THE UNIVERSITY *of* ADELAIDE

Investigation of Higgs Portal Dark Matter Models

From Collider, Indirect and Direct Searches to Electroweak Baryogenesis

Ankit Beniwal

PRINCIPAL SUPERVISOR: Dr. Martin J. White

CO-SUPERVISOR: Prof. Anthony G. Williams

A dissertation submitted towards the degree in

Doctor of Philosophy

Department of Physics

School of Physical Sciences

University of Adelaide

July 2018

To my loving parents and sister.

Declaration

I certify that this work contains no material which has been accepted for the award of any other degree or diploma in my name, in any university or other tertiary institution and, to the best of my knowledge and belief, contains no material previously published or written by another person, except where due reference has been made in the text. In addition, I certify that no part of this work will, in the future, be used in a submission in my name, for any other degree or diploma in any university or other tertiary institution without the prior approval of the University of Adelaide and where applicable, any partner institution responsible for the joint-award of this degree.

I give permission for the digital version of my thesis to be made available on the web, via the University's digital research repository, the Library Search and also through web search engines, unless permission has been granted by the University to restrict access for a period of time.

Signature   Date ___06/07/2018___

Acknowledgements

First and foremost, I would like to thank my principal supervisor, Dr. Martin J. White, for his support, encouragement and dedication towards my research. You have taught me a lot about the challenges and benefits of undertaking research in physics. I also thank you for getting me into Formula 1. I look forward to a competitive F1 championship fight this year. I also thank my co-supervisor, Prof. Anthony G. Williams, for sharing his experience in the field and providing guidance during my PhD candidature. More importantly, I have learned to make clear plans and present my ideas in a pedagogical manner.

I acknowledge the support received from the Centre of Excellence in Particle Physics (CoEPP) at the University of Adelaide. In particular, I would like to thank S. Johnson and S. Santucci for their help in sorting out countless administrative tasks such as arranging my weekly meetings, booking flights, transport and accommodation for interstate as well as international workshops/conferences. I also thank S. Crosby and L. Boland from the Research Computing Team at CoEPP for answering my queries and allocating computer resources for my project. Some of the results presented in this thesis would not have been possible without their support.

During the course of my PhD candidature, I had the privilege of working with some of the world-renowned experts in my area of research. In particular, I enjoyed my collaboration with P. Scott, C. Weniger, C. Savage, J. D. Wells and M. Lewicki. I also had the pleasure of meeting other members of the GAMBIT collaboration during my international trip.

I would also like to thank my fellow PhD and master students. It was a great experience to engage in conversations with all of you from time-to-time and share interesting ideas around the office. In particular, our weekly symmetry for students (S4S) meeting is a great way to broaden our horizons and learn new concepts beside our own field of research.

Last but not least, I would like to thank my mum, dad, sister and Timmy for their unconditional love and support. None of this work would have possible without their support.

Abstract

This thesis addresses two limitations of the Standard Model (SM) of particle physics, namely dark matter (DM) and the origin of matter-antimatter asymmetry. Specifically, we study the Higgs portal DM models where the DM-SM interaction proceeds via a SM Higgs boson. Such models lead to a rich DM phenomenology that can be tested at collider, indirect and direct search experiments.

This thesis is composed of three parts. In the first part, we provide a brief background on the SM and follow the road that led to the Higgs boson discovery. We also present evidence for the existence of DM and motivate the observed baryon asymmetry in our universe.

In the second part of this thesis, we present results from a combined analysis of effective scalar, vector, Majorana and Dirac fermion Higgs portal DM models. For the fermion models, we include both CP-even and CP-odd terms. The parameter space of all models is constrained using the DM relic density, limits on the Higgs invisible branching ratio from the Large Hadron Collider (LHC) as well as indirect and direct DM detection experiments. In line with previous studies, we find that direct detection experiments will continue to exclude much of the model parameter space. For the CP-odd case, indirect searches are the only probe for accessing the high mass range of the theory.

We also study the scalar singlet model in light of electroweak baryogenesis (EWBG). By requiring a large scalar-SM Higgs coupling, the model can explain the observed matter-antimatter asymmetry via a strong first-order electroweak phase transition. This has important implications for EWBG that can be tested using collider, gravitational wave (GW) and direct detection signals. We find that the new scalar *cannot* simultaneously account for the observed DM abundance and matter-antimatter asymmetry. However, a large portion of the model parameter space can lead to a sizeable GW signal.

In the third part of this thesis, we focus on global fits. In particular, we perform a global fit of the extended scalar singlet model with a fermionic DM candidate. In this model, the new scalar mixes with the SM Higgs boson, leading to two scalar mediators. By coupling to the new scalar, a Dirac fermion field can play the role of a DM candidate. From our 7-dimensional scans of the model using *only* the EWBG constraint, we find that EWBG is viable in all parts of the model parameter space provided the scalar-fermion DM coupling $g_S \lesssim 5.62$. On the other hand, the combined constraints from the DM relic density, direct detection limit from the PandaX-II experiment, EWBG, electroweak precision observables

and Higgs searches at colliders place an upper limit on some of the model parameters. We also compute the GW spectra of viable points and check their detection prospects at current or future GW experiments.

Lastly, we present preliminary results from global fits of the vector and Dirac fermion Higgs portal DM models using the GAMBIT software. After motivating and outlining the benefits of using GAMBIT for global fits, we perform scans of the model parameter space using the same set of constraints, model parameter ranges, nuclear and astrophysical parameter values as our previous study. For the Dirac fermion model, we allow the scalar-pseudoscalar mixing parameter ξ to vary in our scans. We find that our preliminary results using GAMBIT are in good agreement with those obtained in our previous study. This is used to motivate a future study of these models using the GAMBIT software.

Table of Contents

List of Figures

List of Tables

List of Abbreviations

ATLAS   A Toroidal LHC ApparatuS

BBN   Big Bang Nucleosynthesis

BBO   Big Bang Observer

BSM   Beyond the Standard Model

CMB   Cosmic Microwave Background

CMS   Compact Muon Solenoid

CP   Charge Parity

CPV   Charge Parity Violation

DM   Dark Matter

dSphs   Dwarf Spheroidals

EW   ElectroWeak

EWBG   ElectroWeak BaryoGenesis

EWPO   ElectroWeak Precision Observables

EWPT   ElectroWeak Phase Transition

EWSB   ElectroWeak Symmetry Breaking

Fermi-LAT Fermi Large Area Telescope

GAMBIT   Global And Modular BSM Inference Tool

GW   Gravitational Waves

LEP   Large Electron-Positron

LHC	Large Hadron Collider
LIGO	Laser Interferometer Gravitational-Wave Observatory
LISA	Laser Interferometer Space Antenna
NFW	Navarro-Frenk-White profile
PT	Phase Transition
SD	Spin-Dependent
SI	Spin-Independent
SM	Standard Model
SSB	Spontaneous Symmetry Breaking
UV	UltraViolet
VEV	Vacuum Expectation Value
WIMPs	Weakly Interacting Massive Particles
WMAP	Wilkinson Microwave Anisotropy Probe

Chapter 1

Introduction

In this thesis, we aim to address two limitations of the Standard Model (SM) of particle physics, namely in providing a particle candidate for dark matter (DM) and an explanation for the matter-antimatter asymmetry. It is composed of three parts. In the first part, we present a pedagogical review of the SM (chapter 2), follow the road that led to the Higgs boson discovery (chapter 3), and a review on DM (chapter 4) and electroweak baryogenesis (EWBG) (chapter 5). The remaining two parts are based on the list of papers in Appendix A.

In the second part of this thesis, we study the phenomenology of effective Higgs portal DM models. In these models, the DM-SM interaction proceeds via a SM Higgs boson. In chapter 6, we perform a combined analysis of scalar, vector, Majorana and Dirac fermion Higgs portal models. For the fermion DM models, we include both CP-conserving and CP-violating interactions. We find that the parameter space of all models is constrained by the DM relic density, Higgs invisible decay as well as indirect and direct detection experiments. The CP-violating case is the least constrained scenario as it leads to weak direct detection limits. In general, two allowed regions remain, one near the Higgs resonance $m_X \sim m_h/2$, and another at higher DM masses.

In chapter 7, we test the viability and detection prospects of the scalar singlet model to facilitate EWBG and serve as a DM candidate. By studying the collider, DM and gravitational wave (GW) signals of this scenario, we find that a significant portion of the model parameter space will be accessible at future GW experiments but is beyond the reach of future collider experiments. More importantly, we find that the model *cannot* simultaneously explain the observed DM abundance and facilitate a strong first-order electroweak phase transition (EWPT). This leads to only two allowed regions where EWBG is viable and direct detection limits are small, namely a region close to the Higgs resonance $m_S \sim m_h/2$ and the other at $m_S > 700\,\text{GeV}$. However, all the DM constraints can be avoided by requiring the new scalar S to serve as a mediator between a new DM candidate and SM particles; in this case, the details of the EWPT essentially remains the same. Lastly, we study a scenario with modified cosmological history by employing

a simple model with a new energy content ρ_N that redshifts faster than radiation, i.e., $\rho_N \propto a^{-n}$ where $n > 4$. This modification has significant implications for both EWBG and the observed DM abundance. However, the case of high DM abundance is severely constrained by direct detection experiments. Thus, no new parameter space opens up.

In the third part of this thesis, we focus on global fits. In chapter 8, we perform a comprehensive and up-to-date study of the extended scalar singlet model with a fermionic DM candidate. This model is a generalisation of the scalar Higgs portal model studied in chapter 6. By relaxing the assumed $\mathbb{Z}_2$ symmetry required to ensure the stability of DM particles, the new scalar acquires a non-zero vacuum expectation value (VEV). Due to additional interaction terms, the new scalar mixes with the SM Higgs boson. In this case, the interaction eigenstates are rotated into the physical mass eigenstates (h, H). The model parameter space is constrained using the *Planck* measured DM relic density, direct detection limit from the PandaX-II experiment, EWBG, electroweak precision observables and Higgs searches at colliders.

From our 7-dimensional scans of the model parameter space using *only* the EWBG constraint, we find that the model can facilitate EWBG provided the scalar-fermion DM coupling $g_S \lesssim 5.62$. On the other hand, a strong upper limit on the second scalar mass m_H, the fermion DM mass m_ψ and g_S is obtained from our global fit. We also confirm that the model can explain (at least a part of) the observed DM abundance and baryon asymmetry. From the viable points that satisfy all of the above constraints, the GW spectra from the EWPT are computed. In particular, we find that the GW spectra of viable points are often within reach of future GW experiments such as LISA, DECIGO and BBO. On the other hand, experiments such as LIGO, EPTA and SKA will be immune to such low-frequency GW signals.

In chapter 9, we present preliminary results from a global fit of the vector and Dirac fermion Higgs portal models using the GAMBIT software. After a brief discussion on the key benefits of using GAMBIT for global fits, we present our model results using the same set of parameters used in chapter 6 for a direct comparison. We also extend the analysis of the Dirac fermion model by allowing the scalar-pseudoscalar mixing parameter ξ to vary in our scans. As the phenomenology of these models is strongly dependent on the SM Higgs boson mass m_h (especially near the Higgs resonance), we allow m_h to vary by more than 4σ from its measured value. We find that our preliminary results are in good agreement with the ones presented in chapter 6.

Lastly, we discuss various ways of improving upon the work presented in chapter 6 for the vector and fermion Higgs portal models. We outline the details for performing a more comprehensive study using the GAMBIT software. This includes a combination of results from multiple indirect and direct search experiments, inclusion of the most important nuclear, astrophysical and SM nuisance parameters, and both frequentist and Bayesian analysis (e.g., model comparison, prior sensitivity studies).

Part I

Background

Chapter 2

The Standard Model of Particle Physics

2.1 Introduction

The main goal of particle physics is to identify the fundamental constituents of matter and understand the forces acting on them [34]. From the microscopic details, all other entities can be constructed as composites of the elementary building blocks. This involves a two-fold aspect: matter on the one hand and forces on the other. The underlying assumption is that the smallest units of matter interact in the simplest ways or there is a deep connection between the units of matter and the fundamental forces. This joint matter/force connection is perfectly illustrated in Thomson's discovery of the electron in 1897 and Maxwell's theory of electromagnetism which together marked the birth of modern particle physics.

In the last 100 years or so, the story of particle physics has revolved around the discovery and study of two non-electromagnetic forces, namely the *weak* and *strong* forces. In the latter quarter of the 20th century, particle physicists from all around the world identified a collection of matter units and tested the theories related to the weak and strong forces. These theories incorporated and generalised the original electron/electromagnetic-field relation in an elegant way and formed part of what is known as the Standard Model (SM) of particle physics.

The particle content of the SM is as follows. The matter units are known as *fermions* with spin $s = 1/2$.[1] They come in two types: *leptons* and *quarks*. Both of them appear structureless at the smallest length scales that are currently probed by the highest energy colliders, e.g., the Large Hadron Collider (LHC). The leptons (meaning *light*) come in three generations (electron e^-, muon μ^-, tau τ^-) along with their associated neutrinos (ν_e, ν_μ, ν_τ). If they are electrically charged, they interact via both the electromagnetic and weak force, otherwise they only interact via the weak force. On the other hand, quarks are the fundamental constituents of hadrons (meaning *heavy*). They also come in three generations and are characterised by either being *up-type* (up u, charm c, top t) or *down-*

---

[1]The spin of an elementary particle comes in either integer or half-integer multiples of $\hbar \equiv h/2\pi$ where $h = 6.626 \times 10^{-34}$ J s [3] is the Planck constant.
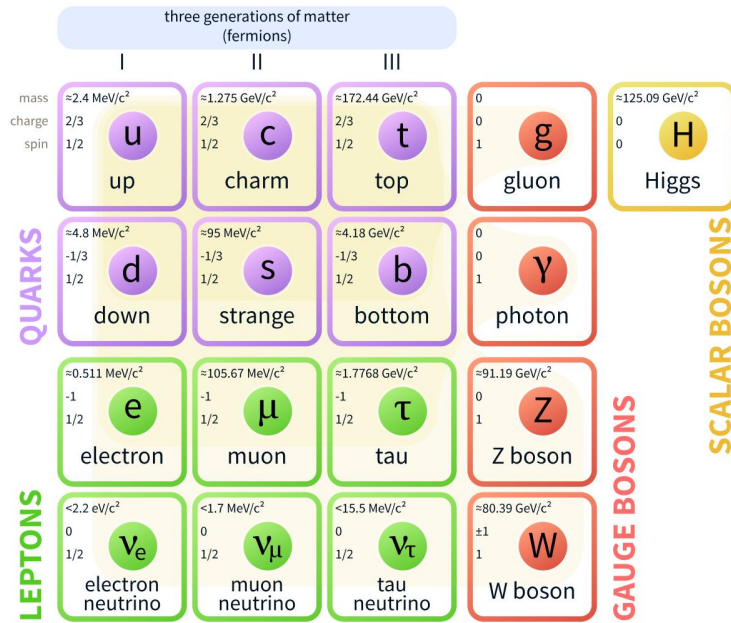
Figure 2.1: Elementary particles of the Standard Model (SM). Figure from Ref. [1].

type (down *d*, strange *s*, bottom *b*) quarks. They interact via the strong, electromagnetic and weak forces. All of the fundamental forces are mediated by an exchange of *bosons* with spin $s = 1$. For instance, a massless photon γ mediates the electromagnetic force, eight massless gluons g_i where $i = 1, \dots, 8$ mediate the strong force and the massive $W^\pm/Z$ bosons mediate the weak force. In addition, the SM also contains a spin-0 particle known as the Higgs boson *h*. It is responsible for giving mass to all of the elementary particles. The full particle content of the SM is shown in Fig. 2.1.

The 1979 Nobel Prize in Physics was collectively awarded to S. Glashow, A. Salam and S. Weinberg for their contributions in unifying the electromagnetic and weak forces into the Electroweak (EW) force. It is a generalisation of the quantum theory of electromagnetism, namely Quantum Electrodynamics (QED) and the quantum theory of the strong force, namely Quantum Chromodynamics (QCD). In the SM, the three quantum field theories (QFTs) are described by *gauge fields*, although each one is realised in a different way.

The SM does not account for the most familiar force, namely gravity. Although all matter objects feel the effects of gravity due to their mass, the resulting effect is many orders of magnitude smaller than the weak force, at least at the length scales relevant to quarks and leptons. Despite the lingering promise of *string theory* and its variants as an attempt to unify quantum mechanics with general relativity (GR) into a quantum theory of gravity, it is fair to say that the vision for unification of all known forces (something that possessed A. Einstein during the later stages of his life) is still a long way away from realisation.

In this chapter, we provide a pedagogical review of the SM based on Refs. [4, 35, 36]. We start by introducing the principle of gauge invariance and describe the theories related

to the electromagnetic, strong and weak forces. We will find that the requirement of a local gauge invariance forbids mass terms for the fermions and gauge bosons. To generate particle masses, we will use the well-known *Higgs mechanism*. In turn, this would lead to the origin of quark mixing in the fermion sector.

2.2 Gauge Invariance

The principle of gauge invariance has played an important role in the development of QFTs in the SM. In simple terms, it specifies a procedure for promoting a global symmetry of a free model Lagrangian density $\mathscr{L}$ into a local one, i.e., dependent on space-time coordinates $x \equiv (t, \boldsymbol{x})$. This is achieved by adding new gauge fields which transform in just the right way to leave $\mathscr{L}$ invariant (or unchanged) under a local gauge transformation. The number of gauge fields required to achieve this always matches with the number of generators of the underlying symmetry group. Once the kinetic terms for the gauge fields are added, interaction terms are generated between the matter and gauge fields. As a result, a quanta of the gauge field (a boson particle) acts as a force carrier and mediates the resulting interaction.

From a theoretical point of view, the SM is a collection of QFTs based on the following local gauge symmetry

$$G_{\text{SM}} \supset SU(3)_C \otimes SU(2)_L \otimes U(1)_Y, \tag{2.1}$$

where $SU(3)_C$ is the gauge symmetry group of the strong interactions and $SU(2)_L \otimes U(1)_Y$ is the gauge symmetry group of the electroweak interactions. The symmetry group $U(1)_{\text{EM}}$ of the electromagnetic interactions is a sub-group of $SU(2)_L \otimes U(1)_Y$. It is in this sense that the electromagnetic and weak forces are unified into the electroweak force.

2.3 Quantum Electrodynamics (QED)

The marriage between Maxwell's theory of electromagnetism and quantum mechanics led to the theory of Quantum Electrodynamics (QED). It is a remarkable theory whose predictions are in excellent agreement with experiments. Being the simplest of the three QFTs in the SM, QED is thus a good starting point.

We start with a physical system that is composed of a free Dirac fermion field ψ with spin $s = 1/2$, mass m and an electric charge Q.[2] The Lagrangian density for a free Dirac fermion field is

$$\mathscr{L}_\psi = \overline{\psi}(i\gamma^\mu \partial_\mu - m)\psi, \tag{2.2}$$

---

[2]From here onwards, the electric charge Q will be expressed in units of a proton charge. Thus, a proton has an electric charge of $+Qe$ where $Q = +1$ and $e = 1.602 \times 10^{-19}$ C [3].

where $\psi \equiv \psi(x)$, $\overline{\psi} \equiv \psi^\dagger \gamma^0$ are the 4-component spinors and γ^μ are the 4×4 gamma matrices. Note that Eq. (2.2) is invariant under the following global $U(1)_Q$ transformation

$$\psi \rightarrow \psi' = e^{-iQ\alpha}\psi, \tag{2.3}$$

where $Q\alpha$ is a global phase and α is a real, space-time independent parameter. This can be easily checked as the terms in Eq. (2.2) transform as

$$\overline{\psi} \rightarrow \overline{\psi}' = (\psi')^\dagger \gamma_0 = \left(e^{-iQ\alpha}\psi\right)^\dagger \gamma_0 = \overline{\psi}e^{iQ\alpha}, \quad \partial_\mu\psi \rightarrow \partial_\mu\psi' = e^{-iQ\alpha}\partial_\mu\psi.$$

To promote the global $U(1)_Q$ symmetry of Eq. (2.2) into a local one, we require the parameter α to depend on the space-time coordinates, i.e., $\alpha \rightarrow \alpha(x)$. In this case, a local $U(1)_Q$ transformation corresponds to

$$\psi \rightarrow \psi' = e^{-iQ\alpha(x)}\psi. \tag{2.4}$$

Under this transformation, the Dirac fermion field ψ and its derivative transforms as

$$\overline{\psi} \rightarrow \overline{\psi}' = \overline{\psi}e^{iQ\alpha(x)}, \quad \partial_\mu\psi \rightarrow \partial_\mu\psi' = e^{-iQ\alpha(x)}\left[\partial_\mu\psi - iQ\psi\partial_\mu\alpha(x)\right]. \tag{2.5}$$

Due to the term $\partial_\mu\alpha(x)$, Eq. (2.2) is not invariant under Eq. (2.4). This is exactly where the principal of gauge invariance comes into play. In particular, we can add a gauge (photon) field A_μ which transform under Eq. (2.4) as

$$A_\mu \rightarrow A'_\mu = A_\mu + \partial_\mu\alpha(x). \tag{2.6}$$

In general, the most economical way of building a local gauge invariant Lagrangian is to replace the normal derivative ∂_μ with a covariant derivative $\mathcal{D}_\mu$. This is known as the method of *minimal substitution*. In the present case, the covariant derivative is defined as

$$\mathcal{D}_\mu \equiv \partial_\mu + iQA_\mu. \tag{2.7}$$

After replacing ∂_μ with $\mathcal{D}_\mu$ in Eq. (2.2), we find that

$$\begin{aligned}
\mathcal{D}_\mu\psi \rightarrow \mathcal{D}'_\mu\psi' &= (\partial_\mu + iQA'_\mu)\psi' \\
&= e^{-iQ\alpha(x)}\left[\partial_\mu\psi - iQ\psi\partial_\mu\alpha(x)\right] + iQ\left[A_\mu + \partial_\mu\alpha(x)\right]e^{-iQ\alpha(x)}\psi \\
&= e^{-iQ\alpha(x)}(\partial_\mu + iQA_\mu)\psi \\
&= e^{-iQ\alpha(x)}\mathcal{D}_\mu\psi.
\end{aligned}$$

Thus, $\mathcal{D}_\mu\psi$ transforms like ψ under Eq. (2.4). Furthermore, the terms in Eq. (2.2) with $\partial_\mu \rightarrow \mathcal{D}_\mu$ transform as

$$\begin{aligned}
\overline{\psi}i\gamma^\mu\mathcal{D}_\mu\psi &\rightarrow \overline{\psi}'i\gamma^\mu\mathcal{D}'_\mu\psi' = \overline{\psi}e^{iQ\alpha(x)}i\gamma^\mu e^{-iQ\alpha(x)}\mathcal{D}_\mu\psi = \overline{\psi}i\gamma^\mu\mathcal{D}_\mu\psi, \\
m\overline{\psi}\psi &\rightarrow m\overline{\psi}'\psi' = m\overline{\psi}e^{iQ\alpha(x)}e^{-iQ\alpha(x)}\psi = m\overline{\psi}\psi.
\end{aligned}$$
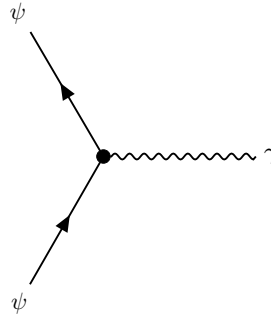
Figure 2.2: Feynman diagram for an interaction between a photon and two fermion fields.

To describe the dynamics of a photon field A_μ, its kinetic term must be included. A gauge invariant combination is given by

$$\mathscr{L}_\gamma = -\frac{1}{4} F_{\mu\nu} F^{\mu\nu}, \tag{2.8}$$

where $F_{\mu\nu} = \partial_\mu A_\nu - \partial_\nu A_\mu$ is the electromagnetic-field strength tensor. Thus, we can write down the QED Lagrangian as

$$\mathscr{L}_{\text{QED}} = \overline{\psi}(i\gamma^\mu \mathcal{D}_\mu - m)\psi - \frac{1}{4} F_{\mu\nu} F^{\mu\nu}. \tag{2.9}$$

This is invariant under both the Lorentz and local $U(1)_Q$ transformations. By comparing the QED Lagrangian against the one in Eq. (2.2), we find that

$$\mathscr{L}_\psi \rightarrow \mathscr{L}_{\text{QED}} = \mathscr{L}_\psi + \mathscr{L}_\gamma + \mathscr{L}_{\text{int}}, \tag{2.10}$$

where

$$\mathscr{L}_{\text{int}} = -Q\overline{\psi}\gamma^\mu A_\mu \psi. \tag{2.11}$$

This term describes an interaction between a photon and two fermion fields. A Feynman diagram for this interaction is shown in Fig. 2.2.

According to the Noether's theorem [37], for every continuous symmetry of $\mathscr{L}$, there is an associated conserved current $J^\mu(x)$ such that $\partial_\mu J^\mu(x) = 0$. In the present case, the invariance of $\mathscr{L}_{\text{QED}}$ under a local $U(1)_Q$ transformation implies that the conserved 4-vector current is

$$J_{\text{EM}}^\mu = Q\overline{\psi}\gamma^\mu \psi, \tag{2.12}$$

whereas the conserved electric charge (or generator) is

$$Q = \int d^3x \, J_{\text{EM}}^0(x). \tag{2.13}$$

Thus, the interaction Lagrangian in Eq. (2.11) can be written as

$$\mathscr{L}_{\text{int}} = -Q\overline{\psi}\gamma^\mu A_\mu \psi = -J_{\text{EM}}^\mu A_\mu. \tag{2.14}$$

An important implication of a local $U(1)_Q$ invariance of the QED Lagrangian is that a mass term for the photon field is not allowed. Under a local $U(1)_Q$ transformation, such a term would break gauge invariance as

$$\frac{1}{2}m_\gamma^2 A_\mu A^\mu \rightarrow \frac{1}{2}m_\gamma^2 A'_\mu (A^\mu)' = \frac{1}{2}m_\gamma^2 \Big(A_\mu + \partial_\mu \alpha(x)\Big)\Big(A^\mu + \partial^\mu \alpha(x)\Big) \neq \frac{1}{2}m_\gamma^2 A_\mu A^\mu.$$

This might sound strange as the photon is a massless particle. However, the same argument holds for the $W^\pm$ and Z bosons in the electroweak theory where they are *known* to be massive. Thus, a new mechanism is required to generate the gauge boson masses in a gauge invariant manner. This is of-course the well-known Higgs mechanism.

2.4   Quantum Chromodynamics (QCD)

The quantum theory of strong interactions is known as Quantum Chromodynamics (QCD). Just like QED, it has successfully passed many experimental tests. It is based on a local *colour* transformation. The associated gauge symmetry group is the non-Abelian Lie group $SU(3)_C$ where C stands for colour. The $SU(3)_C$ group contains 8 gluon fields corresponding to the 8 generators of the $SU(3)_C$ group.

The construction of a local $SU(3)_C$ invariant QCD Lagrangian is similar to the QED case. Once again, we start with the principle of gauge invariance and make the minimal substitution $\partial_\mu \rightarrow \mathcal{D}_\mu$. However, in contrast to the QED case, the $SU(3)_C$ group is non-Abelian.[3] As a result, the covariant derivative for the $SU(3)_C$ group is defined as

$$\mathcal{D}_\mu \equiv \partial_\mu - igt_a G_\mu^a, \tag{2.15}$$

where G_μ^a for $a = 1, \ldots, 8$ are the 8 gluon fields, $\alpha_s \equiv g^2/4\pi$ is the strong coupling constant and $t_a \equiv \lambda_a/2$ are the 8 generators of the $SU(3)_C$ group. The λ_a's are a set of linearly independent 3×3 Gell-Mann matrices.

After adding the kinetic terms for the 8 gluon fields, we can write down a local $SU(3)_C$ invariant QCD Lagrangian as

$$\mathscr{L}_{\text{QCD}} = \sum_f \overline{q}_f (i\gamma^\mu \mathcal{D}_\mu - m_f) q_f - \frac{1}{4} G_{\mu\nu}^a G_a^{\mu\nu}, \tag{2.16}$$

where the sum runs over the 6 quark types (or *flavours*). The non-Abelian field strength tensor is given by

$$G_{\mu\nu}^a = \partial_\mu G_\nu^a - \partial_\nu G_\mu^a + g f^{abc} G_\mu^b G_\nu^c, \tag{2.17}$$

where f^{abc} for $a, b, c = 1, \ldots, 8$ are the structure constants of the $SU(3)_C$ group. They are related to the group generators t_a by

$$[t_a, t_b] \equiv t_a t_b - t_b t_a = i f^{abc} t_c. \tag{2.18}$$

---

[3]In group theory, this corresponds to non-commuting generators of the group, i.e., if A and B are the two generators of such a group, then $[A, B] \equiv AB - BA \neq 0$. In QED, there is only 1 generator, namely the electric charge Q which commutes with itself, thus $U(1)_Q$ is an Abelian group.
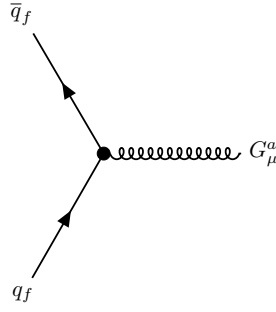
Figure 2.3: Feynman diagram for an interaction between a gluon and two quark fields.
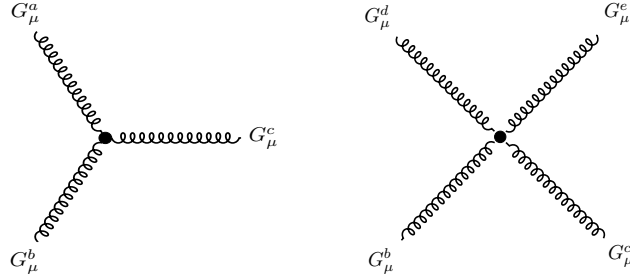
Figure 2.4: Feynman diagrams for the self-interaction of three (*left*) and four (*right*) gluon fields.

The replacement $\partial_\mu \to \mathcal{D}_\mu$ in Eq. (2.16) also generates the following interaction term

$$\mathcal{L}_{\text{int}} = g \sum_f \overline{q}_f \gamma^\mu t_a G_\mu^a q_f. \tag{2.19}$$

This term describes an interaction between a gluon and two quark fields. A Feynman diagram for this interaction is shown in Fig. 2.3.

It is interesting to expand out the kinetic term for the gluon fields as

$$-\frac{1}{4} G_{\mu\nu}^a G_a^{\mu\nu} = \frac{1}{4}(\partial_\mu G_\nu^a - \partial_\nu G_\mu^a)^2 - g f^{abc} \partial^\mu G_a^\nu G_\mu^b G_\nu^c - \frac{1}{4} g^2 f^{abc} f^{ade} G_b^\mu G_c^\nu G_\mu^d G_\nu^e.$$

The first term is analogous to a kinetic term for the photon field A_μ, although for 8 gluon fields. However, the second and third terms arise as a consequence of the non-Abelian nature of the $SU(3)_C$ group. They describe the self-interaction of three and four gluon fields respectively. A Feynman diagram for this interaction is shown in Fig. 2.4. This makes QCD much more interesting and phenomenologically challenging than QED.

2.5   The Electroweak (EW) theory

The Electroweak (EW) theory provides a unified description of the electromagnetic and weak interactions. It is also known as the Glashow-Weinberg-Salam (GWS) theory.

The gauge group for the EW theory is a direct product of two groups

$$G_{\text{EW}} = SU(2)_L \otimes U(1)_Y, \tag{2.20}$$
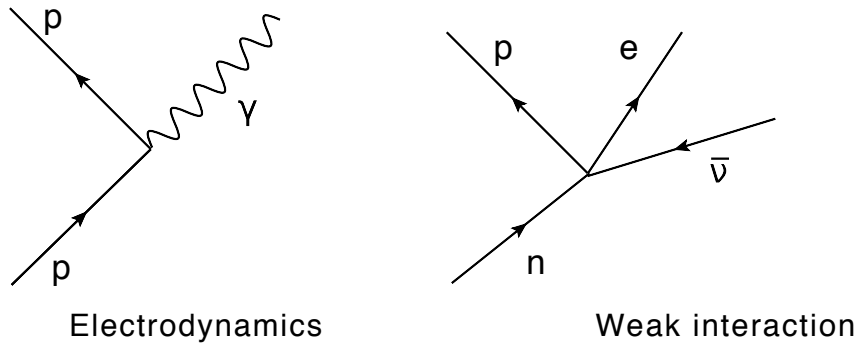
Figure 2.5: Fermi's analogy of the neutron β-decay (*right*) with the photon-proton interaction (*left*). Figure from Ref. [38].

where $SU(2)_L$ acts on the weak isospin T and $U(1)_Y$ acts on the weak hypercharge Y. For the direct product representation in Eq. (2.20), we can write down a covariant derivative that acts on a matter field with weak isospin $1/2$ and weak hypercharge Y as

$$\mathcal{D}_\mu \equiv \partial_\mu + ig\frac{1}{2}\tau_a W_\mu^a + ig'\frac{1}{2}YB_\mu, \tag{2.21}$$

where τ_a are the 2×2 Pauli spin matrices, W_μ^a and B_μ are the gauge fields of the $SU(2)_L$ and $U(1)_Y$ group respectively. The parameters g and g' are two independent couplings of the EW theory.

Before writing down the EW Lagrangian, we take a step back and motivate the need for unification of the electromagnetic and weak forces.

2.5.1 The Fermi theory of weak interactions

The first QFT of weak interactions was proposed by E. Fermi in 1934 to describe the nuclear β-decays [38]. Nowadays, it provides a low-energy effective field theory (EFT) description of the full EW theory.

At the quantum level, the electromagnetic interaction between two protons occur via a photon exchange. By drawing an analogy from this process, Fermi pictured the β-decay of a neutron as a production of a proton and an electron-neutrino pair. This is shown in Fig. 2.5.

In Fermi's theory of weak interactions, the interaction Lagrangian for a neutron β-decay is

$$\mathcal{L}_F = \frac{G_F}{\sqrt{2}} \left(\bar{p}n\,\bar{e}\nu + \bar{n}p\,\bar{\nu}e \right), \tag{2.22}$$

where the particle symbols p, n, e and ν represent the corresponding field operators. The strength of the weak interaction is characterised by the dimensionful Fermi coupling [3]

$$G_F = 1.1663787 \times 10^{-5}\,\text{GeV}^{-2}. \tag{2.23}$$
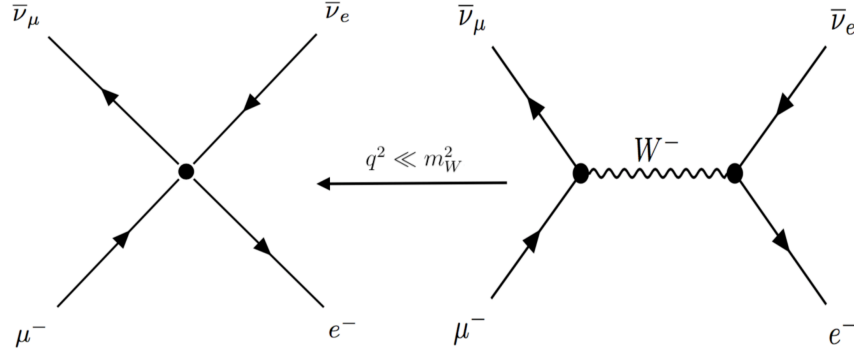
Figure 2.6: Feynman diagram for the process $\overline{\nu}_\mu + \mu^- \rightarrow \overline{\nu}_e + e^-$ in the Fermi (*left*) and electroweak (*right*) theory.

Due to the smallness of the Fermi coupling, the weak interactions are considered as *weak*. The two terms in Eq. (2.22) lead to a neutron and proton decay as

$$n \rightarrow p + e^- + \overline{\nu}_e, \quad p \rightarrow n + e^+ + \nu_e. \tag{2.24}$$

Although, protons do not decay in free space as they are lighter than neutrons, such decays can occur when nuclei are involved. These two processes describe all nuclear β-decays.

The Fermi theory stood the test of time despite many amendments which were successfully incorporated into the theory. However, it was later realised that it could not be the full theory. Thus, it had to be ultraviolet (UV) completed. This can be illustrated by considering the following muon-neutrino interaction

$$\overline{\nu}_\mu + \mu^- \rightarrow \overline{\nu}_e + e^-. \tag{2.25}$$

In the Fermi theory, this process is described by a four-point contact interaction as shown in the left panel of Fig. 2.6. The scattering cross-section has the following form

$$\sigma \propto G_F^2 E^2, \tag{2.26}$$

where G_F is the Fermi coupling and E is the centre-of-mass (c.o.m.) energy. Clearly, the cross-section grows with the interaction energy, i.e., the theory is ultraviolet divergent. However, from the partial wave analysis, the total cross-section is [39]

$$\sigma = \int \frac{d\sigma}{d\Omega} d\Omega = \frac{4\pi}{k^2} \sum_{l=0}^{\infty} (2l + 1) \sin^2 \delta_l, \tag{2.27}$$

where k is the c.o.m. momentum, δ_l is the scattering phase shift and l is the corresponding angular momentum. As $\sin^2 \delta_l \leq 1$, we get

$$\sigma \leq \frac{4\pi}{k^2}(2l + 1) \tag{2.28}$$

for any given value of l. Thus, the scattering cross-section is expected to decrease with the c.o.m. momentum/energy. This statement is in contradiction with Eq. (2.26). Thus, the Fermi theory violates unitarity.

The unitarity violation in weak interactions can be removed by introducing the $W^{\pm}/Z$ bosons. This equates to a UV-completion of the Fermi theory by the electroweak theory. As a result, the process in Eq. (2.25) can be described by an exchange of a W^- boson. This process is shown in the right panel of Fig. 2.6.

2.5.2 Parity violation and $V - A$ currents

The laws of physics were originally thought to be the same under a parity transformation

$$t \rightarrow t' = t, \quad x \rightarrow x' = -x, \quad y \rightarrow y' = -y, \quad z \rightarrow z' = -z. \tag{2.29}$$

It was known that parity conservation holds in classical Newtonian gravity, electromagnetism and strong interactions. However, in 1956, T. D. Lee and C. N. Yang suggested that weak interactions might violate parity. They subsequently suggested experiments where parity violation could be tested in the weak interactions. This lead C. S. Wu and her collaborators to conduct a famous experiment using cooled ^{60}Co atoms [40].

The experimental setup used by C. S. Wu was as follows. The ^{60}Co atoms were cooled down to 0.01 K such that the interaction between the magnetic moments of the nuclei and the magnetic field could overcome the tendency to thermal disorder. The nuclear spins were aligned parallel to the direction of the magnetic field. The polarised ^{60}Co atoms decay to an excited state of ^{60}Ni via the following β-decay process

$$^{60}\text{Co} \longrightarrow {}^{60}\text{Ni}^* + e^- + \overline{\nu}_e. \tag{2.30}$$

In the weak interactions, parity violation was established by observing a forward-backward decay asymmetry, i.e., fewer electrons were emitted in the forward hemisphere than in the backward hemisphere with respect to the spin of the decaying nuclei. This is illustrated in Fig. 2.7. Under a parity transformation, particle's momenta $\boldsymbol{p}$ is reversed, whereas its orbital angular momenta $\boldsymbol{L} = \boldsymbol{r} \times \boldsymbol{p}$ (and by analogy, their spin angular momenta $\boldsymbol{S}$) remains the same. In the rest frame of the decaying nuclei, the effect would be a reversal of the electron's velocity while leaving the nuclear spins unchanged. Parity invariance would require the rates of the two processes to be equal, i.e., an equal number of electrons emitted in the forward and backward hemispheres with respect to the nuclear spins. This was in contradiction with what was observed. In fact, the effect was so large that the parity was said to be *maximally violated*.

The fact that weak interactions violated parity meant that a new Lagrangian was required for the EW theory. The QED and QCD currents are both vector-like ($\propto \overline{\psi} \gamma_\mu \psi$) which conserve parity. Thus, a linear combination of the vector (V) and axial-vector (A) current was required. Experimentally, the form of the parity-violating current was fixed to be $V - A$. Thus, the EW Lagrangian contains a product of the form $\gamma_\mu(1 - \gamma_5)$.

To unify the weak and electromagnetic forces, their currents must be of the same form. Due to the $V - A$ nature of the weak current, the matrix $1 - \gamma_5$ can be absorbed into the
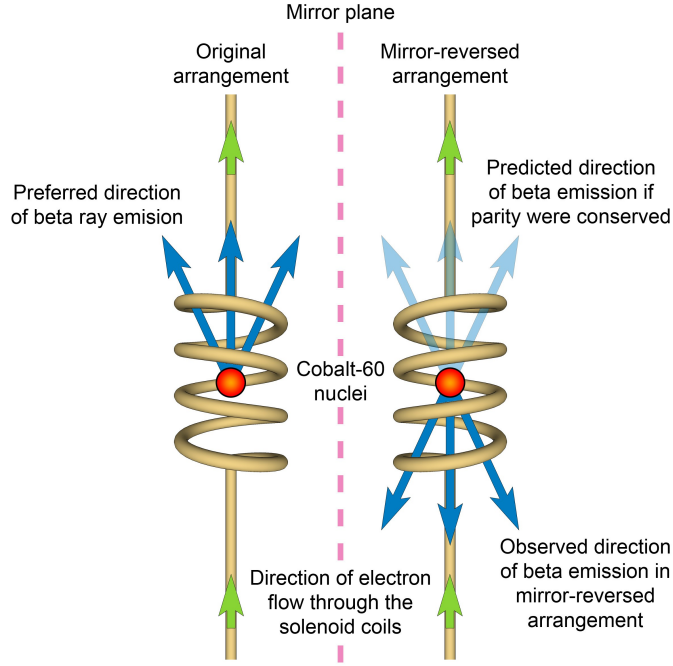
Figure 2.7: Effect of parity transformation on the β-decay of ^{60}Co atoms. Figure from Ref. [2].

definition of the Dirac fermion spinors. The action of the matrix $1 - \gamma_5$ on a Dirac spinor ψ is to split it into its left- and right-handed chiral modes. For massless particles, chirality is the same as helicity.[4]

We can define two projection operators which project out the left- and right-handed components of a Dirac spinor as

$$\mathcal{P}_\pm = \frac{1 \pm \gamma^5}{2}. \tag{2.31}$$

Thus, we can write

$$\psi = \psi_L + \psi_R = (\mathcal{P}_- + \mathcal{P}_+)\psi, \quad \overline{\psi} = \overline{\psi}_L + \overline{\psi}_R = \overline{\psi}(\mathcal{P}_+ + \mathcal{P}_-). \tag{2.32}$$

Using the properties of the γ_5 matrix, one can easily check that the projection operators satisfy the following relations

$$\mathcal{P}_\pm^2 = \mathcal{P}_\pm, \quad \mathcal{P}_+\mathcal{P}_- = 0, \quad \mathcal{P}_\pm^\dagger = \mathcal{P}_\pm. \tag{2.33}$$

Using the above relations, we can see that the vector current $\overline{\psi}\gamma_\mu\psi$ preserves chirality. On the other hand, the mass term $m\overline{\psi}\psi$ mixes states of different chirality as

$$m\overline{\psi}\psi = m\overline{\psi}(\mathcal{P}_+ + \mathcal{P}_-)(\mathcal{P}_- + \mathcal{P}_+)\psi = m\overline{\psi}(\mathcal{P}_+\mathcal{P}_+ + \mathcal{P}_-\mathcal{P}_-)\psi = m(\overline{\psi}_L\psi_R + \overline{\psi}_R\psi_L).$$

By absorbing the $(1 - \gamma^5)/2$ term into the definition of a Dirac fermion spinor, the weak currents look like vector currents but *only* involving left-handed particles. In contrast, QED involves both left- and right-handed particles.

---

[4]Helicity refers to the projection of a particle spin s along its momentum p. A left- (right-)handed helicity state has its spin aligned opposite (parallel) to the direction of motion.

2.5.3 Weak isospin and hypercharge

In complete analogy with a proton p and neutron n which forms a 2-component isospin I eigenstate of a nucleon, we can construct weak $SU(2)_L$ doublets that contain left-handed spinor fields as

$$\begin{pmatrix} \nu_e \\ e \end{pmatrix}_L, \quad \begin{pmatrix} u \\ d \end{pmatrix}_L. \tag{2.34}$$

Using this construction, the weak $SU(2)_L$ current can be written as

$$J_i^\mu = \frac{1}{2} \begin{pmatrix} \bar\nu_e & \bar e \end{pmatrix}_L \gamma^\mu \tau_i \begin{pmatrix} \nu_e \\ e \end{pmatrix}_L, \tag{2.35}$$

where τ's are the Pauli spin matrices. The third current ($i = 3$) is known as the *neutral current* since it does not change the charge of the particles involved in the interaction. It is given by

$$J_3^\mu = \frac{1}{2} \begin{pmatrix} \bar\nu_e & \bar e \end{pmatrix}_L \gamma^\mu \tau_3 \begin{pmatrix} \nu_e \\ e \end{pmatrix}_L. \tag{2.36}$$

On the other hand, the electromagnetic current for an electron e is

$$J_{\text{EM}}^\mu = Q\bar e \gamma^\mu e = Q(\bar e_L \gamma^\mu e_L + \bar e_R \gamma^\mu e_R), \tag{2.37}$$

where Q is the electromagnetic charge operator. As mentioned earlier, J_{EM}^μ is invariant under local $U(1)_Q$ transformations. However, it is not invariant under local $SU(2)_L$ transformations. This is so because Eq. (2.37) contains e_L instead of the $SU(2)_L$ doublet. To solve this problem, we can construct an $SU(2)_L$ invariant $U(1)_Y$ current as

$$J_Y^\mu = Y_L \begin{pmatrix} \bar\nu_e & \bar e \end{pmatrix}_L \gamma^\mu \begin{pmatrix} \nu_e \\ e \end{pmatrix}_L + Y_R \bar e_R \gamma^\mu e_R, \tag{2.38}$$

where the *hypercharges* Y_L and Y_R are the conserved charge operators associated with the $U(1)_Y$ symmetry. The crucial point here is that the hypercharges differ for the left- and right-handed fields.

By inspection, we can see that the current J_Y^μ is some linear combination of the weak neutral and electromagnetic currents in Eqs. (2.36) and (2.37) respectively. This implies that the hypercharge Y is related to the electromagnetic charge Q and the third component of the weak isospin T_3. We can obtain the exact relation by writing J_{EM}^μ as a linear combination of J_3^μ and $J_Y^\mu/2$.[5] Noting that the third Pauli spin matrix τ_3 is

$$\tau_3 = \begin{pmatrix} 1 & 0 \\ 0 & -1 \end{pmatrix},$$

---

[5] The factor of $1/2$ is included by convention.

	T	T_3	Q	Y
U_L	1/2	1/2	2/3	1/3
D_L	1/2	−1/2	−1/3	1/3
U_R	0	0	2/3	4/3
D_R	0	0	−1/3	−2/3
$(\nu_l)_L$	1/2	1/2	0	−1
l_L^-	1/2	−1/2	−1	−1
$(\nu_l)_R$	0	0	0	0
l_R^-	0	0	−1	−2

Table 2.1: Weak quantum numbers of quarks and leptons. Here $U \in (u, c, t)$, $D \in (d, s, b)$ and $l \in (e, \mu, \tau)$.

the electromagnetic current is

$$Q\bar{e}_L\gamma^\mu e_L + Q\bar{e}_R\gamma^\mu e_R = \frac{1}{2}(\bar{\nu}_e)_L\gamma^\mu(\nu_e)_L - \frac{1}{2}\bar{e}_L\gamma^\mu e_L + \frac{1}{2}Y_R\,\bar{e}_R\gamma^\mu e_R + \frac{1}{2}Y_L\left(\begin{array}{cc}\bar{\nu}_e & \bar{e}\end{array}\right)_L\gamma^\mu\left(\begin{array}{c}\nu_e \\ e\end{array}\right)_L.$$

By matching the coefficient of like terms on both sides, we find that

$$Y_R = 2Q, \quad Y_L = 2Q + 1. \tag{2.39}$$

For the left- and right-handed fields, the third component of the weak isospin is

$$T_3(e_R) = 0, \quad T_3((\nu_e)_L) = +1/2, \quad T_3(e_L) = -1/2.$$

Using the above results, we arrive at the following relation

$$Y = 2(Q - T_3). \tag{2.40}$$

Using this relation, we can compute the weak quantum numbers of quarks and leptons. The result is summarised in Table 2.1.

2.5.4 The Electroweak Lagrangian

We start by defining the $SU(2)_L$ doublets containing the left-handed fields as

$$L_L = \begin{pmatrix}\nu_l \\ l\end{pmatrix}_L, \quad Q_L = \begin{pmatrix}U \\ D\end{pmatrix}_L, \tag{2.41}$$

where $l = (e, \mu, \tau)$, $U = (u, c, t)$ and $D = (d, s, b)$. After including the kinetic terms for the gauge fields, the EW Lagrangian can be written as

$$\mathscr{L}_{\text{EW}} = \sum_{l=e,\mu,\tau} \bar{L}_L i\gamma^\mu \mathcal{D}_\mu L_L + \bar{l}_R i\gamma^\mu \mathcal{D}_\mu l_R + (\bar{\nu}_l)_R i\gamma^\mu \mathcal{D}_\mu (\nu_l)_R - \frac{1}{4}W_{\mu\nu}W^{\mu\nu}$$

$$+ \sum_{\substack{D=d,s,b \\ U=u,c,t}} \bar{Q}_L i\gamma^\mu \mathcal{D}_\mu Q_L + \bar{U}_R i\gamma^\mu \mathcal{D}_\mu U_R + \bar{D}_R i\gamma^\mu \mathcal{D}_\mu D_R - \frac{1}{4}B_{\mu\nu}B^{\mu\nu}, \tag{2.42}$$

where

$$W_{\mu\nu} = \partial_\mu W_\nu - \partial_\nu W_\mu - ig\left[W_\mu, W_\nu\right], \quad B_{\mu\nu} = \partial_\mu B_\nu - \partial_\nu B_\mu, \tag{2.43}$$

are the $SU(2)_L$ and $U(1)_Y$ field strength tensors respectively.

In analogy with QED, a mass term for the gauge fields is forbidden by the local $SU(2)_L \otimes U(1)_Y$ invariance of Eq. (2.42). However, it is known that the mediators of the weak force, namely the $W^\pm$ and Z bosons, are massive. Thus, a new mechanism is required to generate the gauge boson masses in a gauge invariant way. In the SM, this is achieved by the well-known *Higgs mechanism*.

The Higgs mechanism relies on the concept of spontaneous symmetry breaking (SSB) as discussed in Appendix B. In the SM, the EW symmetry is broken when a scalar field acquires a non-zero vacuum expectation value (VEV). Once a vacuum state is chosen and the matter fields are expanded around the VEV, the vacuum state no longer respects the symmetries of the original Lagrangian. This way of obtaining an asymmetric ground state from a Lagrangian that respects a local gauge symmetry is the reason why the symmetry is broken *spontaneously*. As a result, the physical particle spectrum not only contains the massive gauge bosons and fermions but also a Higgs boson particle, a quantum of the Higgs field.

2.6   The Higgs mechanism

The Higgs mechanism was developed in 1964 by three independent groups: R. Brout and F. Englert [41]; P. Higgs [42–44]; and G. Guralnik, C. R. Hagen and T. Kibble [45, 46].

To break the local $SU(2)_L \otimes U(1)_Y$ gauge symmetry of the EW Lagrangian, we follow the ingredients of the Higgs mechanism [4].

1. Add an isospin Higgs doublet

$$\Phi = \begin{pmatrix} \phi_+ \\ \phi_0 \end{pmatrix} = \frac{1}{\sqrt{2}} \begin{pmatrix} \chi_1 + i\chi_2 \\ \phi + i\chi_3 \end{pmatrix}. \tag{2.44}$$

   To retain all the symmetries of the Lagrangian, we can only add $SU(2)_L \otimes U(1)_Y$ multiplets. Here we have added a left-handed doublet with a weak isospin $T = 1/2$. The electrical charges of the upper and lower components are chosen to ensure that the hypercharge Y is equal to $+1$. The weak quantum numbers for the components of the Higgs doublet are summarised in Table 2.2.

2. Add a potential $V(\Phi)$ for the scalar field which spontaneously breaks the $SU(2)_L \otimes U(1)_Y$ symmetry

$$V(\Phi) = \mu^2 \Phi^\dagger \Phi + \lambda(\Phi^\dagger \Phi)^2, \tag{2.45}$$

   where $\mu^2 < 0$ and $\lambda > 0$. The part of the Lagrangian involving the scalar field is

$$\mathcal{L}_{\text{scalar}} = (\mathcal{D}_\mu \Phi)^\dagger (\mathcal{D}^\mu \Phi) - V(\Phi^\dagger, \Phi), \tag{2.46}$$

	T	T_3	Q	Y
ϕ_+	$1/2$	$1/2$	1	1
ϕ_0	$1/2$	$-1/2$	1	0

Table 2.2: Weak quantum numbers for the components of the Higgs doublet.

where

$$\mathcal{D}_\mu \equiv \partial_\mu + ig\frac{1}{2}\tau_a W_\mu^a + ig'\frac{1}{2}Y B_\mu \tag{2.47}$$

is the covariant derivative for the $SU(2)_L \otimes U(1)_Y$ gauge group.

3. Choose a vacuum configuration. Any choice for the vacuum state that breaks the symmetry will generate a mass term for the corresponding gauge boson of the underlying symmetry group. In the present case, we choose the vacuum configuration in the *unitary gauge* as

$$\Phi = \Phi_0 = \frac{1}{\sqrt{2}}\begin{pmatrix} 0 \\ v + h \end{pmatrix}, \tag{2.48}$$

where h is the physical SM Higgs field. The above configuration is electrically neutral as $T = 1/2$, $T_3 = -1/2$ and with $Y = +1$, Eq. (2.40) gives $Q = 0$.

It is easy to check that the vacuum state in Eq. (2.48) breaks the $SU(2)_L \otimes U(1)_Y$ symmetry while leaving the $U(1)_{\text{EM}}$ symmetry unbroken. By invariance, we mean

$$e^{i\alpha Z}\Phi_0 = \Phi_0,$$

where Z is the associated rotation. Under infinitesimal rotations, we get

$$(1 + i\alpha Z)\Phi_0 = \Phi_0 \implies Z\Phi_0 = 0.$$

For the $SU(2)_L$ and $U(1)_Y$ groups, this condition gives

$$SU(2)_L : \quad \tau_1\Phi_0 = \begin{pmatrix} 0 & 1 \\ 1 & 0 \end{pmatrix}\frac{1}{\sqrt{2}}\begin{pmatrix} 0 \\ v + h \end{pmatrix} = \frac{1}{\sqrt{2}}\begin{pmatrix} v + h \\ 0 \end{pmatrix} \neq 0,$$

$$\tau_2\Phi_0 = \begin{pmatrix} 0 & -i \\ i & 0 \end{pmatrix}\frac{1}{\sqrt{2}}\begin{pmatrix} 0 \\ v + h \end{pmatrix} = -\frac{i}{\sqrt{2}}\begin{pmatrix} v + h \\ 0 \end{pmatrix} \neq 0,$$

$$\tau_3\Phi_0 = \begin{pmatrix} 1 & 0 \\ 0 & -1 \end{pmatrix}\frac{1}{\sqrt{2}}\begin{pmatrix} 0 \\ v + h \end{pmatrix} = -\frac{1}{\sqrt{2}}\begin{pmatrix} 0 \\ v + h \end{pmatrix} \neq 0,$$

$$U(1)_Y : \quad Y\Phi_0 = Y_{\Phi_0}\frac{1}{\sqrt{2}}\begin{pmatrix} 0 \\ v + h \end{pmatrix} = +\frac{1}{\sqrt{2}}\begin{pmatrix} 0 \\ v + h \end{pmatrix} \neq 0.$$

Thus, all 4 gauge bosons (W_μ^1, W_μ^2, W_μ^3, B_μ) acquire mass via the Higgs mechanism. The W_μ^1 and W_μ^2 fields mix with each other to form the charged W_μ^+ and W_μ^- bosons, whereas the W_μ^3 and B_μ fields mix to form the neutral Z boson and photon γ.
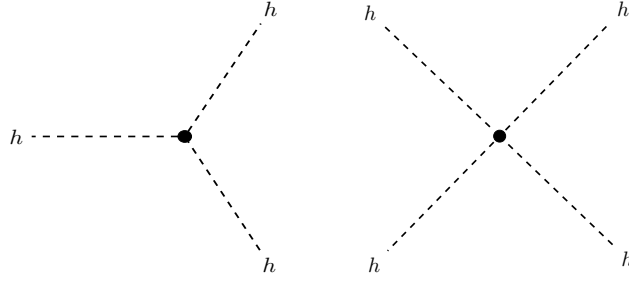
Figure 2.8: Cubic and quartic self-interactions between the Higgs bosons.

When computing the masses of the physical eigenstates, we find that one of the combination remains massless, namely the photon field A_μ. This is true as the vacuum state Φ_0 respects the $U(1)_{\text{EM}}$ symmetry

$$U(1)_{\text{EM}} : \quad Q\Phi_0 = \frac{1}{2}(T_3 + Y)\Phi_0 = \begin{pmatrix} 1 & 0 \\ 0 & 0 \end{pmatrix} \frac{1}{\sqrt{2}} \begin{pmatrix} 0 \\ v + h \end{pmatrix} = 0.$$

Thus, it is not a surprise that the vacuum state in Eq. (2.48) respects a local $U(1)_{\text{EM}}$ transformation

$$\Phi_0 \rightarrow \Phi_0' = e^{-iQ_{\Phi_0}\alpha(x)}\Phi_0 = \Phi_0.$$

2.6.1 Gauge boson masses

We start by studying the scalar Lagrangian in Eq. (2.46). After expanding the potential around the VEV and using the relation $\mu^2 = -\lambda v^2$, we get

$$V(h) = -\frac{1}{2}\lambda v^2 (v + h)^2 + \frac{1}{4}\lambda(v + h)^4 = \lambda v^2 h^2 - \frac{1}{4}\lambda v^4 + \lambda v h^3 + \frac{1}{4}\lambda h^4. \tag{2.49}$$

The first term represents a mass term for the Higgs field h, namely

$$m_h = \sqrt{2\lambda v^2} = \sqrt{-2\mu^2} > 0. \tag{2.50}$$

Although the Higgs VEV v is known as $v = (\sqrt{2}G_F)^{-1/2} = 246.22\,\text{GeV}$, the Higgs quartic coupling λ is a free parameter. Thus, the Higgs boson mass is *not* predicted by the SM. The last two terms in Eq. (2.49) represent cubic and quartic self-interactions between the Higgs bosons. A Feynman diagram for the self-interactions is shown in Fig. 2.8.

To compute the gauge boson masses, we expand the covariant derivative in Eq. (2.47) as

$$\mathcal{D}_\mu = \partial_\mu + \frac{i}{2} \begin{pmatrix} gW_\mu^3 + g'YB_\mu & g(W_\mu^1 - iW_\mu^2) \\ g(W_\mu^1 + iW_\mu^2) & -gW_\mu^3 + g'YB_\mu \end{pmatrix} \equiv \partial_\mu + \frac{i}{2}\mathcal{W}_\mu,$$

where $\mathcal{W}_\mu^\dagger = \mathcal{W}_\mu$. With $Y = +1$, we get

$$\mathcal{D}_\mu\Phi = \frac{1}{\sqrt{2}}\left(\partial_\mu + \frac{i}{2}\mathcal{W}_\mu\right)\begin{pmatrix} 0 \\ v+h \end{pmatrix} = \frac{1}{\sqrt{2}}\begin{pmatrix} 0 \\ \partial_\mu h \end{pmatrix} + \frac{i}{2\sqrt{2}}\mathcal{W}_\mu\begin{pmatrix} 0 \\ v+h \end{pmatrix},$$

$$(\mathcal{D}^\mu\Phi)^\dagger = \left[\frac{1}{\sqrt{2}}\left(\partial^\mu + \frac{i}{2}\mathcal{W}^\mu\right)\begin{pmatrix} 0 \\ v+h \end{pmatrix}\right]^\dagger = \frac{1}{\sqrt{2}}\begin{pmatrix} 0 & \partial^\mu h \end{pmatrix} - \frac{i}{2\sqrt{2}}\begin{pmatrix} 0 & v+h \end{pmatrix}\mathcal{W}^\mu.$$

Thus, the kinetic term expands to

$$(\mathcal{D}^\mu\Phi)^\dagger(\mathcal{D}_\mu\Phi) = \frac{1}{2}(\partial_\mu h)^2 + \frac{i}{4}\begin{pmatrix} 0 & \partial^\mu h \end{pmatrix}\mathcal{W}_\mu\begin{pmatrix} 0 \\ v+h \end{pmatrix} - \frac{i}{4}\begin{pmatrix} 0 & v+h \end{pmatrix}\mathcal{W}^\mu\begin{pmatrix} 0 \\ \partial_\mu h \end{pmatrix}$$

$$+ \frac{1}{8}\begin{pmatrix} 0 & v+h \end{pmatrix}\mathcal{W}^\mu\mathcal{W}_\mu\begin{pmatrix} 0 \\ v+h \end{pmatrix}.$$

Now, we can make use of the following matrix multiplication property

$$\begin{pmatrix} 0 & x \end{pmatrix}\begin{pmatrix} A_{11} & A_{12} \\ A_{21} & A_{22} \end{pmatrix}\begin{pmatrix} 0 \\ y \end{pmatrix} = xA_{22}y.$$

Using this property, the kinetic term simplifies to (ignoring terms of the form $\partial_\mu h(v+h)$)

$$(\mathcal{D}^\mu\Phi)^\dagger(\mathcal{D}_\mu\Phi) = \frac{1}{2}(\partial_\mu h)^2 + \frac{1}{8}(v+h)^2[\mathcal{W}_\mu\mathcal{W}^\mu]_{22},$$

where $[\mathcal{W}_\mu\mathcal{W}^\mu]_{22}$ refers to the $(2,2)$ component of $\mathcal{W}_\mu\mathcal{W}^\mu$. To simplify notation, we can define the charged $W_\mu^\pm$ fields as

$$W_\mu^\pm \equiv \frac{1}{\sqrt{2}}(W_\mu^1 \mp iW_\mu^2). \tag{2.51}$$

Thus, the elements of the $\mathcal{W}_\mu$ matrix are

$$\mathcal{W}_\mu = \begin{pmatrix} gW_\mu^3 + g'B_\mu & \sqrt{2}gW_\mu^+ \\ \sqrt{2}gW_\mu^- & -gW_\mu^3 + g'B_\mu \end{pmatrix}.$$

The final expression for the kinetic term is

$$(\mathcal{D}^\mu\Phi)^\dagger(\mathcal{D}_\mu\Phi) = \frac{1}{2}(\partial_\mu h)^2 + \frac{1}{8}(v+h)^2\left[2g^2W_\mu^-(W^+)^\mu + (gW_\mu^3 - g'B_\mu)^2\right]. \tag{2.52}$$

Since $W_\mu^+ = (W_\mu^-)^\dagger$, the above expression contains a mass term for 3 gauge boson fields, namely W^+, W^- and a combination of the vector fields $(gW_\mu^3 - g'B_\mu)$. The mass of the $W^\pm$ boson is

$$m_{W^\pm} = \frac{1}{\sqrt{2}}vg. \tag{2.53}$$

The neutral boson Z_μ and the photon A_μ fields can be defined as

$$Z_\mu \equiv \frac{1}{\sqrt{g^2 + g'^2}}\left(gW_\mu^3 - g'B_\mu\right), \quad A_\mu \equiv \frac{1}{\sqrt{g^2 + g'^2}}\left(g'W_\mu^3 + gB_\mu\right). \tag{2.54}$$
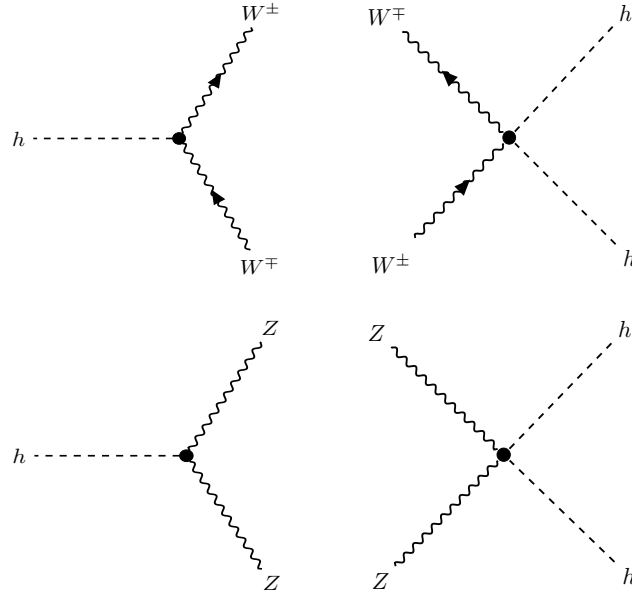
Figure 2.9: Cubic and quartic interactions between the Higgs and gauge bosons.

Thus, the last term in Eq. (2.52) expands to

$$\frac{1}{8}v^2(gW_\mu^3 - g'B_\mu)^2 = \frac{1}{8}v^2(g^2 + g'^2)Z_\mu Z^\mu.$$

This corresponds to a mass term for the Z boson, namely

$$m_Z = \frac{1}{2}v\sqrt{g^2 + g'^2}. \tag{2.55}$$

With no mass term for the photon field A_μ in Eq. (2.52), we get

$$m_\gamma = 0. \tag{2.56}$$

The remaining terms in Eq. (2.52) describe the cubic and quartic interactions between the Higgs and gauge bosons. These are shown by the Feynman diagrams in Fig. 2.9.

2.6.2 The Weinberg angle

It is convenient to re-write the expressions for the Z_μ and A_μ fields as

$$\begin{pmatrix} Z_\mu \\ A_\mu \end{pmatrix} = \begin{pmatrix} \cos\theta_W & -\sin\theta_W \\ \sin\theta_W & \cos\theta_W \end{pmatrix} \begin{pmatrix} W_\mu^3 \\ B_\mu \end{pmatrix}, \tag{2.57}$$

where θ_W is the Weinberg angle. It describes the mixing between the W_μ^3 and B_μ fields, which together form the physical Z boson and the photon. It is related to the parameters g and g' by the following relation

$$\cos\theta_W = \frac{g}{\sqrt{g^2 + g'^2}}. \tag{2.58}$$

Thus, the $W^\pm$ and Z boson masses are related to each other by

$$\frac{m_{W^\pm}}{m_Z} = \frac{g}{\sqrt{g^2 + g'^2}} = \cos\theta_W. \tag{2.59}$$

As g and g' are free parameters, the SM makes no prediction for $m_{W^\pm}$ and m_Z. The experimentally measured values for the gauge boson masses are [3]

$$m_{W^\pm} = 80.385 \pm 0.015\,\text{GeV}, \quad m_Z = 91.1876 \pm 0.0021\,\text{GeV}. \tag{2.60}$$

Thus, the Weinberg angle at tree-level is

$$\theta_W \simeq 28.17°. \tag{2.61}$$

2.6.3 Interactions in mass eigenstate basis

Up until now, we have written down the EW Lagrangian in terms of W_μ^1, W_μ^2, W_μ^3 and B_μ fields, i.e., fields defined in the *weak eigenstate basis*. After electroweak symmetry breaking (EWSB), we generated mass terms that contained a linear combination of fields defined in the weak eigenstate basis. Instead, the physical $W^\pm$ and Z bosons were defined in the *mass eigenstate basis* as they propagate in a given particle physics experiment.

To study the type of interactions in the mass eigenstate basis, we can start by writing down the covariant derivative as

$$\mathcal{D}_\mu = \partial_\mu + ig \sum_{a=1}^{3} T_a W_\mu^a + ig'\frac{1}{2}Y B_\mu, \tag{2.62}$$

where T_a for $a = 1, 2, 3$ are the components of the weak isospin T. They are related to the Pauli matrices τ_a by $T_a = \tau_a/2$. Using Eq. (2.51), we can write

$$W_\mu^1 = \frac{1}{\sqrt{2}}\left(W_\mu^+ + W_\mu^-\right), \quad W_\mu^2 = \frac{i}{\sqrt{2}}\left(W_\mu^+ - W_\mu^-\right)$$

such that

$$\begin{aligned}
T_1 W_\mu^1 + T_2 W_\mu^2 &= \frac{T_1}{\sqrt{2}}\left(W_\mu^+ + W_\mu^-\right) + \frac{iT_2}{\sqrt{2}}\left(W_\mu^+ - W_\mu^-\right) \\
&= \frac{1}{\sqrt{2}}\left[W_\mu^+\left(T_1 + iT_2\right) + W_\mu^-\left(T_1 - iT_2\right)\right] \\
&= \frac{1}{\sqrt{2}}\left(W_\mu^+ T_+ + W_\mu^- T_-\right),
\end{aligned}$$

where T_+ and T_- are the raising and lowering operators of the $SU(2)_L$ group respectively. With the Z_μ and A_μ fields defined in Eq. (2.54), we can write

$$W_\mu^3 = \frac{1}{\sqrt{g^2 + g'^2}}\left(g Z_\mu + g' A_\mu\right), \quad B_\mu = \frac{1}{\sqrt{g^2 + g'^2}}\left(g A_\mu - g' Z_\mu\right)$$

such that

$$
igT_3 W_\mu^3 + ig' \frac{1}{2} Y B_\mu = \frac{ig}{\sqrt{g^2 + g'^2}} T_3 \left(g Z_\mu + g' A_\mu \right) + \frac{ig'}{2\sqrt{g^2 + g'^2}} Y \left(g A_\mu - g' Z_\mu \right)
$$

$$
= \frac{i}{\sqrt{g^2 + g'^2}} Z_\mu \left(g^2 T_3 - g'^2 \frac{Y}{2} \right) + \frac{igg'}{\sqrt{g^2 + g'^2}} A_\mu \left(T_3 + \frac{Y}{2} \right).
$$

Using Eq. (2.40), the last term in brackets is just the electric charge Q, namely

$$
Q = T_3 + \frac{Y}{2}.
$$

As Q is expressed in units of an electron charge e, it can be related to the parameters g and g' by

$$
e = \frac{gg'}{\sqrt{g^2 + g'^2}}. \tag{2.63}
$$

Using the relation $Y = 2(Q - T_3)$ in Eq. (2.40), we can write

$$
\frac{i}{\sqrt{g^2 + g'^2}} Z_\mu \left(g^2 T_3 - g'^2 \frac{Y}{2} \right) = \frac{i}{\sqrt{g^2 + g'^2}} Z_\mu \left[\left(g^2 + g'^2 \right) T_3 - g'^2 Q \right].
$$

Using Eq. (2.58), we can write

$$
\sqrt{g^2 + g'^2} = \frac{g}{\cos \theta_W}.
$$

Finally, the covariant derivative expands to

$$
\mathcal{D}_\mu = \partial_\mu + ig \left(T_1 W_\mu^1 + T_2 W_2^\mu + T_3 W_3^\mu \right) + ig' \frac{1}{2} Y B_\mu
$$

$$
= \partial_\mu + \frac{ig}{\sqrt{2}} \left(W_\mu^+ T_+ + W_\mu^- T_- \right) + \frac{ig}{\cos \theta_W} Z_\mu (T_3 - Q \sin^2 \theta_W) + iQe A_\mu.
$$

Now, we can explicitly write down the expressions for the fermion fields in Eq. (2.42). For the first generation of quarks and leptons, say $l = e$, $U = u$ and $D = d$, we get

$$
\mathscr{L}_{\text{EW}} \supset \left(\overline{\nu}_e \quad \overline{e} \right)_L i\gamma^\mu \mathcal{D}_\mu \begin{pmatrix} \nu_e \\ e \end{pmatrix}_L + \overline{e}_R i\gamma^\mu \mathcal{D}_\mu e_R + (\overline{\nu}_e)_R i\gamma^\mu \mathcal{D}_\mu (\nu_e)_R
$$

$$
+ \left(\overline{u} \quad \overline{d} \right)_L i\gamma^\mu \mathcal{D}_\mu \begin{pmatrix} u \\ d \end{pmatrix}_L + u_R i\gamma^\mu \mathcal{D}_\mu u_R + \overline{d}_R i\gamma^\mu \mathcal{D}_\mu d_R
$$

$$
= \left(\overline{\nu}_e \quad \overline{e} \right)_L i\gamma^\mu \partial_\mu \begin{pmatrix} \nu_e \\ e \end{pmatrix}_L + \overline{e}_R i\gamma^\mu \partial_\mu e_R + (\overline{\nu}_e)_R i\gamma^\mu \partial_\mu (\nu_e)_R
$$

$$
+ \left(\overline{u} \quad \overline{d} \right)_L i\gamma^\mu \partial_\mu \begin{pmatrix} u \\ d \end{pmatrix}_L + u_R i\gamma^\mu \partial_\mu u_R + \overline{d}_R i\gamma^\mu \partial_\mu d_R
$$

$$
- \frac{g}{\sqrt{2}} \left[W_\mu^+ (J^+)^\mu + W_\mu^- (J^-)^\mu \right] - \frac{g}{\cos \theta_W} Z_\mu J_Z^\mu - e A_\mu J_{\text{EM}}^\mu,
$$

f	T_3^f	Q_f	g_L	g_R
$(\nu_e)_L$	$+\frac{1}{2}$	0	$+\frac{1}{2}$	0
$(\nu_e)_R$	0	0	0	0
e_L	$-\frac{1}{2}$	-1	$-\frac{1}{2} + \sin^2\theta_W$	0
e_R	0	-1	0	$+\sin^2\theta_W$
u_L	$+\frac{1}{2}$	$+\frac{2}{3}$	$\frac{1}{2} - \frac{2}{3}\sin^2\theta_W$	0
u_R	0	$+\frac{2}{3}$	0	$-\frac{2}{3}\sin^2\theta_W$
d_L	$-\frac{1}{2}$	$-\frac{1}{3}$	$-\frac{1}{2} + \frac{1}{3}\sin^2\theta_W$	0
d_R	0	$-\frac{1}{3}$	0	$+\frac{1}{3}\sin^2\theta_W$

Table 2.3: Coupling strength between the first generation of quarks/leptons and neutral Z boson.

where the vector currents are given by

$$(J^+)^\mu = (\bar{\nu}_e)_L \gamma^\mu e_L + \bar{u}_L \gamma^\mu d_L, \quad J_Z^\mu = \sum_{f=\nu_e,\,e}^{u,\,d} g_L^f \bar{f}_L \gamma^\mu f_L + g_R^f \bar{f}_R \gamma^\mu f_R,$$

$$(J^-)^\mu = \bar{e}_L \gamma^\mu (\nu_e)_L + \bar{d}_L \gamma^\mu u_L, \quad J_{\text{EM}}^\mu = -\bar{e}\gamma^\mu e + \frac{2}{3}\bar{u}\gamma^\mu u - \frac{1}{3}\bar{d}\gamma^\mu d.$$

Note that the electromagnetic current J_{EM}^μ agrees with Eq. (2.12). The couplings g_L^f and g_R^f are given by

$$g_L^f = T_3^f - Q_f \sin^2\theta_W, \quad g_R^f = -Q_f \sin^2\theta_W.$$

Using these relations, we can calculate the coupling strength between the Z boson and left-/right-handed fermion fields. These are tabulated in Table 2.3.

2.7 Fermion masses

The mass term for a fermion field is

$$m_\psi \bar{\psi}\psi = m_\psi (\bar{\psi}_R + \bar{\psi}_L)(\psi_L + \psi_R) = m_\psi (\bar{\psi}_R \psi_L + \bar{\psi}_L \psi_R). \tag{2.64}$$

Such a term is *not* allowed by a local $SU(2)_L \otimes U(1)_Y$ invariance as the left-handed fields form a part of the isospin doublet, whereas the right-handed fields are isospin singlets. Under the $SU(2)_L \otimes U(1)_Y$ symmetry, they transform as

$$\psi_L \rightarrow \psi_L' = \psi_L e^{iW_\mu^a T_a + i\alpha Y}, \quad \psi_R \rightarrow \psi_R' = \psi_R e^{i\alpha Y}.$$

Thus, a fermion mass term is not invariant under all local $SU(2)_L \otimes U(1)_Y$ transformations.

For a fermion mass term to be gauge invariant, it must be a *singlet* under local $SU(2)_L$ and $U(1)_Y$ transformations. This can be achieved by using the definition of the Higgs
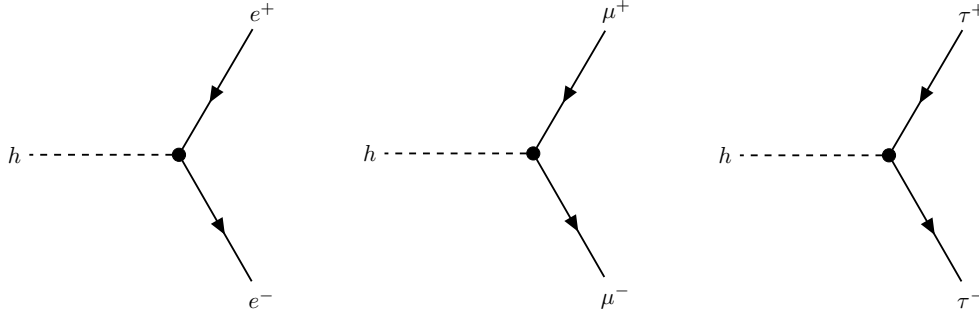
Figure 2.10: Feynman diagrams for an interaction between the Higgs boson and two leptons.

doublet. In particular, one can show that the Higgs field has exactly the right quantum numbers to form an $SU(2)_L$ and $U(1)_Y$ singlet. The gauge invariant mass term for a fermion field is

$$\mathscr{L}_{\text{fermion-mass}} = -\lambda_\psi \left[\overline{\psi}_L \Phi \psi_R + \overline{\psi}_R \Phi^\dagger \psi_L \right], \tag{2.65}$$

where λ_ψ is the fermion Yukawa coupling. After expanding the Higgs doublet, we will see that this expression not only generates a mass term for the fermion field but also an interaction term for the Higgs boson and fermion fields.

2.7.1   Lepton masses

The lepton fields form a part of the isospin doublet

$$L_l = \begin{pmatrix} \nu_l \\ l \end{pmatrix}_L,$$

where $l \in (e, \mu, \tau)$. The lepton mass term in Eq. (2.65) expands to

$$\begin{aligned}
\mathscr{L}_{\text{lepton-masses}} &= - \sum_{l=e,\mu,\tau} \lambda_l \frac{1}{\sqrt{2}} \left[\begin{pmatrix} \overline{\nu}_l & \overline{l} \end{pmatrix}_L \begin{pmatrix} 0 \\ v+h \end{pmatrix} l_R + \overline{l}_R \begin{pmatrix} 0 & v+h \end{pmatrix} \begin{pmatrix} \nu_l \\ l \end{pmatrix}_L \right] \\
&= - \sum_{l=e,\mu,\tau} \frac{\lambda_l}{\sqrt{2}} (v+h) \left(\overline{l}_L l_R + \overline{l}_R l_L \right) \\
&= - \sum_{l=e,\mu,\tau} \frac{\lambda_l}{\sqrt{2}} (v+h) \overline{l} l \\
&= - \sum_{l=e,\mu,\tau} \frac{\lambda_l v}{\sqrt{2}} \overline{l} l - \sum_{l=e,\mu,\tau} \frac{\lambda_l}{\sqrt{2}} h \overline{l} l.
\end{aligned}$$

The first term in the above expression represents a mass term for the lepton l, namely

$$m_l = \frac{\lambda_l v}{\sqrt{2}}. \tag{2.66}$$

The second term represents an interaction between the Higgs boson and two lepton fields. A Feynman diagram for this interaction is shown in Fig. 2.10.

It is conventional to express the Yukawa coupling as

$$\lambda_l = \sqrt{2}\,\frac{m_l}{v}. \tag{2.67}$$

Thus, the Higgs field couples more strongly to the heavier leptons. As the Yukawa coupling λ_l is a free parameter, the lepton masses are *not* predicted by the Higgs mechanism.

2.7.2 Quark masses

Notice that the fermion mass term in Eq. (2.65) only generates mass for the down-type quarks (d, s, b). To generate mass for the up-type quarks (u, c, t), another term is required in the Lagrangian. Luckily, such a term can be constructed using the definition of the Higgs doublet. For the up-type quarks, the mass term has the form

$$\mathscr{L}_{\text{up-type}} = \lambda_f \overline{\psi}_L \widetilde{\Phi}^c \phi_R + h.c., \tag{2.68}$$

where $h.c.$ is a shorthand for the Hermitian conjugate and

$$\widetilde{\Phi}^c = -i\tau_2 \Phi^* = -\frac{1}{\sqrt{2}}\begin{pmatrix} v + h \\ 0 \end{pmatrix}.$$

Thus, a mass term for the up- and down-type quarks is (ignoring the $h.c.$ term)

$$\text{down-type}: \quad \lambda_d \begin{pmatrix} \overline{u} & \overline{d} \end{pmatrix}_L \Phi d_R = \lambda_d \begin{pmatrix} \overline{u} & \overline{d} \end{pmatrix}_L \begin{pmatrix} 0 \\ v \end{pmatrix} d_R = \lambda_d v\, \overline{d}_L d_R,$$

$$\text{up-type}: \quad \lambda_u \begin{pmatrix} \overline{u} & \overline{d} \end{pmatrix}_L \widetilde{\Phi}^c u_R = \lambda_u \begin{pmatrix} \overline{u} & \overline{d} \end{pmatrix}_L \begin{pmatrix} v \\ 0 \end{pmatrix} u_R = \lambda_u v\, \overline{u}_L u_R.$$

However, this does not explain the full story. If we look at these terms in more detail, we find that one can construct more fermion mass-type terms in the Lagrangian that does not have an easy interpretation. Getting rid of these terms lead us to the origin of quark mixing in the fermion sector.

2.8 Origin of the quark mixing

We begin by discussing the consequences of allowing all possible quark 'mass-like' terms, and studying the links between the Yukawa couplings and quark mixing in the SM, i.e., the difference between mass and interaction eigenstates.

The spinor fields ψ for the three fermion generations can be written in five interaction representations, see Table 2.4. In this notation, $Q^I_{Li}(\mathbf{3}, \mathbf{2}, +1/3)$ describes an $SU(3)_C$ triplet and an $SU(2)_L$ doublet with hypercharge $Y = +1/3$. The superscript I denotes that the fermion field is expressed in the interaction eigenstate basis. The subscript i runs over the

three generations (or *families*) of quarks/leptons. Explicitly, $Q_{Li}^I(\mathbf{3}, \mathbf{2}, +1/3)$ is a shorthand for

$$Q_{Li}^I(\mathbf{3}, \mathbf{2}, +1/3) \in \left\{ \begin{pmatrix} u_g^I & u_r^I & u_b^I \\ d_g^I & d_r^I & d_b^I \end{pmatrix}, \begin{pmatrix} c_g^I & c_r^I & c_b^I \\ s_g^I & s_r^I & s_b^I \end{pmatrix}, \begin{pmatrix} t_g^I & t_r^I & t_b^I \\ b_g^I & b_r^I & b_b^I \end{pmatrix} \right\},$$

where g, r, b are the three possible quark colours.

Earlier, we saw that the Higgs doublet Φ can be used to construct mass terms for the fermion fields. For the up- and down-type fermions, we can write (ignoring the $h.c.$ term)

$$\begin{aligned} \mathcal{L}_{\text{quarks}} &= -\Lambda_{\text{down}} \overline{\psi}_L \Phi \psi_R - \Lambda_{\text{up}} \overline{\psi}_L \widetilde{\Phi}^c \psi_R \\ &= -\Lambda_{\text{down}} \frac{v}{\sqrt{2}} \overline{d}^I d^I - \Lambda_{\text{up}} \frac{v}{\sqrt{2}} \overline{u}^I u^I \\ &= -m_d \overline{d}^I d^I - m_u \overline{u}^I u^I, \end{aligned}$$

where the interaction strength between the Higgs boson and fermions, the so-called Yukawa couplings, have again been added. All of this sounds straightforward. However, there are additional complications. In the most general realisations, the Λ's are matrices. As we will see below, this leads to a mixing between different flavours. Ignoring the $h.c.$ term again, the expression for the fermion mass term is

$$- \mathcal{L}_{\text{Yukawa}} = Y_{ij} \overline{\psi_{Li}} \Phi \psi_{Rj} = Y_{ij}^d \overline{Q_{Li}^I} \Phi d_{Rj}^I + Y_{ij}^u \overline{Q_{Li}^I} \widetilde{\Phi}^c u_{Rj}^I + Y_{ij}^l \overline{L_{Li}^I} \Phi l_{Rj}^I. \qquad (2.69)$$

The matrices Y_{ij}^d, Y_{ij}^u and Y_{ij}^l are arbitrary complex matrices which connect the flavour eigenstates. As terms such as Y_{uc} and Y_{us} will also appear, they do not have an easy interpretation.

We can expand out the $Y_{ij}^d \overline{Q_{Li}^I} \Phi d_{Rj}^I$ term in Eq. (2.69) as

$$Y_{ij}^d \overline{Q_{Li}^I} \Phi d_{Rj}^I = Y_{ij}^d \overline{(\text{up-type} \quad \text{down-type})_{iL}^I} \begin{pmatrix} \phi_+ \\ \phi_0 \end{pmatrix} (\text{down-type})_{Rj}^I$$

$$= \begin{pmatrix} Y_{11} \overline{(u \ d)_L^I} \begin{pmatrix} \phi_+ \\ \phi_0 \end{pmatrix} & Y_{12} \overline{(u \ d)_L^I} \begin{pmatrix} \phi_+ \\ \phi_0 \end{pmatrix} & Y_{13} \overline{(u \ d)_L^I} \begin{pmatrix} \phi_+ \\ \phi_0 \end{pmatrix} \\ Y_{21} \overline{(c \ s)_L^I} \begin{pmatrix} \phi_+ \\ \phi_0 \end{pmatrix} & Y_{22} \overline{(c \ s)_L^I} \begin{pmatrix} \phi_+ \\ \phi_0 \end{pmatrix} & Y_{23} \overline{(c \ s)_L^I} \begin{pmatrix} \phi_+ \\ \phi_0 \end{pmatrix} \\ Y_{31} \overline{(t \ b)_L^I} \begin{pmatrix} \phi_+ \\ \phi_0 \end{pmatrix} & Y_{32} \overline{(t \ b)_L^I} \begin{pmatrix} \phi_+ \\ \phi_0 \end{pmatrix} & Y_{33} \overline{(u \ d)_L^I} \begin{pmatrix} \phi_+ \\ \phi_0 \end{pmatrix} \end{pmatrix} \begin{pmatrix} d_R^I \\ s_R^I \\ b_R^I \end{pmatrix}.$$

After EWSB, we get

$$\begin{aligned} -\mathcal{L}_{\text{Yukawa}}^{\text{quarks}} &= Y_{ij}^d \overline{Q_{Li}^I} \Phi d_{Rj}^I + Y_{ij}^u \overline{Q_{Li}^I} \widetilde{\Phi}^c u_{Rj}^I \\ &= Y_{ij}^d \overline{d_{Li}^I} \frac{v}{\sqrt{2}} d_{Rj}^I + Y_{ij}^u \overline{u_{Li}^I} \frac{v}{\sqrt{2}} u_{Rj}^I + \dots \\ &= M_{ij}^d \overline{d_{Li}^I} d_{Rj}^I + M_{ij}^u \overline{u_{Li}^I} u_{Rj}^I + \dots, \end{aligned}$$

General spinor field	Ψ^I (color, weak isospin, hypercharge)
left-handed quarks	$Q^I_{Li}(\mathbf{3}, \mathbf{2}, +1/3)$
right-handed up-type quarks	$u^I_{Ri}(\mathbf{3}, \mathbf{1}, +4/3)$
right-handed down-type quarks	$d^I_{Ri}(\mathbf{3}, \mathbf{1}, +1/3)$
left-handed leptons	$L^I_{Li}(\mathbf{1}, \mathbf{2}, -1)$
right-handed leptons	$L^I_{Ri}(\mathbf{1}, \mathbf{1}, -2)$

Table 2.4: Spinor fields for the three fermion generations in five interaction representations.

where we have omitted the Higgs-quark interaction terms. Note that the d's and u's in the above expression still represent the three down-type and up-type quarks respectively, so the mixed terms are still present.

To obtain the mass eigenstates, we must diagonalise the matrices M^d and M^u. This is achieved using two unitary matrices V^d and V^u such that

$$M^d_{\mathrm{diag}} = V^d_L M^d V^{d\dagger}_R, \quad M^u_{\mathrm{diag}} = V^u_L M^d V^{u\dagger}_R.$$

Using the requirement that the matrices V are unitary ($V^{d\dagger}_L V^d_L = \mathbb{1}$), we get (leaving out the $h.c.$ terms from the Lagrangian)

$$
\begin{aligned}
-\mathcal{L}^{\mathrm{quarks}}_{\mathrm{Yukawa}} &= \overline{d^I_{Li}} M^d_{ij} d^I_{Rj} + \overline{u^I_{Li}} M^u_{ij} u^I_{Rj} + \dots \\
&= \overline{d^I_{Li}} V^{d\dagger}_L V^d_L M^d_{ij} V^{d\dagger}_R V^d_R d^I_{Rj} + \overline{u^I_{Li}} V^{u\dagger}_L V^u_L M^u_{ij} V^{u\dagger}_R V^u_R u^I_{Rj} + \dots \\
&= \overline{d_{Li}} (M^d_{ij})_{\mathrm{diag}} d_{Rj} + \overline{u_{Li}} (M^u_{ij})_{\mathrm{diag}} u_{Rj} + \dots,
\end{aligned}
$$

where the matrices V have been absorbed in the quark states in the last line. Now, the up- and down-type quarks are no longer the interaction states u^I and d^I but are simply u and d quarks in the mass eigenstate basis, namely

$$d_{Li} = (V^d_L)_{ij} d^I_{Lj}, \quad d_{Ri} = (V^d_R)_{ij} d^I_{Rj}, \tag{2.70}$$

$$u_{Li} = (V^u_L)_{ij} u^I_{Lj}, \quad u_{Ri} = (V^u_R)_{ij} u^I_{Rj}. \tag{2.71}$$

2.8.1 The Cabibbo-Kobayashi-Maskawa (CKM) matrix

The combination of matrices $(V^d_L V^{u\dagger}_L)_{ij}$, a unitary 3×3 matrix, is known as the Cabibbo-Kobayashi-Maskawa (CKM) matrix (V_{CKM}) [47]. The weak eigenstates (states produced from W decay) are not the same as the mass eigenstates. Instead, they are different mixtures of the mass eigenstates.

The CKM matrix is a 3-dimensional generalisation of the Cabibbo theory used to describe only two quark generations [48]. In the Cabibbo theory, the objects which couple to an up quark via charged current interactions are a superposition of down-type quarks

$$d^I = V_{ud} d + V_{us} s. \tag{2.72}$$

This can written as

$$d^I = \cos\theta_C \, d + \sin\theta_C \, s, \tag{2.73}$$

where θ_C is the Cabibbo angle. However, when the charm quark was discovered in 1974, it was found that the down and strange quark could also decay to either up or charm quark. This led to two sets of equations

$$\begin{pmatrix} d^I \\ s^I \end{pmatrix} = \begin{pmatrix} V_{ud} & V_{us} \\ V_{cd} & V_{cs} \end{pmatrix} \begin{pmatrix} d \\ s \end{pmatrix} = \begin{pmatrix} \cos\theta_C & \sin\theta_C \\ -\sin\theta_C & \cos\theta_C \end{pmatrix} \begin{pmatrix} d \\ s \end{pmatrix}. \tag{2.74}$$

The term $|V_{ij}|^2$ represents the probability of a quark flavour i decaying into a quark flavour j. Using the currently accepted values for $|V_{us}|$ and $|V_{ud}|$ [3], the Cabibbo angle is

$$\tan\theta_C = \frac{|V_{us}|}{|V_{ud}|} = \frac{0.22506}{0.97434} \implies \theta_C = 13.01°. \tag{2.75}$$

The generalisation of the Cabibbo theory to three quark generations corresponds to the CMK matrix. By convention, the interaction and mass eigenstates are equal for the up-type quarks, whereas for the down-type quarks, they are chosen to be rotated. In going from interaction to mass eigenstate basis, we can write

$$u_i^I = u_i, \quad d_i^I = V_{\text{CKM}} d_j,$$

or more explicitly,

$$\begin{pmatrix} d^I \\ s^I \\ b^I \end{pmatrix} = \begin{pmatrix} V_{ud} & V_{us} & V_{ub} \\ V_{cd} & V_{cs} & V_{cb} \\ V_{td} & V_{ts} & V_{tb} \end{pmatrix} \begin{pmatrix} d \\ s \\ b \end{pmatrix}. \tag{2.76}$$

From this definition of V_{CKM}, it follows that the transition from a down-type quark to an up-type quark is described by V_{ud}, whereas the transition from an up-type quark to a down-type quark is described by V_{ud}^*.

It is useful to count the number of parameters in the CKM matrix that appear in experiments and thus are physically important [35]. For a complex $F \times F$ matrix where F is the number of families, there are $2F^2$ parameters in total. As V_{CKM} is a unitary matrix, we get F^2 constraints from the following condition

$$(V_{\text{CKM}}^\dagger V_{\text{CKM}})_{nm} = \delta_{nm}.$$

Thus, we get F^2 real parameters. As the relative phase of quark fields is impossible to observe, there are $2F-1$ relative phases. Hence, the total number of observable parameters are

$$F^2 - (2F - 1) = (F - 1)^2 = \frac{F(F - 1)}{2} + \frac{(F - 1)(F - 2)}{2},$$

where $F(F - 1)/2$ parameters are real and known as *Euler angles*. The remaining $(F - 1)(F - 2)/2$ parameters are complex phases which results in CP violation [49, 50]. The

fact that CP violation in the CKM matrix arises only when $F \geq 3$ was one of the early motivations behind extending the number of families in the quark model.

To parametrise the CKM matrix, we require four independent parameters. Many parameterisations have been proposed but the three most common ones are as follows.

1. *KM parametrisation*: The original parameterisation of the CKM matrix by Kobayashi and Maskawa used three Euler angles $(\theta_1, \theta_2, \theta_3)$ and a CP-violating phase δ. Denoting the cosines and sines of the angles by c_i and s_i respectively, we can write

$$
V_{\text{CKM}} = \begin{pmatrix} c_1 & -s_1 c_3 & -s_1 s_3 \\ s_1 c_2 & c_1 c_2 c_3 - s_2 s_3 e i \delta & c_1 c_2 s_3 + s_2 c_3 e^{i\delta} \\ s_1 s_2 & c_1 s_2 c_3 + c_2 s_3 e^{i\delta} & c_1 s_2 s_3 - c_2 c_3 e^{i\delta} \end{pmatrix}.
\tag{2.77}
$$

2. *Standard parametrisation*: A standard parameterisation of the CKM matrix uses three Euler angles $(\theta_{12}, \theta_{23}, \theta_{13})$ and one CP-violating phase δ_{13}. Couplings between the quark generation i and j vanish if $\theta_{ij} = 0$. Denoting the cosines and sines of the angles by c_{ij} and s_{ij} respectively, we can write

$$
V_{\text{CKM}} = \begin{pmatrix} 1 & 0 & 0 \\ 0 & c_{23} & s_{23} \\ 0 & -s_{23} & c_{23} \end{pmatrix} \begin{pmatrix} c_{13} & 0 & s_{13}e^{-i\delta_{13}} \\ 0 & 1 & 0 \\ -s_{13}e^{i\delta_{13}} & 0 & c_{13} \end{pmatrix} \begin{pmatrix} c_{12} & s_{12} & 0 \\ -s_{12} & c_{12} & 0 \\ 0 & 0 & 1 \end{pmatrix}
$$

$$
= \begin{pmatrix} c_{12}c_{13} & s_{12}c_{13} & s_{13}e^{-i\delta_{13}} \\ -s_{12}c_{23} - c_{12}s_{23}s_{13}e^{i\delta_{13}} & c_{12}c_{23} - s_{12}s_{23}s_{13}e^{i\delta_{13}} & s_{23}c_{13} \\ s_{12}s_{23} - c_{12}c_{23}s_{13}e^{i\delta_{13}} & -c_{12}s_{23} - s_{12}c_{23}s_{13}e^{i\delta_{13}} & c_{23}c_{13} \end{pmatrix}.
\tag{2.78}
$$

The currently accepted values for the standard parameters are [3]

$$
\theta_{12} = 13.04 \pm 0.05°, \quad \theta_{13} = 0.201 \pm 0.011°,
$$

$$
\theta_{23} = 2.38 \pm 0.06°, \quad \delta_{13} = 1.20 \pm 0.08 \,\text{rad}.
$$

3. *Wolfenstein parametrisation*: A third parametrisation of the CKM matrix was introduced by L. Wolfenstein and involves four parameters λ, A, ρ and η [51]. These parameters have the property that they are all of $O(1)$. They are related to the standard parametrisation by [3]

$$
\lambda = s_{12} = \frac{|V_{us}|}{\sqrt{|V_{ud}|^2 + |V_{us}|^2}}, \quad A\lambda^2 = s_{23} = \lambda \left| \frac{V_{cb}}{V_{us}} \right|,
$$

$$
A\lambda^3(\rho + i\eta) = s_{13}e^{i\delta} = V_{ub}^* = \frac{A\lambda^3(\overline{\rho} + i\overline{\eta})\sqrt{1 - A^2\lambda^4}}{\sqrt{1 - \lambda^2}\left[1 - A^2\lambda^4(\overline{\rho} + i\overline{\eta})\right]}.
\tag{2.79}
$$

These relations ensure that $\overline{\rho} + i\overline{\eta} = -(V_{ud}V_{ub}^*)/(V_{cd}V_{cb}^*)$ is independent of the phase convention. In addition, when the CKM matrix is written in terms of λ, A, $\overline{\rho}$ and $\overline{\eta}$,
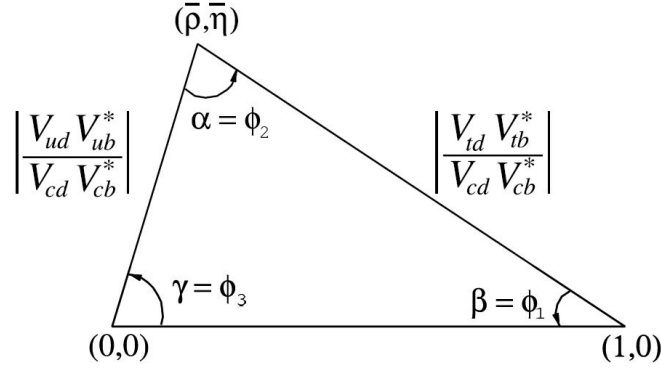
Figure 2.11: The unitary triangle in the Wolfenstein parameterisation. Figure from Ref. [3].

it remains unitary to all orders in λ. We can write V_{CKM} to $O(\lambda^4)$ either in terms of $\overline{\rho}$ and $\overline{\eta}$, or more traditionally as

$$
V_{\text{CKM}} = \begin{pmatrix} 1 - \lambda^2/2 & \lambda & A\lambda^3(\rho - i\eta) \\ -\lambda & 1 - \lambda^2/2 & A\lambda^2 \\ A\lambda^3(1 - \rho - i\eta) & -A\lambda^2 & 1 \end{pmatrix} + O(\lambda^4). \tag{2.80}
$$

By measuring $\rho - i\eta$, the CP violation in the SM can be measured.

The CKM matrix elements are fundamental parameters of the SM, so their precise determination is important. The unitarity of the CKM matrix acts as a strong constraint on new physics

$$
\sum_i V_{ij}V_{ik}^* = \delta_{jk}, \quad \sum_j V_{ij}V_{kj}^* = \delta_{ik}. \tag{2.81}
$$

Thus, there are six vanishing combinations (three for the rows and three for the columns). Each can be represented as triangles in a complex plane. Some of these triangles are obtained by taking scalar products of the neighbouring rows or columns which are nearly degenerate. The most commonly used *unitary triangle* arises from

$$
V_{ud}V_{ub}^* + V_{cd}V_{cb}^* + V_{td}V_{tb}^* = 0. \tag{2.82}
$$

In the above expression, the best known elements are V_{cd} and V_{cb}. After dividing the above expression by $V_{cd}V_{cb}^*$, we get

$$
\frac{V_{ud}V_{ub}^*}{V_{cd}V_{cb}^*} + 1 + \frac{V_{td}V_{tb}^*}{V_{cd}V_{cb}^*} = 0. \tag{2.83}
$$

The resulting unitarity triangle is shown in Fig. 2.11. Its vertices are exactly at $(0, 0)$, $(1, 0)$ and $(\overline{\rho}, \overline{\eta})$ due to the definition in Eq. (2.79). An important goal of flavour physics is to constrain the CKM matrix elements. Many measurements can be conveniently displayed and compared in the $(\overline{\rho}, \overline{\eta})$ plane to reveal if there are any departures from the unitary condition, i.e., any source of new physics.
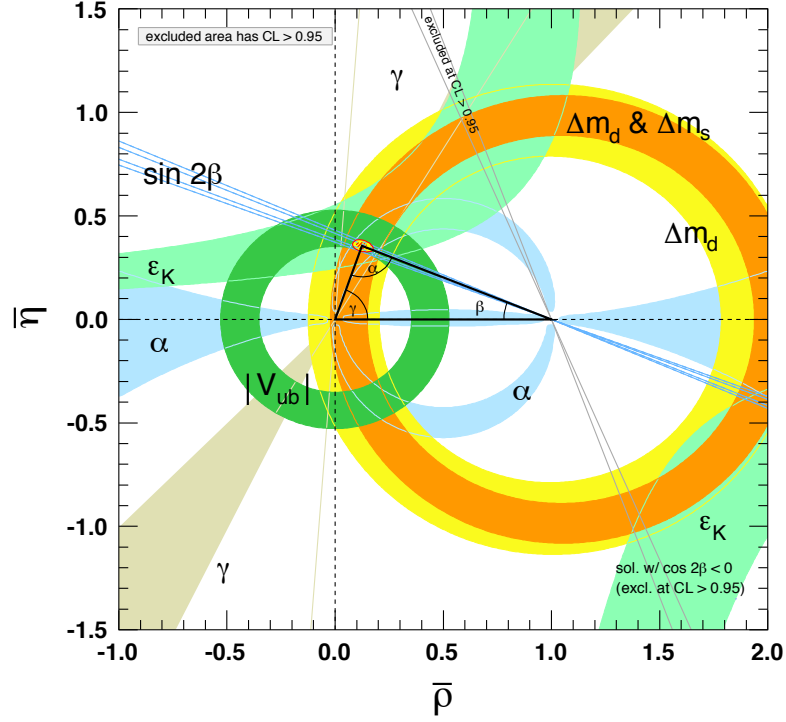
Figure 2.12: Constraints on the $(\overline{\rho}, \overline{\eta})$ plane from various measurements and a global fit. The shaded regions are at 95% C.L. Figure from Ref. [3].

The CKM matrix elements can be determined more precisely using a global fit of all available measurements and imposing the unitarity condition in all three generations. The fit must also use theory predictions for the hadronic matrix elements which often have significant uncertainties. Several approaches can be used to combine the experimental data. For instance, CKMFitter [52] uses frequentist statistics, whereas UTfit [53, 54] uses the Bayesian approach. Both of these approaches give similar results. The fit for the Wolfenstein parameters give [3]

$$\lambda = 0.22506 \pm 0.00050, \quad A = 0.811 \pm 0.026,$$
$$\rho = 0.124^{+0.019}_{-0.018}, \quad \eta = 0.356 \pm 0.011.$$

The magnitudes of all nine CKM elements are [3]

$$V_{\text{CKM}} = \begin{pmatrix} 0.97434^{+0.00011}_{-0.00012} & 0.22506 \pm 0.00050 & 0.00357 \pm 0.00015 \\ 0.22492 \pm 0.00050 & 0.97351 \pm 0.00013 & 0.0411 \pm 0.00013 \\ 0.00875^{+0.00032}_{-0.00033} & 0.0403 \pm 0.0013 & 0.99915 \pm 0.00005 \end{pmatrix}. \quad (2.84)$$

In Fig. 2.12, we show constraints on the $(\overline{\rho}, \overline{\eta})$ plane from various measurements and a global fit. The shaded regions are at 95% C.L. and overlaps consistently around the global fit region.

In principle, a matrix similar to the CKM matrix must also exist for leptons. In contrast to quarks, the charged leptons (e, μ, τ) are chosen to be the mass eigenstates, whereas a

rotation between the interaction and mass eigenstates occur in the neutrino sector. The resulting mixing matrix is known as the Pontecorvo-Maki-Nakagawa-Sakata (PMNS) matrix [55]. It was recently used to solve the solar neutrino problem [3].

Chapter 3

Road to the Higgs boson discovery

3.1 Introduction

In the SM, the Higgs mechanism offers a simple and economical solution to the problem of electroweak symmetry breaking (EWSB). By introducing a pair of complex scalar fields with a non-trivial potential and suitable interaction terms with all matter fields, it achieves the main goal of generating mass for both the weak force carriers and all elementary fermions. In addition, it introduces a new spin-0 particle known as the Higgs boson h to the particle content of the SM.

In 2012, the ATLAS [10] and CMS [56] experiments at the LHC found strong evidence for the existence of a SM-like Higgs boson with a mass around 125-127 GeV. This discovery was marked as a key milestone in the history of particle physics.

In this chapter, we follow the road that led to the Higgs boson discovery in 2012 [4, 7, 57]. We start by imposing various theoretical constraints on the Higgs boson mass. Using the details outlined in chapter 2, we compute the Higgs decay branching ratios as a function of its mass. These are used to determine the primary search channels for Higgs mass exclusion at the LEP and Tevatron experiments along with its discovery at the LHC.

3.2 Theoretical constraints on the Higgs boson mass

The Higgs boson mass m_h is *not* predicted by the SM. However, it is possible to place theoretical upper and lower limits on m_h if one assumes that no new physics enters between the electroweak and a higher energy scale Λ. Below the energy scale Λ, the SM is considered as an extremely successful effective field theory (EFT). Above this scale, the SM has to be embedded into a more general theory which gives rise to new physics phenomenon. From this point of view, the Higgs sector of the SM contains two parameters, namely the Higgs boson mass m_h and the scale of new physics Λ.

We start by providing a brief description of various theoretical constraints that can be

placed on m_h. In particular, we focus on the constraints from unitarity, triviality, vacuum stability, fine-tuning and electroweak precision tests.

3.2.1   Unitarity

Without the Higgs field, the amplitudes for the elastic scattering of longitudinal gauge bosons $V_L V_L \to V_L V_L$, where $V \in (W^\pm, Z)$, are proportional to m_h^2. The Feynman diagrams for the scattering of $W^\pm$ bosons at high energies are shown in Fig. 3.1. These results can be obtained using the electroweak equivalence theorem [58] which is valid in the high energy limit, i.e., for energies $s = Q^2 \gg m_V^2$. According to the equivalence theorem, the scattering amplitudes for longitudinal gauge bosons can be expressed in terms of the scattering amplitudes for the corresponding Goldstone bosons as

$$\mathcal{A}(V_L^1 \ldots V_L^n \to V_L^1 \ldots V_L^m) = (i)^n (-i)^m \mathcal{A}(w^1 \ldots w^n \to w^1 \ldots w^m) + O\left(\frac{m_V^2}{s}\right),$$

where w^i is the Goldstone boson associated with the longitudinal component of the gauge boson V^i. In the high energy limit, the scattering amplitude for $W_L^+ W_L^- \to W_L^+ W_L^-$ satisfies

$$\mathcal{A}(W_L^+ W_L^- \to W_L^+ W_L^-) = \mathcal{A}(w^+ w^- \to w^+ w^-) + O\left(\frac{m_W^2}{s}\right), \tag{3.1}$$

where

$$\mathcal{A}(w^+ w^- \to w^+ w^-) = -\frac{m_h^2}{v^2}\left(\frac{s}{s - m_h^2} + \frac{t}{t - m_h^2}\right). \tag{3.2}$$

Using a partial wave decomposition, the amplitude $\mathcal{A}$ can be written as

$$\mathcal{A} = 16\pi \sum_{l=0}^{\infty} (2l + 1) P_l(\cos\theta) a_l, \tag{3.3}$$

where a_l is the partial wave amplitude with spin l and $P_l(\cos\theta)$ are the Legendre polynomials. In terms of the partial wave amplitudes, the scattering cross-section corresponding to $\mathcal{A}$ is

$$\sigma = \frac{16\pi}{s} \sum_{l=0}^{\infty} (2l + 1)|a_l|^2. \tag{3.4}$$

Using the optical theorem, we can impose a unitarity constraint by writing

$$\sigma = \frac{16\pi}{s} \sum_{l=0}^{\infty} (2l + 1)|a_l|^2 = \frac{1}{s}\text{Im}[\mathcal{A}(\theta = 0)], \tag{3.5}$$

where $\mathcal{A}(\theta = 0)$ refers to the scattering amplitude in the forward direction. The last equality implies that

$$|a_l|^2 = \text{Re}(a_l)^2 + \text{Im}(a_l)^2 = \text{Im}(a_l) \implies |\text{Re}(a_l)| \le \frac{1}{2}. \tag{3.6}$$
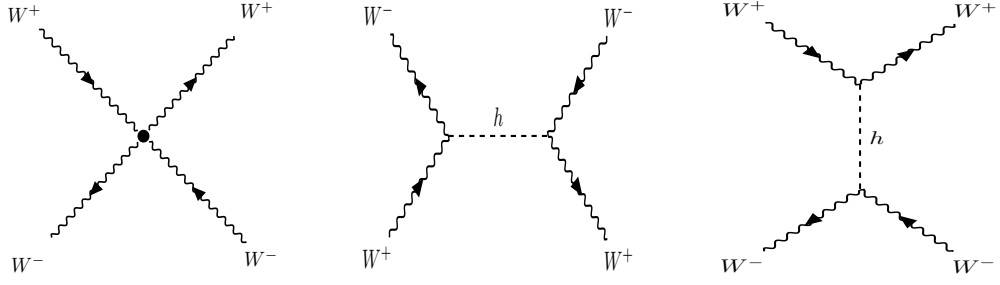
Figure 3.1: Feynman diagrams for the scattering of $W^\pm$ bosons at high energies.

Using Eq. (3.6), we can use different partial wave amplitudes to constrain m_h. For instance, the $J = 0$ partial wave amplitude a_0 for the $W_L^+ W_L^- \to W_L^+ W_L^-$ scattering is

$$a_0 = \frac{1}{16\pi s} \int_{-s}^{0} \mathcal{A}\, dt = -\frac{m_h^2}{16\pi v^2} \left[2 + \frac{m_h^2}{s - m_h^2} - \frac{m_h^2}{s} \log\left(1 + \frac{s}{m_h^2}\right) \right]. \qquad (3.7)$$

In the high energy limit $s \gg m_h^2$, a_0 reduces to

$$a_0 \xrightarrow{s \gg m_h^2} -\frac{m_h^2}{8\pi v^2}. \qquad (3.8)$$

Using Eq. (3.6), this implies

$$m_h \lesssim 870\,\text{GeV}. \qquad (3.9)$$

A stronger constraint can be obtained by using different longitudinal gauge boson scattering amplitudes. For instance, if we consider a coupled channel such as $W_L^+ W_L^- \to Z_L Z_L$, the lower bound becomes

$$m_h \lesssim 710\,\text{GeV}. \qquad (3.10)$$

Taking a different point of view, we can observe that if no Higgs boson exists, or equivalently if $m_h^2 \gg s$, Eq. (3.6) gives an indication on the critical energy scale Λ above which new physics is expected to appear. Indeed, by considering the $W_L^+ W_L^- \to W_L^+ W_L^-$ scattering, we find that

$$a_0(w^+ w^- \to w^+ w^-) \xrightarrow{m_h^2 \gg s} -\frac{s}{32\pi v^2}. \qquad (3.11)$$

Using Eq. (3.6), this gives

$$\Lambda \lesssim 1.8\,\text{TeV}. \qquad (3.12)$$

With more constrained channels, the bound can be reduced to

$$\Lambda \lesssim 1.2\,\text{TeV}. \qquad (3.13)$$

This is very suggestive as it indicates that the scale of new physics is roughly around 1-2 TeV. More importantly, it matches with the range of energies probed by the Tevatron and the LHC.
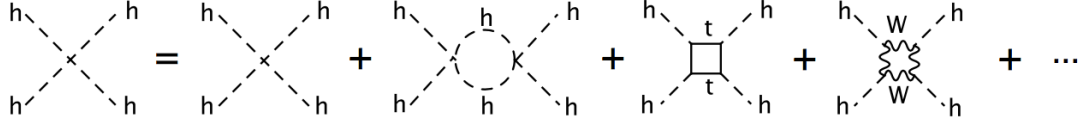
Figure 3.2: 1-loop contributions to the running of the Higgs quartic self-coupling λ. Figure from Ref. [4].

3.2.2 Triviality

The running of the Higgs quartic self-coupling λ with the energy scale Q can be used to place both a theoretical upper *and* lower limit on the Higgs boson mass. After including only the lowest order terms in all relevant couplings, its dependency on the energy scale Q is described by the following renormalisation group equation (RGE) [4]

$$\beta_\lambda \equiv \frac{d\lambda}{dt} = \frac{3}{4\pi^2}\left[\lambda^2 + \frac{1}{2}\lambda y_t^2 - \frac{1}{4}y_t^4 + \mathcal{B}(g,g')\right], \tag{3.14}$$

where $t = \log(Q^2/Q_0^2)$, Q_0 is a reference energy scale and $y = m_t/v$ is the top quark Yukawa coupling. The contribution from the gauge bosons is small and explicitly given by

$$\mathcal{B}(g,g') = -\frac{1}{8}\lambda(3g^2 + g'^2) + \frac{1}{64}(3g^4 + 2g^2g'^2 + g'^4). \tag{3.15}$$

The terms involving the mass of the Higgs boson, top quark and gauge bosons can be understood by looking at the effective quartic coupling at higher energy scales where the contributions from higher order diagrams appear. This is illustrated in Fig. 3.2.

For large m_h, or equivalently for large λ as $m_h^2 = 2\lambda v^2$ in Eq. (2.50), the first term in Eq. (3.14) dominates. In this case, we get

$$\lambda(Q) = \lambda(Q_0)\left[1 - \frac{3}{4\pi^2}\lambda(Q_0)\log\left(\frac{Q^2}{Q_0^2}\right)\right]^{-1}. \tag{3.16}$$

When the energy scale Q grows, the denominator in Eq. (3.16) can vanish. When this happens, $\lambda(Q)$ hits a pole known as the *Landau pole*. A triviality condition must be imposed if λ becomes infinite. This can be avoided if the denominator never vanishes, i.e., $\lambda(Q)$ remains finite such that $1/\lambda(Q) > 0$. After setting $Q = \Lambda$ and $Q_0 = v$ in Eq. (3.16), we get

$$m_h^2 < \frac{8\pi^2 v^2}{3\log(\Lambda^2/v^2)}. \tag{3.17}$$

For a grand unified theory (GUT) with $\Lambda = 10^{16}$ GeV, the upper limit is $m_h \leq 160$ GeV. For higher energy scales Λ, the upper limit on m_h decreases.
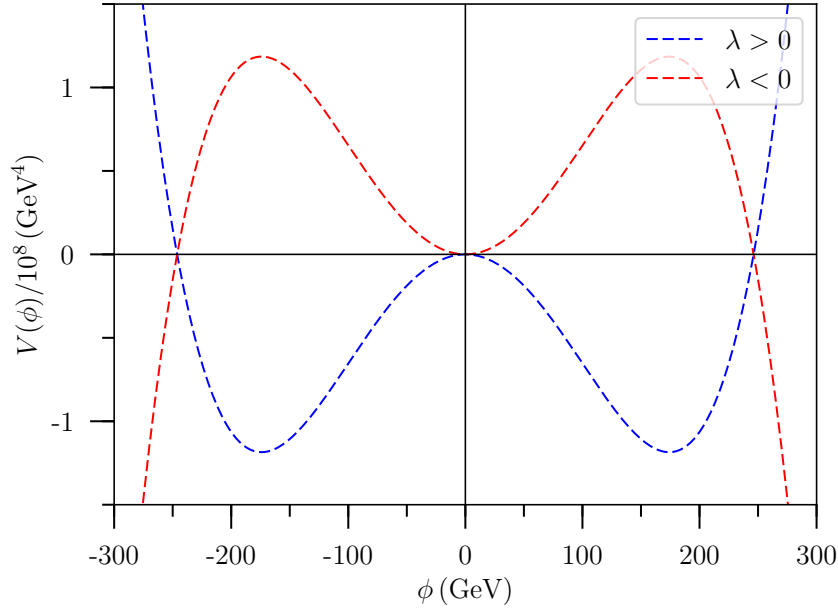
Figure 3.3: Dependence of the Higgs potential on the sign of the Higgs quartic coupling λ. When $\lambda > 0$, two stable degenerate minima exists at $\text{Re}(\phi) = \pm v/\sqrt{2}$ where $v = 246.22$ GeV is the SM Higgs VEV. However, if $\lambda < 0$, the potential is unbounded from below and no stable minima exists.

3.2.3 Vacuum stability

For small m_h, or equivalently for small λ, the top quark Yukawa term in Eq. (3.14) dominates. In this case, we get

$$\lambda(\Lambda) = \lambda(v) - \frac{3}{4\pi^2} y_t^4 \log\left(\frac{\Lambda^2}{v^2}\right). \tag{3.18}$$

When $\lambda(\Lambda) < 0$, the SM Higgs potential is unbounded from below as shown in Fig. 3.3. In this case, no stable minimum exists and a consistent theory cannot be constructed.

For the electroweak vacuum to be a stable minimum of the potential up to an energy scale Λ, the Higgs quartic self-coupling must remain positive, i.e., $\lambda(\Lambda) > 0$. This gives the following lower bound on the Higgs boson mass

$$m_h^2 > \frac{3v^2}{2\pi^2} y_t^4 \log\left(\frac{\Lambda^2}{v^2}\right). \tag{3.19}$$

3.2.4 Electroweak precision measurements

In the SM, virtual excitations of the Higgs field contribute to several physical observables such as the W boson mass, leptonic and hadronic asymmetries, and other electroweak precision observables (EWPO). By performing a precision fit to all measured electroweak observables, the Higgs boson mass can be extracted indirectly. Extensive studies have been carried out in this direction by the LEP Electroweak and Higgs Working Groups [59, 60].
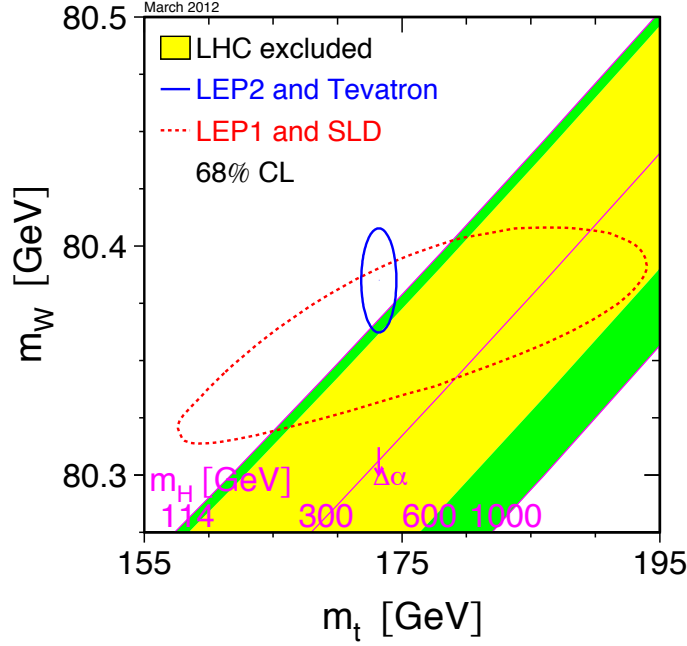
Figure 3.4: Comparison between the indirect (LEP1, SLD; dotted red contour) and direct (LEP2, Tevatron; solid blue contour) measurements of m_W and m_t. In both cases, 68% C.L. contours are shown. The arrow labelled $\Delta\alpha$ shows the variation of the SM relation if the fine-structure constant $\alpha(m_Z^2)$ is varied by 1σ from its central value. Figure from Ref. [59].

The correlations between the Higgs boson mass m_h, the W boson mass m_W, the top quark mass m_t and the precision data are shown in Figs. 3.4 and 3.5. Apart from an excellent agreement between the indirect determination of m_W, m_t and their experimental measurements, the 68% C.L. contours from the LEP, SLD and Tevatron experiments in Fig. 3.4 favour a SM-like Higgs boson with a mass below 200 GeV. Thus, if no new physics exists around the weak scale, all available electroweak precision data are consistent with $m_h = 94^{+29}_{-24}$ GeV for $m_t = 173.2 \pm 0.9$ GeV.

The exact value of the Higgs boson mass from the electroweak precision fit strongly depends on the theoretical predictions of physical observables. In general, these observables include strong and electroweak corrections at different orders in the perturbation theory. For instance, the magenta arrow in Fig. 3.4 shows how the yellow band would move if the QED fine-structure constant $\alpha(m_Z^2)$ is varied by 1σ from its central value. This variation also depends on the fit input parameters. In Fig. 3.5, we can see that m_h grows for larger m_t and smaller m_W.

3.2.5   Fine-tuning

One aspect of the Higgs sector that is traditionally perceived as problematic is that higher order corrections to the square of the Higgs boson mass parameter μ^2 generate quadratic ultraviolet divergences. This is expected in a ϕ^4 theory. It does not pose a renormalisability problem as a ϕ^4 theory is in fact renormalisable. However, these quadratic divergences
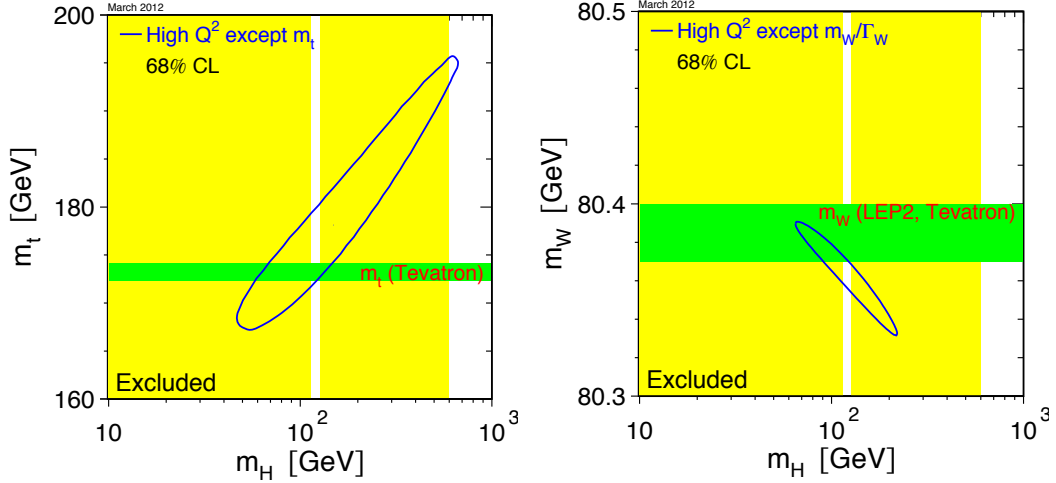
Figure 3.5: The 68% C.L. contours in the (m_h, m_t) (*left*) and (m_h, m_W) (*right*) plane. The precision fit includes all data except the direct measurement of m_t as indicated by the shaded horizontal band of $\pm 1\sigma$ width. The vertical band shows the 95% C.L. exclusion limit on the Higgs boson mass from direct Higgs searches. Figure from Ref. [59].

leave an inelegant feature that the Higgs boson renormalised mass squared has to result from an *adjusted* or a *fine-tuned* balance between μ^2 and a counterterm that is proportional to the ultraviolet cut-off scale. If the physical Higgs boson mass is around the electroweak scale, this can cause a fine-tuning of several orders of magnitude when the scale of new physics Λ is well above the electroweak scale. Ultimately, this is related to a symmetry principle or a lack thereof. Indeed, setting the scalar masses to zero in the Lagrangian does not restore any symmetry to the model. Thus, the scalar masses are not protected against large corrections.

The condition of no fine-tuning in the SM can be softened and translated into a maximum amount of allowed fine-tuning [61]. This can be directly related to the scale of new physics. As discussed earlier, the tree-level Higgs boson mass after EWSB is $m_h^2 = -2\mu^2$. Higher order corrections to m_h^2 can be calculated as loop corrections to μ^2. By interpreting the SM as an effective theory limit of a more general theory at scale Λ, the most general form of μ^2 with all loop corrections is given by

$$\widetilde{\mu}^2 = \mu^2 + \Lambda^2 \sum_{n=0}^{\infty} c_n(\lambda_i) \log^n\left(\frac{\Lambda}{Q}\right), \tag{3.20}$$

where Q is the renormalisation scale and λ_i are a set of input parameters/couplings. The coefficients c_n can be deduced from the calculation of the effective potential V_{eff} at each loop order. As originally pointed out by Veltman [62], there is no fine-tuning problem if the coefficients of Λ^2 in Eq. (3.20) are zero, i.e., if the loop corrections to μ^2 vanish. This condition is known as the *Veltman condition*. Usually, it is overconstraining as the number of independent c_n (which are set to zero by the Veltman condition) can be larger than the number of input parameters λ_i. However, the Veltman condition can be relaxed by requiring that only the sum of a finite number of terms in the coefficient of Λ^2 is zero,

namely

$$\sum_{n=0}^{n_{\max}} c_n(\lambda_i) \log^n \left(\frac{\Lambda}{m_h} \right) = 0, \tag{3.21}$$

where the renormalisation scale Q has been arbitrarily set to m_h and the order n has been set to $n_{\max}$ by the required order of loop in the calculation of V_{eff}. This is based on the fact that higher orders in n come from higher loop effects which are suppressed by powers of the loop factor $1/(16\pi^2)$. By limiting n to $n_{\max}$, Eq. (3.21) can be solved. Indeed, if the scale of new physics Λ is not too far from the electroweak scale, the Veltman condition in Eq. (3.21) can be softened further by requiring

$$\sum_{n=0}^{n_{\max}} c_n(\lambda_i) \log^n \left(\frac{\Lambda}{m_h} \right) < \frac{v^2}{\Lambda^2}. \tag{3.22}$$

This condition determines a value of $\Lambda_{\max}$ such that for $\Lambda \leq \Lambda_{\max}$, the stability of the electroweak scale does not require any dramatic cancellation in $\widetilde{\mu}^2$. In other words, the renormalisation of the SM Higgs boson mass does not require any fine-tuning. For instance, when $n_{\max} = 0$,

$$c_0 = \frac{3}{32\pi^2 v^2} (2m_W^2 + m_Z^2 + m_h^2 - 4m_t^2) \tag{3.23}$$

and the stability of the electroweak scale is assured to scales up to Λ of the order of $4\pi v \simeq 2\,\text{TeV}$. For $n_{\max} = 1$, Λ can pushed up to a maximum of about $15\,\text{TeV}$, whereas for $n_{\max} = 2$, it can be roughly up to $50\,\text{TeV}$. Thus, in going up to 2-loop order, we can assure that the SM Higgs sector is free of fine-tuning up to scales which are well beyond where we hope to discover new physics.

For each value of $n_{\max}$ and $\Lambda_{\max}$, m_h becomes a function of the cut-off scale Λ. The amount of fine-tuning allowed in the theory limits the (Λ, m_h) plane. This is shown in Fig. 3.6 where the constraints from triviality, vacuum stability and electroweak precision fits are also imposed.[1]

3.3   Higgs decay branching ratios

In the SM, the Higgs boson can decay into various final states (or channels). For each channel, different search strategies are required to probe the properties of a SM-like Higgs boson. A precise determination of both the production cross-section and the decay width as well as their respective uncertainties is essential for correctly interpreting the experimental data. Here we provide a brief summary of the main decay channels of a SM-like Higgs boson and point out the main source of uncertainties in the calculation of its decay width/rate.

---

[1]For the observed Higgs boson mass around $125\,\text{GeV}$, the electroweak vacuum is in fact metastable if no new physics exist beyond the SM [63]. Intriguingly, the electroweak vacuum sits at the boundary of stability; this near-criticality makes our vacuum extremely long-lived.
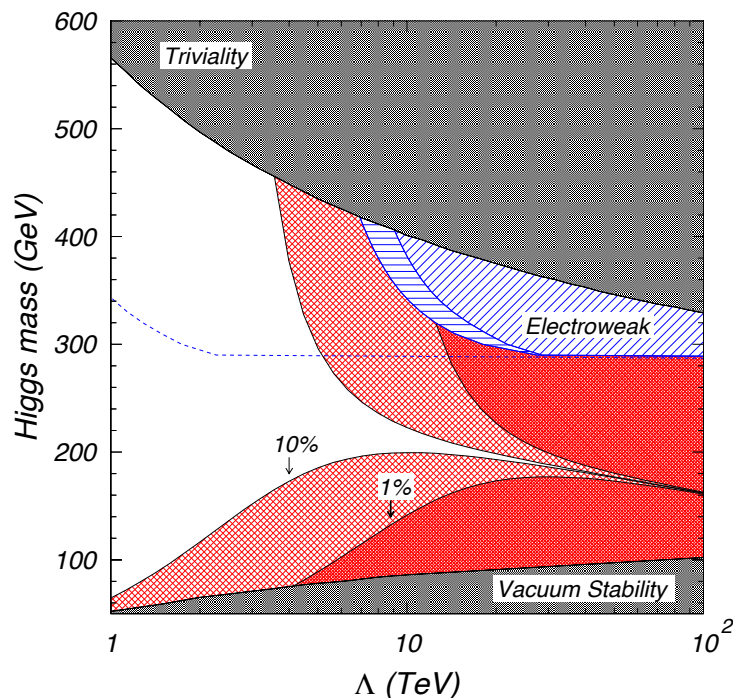
Figure 3.6: The SM Higgs boson mass as a function of the scale of new physics Λ. Constraints from triviality (dark shaded region at the top), vacuum stability (dark shaded region at the bottom) and electroweak precision fits (hatched blue region) are also shown. The white region is consistent with these constraints and corresponds to a fine-tuning of less than 10%. Figure from Ref. [61].

In chapter 2, we computed the coupling strengths between a SM Higgs boson and gauge bosons/fermions. At tree-level, the SM Higgs boson can decay into a pair of electroweak gauge bosons ($h \rightarrow W^+W^-/ZZ$), quarks ($h \rightarrow q\bar{q}$) or leptons ($h \rightarrow l\bar{l}$). At 1-loop, it can decay into two photons ($h \rightarrow \gamma\gamma$), two gluons ($h \rightarrow gg$) or a photon and a Z boson ($h \rightarrow \gamma Z$). The Higgs branching ratios and total decay width as a function of its mass are shown in the left and right panels of Fig. 3.7.

From the branching ratio plot in Fig. 3.7, we can see that a light SM Higgs boson ($m_h \lesssim 140\,\text{GeV}$) behaves very differently from a heavy Higgs boson ($m_h \gtrsim 140\,\text{GeV}$). For $m_h \lesssim 140\,\text{GeV}$, the Higgs boson mainly decays into $b\bar{b}$ and hierarchically into other lighter fermions. Loop induced processes such as $h \rightarrow gg$ also plays an important role in this region. However, this decay mode is almost useless at hadron colliders due to the large hadronic backgrounds. Although the branching ratio of $h \rightarrow \gamma\gamma$ decay is small, it offers an interesting phenomenology as the diphoton signal can be seen over large hadronic backgrounds.

In the high mass range, the Higgs boson mainly decays into W^+W^- and ZZ final states. All fermion and loop-induced decays are suppressed, except for the $h \rightarrow t\bar{t}$ decay when the Higgs boson mass is above the $t\bar{t}$ production threshold. In the intermediate mass region $m_h \sim 160\,\text{GeV}$ (i.e., below the W^+W^- and ZZ production threshold), the Higgs boson can decay into $WW^{(*)}$ and $ZZ^{(*)}$ where one of two gauge bosons is off-shell. At these masses,
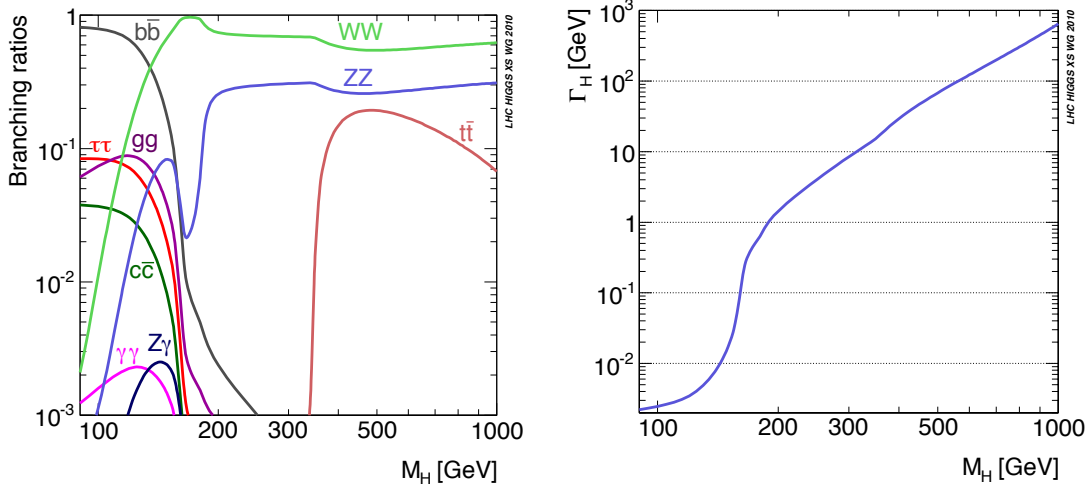
Figure 3.7: Branching ratios (*left*) and total decay width (*right*) of a SM Higgs boson as a function of its mass m_H. Figure from Ref. [5].
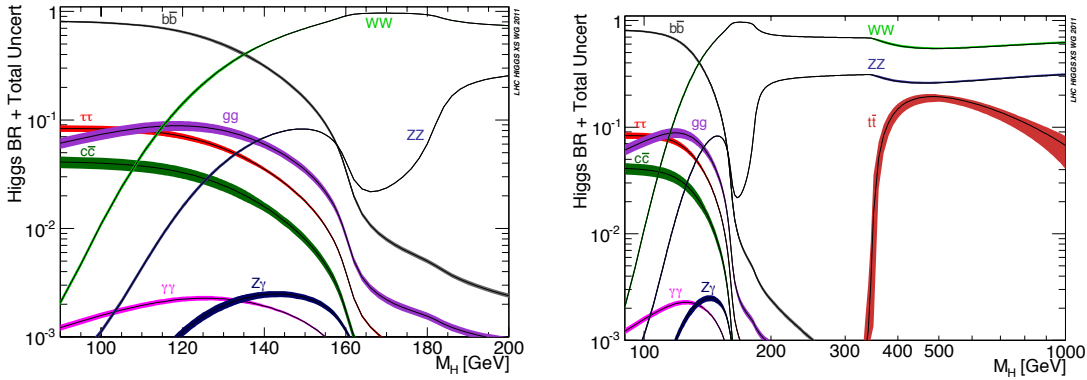
Figure 3.8: Branching ratios with theoretical uncertainties of a SM Higgs boson in the low (*left*) and high (*right*) mass range. Figure from Ref. [6].

the large hWW and hZZ coupling can compensate for the suppression in the two-body decay via $h \rightarrow b\bar{b}$. The different decay modes of light vs heavy Higgs boson determines the search strategies employed at the lepton and hadron colliders.

In Fig. 3.8, we re-plot the SM Higgs branching ratios after accounting for all available QCD and EW radiative corrections. The problem in computing the relevant orders of the QCD and EW corrections has been thoroughly investigated in the literature. Nowadays, these corrections are included in the public codes such as HDECAY [64]. Indeed, it is more accurate to represent each curve in the left panel of Fig. 3.7 as a band to account for the parametric (e.g., variation of the input parameters α_s, m_c, m_b and m_t) and theoretical (e.g., approximations made in theoretical calculations) uncertainties. Moreover, for the $h \rightarrow WW$ and $h \rightarrow ZZ$ decays, the full decay chains into all possible four-fermion final states have been computed with Next-Leading-Order (NLO) QCD and EW corrections. These have been used to estimate the overall uncertainties shown in Fig. 3.8.

The theoretical uncertainties are most relevant for the $h \rightarrow gg$, $h \rightarrow Z\gamma$ and $h \rightarrow t\bar{t}$ decays where they can reach up to $\mathcal{O}(10\%)$. For the $h \rightarrow b\bar{b}$, $h \rightarrow c\bar{c}$ and $h \rightarrow \tau^+\tau^-$

decays, the uncertainties are below a few percent. Parametric uncertainties are most relevant for the $h \to c\bar{c}$ and $h \to gg$ decays which can reach up to $\mathcal{O}(10\%)$ and $\mathcal{O}(5\%)$ respectively. These are mainly induced by the parametric uncertainties in α_s and m_c. For the $h \to \gamma\gamma$ decay, the total uncertainty can reach up to 5% in the relevant Higgs mass range. Both the theoretical and parametric uncertainties in the $h \to ZZ$ and $H \to WW$ decays are at the level of 1% over the full Higgs mass range.

3.3.1   Higgs decay into gauge bosons

The tree-level decay rate for $h \to VV$ where $V \in (W^\pm, Z)$ is [7]

$$\Gamma(h \to VV) = \frac{G_F m_h^3}{16\sqrt{2}\pi} \delta_V \left(1 - \tau_V + \frac{3}{4}\tau_V^2\right)\beta_V, \qquad (3.24)$$

where $\beta_V = \sqrt{1 - \tau_V}$, $\tau_V = 4m_V^2/m_h^2$, $\delta_W = 2$ and $\delta_Z = 1$. Below the W^+W^- and ZZ production threshold, the SM Higgs boson can decay into gauge bosons via three (four)-body decays which are mediated by $WW^{(*)}(W^{(*)}W^{(*)})$ or $ZZ^{(*)}(Z^{(*)}Z^{(*)})$. As evident in Fig. 3.7, the off-shell decays $h \to WW^{(*)}$ and $h \to ZZ^{(*)}$ are relevant in the intermediate mass range around $m_h \simeq 160\,\text{GeV}$ where they compete and overcome the $h \to b\bar{b}$ decay mode.

The decay rates for $h \to VV^* \to Vf_i\bar{f}_i$ are given by [7]

$$\Gamma(h \to WW^{(*)}) = \frac{3g^4 m_h}{512\pi^3}\mathcal{F}\left(\frac{m_W}{m_h}\right), \qquad (3.25)$$

$$\Gamma(h \to ZZ^{(*)}) = \frac{g^4 m_h}{2048(1 - s_W^2)^2\pi^3}\left(7 - \frac{40}{3}s_W^2 + \frac{160}{9}s_W^4\right)\mathcal{F}\left(\frac{m_Z}{m_h}\right), \qquad (3.26)$$

where $s_W = \sin\theta_W$ is the sine of the Weinberg angle. The function $\mathcal{F}(x)$ is given by

$$\mathcal{F}(x) = -(1 - x^2)\left(\frac{47}{2}x^2 - \frac{13}{2} + \frac{1}{x^2}\right) - 3(1 - 6x^2 + 4x^4)\log(x)$$
$$+ \frac{3(1 - 8x^2 + 20x^4)}{\sqrt{4x^2 - 1}}\arccos\left(\frac{3x^2 - 1}{2x^3}\right).$$

3.3.2   Higgs decay into fermions

The tree-level decay rate for $h \to f\bar{f}$ where $f \in (q, l)$ is [7]

$$\Gamma(h \to f\bar{f}) = \frac{G_F m_h}{4\sqrt{2}\pi}N_c m_f^2\beta_f^3, \qquad (3.27)$$

where $\beta_f = \sqrt{1 - \tau_f}$, $\tau_f = 4m_f^2/m_h^2$, $N_c = 1\,(3)$ for leptons l (quarks q). The QCD corrections dominate over other radiative corrections and modify the rate by

$$\Gamma(h \to q\bar{q})_{\text{QCD}} = \frac{3G_F m_h}{4\sqrt{2}\pi}\overline{m}_q^2(m_h)\beta_q^3\left[\Delta_{\text{QCD}} + \Delta_t\right], \qquad (3.28)$$
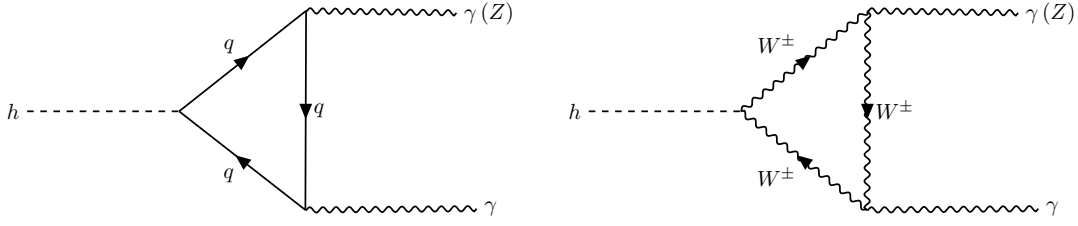
Figure 3.9: Feynman diagrams for the Higgs decay into two photons via a quark (*left*) and $W^\pm$ boson (*right*) loop.

where Δ_t denotes the QCD corrections arising from a top quark loop. Up to 3-loop order, these are given by

$$\Delta_{\text{QCD}} = 1 + 5.67 \left(\frac{\alpha_s(m_h)}{\pi} \right) + (35.94 - 1.36 N_f) \left(\frac{\alpha_s(m_h)}{\pi} \right)^2$$
$$+ (164.14 - 25.77 N_f + 0.26 N_f^2) \left(\frac{\alpha_s(m_h)}{\pi} \right)^3,$$

$$\Delta_t = \left(\frac{\alpha_s(m_h)}{\pi} \right)^2 \left[1.57 - \frac{2}{3} \log \left(\frac{m_h^2}{m_t^2} \right) + \frac{1}{9} \log^2 \left(\frac{\overline{m}_q^2(m_h)}{m_h^2} \right) \right],$$

where $\alpha_s(m_h)$ and $\overline{m}_q(m_h)$ are the renormalised running QCD coupling and quark mass in the $\overline{MS}$ scheme.

3.3.3   Loop-induced Higgs decays

The $h\gamma\gamma$ and $h\gamma Z$ couplings are induced at 1-loop via a fermion and a $W^\pm$ boson loop. These interactions are shown by the Feynman diagrams in Fig. 3.9. At the lowest order, the decay rate for $h \to \gamma\gamma$ is [7]

$$\Gamma(h \to \gamma\gamma) = \frac{G_F \alpha^2 m_h^3}{128 \sqrt{2} \pi^3} \left| \sum_f N_c^f Q_f^2 \mathcal{A}_f^h(\tau_f) + \mathcal{A}_W^h(\tau_W) \right|^2, \qquad (3.29)$$

where $N_c^f = 1$ (3) for $f = l$ (q), $\tau_f = 4m_f^2/m_h^2$, $\tau_W = 4m_W^2/m_h^2$ and Q_f is the electric charge of the fermion f. The form factors $\mathcal{A}_f^h$ and $\mathcal{A}_W^h$ are given by

$$\mathcal{A}_f^h = 2\tau \left[1 + (1 - \tau) f(\tau) \right], \quad \mathcal{A}_W^h = - \left[2 + 3\tau + 3\tau(2 - \tau) f(\tau) \right], \qquad (3.30)$$

where

$$f(\tau) = \begin{cases} \arcsin^2(1/\sqrt{\tau}), & \tau \geq 1, \\ -\frac{1}{4} \left[\log \left(\frac{1 + \sqrt{1-\tau}}{1 - \sqrt{1-\tau}} \right) - i\pi \right]^2, & \tau < 1. \end{cases} \qquad (3.31)$$

The decay rate for $h \to \gamma Z$ is given by [7]

$$\Gamma(h \to \gamma Z) = \frac{G_F^2 m_W^2 \alpha m_h^3}{64\pi^4} \left(1 - \frac{m_Z^2}{m_h^2} \right)^3 \left| \sum_f \mathcal{A}_f^h(\tau_f, \lambda_f) + \mathcal{A}_W^h(\tau_W, \lambda_W) \right|^2, \qquad (3.32)$$

where $\tau_i = 4m_i^2/m_h^2$ and $\lambda_i = 4m_i^2/m_Z^2$ for $i \in (f, W)$. The form factors $\mathcal{A}_f^h(\tau, \lambda)$ and $\mathcal{A}_W^h(\tau, \lambda)$ are

$$\mathcal{A}_f^h(\tau, \lambda) = \frac{2N_c^f Q_f \left(I_3^f - 2Q_f \sin^2 \theta_W\right)}{\cos \theta_W} [\mathcal{I}_1(\tau, \lambda) - \mathcal{I}_2(\tau, \lambda)],$$

$$\mathcal{A}_W^h(\tau, \lambda) = \cos \theta_W \left\{ \left[\left(1 + \frac{2}{\tau}\right) \tan^2 \theta_W - \left(5 + \frac{2}{\tau}\right) \right] \mathcal{I}_1(\tau, \lambda) \right.$$
$$\left. + 4 \left(3 - \tan^2 \theta_W\right) \mathcal{I}_2(\tau, \lambda) \right\},$$

where I_3^f is the weak isospin of the fermion f and

$$\mathcal{I}_1(\tau, \lambda) = \frac{\tau \lambda}{2(\tau - \lambda)} + \frac{\tau^2 \lambda^2}{2(\tau - \lambda)^2} [f(\tau) - f(\lambda)] + \frac{\tau^2 \lambda}{(\tau - \lambda)^2} [g(\tau) - g(\lambda)],$$

$$\mathcal{I}_2(\tau, \lambda) = -\frac{\tau \lambda}{2(\tau - \lambda)} [f(\tau) - f(\lambda)].$$

The function $f(\tau)$ is same as in Eq. (3.31), whereas $g(\tau)$ is defined as

$$g(\tau) = \begin{cases} \sqrt{\tau - 1} \arcsin(1/\sqrt{\tau}), & \tau \geq 1, \\ \frac{\sqrt{1-\tau}}{2} \left[\log \left(\frac{1 + \sqrt{1-\tau}}{1 - \sqrt{1-\tau}} \right) - i\pi \right], & \tau < 1. \end{cases}$$

For the $h \to \gamma\gamma$ and $h \to \gamma Z$ decays, the QCD and EW corrections are small. For more details about these corrections, see Ref. [57].

The $h \to gg$ decay is only induced by a fermion loop. At the lowest order, the decay rate is given by [7]

$$\Gamma(h \to gg) = \frac{G_f \alpha_s^2 m_h^3}{36\sqrt{2}\pi^3} \left| \frac{3}{4} \sum_q \mathcal{A}_q^h(\tau_q) \right|^2, \tag{3.33}$$

where $\tau_q = 4m_q^2/m_h^2$ and $\mathcal{A}_q^h$ is same as $\mathcal{A}_f^h$ in Eq. (3.30). For this decay mode, the QCD corrections have been calculated up to Next-to-Next-to-leading-order (NNLO) in the $m_t \to \infty$ limit [7].

3.4 Higgs searches at colliders

The search for a SM-like Higgs boson was one of the main goals of both the Tevatron and the LHC. The LEP experiment finished its run after setting a lower bound on a SM-like Higgs boson mass of roughly 114.4 GeV. On the other hand, the Tevatron experiment excluded various Higgs boson masses and actively analysed the data collected during its second run.

Since the start of the LHC, it has broken records in collecting huge amounts of data to confirm and extend the Tevatron exclusion bounds. It also promised to confirm or exclude the existence of a SM-like Higgs boson by the end of 2012. Indeed, on 4th July 2012,
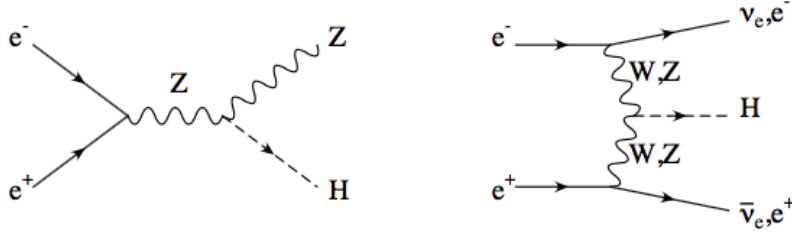
Figure 3.10: Dominant production modes for a SM-like Higgs boson at the LEP experiment. Figure from Ref. [7].

both the ATLAS and CMS experiments at the LHC announced the discovery of a SM-like Higgs boson with a mass around 125 GeV. Only 2 days prior to the announcement, the CDF and DØ experiments at the Tevatron presented their results and showed how their 2012 dataset would confirm or at least not contradict a Higgs boson discovery with a mass around 126 GeV.

3.4.1 Direct bounds from LEP

The LEP experiment performed a search for a SM-like Higgs boson between $\sqrt{s} = 189$ GeV and 209 GeV. At these energies, the Higgs boson is mainly produced via a Z boson Higgs-stralung process, $e^+e^- \to Z^{(*)} \to hZ$ and to a lesser extent via a $W^\pm/Z$-fusion, $e^+e^- \to W^+W^-/ZZ \to h\nu_e\bar{\nu}_e/he^+e^-$. These two production modes are shown by the Feynman diagrams in Fig. 3.10.

When a Higgs boson is produced, it mainly decays into $b\bar{b}$ and more rarely into $\tau^+\tau^-$. The four LEP experiments looked for the following search channels: a four jet final state ($h \to b\bar{b}$, $Z \to q\bar{q}$); a final state with missing energy ($h \to b\bar{b}$, $Z \to \nu\bar{\nu}$); a leptonic final state, ($h \to b\bar{b}$, $Z \to l^+l^-$); and a τ-lepton final state ($h \to b\bar{b}$, $Z \to \tau^+\tau^-$ and $h \to \tau^+\tau^-$, $Z \to q\bar{q}$). In the absence of a statistically significant signal, the LEP experiment placed a 95% C.L. lower limit on a SM-like Higgs boson of $m_h > 114.4$ GeV.

3.4.2 Higgs production at hadron colliders

At the hadron colliders, a SM-like Higgs boson can be produced via the parton level processes shown in Figs. 3.11 and 3.12.

The production cross sections for a SM-like Higgs boson at the Tevatron ($\sqrt{s} = 1.96$ TeV) and the LHC ($\sqrt{s} = 14$ TeV) are shown in Fig. 3.13. They incorporate the QCD corrections to known orders and include up-to-date input parameters. The leading production mode is the gluon fusion, $gg \to h$. Although it is a loop-induced process, its contribution to the total production cross-section is enhanced by the top quark loop. For light and intermediate Higgs boson masses, the large cross-section for this process has to compete with a large hadronic background as the Higgs boson mainly decays into $b\bar{b}$. There is no other non-hadronic probe that can be used to distinguish this mode from the
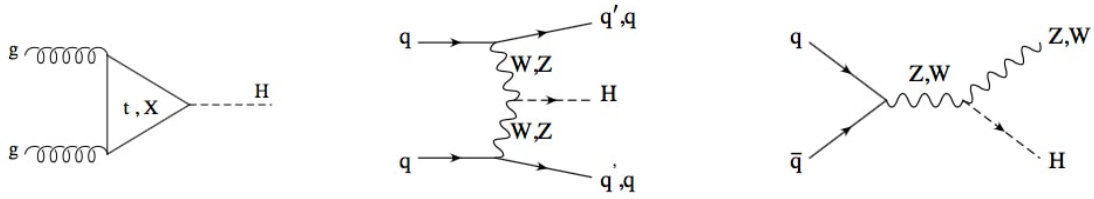
Figure 3.11: Leading production modes for a SM-like Higgs boson at the hadron colliders such as gluon fusion ($gg \rightarrow h$) (*left*), vector boson fusion ($q\bar{q} \rightarrow q\bar{q}h$) (*center*) and Higgs-stralung ($q\bar{q} \rightarrow Wh/Zh$) (*right*). Figure from Ref. [7].
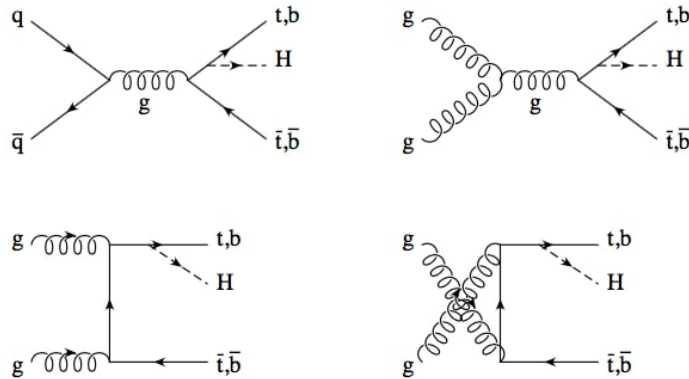
Figure 3.12: SM Higgs production at hadron colliders with heavy quarks. Figure from Ref. [7].

overall hadronic activity in the detector. To beat the background, one has to employ a sub-leading Higgs decay mode such as $h \rightarrow \gamma\gamma$. However, this dilutes the large cross-section to some extent. For Higgs masses above the ZZ threshold, the gluon fusion process and $h \rightarrow ZZ$ decay produces a very distinctive signal and makes this mode a golden channel for detection. For this reason, the gluon fusion process plays an important role at the LHC over the entire Higgs mass range. At the Tevatron, this production mechanism can only be considered if the Higgs boson mass is very close to the maximum energy limit of the machine, i.e., roughly 200 GeV.

The weak boson fusion, $q\bar{q} \rightarrow q\bar{q}h$ and associated W/Z production, $q\bar{q} \rightarrow Wh/Zh$ also have large cross sections of different relative sizes at the Tevatron and the LHC. At the Tevatron, $q\bar{q} \rightarrow Wh/Zh$ is only important if a relatively light Higgs boson, $m_h \leq 200$ GeV is accessible. In this mass range, $gg \rightarrow h$ and $h \rightarrow \gamma\gamma$ cross sections are too small, whereas $q\bar{q} \rightarrow q\bar{q}h$ is suppressed (as the initial states involve a proton and an antiproton). On the other hand, $q\bar{q} \rightarrow q\bar{q}h$ becomes instrumental at the LHC with a *pp* initial state for light and intermediate Higgs boson masses. With its characteristic final state configuration consisting of two forward jets, it greatly helps in disentangling this signal from the hadronic background using different Higgs decay modes.

Finally, the production of a SM-like Higgs boson with heavy quarks in the two channels $q\bar{q}/gg \rightarrow Q\bar{Q}h$, where $Q \in (b, t)$, is a sub-leading process at both the Tevatron and the
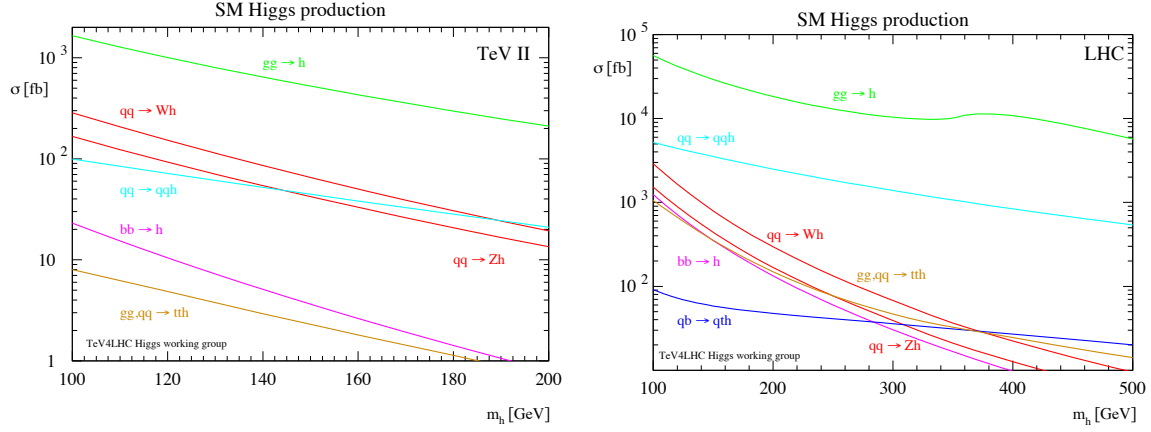
Figure 3.13: *Left panel*: SM Higgs production cross-section at the Tevatron, Run II ($\sqrt{s}$ = 1.96 TeV). *Right panel*: SM Higgs production cross-section at the LHC ($\sqrt{s}$ = 14 TeV). Figure from Ref. [8].

LHC but has a great physics potential. The associated production with $t\bar{t}$ is too small to be relevant for the Tevatron, but it plays an important role at the LHC where enough statistics is available to exploit the signature of a $t\bar{t}h$, $h \to b\bar{b}$ final state. Although this decay mode was not used for the Higgs boson discovery, it certainly provides a way of measuring the top quark Yukawa coupling. On the other hand, the production of a SM Higgs boson with a $b\bar{b}$ pair is small as the bottom quark Yukawa coupling is suppressed by the bottom quark mass m_b. Thus, the $h \to b\bar{b}$ decay mode is one of many ideal channels in searching for signs of new physics.

3.4.2.1   Higgs searches at the Tevatron

The CDF and DØ collaborations presented their combined results from direct searches for a SM-like Higgs boson in $p\bar{p}$ collisions at $\sqrt{s}$ = 1.96 TeV [9]. They combined their results from all Tevatron searches in the mass range of 100–200 GeV. Their analyses sought signals of a SM-like Higgs produced through an associated production with a gauge boson, $q\bar{q} \to hW/Z$, via gluon fusion, $gg \to h$ and vector boson fusion, $q\bar{q} \to hq\bar{q}$ corresponding to integrated luminosities from 5.4 to 10 fb^{-1}. They studied the $h \to b\bar{b}$, $h \to W^+W^-$, $h \to ZZ$, $h \to \tau^+\tau^-$ and $h \to \gamma\gamma$ decay modes. The strongest sensitivity was reached using $h \to W^+W^-$ (where W decays leptonically) in the $m_h > 125$ GeV region and $q\bar{q} \to hW/Z$, $h \to b\bar{b}$ (where W or Z decays leptonically) in the $m_h < 125$ GeV mass region.

To quantify the expected sensitivity across the entire mass range, CDF and DØ collaborations studied the distribution of log-likelihood ratios (LLR) for two different hypothesis (signal-plus-background or background-only). Their results were presented in terms of LLR$_b$ and LLR$_{s+b}$ defined as

$$\text{LLR} = -2\log\frac{p(\text{data}|H_1)}{p(\text{data}|H_0)}, \tag{3.34}$$

where H_1 denotes the test hypothesis which admits the presence of SM backgrounds and a Higgs boson signal, whereas H_0 is the null hypothesis, i.e., SM background only. The data is either an ensemble of pseudo-experimental data constructed from the expected signal and background events or the observed experimental data. The probabilities p are computed using the best-fit values of the nuisance parameters for each pseudo-experiment, separately for each of the two hypotheses, and include the Poisson probabilities of observing the data multiplied by Gaussian priors for the values of the nuisance parameters.

The CL_s technique involves computation of two p-values, CL_{s+b} and CL_b [65, 66]. The latter is defined by

$$1 - \mathrm{CL}_b = p(\mathrm{LLR} \leq \mathrm{LLR}_{\mathrm{obs}}|H_0), \tag{3.35}$$

where $\mathrm{LLR}_{\mathrm{obs}}$ is the value of the test statistic computed for the data and $1 - \mathrm{CL}_b$ is the probability of observing a signal-plus-background-like outcome without the presence of a signal, i.e., the probability that an upward fluctuation of the background provides a signal-plus-background-like response as observed in data. The other p-value is defined by

$$\mathrm{CL}_{s+b} = p(\mathrm{LLR} \geq \mathrm{LLR}_{\mathrm{obs}}|H_1). \tag{3.36}$$

This corresponds to the probability of measuring a downward fluctuation in the sum of signal and background in the data. A small value of CL_{s+b} reflects inconsistency with H_1. It is also possible to observe a downward fluctuation in the data even when a signal is absent. A small value of CL_{s+b} is possible even if the expected signal is small to be untestable with an experiment. To minimise the possibility of excluding a signal with insufficient sensitivity (an outcome that is expected about 5% of the time at the 95% C.L. for full coverage), we can use the quantity

$$\mathrm{CL}_s = \frac{\mathrm{CL}_{s+b}}{\mathrm{CL}_b}. \tag{3.37}$$

If $\mathrm{CL}_s < 0.05$ for a particular choice of H_1, that hypothesis is deemed to be excluded at 95% C.L. In an analogous way, the expected CL_b, CL_{s+b} and CL_s values are computed from the median of the LLR distribution for the background-only hypothesis.

In the left panel of Fig. 3.14, we show the LLR distributions for the combined CDF and DØ analyses as a function of the Higgs boson mass. The solid black line represents the observed experimental data $\mathrm{LLR}_{\mathrm{obs}}$. The dashed black and red lines represent the median for the background-only hypothesis LLR_b and the signal-plus-background hypothesis LLR_{s+b}. The shaded bands represent the 1σ and 2σ departures from the median for LLR_b, assuming no signal is present, i.e., only statistical fluctuations and systematic effects. The separation between the medians of the LLR_b and LLR_{s+b} distributions provide a measure of the discriminating power of the search. Moreover, the value of $\mathrm{LLR}_{\mathrm{obs}}$ relative to LLR_{s+b} or LLR_b indicates if the data distribution resembles the case in which a signal is present or
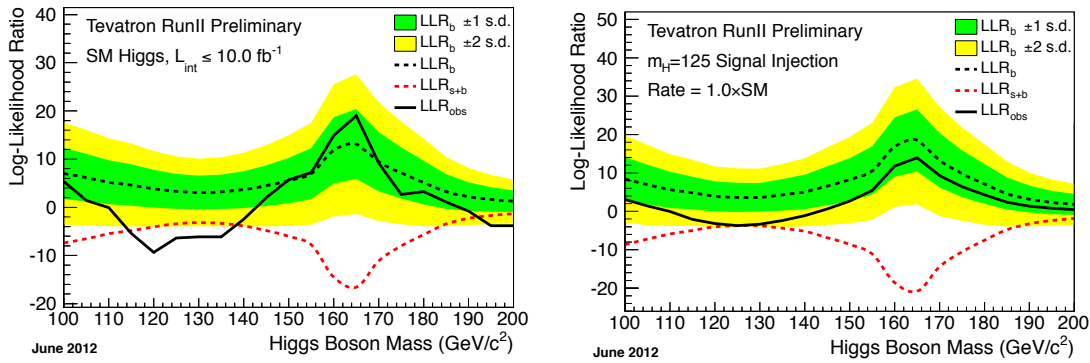
Figure 3.14: *Left panel*: Distribution of the log-likelihood ratio (LLR) as a function of the Higgs boson mass for the combined CDF and DØ analyses. *Right panel*: Same as in the left panel except the solid black corresponds to an artificially injected signal for a SM-like Higgs boson with m_h = 125 GeV. Figures from Ref. [9].

not. With this point in mind, we can see that the data is consistent with a background-only hypothesis for $m_h > 145$ GeV except above 190 GeV where the signal-plus-background and background only hypotheses cannot be easily separated. For m_h between 110 and 140 GeV, an excess is seen in the data that is consistent with the expectation for a SM-like Higgs boson in this mass range. The ability to separate LLR_{s+b} from LLR_b in this mass region, as indicated by the separation of the LLR_{s+b} and LLR_b values, is at the 2σ level. These results can be compared against an artificially injected signal for a SM-like Higgs boson with m_h = 125 GeV. This is shown in the right panel of Fig. 3.14 where the solid black line represents the artificial injected Higgs signal at m_h = 125 GeV.

The CDF and DØ collaborations have presented limits on $\mu \equiv \sigma/\sigma_{SM}$ as a function of the Higgs boson mass. This is shown in Fig. 3.15. It shows all the existing limits from LEP and the LHC up until the Higgs boson discovery. The line patterns and colours have the same meaning as in Fig. 3.14. The combined analysis excludes two Higgs mass regions, namely 100 GeV < m_h < 103 GeV and 147 GeV < m_h < 180 GeV at 95% C.L.

On the other hand, if the solid black line is above $\mu = 1$ and also somewhat above the dotted black line, it might hint that a Higgs boson exists at that mass value. If the solid black line is at the upper edge of the yellow band, there may be 95% certainty that this is above the expectation. It could point towards the existence of a SM-like Higgs boson, a sign of background processes or systematic errors that are not well understood. Indeed in Fig. 3.15, we can see that the limit (black solid curve) goes above the upper edge of the yellow band in a region between 115 and 140 GeV. This could point to the fact that a Higgs boson may indeed be contributing to the data in that mass region. Nevertheless, in the same region, the calculated (expected) background has not yet reached the same level of sensitivity as the black dashed line. In this case, the indication of a Higgs-like fluctuation is statistically weak. This excess causes the observed limits to be less stringent than expected.
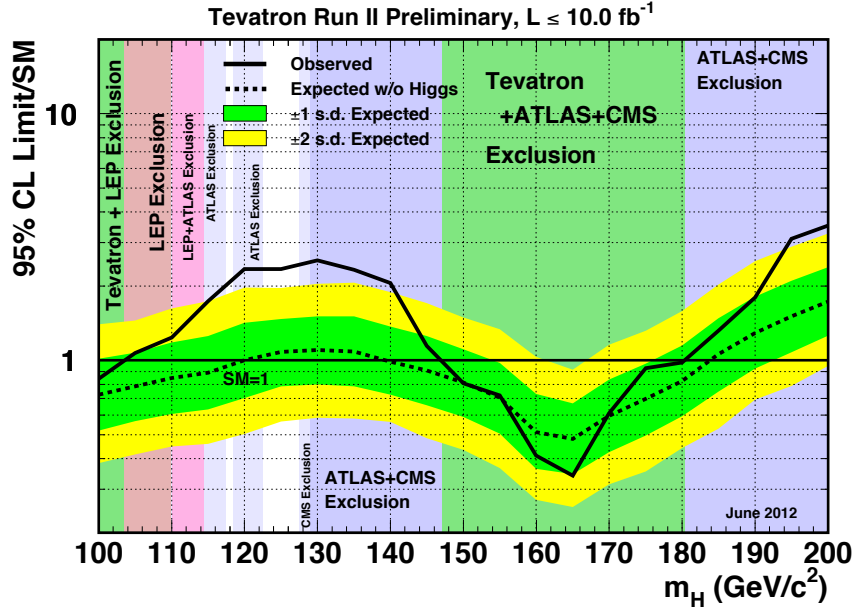
Figure 3.15: Expected and observed upper limits on the ratio of the SM Higgs production cross-section and SM expectation at the 95% C.L. from the combined CDF and DØ analysis. Figure from Ref. [9].

3.4.2.2 Higgs searches at the LHC

Since the start of the LHC, it has and is continuing to accumulate an unprecedented amount of data. In 2011, the LHC delivered an integrated luminosity of up to $5.1 \, \text{fb}^{-1}$ at $\sqrt{s} = 7 \, \text{TeV}$ to the ATLAS and CMS experiments, thus fulfilling all the data quality requirements to search for a SM-like Higgs boson. In 2012, the center-of-mass energy $\sqrt{s}$ was increased up to $8 \, \text{TeV}$. The accelerator delivered up to an extra $5.9 \, \text{fb}^{-1}$ of data by July 2012. On 4th July 2012, the discovery of a SM-like Higgs boson was announced to the world by the ATLAS and CMS collaborations. With the statistical and systematic uncertainties, the measured SM-like Higgs boson mass was

$$m_h = 126.0 \pm 0.4 \, (\text{stat.}) \pm 0.4 \, (\text{syst.}) \, \text{GeV} \tag{3.38}$$

by ATLAS [10] and

$$m_h = 125.3 \pm 0.4 \, (\text{stat.}) \pm 0.5 \, (\text{syst.}) \, \text{GeV} \tag{3.39}$$

by CMS [56] experiments. At the same time, the 95% C.L. exclusion limits for a SM-like Higgs boson were updated by ATLAS to $110 \, \text{GeV} < m_h < 122.6 \, \text{GeV}$ and $129.7 \, \text{GeV} < m_h < 558 \, \text{GeV}$, and by CMS to $110 \, \text{GeV} < m_h < 122.5 \, \text{GeV}$ and $127 \, \text{GeV} < m_h < 600 \, \text{GeV}$.

The LHC experiments have searched for a SM-like Higgs boson in the mass range between the experimental LEP bound of $114 \, \text{GeV}$ and roughly $600 \, \text{GeV}$. The main production modes in this mass range are gluon fusion ($gg \rightarrow h$) followed by the vector boson fusion ($q\bar{q} \rightarrow Vq\bar{q}$), and associated production with weak gauge bosons ($q\bar{q} \rightarrow Zh/Wh$) and
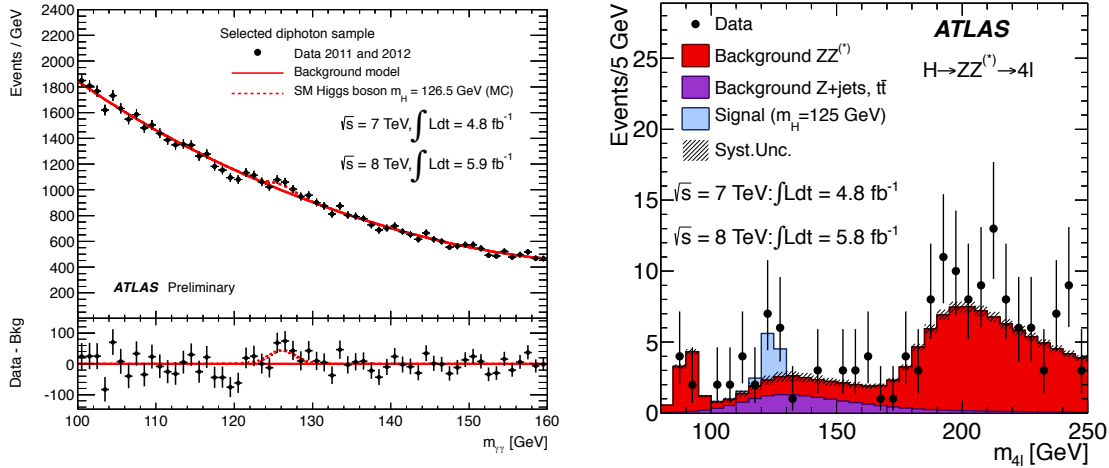
Figure 3.16: Distributions of the reconstructed invariant mass for the selected candidate events along with the total background and signal expected in the $h \to \gamma\gamma$ (*left*) and $h \to ZZ^{(*)} \to 4l$ (*right*) channels. The datasets used correspond to integrated luminosities of roughly 4.8 fb^{-1} collected at $\sqrt{s} = 7$ TeV in 2011 and 5.8 fb^{-1} at $\sqrt{s} = 8$ TeV in 2012. Figure from Ref. [10].

top quarks ($q\bar{q}, gg \to t\bar{t}h$). In the combined analysis, $h \to \gamma\gamma$, $h \to ZZ^{(*)}$, $h \to WW^{(*)}$, $h \to b\bar{b}$ and $h \to \tau^+\tau^-$ decay modes were considered.

The crucial decay modes in the discovery were $h \to \gamma\gamma$ in the low mass range and $h \to ZZ^{(*)} \to 4l$ over the entire mass range. Both decay modes provide a high-resolution invariant mass for fully reconstructed candidates in the respective mass regions. As is evident in Fig. 3.16, a clear excess in the experimental data is found around 125–127 GeV in both search channels.

The dominant systematic uncertainties are on the measurement of the integrated luminosity, theoretical predictions of the signal production cross sections and decay branching ratios, as well as those related to detector response which impact the reconstruction analyses. For more details on the uncertainties associated with the measurement of the integrated luminosity and detector responses, see Refs. [10, 56, 67, 68].

In Fig. 3.17, we show the 95% C.L. upper limits on the signal strength $\mu \equiv \sigma/\sigma_{\text{SM}}$ from ATLAS and CMS experiments [10, 56]. The various curves and bands have the same meaning as in Fig. 3.14. We can see that the observed cross-section limits exceed the expected background well beyond the 2σ level in a region where the expected background is determined with enough sensitivity to test the SM Higgs hypothesis.

After the Higgs boson was discovered at the LHC, the ATLAS and CMS experiments measured the properties of the new particle such as its spin, CP and coupling strengths to SM particles, and found them to be consistent (within uncertainties) with the SM expectation [69–73]. In Ref. [74], ATLAS and CMS experiments published a combined measurement of the Higgs boson mass using the LHC data for the $h \to \gamma\gamma$ and $h \to ZZ \to 4l$ decay channels at $\sqrt{s} = 7$ and 8 TeV. The combined mass measurement gives

$$m_h = 125.09 \pm 0.21 \, (\text{stat.}) \pm 0.11 \, (\text{stat.}) \, \text{GeV}, \tag{3.40}$$

ATLAS Preliminary 2011 + 2012 Data
Obs. $\sqrt{s}$ = 7 TeV: $\int$Ldt = 4.6-4.8 fb^{-1}
Exp. $\sqrt{s}$ = 8 TeV: $\int$Ldt = 5.8-5.9 fb^{-1}
±1 σ
±2 σ

ATLAS Preliminary 2011 + 2012 Data
- Obs. $\sqrt{s}$ = 7 TeV $\int$Ldt = 4.6-4.8 fb^{-1}
- Exp. $\sqrt{s}$ = 8 TeV $\int$Ldt = 5.8-5.9 fb^{-1}
±1 σ
±2 σ

CLs Limits

m_H [GeV]

CMS Preliminary
$\sqrt{s}$ = 7 TeV, L = 5.1 fb^{-1}
$\sqrt{s}$ = 8 TeV, L = 5.3 fb^{-1}
- Observed
- Expected (68%)
- Expected (95%)

95% CL limit on σ/σ_{SMH}

Higgs boson mass (GeV)
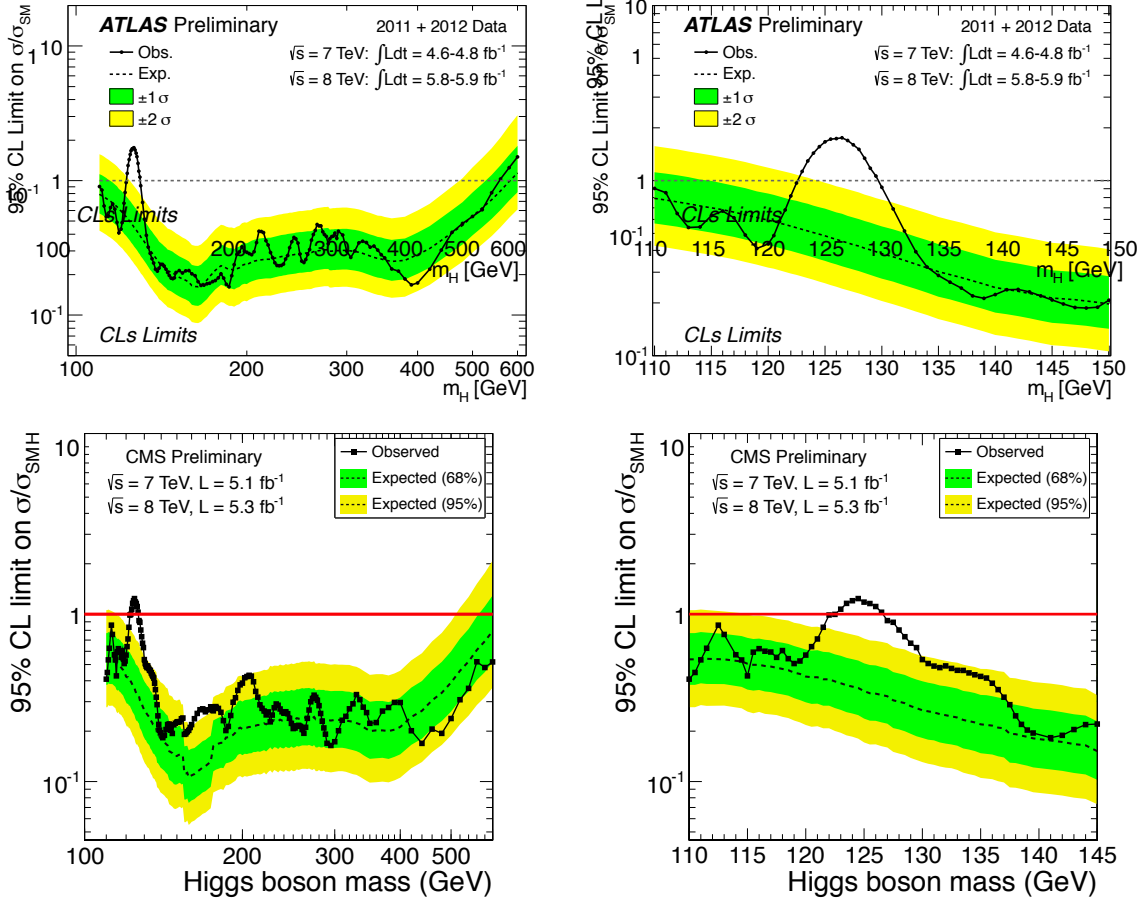
Figure 3.107: 95% C.L. upper limits on the signal strength $\mu = \sigma/\sigma_{SM}$ for light (*right*) and heavy (*left*) Higgs boson masses from the ATLAS (*top row*) and CMS (*bottom row*) experiments. The solid black curve corresponds to the observed limit, whereas the black dashed curve shows the median expected limit in the absence of a signal together with the 1σ (green) and 2σ (yellow) bands. The datasets used correspond to integrated luminosities of up to 4.8 fb^{-1} at $\sqrt{s}$ = 7 TeV (2011) and 5.8 fb^{-1} at $\sqrt{s}$ = 8 TeV (2012) for ATLAS, and up to 5.1 fb^{-1} at $\sqrt{s}$ = 7 TeV (2011) and 5.3 fb^{-1} at $\sqrt{s}$ = 8 TeV (2012) for CMS experiments. Figure from Refs. [10, 56].

where the total uncertainty is dominated by the statistical component.

The ATLAS and CMS measurements of the Higgs boson production and decay rates, and constraints on its coupling to vector bosons and fermions were combined in Ref. [11]. The main production processes used in the combination were gluon fusion (ggF), vector boson fusion (VBF), associated production with vector bosons (Vh where $V = W, Z$) and a pair of top quarks (tth). The decay modes used in the analysis were $h \to ZZ$, $h \to W^+W^-$, $h \to \gamma\gamma$, $h \to \tau^+\tau^-$, $h \to b\bar{b}$ and $h \to \mu^+\mu^-$. For $m_h = 125.09$ GeV from Eq. (3.40), its decay branching ratios are summarised in Table 3.1.

The signal strength μ is defined as the ratio of the measured Higgs boson rate to its SM prediction. For a specific production process and decay mode $i \to h \to f$, the signal strength for the production μ_i and decay μ^f is defined as

$$\mu_i = \frac{\sigma_i}{(\sigma_i)_{\mathrm{SM}}}, \quad \mu^f = \frac{\mathrm{B}^f}{(\mathrm{B}^f)_{\mathrm{SM}}}. \tag{3.41}$$

Decay mode	Branching ratio [%]
$h \to b\bar{b}$	57.5 ± 1.9
$h \to W^+W^-$	21.6 ± 0.9
$h \to gg$	8.56 ± 0.86
$h \to \tau^+\tau^-$	6.30 ± 0.36
$h \to c\bar{c}$	2.90 ± 0.35
$h \to ZZ$	2.67 ± 0.11
$h \to \gamma\gamma$	0.228 ± 0.011
$h \to Z\gamma$	0.155 ± 0.014
$h \to \mu^+\mu^-$	0.022 ± 0.001

Table 3.1: SM predictions for the decay branching ratios of a Higgs boson with $m_h = 125.09\,\text{GeV}$ together with their uncertainties. Table from Ref. [33].

Here σ_i ($i = ggF$, VBF, Wh, Zh, tth) and B^f ($f = ZZ$, W^+W^-, $\gamma\gamma$, $\tau^+\tau^-$, $b\bar{b}$, $\mu^+\mu^-$) are the production cross-section for $i \to h$ and decay branching ratio for $h \to f$ respectively. The subscript "SM" refers to their respective SM predictions, thus by definition, $\mu_i = 1$ and $\mu^f = 1$ in the SM. As σ_i and B^f cannot be separated without additional assumptions, only the product of μ_i and μ^f can be measured experimentally. This leads to a signal strength μ_i^f for the combined production and decay as

$$\mu_i^f = \frac{\sigma_i \cdot B^f}{(\sigma_i)_{\text{SM}} \cdot (B^f)_{\text{SM}}} = \mu_i \cdot \mu^f. \tag{3.42}$$

The production and decay mode of the Higgs boson can be factorised such that the cross-section times branching ratio of an individual channel $\sigma(i \to h \to f)$ contributing to a measured signal yield can be parametrised as

$$\sigma_i \cdot B^f = \frac{\sigma_i(\vec{k}) \cdot \Gamma^f(\vec{k})}{\Gamma_h}, \tag{3.43}$$

where Γ_h is the total decay width of the Higgs boson and Γ^f is the partial width for Higgs boson decay into final state f. A set of coupling modifiers $\vec{k}$ is introduced to parametrise possible deviations of the Higgs boson coupling to SM bosons and fermions from the SM expectation.

In Fig. 3.18, we show the best-fit values of $\sigma_i \cdot B^f$ for each channel $i \to h \to f$ from combined ATLAS and CMS measurements [11]. The fit results are normalised to the SM predictions for the various parameters and the shaded bands indicate the theoretical uncertainties in these predictions. Only 20 parameters are shown as some are either not measured with a meaningful precision (e.g., the $h \to ZZ$ decay mode for the Wh, Zh and tth production processes) or not measured at all and thus fixed to their corresponding SM predictions (e.g., the $h \to b\bar{b}$ decay mode for the ggF and VBF production processes).

The global signal strength is the most precisely measured Higgs boson coupling-related observable, but this simple parameterisation is very model dependent as all Higgs boson
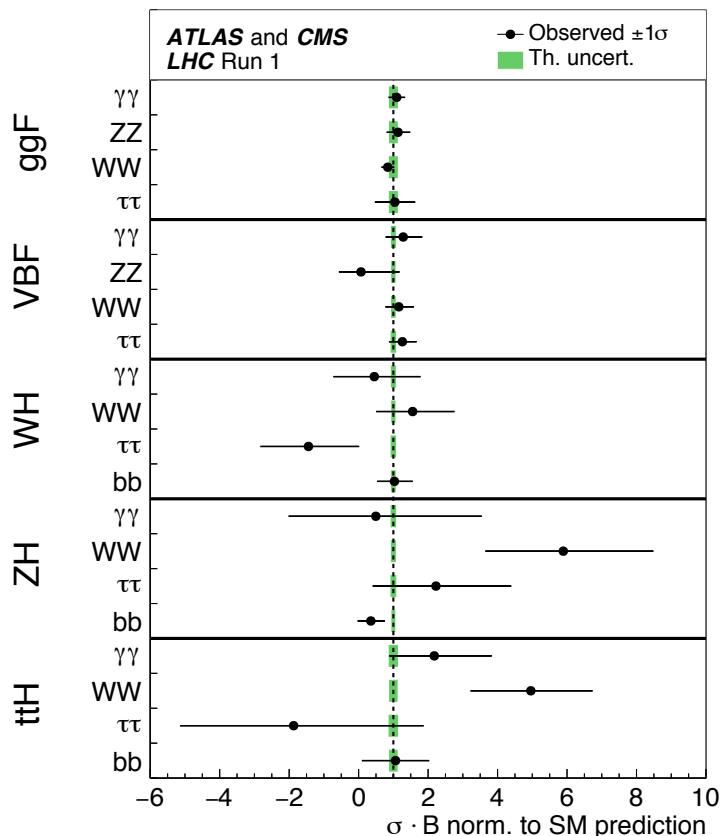
Figure 3.18: Best fit values of $\sigma_i \cdot B^f$ for each channel $i \to h \to f$ used in the combined ATLAS and CMS measurements. The dataset used corresponds to integrated luminosities per experiment of roughly 5 fb^{-1} at $\sqrt{s} = 7$ TeV (2011) and 20 fb^{-1} at $\sqrt{s} = 8$ TeV (2012). Figure from Ref. [11].

production and decay measurements are combined assuming that their ratios are the same as in the SM. The compatibility of the measurements with the SM can be tested in a less model-dependent way by relaxing these assumptions separately for the production cross sections and the decay branching ratios.

Assuming the SM values for the Higgs boson branching ratios, namely $\mu^f = 1$ in Eq. (3.41), five main Higgs boson production processes can be explored with independent signal strengths: μ_{ggF}, μ_{VBF}, μ_{Wh}, μ_{Zh} and μ_{tth}. A combined analysis of the ATLAS and CMS data is performed using these signal strengths as parameters of interest. The results are shown in Fig. 3.19 along with their total uncertainties. The *p*-value of the compatibility between the data and the SM predictions is roughly 24%.

The Higgs boson decays were also studied using six independent signal strengths, one for each decay channel included in the combination, assuming that the Higgs boson production cross sections are same as in the SM. Unlike the production signal strengths in Fig. 3.19, the decay-based signal strengths are independent of the collision centre-of-mass energy, thus the $\sqrt{s} = 7$ and 8 TeV data sets can be combined without additional assumptions. The best-fit results are shown in Fig. 3.20 for the combined ATLAS and CMS, and separately for each experiment. The *p*-value for the compatibility between the
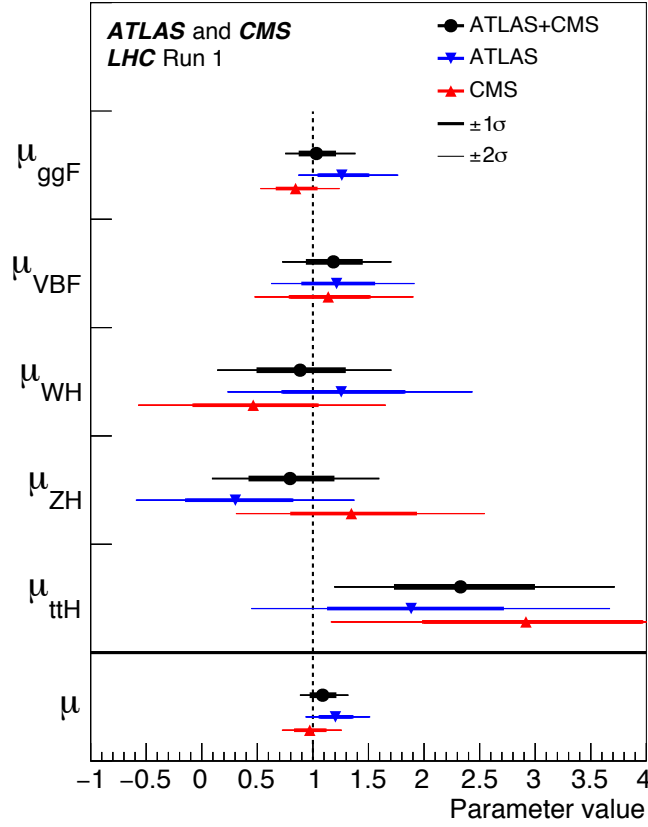
Figure 3.19: Best fit results for the production signal strengths μ_i from the combined ATLAS and CMS data. Results from each experiment are also shown. The error bars show the 1σ (thick lines) and 2σ (thin lines) C.L. intervals. The combined measurement of the global signal strength μ is also shown. The integrated luminosities per experiment and year of the dataset are same as in Fig. 3.18. Figure from Ref. [11].

data and SM predictions is about 75%.

The simplest and most restrictive signal strength parameterisation is to assume that the values of the signal strength μ_i^f defined in Eq. (3.41) are same for all production processes i and decay modes f. In this case, the SM prediction of signal yields in all categories are scaled by a global signal strength μ. Such a parameterisation provides the simplest test for the compatibility of the experimental data and SM predictions. A fit to the ATLAS and CMS data at $\sqrt{s} = 7$ and 8 TeV with μ as the parameter of interest gives the following best fit value

$$\mu = 1.09^{+0.11}_{-0.10} = 1.09^{+0.07}_{-0.07} \text{ (stat) } ^{+0.04}_{-0.04} \text{ (expt) } ^{+0.03}_{-0.03} \text{ (th-bgd) } ^{+0.07}_{-0.06} \text{ (th-sig)}, \tag{3.44}$$

where "stat" refers to uncertainties that are statistical in nature, "expt" refers to experimental uncertainties (e.g., detector-level quantities such as reconstruction efficiencies, momentum and energy resolution, etc) and those related to the finite size of the MC simulation samples, "th-bgd" refers to the theoretical uncertainties in the background only processes, and "th-sig" refers to the theoretical uncertainties that affect the Higgs boson signals. The result
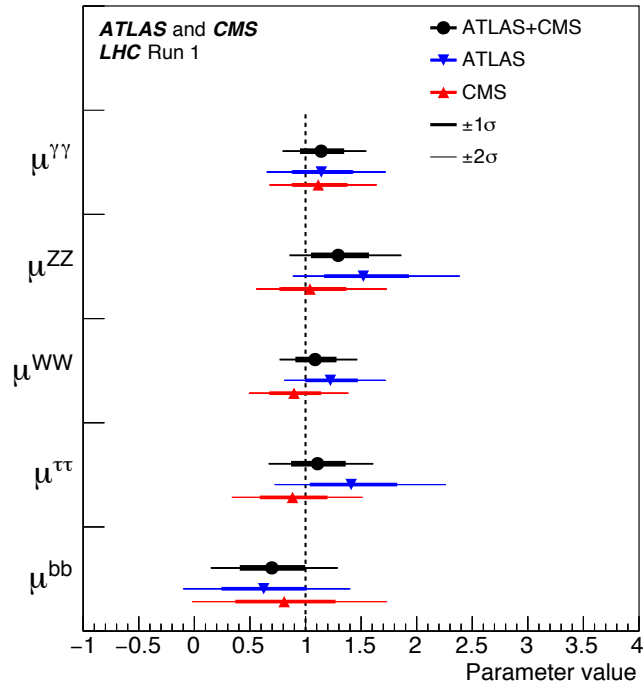
Figure 3.20: Best fit results for the decay signal strengths from the combined ATLAS and CMS data. Results from each experiment are also shown. The error bars show the 1σ (thick lines) and 2σ (thin lines) C.L. intervals. The integrated luminosities per experiment and year of the dataset are same as in Fig. 3.18. Figure from Ref. [11].

in Eq. (3.44) is consistent with the SM expectation of $\mu = 1$ within less than 1σ and the p-value of the compatibility between the data and SM predictions is about 40% [11].

Chapter 4

Dark Matter

4.1 Introduction

One of the most astounding facts of nature is that ordinary baryonic matter is not the dominant form of matter. Rather, a new form of matter known as dark matter (DM) fills our universe. It is invisible, non-luminous and roughly 5 times more abundant than ordinary matter [75]. Although its presence is yet to be detected in Earth-based laboratories, there is compelling astrophysical evidence to support its existence.

A complete understanding of DM requires knowledge from several branches of physics and astronomy. For instance, the creation of DM in the early universe is best understood through statistical mechanics and thermodynamics. On the other hand, particle physics is required to propose viable DM candidates and to predict the form of interactions with SM particles. On large scales, astrophysics and cosmology dictate the behaviour of the DM particles. Other areas of physics also come into play which makes the study of DM a diverse and interdisciplinary field.

In the field of astronomy, we rely on light (or photons) arriving from distant celestial bodies to infer their properties. For instance, when we notice dark patches against a bright background field in a distant nebula, we expect that the incoming light is absorbed by the interstellar medium. Thus, the process of photon emission and absorption allows us to trace the baryonic matter content in the universe. With the advent of modern ground- and space-based telescopes, we can detect photons from celestial bodies in different regions of the electromagnetic spectrum. These range from long wavelength radio waves to short wavelength cosmic rays.

In this chapter, we give a general overview of DM based on Refs. [12,76–82]. We begin by presenting various pieces of astrophysical evidence to support its existence. These range from observations of galactic rotation curves, the cosmic microwave background (CMB), large-scale structure to results from N-body simulations and observations of collisions of galaxy clusters. Based on the inferred properties of the DM particles, we propose viable DM candidates and discuss their production in the early universe. We also discuss various

detection methods for probing the nature of DM in the universe today. In Appendix C, we provide a summary of the Big Bang cosmology and various details used in computing the present-day abundance of the DM particles.

4.2 Evidence

4.2.1 Galactic rotation curves

Traditionally, astronomers have relied on photometry to estimate the mass of celestial objects, especially using well-defined mass-to-luminosity ratios M/L. For instance, the M/L ratio of our Sun is $M_\odot/L_\odot = 5.31 \times 10^3 \, \text{kg W}^{-1}$. Thus, the M/L ratio of celestial bodies can be measured in terms of the Sun's mass and luminosity such that $M_\odot/L_\odot = 1$ by definition. By measuring the light output from a distant object (e.g., nebulae, galaxies or clusters of galaxies), we can use the M/L ratios to estimate the mass of a distant object.

In the early 1930s, J. H. Oort discovered that the motion of stars in the Milky Way required a presence of far more galactic mass than was previously imagined. By measuring the Doppler shift of stars moving near the galactic plane, Oort was able to calculate their velocities [83]. From his finding, he made a startling discovery that the stars in the Milky Way move far too quickly, even allowing them to escape the gravitational pull of the luminous matter in the galaxy. As galaxies do not fly apart, Oort postulated that more mass was required in the Milky Way to hold these stars in their observed orbits.[1]

In 1933, a Swiss astronomer named F. Zwicky found similar indications of the missing mass but on a much larger scale. Using the Doppler shift of galaxies in the Coma cluster, Zwicky was able to calculate the velocity dispersion of galaxies in the cluster. Their speeds depended on the total mass of the cluster as each galaxy is gravitationally pulled by other galaxies. After knowing the velocity dispersion of individual galaxies, i.e., their kinetic energies, Zwicky was able to estimate the mass of the cluster using the Virial theorem [84]. Assuming only gravitational interactions and Newtonian gravity, i.e., $F \propto 1/r^2$ where r is the distance from the GC, the Virial theorem states that

$$\langle T \rangle = -\frac{1}{2}\langle U \rangle, \tag{4.1}$$

where $\langle T \rangle$ is the average kinetic energy and $\langle U \rangle$ is the average potential energy. Using this theorem, Zwicky calculated the total mass of the cluster to be roughly $4.5 \times 10^{13} \, M_\odot$. With his observation of around 1000 nebulae in the Coma cluster, the average mass of each nebula was estimated to be around $4.5 \times 10^{10} \, M_\odot$. However, this result came to Zwicky and others as a surprise since the measurement of cluster's luminosity using standard M/L

---

[1]It was also pointed out that 85% of the light from the GC could have been obscured by dust and intervening matter, or that the measurement of star velocities was in error.

ratios implied a cluster mass of only about 2% of this value.[2] In essence, the luminous matter only accounted for a small fraction of the total cluster mass. A vast majority of the cluster's mass is missing or non-luminous.

After 40 years following the discoveries of Oort, Zwicky, and others, V. Rubin and W. Ford performed an extensive study of the rotation curves of 60 isolated galaxies [85, 86]. The galaxies were chosen in such a way that the material on one side of the GC was approaching our galaxy while on the other side, it was receding away. Thus, an analysis of the spectral lines (or Doppler shifts) gave the rotational velocity of different regions in the target galaxy. In addition, the position along the spectral lines gave angular information about the distance of a point from the GC. Ideally, one should target individual stars to determine their rotational velocities. However, stars in distant galaxies are too faint to see. Thus, V. Rubin used hydrogen and helium gas clouds surrounding the hot stars as tracers of the rotational profile.

In classical Newtonian physics, the orbit of stars within a galaxy should closely mimic the rotation of planets in our solar system. Within our solar system, the rotation speed $v(r)$ of a planet at a distance r from the Sun is

$$v(r) = \sqrt{\frac{G_N M(r)}{r}}, \tag{4.2}$$

where $G_N = 6.674 \times 10^{-11} \, \mathrm{m^3 \, kg^{-1} \, s^{-2}}$ is Newton's gravitational constant,

$$M(r) = 4\pi \int_0^r dr' \, (r')^2 \rho(r') \tag{4.3}$$

is the total gravitational mass contained within a radius r from the Sun and $\rho(r')$ is a spherically-symmetric mass density profile. Thus, we expect $v(r) \propto 1/\sqrt{r}$ beyond the optical disk. This is known as the *Keplerian* behaviour.

However, Rubin's results showed an extreme deviation from the Keplerian behaviour. The collected data implied that the rotation curve of stars continue to *rise* with distance from the GC and ultimately approaches a constant steady value. This is shown for the Andromeda (M31) galaxy in Fig. 4.1. The result implied that $M(r) \propto r$ and $\rho(r') \propto 1/(r')^2$, i.e., an extended halo of DM must exist beyond the optical disk.

An intuitive way to understand Rubin's result is by following a simplified model. Consider the galaxy as a uniform sphere of mass and apply Gauss's Law for gravity as

$$\int_S \boldsymbol{g} \cdot \boldsymbol{dA} = 4\pi G_N M_{\mathrm{encl}}. \tag{4.4}$$

The left-hand side is the flux of gravitational field $\boldsymbol{g}$ passing through a closed surface S, whereas the right-hand side is proportional to the total mass enclosed by that surface. As the radius of the Gaussian surface increases, more mass is enclosed within the surface S and

---

[2]Although it was not known to Zwicky at the time, roughly 10% of the cluster mass is contained in the intracluster gas which slightly alleviates but does not solve the issue of missing mass.
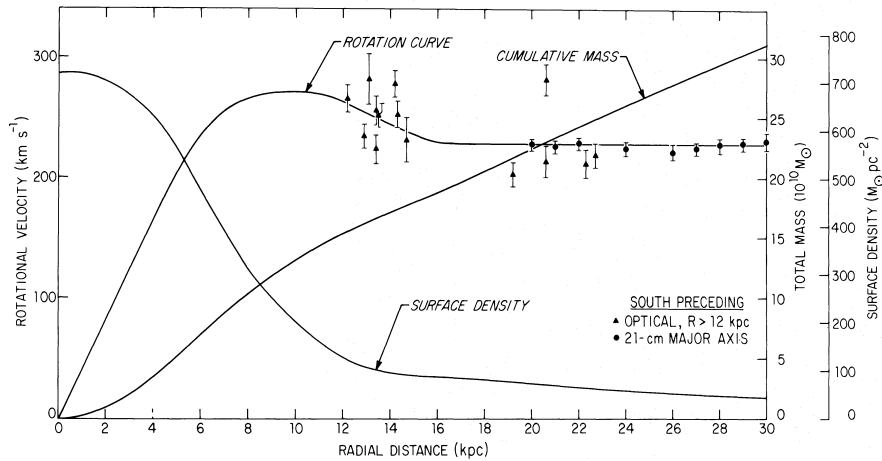
Figure 4.1: Rotation curve of the Andromeda (M31) galaxy. The filled triangles show the optical data as taken by Rubin and Ford (1970) [85], whereas the filled circles indicate the 21 cm measurements made using the 300 ft radio telescope. Figure from Ref. [87].

the gravitational field grows; the velocities can grow or remain constant as a function of the radius r since the exact behaviour depends on the mass density profile $M(r)$ in Eq. (4.2). On the other hand, if the enclosed mass decreases or remains constant as the Gaussian surface grows, the gravitational field will fall, leading to smaller rotational velocities as r increases. The former condition applies for the luminous matter near the GC, whereas on the outskirts of the galaxy, where little or no additional mass is being added, the latter condition applies. If the rotational velocities remain constant with increasing radius, the mass inside this radius must be increasing. As the density of luminous matter falls outside the central bulge of the galaxy, the missing mass must be non-luminous. Thus, mass (unlike luminosity) is not concentrated near the center of galaxies. More importantly, the distribution of light in a galaxy is not a complete guide to its total mass distribution.

4.2.2 Microlensing

In the 1970s, gravitational lensing offered a new way to probe the amount and distribution of DM in the universe. It is a direct result of Einstein's Theory of General Relativity (GR) which postulates that the universe exists within a flexible fabric of space-time. Massive objects bend this fabric and affect the motion of bodies (including light) around them. Thus, cosmologists look for a relatively close, massive object (e.g., cluster of galaxies) behind which a distant, bright object (e.g., a galaxy or a quasar) is located. If the distant galaxy is *directly* behind the cluster, a complete *Einstein ring* appears, i.e., an image in which the closer object is at the center and the ring is a lensed image of the more distant object. A schematic diagram of this lensing effect is shown in Fig. 4.2. As the likelihood of two appropriately bright and distant objects lining up perfectly with the Earth is rather low, we often see distorted images known as *arclets* or partial Einstein rings.

In 1979, D. Walsh *et al.* observed the first gravitational lensing effect [89]. While
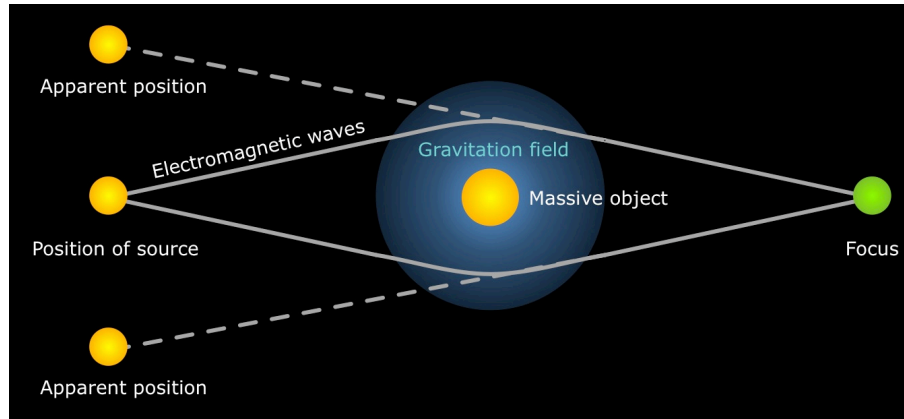
Figure 4.2: A schematic diagram of the gravitational lensing effect. The gravity of a foreground object distorts the light coming from a distant object. Figure from Ref. [88].

working at the Kitt Peak National Observatory, they found two distant objects that were separated only by 5.6 arc seconds with very similar redshifts, magnitudes and spectra. In 1988, similar observations were made by R. Lynds and V. Petrosian where multiple arclets were seen within clusters [90].

By studying the distorted image of a distant galaxy, we can infer the amount of mass within the lensing cluster. This is achieved using the following expression for the Einstein radius θ_E as

$$\theta_E = \sqrt{\frac{4G_N M}{c^2} \frac{d_{LS}}{d_L d_S}}, \tag{4.5}$$

where M denotes the total mass of the lensing cluster, d_{LS} is the distance between the lens and source, d_L is the distance to the lens and d_S is the distance to the source. However, using this expression, astronomers found that the calculated cluster mass is much larger than the mass inferred from a cluster's luminosity. For instance, A. Bargemen, R. Lynds and V. Petrosian determined that the M/L ratio of the Abell 370 cluster should be roughly 10^2–$10^3 M_\odot/L_\odot$. This places a constraint on the DM distribution within the cluster. For the galaxy cluster CL0024+1654, this is illustrated in Fig. 4.3. Thus, a vast amount of DM is required in the cluster.

Initially, astrophysical objects made up of baryonic matter were thought to account for DM. As DM is invisible and non-luminous in nature, possible astrophysical DM candidates were thought to be brown dwarfs, primordial black holes and neutron stars [93]. All of these are collectively classified as Massive Compact Halo Objects (MACHOs).

By combining theory with observations, MACHOs have been ruled as a solution to the missing mass problem in the Milky Way. Using the Hubble Space Telescope (HST) data, it was shown that low mass stars could be at most 3% of the total DM in the Milky Way [94]. A combination of theory and Hipparchos parallax data ruled out substellar objects or brown dwarfs as the primary constituent of galaxy's DM [95]. Stellar remnants were also potential DM candidates. Bounds on white dwarfs as DM candidates come from
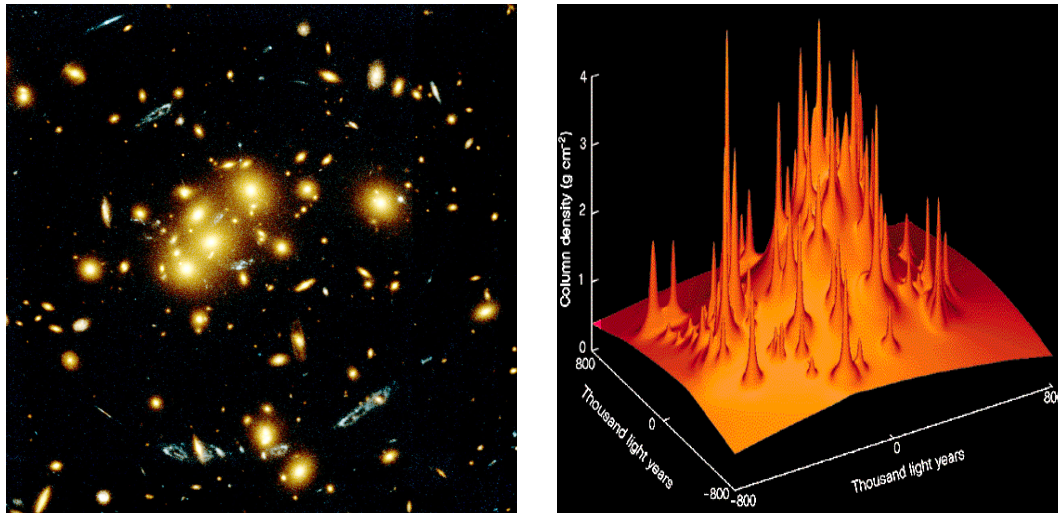
Figure 4.3: *Left panel*: Gravitational lensing of the background galaxy (shown as blue arcs) by the galaxy cluster CL0024+1654. *Right panel*: Projected density plot of the galaxy cluster CL0024+1654. The sharp peaks correspond to the individual galaxies in the cluster, whereas the smooth background component is due to dark matter. Figure from Refs. [91, 92].

several arguments [96, 97].

To hunt for MACHO-like objects, the MACHO collaboration and EROS-2 survey searched for gravitational microlensing caused by possible MACHOs in the Magellanic Clouds. The MACHO collaboration analysed the skies for such lensing events in a study of 11.9 million stars [98]. However, only 13–17 possible events were detected [99]. In 2007, EROS-2 survey [100] reported only *one* event out of a sample of 7 million stars. Thus, the low number of possible MACHOs can only account for a small fraction of the total non-luminous matter in the galaxy. In addition, these findings revealed that most of the DM can not exist in the form of baryonic astrophysical objects.

4.2.3   Big Bang Nucleosynthesis

Big bang nucleosynthesis (BBN) refers to a period of few seconds to minutes after the big bang. During this time, neutrons and protons fused to form deuterium (^{2}H), helium (^{4}He) and traces of other light elements. In fact, BBN is the largest source of deuterium in the universe as any deuterium produced or found in stars today is immediately fused to form ^{4}He. By measuring the deuterium-to-hydrogen (D/H) ratio in distant, primordial-like regions, astronomers have been able to estimate the D/H abundance directly after BBN. Based on known nuclear physics and reaction rates, BBN elemental abundance can be theoretically calculated. In fact, one of the triumphs of the big bang model is the precise agreement between theory and observational determinations of these light elemental abundances. This is shown in Fig. 4.4.

The D/H abundance is heavily dependent on the overall density of baryons in the early universe. By measuring the D/H abundance, we can obtain the overall baryon abundance
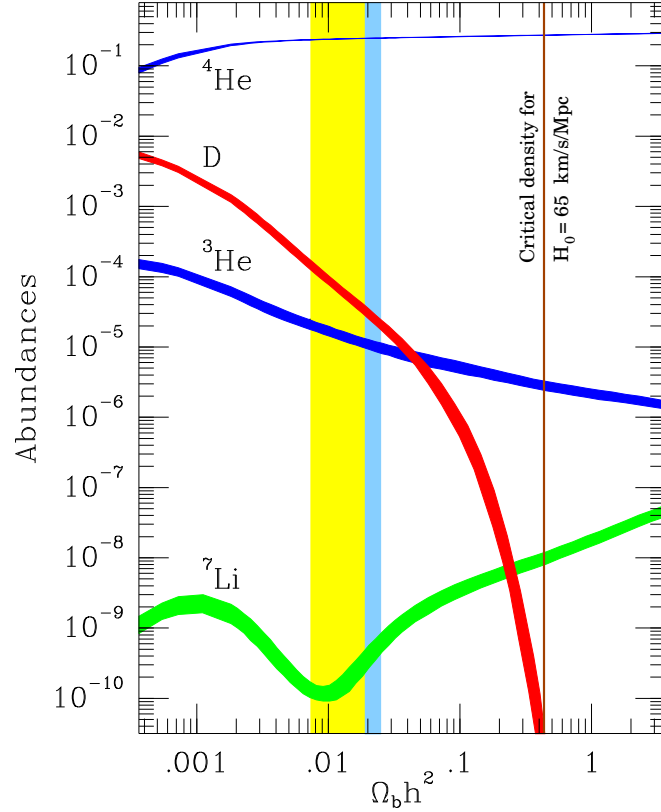
Figure 4.4: Abundance of light elements vs the baryon matter density $\Omega_b = \rho_b/\rho_c$. The width of the curves show 2σ theoretical uncertainties, whereas the vertical band shows where the predicted abundances of light elements agree with the measured values. Figure from Ref. [101].

in the universe today. This is conventionally expressed as $\Omega_b h^2$ where $\Omega_b \equiv \rho_b/\rho_c$ is the density parameter, $\rho_c = 3H_0^2 M_p^2 = 3H_0^2/(8\pi G)$ is the critical mass density and $h = H_0/(100\,\text{km}\,\text{s}^{-1}\,\text{Mpc}^{-1})$ is the reduced Hubble parameter. For more details, see Appendix C.

In Ref. [102], two possible values for $\Omega_b h^2$ are obtained (depending on which deuterium observation is chosen):

$$\Omega_b h^2 = 0.0229 \pm 0.0013, \quad \Omega_b h^2 = 0.0216^{+0.0020}_{-0.0021}. \tag{4.6}$$

Note that both values only account for about 20% of the total matter density in the universe. Thus, the observed D/H abundance provides a strong evidence for the existence of DM.

4.2.4 Cosmic Microwave Background

The cosmic microwave background (CMB) was accidentally discovered by A. Penzias and R. Wilson in 1964. It has an excess background temperature of roughly 2.73 K and provides another way to learn about the composition of the early universe.

Just after the big bang, the universe was in an extremely dense state of hot plasma that went through an initial phase of rapid expansion, then expanded at a slower, steady

rate and cooled for about 380,000 years. After some time, a stage known as the *epoch of recombination* was reached when neutral atoms started to form. As a result, the universe became transparent to electromagnetic radiation (or light). Photons that were initially trapped due to their electromagnetic interactions with charged particles became free to travel unimpeded in the universe. The photons that were released from the *surface of last scattering* have since been travelling to us. Due to the expansion of the universe, they have redshifted and appears today as a uniform background of CMB photons.

4.2.4.1 Cosmic Background Explorer (COBE)

In 1989, the Cosmic Background Explorer (COBE) satellite was launched to verify two fundamental properties of the CMB: its uniformity in temperature ($T \sim 2.73\,\text{K}$) across the sky; and to test if the CMB is nearly a perfect blackbody. Although the temperature fluctuations in the CMB are extraordinarily uniform, COBE's Differential Microwave Radiometer (DMR) discovered small anisotropies (or fluctuations) in the CMB. These fluctuations are caused by two different effects.

1. *Sachs-Wolfe effect* generates large-scale fluctuations. In regions that were more dense at the time of last scattering, lower energy photons were emitted as they had to climb over more powerful potential energy wells than photons emitted from less dense regions.

2. *Acoustic oscillations* generate small-scale fluctuations. Before the decoupling of photons, protons and photons can be modelled as a photon-baryon fluid. This fluid repeatedly went through the following life cycle.

   a) the fluid is compressed as it falls into a gravitational potential;

   b) the pressure of the fluid increases until it forces the fluid to expand outwards;

   c) the pressure of the fluid decreases as it expands until gravity pulls it back; and

   d) the process repeats until photons are decoupled at the time of recombination.

Depending on the life cycle for a portion of fluid after the photon-decoupling, the photons emerge with varying temperatures. Thus, the fluctuations in the CMB are an indication of both the initial density perturbations and the dynamics of the photon-baryon fluid. In this way, temperature fluctuations in the CMB are related to the density of baryons at the time of recombination.

Although the detection of temperature fluctuations in the CMB was a major achievement, the magnitude of the temperature variation puzzled many physicists. The fluctuations in the CMB are extremely small, roughly $30 \pm 5\,\mu\text{K}$, meaning that the CMB is uniform to 1 part in 10^5. In fact, they are too small to solely serve as the seeds of structure formation [103]. Before the time of recombination, ordinary matter could not clump
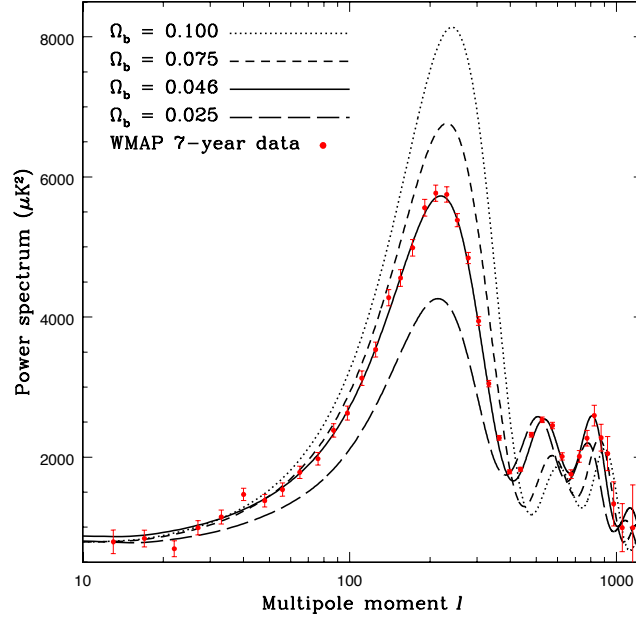
Figure 4.5: The cosmic microwave background (CMB) power spectrum for various values of $\Omega_b = \rho_b/\rho_c$ along with the 7-year WMAP data. Figure from Ref. [12].

into gravitational wells (due to the electromagnetic interactions) and begin the structure formation process. Thus, an electrically neutral form of matter is required to kick-start the structure formation process well before the time of recombination. This can of-course be achieved by introducing DM in the early universe.

4.2.4.2 Wilkinson Microwave Anisotropy Probe (WMAP)

In 2001, the Wilkinson Microwave Anisotropy Probe (WMAP) was launched with the goal of precisely measuring the CMB anisotropies. In particular, it has been able to detect temperature variations in the CMB as small as one-millionth of a degree.

Due to the increased precision of WMAP, the total matter and baryon densities were found to be [104]

$$\Omega_m h^2 = 0.1334^{+0.0056}_{-0.0055}, \quad \Omega_b h^2 = 0.02260 \pm 0.00053. \tag{4.7}$$

Note that the two numbers are different, i.e., baryonic matter is not the dominant form of matter in the universe. In fact, DM with a mass density of $\Omega_{\mathrm{DM}} h^2 = 0.1123 \pm 0.0035$ [104] makes up about 85% of the total matter density in the universe.

An analysis of the CMB allows us to discriminate between DM and ordinary matter as the two components behave differently. Unlike baryons, DM does not play any role in the photon-baryon fluid (as it is electrically neutral). The height of the first peak in the CMB power spectrum is sensitive to the baryon density $\Omega_b = \rho_b/\rho_c$ as shown in Fig. 4.5. Any shift in its value would give inconsistent result between WMAP and other CMB data.
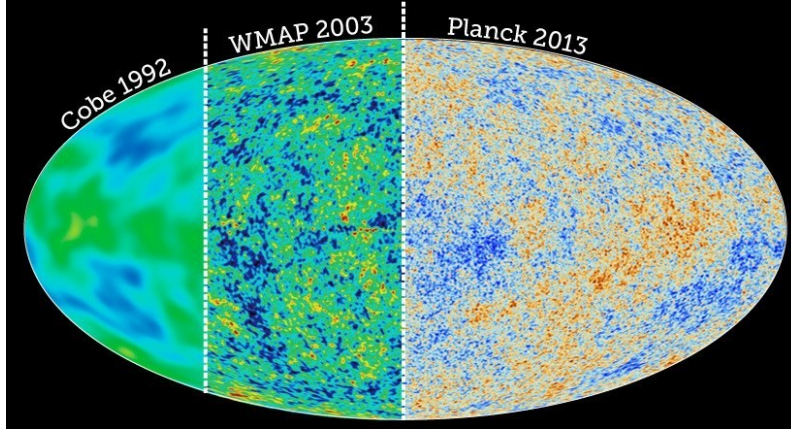
Figure 4.6: Temperature fluctuations in the CMB as measured by the COBE, WMAP and *Planck* satellite. Figure from Ref. [13].

4.2.4.3 *Planck* satellite

The *Planck* satellite (a successor to WMAP) was launched in 2009 to image the temperature and polarization fluctuations in the CMB over the entire sky with higher sensitivity and smaller angular resolution. It provided a major source of information for testing theories of the early universe and the origin of cosmic structure. The resulting map of the CMB by the *Planck* satellite can be compared against COBE and WMAP results in Fig. 4.6.

The *Planck* satellite provides the most accurate estimate of the cosmological parameters, including the average density of baryons and DM in the universe. Based on the 2015 dataset, we know that [75]

$$\Omega_\Lambda = 0.692 \pm 0.012, \qquad \Omega_m = 0.308 \pm 0.012,$$
$$\Omega_b h^2 = 0.02226 \pm 0.00023, \quad \Omega_{\mathrm{DM}} h^2 = 0.1186 \pm 0.0020, \tag{4.8}$$

where $h = H_0/(100\,\mathrm{km\,s^{-1}\,Mpc^{-1}})$ and $H_0 = 67.81 \pm 0.92\,\mathrm{km\,s^{-1}\,Mpc^{-1}}$ is the Hubble constant. These values imply that our universe is made up of roughly 69% dark energy, 26% dark matter and 5% ordinary baryonic matter. In particular, DM is roughly 5 times more abundant than ordinary matter.

4.2.5 Large-scale structures

Evidence for DM is also inferred from analysing the large-scale structures in the universe. By computing the distance to various galaxies using their redshifts, cosmologists have been able to map out the location of more than 1.5 million galaxies. For instance, the Sloan Digital Sky Survey (SDSS) has been able to create 3-dimensional maps of more than 900,000 galaxies, 400,000 stars and 120,000 quasars from its eight years of operation [105]. The observed number of galaxies support the need for DM as the current structure in the universe is a result of initial density perturbations in the early universe. Most likely, these initial density perturbations were quantum fluctuations which were magnified by inflation,

a period of rapid exponential growth about 10^{-35} seconds after the big bang. Assuming that the random fluctuations are Gaussian, the power spectrum $P(k)$ is sufficient to describe the density perturbations.

For a given $P(k)$, we can predict the large-scale structure. The converse is also true: by measuring large-scale structure (e.g., from galaxy counts and surveys), we can experimentally determine the power spectrum $P(k)$. Using this information from the galaxy surveys, the total amount of matter and baryonic matter can be estimated. The peak of $P(k)$ is sensitive to the value of Ω_m, whereas the amount of baryons affect the shape of $P(k)$ due to baryonic acoustic oscillations [106]. Using these techniques, the power spectrum from the Two-degree-Field Galaxy Redshift Survey (2dFGRS) gives

$$\Omega_m = 0.231 \pm 0.021, \quad \Omega_b/\Omega_m = 0.185 \pm 0.046. \tag{4.9}$$

Based on the SDSS data, we find that [107, 108]

$$\Omega_m = 0.286 \pm 0.018, \quad \Omega_{\text{DM}}h^2 = 0.02267 \pm 0.00058. \tag{4.10}$$

These results agree well with both the BBN and CMB predictions.

4.2.6 *N*-body simulations

The need for DM is also seen in *N*-body simulations of large-scale structure. Generally, these simulations take weeks. For instance, the MS-II tracked over 10 billion particles, each with mass $6.89 \times 10^6\ h^{-1}M_\odot$ in a volume of $(100\ h^{-1}\text{Mpc})^3$ to study DM halo structure and formation [109]. Similarly, T. Matteo *et al.* ran simulations to study the role of black holes in structure formation using 20-200 million particles in a volume of $(33.75\ h^{-1}\text{Mpc})^3$ to $(50\ h^{-1}\text{Mpc})^3$ [110].

N-body simulations without DM do not form the familiar filament and void-type structures seen in the observable universe by SDSS and other related surveys on the proper timescales. Additionally, scenarios in which DM is relativistic or *hot* finds that structure formation is retarded or *washed-out* instead of enhanced. This corresponds to a *top-down* formation, i.e., larger structures form first, eventually condensing and fragmenting into the ones that we can see today [111]. However, galaxies have been known to exist less than a billion years after the big bang, and together with the *N*-body simulations of structure formation, a *bottom-up* formation, i.e., stars followed by galaxies and cluster of galaxies is more likely [112]. Thus, not only is DM required in the universe, it must be *cold* or non-relativistic during the period of structure formation [113, 114].

4.2.7 Collision of galaxy clusters

The most recent evidence serves as a *smoking gun* signal for DM. A sub-cluster called the *bullet* collided with a larger galaxy cluster 1E 0657-56. During the collision, the galaxies
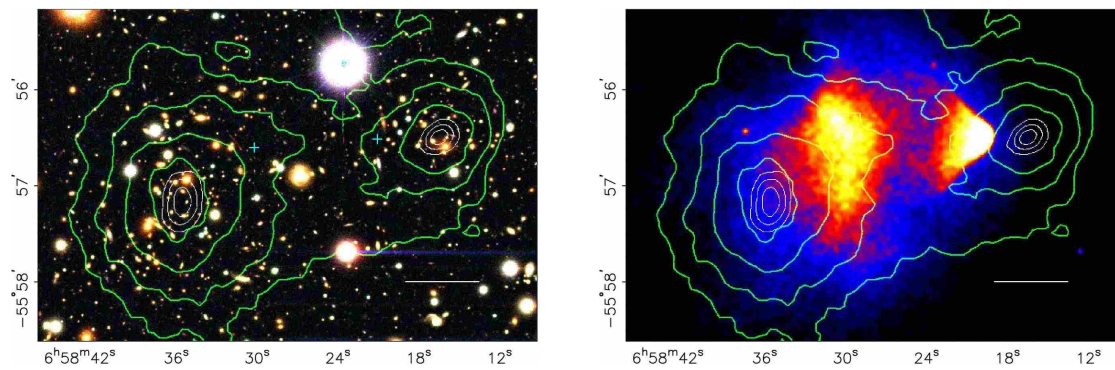
Figure 4.7: *Left panel*: Optical image of the Bullet cluster from the Magellan telescope. *Right panel*: Same as the left panel but in X-rays as measured by the Chandra X-ray telescope. Projected mass density reconstructed from weak lensing is superimposed in both panels (green contours); thin white contours indicate locations of the density peaks for the Bullet and main cluster at 68.3%, 95.5% and 99.7% C.L., separated by 720 kpc. Most of the cluster mass (blue) inferred from weak lensing lies in a location that is different from the cluster's baryonic mass (red). Figure from Ref. [115].

within the two clusters passed through each other without any interaction (as typical distances between galaxies are roughly 1 Mpc or 3.26 light years). As the majority of cluster's baryonic mass resides in the extremely hot gas between the galaxies, the collision compressed the hot gas and created shock waves. This generated high-energy X-rays that were detected by the Chandra X-ray telescope. In the right panel of Fig. 4.7, we can see a clear discrepancy between the regions that produce X-rays (where the majority of the baryonic matter lies) and maps of weak gravitational lensing (where the total mass lies). In particular, the areas of strong X-ray emission and high mass concentration *do not* overlap. Thus, the majority of mass in the cluster is non-baryonic and gravity again pointed back to the missing mass problem [115].

Similar to the bullet cluster, the galaxy cluster MACS J0025.4-1222 was formed as a result of a collision between two clusters. The collision caused a separation between the luminous matter and DM in the two clusters. In mid-2008, it was found that the behaviour of matter within this cluster was strikingly similar to the Bullet cluster [116]; the DM passed through the collision while the intergalactic gas interacted and emitted X-rays. These results confirmed the need for a collisionless DM.

In 2007, the HST detected a ring-like structure of DM from another collision of two massive galaxy clusters one to two billion years ago [117]. The DM in the two clusters collapsed towards the center but some of it began to *slosh* back out, causing the ring-shaped structure to form. By overlapping the distribution of gravitational lensing with the baryonic mass in the combined cluster, the largest discrepancy was seen between the luminous matter and DM.

In 2013, Penny *et al.* presented a study of the Perseus cluster from the HST survey [118]. They noticed that a small number of dwarf spheroidal galaxies were stable while larger

galaxies were being torn apart due to tidal forces caused by the cluster potential. They suggested that a significant amount of DM was holding the galaxies together. By finding the minimum mass required for the dwarf galaxies to survive the cluster's potential, they estimated the amount of DM required in each galaxy. Out of 25 dwarf spheroidal galaxies surveyed within the cluster, only 12 required DM in order to survive the tidal forces from the cluster potential.

4.3 Candidates

It is clear that the evidence for DM exists at small and large scales. However, its true nature is unknown to us. The measurement of the CMB allows us to calculate the present-day abundance of the DM particles, whereas *N*-body simulations of large-scale structures favour cold and collision-less DM.

Despite many successes of the SM, it fails to provide any particle DM candidates. In the SM, the only stable, electrically neutral and weakly interacting particles are the neutrinos. However, they cannot account for all of the DM due to two main reasons. Firstly, as neutrinos are relativistic, they would lead to a *top-down* structure formation which is disfavoured by *N*-body simulations. Secondly, neutrinos are ruled out as the entire solution to the missing mass problem from cosmological observations. The combined results from WMAP and large-scale structure data constrain the neutrino mass to $m_\nu < 0.23$ eV. This corresponds to a cosmological density of $\Omega_\nu h^2 < 0.0072$ [119]. Thus, neutrinos cannot be the only source of DM.

The lack of particle DM candidates in the SM motivates new physics beyond the SM (BSM). The new BSM theories must supplement the SM and provide a viable DM candidate. Many BSM theories predict new particles, often with masses comparable to those of the *W* and *Z* bosons. In many cases, the lightest of the new BSM particles are stable and can serve as DM candidates.

In the following subsection, we discuss two of the most popular particle DM candidates and the theories that lie behind them.

4.3.1 Weakly Interacting Massive Particles (WIMPs)

Among many potential DM candidates, the class of Weakly Interacting Massive Particles (WIMPs) is popular. They appear in well-motivated BSM theories. In addition, a GeV-scale WIMP with a weak interaction cross-section can naturally reproduce the observed DM abundance, leading to the so-called *WIMP miracle* [76, 120].

In the WIMP scenario, there are two possible approaches for specifying the WIMP-SM couplings as discussed below.

4.3.1.1   Top-down approach

In this approach, WIMPs are included amongst the new particle content of a BSM theory at high energies. From the details of the theory, one can derive the WIMP-SM interactions. Two popular examples that employ this approach are discussed below.

- *Supersymmetric candidates*: Supersymmetry (SUSY) introduces an additional symmetry to the SM and allows for an inter-conversion between fermions and bosons. Essentially, every fermion in the SM is associated with a supersymmetric boson and vice versa. Thus, adding SUSY into the SM effectively doubles the number of particles. Although this might seem like an unnecessary complication, SUSY has very attractive theoretical features, namely in solving the hierarchy and fine-tuning/naturalness problem [121, 122].

  In SUSY, the stability of the lightest supersymmetric particle (LSP) is guaranteed by *R*-parity [76]

  $$R \equiv (-1)^{3B+L+2s}, \tag{4.11}$$

  where $B\,(L)$ is the baryon (lepton) number and s is the particle spin. An *R*-parity of $+1$ is assigned to all SM fields and -1 to all superpartners. Thus, an even number of SUSY particles must appear in every interaction, and forbids the decay of the LSP. If the LSP is electrically neutral, it is an excellent DM candidate.

  In the particle content of the SM with SUSY, there are three potential DM candidates, namely

  - the neutralino (a superposition of the neutral superpartners of the Higgs and gauge bosons);
  - the sneutrino (the superpartner of the neutrino); and
  - the gravitino (the superpartner of the graviton which would come from a quantum theory of gravity).

  However, sneutrinos annihilate very quickly in the early universe, and their relic densities are too low to be cosmologically significant [123]. In addition, gravitinos behave as hot DM particles depending on their mass, and are disfavoured by *N*-body simulations of large-scale structure [124]. Thus, the neutralino is the preferred DM candidate in the SM with SUSY. Its relic abundance can be sizeable and of cosmological significance. The detection rates for neutralinos are high enough to be accessible in the laboratory but not high enough to be experimentally ruled out.

- *Extra dimensions*: DM candidates can come from theories of extra spatial dimensions. The idea of extra spatial dimensions was first initiated by T. Kaluza and O. Klein in early 1920s. After writing down the general theory of relativity in five

dimensions, they were able to recover four-dimensional gravity, Maxwell's equations for a vector field and an extra scalar particle [125, 126]. In their study, Klein explained the non-observation of the fifth-dimension by compactifying it on a circle with an extremely small radius about 10^{-35} cm. Initially, KK theories were on a quest to become a grand unified theory (GUT). However, the emergence of weak and strong nuclear forces as fundamental forces of nature hindered their progress.

In the late-1990s, two new scenarios with extra dimensions appeared. In Ref. [127], A. Hamed, G. Dvali and S. Dimpoulos tried to solve the hierarchy problem by assuming the existence of large extra dimensions. They made an assertion that the electroweak scale is the only fundamental scale in nature. In addition, they stated that the Planck scale appears small due to the presence of the extra spatial dimensions. On the other hand, L. Randall and R. Sundum proposed infinitely large extra dimensions that were unobservable at low energies. Their reasoning behind the weakness of gravity was that it was the only force that could *leak-out* into the extra dimensions.

In theories where extra spatial dimensions are compactified, particles that can propagate in these dimensions have their momenta quantised as $p^2 \sim 1/R^2$ where p is the particle momentum and R is the size of the extra dimension. Thus, for each particle that is free to move in these extra dimensions, a set of Fourier modes called KK states appear. These modes have mass $m^2 = n^2/R^2 + m_0^2$ where m_0 is the usual SM particle mass and n is the mode number. Each SM particle is associated with an infinite tower of excited KK states. If translational invariance along the fifth-dimension is postulated, a new discrete symmetry called the Kaluza-Klein parity exists, and the lightest Kaluza-Klein particle (LKP) can be a stable DM candidate. In most models, the LKP is the first excitation of the photon. While working within the framework of Universal Extra Dimensions (UED) [128], Servant and Tait (2013) showed that the LKP could be a DM candidate if its mass lies between 500 and 1200 GeV [129]. Additional motivation for extra-dimensional theories of DM comes from proton stability and cancellation of gauge anomalies from three generations of fermions [130].

4.3.1.2   Bottom-up approach

In the bottom-up approach, effective field theories (EFTs) are constructed from the lowest-dimensional operators allowed in a weak scale interaction Lagrangian. In this scenario, the WIMP-SM interaction takes the following form

$$\mathscr{L}_{\text{int}} \supset \frac{1}{\Lambda^n} O_{\text{DM}} O_{\text{SM}}, \tag{4.12}$$
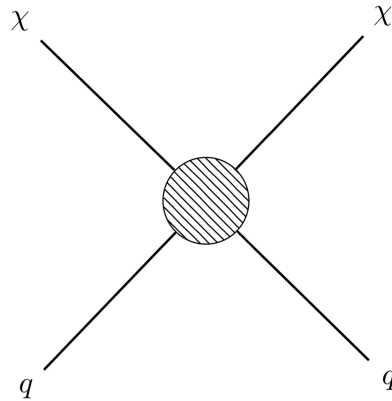
Figure 4.8: Feynman diagram for a contact interaction between a fermion DM χ and SM quark q.

where Λ is the EFT cutoff scale and O_{DM} (O_{SM}) are the DM (SM) operators, which are singlets under the SM gauge group. Thus, the WIMP-SM interaction is described by a set of non-renormalisable operators. For instance, a fermion DM χ can couple to a SM quark q via the following dimension-6 operator

$$\mathscr{L}_{\text{EFT}} = \frac{1}{\Lambda^2} \left(\overline{\chi} \gamma_\mu \chi \right) \left(\overline{q} \gamma^\mu q \right), \tag{4.13}$$

where the strength of the interaction is governed by the energy scale Λ. It is raised to an appropriate power to ensure that the interaction Lagrangian has a mass-dimension of 4. A Feynman diagram for this interaction is shown in Fig. 4.8.

The main advantage of using an EFT approach is that each operator and energy scale can describe a range of processes. For instance, depending on the direction of the arrow of time in Fig. 4.8, the dimension-6 operator in Eq. (4.13) describes the process of DM annihilation $\overline{\chi}\chi \rightarrow \overline{q}q$, scattering off quarks $\chi q \rightarrow \chi q$ and production at colliders $\overline{q}q \rightarrow \overline{\chi}\chi$. In this case, the calculation of physical observables is based on a Taylor series expansion in E^n/Λ^n which is truncated at an appropriate interaction energy scale. Thus, EFTs provide a consistent description of a higher-order process as long as the interaction energy scale lies below the energy scale Λ. The EFT description is most valid when the energy scales of the operator and the interaction are well-separated.

Although EFTs provide a simple and economical way of capturing the higher-order processes, the validity of EFTs for DM searches at colliders has been questioned [131–134] and the limitations of its use are now recognised in the particle physics community. The effective operators offer a tool to describe the effects of heavy mediators in a low-energy theory where such particles are integrated out. Due to the range of energies delivered by the colliders such as the LHC, one can directly produce an on-shell mediator particle. In this case, the EFT description fails completely. This simple point demands a careful and consistent check of the EFT validity in the context of DM searches at the LHC, or even better, a newer approach for DM searches at the LHC.

A way out of this deadlock is to resort to full-fledged models of new physics comprising

a DM candidate, i.e., using the top-down approach as discussed earlier. Models that are connected to the solution of the hierarchy problem such as supersymmetric (SUSY) or composite Higgs models are already being thoroughly studied. In addition, searches for DM within a complete framework of particle physics models are currently a subject of research. On the other hand, more fundamental physics frameworks involve many parameters. Thus, the inverse problem, i.e., using experimental results to understand the theory space necessarily involves a large number of degeneracies. This is a severe problem, particularly for DM where the only precisely known property is its thermal relic density.

An alternative approach is based on *simplified models* [135, 136]. In these models, the WIMP-SM interaction occurs via a "mediator" field which propagates the degrees of freedom of a UV theory. By increasing the number of parameters to specify the unknown DM interactions, one gains a complete theoretical control. For heavy mediators, they can be *integrated out* and the EFT situation is recovered.

When building a simplified DM model, one wishes to extend the SM by adding new degrees of freedom: not too many, otherwise, simplicity is lost; not too few, otherwise, the relevant physics is not completely captured. To this end, one builds simplified models based on the following general prescriptions:

- the SM is extended by adding a new stable DM candidate; and

- the new Lagrangian operators of the models are renormalizable and consistent with symmetries such as Lorentz invariance, SM gauge invariance and DM stability.

In addition to these exact symmetries, the SM has other important global symmetries. Baryon *B* and lepton *L* numbers are anomalous, but they can be treated as exact symmetries at the renormalizable level. Thus, simplified models must respect *B* and *L*.

On the other hand, the flavour symmetry of the SM can be broken by new physics but this breaking should be sufficiently small to agree with high-precision flavour experiments. A very convenient approach to deal with this is to either impose that the new physics respects the SM flavour symmetry or that the breaking of the symmetry is associated with the quark Yukawa matrices. This idea is known as Minimal Flavour Violation (MFV) [137]. It also allows us to keep small CP-violating effects which are possibly induced by new physics.

Simplified models have appealing features as well as limitations. Despite being simple and effective, they are not the only way to go. In fact, one can look for alternative scenarios which can still offer diverse phenomenology [138]. On the other hand, simplified models retain some of the virtues of other extreme approaches: a small number of manageable parameters for simpler search strategies, and close contact with ultraviolet (UV) completions, which reduce to the simplified models in some particular low-energy limit. Moreover, one can exploit the direct searches for the mediator as a complementary
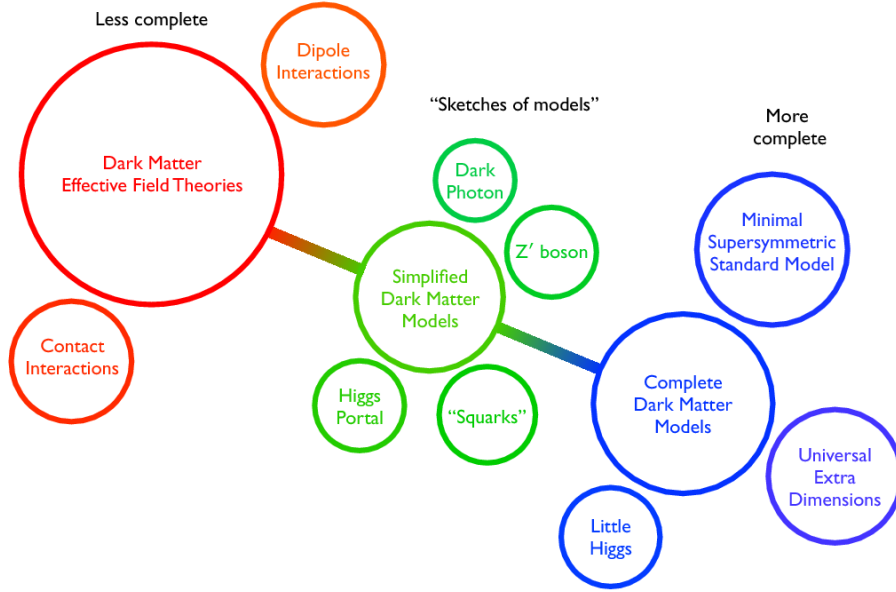
Figure 4.9: Artistic view of the DM theory space. Figure from Ref. [14].

tool to explore the dark sector. An artistic view of the DM theory space is shown in Fig. 4.9.

The EFT interaction in Eq. (4.13) provides a low-energy description of the following simplified model with a Z' mediator field

$$\mathscr{L}_{\text{int}} \supset -Z'_\mu \left(g_\chi \overline{\chi} \gamma^\mu \chi + \sum_q g_q \overline{q} \gamma^\mu q \right). \tag{4.14}$$

Here the mediator Z' couples to a Dirac fermion DM χ with coupling g_χ and to the SM quarks with coupling g_q. A Feynman diagram for this interaction is shown in Fig. 4.10.

At energies below the mediator mass $m_{Z'}$, the heavy mediator can be integrated out. In this case, we are left with the EFT in Eq. (4.13) where the interactions between DM and quarks are described by a tower of effective operators. The expansion in terms of this tower of operators can be viewed as the expansion of the mediator propagator as

$$\frac{g_q g_\chi}{m_{Z'}^2 - Q^2} = \frac{g_q g_\chi}{m_{Z'}^2} \left[1 + \frac{Q^2}{m_{Z'}^2} + O\left(\frac{Q^4}{m_{Z'}^4} \right) \right], \tag{4.15}$$

where Q^2 is the momentum transfer for a given process. In the low-energy limit $Q^2 \ll m_{Z'}^2$, only the leading order term $1/m_{Z'}^2$ is relevant. Thus, the parameters of the high-energy theory and scale Λ associated with the dimension-6 operator of the low-energy EFT in Eq. (4.13) can be connected via

$$\Lambda = \frac{m_{Z'}}{\sqrt{g_q g_\chi}}. \tag{4.16}$$

An example of a simplified model with a well-resolved mediator is the so-called *Higgs portal* scenario [139–148]. In these models, the WIMP-SM interaction occurs via a SM
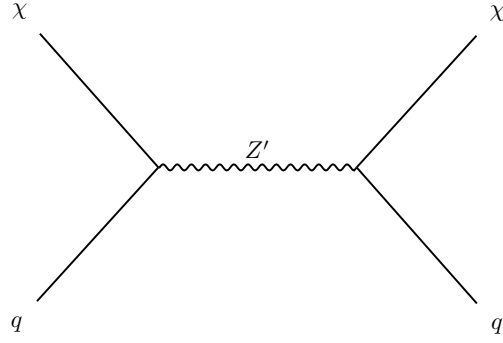
Figure 4.10: Feynman diagram for an interaction between a fermion DM χ and a SM quark q via a Z' portal.

Higgs boson as

$$\mathscr{L}_{\mathrm{SM}} \supset \frac{1}{\Lambda^n} O_{\mathrm{DM}} \Phi^\dagger \Phi, \tag{4.17}$$

where Φ is the SM Higgs doublet. This is motivated by the simplicity of the model in the required BSM particle content, and by the fact that the operator $\Phi^\dagger \Phi$ is one of the two lowest-dimensional gauge invariant operators in the SM (the other being the hypercharge field strength tensor $B_{\mu\nu}$). With the recent discovery of a SM-like Higgs boson at the LHC [10, 56], it opens up a new window to probe the possible connections between the Higgs boson and DM.

4.3.2 Axions

Axions were first proposed by R. Peccei and H. Quinn in 1977 to solve the *strong CP problem* [149]. In essence, the Lagrangian for the strong force contains a term that gives an arbitrarily large electric dipole moment to the neutron. As no such dipole moment is observed for the neutron, Peccei and Quinn postulated that a new symmetry must prevent the appearance of such a term (similar to the gauge invariance of the QED Lagrangian which keeps the photon massless). They further theorised that the symmetry is slightly broken and leads to a new, very light scalar particle called the *axion*. Although the particle is expected to be extremely light with mass in the μeV range, it can exist in sufficient numbers today to act as cold DM.

Axions should couple to photons and can be searched for using precisely tuned radio frequency (RF) cavities. Inside the magnetic field of an RF cavity, an axion can be converted into a photon which would show up as an excess power in the cavity. In a unique blend of particle and astrophysics, limits on axions have been placed through observations of red giant stars. If axions exist, they can offer another cooling mechanism which can be constrained by studying how quickly red giant stars cool down [150]. The ADMX experiment has already excluded a portion of the axion mass range and is continuing to search for axions with a mass of roughly 10 μeV [151]. A different technique involving a search for keV photons from axion-photon conversion in the Sun (via the Primakoff effect)

has been used in the KEK, CAST and IAXO observatories. Such *axion helioscopes* are sensitive to the higher end of the axion mass range. In addition, new ideas for axion searches including the Cosmic Axion Spin Precession Experiment (CASPEr) [152], broadband and resonant approaches [153] have been proposed. Axion searches will continue to reach into the theoretically best-motivated regions of the axion mass and coupling parameter space.

In addition to the well-motivated particle DM candidates introduced above, other exotic DM candidates can also exist. These include Q-balls, WIMPzillas, branons and GIMPs [154–156].

4.4   Relic density of WIMPs

In the early universe, energetic and massive particles were created. They remained in thermal equilibrium via mechanisms such as pair production or collisions with other particles. However, as the universe expanded and cooled, two main changes occurred. First, lighter particles no longer had sufficient kinetic (thermal) energy to produce heavier particles through interactions, and second, the universe's expansion diluted the number of particles such that interactions occurred less frequently or ceased altogether. At some point, the density of heavier particles or a particular particle species became too low to support frequent interactions and conditions for thermal equilibrium were violated. After this stage, particles freeze-out and their comoving number density (no longer affected by interactions) remained constant. The exact moment or temperature of freeze-out is calculated by equating the reaction rate Γ to the Hubble rate H, see Appendix C for more details. The density of a specific particle species remaining at the time of freeze-out is known as the relic density. It remains constant with the expansion of the universe.

For a Majorana fermion WIMP χ, the evolution of its number density dn/dt is governed by the following Boltzmann equation [157]

$$\frac{1}{a^3}\frac{d}{dt}(na^3) = \frac{dn}{dt} + 3Hn = \langle\sigma v_{\rm rel}\rangle(n_{\rm eq}^2 - n^2), \qquad (4.18)$$

where $H \equiv \dot{a}/a$ is the Hubble parameter, $\langle\sigma v_{\rm rel}\rangle$ is a thermal average of the WIMP annihilation cross-section σ times its relative velocity $v_{\rm rel}$ and $n_{\rm eq}$ is the equilibrium number density of WIMPs. Depending on the relative velocity of the WIMP χ, the equilibrium number density is

$$n_{\rm eq}(T) = \begin{cases} \frac{3}{4}\frac{\zeta_3}{\pi^2}g_\chi T^3, & \text{relativistic, } T \gg m, \\ g_\chi\left(\frac{m_\chi T}{2\pi}\right)^{3/2} e^{-m_\chi/T}, & \text{non-relativistic, } T \ll m, \end{cases} \qquad (4.19)$$

where $\zeta_3 \simeq 1.202$ and g_χ is the number of degrees of freedom of χ, see Appendix C for more details. Thus, if χ remains in thermal equilibrium, $n = n_{\rm eq}$ and its abundance decreases exponentially. However, when the χ abundance is small, equilibrium cannot be maintained due to a reduced number density. Consequently, the WIMP χ freezes out.

As the dynamics leading to freeze-out occurs during the radiation dominated era of the universe, it is useful to recast physical quantities in terms of the CMB photons. The total radiation density ρ_R can be written in terms of the photon energy density ρ_γ as $\rho_R = (g_\rho/g_\gamma)\rho_\gamma$ where g_ρ counts the relativistic ($T > m$) degrees of freedom as

$$g_\rho \equiv \sum_b g_b \left(\frac{T_b}{T_\gamma}\right)^4 + \frac{7}{8} \sum_f g_f \left(\frac{T_f}{T_\gamma}\right)^4. \tag{4.20}$$

Here b (f) refers to bosons (fermions). For particles that are in thermodynamic equilibrium with photons, $T_{b,f} = T_\gamma$. If relativistic particles are present which are decoupled from photons, it is necessary to distinguish between two kinds of g: g_ρ in Eq. (4.20) and g_s which is associated with the total entropy density, namely

$$g_s \equiv \sum_b g_b \left(\frac{T_b}{T_\gamma}\right)^3 + \frac{7}{8} \sum_f g_f \left(\frac{T_f}{T_\gamma}\right)^3. \tag{4.21}$$

Note that g_ρ and g_s differs only when relativistic particles are present that are not in equilibrium with the photons, i.e., when $T_{b,f} \neq T_\gamma$. For the SM particle content, this only occurs for $T \lesssim m_e$ when the $e^\pm$ pairs annihilate and heat up the photons relative to the neutrinos (such that $T_\gamma > T_\nu$) after the neutrinos have decoupled ($T_{\nu,\text{dec}} \sim 2\text{–}3$ MeV).

The entropy of the universe in a comoving volume $S \equiv sa^3 = (2\pi^2/45)g_s T^3 a^3$ is conserved. Thus, the evolution equation in Eq. (4.18) can be written in terms of $Y \equiv n/s$ and $x \equiv m_\chi/T$ where

$$Y_{\text{eq}} = \frac{n_{\text{eq}}}{s} = \frac{45}{2\pi^4} \sqrt{\frac{\pi}{8}} \frac{g_\chi}{g_s} x^{3/2} e^{-x}. \tag{4.22}$$

Conservation of entropy also allows us to relate changes in the scale factor a and temperature T. During radiation dominated epochs, the expansion rate of the universe, namely H is related to the total energy density by $H \equiv \dot{a}/a = \sqrt{\rho_R/(3M_p^2)}$ where $\rho_R = (\pi^2/30)g_\rho T^4$. Thus, the evolution equation can be written as

$$\frac{dY}{dx} = \frac{s\langle \sigma v_{\text{rel}}\rangle}{Hx} \left[1 + \frac{1}{3}\frac{d(\ln g_s)}{d(\ln T)}\right] \left(Y_{\text{eq}}^2 - Y^2\right). \tag{4.23}$$

This expression makes it clear that the only source of uncertainty and model dependence comes from $g(T)$, which enters directly in $S \propto g_s T^3$ and $H \propto g_\rho^{1/2} T^2$. For our choice of WIMP masses, $10\,\text{MeV} \lesssim m_\chi \lesssim 10\,\text{TeV}$, we set $g = g_\rho = g_s$ and $T_b = T_f = T$. We rely on the values of $g(T)$ obtained in Ref. [158].

We assume that the WIMP χ begins in thermal equilibrium for $x \gtrsim 1$ and solve Eq. (4.23) for $Y_0 = Y(t = t_0, T = T_0)$ as $x \to \infty$ ($x \gg 1$) where $T_0 = 2.7255 \pm 0.0006$ K [3] is the present day CMB temperature. The WIMP relic density ρ_χ can be expressed in terms of the density parameter Ω_χ as

$$\Omega_\chi h^2 \equiv \frac{\rho_\chi}{\rho_c} h^2 = \frac{m_\chi s_0 Y_0}{\rho_c} h^2. \tag{4.24}$$
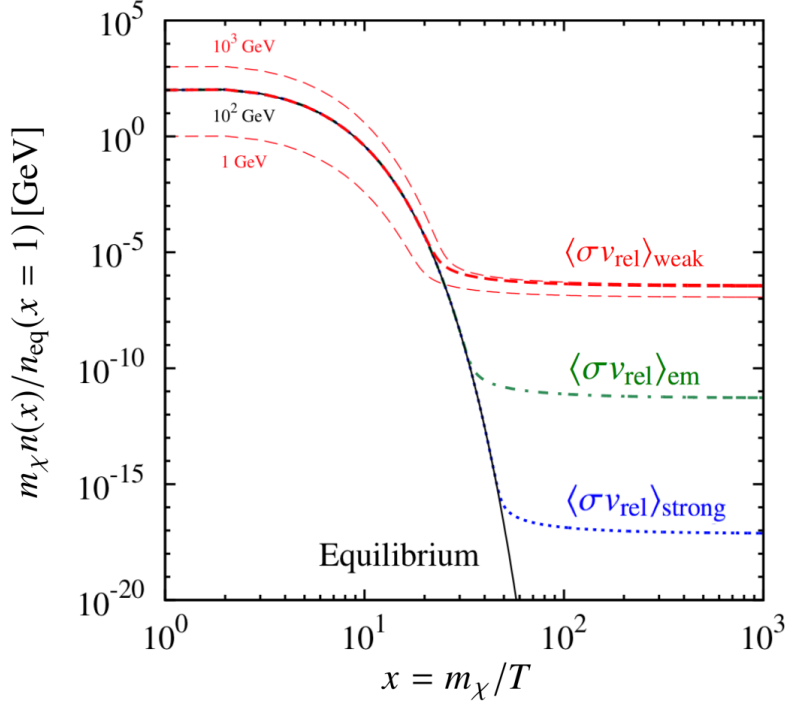
Figure 4.11: Evolution of the WIMP χ abundance as a function of $x \equiv m_\chi/T$. The thick curves show the WIMP mass density $m_\chi n(x)$ normalized to the initial equilibrium number density $n_{eq}(x = 1)$ for different choices of annihilation cross-section $\langle \sigma v_{rel} \rangle$ and WIMP mass m_χ. Results for $m_\chi = 100\,\mathrm{GeV}$ are shown for weak interactions, $\langle \sigma v_{rel} \rangle = 2 \times 10^{-26}\,\mathrm{cm^3\,s^{-1}}$ (dashed red), electromagnetic interactions, $\langle \sigma v_{rel} \rangle = 2 \times 10^{-21}\,\mathrm{cm^3\,s^{-1}}$ (dot-dashed green), and strong interactions, $\langle \sigma v_{rel} \rangle = 2 \times 10^{-15}\,\mathrm{cm^3\,s^{-1}}$ (dotted blue). For the weak-scale annihilation cross-section, the thin dashed curves show the dependence of the WIMP abundance on its mass for $m_\chi = 10^3\,\mathrm{GeV}$ (upper dashed curve) and $m_\chi = 1\,\mathrm{GeV}$ (lower dashed curve). The solid black curve shows the evolution of the equilibrium abundance for $m_\chi = 100\,\mathrm{GeV}$. Figure based on Ref. [157].

In Fig. 4.11, we show the evolution of the WIMP mass density $m_\chi n(x)$ normalized to its initial equilibrium value $n_{eq}(x = 1)$ as a function of $x = m_\chi/T$ (a proxy for "time") for different values of $\langle \sigma v_{rel} \rangle$. In this definition, the final asymptotic value is proportional to the WIMP relic abundance $\Omega_\chi h^2$. During the early universe when the WIMP is relativistic ($T \gtrsim m_\chi$, $x \lesssim 1$), the production and annihilation rates far exceed the expansion rate H and $n = n_{eq}$ is a very accurate, approximate solution of Eq. (4.18). Even when $T \lesssim m_\chi$ and $x \gtrsim 1$, the actual WIMP number density closely tracks its equilibrium value. When the universe expands and cools ($T \lesssim m_\chi$), the WIMP production rate is exponentially suppressed as evident from the rapid drop in n_{eq}. Annihilations continue to take place at a lower rate due to an exponentially suppressed production rate. At some point, equilibrium can no longer be maintained and n deviates from n_{eq}. However, even for $x \gtrsim 1$, the annihilation rate is still very fast compared to the expansion rate and n continues to decrease, but more slowly than n_{eq}. For some value of $T \ll m_\chi$ and $x \gg 1$, WIMPs become so rare that residual annihilations also cease and their number stops evolving in a comoving volume. As a result, they freeze-out and leave behind a thermal relic.

It is also evident from Fig. 4.11 that a large annihilation cross $\langle \sigma v_{\mathrm{rel}} \rangle$ allows χ to maintain equilibrium for large values of $x = m_\chi / T$, i.e., up to low temperatures. This leads to a smaller relic abundance in the universe today. On the other hand, χ would freeze-out earlier than expected if its annihilation cross-section is small. This would lead to a large relic abundance in the universe today. In fact, WIMPs with a weak-scale interaction cross-section can naturally reproduce the observed DM relic abundance. This is one of the reasons why WIMPs are well-motivated DM candidates. For higher WIMP masses, $m_\chi \gtrsim 10\,\mathrm{GeV}$, the relic abundance is insensitive to m_χ, whereas for lower WIMP masses, it is strongly sensitively to m_χ. Thus, for the same value of $\langle \sigma v_{\mathrm{rel}} \rangle$, increasing the WIMP mass can result in a factor of two difference in its relic density.

4.5 Detection methods

The detection or creation of DM offers the key to determine its properties and role in the formation of structure in the universe. Many experiments are searching for signs of a WIMP-like DM using different detection methods. Although the production of DM in a particle accelerator such as the LHC would be ideal (as we would have better control over a repeatable experiment), direct and indirect detection also plays an important role in the search. This complementarity is illustrated in Fig. 4.12. For a recent review on direct and indirect DM searches, see Refs. [159, 160].

In the following subsections, we discuss the detection methods for DM in more detail. In doing so, we assume that the local DM distribution is at rest in the Milky Way halo. Other possibilities such as DM clumps and velocity streams due to an incomplete virialization are also possible [161].

4.5.1 Collider searches

As DM particles are assumed to be electrically neutral and cosmologically stable, they would appear as missing energies at collider experiments [16]. Thus, collider searches for DM are based on the detection of the visible counterpart of a signal such as jets and/or charged leptons. An important aspect of collider searches is that it offers a complementary probe for DM but cannot determine exactly if a signal is due to DM as any neutral particle that decays outside the detector would carry away the missing energy. Only direct and indirect detection methods can provide a way to confirm whether a potential signal is truly due to DM.

The most commonly used experimental strategies for DM searches at the LHC are as follows [17].

- *Mono-jet searches*: If a pair of DM particles can be produced from *pp* collisions, it should also produce one or more QCD jets from initial state radiation (ISR).
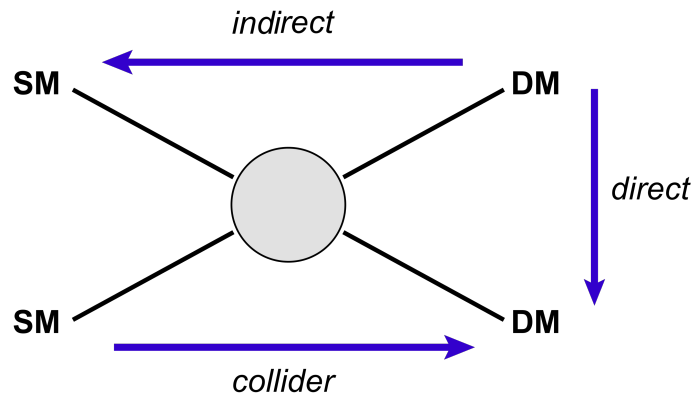
Figure 4.12: Detection methods for dark matter (DM). Figure from Ref. [15].

Searches for events where a jet with high transverse momentum p_T is produced in association with large missing transverse momentum $\not{E}_T$ have become emblematic for DM searches at the LHC. Typically, mono-jet searches only impose a strict veto on events containing leptons but do include events with several high p_T jets.

In some models, the DM particles are produced preferentially in association with one or more bottom quarks [162, 163]. Searches for such models are conceptually similar to mono-jet searches except that they require at least one hard jet to pass *b*-tagging requirements [164–166].

- *Mono-V searches*: Similar to the mono-jet events, DM may also be produced together with a vector boson $V \in (\gamma, W, Z)$ which is radiated off a quark in the initial state. While the corresponding production cross-section is significantly smaller than for the QCD radiation, the process is much cleaner and can be searched for with higher sensitivity. Moreover, if DM particles couple directly to a pair of gauge bosons, mono-*V* processes can be the dominant way to produce DM at the LHC [167].

  Mono-photon searches are among the simplest searches for DM, and typically require only the presence of a high p_T photon and no isolated leptons [168]. Although both detector effects (e.g., electron or jet misidentification) and beam-induced events can potentially fake mono-photon events, background levels are typically very low, and the experimental sensitivity is limited only by statistics.

- *Invisible Higgs decays*: If the DM mass is less than half the SM Higgs boson mass, it may be possible to produce pairs of DM particles in Higgs decays. Such invisible Higgs decays can be searched for in a number of different ways. Firstly, indirect constraints can be obtained by combining the visible decay modes in order to construct an upper bound on all unobserved decay channels. This approach, however, requires an assumption on the Higgs production cross-section, which is typically taken to be given by the SM prediction. Secondly, one can directly search

for invisible Higgs decays by triggering on the particles that signal the production of a Higgs boson. The two most relevant production modes in this context are vector boson fusion (VBF) and association production of a massive vector boson (Vh). However, the gluon fusion mode can also be interesting if the Higgs boson is produced with an additional jet from ISR.

LHC searches for the associated production of a Higgs boson and a massive vector boson followed by an invisible decay of the Higgs boson are conceptually very similar to the mono-V signatures as discussed earlier. They can be searched for both in the leptonic decays of a Z boson or in the hadronic decays of a W or Z boson [169–171]. On the other hand, the jet-associated gluon fusion production mode essentially yields a mono-jet signature [169].

A truly novel signature is obtained in the VBF case [172]. In this channel, the production of a Higgs boson is signalled by the presence of two jets with large separation in pseudorapidity and large invariant mass [169, 173]. This distinctive topology can be exploited to discriminate hypothetical invisible Higgs decays from the large SM backgrounds. Indeed, searches for invisible Higgs decays in the VBF production mode typically yield the strongest upper limits on the Higgs invisible branching ratio $\mathcal{BR}_{\mathrm{inv}}$.

Combinations of the various direct searches for invisible Higgs decays have been performed by both the ATLAS [174] and CMS [169] experiments.[3] The resulting upper bounds at 95% C.L. on the Higgs invisible branching ratio are $\mathcal{BR}_{\mathrm{inv}} < 0.25$ and $\mathcal{BR}_{\mathrm{inv}} < 0.24$ respectively. These bounds are comparable to the ones obtained indirectly from the visible Higgs decay modes [11, 174].

In the EFT approach, the strongest constraints on the suppression scale Λ from hadron colliders are obtained for effective operators involving quarks and gluons. Another interesting possibility includes contact interactions between the DM particles and SM gauge bosons [167, 175, 176] or Higgs bosons [177]. In such a set-up, any gauge boson or Higgs boson produced at the LHC can radiate off a pair of DM particles, potentially leading to mono-V or mono-Higgs signals.

For the Higgs portal models introduced earlier, one of the simplest ways to couple a fermionic DM to the SM is via the following dimension-5 operator

$$\mathscr{L}_{\mathrm{int}} \supset \frac{1}{\Lambda} \Phi^{\dagger}\Phi\,\bar{\chi}\chi, \tag{4.25}$$

where Φ is the SM Higgs doublet. After EWSB, this operator gives rise to an $h\bar{\chi}\chi$ vertex where h is the physical Higgs boson. For $m_{\chi} < m_h/2$, this interaction leads to an invisible Higgs decay, which is strongly constrained by the experimental data. On

---

[3]The latter includes first results from data taken at $\sqrt{s} = 13\,\mathrm{TeV}$.
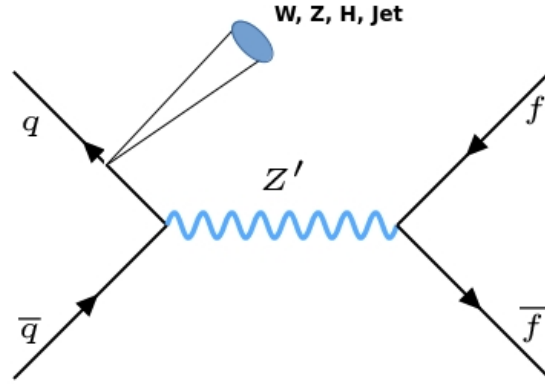
Figure 4.13: Mono-X searches for DM f in the case of a Z' portal model. Figure from Ref. [16].

the other hand, for $m_\chi > m_h/2$, the DM production cross-section at the LHC is strongly suppressed [139]. For a scalar singlet DM model, the corresponding Higgs portal operator is in fact renormalizable, leading to the simplest model for DM production at the LHC.

The original appeal of the EFT approach was based on the idea that bounds on effective operators are model-independent, in the sense that it is not necessary at any point of the analysis to specify the details of the underlying UV completion. However, this hope has been challenged by two related observations. Firstly, it has become clear that there are many interesting models describing the production of DM at the LHC which are not correctly captured by the EFT approach [178–180]. In other words, these models predict kinematic distributions that differ significantly from the ones obtained from contact interactions. Secondly, it was shown that, at least for certain values of the suppression scale Λ, the effective operator approach makes unphysical predictions so that it becomes impossible to find a plausible UV completion [180–182].

Both of these observations are connected to the way in which effective operators are obtained from a more fundamental theory. For instance, for the EFT interaction in Eq. (4.13), there is a condition which defines the point at which the EFT description breaks down for DM searches at the LHC. These searches include mono-jet and mono-V signals as shown by the Feynman diagram in Fig. 4.13. The Z' mediator in Eq. (4.14) must carry at least enough energy to produce DM at rest, i.e., $Q > 2m_\chi$. Combining this with Eq. (4.16) and the EFT validity limit $Q \ll m_{Z'}$ gives

$$\Lambda > \frac{Q}{\sqrt{g_q g_\chi}} > \frac{2m_\chi}{\sqrt{g_q g_\chi}}. \tag{4.26}$$

In the extreme case when the couplings are as large as possible while remaining in the perturbative regime, $g_q, g_\chi < 4\pi$, we get

$$\Lambda > \frac{m_\chi}{2\pi}. \tag{4.27}$$

This condition is necessary but not enough to ensure the validity of the EFT approximation. A better measure of the validity comes from comparing Q and $m_{Z'}$. This defines the following three regions as shown in Fig. 4.14.
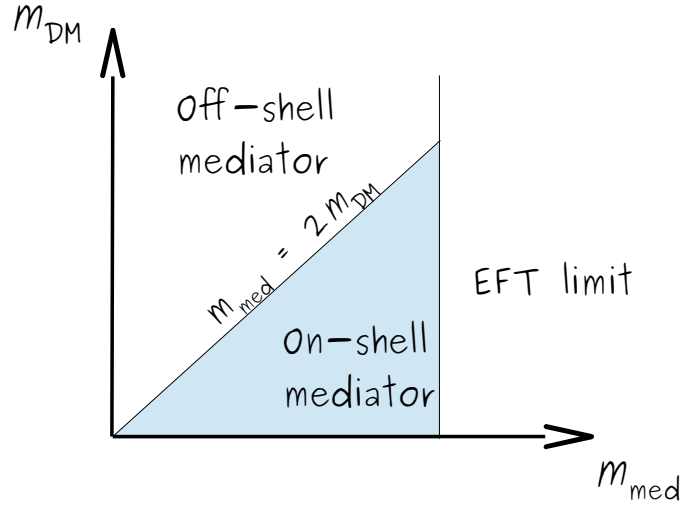
Figure 4.14: A sketch of the mediator-DM mass plane used to present experimental results for simplified DM models. Figure from Ref. [17].

1. When $Q^2 < m_{Z'}^2 \equiv g_q g_\chi \Lambda^2$, the approximation in Eq. (4.15) holds. This is the only region where the EFT approximation is valid.

2. In the region where $Q^2 \sim m_{Z'}^2$, the production cross-section undergoes a resonant enhancement. The EFT approximation misses this enhancement and gives conservative results with respect to the full theory.

3. When $Q^2 \gg m_{Z'}^2$, the expansion in Eq. (4.15) fails and the signal cross-section falls like Q^{-1} rather than $m_{Z'}^{-1}$. In this region, the EFT constraints will be stronger than the full theory.

Another issue that can arise when high-energy collisions at the LHC are dealt using the EFT approach is the unitarity violation of the S-matrix. When adopting the EFT description, the condition of unitarity preservation sets an energy scale above which the contact interaction is not reliable. In this case, a UV-completion of the EFT operator must be considered. For the operator in Eq. (4.13), the unitarity constraint translates to [181]

$$\Lambda > \left[\left(1 - \frac{4m_\chi^2}{s} \right) s \frac{\sqrt{3}}{4\pi} \right]^{1/2}, \tag{4.28}$$

where $\sqrt{s}$ is the centre-of-mass energy of the initial state for the process $q\bar{q} \to \overline{\chi}\chi + $ jets.

4.5.2 Direct detection

The idea behind direct DM detection is very simple: set up a very sensitive device containing a large amount of an element(s) and detect very small motions or interactions with the atoms within it. If DM is everywhere in the universe, it should be travelling around (and through) the Earth, and thus a detection apparatus at all times. Although DM

is weakly interacting, it may occasionally bump into the nucleus of a detector atom and deposit some non-zero energy that can be detected. However, the energy deposited by a WIMP is quite small. By estimating the WIMP velocity around $220\,\mathrm{km\,s^{-1}}$ and a mass of roughly $100\,\mathrm{GeV}$, the nuclear recoil energy is

$$T = \frac{1}{2}mv^2 = \frac{1}{2}(1.78 \times 10^{-25}\,\mathrm{kg})(2.2 \times 10^5\,\mathrm{m\,s^{-1}})^2 \simeq 4.314 \times 10^{-15}\,\mathrm{J} \simeq 26.9\,\mathrm{keV}. \quad (4.29)$$

This only provides an upper limit; the actual amount would certainly be smaller as it is unlikely for a weakly interacting particle to be completely stopped within the detector. In contrast, natural radioactive elements emit MeV-scale energies. This makes a keV-scale energy event nearly impossible to find. For this reason, direct detection experiments must be radioactively clean and shielded from other background sources such as cosmic rays.

The recoil energy E of a nucleus with mass M after scattering off a WIMP with mass m is

$$E = \frac{\mu^2 v^2}{M}(1 - \cos\theta), \quad (4.30)$$

where $\mu = mM/(m + M)$ is the WIMP-nucleus reduced mass, v is the speed of the WIMP relative to the nucleus and θ is the scattering angle in the centre-of-mass (c.o.m.) frame.

A signal from WIMP will have very specific characteristics. Firstly, events should be uniformly distributed throughout the detector as the local DM density $\rho_\odot$ is assumed to be homogeneous, and the cross-section for the WIMP-nucleus interaction remains constant. Secondly, the WIMP-nucleus interaction is a single-site event, whereas events initiated by cosmic rays or radioactive elements will be multi-site. Thus, direct detection experiments have an *anti-coincidence veto system* to avoid events which are caused by the same incoming particles.

The interactions of a WIMP with the detector material can be classified into the following two categories:

1. *Elastic and inelastic scattering*: In elastic scattering, the WIMP-nucleus interaction occurs as a whole. This results in a nuclear recoil with energies of the order of few keVs. However, in inelastic scattering, all of the energy does not go into the nuclear recoil; rather a nucleus is excited into a higher energy state (for instance, the $5/2^+$ state in ^{73}Ge) which decays by photon emission. If the excited state is long-lived, the decay signal can be separated from the nuclear recoil event; this leads to a better background discrimination. However, inelastic scattering cross sections are generally smaller than the elastic ones due to a lack of coherence, i.e., the interaction is with individual nucleons rather than the nucleus as a whole [183];

2. *Spin-dependent and spin-independent scattering*: A spin-dependent (SD) scattering occurs when the spin of a WIMP couples to the spin content of a nucleon. On the other hand, a spin-independent (SI) scattering does not depend on this coupling and
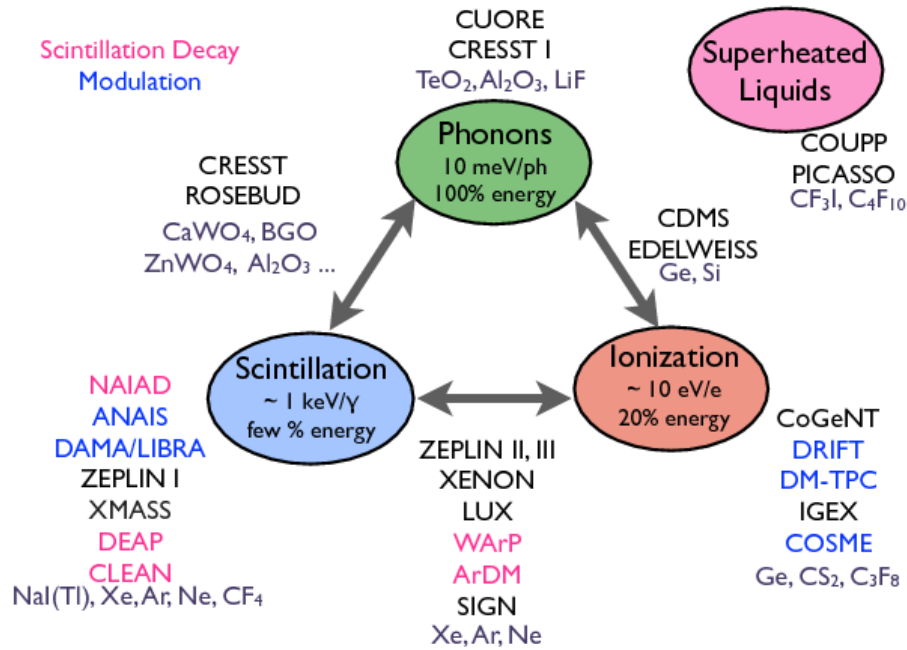
Figure 4.15: Detection techniques used by various direct DM detection experiments. Figure from Ref. [18].

has the advantage of higher cross sections with larger nuclei due to coherence, i.e., the WIMP interacts with the nucleus as a whole.

A recoil event can take one of the following three forms:

1. *Phonon/Thermal*: It appears as a vibration (detected as a rise in temperature) in the crystal lattice of the detector due to a slight movement of a nucleus from a WIMP-nucleus interaction. Using an extremely sensitive thermometer system which is placed around the detector, one can record any temperature variations caused by the nuclear recoil;

2. *Ionisation*: An incident particle (such as a WIMP) can pass enough energy to an electron in the detector to escape the pull of its nucleus. This event is recorded by placing a small electric field in the detector which pushes the electron to a detector wall where it can be registered and counted as an ionisation event;

3. *Scintillation*: This type of recoil event occurs when an electron absorbs enough energy to climb to a higher energy state. After a short time, the electron loses this energy and emits a photon which can be collected by photomultipliers and converted into an electric signal for further analysis.

In general, a detector is set up to record two of these WIMP signals as shown in Fig. 4.15. As a result, background events can be recognised on an event-by-event basis and discarded, thereby allowing for possible DM signatures to be counted and analysed.

To compute the expected number of recoil events N in a detector within a range of recoil energy (E_1, E_2), we take a sum over the nuclear species i in the detector as

$$N = \sum_i \int_{E_1}^{E_2} dE \, \frac{dR_i}{dE} \mathcal{M}_i \mathcal{T}_i \epsilon_i(E), \tag{4.31}$$

where dR_i/dE is the expected recoil rate off nuclear species i (in units of cpd kg^{-1} keV^{-1} where cpd is counts/day), $\mathcal{M}_i$ is the total mass of nuclei of species i in the detector that is active for time $\mathcal{T}_i$ and $\epsilon_i(E)$ is the counting efficiency for nuclear recoils with energy E. The differential rate $\mathrm{d}R_i/\mathrm{d}E$ is given by

$$\frac{dR_i}{dE} = \frac{\rho_\odot \sigma_i |F_i(E)|^2}{2m\mu_i^2} \int_{v > v_{\min}} d^3v \, \frac{f(\boldsymbol{v}, t)}{v}, \tag{4.32}$$

where $\rho_\odot$ is the local DM density, σ_i is the WIMP-nucleus cross-section, $F_i(E)$ is the nuclear form factor which accounts for the fact that a nucleus is not a simple point-like object, m is the WIMP mass, μ_i is the reduced mass, v is the WIMP velocity with respect to the detector and $f(\boldsymbol{v}, t)$ is the WIMP velocity distribution (commonly assumed to be a Maxwell-Boltzmann distribution) in the reference frame of the detector. The lower limit on the integral is

$$v_{\min} = \sqrt{\frac{\mathcal{M}_i E}{2\mu_i^2}}. \tag{4.33}$$

This corresponds to the minimum WIMP velocity that can initiate a nuclear recoil with energy E. The nuclear physics uncertainties are locked into the form factor $F_i(E)$, whereas the main astrophysical uncertainties lie in the WIMP velocity distribution $f(\boldsymbol{v}, t)$ and the local DM density $\rho_\odot$.

The DM halo in our local neighbourhood is most likely dominated by a smooth and well-mixed (virialized) component with an average density of $\rho_\odot \simeq 0.4\,\text{GeV cm}^{-3}$ [184]. The simplest model for this smooth component is often taken to be the Standard Halo Model (SHM) of an isothermal sphere with an isotropic, Maxwell-Boltzmann velocity distribution and a root-mean-square (RMS) velocity dispersion σ_v [185]. The Maxwell-Boltzmann velocity distribution is given by

$$\tilde{f}(v) = \begin{cases} \frac{1}{N_{\text{esc}}} \left(\frac{3}{2\pi\sigma_v^2}\right)^{3/2} e^{-3v^2/2\sigma_v^2}, & |v| < v_{\text{esc}}, \\ 0, & \text{otherwise}, \end{cases} \tag{4.34}$$

where

$$N_{\text{esc}} = \operatorname{erf}\left(\frac{v_{\text{esc}}}{\bar{v}}\right) - \frac{2}{\sqrt{\pi}} \frac{v_{\text{esc}}}{\bar{v}} \exp\left(-\frac{v_{\text{esc}}^2}{\bar{v}^2}\right). \tag{4.35}$$

Here $\bar{v} = \sqrt{2/3}\sigma_v \simeq 235\,\text{km s}^{-1}$ is the most probable speed [186–188] and $v_{\text{esc}} = 550\,\text{km}$ s^{-1} is the galactic escape speed.

In recent years, the use of a Maxwellian velocity distribution has been questioned. However, it was also shown that the results with DM using a Maxwellian distribution are
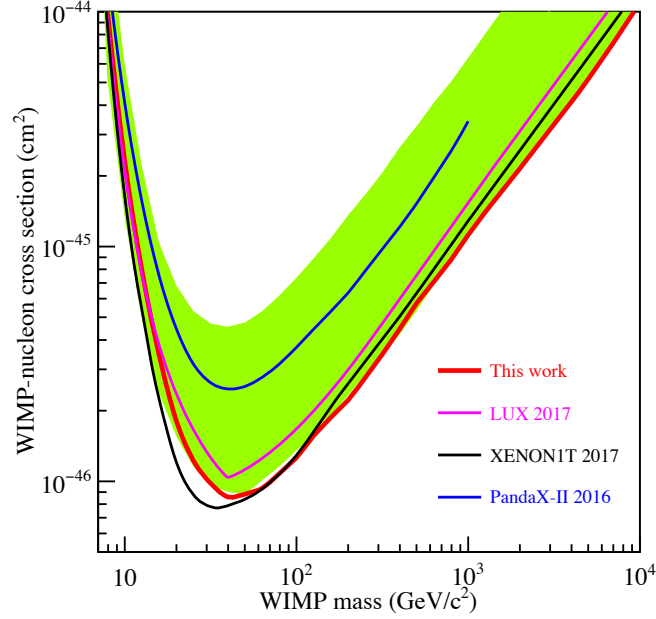
Figure 4.16: Upper limits on the WIMP-nucleon cross-section vs WIMP mass at 90% C.L. from the PandaX-II 2017 (red), PandaX-II 2016 (blue), XENON1T 2017 (black) and LUX 2017 (magenta) experiments. Figure from Ref. [19].

consistent with the ones where baryons are included in the *N*-body simulations [189–191]. Thus, the Maxwellian distribution is a perfectly good approximation when comparing results from DM search experiments with data.

From Eq. (4.31), we can see that a detector should ideally have a large mass, operate for a long period of time, and be properly shielded against background radiation. By comparing the observed number of signal events against the predicted ones from Eq. (4.31), an upper limit can be placed on the WIMP-nucleon cross-section (since different detection experiments use different target material). Thus, negative results from direct detection experiments do not go to waste; instead, they allow us to make statements about the existence of WIMPs in certain regions of the parameter space for a given DM theory and extend searches towards more sensitive regions. Fortunately, the current generation of direct detection experiments is employing advanced detection techniques to probe the WIMP-nucleon cross-section with increasing sensitivity. Currently, the best upper limits on the SI WIMP-nucleon cross-section come from the PandaX-II (2017) [19], XENON1T (2017) [192] and LUX (2017) [193] experiments. The results are shown in Fig. 4.16.

Although SI scattering gives a larger interaction rate in most WIMP models, SD scattering can explore the parameter space where scalar interactions are less probable. For this reason, experiments that are searching for SD interactions have placed competitive upper limits on the WIMP interactions. However, the coupling of the WIMP spin to protons and neutrons can be substantially different. Thus, SD experiments can only constrain one of the two SD cross sections, σ_{SD}^p or σ_{SD}^n. For the spin-dependent WIMP-proton interaction, the best upper limits come from the LUX (2016) [194], PandaX-II
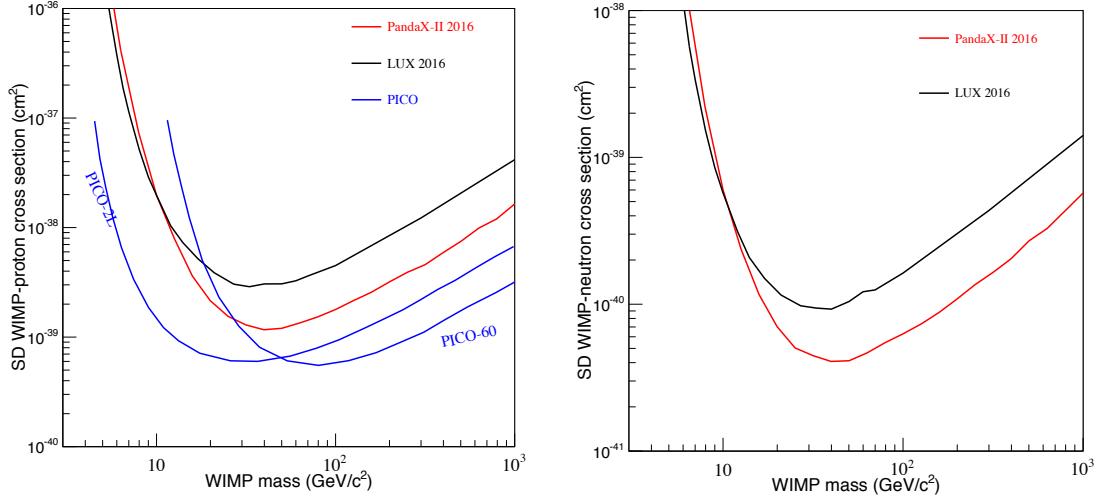
Figure 4.17: Upper limits on the spin-dependent WIMP-proton (*left*) and WIMP-neutron (*right*) cross-section vs WIMP mass. Figure from Ref. [20].

(2016) [195] and PICO [24, 196] experiments, whereas for the spin-dependent WIMP-neutron interaction, they come from the LUX (2016) [194] and PandaX-II (2016) [195] experiments. The results are shown in Fig. 4.17.

The DM signal is expected to modulate throughout the year. As the Sun orbits around the GC, Earth-based detectors effectively move into a *wind* of WIMPs. As WIMPs are moving in random directions in the galaxy, the motion of the Sun creates (on average) a relative velocity between us and the WIMP wind. In addition, the relative velocity of the Earth with the WIMP wind also varies over a year due to its orbit around the Sun. This effect is shown in Fig. 4.18. Thus, the count rate is expected to modulate sinusoidally over the year, peaking in June and with a minimum in December. The annually modulating recoil rate can be approximated by [185]

$$\frac{dR}{dE}(E,t) \simeq S_0(E) + S_m(E)\cos\left[\omega(t - t_0)\right], \tag{4.36}$$

where $|S_m| \ll S_0$, S_0 is the time-averaged rate, S_m is the modulation amplitude, $\omega = 2\pi/\text{year}$ and t_0 is the phase of the modulation. The variation of the WIMP flux over a year is only about 7%. This means that many events are required to see such a small modulation. These among other indications can help experiments to decide whether the observed signals are truly from WIMPs or background sources.

The Dark Matter (DAMA) experiment has reported an annual modulation in the scattering events of around 7% [197]. This experiment uses NaI crystals at the Gran Sasso tunnel under the Apennine mountains near Rome. It has observed exactly the expected annular modulation with the correct phase as shown in Fig. 4.19. In fact, DAMA has collected 10 years of cycles corresponding to 9σ detection of annual modulation.

However, the DAMA results are puzzling as no other direct detection experiment to date has seen such a signal. From Fig. 4.20, we might think that other experiments rule
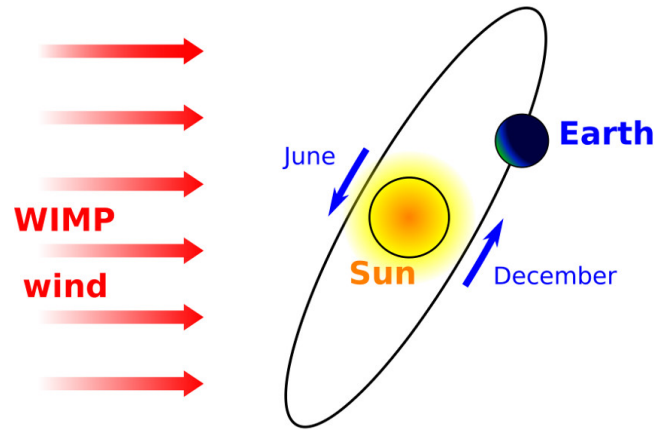
Figure 4.18: A simplified picture of the WIMP velocities as seen from the Sun and Earth. Due to the rotation of the Sun around the galactic center in essentially a non-rotating DM halo, the solar system experiences an effective WIMP wind which causes an annual modulation in the DM signal measured on Earth. The Earth's orbit is inclined at about 60° with respect to the plane of the disk. Figure from Ref. [185].
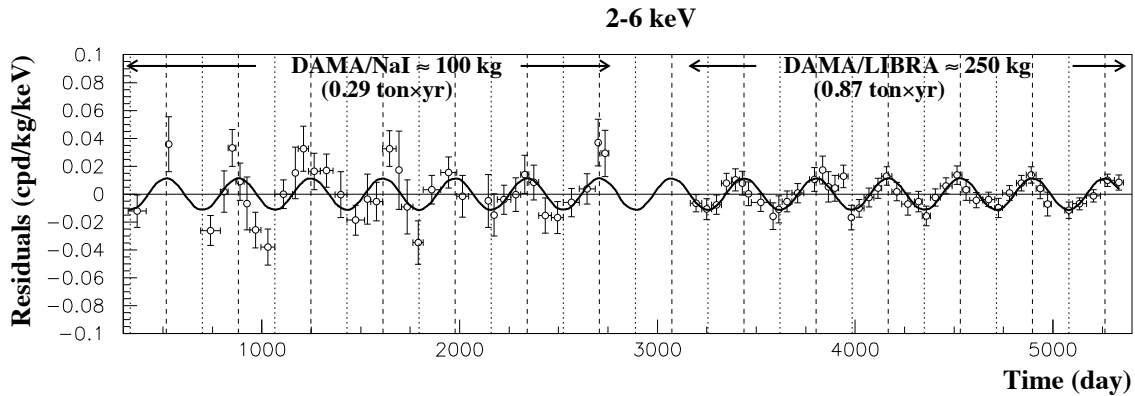
Figure 4.19: Results from the DAMA/NaI and DAMA/LIBRA experiment which shows a 9σ detection of annual modulation. Figure from Ref. [21].

out the DAMA signals as being due to WIMPs. However, this may not be true for all experiments as each experiment uses different target materials. The DAMA experiment is the only one to date that uses NaI crystals. Other experiments such as LUX [193] and XENON100 [198] experiments use xenon, whereas CDMS (and SuperCDMS) [199] uses germanium crystals, i.e., far heavier nuclei than the NaI crystals used in DAMA.

A theoretical input is required to compare DAMA results against other experiments. For instance, if we assume that the WIMP-nucleon scattering is nuclear spin-independent such that the cross-section scales as A^2 where A is the total number of nucleons, we can plot the different experimental limits on the WIMP-nucleon cross-section vs WIMP mass as in Figs. 4.16 and 4.20. The signals in DAMA experiment can be explained by a 10 GeV WIMP if it scatters off the sodium (Na) atom, whereas the signal can be explained by an 80 GeV WIMP if it scatters off the iodine (I) atom. The higher WIMP masses are in severe conflict with bounds from other experiments, while the lower mass region
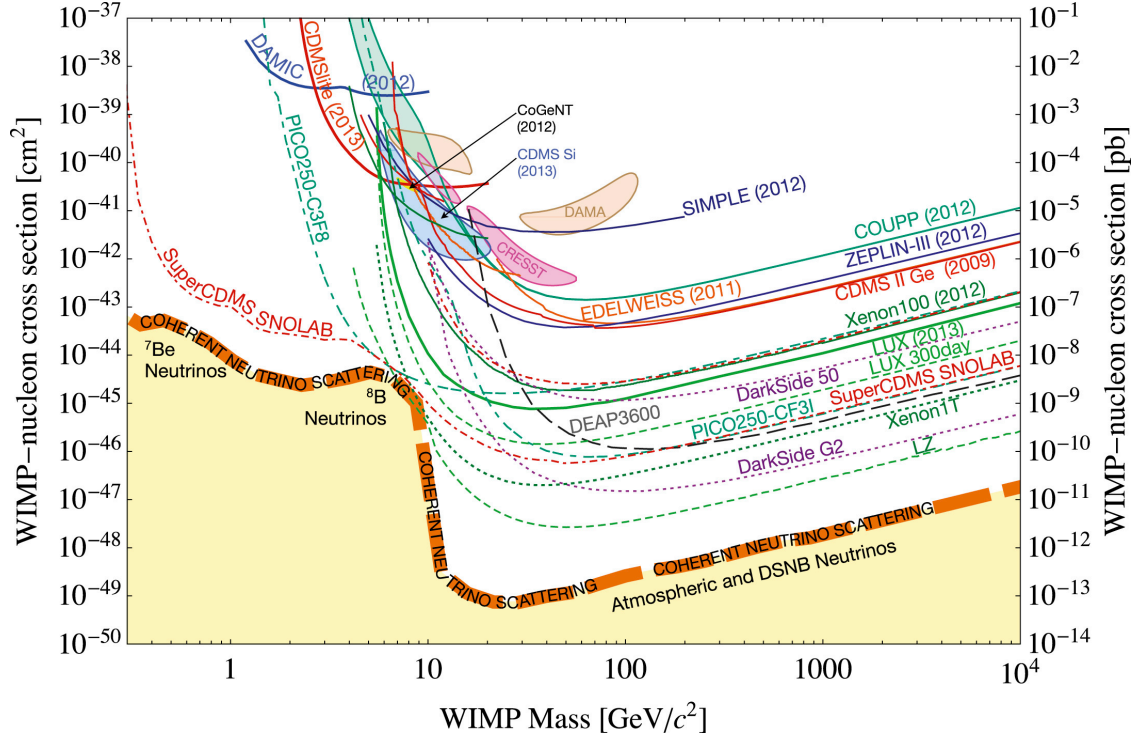
Figure 4.20: Upper limits on the SI WIMP-nucleon cross-section (solid lines) and hints of WIMP signals (closed contours) from current DM detection experiments, and projections (dashed) limits for planned direct detection experiments. In regions below the solid orange band, coherent neutrino scattering from solar neutrinos, atmospheric neutrinos and diffuse supernova neutrinos will dominate [205]. Figure from Ref. [206].

also appears to be ruled out. If we abandon the A^2 scaling of the WIMP-nucleon cross-section, this comparison plot is no longer valid. For all known theoretical assumptions, it is hard to reconcile the positive results of DAMA with the negative results of other experiments [200]. Many alternate explanations for the DAMA results have been proposed (e.g. radon contamination, muons) but all of them are shown to be incorrect. The reason DAMA remains interesting today is that there is no other non-WIMP explanation for the annual modulation.

To verify the DAMA results, further experimental tests using the same detector material as DAMA are required. In particular, DAMA-like experiments in the southern hemisphere would be ideal to rule out seasonal variations. Some of the proposed experiments include SABRE [201], COSINE-100 [202], DM-Ice [203] and ANAIS [204]. In the next 5 years or so, we can hope to either confirm or refute the long-standing DAMA signal.

4.5.3 Indirect detection

Indirect detection focus on searching for signs of SM particles produced from the annihilation or decay of the DM particles in our galaxy or throughout the cosmos [160,207]. Not only do they offer a unique advantage of being able to identify particle DM in an astro-

physical context, they also provide an independent means of mapping the DM distribution, and yield insight into the gravitational interplay between DM and other components of the universe.

Many particle DM candidates may annihilate or decay and produce indirect signals. Among such candidates, WIMPs are the focus of most indirect searches. WIMPs typically have a weak-scale mass, although more massive candidates such as *wimpzillas* have been proposed; their decay may result in ultra-high-energy cosmic rays which motivates indirect searches with those observations. The right-handed or *sterile* neutrino is another viable DM candidate in many scenarios. They can yield indirect signals via their radiative decay into an active neutrino.

Most channels from DM annihilation or decay involve unstable SM particles which quickly decay or hadronize into stable states such as protons, neutrinos, electrons and positrons, protons and antiprotons, and heavier nuclei and anti-nuclei. Thus, a potential signal for the existence of DM is WIMP-WIMP annihilation. As the annihilation rate of WIMPs is proportional to the square of the DM density ($\Gamma_A \propto \rho_{\mathrm{DM}}^2$), natural places to look for DM annihilations are those expected to have high WIMP densities such as the Sun, Earth and the GC. Due to their weak-scale masses (from tens of GeV to several TeV), they imply a similar energy scale for the prompt observable products from DM annihilation. Thus, indirect searches for WIMPs are focused largely on gamma rays, neutrinos and high-energy cosmic rays.

4.5.3.1 Gamma rays

Gamma rays are excellent astroparticle for indirect searches for WIMPs. The mass scale of the WIMP imply that a sizeable fraction of the emission generated by their annihilation or decay would end up at gamma-ray energies. Furthermore, gamma rays can travel to the observer without deflection, which allows for mapping of the signal sources. Together, the spatial and spectral signatures can be extremely useful for understanding the DM properties via indirect searches.

One way of producing gamma rays from WIMP annihilation is from a quark-anti-quark final state, which produces a particle jet along with gamma rays. The quark anti-quark fragmentation process has been thoroughly studied at accelerators and is well understood; the creation and propagation of gamma rays from such a jet is a fairly predictable process. The second form of gamma-ray production is the direct decay of WIMPs into gamma rays such as $\overline{\chi}\chi \rightarrow \gamma\gamma, \gamma Z$. These modes will produce a *gamma-ray line* with energy equal to the WIMP mass. As mentioned earlier, a typical WIMP can have a mass on the order of a few GeV. Thus, the resulting gamma rays would be extremely high in energy. Although the flux is small and quite difficult to detect, observing such a gamma-ray line would be a *smoking gun* signal of DM annihilation. The gamma-ray spectrum from the DM annihilation into various SM final states is shown in Fig. 4.21.
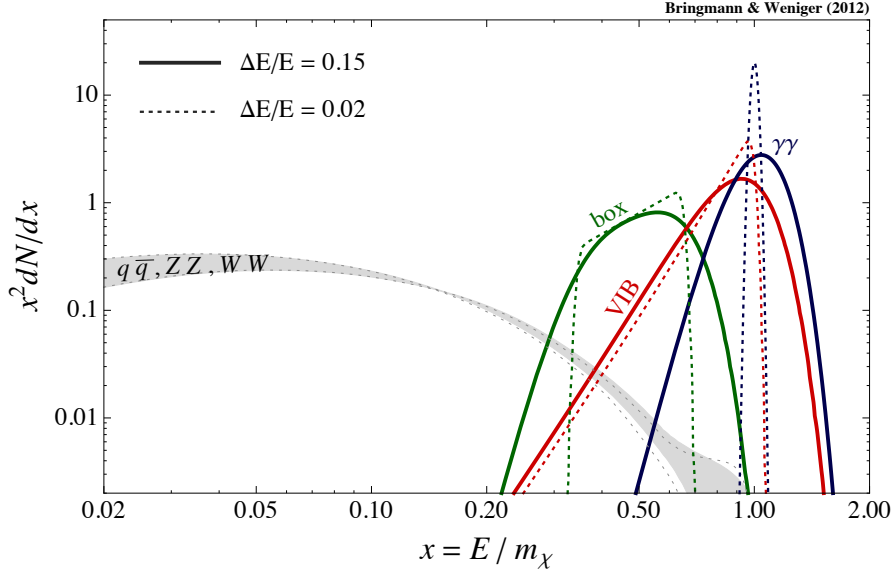
Figure 4.21: Energy spectrum of photons for the $\gamma\gamma$ final state without (blue) and with (red) virtual bremsstrahlung. The box-shaped spectrum (green) can be produced if the DM annihilates into a new state, which subsequently decays into photons. The dotted and solid lines compare the photon energy spectrum for energy resolution $\Delta E/E = 0.02$ and 0.15 respectively. The gray band corresponds to the photon energy spectrum from the DM annihilation into gauge bosons and quarks. Figure from Ref. [78].

The prompt flux emitted from the annihilation or decay of DM particles can be factored into a part that depends on the particle physics model for DM and a part that is determined by the DM distribution. The latter is known as the *J-factor* and is defined as

$$J_{\mathrm{ann}}(\psi) = \int_{\mathrm{l.o.s.}} \rho_{\mathrm{DM}}^2(\psi, l)\, dl \tag{4.37}$$

for DM annihilation and

$$J_{\mathrm{dec}}(\psi) = \int_{\mathrm{l.o.s.}} \rho_{\mathrm{DM}}(\psi, l)\, dl \tag{4.38}$$

for DM decay. Here ψ is the sky direction, l is the distance along the line-of-sight (l.o.s.) and ρ_{DM} is the DM density distribution. Usually, the J-factor is given in terms of an integral of $J(\psi)$ over a specific angular region.

The differential gamma-ray flux per unit solid angle and energy in a region $\Delta\Omega$ towards a direction ψ is [207–209]

$$\frac{d\Phi_{\mathrm{ann}}}{d\Omega\, dE} = \frac{\langle \sigma v_{\mathrm{rel}} \rangle}{2m_\chi^2} \frac{dN_\gamma}{dE} \frac{1}{4\pi} J_{\mathrm{ann}}(\psi) \tag{4.39}$$

for DM annihilation and

$$\frac{d\Phi_{\mathrm{dec}}}{d\Omega\, dE} = \frac{1}{m_\chi \tau} \frac{dN_\gamma}{dE} \frac{1}{4\pi} J_{\mathrm{dec}}(\psi) \tag{4.40}$$

for DM decay. Here τ is the lifetime for the DM particle, $\langle \sigma v_{\mathrm{rel}} \rangle$ is the velocity-averaged DM annihilation cross-section and dN_γ/dE is the differential gamma-ray spectrum per

annihilation or decay.[4] The factor of 2 in the denominator of Eq. (4.39) applies to a self-conjugate DM, and becomes a factor of 4 if the DM particle is not its own antiparticle.

In the past few years, the *Fermi* Large Area Telescope (*Fermi*-LAT) has discovered a gamma-ray excess towards the GC. It can be explained by the annihilation of a 40 GeV WIMP [210, 211]. More recent studies of the cosmic ray backgrounds have widened the possible range of WIMP masses [212]. However, studies have also shown that a point source explanation (e.g., pulsars) is at least as likely as a DM explanation [213–215]. Although a DM explanation for the excess sounds tantalising, it requires further proof due to the large uncertainties in the astrophysical backgrounds near the GC.

4.5.3.2 Neutrinos

Another indirect product of WIMP annihilations is neutrinos. Just like gamma rays, they preserve spectral information and point back to the source, making them a useful astroparticle for indirect searches. Detection of astrophysical neutrinos generally involves instrumenting a large volume of water or ice and detecting the Cherenkov light produced in the detector medium as the products of neutrino interactions pass through it. Large volumes are needed to gain sufficient statistics for neutrino-based DM searches.

As WIMPs travel through the universe and matter, they can lose small amounts of energy due to scattering off of nuclei. Thus, WIMPs can gather at the center of large gravitating bodies such as the Sun, thereby increasing their density until their annihilation rate equals half the capture rate (as two WIMPs are required for annihilation, whereas only one is required for capture). For many of the particle physics models, the WIMP annihilation and capture rates are at (or nearly at) equilibrium in the Sun. This equilibrium allows for a steady annihilation rate and a constant flow of neutrinos emanating from within the Sun. As neutrinos interact very weakly with ordinary baryonic matter in the Sun, they can travel straight to Earth. On the other hand, most DM models predict that the Earth has not yet reached such an equilibrium; it is less massive than the Sun, so it causes less WIMP scattering and has a much smaller gravitational potential well. Thus, neutrino telescopes usually focus on neutrino flux coming from the Sun rather than the Earth.

The differential neutrino flux from WIMP annihilation into a final state f is given by [12]

$$\frac{dN_\nu}{dE_\nu} = \frac{\Gamma_A}{4\pi D^2} \sum_f \mathcal{B}_f \frac{dN_\nu^f}{dE_\nu}, \tag{4.41}$$

where Γ_A is the annihilation rate of WIMPs in the Sun or Earth, D is the distance of the detector from the source (the central region of the Sun or Earth), f is the final state from the WIMP pair annihilation and $\mathcal{B}_f$ is the branching ratio into a final state f. The parameter dN_ν^f/dE_ν is the energy distribution of neutrinos generated by a final

---

[4]Specifically, it is a given by $dN_\gamma/dE = \sum_f \mathcal{B}_f \, dN_\gamma^f/dE$ where $\mathcal{B}_f$ is the branching ratio into a SM final state f.

state f [216]. Depending on the WIMP mass and its composition, annihilation processes include $\overline{\chi}\chi \rightarrow t\bar{t}$, $b\bar{b}$, $c\bar{c}$, ZZ, W^+W^- and $\tau^+\tau^-$, which decay to neutrinos among other products. For WIMPs lighter than the W mass, annihilation into $b\bar{b}$ and $\tau^+\tau^-$ states are the most common ones, yielding neutrinos with energies around 30 GeV. WIMP with heavier masses can annihilate into Higgs and gauge bosons, top and bottom quarks, and muons to produce high-energy neutrinos which are much easier to detect in neutrino telescopes. Thus, the detection of neutrinos heavily depends on the WIMP mass, annihilation rate, and density of WIMPs in the Sun and several other factors.

When neutrinos pass through the Earth, they can interact with the hydrogen, oxygen and other atoms around the optical modules in a neutrino detector. Electrons, muons and taus produced by such events are extremely energetic and travel faster than the speed of light in the medium. These particles are optically detected by their Cherenkov radiation. This technique is used in a cubic kilometer IceCube detector to constrain the spin-dependent WIMP-proton cross-section.[5] In fact, IceCube currently provides the best upper limits on the SD WIMP-proton cross-section for higher WIMP masses depending on the final state from the WIMP annihilation. The results are shown in Fig. 4.22.

4.5.3.3 Antimatter

Antimatter can provide an excellent signal of WIMP annihilation as it is relatively rare in the universe, and many of the astrophysical processes that create antimatter are well understood. For instance, the annihilation of WIMPs can produce antiprotons via $\overline{\chi}\chi \rightarrow q\bar{q}$ through hadronization (where the dominant annihilation process yields b quarks and anti-quarks), and positrons via secondary products such as W^+W^- and ZZ where $W/Z \rightarrow e^+\nu_e$. Unlike the production of gamma rays and neutrinos, these final products are electrically charged. Thus, they are affected by the magnetic fields in space and can lose energy due to inverse Compton, bremsstrahlung and synchrotron processes. Thus, one cannot make any conclusions about where the WIMP annihilation actually took place. Instead, the flux of antimatter particles from the galactic halo are studied as a whole, rather than dense regions such as the GC or large astrophysical objects.

Experimental searches for antimatter must be conducted near the top of the Earth's atmosphere or preferably in space. Various cosmic rays and their consequential particle showers can create large and uncertain backgrounds, thus making it difficult to perform robust analyses. It is also important to consider and subtract any potential backgrounds arising from cosmic rays that reach the edges of our atmosphere.

Recently, results from the PAMELA (a Payload for Antimatter Matter Exploration and Light-nuclei Astrophysics) satellite were released. The results indicated a sharp increase in the positron fraction over an energy range of 1.5–100 GeV. The authors concluded that

---

[5]For the Sun, this is possible as the capture rate (proportional to the DM-nucleon cross-section) is twice the annihilation rate (proportional to the DM annihilation cross-section).
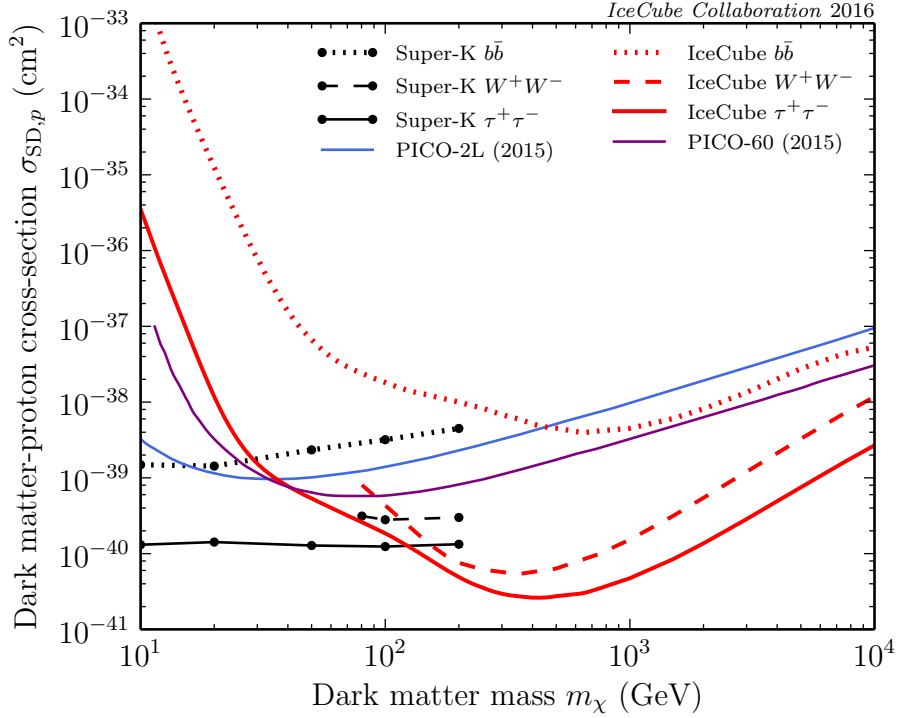
Figure 4.22: Comparison between the IceCube limits and latest constraints from Super-Kamiokande [22] and PICO [23, 24]. Depending on the DM annihilation channel, IceCube provides the best upper limits for WIMP masses above ∼ 100–200 GeV. On the other hand, Super-K is more sensitive to low WIMP masses. When the annihilation spectrum is soft or heavily suppressed, the PICO experiment provides stronger upper limits than neutrino telescopes; other direct detection limits are weaker. Figure from Ref. [217].

an astrophysical object or DM annihilation must account for the abundance of cosmic-ray positrons [218]. The data from PAMELA also required heavy WIMP candidates or large boost factors associated with non-uniform clumps in the DM distribution, thus constraining the nature of the possible DM models. The Advanced Thin Ionisation Calorimeter (ATIC), a balloon-based experiment, also reported an excess of e^- or e^+ at 300–800 GeV. However, results from the *Fermi*-LAT [219] and High Energy Stereoscopic System (HESS) [220] did not see the same electron-positron excess as ATIC, which leaves the issue far from settled. However, *Fermi*-LAT did see an excess similar to that of PAMELA. Further data is needed to determine if the excess gamma-ray and antimatter fluxes are indeed signals of DM annihilation or signatures of local astrophysical objects/backgrounds.

Similarly, the Alpha Magnetic Spectrometer (AMS) experiment has found an excess of positrons [221]. However, this excess is not likely caused by WIMP annihilation [222]. First, it was pointed out that such a positron excess would also generate gamma rays from dwarf galaxies which were not seen in the *Fermi*-LAT data. Using the *Fermi*-LAT bounds on gamma rays from dwarf galaxies, one finds that all WIMP annihilation channels are excluded as an explanation for the AMS data, except one where a mediator decays to four muons [223]. Second, the *Planck* satellite examined the effects of such an excess on the

CMB and ruled out a large portion of the model parameter space [75]. Thus, it is far more likely that the AMS positron excess is due to pulsars or other point sources than due to the WIMP annihilation. As with other experimental probes, more data is required to make any definitive statements.

Chapter 5

Electroweak Baryogenesis

5.1 Introduction

From our everyday lives, it is evident that there is more matter than antimatter. In nature, antimatter is mainly found in the form of cosmic rays, e.g., antiprotons $\overline{p}$. Their flux with respect to protons is

$$\frac{\Phi_{\overline{p}}}{\Phi_p} \sim 10^{-4}. \tag{5.1}$$

This ratio is consistent with $\overline{p}$ production via high energy collisions with ordinary matter. On Earth, antimatter is much harder to produce and store in laboratories, e.g., e^+ $(\overline{p})$ production at the former LEP (Tevatron) experiment.

In this chapter, we review the topic of electroweak baryogenesis (EWBG) based on Refs. [25, 26]. We start by motivating the presence of baryon asymmetry in our universe, outline the three Sakharov conditions required by any baryon-generating theory and check if these conditions are fulfilled in the SM. To study the details of the electroweak phase transition (EWPT), we will describe both the perturbative and non-perturbative methods. This will allow us to propose simple extensions of the SM, and discuss possible collider, indirect and gravitational wave (GW) signals.

5.2 Baryon asymmetry

The asymmetry between matter and antimatter can be characterised in terms of the baryon-to-photon ratio as

$$\eta \equiv \frac{n_b - n_{\overline{b}}}{n_\gamma}, \tag{5.2}$$

where n_b $(n_{\overline{b}})$ is the number density of baryons (antibaryons), $n_\gamma = \zeta_3 g_* T^3/\pi^2$ is the number density of photons, $g_* = 2$ is the number of spin polarization states for photons and $\zeta_3 \simeq 1.2021$. The ratio in Eq. (5.2) provides a useful measure of the asymmetry as it remains constant with the expansion of the universe, at least at late times. At earlier
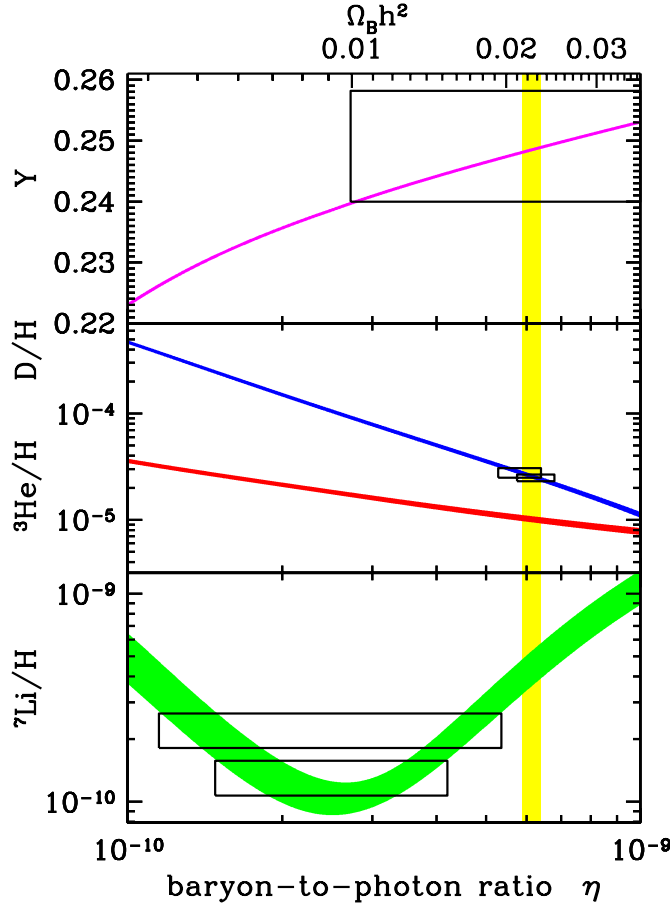
Figure 5.1: Primordial abundance of light elements vs the baryon-to-photon ratio η. The range of η values allowed by the CMB data is shown as the vertical yellow band. Figure from Ref. [25].

times (or high temperatures), many heavier particles were in thermal equilibrium which later annihilated to produce more photons but not many baryons. In this case, the entropy density s is a better quantity to compare against the baryon number density. Thus, we can consider

$$\frac{n_b - n_{\bar{b}}}{s} = \frac{1}{7.04}\eta, \tag{5.3}$$

where the conversion factor is valid in the present universe from the time when neutrinos went out of thermal equilibrium and positrons annihilated.

The baryon-to-photon ratio η was historically determined using the big bang nucleosynthesis. The abundance of light elements ^{3}He, ^{4}He, D, ^{6}Li and ^{7}Li are sensitive to the values of η [3]. A comparison between the theoretical predictions and measured experimental values for η is made in Fig. 5.1. The boxes represent the regions that are consistent with the experimentally determined values for η. As the smallest error bars appear in the deuterium (D/H) abundance, we get

$$\eta = 10^{-10} \times \begin{cases} 6.28 \pm 0.35 \\ 5.92 \pm 0.56 \end{cases} \tag{5.4}$$
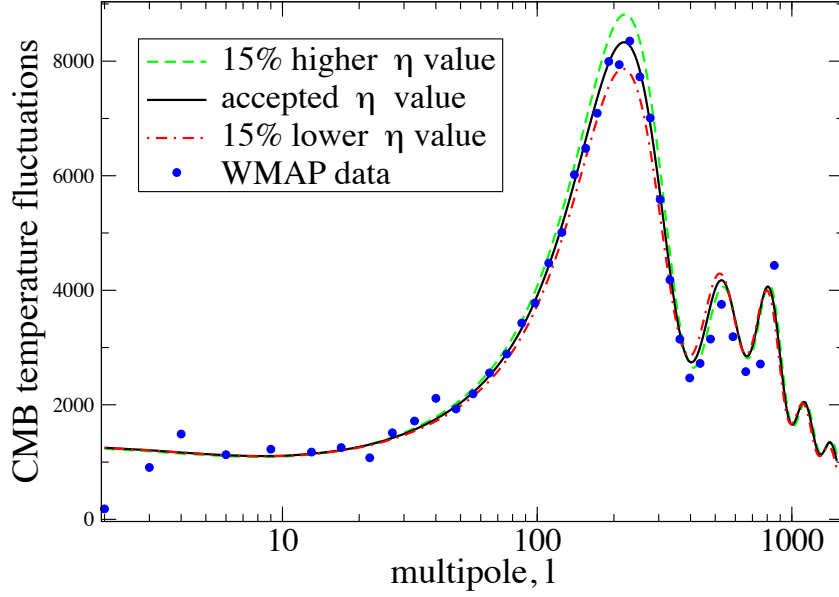
Figure 5.2: Dependence of the CMB Doppler peaks on η. Figure from Ref. [25].

for the two experimental determinations shown in Fig. 5.1. These values are consistent with the ^{4}He abundance, however they are marginally inconsistent with the ^{7}Li abundance.[1]

In recent years, the CMB has provided an independent way of measuring the baryon asymmetry. The relative size of the Doppler peaks in the CMB temperature anisotropies is sensitive to the values of η [225]. This is illustrated in Fig. 5.2. Using the first year data from the WMAP, we get [102]

$$\Omega_b h^2 = 0.0224 \pm 0.0009. \qquad (5.5)$$

This corresponds to

$$\eta = (6.14 \pm 0.25) \times 10^{-10}. \qquad (5.6)$$

Thus, the CMB provides a more accurate estimate of η than the BBN determination. Apart from the lithium problem, the above result is in good agreement with the BBN value. The range of η values allowed by the CMB data is shown as the vertical yellow band in Fig. 5.1.

From these measurements, it is clear that a matter-antimatter asymmetry exists in our universe. The key question is why the asymmetry exists in the first place. After all, if the universe started out without any baryon asymmetry, the big bang should produce equal numbers of particles and antiparticles, yet this is not the case. One might wonder if the universe is baryon symmetric on large scales and is separated into regions which are dominated by either baryons or antibaryons. However, it is well-known that in the least dense regions of the universe, there are hydrogen gas clouds. Thus, an excess of gamma rays would be expected from the matter-antimatter annihilation in regions between the baryon and antibaryon dominated regions. Such gamma-ray excesses have not been seen

---

[1]This is the well-known primordial *Lithium problem* [224].

so far. This suggests that the matter/antimatter dominated regions have to be as large as the observable universe today. Thus, there is no plausible way of separating baryons and antibaryons from each other.

It is interesting to note that in a homogeneous, baryon symmetric universe, some baryon asymmetry is generated as annihilations are not 100% efficient. In this case, the freeze-out abundance of baryons and antibaryons is expected to be [226]

$$\frac{n_b}{n_\gamma} = \frac{n_{\bar{b}}}{n_\gamma} \simeq 10^{-20}.$$
(5.7)

This is about 10 orders of magnitude smaller than the value of η determined from the BBN or CMB. Thus, an unknown mechanism must be responsible for generating the observed matter-antimatter asymmetry in our universe.

5.3 Sakharov conditions

During the early days of big bang cosmology, baryon asymmetry was considered as an initial condition. However, in the context of inflation, this idea is no longer supported as any baryon asymmetry existing before inflation would be washed out by the production of entropy during the re-heating process. Thus, the baron asymmetry must be generated *dynamically*.

In 1967, A. Sakharov realised the need for a dynamic generation of baryon asymmetry from symmetric initial conditions [227]. He outlined three necessary conditions that would result in an imbalance between matter and antimatter number densities.

5.3.1 B violation

The generation of baryon asymmetry requires baryon number B violating processes. In the SM, B is violated by the triangle anomaly which spoils the conservation of left-handed baryon and lepton current [25], namely

$$\partial_\mu J^\mu_{B_L+L_L} = \frac{3g^2}{32\pi^2} \epsilon_{\alpha\beta\gamma\delta} W_a^{\alpha\beta} W_a^{\gamma\delta},$$
(5.8)

where $W_a^{\alpha\beta}$ is the $SU(2)$ field strength tensor. This leads to a non-perturbative *sphaleron process* as shown in Fig. 5.3. It involves 9 left-handed $SU(2)$ quark doublets (3 from each generation) and 3 left-handed leptons (one from each generation). This process violates B and L by 3 units each, i.e.,

$$\Delta B = \Delta L = \pm 3.$$
(5.9)
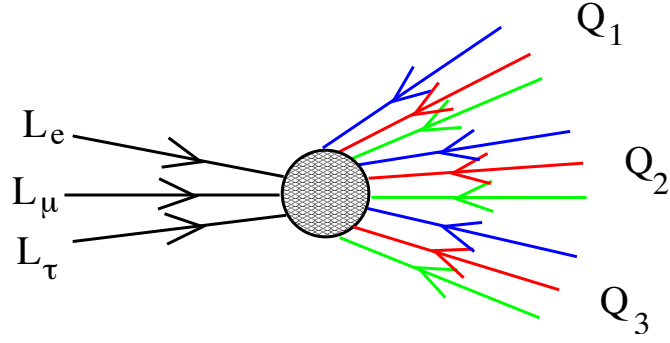
Figure 5.3: The non-perturbative sphaleron process which violates B and L by 3 units. Figure from Ref. [25].

5.3.2 Departure from thermal equilibrium

To understand this requirement, consider a hypothetical process

$$X \rightarrow Y + Z, \tag{5.10}$$

where X (Y) represents some initial (final) state with $B = 0$ and Z represents the excess baryons produced by the process with $B \neq 0$. If the process is in thermal equilibrium, the inverse process $Y + Z \rightarrow X$ also occurs at the same rate such that

$$\Gamma(Y + Z \rightarrow X) = \Gamma(X \rightarrow Y + Z). \tag{5.11}$$

In this case, no net asymmetry is generated as the inverse process destroys the excess baryons as fast as Eq. (5.10) creates it. Thus, a departure from thermal equilibrium is essential for generating any baryon asymmetry.

The classic example of a departure from thermal equilibrium is that arising from out-of-equilibrium decays. In this case, X is a heavy particle with mass $m_X > T$ at the time of decay $\tau = \hbar/\Gamma$. As the energy of the final state $Y + Z$ is of the order T, there is not enough energy to produce the heavier X boson from the inverse process $Y + Z \rightarrow X$. This results in a Boltzmann-suppressed rate, i.e.,

$$\Gamma(Y + Z \rightarrow X) \sim e^{-m_X/T}. \tag{5.12}$$

Thus, the original process $X \rightarrow Y + Z$ can generate the observed baryon asymmetry.

5.3.3 C and CP violation

Suppose the above process $X \rightarrow Y + Z$ has a charge conjugation C symmetry. This implies that the charge conjugated process $\overline{X} \rightarrow \overline{Y} + \overline{Z}$ occurs at the same rate, i.e.,

$$\Gamma(\overline{X} \rightarrow \overline{Y} + \overline{Z}) = \Gamma(X \rightarrow Y + Z). \tag{5.13}$$

In this case, the net rate of baryon production is

$$\frac{dB}{dt} \propto \Gamma(\overline{X} \rightarrow \overline{Y} + \overline{Z}) - \Gamma(X \rightarrow Y + Z). \tag{5.14}$$

Thus, no net asymmetry is generated if C is a symmetry. However, even if C is violated, it is not enough. In addition, the combined charge conjugation and parity CP symmetry must also be violated. To understand this requirement, we consider a scenario where X decays into two left-handed or right-handed quarks as

$$X \to q_L\,q_L, \quad X \to q_R\,q_R. \tag{5.15}$$

Under CP, $q_L \to \overline{q}_R$ where $\overline{q}_R$ is the left-handed antiparticle of q_R, see Eq. (2.32), whereas under C, $q_L \to \overline{q}_L$. Although C violation implies that

$$\Gamma(X \to q_L\,q_L) \neq \Gamma(\overline{X} \to \overline{q}_L\,\overline{q}_L), \tag{5.16}$$

$$\Gamma(X \to q_R\,q_R) \neq \Gamma(\overline{X} \to \overline{q}_R\,\overline{q}_R), \tag{5.17}$$

CP conservation would imply

$$\Gamma(X \to q_L\,q_L) = \Gamma(\overline{X} \to \overline{q}_R\,\overline{q}_R), \tag{5.18}$$

$$\Gamma(X \to q_R\,q_R) = \Gamma(\overline{X} \to \overline{q}_L\,\overline{q}_L). \tag{5.19}$$

This means that

$$\Gamma(X \to q_L\,q_L) + \Gamma(X \to q_R\,q_R) = \Gamma(\overline{X} \to \overline{q}_R\,\overline{q}_R) + \Gamma(\overline{X} \to \overline{q}_L\,\overline{q}_L). \tag{5.20}$$

If the initial state contains equal numbers of X and $\overline{X}$, we will end up with no net asymmetry. The best we can hope to achieve is an asymmetry between left- and right-handed quarks. However, this does not correspond to a baryon asymmetry.

Now, suppose that the process $X \to qq$ violates both C and CP symmetries, i.e.,

$$\Gamma(X \to qq) \neq \Gamma(\overline{X} \to \overline{q}\,\overline{q}), \tag{5.21}$$

where we have ignored the distinctions between q_L and q_R for convenience. We can imagine that if all X's decay into qq and all $\overline{X}$'s decay into $\overline{q}\,\overline{q}$ when $n_X = n_{\overline{X}}$ initially, we will eventually end up with equal numbers of q and $\overline{q}$, although there was temporarily an excess. To avoid such outcomes, there must be at least one competing channel $X \to Y$, $\overline{X} \to \overline{Y}$ such that

$$\Gamma(X \to Y) \neq \Gamma(\overline{X} \to \overline{Y}). \tag{5.22}$$

In this channel, Y should have a different baryon number than qq. Thus, a baryon asymmetry will develop by the time all X's have decayed. The CPT theorem with the requirement of B violation guarantees that there is no other competing decay channel with the correct properties [228]. It also implies that the total decay rates of X and $\overline{X}$ are equal, i.e.,

$$\Gamma(X \to qq) + \Gamma(X \to Y) = \Gamma(\overline{X} \to \overline{q}\,\overline{q}) + \Gamma(\overline{X} \to \overline{Y}). \tag{5.23}$$

As B violation is required, Y should have a different baryon number than qq. Otherwise, we can consistently assign a baryon number of 2/3 to X which does not result in any B violation.

5.4 B and CP violation in the SM

5.4.1 B violation

The SM has a usable source of B violation. In 1976, 't Hooft showed that the triangle anomaly violates baryon number B through a non-perturbative process [229]. As we have seen in Eq. (5.8), the baryon current is not conserved in the presence of external W boson field strengths. However, this B violation does not manifest itself in any perturbative process. Instead, it is associated with the vacuum structure of $SU(N)$ gauge theories with spontaneously broken symmetry. To explain this, we introduce the concept of a Chern-Simons number as

$$N_{\mathrm{CS}} = \int d^3x\, K^0, \tag{5.24}$$

where the current K^μ is given by

$$K^\mu = \frac{g^2}{32\pi^2} \epsilon^{\mu\nu\alpha\beta} \left(F_{\nu\alpha}^a A_\beta^a - \frac{g}{3} \epsilon_{abc} A_\nu^a A_\alpha^b A_\beta^c \right). \tag{5.25}$$

This current has the property that

$$\partial_\mu K^\mu = \frac{g^2}{32\pi^2} F_{\mu\nu}^a \widetilde{F}_a^{\mu\nu}. \tag{5.26}$$

In reality, the Chern-Simons number has a topological nature which can be seen by considering configurations that are pure gauge at some initial time t_0 and final time t_1. It can be shown that

$$N_{\mathrm{CS}}(t_1) - N_{\mathrm{CS}}(t_0) = \int_{t_0}^{t_1} dt \int d^3x\, \partial_\mu K^\mu = \omega, \tag{5.27}$$

where ω is an integer called the winding number. The gauge field is a map from the physical space to the manifold of the gauge group.

We are mainly interested in the vacuum structure of the $SU(2)$ gauge theory. We consider a family of static gauge field configurations with continuously varying N_{CS}. Those configurations with integer values turn out to be pure gauge everywhere with vanishing field strength and zero energy. To interpolate between two such configurations, one must pass through other configurations with non-vanishing field strengths. The form of the energy vs Chern-Simons number N_{CS} is shown in Fig. 5.4.

Each minimum is a valid perturbative vacuum state of the theory. They are called n-vacua. The height of the energy barrier is given by

$$E_{\mathrm{sph}} = f\left(\frac{\lambda}{g^2}\right) \frac{4\pi v}{g} \simeq \frac{8\pi v}{g} = \frac{2m_W}{\alpha_W} f\left(\frac{\lambda}{g^2}\right), \tag{5.28}$$

where $v = 174\,\mathrm{GeV}$ is the VEV of the Higgs field, λ is the Higgs quartic coupling and $\alpha_W = g^2/4\pi \sim 1/30$. The function f ranges between $f(0) = 1.56$ and $f(\infty) = 2.72$.
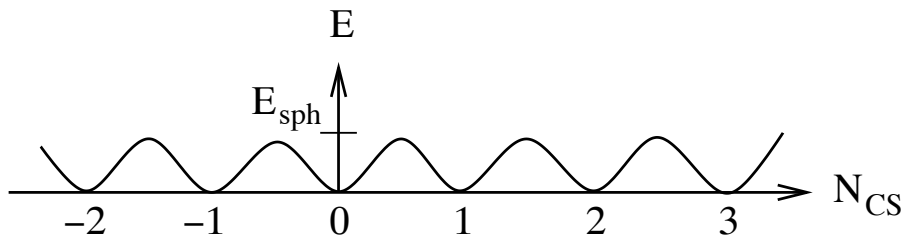
Figure 5.4: Energy of the gauge field configurations vs the Chern-Simons number N_{CS}. Figure from Ref. [25].

It was 't Hooft who showed that tunnelling between n-vacua through field configurations occur via *instantons*. This is relevant for B violation via the following relation

$$\partial_\mu J^\mu_{B_L+L_L} = N_f \partial_\mu K^\mu, \tag{5.29}$$

where $N_f = 3$ is the number of families. After integrating over space and time coordinates, the spatial divergence integrates to zero and we are left with

$$3\frac{d}{dt}N_{\mathrm{CS}} = \frac{d}{dt}B = \frac{d}{dt}L. \tag{5.30}$$

Thus, each instanton transition violates B and L by 3 units. The transition causes simultaneous generation of 9 quarks and 3 leptons with each generation represented equally. However, the transition amplitude is

$$\mathcal{A} \sim e^{-8\pi^2/g^2} \sim 10^{-173}. \tag{5.31}$$

This is too small to ever happen during the lifetime of our universe. For this reason, anomalous B violation in the SM was not first considered for baryogenesis. However, in 1985, V. A. Kuzmin, V. A. Rubakov and M. E. Shaposhnikov realised that at high temperatures, these transitions could become unsuppressed due to the availability of thermal energy to hop over the potential barrier instead of tunnelling through it [230]. This occurs when $T \gtrsim 100\,\mathrm{GeV}$, i.e., above the electroweak scale. The finite temperature transitions are known as *sphaleron processes*, a term coined by Klinkhamer and Manton from the Greek meaning "ready to fall." It is the field configuration of the Higgs and W^μ fields which sit at the top of the energy barrier between the n-vacua [231]. A thermal transition between the n-vacua must pass through a configuration that is close to the sphaleron unless $T \gg E_{\mathrm{sph}}$. The sphaleron is a static, saddle point solution of the field equations.

After evaluating the path integral for a sphaleron transition semi-classically, one finds that the amplitude goes as

$$\mathcal{A} \sim e^{-E_{\mathrm{sph}}/T}. \tag{5.32}$$

To find the actual rate of transitions, a more detailed calculation is required [232]. The rate per unit volume of the sphaleron transitions was computed by Khlebnikov and Sha-

poshnikov to be

$$\frac{\Gamma}{V} = \mathcal{B}_0 \left(\frac{E_{\mathrm{sph}}}{T}\right)^3 \left(\frac{m_W(T)}{T}\right)^4 T^4 e^{-E_{\mathrm{sph}}/T}, \tag{5.33}$$

where $\mathcal{B}_0$ is a constant of order one and $m_W(T)$ is the temperature dependent mass of the W boson. However, the above expression is only valid for temperature $T < E_{\mathrm{sph}}$. At $T \gtrsim m_W$, EWSB has not yet occurred and $m_W(T) = 0$. The Higgs VEV vanishes in the symmetry-restored phase and $E_{\mathrm{sph}} = 0$. In this case, there is no barrier between the n-vacua.

Above the EWPT, the rate of sphaleron transitions cannot be computed analytically; instead, lattice computations are required. For many years, the parametric dependence of the sphaleron transition rate was thought to be

$$\frac{\Gamma}{V} = c\alpha_W^4 T^4 \simeq c(g^2 T)^4, \tag{5.34}$$

where $c \sim 1$ and $\alpha_W = g^2/4\pi \sim 1/30$. This is based on an idea that the transverse gauge bosons acquire a thermal mass of order $g^2 T$ which is the only relevant scale in the problem. This determines the form of the above expression by dimensional analysis. However, it was later shown that this form is incorrect [233]. The time scale for sphaleron transition is actually $g^4 T$ instead of $g^2 T$ as in Eq. (5.34). This gives $\Gamma/V \sim \alpha_W^5 T^4$. Recent lattice calculations fix the dimensionless coefficient to be [234]

$$\frac{\Gamma}{V} = (25.4 \pm 2.0)\alpha_W^5 T^4 = (1.06 \pm 0.08) \times 10^{-6} T^4. \tag{5.35}$$

We can determine when the sphalerons were in thermal equilibrium in the early universe. To compute the rate, we must choose a relevant volume. We can take the thermal volume $1/T^3$ which corresponds to the average space occupied by a particle in the thermal bath. Thus, we get

$$\Gamma = 10^{-6} T. \tag{5.36}$$

This should be compared against the Hubble rate $H \sim \sqrt{g_*} T^2/M_p$ such that

$$\frac{\Gamma}{H} \sim \frac{1}{T}. \tag{5.37}$$

At very high temperatures, sphalerons are out of equilibrium as shown in Fig. 5.5. They come into equilibrium when $\Gamma = H$. This corresponds to $T \sim 10^{13}$ GeV. When T falls below the EWPT temperature $T \sim 100$ GeV, the sphaleron rate again falls below H.

5.4.2 CP violation

As the SM provides a useable source of B violation, it is natural to ask if baryogenesis is possible within the SM. Specifically, we can check if the remaining two Sakharov conditions can be satisfied.
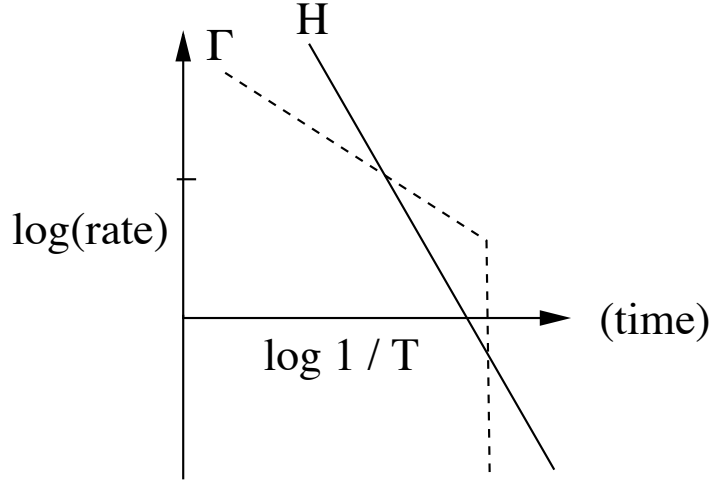
Figure 5.5: Sphaleron transition and Hubble rates vs time. The sharp drop in the sphaleron transition rate occurs at the electroweak phase transition (EWPT) when $T \simeq 100\,\text{GeV}$. Figure from Ref. [25].

In the SM, it is known that CP violation exists in the CKM matrix where

$$V_{\text{CKM}} = \begin{pmatrix} V_{ud} & V_{us} & V_{ub} \\ V_{cd} & V_{cs} & V_{cb} \\ V_{td} & V_{ts} & V_{tb} \end{pmatrix} = \begin{pmatrix} c_1 & -s_1 c_3 & -s_1 s_3 \\ s_1 c_2 & c_1 c_2 c_3 - s_2 s_3 e i\delta & c_1 c_2 s_3 + s_2 c_3 e^{i\delta} \\ s_1 s_2 & c_1 s_2 c_3 + c_2 s_3 e^{i\delta} & c_1 s_2 s_3 - c_2 c_3 e^{i\delta} \end{pmatrix}. \tag{5.38}$$

This is written in the KM parametrisation, whereas in the Wolfenstein parameterisation, V_{ub} and V_{td} contain CP violating phases. The phase residing in the CKM matrix can be changed by field redefinitions. To express the invariant phase, C. Jarlskog showed that one possible invariant combination is [235]

$$J = (m_t^2 - m_c^2)(m_t^2 - m_u^2)(m_c^2 - m_u^2)(m_b^2 - m_s^2)(m_b^2 - m_d^2)(m_s^2 - m_d^2)K, \tag{5.39}$$

where

$$K = s_1^2 s_2 s_3 c_1 c_2 c_3 \sin \delta = \text{Im}(V_{ii} V_{jj} V_{ij}^* V_{ji}^*), \quad i \neq j. \tag{5.40}$$

This can be derived by computing the determinant of the commutator of the up- and down-type quark squared mass matrices as

$$J = \det \left[\mathcal{M}_u^2, \mathcal{M}_d^2 \right] \tag{5.41}$$

which is invariant under field rotations.

The form of J has been used to argue that CP violation in the SM is not enough for baryogenesis. Using the relevant temperature scale of the universe (which must be at least of order $100\,\text{GeV}$ for sphalerons to be effective), one finds a dimensionless measure of the strength of CP violation to be

$$\frac{J}{(100\,\text{GeV})^{12}} \sim 10^{-20}. \tag{5.42}$$

This is too small to account for the measured value of $\eta \sim 10^{-10}$.

In Ref. [235], J was defined in terms of the linear quark mass matrices as in Eq. (5.41) but with linear rather than squared mass differences. In a subsequent paper, it was argued that the sign of a fermion mass has no absolute physical significance. Thus, any physical quantity should depend on the square of the masses. However, this does not have any bearing on the mathematical fact that the original linear mass definition of J is a valid invariant characterisation of the CP phase. If it were the physically correct definition, Eq. (5.41) would be revised to read $J \sim 10^{-10}$ which agrees with $\eta \sim 10^{-10}$.

A more specific criticism towards the above argument comes from Ref. [236]. Here it was shown that the above arguments could not be applied to the $K\overline{K}$ mixing in the neutral kaon system. The authors showed that the CP violating effect is not proportional to J and the relevant scale is much smaller than $100\,\text{GeV}$, rather it is the mass of K^0. The idea that J/T^{12} is the correct measure of CP violation only makes sense if all the ratios of particle masses to temperature are perturbatively small. This is not the case for the top quark mass. Although there is no theorem which proves that it is impossible to find some other mechanism that does work, no convincing demonstrations have been shown so far. Most experts on baryogenesis theories agree that CP violation in the SM is too weak. Thus, new sources of CP violation are required which motivates BSM physics.

5.5 Electroweak baryogenesis

One of the most attractive ways to account for the observed baryon asymmetry is via electroweak baryogenesis (EWBG) [230, 237–242]. It refers to a mechanism that generates the baryon asymmetry during the electroweak epoch.

The assumed initial conditions for EWBG are a hot, radiation-dominated early universe with zero net baryon charge in which the full $SU(2)_L \otimes U(1)_Y$ electroweak symmetry is manifested [243, 244]. As the universe cools down to temperatures below the electroweak scale, $T \lesssim 100\,\text{GeV}$, the Higgs field settles into a vacuum state which spontaneously breaks the electroweak symmetry down to its $U(1)_{\text{EM}}$ subgroup. It is believed that during this phase transition, EWBG is meant to take place.

A successful EWBG requires a strong first-order EWPT. Such a transition proceeds via a nucleation of bubbles of the broken phase within the surrounding plasma in the symmetric phase. This process is shown in Fig. 5.6. As the bubbles expand, they collide and coalesce with other bubbles until only the broken phase remains.

In EWBG, baryon creation takes place in the vicinity of the expanding bubble walls [245]. As shown in Fig. 5.7, this occurs via the following three steps:

1. Particles in the plasma scatter with the bubble walls. If the underlying theory violates CP symmetry, these scattering processes will generate C and CP asymmetries in
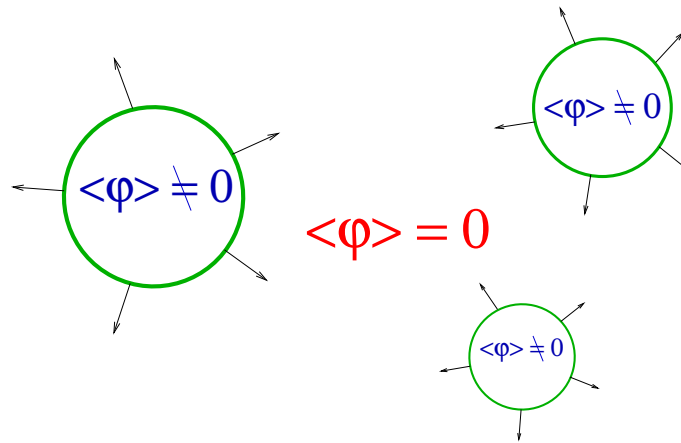
Figure 5.6: Expanding bubbles of the broken phase within the surrounding plasma in the symmetric phase. Figure from Ref. [26].
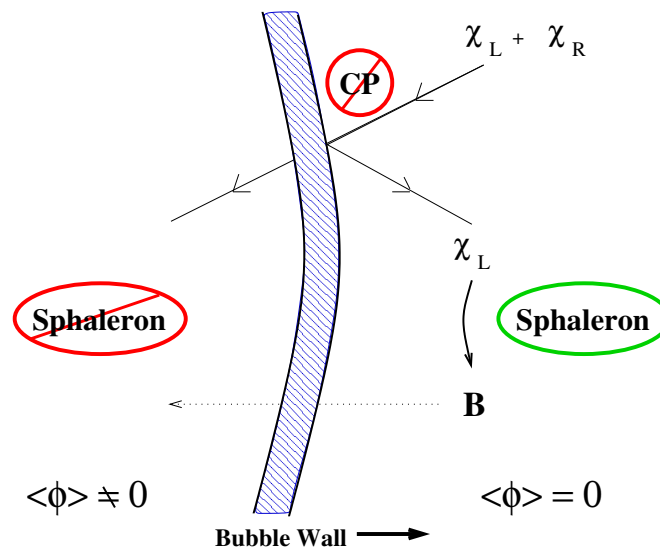
Figure 5.7: Production of baryons in front of the expanding bubble walls. Figure from Ref. [26].

particle number densities in front of the bubble wall;

2. These asymmetries diffuse into the symmetric phase ahead of the bubble wall where they bias electroweak sphaleron transitions to produce more baryons than antibaryons [246];

3. A part of the net baryon charge created outside the bubble wall is swept up by the expanding wall into the broken phase. In this broken phase, the rate of sphaleron transitions is strongly suppressed and can be small enough to avoid washout of baryons created in the first two steps.

The above steps explicitly satisfy the three Sakharov conditions [227]. First, the departure from thermodynamic equilibrium is induced by the passage of the rapidly expanding bubble walls through the cosmological plasma. Second, *B* violation comes from the

rapid sphaleron transitions in the symmetric phase. And third, both C- and CP-violating scattering processes are required at the phase boundaries to create an asymmetry in particle number densities. This biases the sphalerons to create more baryons than antibaryons.

All of the required ingredients for EWBG are present in the SM. However, EWBG is unable to explain the observed baryon asymmetry within the SM alone. The first impediment is that a strongly first-order EWPT is only possible in the SM if the Higgs boson mass lies below 70 GeV [247, 248]. This is much less than the observed Higgs boson mass $m_h = 125$ GeV [10, 56]. Even if the phase transition was first-order, the CP violation induced by the CKM matrix in the SM is not enough to generate large enough chiral asymmetries [249, 250].

An essential feature of all viable realisations of EWBG is BSM physics. The new physics must couple to the SM with at least a moderate strength and must be abundant in the thermal plasma at the time of EWPT. These two conditions together imply that new particles must exist with masses not too far above the electroweak scale and with direct couplings to the SM. Thus, a generic feature of EWBG is that new phenomena should be discovered in the upcoming collider, precision and astrophysical experiments. It is this property of EWBG which sets it apart from other mechanisms for baryon creation.

Due to the detection probes for EWBG, it is particularly important to achieve the most robust theoretical predictions for the baryon asymmetry and associated phenomenological implications. Thus, we review the current progress in various theoretical tools used to compute the baryon asymmetry and detection probes.

5.6 Electroweak phase transition

Baryon creation in EWBG is closely tied to the dynamics of the electroweak phase transition (EWPT). In this transition, the thermal plasma goes from a symmetric state in which the full $SU(2)_L \otimes U(1)_Y$ gauge invariance is manifested to a broken one where only the $U(1)_{\text{EM}}$ electroweak subgroup remains [243, 251–253]. As discussed earlier, the transition must be first-order and proceed via the nucleation of bubbles of the broken phase. We discuss the dynamics of the phase transition and describe its role in EWBG.

The transition from symmetric to broken phase in the SM can be characterised by the VEV of the Higgs field $\Phi \equiv (\phi_+, \phi_0)^T$. A field basis can always be chosen such that only the real component of ϕ_0 develops a non-zero VEV. Thus, we will write

$$\langle \phi_0 \rangle \equiv \phi/\sqrt{2}. \tag{5.43}$$

The symmetric phase corresponds to $\phi = 0$, whereas the broken phase corresponds to $\phi \equiv v \neq 0$. In the unitary gauge, the masses of the $W^\pm/Z$ bosons and fermions are proportional to ϕ. For more details, see chapter 2.

The features of the phase transition that are most relevant for EWBG are its character (first-order, second-order or a crossover), the critical temperature T_c, the bubble nucleation temperature T_n, which describe when the transition takes place, and the sphaleron transition rate Γ_{sph}, which governs the rate of baryon number generation, washout and the bubble nucleation rate. These features have been extensively studied using a broad range of theoretical tools.

The most robust computation of these quantities is performed using non-perturbative, Monte Carlo methods. Due to the level of efforts required to perform such studies, they have only been carried out for a few specific theories of EWBG. Instead, perturbative methods have been used more frequently to study the dynamics of the EWPT in a broad range of BSM scenarios. Perturbative analyses can also help in giving useful insights into some aspects of phase transition dynamics which may be less accessible with Monte Carlo methods. However, it should be noted that the application of perturbation theory to EWPT physics comes with uncertainties and potential ambiguities. For instance, in the SM, one often finds that the transition temperature T_n obtained using perturbative methods is significantly lower than the value obtained from Monte Carlo studies for a fixed Higgs boson mass. Given the widespread use of perturbation theory, we first begin by reviewing this approach to present the conventional treatment and comment on its difficulties. We subsequently review some of the features of the non-perturbative analysis.

5.6.1 Perturbative methods

In a perturbative analysis of the EWPT, a key quantity of interest is the renormalised finite-temperature effective potential V_{eff}. It coincides with the free energy of the cosmological plasma [238, 254, 255] as long as it is reasonably close to the thermodynamic equilibrium. A key feature of the effective potential is that the expectation value of the Higgs field is the one that minimises its value.

At one-loop order, the effective potential is given by [238]

$$V_{\text{eff}}(\phi, T) = V_0(\phi) + V_1(\phi) + V_1^{(T)}(\phi, T), \tag{5.44}$$

where

$$V_0(\phi) = -\frac{1}{2}\mu^2\phi^2 + \frac{1}{4}\lambda\phi^4 \tag{5.45}$$

is the tree-level Higgs potential, $V_1(\phi)$ is the one-loop correction to the effective potential at $T = 0$ and $V_1^{(T)}(\phi, T)$ contains the leading order thermal corrections. The one-loop correction $V_1(\phi)$ is given by [256]

$$V_1(\phi) = \sum_i \frac{n_i(-1)^{2s_i}}{4(4\pi)^2} m_i^4(\phi) \left[\log\left(\frac{m_i^2(\phi)}{\mu^2}\right) - C_i\right], \tag{5.46}$$

where the sum i runs over all particles in the theory, each with n_i degrees of freedom, field-dependent mass $m_i(\phi)$ and spin s_i. We have assumed a mass-independent renormalisation

where μ is the renormalisation scale and C_i are the scheme-dependent constants. Choosing $\mu \sim \max\{m_i(\phi)\}$ optimises the perturbative expansion. We note that the Fadeev-Popov ghosts are massless and decoupled if we work in the *Landau gauge* ($\xi = 0$). In this case, $n_i = 3$ for each vector and Goldstone bosons in the theory.

The thermal corrections at one-loop order are given by [238]

$$V_1^{(T)}(\phi, T) = \frac{T^4}{2\pi^2}\left[\sum_{i=\text{bosons}} n_i J_b\left(\frac{m_i^2}{T^2}\right) + \sum_{j=\text{fermions}} n_j J_f\left(\frac{m_j^2}{T^2}\right)\right], \qquad (5.47)$$

where J_b and J_f are loop functions. For $x \ll 1$, the loop functions expand to [257]

$$J_b(x^2) = -\frac{\pi^4}{45} + \frac{\pi^2}{12}x^2 - \frac{\pi}{6}x^3 - \frac{1}{32}x^4 \log\left(\frac{x^2}{a_b}\right) + O(x^3), \qquad (5.48)$$

$$J_f(x^2) = -\frac{7\pi^4}{360} - \frac{\pi^2}{24}x^2 - \frac{1}{32}x^4 \log\left(\frac{x^2}{a_f}\right) + O(x^3), \qquad (5.49)$$

where $\log(a_b) \simeq 5.4076$ and $\log(a_f) \simeq 2.6351$. For $x \gg 1$, the loop functions reduce to [257]

$$J_b(x^2) \simeq J_f(x^2) = \left(\frac{x}{2\pi}\right)^{3/2} e^{-x}\left[1 + \frac{15}{8x} + O(x^{-2})\right]. \qquad (5.50)$$

In this expression, we can see the familiar Boltzmann suppression of heavier particles when $x = m/T > 1$.

The effect of thermal corrections on the SM Higgs potential can be illustrated by writing down the potential in an approximate form using the high-temperature expansions in Eqs. (5.48) and (5.49). This gives [257]

$$V_{\text{eff}}(\phi, T) \simeq D(T^2 - T_0^2)\phi^2 - ET\phi^3 + \frac{\overline{\lambda}}{4}\phi^4, \qquad (5.51)$$

where D and $\overline{\lambda}$ are slowly varying functions of T only.

In the limit of $E = 0$, the phase transition is *second-order* with a transition temperature of $T = T_0$ and a Higgs VEV for $T < T_0$ of

$$\phi = T_0\sqrt{\frac{2D}{\overline{\lambda}}\left(1 - \frac{T^2}{T_0^2}\right)}. \qquad (5.52)$$

In this case, the effective potential $V_{\text{eff}}(\phi)$ evolves with temperature T as in the right panel of Fig. 5.8.

For $E \neq 0$, the phase transition is *first-order*. Starting from $T \gg T_0$, a second minimum appears away from the origin when $T = T_1$ where

$$T_1 = T_0\sqrt{\frac{8\overline{\lambda}D}{8\overline{\lambda}DT_0^2 - 9E^2}}. \qquad (5.53)$$
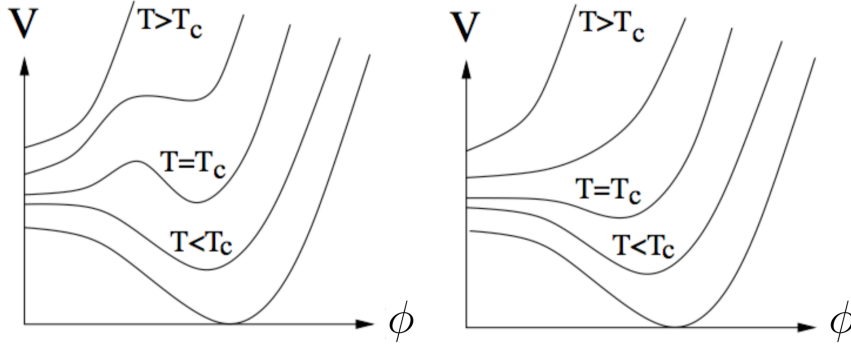
Figure 5.8: Schematic illustration of the evolution of $V_{\text{eff}}(\phi)$ with temperature T for a first- (*left*) and second- (*right*) order phase transition. Figure from Ref. [25].

Here the temperature-dependent coefficients D and $\overline{\lambda}$ are evaluated at $T = T_1$. The second symmetry breaking minimum becomes degenerate with the origin at the *critical temperature* T_c and becomes deeper at lower temperature. This is illustrated in the left panel of Fig. 5.8. The degree to which the phase transition is first-order is typically characterised by ϕ_c/T_c where ϕ_c is the location of the minimum at $T = T_c$. In terms of the parameters in Eq. (5.51), we get

$$\frac{\phi_c}{T_c} = \frac{2E}{\overline{\lambda}}. \tag{5.54}$$

Once the temperature falls below T_c, regions of the cosmological phase tunnel to the deeper broken minimum and the phase transition proceeds via nucleation of bubbles.

Before discussing the dynamics of a first-order phase transition, it is worth examining the validity of the perturbative expansion as given above. This expansion breaks down at very high temperatures when the thermal loop expansion parameter $g^2 T^2/m^2(\phi)$ (where g^2 is the coupling entering in the loop) becomes large [252, 258]. Indeed, we have seen earlier that the leading thermal corrections (generated by loops only) completely change the vacuum structure of the theory by restoring the symmetry at very high temperatures. The breakdown of the perturbative expansion can be postponed by re-summing the most dangerous thermal corrections and incorporating thermal mass corrections in the propagators. The net result of such a *daisy resummation* (or *ring diagrams*) is to generate an additional term in the effective potential given by [259]

$$V_1^{(\text{daisy})}(\phi, T) = -\frac{T}{12\pi} \sum_{\{b\}'} n_b \left[\overline{m}_b^3(\phi, T) - m_b^3(\phi) \right]^{3/2}, \tag{5.55}$$

where the sum runs only over scalars and longitudinal vectors. The parameter $\overline{m}^2$ is the field-dependent thermal squared mass and is given by

$$\overline{m}^2(\phi) = m^2(\phi) + \Pi(T), \tag{5.56}$$

where $\Pi(T) \propto T^2$ is a thermal mass correction.

The daisy corrections are particularly important for a first-order phase transition as they directly affect the crucial cubic term. For instance, suppose that a contribution to

the cubic term comes from a scalar with a zero-temperature mass of $m^2(\phi) = g\phi^2$ and a thermal correction of $\Pi(T) = \kappa T^2$. In this case, the cubic term becomes

$$\Delta E\phi^3 = \frac{1}{12\pi}g^{3/2}\phi^3 \rightarrow \frac{1}{12\pi}\left(g\phi^2 + \kappa T^2\right)^{3/2}. \tag{5.57}$$

When $\Pi(T)$ is large relative to $m^2(\phi)$, the above expression ceases to behave as a cubic in ϕ and the phase transition may no longer be first-order.

In a first-order EWPT, the phase transition proceeds by the nucleation of bubbles of the broken phase within the surrounding plasma of symmetric phase. Bubble nucleation is governed by thermal tunnelling from the local minimum at $\phi = 0$ to a deeper minimum at $\phi \neq 0$ [260]. In nucleating a bubble, there is a competition between the decrease in free energy proportional to the bubble volume and an increase due to the tension of the wall proportional to the bubble surface area. Thus, there is a minimum radius for which a bubble can grow after it is formed, which limits the tunnelling rate. Bubble formation and growth only begin in earnest when this rate exceeds the Hubble rate and occurs at the *nucleation temperature* T_n. After a sufficiently large bubble formation, it expands until it collides with other bubbles until the universe is filled entirely with the broken phase. The typical profile and expansion rate of the bubble walls can be computed from the effective potential by taking account of the frictional effects from scattering with surrounding particles in the plasma [261, 262]. The baryon creation process is very sensitive to the speed and profile of the bubble walls [263].

A first-order EWPT is not enough for a successful EWBG. The transition must be *strongly first-order*. Within the context of perturbation analysis, the quantitative condition for a strongly first-order phase transition is

$$\frac{\phi_c}{T_c} \gtrsim 1. \tag{5.58}$$

This ratio approximates a factor which appears in the sphaleron transition rate in the broken phase within the bubble walls. If this condition is not met, the transitions will wash out the baryon asymmetry created by EWBG. As we will see below, the requirement of a strongly first-order phase transition is one of the reasons why EWBG does not work in the SM. Thus, it provides a strong motivation for new BSM physics.

The condition in Eq. (5.58) is a frequently applied approximation, but a precise calculation of the baryon abundance from EWBG requires a detailed analysis. For one, the relevant temperature for the phase transition dynamics is the slightly lower bubble nucleation temperature rather than the critical temperature, although it is often the case that $T_n \simeq T_c$ [264]. A more serious worry is the lack of *gauge invariance*. In particular, it is well-known that the VEV of the one-loop effective potential at any temperature is gauge-dependent [265–271], so the ratio on the left-hand side of Eq. (5.58) is not a well-defined physical quantity. Moreover, the above procedure for calculating T_c perturbatively

also introduces a spurious gauge-dependence. This becomes clear after expanding the right-hand side of Eq. (5.54) in an arbitrary gauge as

$$\frac{\phi_c}{T_c} = \frac{2E}{\overline{\lambda}} = \frac{3 - \xi^{3/2}}{48\pi\lambda}\left[2g_2^2 + (g_1^2 + g_2^2)^{3/2}\right] + \ldots, \tag{5.59}$$

where the additional terms are ξ-dependent contributions from the one-loop corrections to the Higgs quartic self-coupling. As we saw earlier, the conventional analyses have been performed in the Landau gauge. However, a small change in the choice of the gauge parameter η can significantly alter the ratio ϕ_c/T_c.

To obtain a gauge invariant baryon number preserving condition (BNPC), we require several modifications of the naive perturbative treatment given above. Some of these modifications are discussed below.

1. Determine T_c (or T_n) in a gauge invariant manner by following the evolution of $V_{\text{eff}}(\phi, T)$ and consistently implementing the so-called Nielsen identities [265, 266]. A procedure for doing this involves an $\hbar$-expansion of $V_{\text{eff}}(\phi, T)$ [266, 270, 272]. By generalising this procedure, we can approximate the full daisy resummation in a gauge invariant way and reproduce the trends for T_c found in non-perturbative calculations [270].

2. Perform a gauge invariant computation of the energy of the sphaleron configuration E_{sph}. In the perturbation theory, it is possible to do so in the broken phase by working with the high-temperature effective theory in which the zero-temperature masses are replaced by their gauge invariant Debye masses. The energy E_{sph} depends on a gauge invariant scale $\bar{\phi}(T)$ which is not the same as $\phi(T)$. The fluctuation determinant κ characterises the leading quadratic corrections to the sphaleron action [273, 274].

3. Compute the baryon density n_B at the end of EWPT (corresponding to a time delay of Δt_{EW} after its onset) and compare it with the initial density resulting from the CP violating (CPV) transport dynamics [26]. The resulting ratio is called the *washout factor* and is given by

$$S = \frac{n_B(\Delta t_{\text{EW}})}{n_B(0)}. \tag{5.60}$$

For the baryon asymmetry created by EWBG to be preserved, the washout factor S must not be too small.

The washout factor can be re-written in terms of X defined as $S > e^{-X}$ such that the quantitative BNPC is [270]

$$\frac{4\pi B}{g}\frac{\bar{\phi}(T_c)}{T_c} - 7\log\left(\frac{\bar{\phi}(T_c)}{T_c}\right) > -\log X - \log\left(\frac{\Delta t_{\text{EW}}}{t_H}\right) + \log Q\mathcal{F} + \hbar\log\kappa. \tag{5.61}$$

Here B parametrises the relationship between the scale $\overline{\phi}(T)$ and the sphaleron energy [275, 276]

$$E_{\text{sph}} \simeq B\frac{2m_W}{\alpha_W}\frac{\overline{\phi}(T)}{\phi(0)}, \tag{5.62}$$

where B is a constant of order unity that depends on the mass of the Higgs boson, $\phi(0) = 174\,\text{GeV}$ is the Higgs VEV at $T = 0$ and α_W is the weak coupling. The other quantities in Eq. (5.61) are the Hubble time t_H, a quantity Q characterising the contribution of sphaleron zero modes, a function $\mathcal{F}$ that characterises the dependence of the unstable mode of the sphaleron on $\overline{\phi}(T)$ and a factor κ accounting for fluctuations that are not zero modes. The appearance of logarithms in Eq. (5.61) and the dependence on t_{EW} leads to [232]

$$\frac{dn_B}{dt} \simeq \frac{13N_f}{2}\frac{\Gamma_{\text{ws}}}{VT^3}n_B, \tag{5.63}$$

where N_f is the number of fermion families and

$$\frac{\Gamma_{\text{ws}}}{VT^3} \propto e^{-E_{\text{sph}}/T} \tag{5.64}$$

is the sphaleron rate per unit volume inside the bubble. Qualitatively, the BNPC in Eq. (5.61) corresponds to the requirement that the sphaleron rate in the broken phase during the phase transition is much slower than the Hubble expansion rate H.

The conventionally employed condition in Eq. (5.54) results from replacing the gauge invariant ratio $\overline{\phi}(T_c)/T_c$ by the gauge-dependent one ϕ_c/T_c and making specific choices for the parameters appearing in Eq. (5.61). In particular, it has been assumed that $X = 10$, i.e., by allowing the initial baryon asymmetry to be 5 orders of magnitude larger than what is observed today (an assumption that is questionable in view of recent studies of the CPV transport dynamics). Additional significant uncertainties are associated with the value of the fluctuation determinant κ and the duration of the transition Δt_{EW}. In short, even if one employs an appropriately gauge invariant procedure to determine the degree of baryon number preservation, considerable uncertainty remains on the precise requirement.

Almost all phenomenological studies carried out over the past decade or so have neglected these issues. Even if one places some trust in the use of perturbation theory to analyse EWPT dynamics, it should be clear that considerable amount of work is required to make a robust statement about the presence or absence of a sufficiently strong first-order phase transition in a given BSM scenario. For instance, it may be that a given BSM scenario significantly modifies the dependence of E_{sph} on the gauge invariant scale $\overline{\phi}(T_c)$, the dependence of $\overline{\phi}$ on T_c itself, the duration of the transition or the fluctuation determinant. With this view, conclusions that have been drawn as to the viability of EWBG based on existing perturbative analyses of the scalar field dynamics should be viewed as provisional at best and in an ideal situation, revisited in light of these open theoretical issues.

Lattice	m_h^c (GeV)	Ref.
4D Isotropic	80 ± 7	[287]
4D Anisotropic	72.4 ± 1.7	[288]
3D Isotropic	72.3 ± 0.7	[289]

Table 5.1: Maximum value of the Higgs boson mass m_h^c allowed for a first-order EWPT in the SM as obtained from lattice studies. Table from Ref. [25].

5.6.2   Non-perturbative methods

Dedicated non-perturbative numerical studies of the EWPT have been carried out for the SM [234, 248, 277–286]. Some of the properties studied that are particularly relevant to EWBG are the critical temperature T_c, the weak sphaleron rate Γ_{sph} and the character of the phase transition (first-order, second-order or a crossover) [234, 284, 285]. As we will discuss below, the latent heat L is also critical for the amplitude of gravity wave production [277].

The starting point for EWBG is the process of bubble nucleation which requires a strongly first-order phase transition. In the SM, this requirement is only satisfied for a sufficiently light Higgs boson. It is possible to find the maximum value of the Higgs boson mass for which a first-order phase transition is allowed. Representative results from lattice studies are shown in Table 5.1. The results are obtained using three-dimensional (3D) lattices after carrying out the procedure of dimensional reduction to a 3D effective theory before studying the phase transition properties of the latter using Monte Carlo methods [282]. For 3D or 4D studies, a criterion must be identified to determine the character of the phase transition. Among those employed are the susceptibility associated with the scalar field

$$\chi \propto \langle (\phi^\dagger \phi - \langle \phi^\dagger \phi \rangle)^2 \rangle \tag{5.65}$$

and correlation lengths. The scaling behaviour of χ with lattice volume can be used to determine whether the transition is first-order, second-order or a crossover. For $m_h \gg m_h^c \simeq 75\,\text{GeV}$, as implied by collider searches for a SM-like Higgs boson, the transition appears to be a crossover between the symmetric and broken phases. This is shown in Fig. 5.9.

5.7   Extended scalar sector

The need for a strongly first-order EWPT is one of the two main reasons why EWBG does not work in the SM. This motivates new physics near the electroweak scale. The new physics is also needed to stabilise the electroweak scale and account for dark matter. A broad range of SM extensions has been proposed to strengthen the EWPT and allow for a successful EWBG. Most of them fall in one of the following two groups.
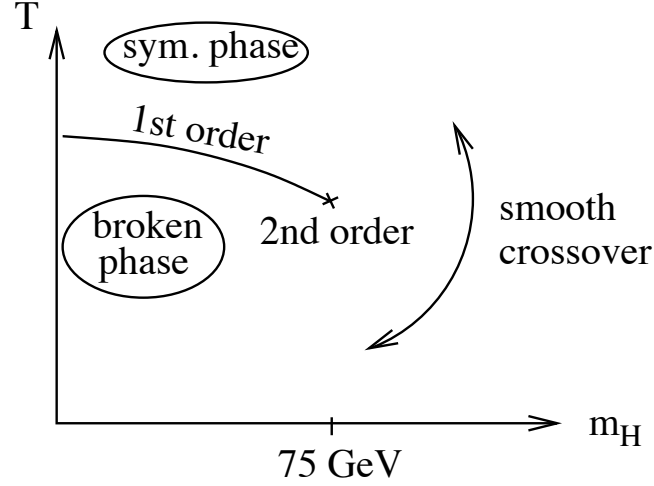
Figure 5.9: Phase diagram for EWPT in the SM. Figure from Ref. [25].

1. In the first group, new scalars can couple to the SM Higgs field and affect the cubic term in the effective potential through loop effects. For instance, the relevant interaction of a new scalar X can be written in the following form [264, 290]

$$\mathcal{L} \supset -M_X^2 |X|^2 - \frac{1}{6} K |X|^4 - Q|X|^2 \Phi^\dagger \Phi, \tag{5.66}$$

where the third term is a *Higgs portal* coupling. Assuming that X does not develop a VEV, its physical mass is

$$m_X^2 = M_X^2 + \frac{1}{2} Q \phi^2. \tag{5.67}$$

Its contribution to the effective potential is

$$\Delta V_{\text{eff}}(\phi, T) \supset +\frac{n_X T}{12\pi} \left[\Pi_X(T) + M_X^2 + \frac{1}{2} Q\phi^2 \right]^{3/2}, \tag{5.68}$$

where $\Pi_X(T)$ is the thermal mass of X and n_X is the number of degrees of freedom. If $Q\phi^2/2$ is much larger than the other terms when $\phi \simeq \phi_c$, this correction gives a strong enhancement to the cubic operator which drives a first-order phase transition. If X is charged under $SU(3)_C$, the contribution to the cubic term is further enhanced at two-loop order by corrections involving virtual gluons [291, 292]. The net result is that a strong first-order EWPT can be obtained for $Q \gtrsim 1$ and $M_X^2 \lesssim 0$ if X is a $SU(3)_C$ triplet, but much larger Q values are required if X is a gauge singlet [292].

2. The second group consists of scalar fields which couple to the Higgs field and develop non-trivial dynamics in the early universe. Thus, the scalar fields directly influence the effective potential. For instance, the Higgs field can be coupled to a new scalar which develops a non-trivial VEV near the electroweak scale [293]. A simple example of this case is

$$\mathcal{L} \supset -m_N^2 N^2 - A_N N^3 - \lambda_N N^4 - (A_H N + \zeta_H N^2)\Phi^\dagger \Phi + \dots, \tag{5.69}$$

where $\Phi = (\phi_+, \phi_0)^T$. These interactions can allow both ϕ_0 and N to develop non-zero VEVs, which results in a mixing between the physical singlet and $SU(2)_L$ scalar in the theory. When the singlet and $SU(2)_L$ mass parameters are similar, it is convenient to track the evolution of VEVs in polar coordinates as [293]

$$\langle \phi_0 \rangle = \varphi \cos \alpha, \quad \langle N \rangle = \varphi \sin \alpha. \tag{5.70}$$

In this parametrisation, one obtains cubic terms in the tree-level potential for φ which can lead to a strong first-order EWPT. The singlet can also strengthen the phase transition by contributing to the loop-induced cubic term in the effective potential or reducing the effective Higgs quartic coupling near the critical temperature [293]. Similar effects arise in gauge extensions of the SM and in theories with two or more $SU(2)_L$ doublets [292, 294, 295].

When the characteristic mass scale Λ_N of the singlet sector is significantly larger than the $SU(2)_L$ one, the singlet can be integrated out of the theory. This gives an effective Higgs interaction of the following form

$$\mathscr{L} \supset \mu^2 \Phi^\dagger \Phi - \lambda (\Phi^\dagger \Phi)^2 - \frac{1}{\Lambda_N^2} (\Phi^\dagger \Phi)^3 + \ldots . \tag{5.71}$$

For $\Lambda_N \leq 1000\,\text{GeV}$, the third term can drive a strong first-order EWPT [296, 297].

In both cases, new scalars with significant coupling to the Higgs field are required. Both mechanisms to enhance the strength of EWPT require new physics below the TeV scale. This is precisely the energy regime that is currently being probed directly by high-energy colliders and indirectly by low energy precision probes.

5.8 Tests for electroweak baryogenesis

Electroweak baryogenesis requires new particles/interactions to obtain a strongly first-order EWPT and sufficient CP violation. The new particles cannot be much heavier than the electroweak scale and must couple to the Higgs field. These two properties together imply that new particles will have observable effects in upcoming high-energy and high-precision experiments.

The prospects for observing new particles directly at the LHC and indirectly via high-sensitivity, low-energy studies of CP-violating observables mean that EWBG is a generally testable or falsifiable baryogenesis scenario. In this way, it contrasts from other scenarios which typically involve high energy scales such as standard thermal leptogenesis or Affleck-Dine baryogenesis. We discuss some of the primary experimental tests for EWBG by considering three frontiers in particle physics: the high-energy frontier; the intensity frontier; and the cosmological frontier.

5.8.1 The high-energy frontier

New particles related to EWBG can potentially be produced at high energy-colliders such as the LHC. This is especially true for new coloured states that can help to strengthen the EWPT, e.g., a new coloured scalar X. These particles must be lighter than about $m_X \lesssim 200\,\text{GeV}$ to have an adequate effect; they also lead to large LHC production cross sections. Such states should also be consistent with existing collider limits.

The new physics required for EWBG must also couple significantly to the $SU(2)_L$ doublet Higgs field. This can potentially induce observable changes in the production and decay properties of the Higgs boson. A very significant effect arises from coloured X scalars which couple to the Higgs field as in Eq. (5.66). Such scalars will contribute in loops to the amplitudes for the Higgs boson production via gluon fusion and Higgs decay to diphotons. Large couplings Q are required to induce a strongly first-order phase transition. In this case, the contribution from gluon fusion interferes constructively with the dominant top quark loop in the SM and destructively with the dominant $W^\pm$ loop for the Higgs decay to diphotons. The net result is an enhancement of the gluon fusion rate that is closely related to the strength of the EWPT and a modest decrease in the branching ratio to diphotons [291].

In Fig. 5.10, we show the enhancement of the gluon fusion rate from X relative to the SM as a function of Q and the mass parameter M_X^2 along with an estimate for where the phase transition is strong enough for EWBG. Gluon fusion is the dominant Higgs production mode at the LHC, whereas the primary decay channels are $\gamma\gamma$, W^+W^- and ZZ. Indeed, the enhancement of the gluon fusion rate as implied by this mechanism for strengthening the EWPT is already strongly constrained by current LHC and Tevatron Higgs searches [291].

New uncoloured X particles that couple to the SM Higgs boson can also help in strengthening the phase transition, although their effects tend to be weaker than the coloured particles. If such an uncoloured state has a non-trivial electric charge, it will modify the Higgs branching ratio into diphotons [291]. As in the coloured case, the interference with the $W^\pm$ loop is destructive when the phase transition is strongly first-order. Thus, the Higgs branching ratio to diphotons is reduced, whereas the gluon fusion rate largely remains unchanged. Uncoloured X particles could potentially be discovered at colliders. In addition, they can also lead to indirect effects on the Higgs quartic self-coupling λ [299–301].

A successful EWBG can also be realised if new scalar fields develop VEVs in the early universe at roughly the same time as the SM Higgs field. A simple example of this scenario is the real singlet model presented in Ref. [294]. In this case, there is an additional fundamental scalar boson in the theory which mixes with the $SU(2)_L$ doublet Higgs excitation. The resulting real scalar mass eigenstates will consist of a SM-like h_1
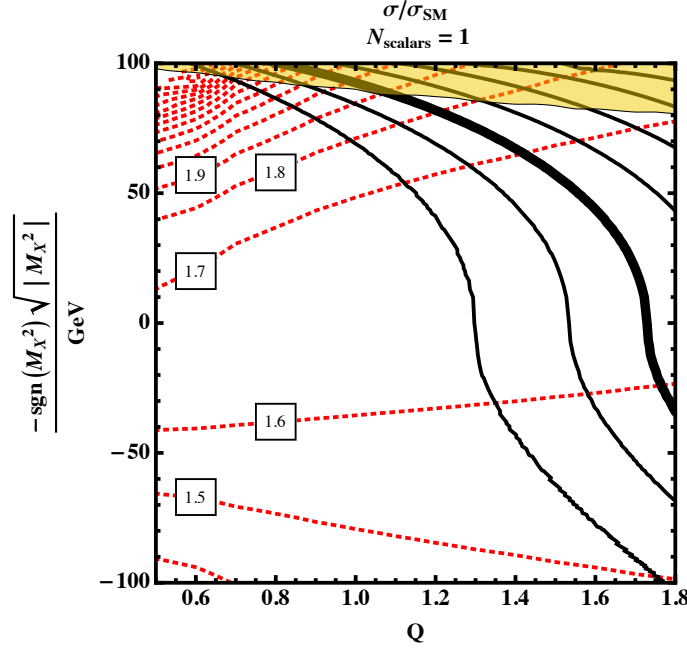
Figure 5.10: Higgs production rates via gluon fusion relative to the SM (red dotted lines) and contours of ϕ_c/T_c (black solid lines) for one new color-triplet scalar for given values of the parameter $-\text{sgn}(M_X^2)\sqrt{|M_X^2|}$ and Q. The thick solid line corresponds to $\phi_c/T_c = 0.9$, whereas the adjacent solid lines show steps of $\Delta(\phi_c/T_c) = 0.2$. Figure from Ref. [298].

and a singlet-like h_2. Decays of h_1 are frequently similar to the SM but can be changed radically if $h_1 \to h_2 h_2$ is kinematically allowed. The decays of the h_2 state are typically inherited from h_1, so the chain $h_1 \to h_2 h_2$ is likely to produce $4b$, $2b\,2\tau$ and 4τ final states which can be distinctive but challenging to find at hadron colliders [302, 303]. On the other hand, the singlet-like h_2 state may have more exotic decay channels if there are other light states in theory, e.g., a light singlet fermion [304]. Generically, one could expect a significant reduction of signal in conventional SM Higgs search channels due to the mixing, $h_1 \to h_2 h_2$ decay if it is kinematically allowed [293] and the appearance of the second state h_2 [305].

New light particles are also needed to induce CP violation in the expanding bubble walls. In many cases, they carry non-trivial electroweak charges and couple to the varying Higgs background. Direct searches for such particles are underway at the LHC and some relevant exclusions have already been presented in Ref. [306]. Even so, the detailed signals are very sensitive to the decay channel of the new states.

5.8.2 The intensity frontier

The most powerful probes for BSM sources of CP violation are searches for the permanent electric dipole moments (EDMs) of the electron, neutron and neutral atoms. In all cases, only null results have been obtained so far. This translates into stringent constraints on new sources of CP violation. Limits on the muon EDM also exist, but they are considerably

weaker than the electron EDM. One expects the 1-loop EDM of an elementary fermion f generated by new field(s) of mass M to go as

$$d_f \sim e \left(\frac{m_f}{M^2} \right) \frac{\alpha_k}{4\pi} \sin\theta, \tag{5.72}$$

where α_k is either the fine structure constant or strong coupling at the scale M and θ is a CP violating phase associated with the new interaction(s). For $\alpha_k = \alpha_{EM}$, the above expression gives

$$d_f \sim \sin\theta \left(\frac{m_f}{\text{MeV}} \right) \left(\frac{1\,\text{TeV}}{M} \right)^2 \times 10^{-26}\, e\,\text{cm}. \tag{5.73}$$

The present limit on the electron EDM is $|d_e| < 10.5 \times 10^{-28}\, e$ cm [307] from an experiment on the Yb-F molecule. This implies

$$|\sin\theta| \lesssim \left(\frac{M}{2\,\text{TeV}} \right)^2. \tag{5.74}$$

Similar constraints can also be placed using the limits on the neutron [308] and ^{199}Hg atomic [309] EDMs as

$$|d_n| < 2.9 \times 10^{-26}\, e\,\text{cm}, \quad |d_A(^{199}\text{Hg})| < 3.1 \times 10^{-29}\, e\,\text{cm}, \tag{5.75}$$

assuming that any contributions from the QCD θ-term are sufficiently small that no cancellation between this source of SM CP violation and that arising from the new interaction occurs. Contributions from the CP violation associated with the CKM matrix first arise at three- (four-) loop order for d_n and d_A (d_e) implying effects that are well below the $10^{-30}\, e$ cm level. The next generation of lepton, neutron and neutral atom EDM searches aim to improve the sensitivity by up to two orders of magnitude. Efforts to reach even higher sensitivity with storage ring hadronic EDM searches are also underway.

The constraints imposed in Eq. (5.74) generally makes EWBG unviable. For the new particles to be sufficiently abundant in the electroweak plasma at $T \sim 100\,\text{GeV}$, their masses should be lighter than $\sim 500\,\text{GeV}$, implying $|\sin\theta| \lesssim 0.01$. In this case, the CP violating sources in the transport equations are suppressed and EWBG becomes untenable. However, there are several ways to evade the one-loop EDM constraints, see e.g., Ref. [26].

5.8.3 The cosmological frontier

A strong first-order phase transition as required for EWBG can produce a cosmological signal in the form of gravitational waves (GW) [310–314]. As discussed earlier, the phase transition proceeds by the formation of bubbles of the broken phase within the surrounding plasma in the symmetric phase. Gravitational background radiation is created by a turbulent expansion of the bubble walls and their subsequent collisions as they coalesce [315, 316, 316]. The net effect of bubble collisions within the current Hubble radius

would be a uniform stochastic background of gravitational radiation with a characteristic spectrum.

The spectrum and intensity of GW generated by a strongly first-order phase transition depends on three parameters. These include the latent heat α released by the phase transition at the nucleation temperature T_n relative to the background radiation energy, the characteristic rate of bubble nucleation β/H and the bubble wall velocity v_b [317]. All three quantities can be calculated from the finite-temperature effective potential V_{eff} in Eq. (5.44).

Estimates of the gravitational wave signals from a strong first-order EWPT suggest that they will be difficult to detect in the foreseeable future [317, 318]. The signal is typically too low in frequency to be picked up by the LIGO experiment, but it might be observable with LISA if the transition is extremely strong [319, 320]. The prospects for discovery are considerably better with DECIGO [321] and BBO [322]. Even in these cases, the signal from the phase transition could be obscured by other GW signals arising from astrophysical processes (e.g., neutron stars, black holes) or inflation [323]. Thus, a significant advancement in background reduction techniques will be required to detect the gravitational radiation from a strongly first-order phase transition.

Part II

Phenomenology of Higgs portal dark matter models

Chapter 6

Higgs portal dark matter models

6.1 Introduction

In chapter 4, we realised that the SM could not provide any particle DM candidates. This forces us to go beyond the SM. Among many potential DM candidates, the class of WIMPs is favoured. They appear in well-motivated BSM theories (e.g., SUSY) and can naturally account for the observed DM abundance via the WIMP miracle [76, 120].

Within the bottom-up EFT approach, Higgs portal DM models are well-motivated. In recent years, they have been a popular topic of interest. The most comprehensive study of the scalar singlet DM model was performed in Ref. [324]. Results from a global fit of the scalar singlet model were presented in Ref. [325] and more recently in Ref. [326]. The scalar, vector and Majorana fermion portal models were studied in Ref. [327] in light of the WMAP and XENON100 data, Higgs invisible width and XENON1T prospects. Current LHC constraints on the scalar singlet model from vector boson fusion, monojet and mono-Z analyses were shown to be weak in Ref. [328]. Similarly, monojet constraints on the vector and fermion portal models were shown to be weak in Ref. [329]. Constraints from perturbativity and electroweak vacuum stability on the scalar model parameter space were first imposed in Ref. [330] and recently in Ref. [331].

Limits on the scalar singlet model from gamma-ray line searches in the Higgs resonance region were recently imposed in Ref. [332]. The LUX limits on the scalar model parameter space were first imposed in Ref. [333]. This study also combined constraints from the antiproton data which were found to be important in the Higgs resonance region; they are competitive with the LUX limits at higher DM masses. For fermion DM models, the corresponding antiproton limits are weak due to a velocity suppressed DM annihilation cross-section σv_{rel}. In all cases, the results were found to be strongly dependent on the chosen propagation model. A combination of the parity-conserving and parity-violating terms in the fermion DM models was first considered in Ref. [334] and more recently in Refs. [335, 336]. In the latter two studies, it was noted that the parity-violating term could generate a significant parity-conserving coupling after EWSB.

In this chapter, we study the phenomenology of effective scalar, vector, Majorana and Dirac fermion Higgs portal DM models based on our work in Ref. [30].[1] For the fermion DM models, we take an admixture of parity-conserving scalar couplings ($\propto \overline{\psi}\psi$) and parity-violating pseudoscalar couplings ($\propto \overline{\psi}i\gamma_5\psi$). With the fast approaching availability of the Cherenkov Telescope Array (CTA), it is an opportune moment to explore its expected reach in these models. As the fermion DM-nucleon cross-section is momentum suppressed, we re-derive the XENON100 and LUX limits using a dedicated code. However, in such cases, the results do not change appreciably, and the impact of direct searches remain negligible. Finally, we perform the same comprehensive study for all portal models and present a consistent set of detailed results.

We start by introducing the four effective Higgs portal DM models. After providing a brief description of various constraints and their implementations, we present our model results and discuss the prospects for detection at current and/or future experiments. A detailed derivation of the physical mass basis required to understand the post-EWSB fermion EFTs is given in Appendix D.

6.2 Models

We assume that the DM fields are SM gauge singlets and consider a scalar (S), vector (V_μ), Majorana (χ) and Dirac (ψ) fermion DM candidate. The following DM model Lagrangians are invariant under the symmetries of the SM [335, 337]

$$\mathscr{L}_S = \mathscr{L}_{\text{SM}} + \frac{1}{2}(\partial_\mu S)(\partial^\mu S) - \frac{1}{2}\mu_S^2 S^2 - \frac{1}{4!}\lambda_S S^4 - \frac{1}{2}\lambda_{hS} S^2 \Phi^\dagger \Phi, \tag{6.1}$$

$$\mathscr{L}_V = \mathscr{L}_{\text{SM}} - \frac{1}{4}W_{\mu\nu}W^{\mu\nu} + \frac{1}{2}\mu_V^2 V_\mu V^\mu - \frac{1}{4!}\lambda_V(V_\mu V^\mu)^2 + \frac{1}{2}\lambda_{hV} V_\mu V^\mu \Phi^\dagger \Phi, \tag{6.2}$$

$$\mathscr{L}_\chi = \mathscr{L}_{\text{SM}} + \frac{1}{2}\overline{\chi}\left(i\slashed{\partial} - \mu_\chi\right)\chi - \frac{1}{2}\frac{\lambda_{h\chi}}{\Lambda_\chi}\left(\cos\theta\,\overline{\chi}\chi + \sin\theta\,\overline{\chi}i\gamma_5\chi\right)\Phi^\dagger\Phi, \tag{6.3}$$

$$\mathscr{L}_\psi = \mathscr{L}_{\text{SM}} + \overline{\psi}\left(i\slashed{\partial} - \mu_\psi\right)\psi - \frac{\lambda_{h\psi}}{\Lambda_\psi}\left(\cos\theta\,\overline{\psi}\psi + \sin\theta\,\overline{\psi}i\gamma_5\psi\right)\Phi^\dagger\Phi, \tag{6.4}$$

where $\mathscr{L}_{\text{SM}}$ is the SM Lagrangian, $W_{\mu\nu} \equiv \partial_\mu V_\nu - \partial_\nu V_\mu$ is the field strength tensor for the vector field V_μ and Φ is the SM Higgs doublet. The parameter θ determines the type of interaction between DM and the Higgs field: $\cos\theta = 1$ corresponds to a pure scalar interaction, whereas $\cos\theta = 0$ corresponds to a pure pseudoscalar interaction.

The DM particles must be stable on cosmological timescales. For our portal models, their stability is guaranteed by imposing an assumed $\mathbb{Z}_2$ symmetry: $X \rightarrow -X$ where $X \in (S, V_\mu, \chi, \psi)$. Under the $\mathbb{Z}_2$ symmetry, the DM fields (S, V_μ, χ, ψ) are odd while the SM fields are even. Thus, the decay of a DM particle into SM particles is forbidden. The

---

[1]As our study was performed in late-2015, some of the constraints included in this chapter are now outdated, e.g., *Planck*, CTA, LUX and XENON100 limits.

imposed symmetry also prohibits linear and cubic terms in the scalar field Lagrangian as well as the kinetic mixing terms between the electromagnetic and vector field strength tensors. As an explicit bare mass term for the DM field is allowed by the $\mathbb{Z}_2$ symmetry, it is included in the above Lagrangians for completeness.

The scalar DM model in Eq. (6.1) was first introduced 30 years ago [338–340]. Being one of the simplest extensions of the SM, it is both theoretically and phenomenologically satisfactory as long as the assumed $\mathbb{Z}_2$ symmetry remains unbroken. It is also renormalizable and valid up to high energy scales provided that the Landau pole is not reached. The vector DM model in Eq. (6.2) is simple, compact and appears renormalizable due to the presence of dimension-2 and dimension-4 operators only. However, in reality, it is non-renormalizable and violates unitarity in a similar fashion to the Fermi theory of weak interactions. Thus, it is an effective model which requires a UV completion. We leave the discussion of UV complete models for a future study; for simple UV completions, see Refs. [341, 342]. Similarly, the fermion DM models in Eqs. (6.3) and (6.4) are non-renormalizable. A suggested UV completion is proposed in Ref. [343] and discussed in more detail in chapter 8.

Once the electroweak symmetry is broken, the SM Higgs field acquires a VEV. In the unitary gauge, we can write

$$\Phi = \frac{1}{\sqrt{2}} \begin{pmatrix} 0 \\ v_0 + h \end{pmatrix}, \tag{6.5}$$

where h is the physical SM Higgs field and $v_0 = 246.22\,\text{GeV}$ is the SM Higgs VEV. Thus, the $\Phi^\dagger \Phi$ term generates mass and interaction terms for the associated DM fields $X \in (S, V_\mu, \chi, \psi)$. These interactions are shown by the Feynman diagrams in Fig. 6.1. Using Eq. (8.7), we can rewrite the model Lagrangians as

$$\mathscr{L}_S = \mathscr{L}_{\text{SM}} + \frac{1}{2}(\partial_\mu S)(\partial^\mu S) - \frac{1}{2}m_S^2 S^2 - \frac{1}{4!}\lambda_S S^4 - \frac{1}{2}\lambda_{hS}\, S^2 \left(v_0 h + \frac{1}{2}h^2 \right), \tag{6.6}$$

$$\mathscr{L}_V = \mathscr{L}_{\text{SM}} - \frac{1}{4}W_{\mu\nu}W^{\mu\nu} + \frac{1}{2}m_V^2 V_\mu V^\mu - \frac{1}{4!}\lambda_V(V_\mu V^\mu)^2 + \frac{1}{2}\lambda_{hV}\, V_\mu V^\mu \left(v_0 h + \frac{1}{2}h^2 \right), \tag{6.7}$$

$$\mathscr{L}_\chi = \mathscr{L}_{\text{SM}} + \frac{1}{2}\overline{\chi} i \slashed{\partial} \chi - \frac{1}{2}\left[\mu_\chi \overline{\chi}\chi + \frac{1}{2}\frac{\lambda_{h\chi}}{\Lambda_\chi} v_0^2 \Big(\cos\theta\, \overline{\chi}\chi + \sin\theta\, \overline{\chi} i\gamma_5 \chi \Big) \right]$$
$$- \frac{1}{2}\frac{\lambda_{h\chi}}{\Lambda_\chi} \left(\cos\theta\, \overline{\chi}\chi + \sin\theta\, \overline{\chi} i\gamma_5 \chi \right) \left(v_0 h + \frac{1}{2}h^2 \right), \tag{6.8}$$

$$\mathscr{L}_\psi = \mathscr{L}_{\text{SM}} + \overline{\psi} i \slashed{\partial} \psi - \left[\mu_\psi \overline{\psi}\psi + \frac{1}{2}\frac{\lambda_{h\psi}}{\Lambda_\psi} v_0^2 \Big(\cos\theta\, \overline{\psi}\psi + \sin\theta\, \overline{\psi} i\gamma_5 \psi \Big) \right]$$
$$- \frac{\lambda_{h\psi}}{\Lambda_\psi} \left(\cos\theta\, \overline{\psi}\psi + \sin\theta\, \overline{\psi} i\gamma_5 \psi \right) \left(v_0 h + \frac{1}{2}h^2 \right), \tag{6.9}$$

where the physical scalar and vector DM masses are

$$m_S^2 = \mu_S^2 + \frac{1}{2}\lambda_{hS} v_0^2, \quad m_V^2 = \mu_V^2 + \frac{1}{2}\lambda_{hV} v_0^2. \tag{6.10}$$
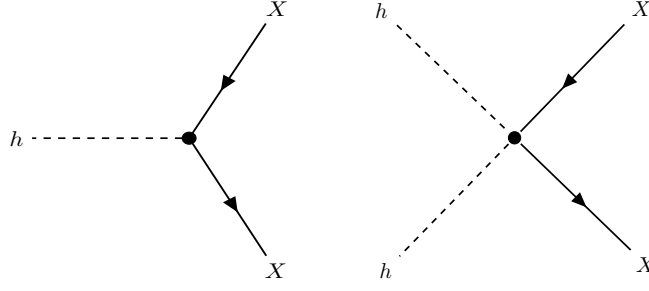
Figure 6.1: Feynman diagrams for an interaction between the SM Higgs boson and DM X where $X \in (S, V_\mu, \chi, \psi)$.

For the fermion DM models, when $\sin\theta \neq 0$, non-mass-type contributions appear which are purely quadratic in the DM fields. To define a real mass, we can redefine the fermion DM fields by performing a chiral rotation. This is achieved by

$$\chi \to e^{i\gamma_5\alpha/2}\,\chi, \quad \psi \to e^{i\gamma_5\alpha/2}\,\psi, \tag{6.11}$$

where α is a real, space-time-independent parameter. After substituting the redefined fields into the fermion DM Lagrangians, we demand the coefficients of the pseudoscalar terms $\overline{\chi}i\gamma_5\chi$ and $\overline{\psi}i\gamma_5\psi$ to vanish in order to go to the real mass basis. As shown in Appendix D, this places a constraint on the allowed values of α as

$$\tan\alpha = \left(-\frac{1}{2}\frac{\lambda_{h\chi,h\psi}}{\Lambda_{\chi,\psi}}v_0^2\sin\theta\right)\left(\mu_{\chi,\psi} + \frac{1}{2}\frac{\lambda_{h\chi,h\psi}}{\Lambda_{\chi,\psi}}v_0^2\cos\theta\right)^{-1}.$$

Thus, the post-EWSB fermion DM Lagrangians are

$$\mathscr{L}_\chi = \mathscr{L}_{\text{SM}} + \frac{1}{2}\overline{\chi}(i\slashed{\partial} - m_\chi)\chi - \frac{1}{2}\frac{\lambda_{h\chi}}{\Lambda_\chi}\Big[\cos\xi\,\overline{\chi}\chi + \sin\xi\,\overline{\chi}i\gamma_5\chi\Big]\left(v_0 h + \frac{1}{2}h^2\right), \tag{6.12}$$

$$\mathscr{L}_\psi = \mathscr{L}_{\text{SM}} + \overline{\psi}(i\slashed{\partial} - m_\psi)\psi - \frac{\lambda_{h\psi}}{\Lambda_\psi}\Big[\cos\xi\,\overline{\psi}\psi + \sin\xi\,\overline{\psi}i\gamma_5\psi\Big]\left(v_0 h + \frac{1}{2}h^2\right), \tag{6.13}$$

where $\xi \equiv \theta + \alpha$,

$$\cos\xi = \frac{\mu_{\chi,\psi}}{m_{\chi,\psi}}\left(\cos\theta + \frac{1}{2}\frac{\lambda_{h\chi,h\psi}}{\Lambda_{\chi,\psi}}\frac{v_0^2}{\mu_{\chi,\psi}}\right), \quad \sin\xi = \frac{\mu_{\chi,\psi}}{m_{\chi,\psi}}\sin\theta,$$

$$m_{\chi,\psi} = \sqrt{\left(\mu_{\chi,\psi} + \frac{1}{2}\frac{\lambda_{h\chi,h\psi}}{\Lambda_{\chi,\psi}}v_0^2\cos\theta\right)^2 + \left(\frac{1}{2}\frac{\lambda_{h\chi,h\psi}}{\Lambda_{\chi,\psi}}v_0^2\sin\theta\right)^2}.$$

The parameter m_χ (m_ψ) is the physical mass of the Majorana (Dirac) fermion DM field.

6.3 Constraints

For the scalar and vector DM models, the free parameters are the DM mass $m_{S,V}$ and its dimensionless coupling $\lambda_{hS,hV}$ with the SM Higgs boson.[2] On the other hand, the fermion

---

[2]The quartic self-coupling $\lambda_{S,V}$ can be ignored as it does not play any role in the DM phenomenology. However, it has important implications on the model parameter space if the constraints from electroweak vacuum stability and model perturbativity are imposed [330, 344–350].
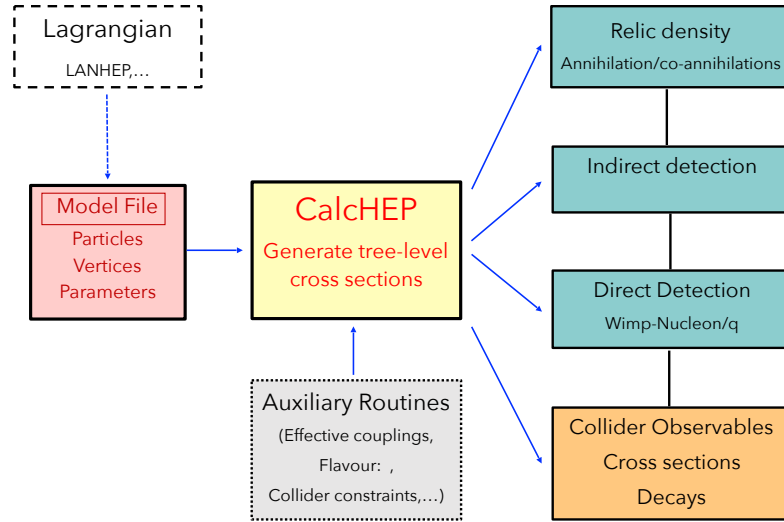
Figure 6.2: A flow chart of `microOMEGAs`. Figure based on Ref. [27].

DM models in Eqs. (6.12) and (6.13) contain three free parameters: $m_{\chi,\psi}$, $\lambda_{h\chi,h\psi}/\Lambda_{\chi,\psi}$ and $\cos\xi$. Thus, we choose to impose constraints on the model parameter space at fixed values of $\cos\xi$. Specifically, we study the following cases: pure scalar interaction ($\cos\xi = 1$); equally mixed scalar-pseudoscalar interaction ($\cos\xi = 1/\sqrt{2}$); and pure pseudoscalar interaction ($\cos\xi = 0$). Thus, the remaining free model parameters are the fermion DM mass $m_{\chi,\psi}$ and its dimensionful coupling $\lambda_{h\chi,h\psi}/\Lambda_{\chi,\psi}$ with the SM Higgs boson.

We use the publicly available software `LanHEP_v3.2.0` [351, 352] to implement the scalar DM model in Eq. (6.1), vector DM model in Eq. (6.2) and the redefined, chiral-rotated fermion DM models in Eqs. (6.12) and (6.13). For the calculation of the model relic density $\Omega_X h^2$, annihilation cross-section $\sigma v_{\rm rel}$ and the gamma-ray yields per annihilation, we rely on the `microOMEGAs_v3.6.9.2` [353] package. A flow chart of `microOMEGAs` is shown in Fig. 6.2. In computing the model relic density, we also take account of DM annihilation into virtual gauge bosons.

In the following subsections, we provide a brief outline of various constraints and their implementations.

6.3.1 Thermal relic density

The best known value for the DM relic density (or abundance) comes from the *Planck* satellite [354]

$$\Omega_{\rm DM}h^2 = 0.1199 \pm 0.0027, \tag{6.14}$$

where $\Omega_{\rm DM} \equiv \rho_{\rm DM}/\rho_c$ is the ratio of the DM mass density to the critical density $\rho_c = 3H_0^2/8\pi G$ and $h = H_0/(100\,{\rm km\,s^{-1}\,Mpc^{-1}})$ is the reduced Hubble constant.

In general, the relic density of WIMPs from an *s*-wave annihilation goes as

$$\Omega_{\rm DM}h^2 \sim \frac{3 \times 10^{-27}\,{\rm cm^3\,s^{-1}}}{\langle \sigma v_{\rm rel} \rangle}, \tag{6.15}$$

where $\langle \sigma v_{\text{rel}} \rangle$ is the velocity-averaged annihilation cross-section. Thus, a small (large) value for $\langle \sigma v_{\text{rel}} \rangle$ leads to an overabundance (underabundance) of WIMPs in the universe today.

For our Higgs portal models, their relic density is mostly determined by the Higgs mediated *s*-channel annihilation into SM particles. A subdominant role is played by the annihilation into *hh* final state via the direct $h^2 X^2$ vertex as well as the Higgs mediated *t*-channel annihilation. As $\langle \sigma v_{\text{rel}} \rangle$ goes as the square of the DM-Higgs coupling, large (small) couplings give a suppressed (enhanced) DM relic density $\Omega_X h^2$ in agreement with Eq. (6.15).

The *Planck* measured DM relic density in Eq. (6.14) places a lower limit on the SM Higgs-DM coupling. For each portal model, we find the coupling(s) at a fixed DM mass which gives the correct relic density using Brent's method [355]. These couplings are the roots (or zeros) of the following function

$$f_\Omega = \Omega_{\text{DM}} h^2 - \Omega_X h^2, \tag{6.16}$$

where $\Omega_X h^2$ is the model relic density as computed in `microMEGAs` and $\Omega_{\text{DM}} h^2 = 0.1199$ is the *Planck* measured central value in Eq. (6.14).

To address the possibility of a multicomponent dark sector where a given model constitutes only a small fraction towards the observed DM abundance, we define a relic abundance parameter as

$$f_{\text{rel}} \equiv \frac{\Omega_X}{\Omega_{\text{DM}}}. \tag{6.17}$$

For plotting purposes, we take $f_{\text{rel}} = 1, 0.1$ and 0.01 corresponding to an X relic abundance of 100%, 10% and 1% respectively.

For DM masses below $m_h/2$, we find multiple values of the SM Higgs-DM coupling which satisfies Eq. (6.16). Naively, we expect $\Omega_X h^2$ to decrease monotonically at large values of λ_{hX} as in Eq. (6.15). However, $\langle \sigma v_{\text{rel}} \rangle$ has an additional dependence on λ_{hX} through the full Higgs boson width $\Gamma_h(\sqrt{s})$ as a function of the center-of-mass energy $\sqrt{s}$. Thus, when λ_{hX} increases, the increasing Higgs boson width counteracts the increase in $\langle \sigma v_{\text{rel}} \rangle$ from λ_{hX} alone and at some point outstrips it such that $\langle \sigma v_{\text{rel}} \rangle$ starts decreasing with increasing λ_{hX}. This causes a minimum relic density $\Omega_X h^2$ for any given DM mass. When such features appear, we always find that only one root is consistent with the Higgs invisible width constraint; this is the one that we show in our results. Indeed, the same feature was also seen in Ref. [324] but was not explicitly commented on in the paper.

In addition, for DM masses below $m_h/2$, we do not find roots of Eq. (6.16) for $f_{\text{rel}} = 0.1$ and 0.01. This is so because the minimum relic density is larger than the value of the contour being drawn. Thus, gaps in our relic density contours appear for $f_{\text{rel}} = 0.1$ and 0.01.

When the DM mass is above $m_h/2$, the relic density monotonically decreases with larger couplings λ_{hX}. This gives a single root (or coupling) at a fixed DM mass. The

Higgs invisible width $\Gamma_{\text{inv}}(h \rightarrow \overline{X}X)$ vanishes in this region as the decay $h \rightarrow \overline{X}X$ is kinematically forbidden.

6.3.2 Higgs invisible width

When $m_X < m_h/2$, the decay $h \rightarrow \overline{X}X$ is kinematically allowed. This contributes to the Higgs invisible width Γ_{inv}. For our Higgs portal models, the Higgs invisible widths are given by [335, 337]

$$\Gamma_{\text{inv}}(h \rightarrow SS) = \frac{\lambda_{hS}^2 v_0^2}{32\pi m_h}\sqrt{1 - \frac{4m_S^2}{m_h^2}}, \tag{6.18}$$

$$\Gamma_{\text{inv}}(h \rightarrow VV) = \frac{\lambda_{hV}^2 v_0^2 m_h^3}{128\pi m_V^4}\left(1 - \frac{4m_V^2}{m_h^2} + \frac{12m_V^4}{m_h^4}\right)\sqrt{1 - \frac{4m_V^2}{m_h^2}}, \tag{6.19}$$

$$\Gamma_{\text{inv}}(h \rightarrow \overline{\chi}\chi) = \frac{m_h v_0^2}{16\pi}\left(\frac{\lambda_{h\chi}}{\Lambda_\chi}\right)^2\left(1 - \frac{4m_\chi^2 \cos^2\xi}{m_h^2}\right)\sqrt{1 - \frac{4m_\chi^2}{m_h^2}}, \tag{6.20}$$

$$\Gamma_{\text{inv}}(h \rightarrow \overline{\psi}\psi) = \frac{m_h v_0^2}{8\pi}\left(\frac{\lambda_{h\psi}}{\Lambda_\psi}\right)^2\left(1 - \frac{4m_\psi^2 \cos^2\xi}{m_h^2}\right)\sqrt{1 - \frac{4m_\psi^2}{m_h^2}}. \tag{6.21}$$

In Ref. [356], an upper limit of 19% was obtained on the SM Higgs invisible branching ratio $\mathcal{BR}(h \rightarrow \overline{X}X)$ at 2σ C.L. using combined fits to all Higgs production and decay channels probed by ATLAS, CMS and the Tevatron.[3] An additional projected upper limit of 5% on $\mathcal{BR}(h \rightarrow \overline{X}X)$ at no more than 1σ C.L. can be further imposed if no additional Higgs decay is detected at the 14 TeV LHC run after 300 fb^{-1} of luminosity data is collected [357].

Using an upper limit of Y ($Y = 0.19$ or 0.05 from above) on $\mathcal{BR}(h \rightarrow \overline{X}X)$, the Higgs invisible width Γ_{inv} can be expressed in terms of the visible contribution Γ_{vis} as

$$\Gamma_{\text{inv}} \leq \frac{Y}{1 - Y}\Gamma_{\text{vis}}, \tag{6.22}$$

where $\Gamma_{\text{vis}} \equiv \Gamma_{\text{SM}} = 4.07$ MeV for $m_h = 125$ GeV [5]. Using the expressions for the Higgs invisible width in Eqs. (6.18)–(6.21), the upper limit on Γ_{inv} can be translated into an upper limit on the SM Higgs-DM coupling as a function of the DM mass.

6.3.3 Indirect detection

Indirect DM searches are based on measuring the fluxes of gamma rays, neutrinos and antimatter produced from DM annihilation in distant regions of the universe. The annihilation flux Φ_{ann} scales as the square of the DM mass density, i.e., $\Phi_{\text{ann}} \propto \rho_{\text{DM}}^2$. Thus,

---

[3]The Higgs invisible branching ratio is defined as $\mathcal{BR}(h \rightarrow \overline{X}X) \equiv \Gamma_{\text{inv}}/(\Gamma_{\text{vis}} + \Gamma_{\text{inv}})$ where Γ_{vis} is the visible/SM contribution to the SM Higgs boson width.

natural targets are those with the highest DM content, e.g., dwarf spheroidal (dSph) galaxies, the galactic centre (GC) and the Sun. Some of the current indirect search experiments include the *Fermi*-LAT [358], HESS [359] and AMS-02 [360]. The CTA is one of the next generation of ground-based gamma-ray telescopes [361].

We impose constraints on the model parameter space from indirect searches using the following combined delta log-likelihood function

$$\Delta \ln \mathcal{L}_{\text{total}} = \Delta \ln \mathcal{L}_{\text{CMB}} + \Delta \ln \mathcal{L}_{\text{dSphs}} + \Delta \ln \mathcal{L}_{\text{CTA}}. \tag{6.23}$$

In general, the combined delta log-likelihood receives contributions from all three indirect searches. However, the CTA delta log-likelihood is only included when *projected* limits are discussed. Each delta log-likelihood depends on the DM mass m_X and its coupling with the SM Higgs boson λ_{hX} via the zero-velocity annihilation cross-section $\langle \sigma v_{\text{rel}} \rangle_0 \equiv \langle \sigma v_{\text{rel}} \rangle|_{v \to 0} \equiv \langle \sigma v_{\text{rel}} \rangle|_{\sqrt{s} \to 2m_X}$, the branching ratio $\mathcal{B}_f$ into a SM final state f and the model relic density $\Omega_X h^2$.[4] The allowed SM final states from the DM annihilation are W^+W^-, ZZ, hh, $\mu^+\mu^-$, $\tau^+\tau^-$ and $\overline{q}q$ where $q = b, c, t$.

We scale all indirect signals by f_{rel}^2 when X constitutes only a small fraction of the observed DM abundance. In regions where $f_{\text{rel}} > 1$, we rescale in the same way and increase the expected signals. This is done for the sake of simplicity and has no practical consequence as the relevant region is robustly excluded by the relic density constraint.

We perform 2D scans in the model parameter space using Brent's method by finding the roots of the following function

$$f_{\text{ID}} = \Delta \ln \mathcal{L}_{\text{total}} - \Delta \ln \mathcal{L}_{\text{C.L.}}, \tag{6.24}$$

where $\Delta \ln \mathcal{L}_{\text{total}}$ is the combined delta log-likelihood from Eq. (6.24) (equal to zero in the case of no DM signal). The term $\Delta \ln \mathcal{L}_{\text{C.L.}}$ is the delta log-likelihood for a fixed C.L. For our study, we consider 1σ and 90% C.L. such that

$$\Delta \ln \mathcal{L}_{\text{C.L.}} = \begin{cases} -0.500000, & 1\sigma \text{ C.L.}, \\ -1.352771, & 90\% \text{ C.L.} \end{cases} \tag{6.25}$$

When imposing current limits from indirect searches, the combined delta log-likelihood function is

$$\Delta \ln \mathcal{L}_{\text{total}} = \Delta \ln \mathcal{L}_{\text{WMAP}} + \Delta \ln \mathcal{L}_{\text{dSphs}}, \tag{6.26}$$

whereas for the projected future limits, the combined delta log-likelihood function is

$$\Delta \ln \mathcal{L}_{\text{total}} = \Delta \ln \mathcal{L}_{\text{Planck}} + \Delta \ln \mathcal{L}_{\text{dSphs}}^{\text{projected}} + \Delta \ln \mathcal{L}_{\text{CTA}}. \tag{6.27}$$

Here $\Delta \ln \mathcal{L}_{\text{dSphs}}^{\text{projected}}$ differs from $\Delta \ln \mathcal{L}_{\text{dSphs}}$ due to the projected *Fermi*-LAT improvements in adding more dwarf galaxies to its search and observing for a longer duration.

---

[4]For indirect searches, DM annihilation occur in the non-relativistic limit with DM speeds $v \sim 10^{-3}c$. In this limit, the centre-of-energy is $\sqrt{s} = 2m_X$.

When $m_X < m_h/2$, we again find multiple values of λ_{hX} which satisfy Eq. (6.24). In these cases, we ignore the root at larger λ_{hX} and choose the one at smaller λ_{hX}. This is done because the root at larger coupling is robustly excluded by the Higgs invisible width constraint.

6.3.3.1 CMB likelihood

The temperature fluctuations and polarization of the CMB are sensitive to the redshift of recombination $z \sim 1100$ as it determines the surface of last scattering. If the decay or annihilation of DM deposits extra electromagnetic radiation after $z \sim 1100$, it can delay the time for recombination and/or produce distortions in the CMB.

When computing the CMB bounds from the DM annihilation, a key quantity of interest is the efficiency $f(z)$ for producing ionising radiation as a function of redshift z. For DM annihilations, $f(z)$ is determined in terms of the electromagnetic power injected per unit volume [362]

$$\frac{dE}{dt\,dV} = f(z)\frac{\langle \sigma v_{\mathrm{rel}} \rangle}{m_X}\Omega_X^2 \rho_c^2 \, c^2 (1+z)^6.\tag{6.28}$$

The bounds on $\langle \sigma v_{\mathrm{rel}} \rangle$ can be encoded in terms of an integral involving $f(z)$ and a set of *principle component* basis functions $e_i(z)$ [363, 364]. In terms of these basis functions, $f(z)$ can be expanded as

$$\varepsilon f(z) = \sum_{i=1}^{\infty} \varepsilon_i e_i(z),$$

where $\varepsilon \equiv \langle \sigma v_{\mathrm{rel}} \rangle / m_X$ and $\varepsilon_i = \varepsilon f(z) \cdot e_i(z)/(e_i(z) \cdot e_i(z))$. The inner product is an integral over z with the integration limits $z_1 = 86.83$ and $z_2 = 1258.2$. For DM annihilations, the basis functions are chosen to maximise the sensitivity to a generally expected z-dependence of the energy injection from annihilating DM in such a way that the most important contributions are described by the lowest components.

It is useful to consider the effective efficiency f_{eff} which is defined in terms of a *universal WIMP annihilation* curve $e_W(z)$ as $f_{\mathrm{eff}} \sim (f \cdot e_W)/(e_W \cdot e_W)$. This has the interpretation that $f_{\mathrm{eff}} < 1$ denotes the average efficiency of energy injection for the annihilation channel under consideration. Using the expansion $e_W = \sum_i c_i e_i$ for WMAP7 [365], only the first principle component is dominant. Thus, for WMAP7, f_{eff} is given by

$$f_{\mathrm{eff}} \equiv \frac{(f \cdot e_1)}{c_1(e_1 \cdot e_1)},$$

where $c_1 = 4.64$. For *Planck* [354], all three principle components contribute and this gives

$$f_{\mathrm{eff}} \equiv \frac{1}{\sqrt{\lambda_1}c_1}\sqrt{\sum_i \lambda_i \left(\frac{f \cdot e_i}{e_i \cdot e_i}\right)^2},$$

where λ_i and e_i are parameters appropriate for *Planck*.

We use the tabulated values of f_{eff} for various SM final states and DM masses from Ref. [362]. For intermediate DM masses, we interpolate the values of f_{eff} in terms of $\log_{10} m_X$. For DM annihilation into multiple channels, the total f_{eff} is a weighted sum of the effective efficiency $f_{\text{eff},f}$ over final states f with branching ratio $\mathcal{B}_f$ as

$$f_{\text{eff}} = \sum_f \mathcal{B}_f f_{\text{eff},f}. \tag{6.29}$$

We impose CMB constraints on the model parameter space at arbitrary C.L. by constructing a delta log-likelihood function for the annihilation cross-section $\langle \sigma v_{\text{rel}} \rangle$, assuming a DM mass m_X and a branching ratio $\mathcal{B}_f$ into final state f. For the *Planck* experiment, the delta log-likelihood function is given by [362]

$$\Delta \ln \mathcal{L}_{\text{Planck}}(\langle \sigma v_{\text{rel}} \rangle | m_X, \mathcal{B}_f) = -\frac{1}{2} f_{\text{eff}}^2 \lambda_1 c_1^2 \left(\frac{\langle \sigma v_{\text{rel}} \rangle}{2 \times 10^{-27} \text{cm}^3 \text{ s}^{-1}} \right)^2 \left(\frac{\text{GeV}}{m_X} \right)^2, \tag{6.30}$$

where $c_1 = 4.64$ and $\lambda_1 = 3.16$.[5] The above expression assumes a linear response on the CMB against the deposited energy which is not accurate for WMAP. However, this can be corrected by the replacement $2 \times 10^{-27} \text{cm}^3 \text{ s}^{-1} \rightarrow 3.2 \times 10^{-27} \text{cm}^3 \text{ s}^{-1}$ and $\lambda_1 = 0.279$. Thus, the delta log-likelihood function for the WMAP experiment is [362]

$$\Delta \ln \mathcal{L}_{\text{WMAP}}(\langle \sigma v_{\text{rel}} \rangle | m_X, \mathcal{B}_f) = -\frac{1}{2} f_{\text{eff}}^2 \lambda_1 c_1^2 \left(\frac{\langle \sigma v_{\text{rel}} \rangle}{3.2 \times 10^{-27} \text{cm}^3 \text{ s}^{-1}} \right)^2 \left(\frac{\text{GeV}}{m_X} \right)^2, \tag{6.31}$$

where $c_1 = 4.64$ and $\lambda_1 = 0.279$.

6.3.3.2 Fermi dwarfs likelihood

The *Fermi*-LAT is a powerful tool in searching for signs of DM annihilation in distant astrophysical sources. It currently provides the strongest upper limits on $\langle \sigma v_{\text{rel}} \rangle$ based on a combined analysis of 15 dwarf galaxies using 6 years of the *Fermi*-LAT data, processed with the new `Pass-8` event-level analysis [367]. For each of the 15 dwarf galaxies included in the analysis, the results are publicly available in the form of tabulated energy times integrated gamma-ray flux ($E\Phi_{\text{ann}}$) in units of $\text{MeV cm}^{-2} \text{ s}^{-1}$ and delta log-likelihoods ($\Delta \ln \mathcal{L}_{\text{dSphs}}$) in 24 energy bins between 500 MeV and 500 GeV.[6]

To calculate $\Delta \ln \mathcal{L}_{\text{dSphs}}$, we use the `gamLike_v1.0.0` package [184]. It is designed to compute delta log-likelihoods from gamma-ray searches. It uses various integration routines to integrate over the input arrays of $\Phi_{\text{PP}}(E)$ in each of the energy bins used by a given experiment. The integrated $\Phi_{\text{PP}}(E)$ values are combined with the J-factors to give an array of integrated gamma-ray fluxes Φ_{ann} in various energy bins. The arrays of integrated flux times energy ($E\Phi_{\text{ann}}$) are compared against the tabulated delta log-likelihood values.

---

[5]This is in fact a projected delta log-likelihood for the *Planck* polarization data, but it agrees very well with the actual constraints in Ref. [366].

[6]https://www-glast.stanford.edu/pub_data/1048/

Finally, $\Delta \ln \mathcal{L}_{\text{dSphs}}$ is calculated at a fixed set of model parameters by summing over the interpolated delta log-likelihood values in each energy bin.

As inputs, the `gamLike` package requires an array of gamma-ray energies E (GeV) and $\Phi_{\text{PP}}(E)$ (cm^3 s^{-1} GeV^{-3}) where

$$\Phi_{\text{PP}}(E) = \kappa \, \frac{\langle \sigma v_{\text{rel}} \rangle}{4\pi m_X^2} \frac{dN_\gamma}{dE}. \tag{6.32}$$

The tabulated results of Ref. [367] are based on gamma-ray energies between 500 MeV and 500 GeV. Thus, we interpolate the differential gamma-ray spectrum dN_γ/dE from `micrOMEGAs` between 500 MeV and the DM mass m_X.[7] Thus, $\Delta \ln \mathcal{L}_{\text{dSphs}}$ entering in Eq. (6.26) is a difference of the log-likelihoods for a DM signal and background-only hypothesis ($\Phi_{\text{PP}} = 0$).

For projected *Fermi*-LAT limits, we assume that *Fermi* operates for at least 10 years in its current survey mode and is able to add as many southern dwarf galaxies in the future as the northern dwarfs now. Assuming that the improvements in the *Fermi*-LAT reach are dominated by the statistical uncertainty, i.e., limits on $\langle \sigma v_{\text{rel}} \rangle$ scale as $\sqrt{N}$ where N is the number of dwarfs, we calculate the projected *Fermi*-LAT sensitivities by scaling the current *Fermi*-LAT limits by a factor of $\sqrt{2 \times 10/6} = \sqrt{20/6} \sim 1.83$.

6.3.3.3 CTA likelihood

The Cherenkov Telescope Array (CTA) is a multinational project to build the next generation of ground-based gamma-ray instruments with sensitivity over energies from a few tens of GeV to 100 TeV. It is intended to improve the flux sensitivities of the current generation of Imaging Atmospheric Cherenkov Telescopes (IACTs) such as MAGIC [368], HESS [220] and VERITAS [369] by an order of magnitude.

The CTA will consist of several tens of telescopes of 2–3 different types with sizes varying between 5 and 25 meters. These will be distributed over an area of several square kilometers. The sensitivity will be a factor of 10 better than current instruments, and the field of view (FoV) will be up to 10° in diameter [29]. It is envisaged as a two-part telescope with both southern and northern sites; CTA South will be relevant for DM searches towards the GC. The first detailed Monte Carlo (MC) analysis was presented in Ref. [370] where 11 different array configurations for CTA South were studied.

We use the array configuration known as *Array I* which provides a balanced configuration with 3 large (~ 24 m aperture), 18 medium (~ 12 m) and 56 small telescopes (~ 4–7 m). The configuration provides a good compromise in sensitivity between low- and high-energy gamma rays [29]. Extensive information on the effective area, background rates, angular and energy resolution is also available for Array I. Previous DM sensitivity studies used a similar array: Array E in Ref. [371] and the Paris-MVA analysis of Array I

---

[7]The differential gamma-ray spectrum dN_γ/dE goes to zero when $E \geq m_X$.

in Ref. [372]. The point-source sensitivities of Arrays E and I agree very well at energies $\lesssim 1$ TeV, whereas Array I is more sensitive (only by a factor of less than 2) at higher energies.

To calculate $\Delta \ln \mathcal{L}_{CTA}$, we follow the analysis of Ref. [29] by using their tabulated values of integrated gamma-ray flux times energy $E\Phi_{ann}$ (MeV cm^{-2} s^{-1}) and delta log-likelihoods ($\Delta \ln \mathcal{L}_{CTA}$) between gamma-ray energies of 25 GeV and 10 TeV. The main features of this study are:

1. Assessing the impacts of all backgrounds such as cosmic ray protons and electrons hitting the atmosphere and diffuse astrophysical emissions. It was found that galactic diffuse emission (GDE) substantially degrades the CTA differential sensitivity, see Fig. 4 of Ref. [29];

2. Using a statistical framework to account for the impacts of differential acceptance uncertainties from sources such as event reconstruction, MC determination of the effective areas and the uncertainty in atmospheric conditions within a FoV on DM search limits from CTA [373]. Specifically, the tabulated results are based on a systematic uncertainty of 1%;

3. Using the Einasto profile [374] to calculate the *J*-factors for the GC. The profile is parametrised as

$$\rho_{DM}(r) \propto \exp\left(-\frac{2}{\alpha}\left[\left(\frac{r}{r_s}\right)^{\alpha} - 1\right]\right). \tag{6.33}$$

It is normalized to a local DM density of $\rho_{\odot} \equiv \rho_{DM}(r_{\odot}) = 0.4$ GeV cm^{-3} by choosing $\alpha = 0.17$, $r_s = 20$ kpc and $r_{\odot} = 8.5$ kpc [375];

4. Using a slightly contracted generalised Navarro-Frenk-White (NFW) profile [376] to indicate an improvement in CTA limits. The profile is parametrised as

$$\rho_{DM}(r) \propto \frac{1}{r^{\gamma}(r_s + r)^{3-\gamma}}, \tag{6.34}$$

where $\gamma = 1.3$ is the inner slope of the profile and $r_s = 20$ kpc is the scale radius. It is normalised in the same way as the Einasto profile, i.e., $\rho_{\odot} = 0.4$ GeV cm^{-3};

5. Performing a *morphological* analysis by covering the area occupied by the two regions of interest (RoIs) in the left panel of Fig. 6.3 and dividing it into $1° \times 1°$ squares. This gives a total of 28 RoIs as shown in the right panel of Fig. 6.3. A morphological analysis allows for proper exploitation of the shape differences between the GDE (concentrated along the Galactic plane) and a DM annihilation signal (spherically distributed around the GC). The resultant constraints are stronger by a factor of a few when compared to the traditional ring analyses.
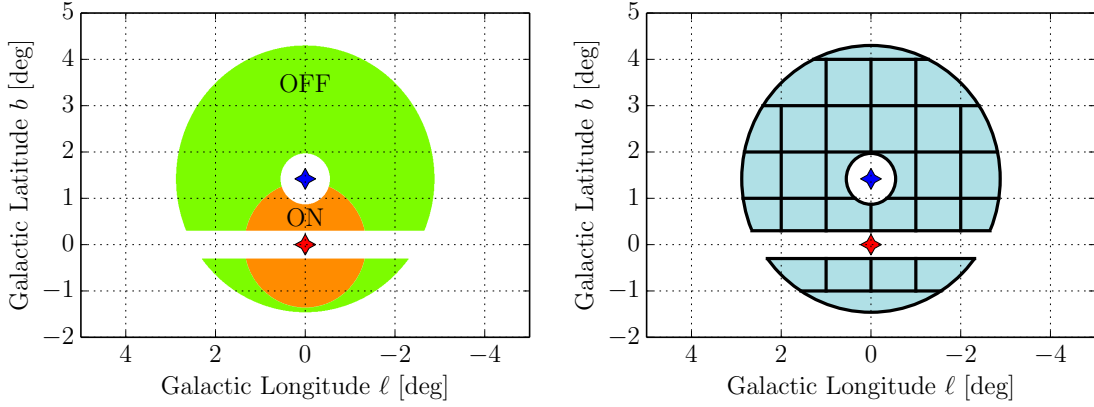
Figure 6.3: *Left panel*: The signal and background regions of interest (RoIs) as used in the ring method of Ref. [28]. *Right panel*: Separation of the signal and background RoIs into 28 sub-RoIs for the morphological analysis of Ref. [29]. Figure from Ref. [29].

In summary, the tabulated results of Ref. [29] are based on a morphological analysis over 28 RoIs, assuming $\gtrsim 100\,\mathrm{h}$ of GC observation by CTA,[8] 1% instrumental systematics, J-factors for the GC using the Einasto profile in Eq. (6.33) and inclusion of all known backgrounds (cosmic-ray electrons/protons and the galactic diffusion emissions).

We use the `gamLike_v1.0.0` package to calculate the CTA delta log-likelihood from the tabulated results of Ref. [29]. As the tabulated results are available for gamma-ray energies between 25 GeV and 10 TeV, the corresponding inputs for the `gamLike` package are arrays of gamma-ray energies E (GeV) between 25 GeV and m_X, and $\Phi_{\mathrm{PP}}(E)$ ($\mathrm{cm^3\,s^{-1}\,GeV^{-3}}$).

In Fig. 7 of Ref. [29], upper limits on $\langle\sigma v_{\mathrm{rel}}\rangle$ from CTA observation of the GC were presented assuming different annihilation channels and DM halo profiles. For the DM annihilation into the $b\bar{b}$ final state, a contracted generalised NFW profile in Eq. (6.34) yields a factor of 6 better limits on $\langle\sigma v_{\mathrm{rel}}\rangle$ when compared against the Einasto profile in Eq. (6.33). This is primarily due to an increase in the GC J-factors by a factor of ~ 2.9 when summing over all RoIs. To extend the expected search capability of CTA towards higher DM masses, we also use these improved limits to see the impacts of using a more optimistic DM distribution.

6.3.4 Direct detection

Direct detection experiments are aimed at measuring the recoil of a nucleus from a collision with a DM particle. The differential rate per day (cpd $\mathrm{kg^{-1}\,keV^{-1}}$ where cpd is counts per day) for a spin-independent (SI) interaction is given by [185, 377]

$$\frac{dR}{dE} = \frac{\rho_\odot}{mM} \int d^3v\, v f(\boldsymbol{v}, t)\frac{d\sigma}{dE}, \tag{6.35}$$

---

[8]As the limits of Ref. [29] are systematics dominated, they are more or less independent of any increase in the CTA observation time beyond 100 h. For our portal models, we calculate the indirect search limits based on 100 h of CTA observation time.

where $\rho_\odot$ is the local DM mass density, $f(\mathbf{v}, t)$ is the time-dependent DM velocity distribution and E is the nuclear recoil energy as defined in chapter 4. In the typical case where the target material contains more than one isotope, the differential rate is a mass-fraction weighted sum over contributions from all isotopes, each of the forms given by Eq. (6.35). The term $d\sigma/dE$ is the momentum-dependent differential SI cross-section and is given by

$$\frac{d\sigma}{dE} = \frac{1}{E_{\max}} \sigma_0 F^2(q) \Theta(q_{\max} - q), \tag{6.36}$$

where $E_{\max} = q_{\max}^2/2M = 2\mu^2 v^2/M$ is the maximum energy transfer in a collision at a relative velocity v, σ_0 is the SI cross-section in the zero-velocity limit[9] and Θ is the Heaviside step function. The term $F(q)$ is the form factor which accounts for the finite size of the nucleus. When DM coherently scatters off the entire nucleus at low momentum transfer, $F^2(q) \to 1$. However, when the de Broglie wavelength of the momentum transfer q becomes comparable to the size of the nucleus, DM becomes sensitive to the internal structure of the nucleus and $F^2(q) < 1$ with $F^2(q) \ll 1$ at high momentum transfers.

It is traditional to define an *effective* SI cross-section as

$$\sigma(q) \equiv \sigma_0 F^2(q) \tag{6.37}$$

such that the dependency on the momentum transfer q is contained entirely within the form factor $F^2(q)$. The *actual* cross-section is

$$\int dq^2 \, \frac{d\sigma(q^2, v)}{dq^2} \tag{6.38}$$

for a given DM-nucleus relative speed v. Using Eq. (6.37), the momentum-dependent differential SI cross-section in Eq. (6.36) simplifies to

$$\frac{d\sigma}{dE} = \frac{M}{2\mu^2 v^2} \sigma(q) \Theta(q_{\max} - q). \tag{6.39}$$

Using this expression, the differential rate per day in Eq. (6.35) simplifies to

$$\frac{dR}{dE} = \frac{1}{2m\mu^2} \sigma(q) \, \rho_\odot \, \eta(v_{\min}(E), t), \tag{6.40}$$

where

$$\eta(v_{\min}(E), t) = \int_{v > v_{\min}(E)} d^3v \, \frac{f(\mathbf{v}, t)}{v} \tag{6.41}$$

is the mean inverse speed and

$$v_{\min}(E) = \sqrt{\frac{ME}{2\mu^2}}$$

is the minimum DM speed that results in a nuclear recoil with energy E. The requirement $q < q_{\max}$ in the Heaviside step function of Eq. (6.36) imposes a lower limit of $v > v_{\min}(E)$ on the integral in Eq. (6.41).

---

[9]Generally, σ_{SI} and σ_{SD} are used to represent this term for nuclear spin-independent (SI) and spin-dependent (SD) interactions respectively.

The main advantage of writing down the recoil spectrum in Eq. (6.40) as opposed to Eq. (6.35) is that the particle physics and astrophysical aspects separate into two distinct factors: $\sigma(q)$ describe the particle physics aspect, whereas $\rho_\odot$ and $\eta(v_{\min}(E), t)$ describes the astrophysical aspect.

For our Higgs portal models, the SI cross-section σ_{SI} is given by

$$\sigma_{\mathrm{SI}} = \frac{\mu^2}{\pi}\left[Z\,G_p^{\mathrm{SI}} + (A-Z)\,G_n^{\mathrm{SI}}\right]^2 + \frac{q^2}{4m_X^2}\frac{\mu^2}{\pi}\left[Z\,\widetilde{G}_p^{\mathrm{SI}} + (A-Z)\,\widetilde{G}_n^{\mathrm{SI}}\right]^2, \qquad (6.42)$$

where $Z\,(A-Z)$ are the number of protons (neutrons) in the nucleus and $G_N^{\mathrm{SI}}\,(\widetilde{G}_N^{\mathrm{SI}})$ for $N \in (p, n)$ are the effective scalar (pseudoscalar) DM-nucleon couplings.[10] For the scalar and vector models, $\widetilde{G}_N^{\mathrm{SI}} = 0$, whereas for the fermion models, both terms contribute towards σ_{SI}. For the fermion models with a pseudoscalar DM-nucleon coupling, the SI cross-section is suppressed by $q^2/4m_X^2$ where $q \sim O(\mathrm{MeV})$ is the momentum transfer [379]. Thus, the resulting direct detection limits are momentum suppressed.

When the effective scalar (pseudoscalar) DM couplings with protons and neutrons are approximately equal, i.e., $\sigma_{\mathrm{SI}}^p \simeq \sigma_{\mathrm{SI}}^n$, the SI cross-section in Eq. (6.42) is enhanced by a factor of A^2 as the matrix elements for the cross-section are a coherent sum over the individual protons and neutrons in the nucleus.

For a SI interaction, the form factor is a Fourier transform of the nucleus mass distribution. As a reasonably accurate approximation, we use the Helm form factor [380]. It was first introduced as a modification to the form factor for a uniform sphere with a Gaussian function to account for the soft edge of the nucleus [381]. It is given by

$$F(q) = 3e^{-q^2 s^2/2}\left[\frac{\sin(qr_n) - qr_n\cos(qr_n)}{(qr_n)^3}\right], \qquad (6.43)$$

where $s \simeq 0.9\,\mathrm{fm}$ and $r_n^2 = c^2 + \frac{7}{3}\pi^2 a^2 - 5s^2$ is the effective nuclear radius with $a \simeq 0.52\,\mathrm{fm}$ and $c \simeq 1.23 A^{1/3} - 0.60\,\mathrm{fm}$.

We use the standard astrophysical parameters, namely the local DM density $\rho_\odot = 0.4\,\mathrm{GeV\,cm^{-3}}$ and the local galactic disk rotation speed $v_{\mathrm{rot}} = 220\,\mathrm{km\,s^{-1}}$ (also equals the most probable speed $\bar{v}$ of the Maxwell-Boltzmann velocity distribution). We take the Galactic escape speed as $v_{\mathrm{esc}} = 544\,\mathrm{km\,s^{-1}}$. For more details, see Ref. [382].

In the standard analysis where only a single component of DM contributes towards the observed DM abundance, the differential rate is proportional to $(\rho_\odot\,\sigma_{\mathrm{SI}})/m$ as in Eq. (6.40). To address the multicomponent scenario, we rescale the limiting value of σ_{SI} by the fraction $f_{\mathrm{rel}} = \Omega_X/\Omega_{\mathrm{DM}}$ where $X \in (S, V_\mu, \chi, \psi)$. Thus, the local energy density of X is $f_{\mathrm{rel}}\,\rho_\odot$.

---

[10]These are analogous to the four-fermion G_F-like couplings [378].

6.3.4.1 Non-fermion models

For the scalar and vector DM models, the SI DM-nucleon cross-section is

$$\sigma_{\text{SI}} = \frac{\mu^2}{\pi} \frac{\lambda_{hX}^2 f_N^2 m_N^2}{4 m_X^2 m_h^4} = \frac{m_N^4}{4\pi(m_X + m_N)^2} \frac{\lambda_{hX}^2 f_N^2}{m_h^4}, \tag{6.44}$$

where $X \in (S, V)$, $m_N = 931\,\text{MeV}$ and $f_N = 0.30$ [324]. The term f_N is related to the hadronic matrix elements by

$$f_N = \sum_{\text{quarks}} f_{Tq}^{(N)} = \sum_{\text{quarks}} \frac{m_q}{m_N} \langle N|\overline{q}q|N \rangle = \frac{2}{9} + \frac{7}{9} \sum_{q=u,d,s} f_{Tq}^{(N)}, \tag{6.45}$$

where the last equality follows from the heavy-quark expansion [383].

For the projected XENON1T [384–386] experiment, we use the 90% C.L. limit from XENON100 [387] and scale it by the relic abundance parameter $f_{\text{rel}} = \Omega_X/\Omega_{\text{DM}}$. Assuming that the sensitivity of XENON1T as a function of the DM mass scales relative to the XENON100 by the exposure ε, we demand that

$$\sigma_{\text{eff}} \equiv \varepsilon f_{\text{rel}} \sigma_{\text{SI}} \leq \sigma_{\text{Xe}}, \tag{6.46}$$

where σ_{Xe} is the 90% C.L. from XENON100 and $\varepsilon = 100$.

For the LUX [388, 389] experiment, we use a Poisson based likelihood [390] in the observed number of signal events N as

$$\mathcal{L}_{\text{Poisson}}(s|N) = P(N|s) = \frac{(b+s)^N e^{-(b+s)}}{N!}, \tag{6.47}$$

where b is the expected number of background events and

$$s = MT \int_0^\infty dE\, \phi(E) \frac{dR}{dE} \tag{6.48}$$

is the expected number of signal events, M is the detector mass, T is the exposure time and $\phi(E)$ is a global efficiency factor which incorporates trigger efficiencies, energy resolution and analysis cuts.

We calculate the LUX log-likelihood using the `LUXCalc_v1.0.1` [391] package. For the LUX analysis region, we use $N = 1$ and $b = 0.64$ [392], whereas for XENON100, we use $N = 2$ and $b = 1$ [387]. The efficiency curves $\phi(E)$ are generated by `TPMC` [393] using the `NEST` [394, 395] model.

As inputs, the `LUXCalc` package require the effective SI scalar DM-nucleon coupling G_N^{SI} and pseudoscalar DM-nucleon coupling $\widetilde{G}_N^{\text{SI}}$. For the scalar and vector DM models, these are given by

$$G_N^{\text{SI}} = \frac{\lambda_{hX} f_N m_N}{2 m_X m_h^2}, \quad \widetilde{G}_N^{\text{SI}} = 0, \tag{6.49}$$

where $X \in (S, V)$. The pseudoscalar effective DM-nucleon couplings are zero as the DM-nucleon interaction for the non-fermion models is mediated by a spin-0 boson.

6.3.4.2 Fermion models

Given that the mediator h is a spin-0 boson with scalar coupling to nucleons (specifically quarks), the DM-nucleon interaction is nucleon-spin independent. In the fermion DM models, a mixing between a pure scalar ($\cos \xi = 1$) and a pure pseudoscalar ($\cos \xi = 0$) interaction occurs.

For a pure pseudoscalar interaction, the SI cross-section is suppressed by a factor of $q^2/4m_X^2$ [379] where $q \sim O(\text{MeV})$ is the momentum transfer. Thus, a direct comparison between the analytical expression for the SI cross-section and XENON100/LUX limits is inaccurate. To remedy this, we use a generalized and augmented version of `LUXCalc` by including the $q^2/4m_X^2$ factor in the differential rate per day dR/dE.

For the fermion DM models, the effective scalar and pseudoscalar DM-nucleon couplings are given by

$$G_N^{\text{SI}} = \frac{\lambda_{hX}}{\Lambda_X} \frac{f_N m_N \cos \xi}{m_h^2}, \quad \widetilde{G}_N^{\text{SI}} = \frac{\lambda_{hX}}{\Lambda_X} \frac{f_N m_N \sin \xi}{m_h^2}, \tag{6.50}$$

where $X \in (\chi, \psi)$. For the XENON1T experiment, the expected improvement in sensitivity over XENON100 is $\varepsilon = 100$, whereas for the LUX experiment, limits are derived with $\varepsilon = 1$.

With the inclusion of a momentum-suppressed term in the differential rate per day, we perform 2D scans in the $(m_X, \lambda_{hX}/\Lambda_X)$ plane where $X \in (\chi, \psi)$ using the Brent's method. The function for the root-finding algorithm is

$$f_{\text{DD}} = \Delta \ln \mathcal{L}_{\text{Poisson}} - \Delta \ln \mathcal{L}_{90\% \text{ C.L.}}, \tag{6.51}$$

where $\Delta \ln \mathcal{L}_{\text{Poisson}}$ is the difference between a Poisson likelihood in Eq. (6.47) for a DM signal ($s \neq 0$) and no DM signal ($s = 0$). The parameter $\Delta \ln \mathcal{L}_{90\% \text{ C.L.}} = -1.352771$ is the delta log-likelihood for a 90% C.L as in Eq. (6.25).

6.3.5 Validity of the fermion EFTs

Due to the presence of dimension-5 effective operators in the fermion DM models, it is important to check the validity of the EFT approximation. As discussed in chapter 4, an EFT is valid as long as the momentum exchange q involved in an interaction is below the mass of the underlying mediator φ. Thus, the mediator mass m_φ dominates the denominator of the internal propagator and allows q to be neglected. In this case, φ is said to be *integrated out*.

A non-renormalizable effective operator (as in the fermion EFTs) is valid only if its dimensionful coupling implies a mediator mass that is below the interaction scale of a given process. For DM annihilation, it is $q \sim \sqrt{s} = 2m_X$ where $X \in (\chi, \psi)$. Thus, the fermion EFTs are valid for indirect detection when $m_\varphi > 2m_X$. For direct detection

experiments, the momentum exchange occurs deep in the non-relativistic regime where $q \sim O(\text{MeV})$. This means that the fermion EFTs are valid for direct detection when $m_\varphi > O(\text{MeV})$.

To find the values of λ_{hX}/Λ_X which are consistent with the EFT approximation, it is instructive to consider a simple UV completion of the fermion EFTs. Assume that φ is a new scalar which interacts with the fermion DM field X and the Higgs doublet Φ via dimensionless couplings $g_{\varphi X}$ and $g_{\varphi\Phi}$ respectively [343].[11] In the EFT limit, $q^2 \ll m_\varphi^2$ such that

$$\frac{\lambda_{hX}}{\Lambda_X} \simeq \frac{g_{\varphi X}\tilde{g}_{\varphi\Phi}}{m_\varphi^2}, \tag{6.52}$$

where $\tilde{g}_{\varphi\Phi} = m'g_{\varphi\Phi}$ and m' is some characteristic mass scale of the new coupling, e.g., from a new Yukawa-type interaction.

To place an upper limit on the values of λ_{hX}/Λ_X where the EFT approximation is valid in *some* UV completion, we require m_φ to be as small as possible (i.e., $2m_X$ for the DM annihilation) and the product $m'g_{\varphi X}g_{\varphi\Phi}$ to be as large as possible. The largest value m' can realistically take is simply m_φ (as it would otherwise have already been integrated out). This gives

$$\frac{\lambda_{hX}}{\Lambda_X} \simeq \frac{g_{\varphi X}g_{\varphi\Phi}}{m_\varphi}. \tag{6.53}$$

For the EFT itself to remain perturbative, we also require $g_{\varphi X}g_{\varphi\Phi} \lesssim 4\pi$. Thus, the approximate values of λ_{hX}/Λ_X above which we generically expect to receive corrections from UV effects in DM annihilation are $\lambda_{hX}/\Lambda_X \gtrsim 4\pi/2m_X$. This is the value at which the EFT is *guaranteed* to break down for indirect detection and relic density calculations. Depending on the UV completion, e.g., for weakly coupled theories, this scale can even be lower. In contrast, the EFT approximation is perfectly valid for direct detection as long as the mediator mass is above a few MeV, implying $\log_{10}(\lambda_{hX}/\Lambda_X \text{ GeV}) \lesssim 2$.

In presenting our fermion model results, we show the regions where the EFT approximation breaks down for DM annihilation, i.e., when $\lambda_{hX}/\Lambda_X > 4\pi/2m_X$. Whilst the use of fermion EFTs is valid for direct searches at all values of the coupling that we show in our plots, by choosing to rescale the direct search limits by the relic abundance parameter $f_{\text{rel}} \equiv \Omega_X/\Omega_{\text{DM}}$ which is itself subject to UV corrections, they are indirectly affected when $\lambda_{hX}/\Lambda_X > 4\pi/2m_X$.

---

[11]In this specific UV completion, the new scalar φ mixes with the SM Higgs boson h and modifies the SM-like Higgs coupling to SM gauge bosons and fermions. In general, this mixing should be strongly suppressed for $m_\varphi \gg m_h$, i.e., when the EFT is valid, but the presence and strength of this interaction is ultimately highly dependent on the details of the UV completion. For our study in line with the EFT assumption, we assume that such modifications are absent, i.e., the Higgs production cross-section and visible decay widths are same as in the SM.
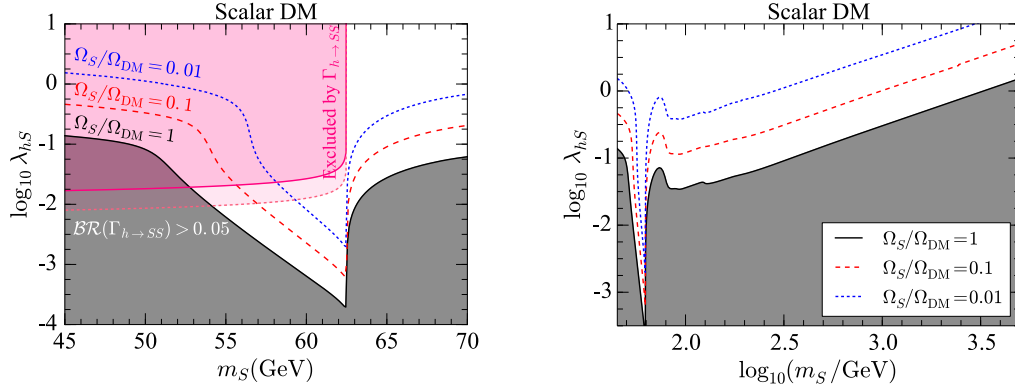
Figure 6.4: Contours of fixed scalar relic density for $f_{\rm rel} = 1$ (black solid), 0.1 (red dashed) and 0.01 (blue dotted). The grey shaded region is excluded by the relic density constraint. *Left panel*: A close-up of the resonantly enhanced annihilation region, $m_S \sim m_h/2$. Larger values of λ_{hS} are excluded by an upper limit of 19% (pink solid) at 2σ C.L. or 5% (pink dotted) at 1σ C.L. on $\mathcal{BR}(h \to SS)$. *Right panel*: Relic density contours for the full range of m_S.

6.4 Results

After giving an outline of various constraints and their implementations, we present our model results. As our study is a generalization of the scalar singlet analysis in Ref. [324] to nonscalar models, we start by presenting our scalar model results obtained from `microMEGAs` to validate their consistency.

Although QCD corrections from quark final states at low scalar masses were included in Ref. [324], they are absent in our analysis as their inclusion in either `microMEGAs` or `LanHEP` is rather nontrivial, given the fact that `microMEGAs` relies heavily on autogenerated `LanHEP` codes.

In computing the model relic density in `microMEGAs`, we found a local step-function reduction of 5–12% in a small range of couplings over the mass range $100 \lesssim m_{S,V}/\text{GeV} \lesssim 400$ and $5 \lesssim m_{\chi,\psi}/\text{TeV} \lesssim 180$. This feature is not seen in the annihilation cross-section, relic densities from the `microMEGAs` routines employing the freeze-out approximation, or in Ref. [324] for the scalar DM model. Away from this feature, the `microMEGAs` calculated relic densities are in good agreement with the freeze-out approximation and Ref. [324]. The drop appears symptomatic of a numerical error in the full `microMEGAs` Boltzmann solver, possibly due to poor convergence properties. As the regions where this occurs are only a few tenths of a unit-wide in the log of λ_{hX} or λ_{hX}/Λ_X as appropriate, we simply omit them from our limit curves and interpolate across the small gap.

6.4.1 Scalar model

We perform scans in the (m_S, λ_{hS}) plane and generate contours of fixed scalar relic density $\Omega_S h^2$ for $f_{\rm rel} = 1$ (black solid), 0.1 (red dashed) and 0.01 (blue dotted) as shown in Fig. 6.4.
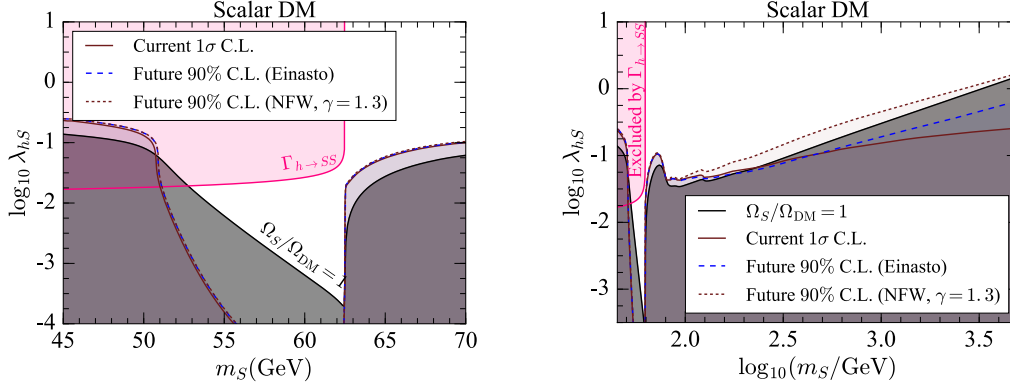
Figure 6.5: Indirect search limits on the scalar model parameter space. The grey and pink shaded regions are excluded respectively by the observed DM relic density and an upper limit of 19% on $\mathcal{BR}(h \to SS)$ at 2σ C.L. Values of λ_{hS} below the current 1σ C.L. (brown solid) curve are excluded at more than 1σ C.L. Regions below the future 90% C.L. curve with the Einasto (blue dashed) and contracted NFW (brown dotted) profile will be excluded. *Left panel*: A close-up of the resonantly enhanced annihilation region, $m_S \sim m_h/2$. *Right panel*: The full range of m_S.

Values of λ_{hS} in the grey shaded region are excluded by the relic density constraint as they lead to an overabundance of DM.

In the region $m_S < m_h/2$, an upper limit of 19% (pink solid) at 2σ C.L. and 5% (pink dotted) at 1σ C.L. on the Higgs invisible branching ratio $\mathcal{BR}(h \to SS)$ exclude couplings larger than $\log_{10} \lambda_{hS} \sim -1.75$ and $\log_{10} \lambda_{hS} \sim -2.1$ respectively. The combined constraints on the scalar relic density and Higgs invisible width exclude low scalar masses apart from a small triangular region between $54\,\mathrm{GeV}$ and $m_h/2$. Near the resonance $m_S \sim m_h/2$, the annihilation cross-section σv_{rel} is enhanced. Thus, the relic density contours move to lower values of λ_{hS} to compensate for the enhancement. Above $m_S > m_h/2$, the relic density contours scale essentially linearly with $\log_{10} m_S$.

In Fig. 6.5, we show the combined sensitivity of indirect searches to various regions of the scalar model parameter space. For the current limits involving a combined analysis of 15 dwarf galaxies by *Fermi*-LAT and 7-year observations of the CMB (WMAP7), we only present 1σ C.L. (brown solid). The region $m_h/2 \lesssim m_S < 70\,\mathrm{GeV}$ with $\log_{10} \lambda_{hS} \in [-2.5, -1]$ can be seen to be in tension with the current indirect searches at slightly more than 1σ C.L. The same can be said about the scalar masses below $\sim 51\,\mathrm{GeV}$; this region is currently excluded by the Higgs invisible width constraint at more than 2σ C.L. In extending the current indirect search limits to higher scalar masses, we find that scalar masses up to $\sim 232\,\mathrm{GeV}$ are excluded by the current indirect searches at more than 1σ C.L. if S makes up all of the dark matter.

The combined future limits incorporate the *Planck* polarization data, $\gtrsim 100\,\mathrm{h}$ GC observation by CTA and extended improvements in the *Fermi*-LAT data from the addition of more southern dwarf galaxies in its search. Due to better exposure, future indirect DM searches will be sensitive enough to probe higher scalar DM masses, if S makes up all of
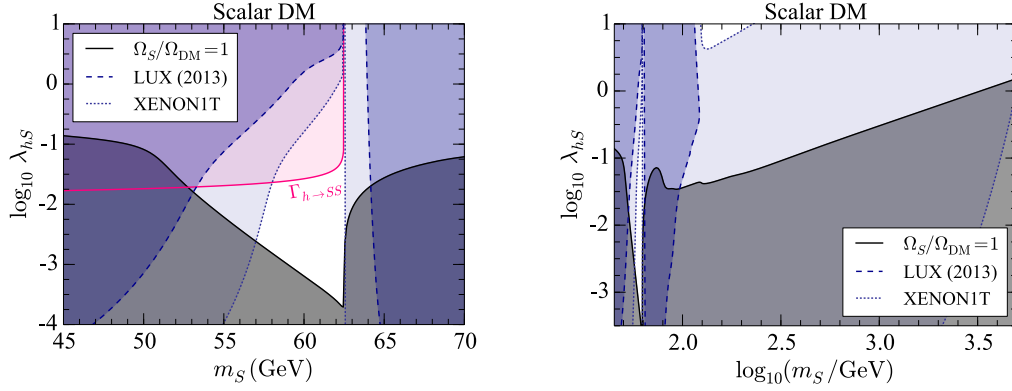
Figure 6.6: Direct search limits on the scalar model parameter space. The grey shaded region is ruled out by the observed DM relic density. Regions excluded by the LUX (XENON1T) experiment are delineated with blue dashed (blue dotted) curves and dark (light) shadings. *Left panel*: A close-up of the resonantly enhanced annihilation region, $m_S \sim m_h/2$. The pink shaded region is excluded by an upper limit of 19% on $\mathcal{BR}(h \to SS)$ at 2σ C.L. *Right panel*: The full range of m_S.

the dark matter. At low scalar masses, future DM searches will be relatively insensitive to the assumed DM density profile (Einasto or a contracted NFW). This is due to the fact that the *Fermi*-LAT delta log-likelihood dominates in this region. However, at high scalar masses, the CTA delta log-likelihood entering in Eq. (6.27) dominates the combined delta log-likelihood. Thus, the upcoming CTA experiment will be able to exclude scalar masses up to $\sim 176\,\text{GeV}$ (Einasto profile) and $\sim 9\,\text{TeV}$ (a contracted NFW profile) at more than 90% C.L., if S makes up all of the dark matter.

The resulting limits in the (m_S, λ_{hS}) plane from the LUX (blue dashed) and the projected XENON1T (blue dotted) experiment are shown in Fig. 6.6. In the left panel near the resonance $m_S \sim m_h/2$, a small triangular region will continue to evade detection at the LUX and projected XENON1T experiments. At high scalar masses, the LUX experiment excludes masses up to $120\,\text{GeV}$ for a narrow range of λ_{hS} values. Most of the remaining parameter space will be tested and ruled out by the XENON1T experiment for a wide range of λ_{hS} values. In particular, it will be able to exclude scalar masses up to $10\,\text{TeV}$, if S makes up all of the dark matter.

6.4.2 Vector model

The contours of fixed vector relic density $\Omega_V h^2$ for $f_{\text{rel}} = 1$ (black solid), 0.1 (red dashed) and 0.01 (blue dotted) are shown in Fig. 6.7. For $f_{\text{rel}} = 0.1$ (0.01), no values of λ_{hV} satisfy Eq. (6.16) for vector masses below $46\,(56)\,\text{GeV}$. The minimum relic density below these masses stays above the values of the contour being drawn, thus leaving gaps that are evident in the left panel of Fig. 6.7.

For $m_V < m_h/2$, upper limits on $\mathcal{BR}(h \to VV)$ of 19% (pink solid) at 2σ C.L. and 5% (pink dotted) at 1σ C.L. exclude couplings larger than $\log_{10} \lambda_{hV} \sim -2.28$ and
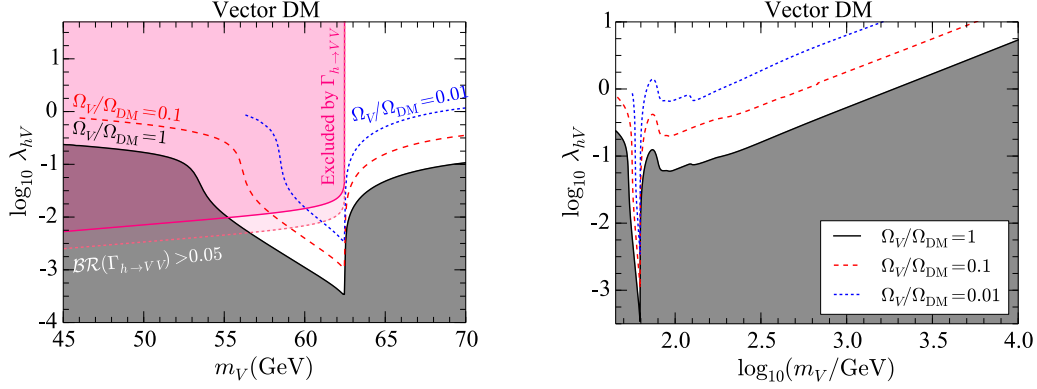
Figure 6.7: Same as Fig. 6.4 but for the vector DM model.
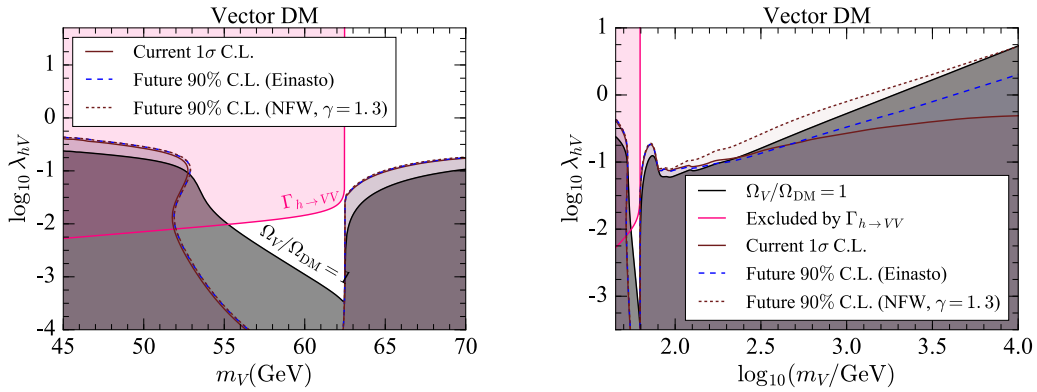
Figure 6.8: Same as Fig. 6.5 but for the vector DM model.

$\log_{10} \lambda_{hV} \sim -2.6$ respectively. The combined constraints on the vector relic density and Higgs invisible width exclude most of the low vector masses apart from a small triangular region between 56.5 GeV and $m_h/2$. Above $m_V > m_h/2$, the relic density contours scale linearly with $\log_{10} m_V$ in a similar fashion to the scalar model.

The combined sensitivity of indirect searches to various regions in the (m_V, λ_{hV}) plane is shown in Fig. 6.8. The current limits involve contributions from WMAP7 and the combined analysis of 15 dwarf galaxies by *Fermi*-LAT. The region $m_h/2 \leq m_V \leq 70$ GeV with $\log_{10} \lambda_{hV} \in [-2.5, -0.75]$ can be seen to be in tension with the current indirect searches. The same is true for vector masses below ~ 52.5 GeV; this region is already excluded by the Higgs invisible width constraint at more than 2σ C.L. Vector DM masses up to ~ 230 GeV are excluded by the current indirect searches at more than 1σ C.L., if V makes up all of the dark matter.

Limits from future indirect searches will be able to probe parts of the parameter space that are not already excluded by the current indirect searches or relic density constraints. In particular, future indirect searches based on the Einasto and contracted NFW DM profiles will exclude vector masses up to ~ 173 GeV and ~ 9 TeV respectively at more than 90% C.L., if V makes up all of the dark matter.
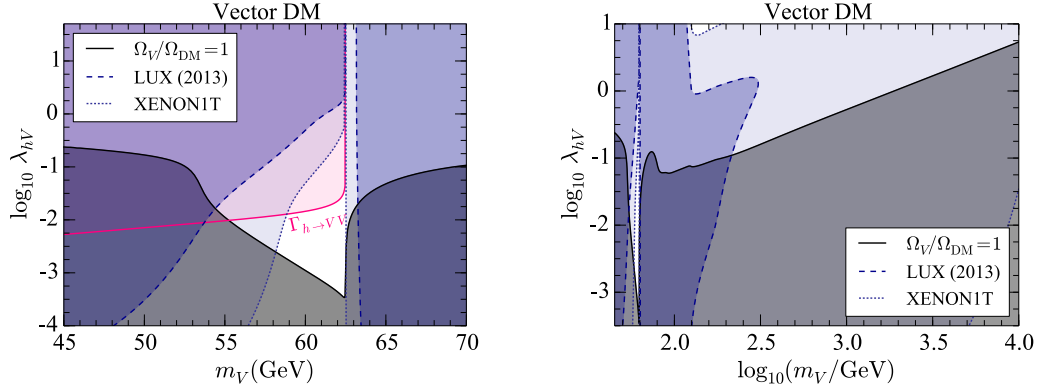
Figure 6.9: Same as Fig. 6.6 but for the vector DM model.

Limits from the LUX (blue dashed) and the projected XENON1T (blue dotted) experiment in the (m_V, λ_{hV}) plane are shown in Fig. 6.9. The LUX experiment excludes vector DM masses up to ~ 300 GeV for a moderate range of λ_{hV} values, whereas the projected XENON1T experiment will exclude parts of the model parameter space that are not already ruled out by the DM relic density and Higgs invisible width constraints. In particular, it will be able to exclude vector masses up to ~ 30 TeV, if V makes up all of the dark matter.

6.4.3 Majorana fermion model

The contours of fixed Majorana relic density in the $(m_\chi, \lambda_{h\chi}/\Lambda_\chi)$ plane for $f_{rel} = 1$ (black solid), 0.1 (red dashed) and 0.01 (blue dotted) are plotted in Fig. 6.10. In each row, contours are drawn at fixed values of $\cos\xi$: $\cos\xi = 1$ for a pure scalar interaction (top row), $\cos\xi = 1/\sqrt{2}$ for an equal mix between the scalar and pseudoscalar terms (middle row), and $\cos\xi = 0$ for a pure pseudoscalar interaction (bottom row). When the SM Higgs-Majorana fermion DM interaction changes from pure scalar to pure pseudoscalar, the Majorana relic density contours move towards lower values of $\lambda_{h\chi}/\Lambda_\chi$.

In the region $m_\chi < m_h/2$, most values of $\lambda_{h\chi}/\Lambda_\chi$ for $\cos\xi = 1$, $1/\sqrt{2}$ and 0 are excluded by the combined constraints on the Majorana relic density and Higgs invisible width; a small triangular region remains which continues to evade these limits in a similar fashion to the scalar and vector DM models. Above Majorana fermion masses of ~ 300 GeV, the relic density contours for $\cos\xi = 1/\sqrt{2}$ and 0 essentially remain constant and independent of the coupling $\lambda_{h\chi}/\Lambda_\chi$. When $f_{rel} = 0.1$ or 0.01, the relic density contours at higher DM masses lie in the green shaded region where $\lambda_{h\chi}/\Lambda_\chi > 4\pi/2m_\chi$. Thus, the validity of our results in these regions cannot be guaranteed within the EFT framework.

The combined sensitivity of indirect searches to various regions in the $(m_\chi, \lambda_{h\chi}/\Lambda_\chi)$ plane is shown in Fig. 6.11 for $\cos\xi = 1$ (top row), $1/\sqrt{2}$ (middle row) and 0 (bottom row).

a). Pure scalar interaction, $\cos\xi = 1$.

b). Equally mixed scalar-pseudoscalar interaction, $\cos\xi = 1/\sqrt{2}$.

c). Pure pseudoscalar interaction, $\cos\xi = 0$.
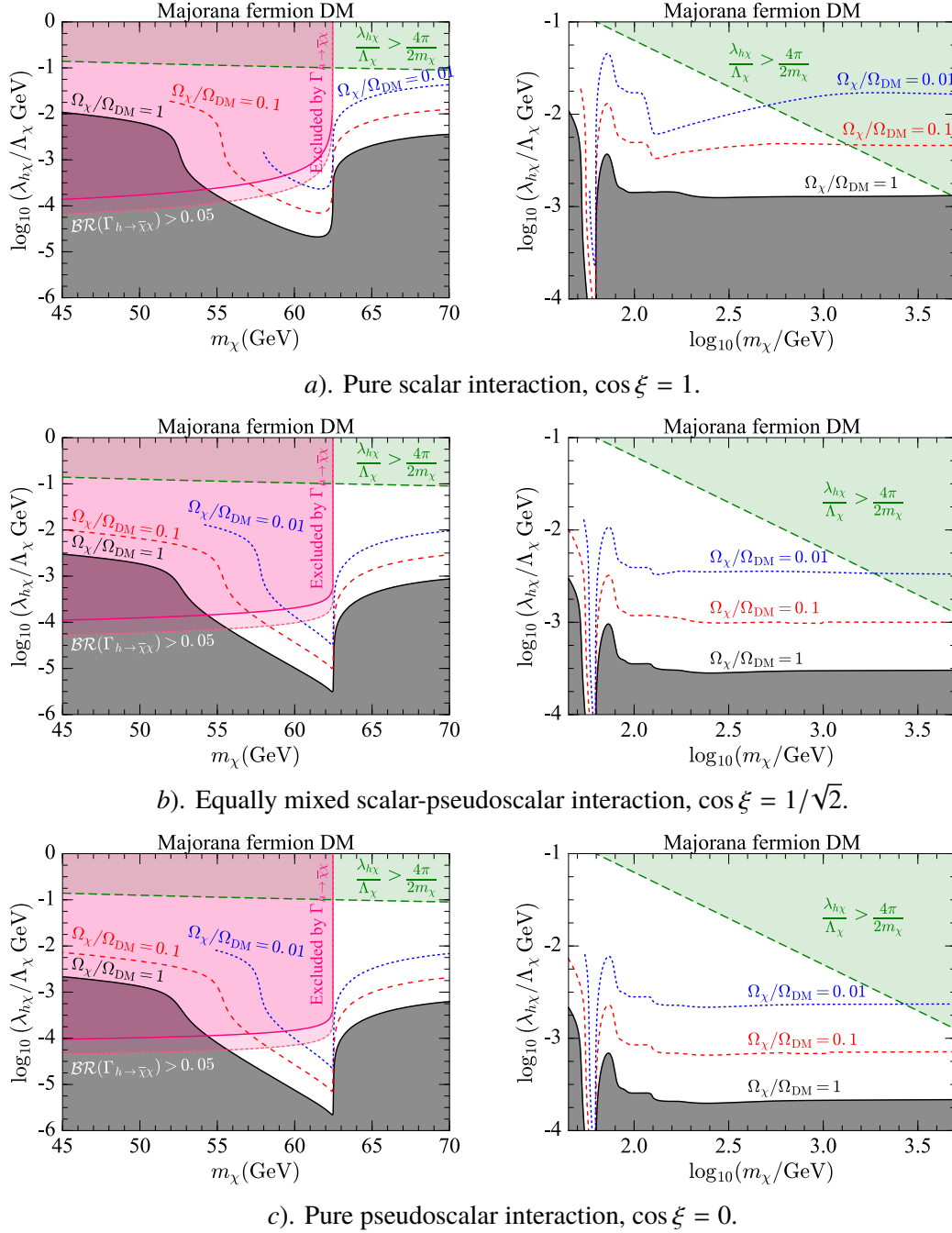
Figure 6.10: Same as Fig. 6.4 but for the Majorana fermion DM model. The green shaded region is where the EFT approximation of the full theory breaks down for $\lambda_{h\chi}/\Lambda_\chi > 4\pi/2m_\chi$.

In the case of $\cos\xi = 1$, the annihilation cross-section $\sigma v_{\rm rel}$ entering in the calculation of indirect detection rates receives a v^2 suppression where $v \sim 10^{-3}\,c$ is the typical speed of DM particles in the local halo. Thus, the resulting indirect search limits are weak and no exclusion is possible.

When interactions are pure pseudoscalar, the velocity suppression of $\sigma v_{\rm rel}$ is completely lifted. Thus, the indirect detection limits become nontrivial. In the case of $\cos\xi = 1/\sqrt{2}$ and 0, Majorana masses between $m_h/2$ and $70\,{\rm GeV}$ with $\log_{10}(\lambda_{h\chi}/\Lambda_\chi\,{\rm GeV}) \in$

a). Pure scalar interaction, $\cos\xi = 1$.

b). Equally mixed scalar-pseudoscalar interaction, $\cos\xi = 1/\sqrt{2}$.

c). Pure pseudoscalar interaction, $\cos\xi = 0$.
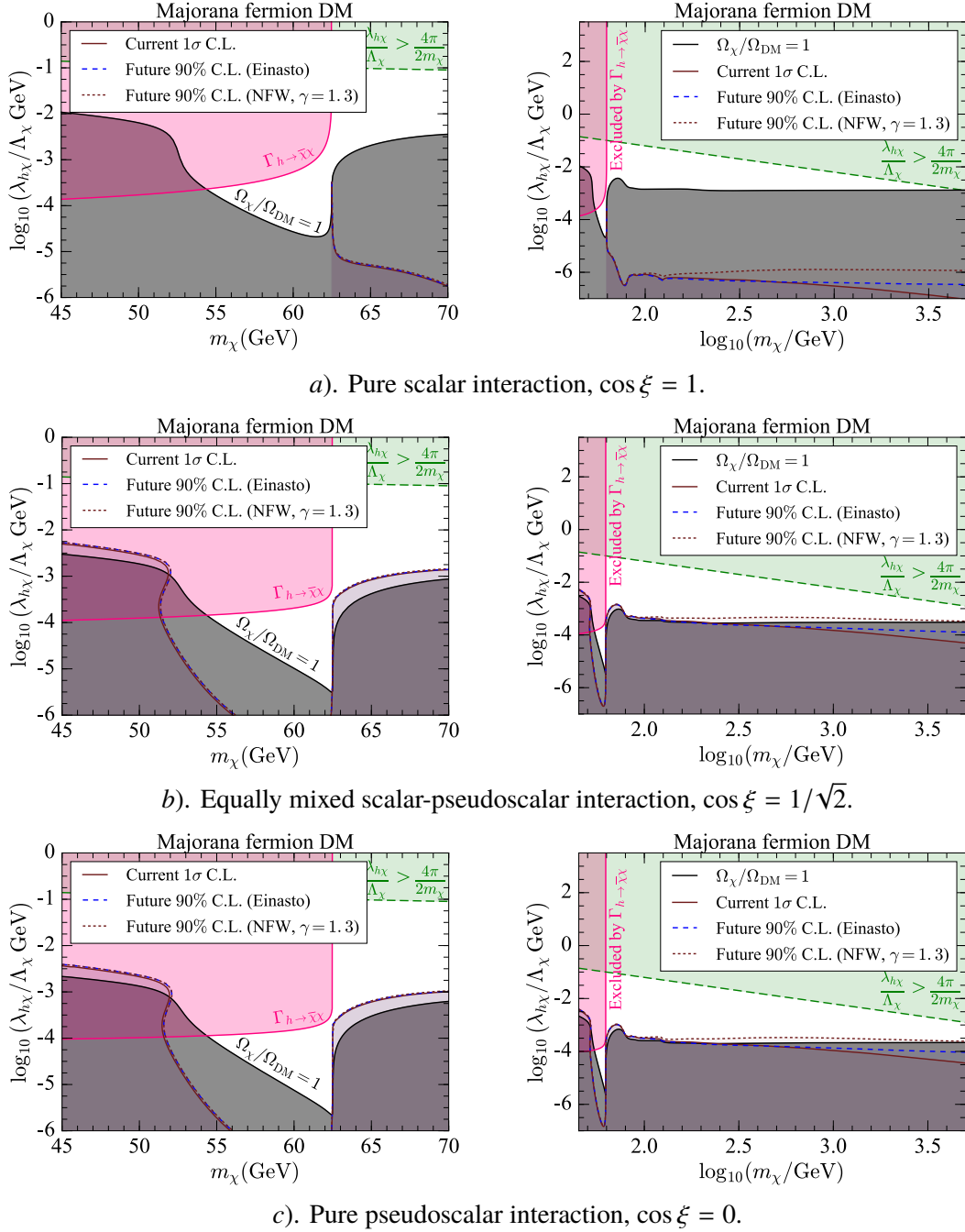
Figure 6.11: Same as Fig. 6.5 but for the Majorana fermion DM model. The green shaded region is where the EFT approximation of the full theory breaks down for $\lambda_{h\chi}/\Lambda_\chi > 4\pi/2m_\chi$.

$[-4.1, -2.8]$ can be seen to be in tension with the current indirect searches at more than 1σ C.L. A small triangular region around $m_\chi \lesssim m_h/2$ will continue to evade the current and future indirect searches.

To illustrate the degree to which different indirect searches contribute to the resulting limits, we show the breakdown of the current 1σ C.L. and future 90% C.L. (NFW, $\gamma = 1.3$) indirect search limits for a pure pseudoscalar coupling ($\cos\xi = 0$) in Figs. 6.12 and 6.13. Current indirect search limits incorporate the WMAP 7-year observations of the CMB and
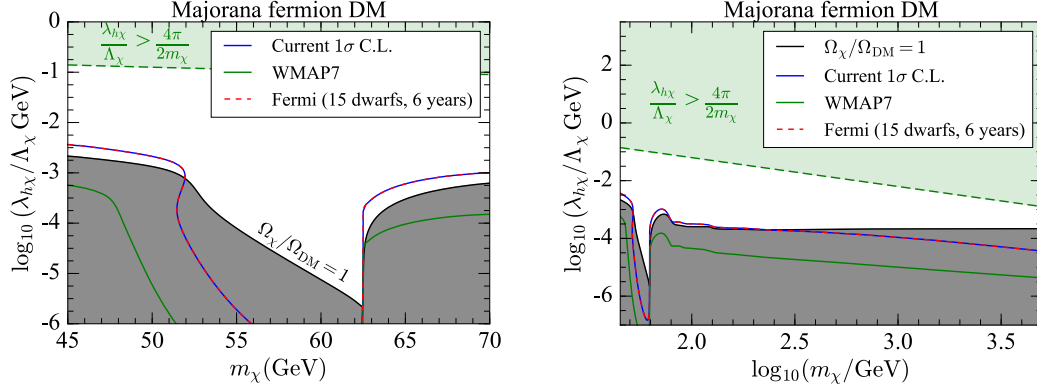
Figure 6.12: Breakdown of the current 1σ C.L. (blue solid) indirect search limit in the Majorana fermion model parameter space when $\cos\xi = 0$. The grey shaded region is excluded by the relic density constraint. The green shaded region is where the EFT approximation of the full theory breaks down for $\lambda_{h\chi}/\Lambda_\chi > 4\pi/2m_\chi$. *Left panel*: A close-up of the resonantly enhanced annihilation region, $m_\chi \sim m_h/2$. *Right panel*: The full range of m_χ.
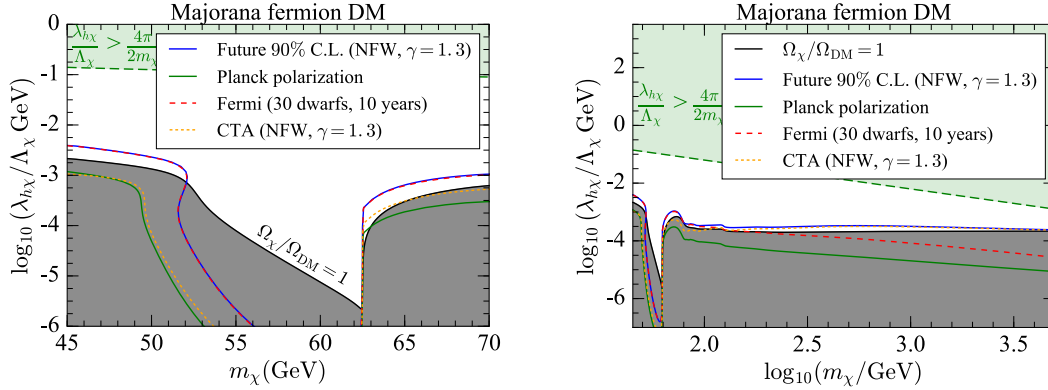
Figure 6.13: Same as Fig. 6.12 but for the future 90% C.L. (NFW, $\gamma = 1.3$).

a combined analysis of 15 dwarf galaxies using 6 years of the *Fermi*-LAT data. Projected future limits include contributions from the *Planck* polarization data, projected *Fermi*-LAT limits based on the discovery of a further 15 southern dwarf galaxies over 10 years, and projected CTA limits from the GC. At low DM masses, limits from the *Fermi*-LAT are strongest, whereas at higher DM masses, limits from the upcoming CTA experiment will be strongest. Constraints from the CMB are weak in all parts of the model parameter space. Future indirect searches will be sensitive enough to exclude Majorana fermion masses up ~ 12 TeV (NFW, $\gamma = 1.3$) at more than 90% C.L., if χ makes up all of the dark matter.

In Fig. 6.14, we present direct search limits from the LUX (blue dashed) and projected XENON1T (blue dotted) experiment in the $(m_\chi, \lambda_{h\chi}/\Lambda_\chi)$ plane for $\cos\xi = 1$ (top row), $1/\sqrt{2}$ (middle row) and 0 (bottom row). Although the use of an EFT at direct search experiments is perfectly valid, our LUX and projected XENON1T limits within the green shaded regions are subjected to UV corrections. This is due to the scaling of our limits by the relic abundance parameter $f_{rel} = \Omega_\chi/\Omega_{DM}$. Thus, values of $\lambda_{h\chi}/\Lambda_\chi$ in the green

shaded region for the Majorana fermion masses above ~ 4.76 TeV ($\cos \xi = 1$), ~ 20.3 TeV ($\cos \xi = 1/\sqrt{2}$) and ~ 28 TeV ($\cos \xi = 0$) cannot be guaranteed to validate the use of EFT approximation in DM annihilations.

When $\cos \xi = 0$, the SI cross-section is momentum suppressed by a factor of $q^2/4m_\chi^2$ where $q \sim O(\text{MeV})$. Thus, the expected number of signal events is small. In fact, the imposed direct search limits are significantly weaker than the Higgs invisible width constraint at 2σ C.L. Thus, the higher Majorana mass range with a pure pseudoscalar coupling will be inaccessible at the XENON1T experiment. This coincides with better prospects from indirect detection (see the bottom row in Fig. 6.11), making the latter class of observations the *only* type of experiment capable of probing the higher DM mass range if nature chooses to have DM interact with the SM Higgs boson only by a pure pseudoscalar coupling.

When interactions are pure scalar in nature, the momentum suppression of the SI cross-section is lifted. In the case of an equal mixing between the scalar and pseudoscalar terms, although the DM-nucleon effective couplings (G_N^{SI}, $\widetilde{G}_N^{\text{SI}}$) are equal, the pseudoscalar effective couplings ($\widetilde{G}_N^{\text{SI}}$) still carry a momentum dependence of the form $q^2/4m_\chi^2$ as is evident in Eq. (6.42). Thus, the direct search limits are strongest in the case of a pure scalar interaction, moderate for an equal mix between the scalar and pseudoscalar terms, and weakest in the case of a pure pseudoscalar interaction.

For Majorana fermion masses above 70 GeV, direct detection experiments will continue to exclude large portions of the model parameter space provided the EFT approximation remains valid for the model to account for all of the dark matter. The LUX experiment currently excludes Majorana fermion masses up to ~ 4.7 TeV ($\cos \xi = 1$) and ~ 200 GeV ($\cos \xi = 1/\sqrt{2}$). Further exclusion will also be possible with the projected XENON1T experiment.

6.4.4 Dirac fermion model

The Dirac fermion model is analogous to the Majorana fermion model. An aspect that separates them is the conventional factor of $1/2$ in front of each fermion bilinear $\overline{\chi}\chi$ in defining a Majorana fermion field χ. This factor of $1/2$ accounts for the field normalization and self-conjugation. Thus, the results for the Majorana fermion model carries over to the Dirac fermion model in a relatively straightforward way once the factor of $1/2$ is accounted.

In Fig. 6.15, we show the contours of fixed Dirac relic density in (m_ψ, $\lambda_{h\psi}/\Lambda_\psi$) plane for $f_{\text{rel}} = 1$ (black solid), 0.1 (red dashed) and 0.01 (blue dotted). Analogous to the Majorana fermion model, contours in each row are generated at fixed values of $\cos \xi$: $\cos \xi = 1$ for a pure scalar interaction (top row), $\cos \xi = 1/\sqrt{2}$ for an equal mix between the scalar and pseudoscalar terms (middle row), and $\cos \xi = 0$ for a pure pseudoscalar

a). Pure scalar interaction, $\cos \xi = 1$.

b). Equally mixed scalar-pseudoscalar interaction, $\cos \xi = 1/\sqrt{2}$.

c). Pure pseudoscalar interaction, $\cos \xi = 0$.
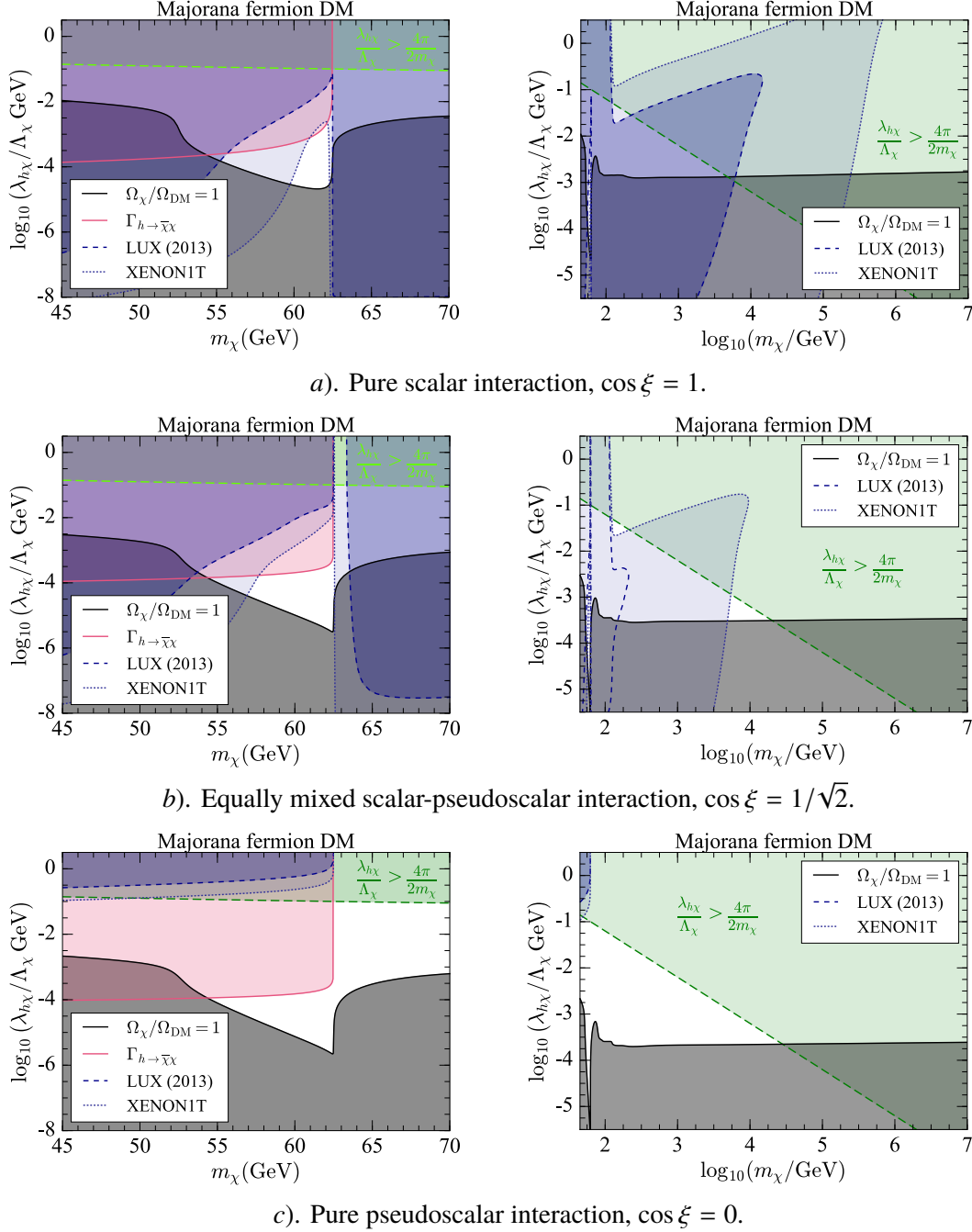
Figure 6.14: Same as Fig. 6.6 but for the Majorana fermion DM model. Although EFTs are valid at direct search experiments, our scaling of the LUX/XENON1T limits by the relic abundance parameter $f_{\rm rel} = \Omega_\chi/\Omega_{\rm DM}$ introduces a sensitivity to UV corrections when the EFT approximation in DM annihilations breaks down for $\lambda_{h\chi}/\Lambda_\chi > 4\pi/2m_\chi$.

interaction (bottom row). For $m_\psi < m_h/2$, most of the model parameter space except for a small triangular region between $\sim 57.5\,\mathrm{GeV}$ and $m_h/2$ is excluded by the combined constraints on the Dirac fermion relic density and Higgs invisible width. Similar to the Majorana fermion model, roots of Eq. (6.16) for $f_{\rm rel} = 0.1$ and 0.01 do not exist when $m_\psi < m_h/2$. At higher Dirac fermion masses, the relic density contours continue to increase and ultimately become independent of the coupling $\lambda_{h\psi}/\Lambda_\psi$.

a). Pure scalar interaction, $\cos\xi = 1$.

b). Equally mixed scalar-pseudoscalar interaction, $\cos\xi = 1/\sqrt{2}$.

c). Pure pseudoscalar interaction, $\cos\xi = 0$.
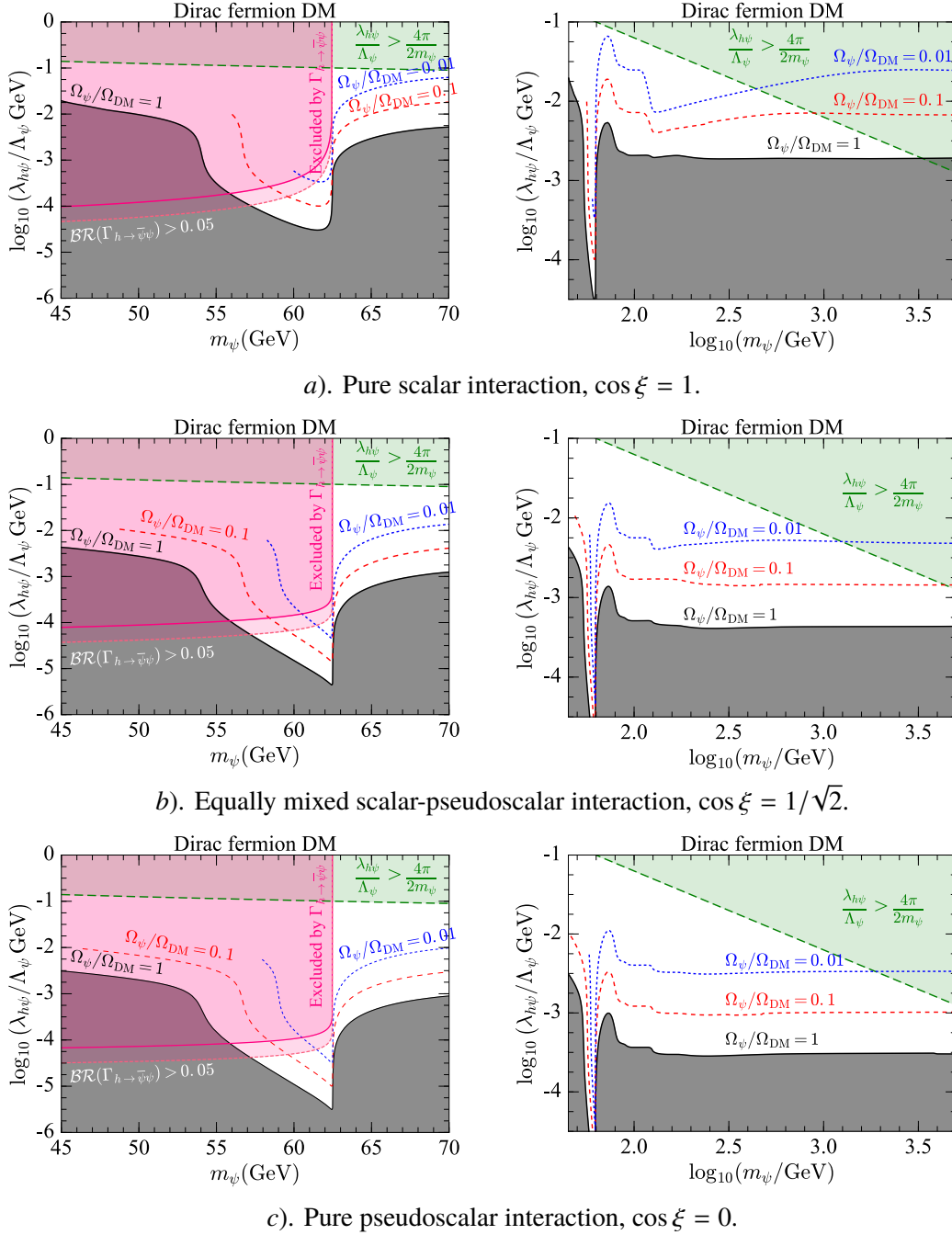
Figure 6.15: Same as Fig. 6.10 but for the Dirac fermion DM model.

The sensitivity of indirect searches to various regions in the $(m_\psi, \lambda_{h\psi}/\Lambda_\psi)$ plane when $\cos\xi = 1$ (top row), $1/\sqrt{2}$ (middle row) and 0 (bottom row) is shown in Fig. 6.16. Again, in the case of $\cos\xi = 1$, the annihilation cross-section $\sigma v_{\rm rel}$ is velocity suppressed. Thus, the resulting indirect search limits are weak. In fact, the relic density constraint alone is strong enough to exclude the entire region probed by the indirect search experiments in this case.

When interactions are pure pseudoscalar in nature, the velocity suppression of $\sigma v_{\rm rel}$ is lifted. Thus, parts of the model parameter space can be excluded by the indirect

a). Pure scalar interaction, $\cos\xi = 1$.

b). Equally mixed scalar-pseudoscalar interaction, $\cos\xi = 1/\sqrt{2}$.

c). Pure pseudoscalar interaction, $\cos\xi = 0$.
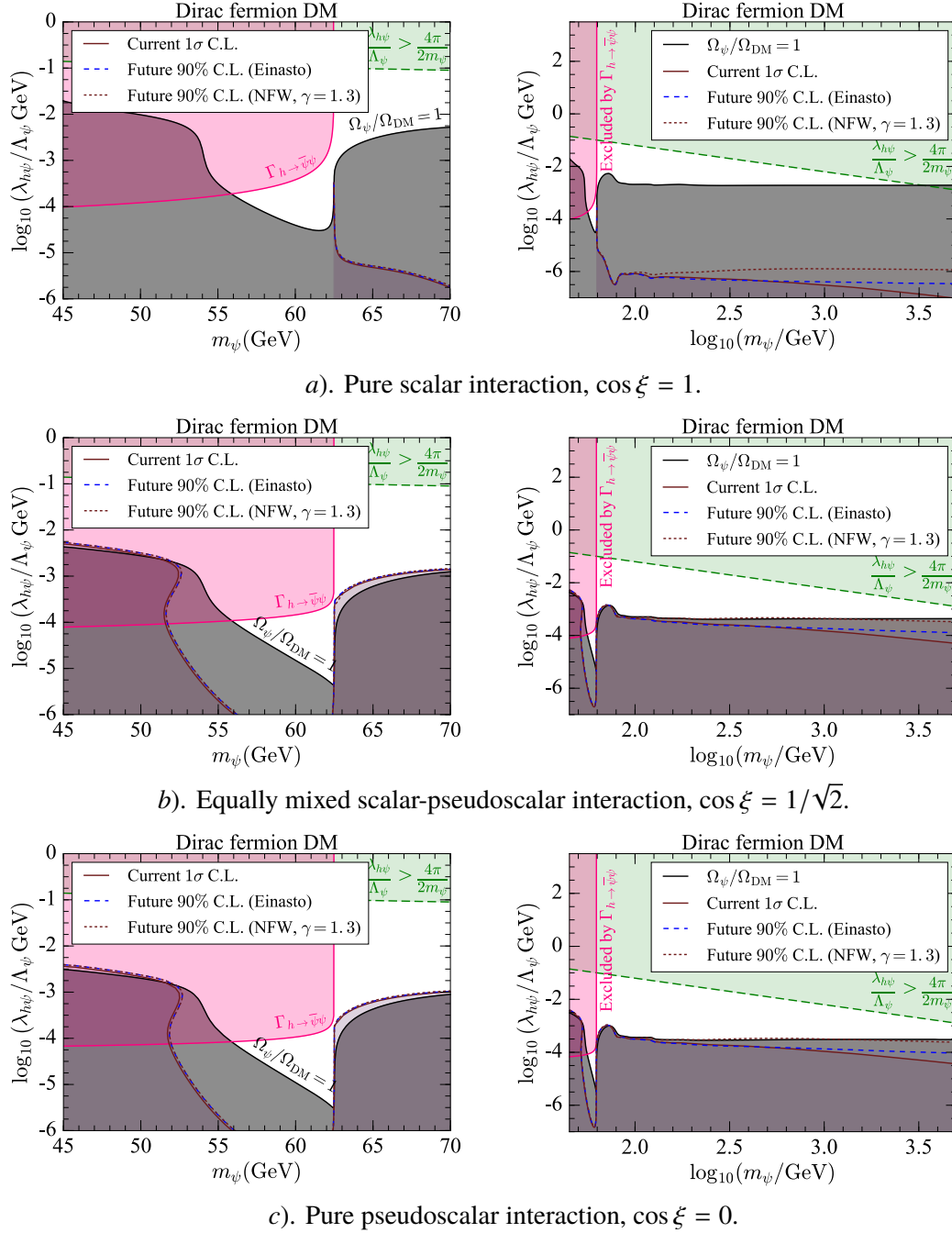
Figure 6.16: Same as Fig. 6.11 but for the Dirac fermion DM model.

search experiments. With the strongest indirect limits in the case of a pure pseudoscalar interaction, Dirac fermion masses between $m_h/2$ and $70\,\mathrm{GeV}$ for $\log_{10}(\lambda_{h\psi}/\Lambda_\psi\,\mathrm{GeV}) \in [-4, -3]$ can be seen to be in tension with the current indirect search limits. Similarly, Dirac fermion masses below $\sim 51.5\,\mathrm{GeV}$ are in tension with the current indirect searches at more than 1σ C.L. On the other hand, future indirect searches will be able to exclude Dirac fermion masses up to $\sim 74\,\mathrm{GeV}$ (Einasto), and between $166\,\mathrm{GeV}$ and $1.3\,\mathrm{TeV}$ (contracted NFW profile) in the case of a $\cos\xi = 0$, if ψ makes up all of the dark matter.

In Fig. 6.17, we present direct search limits in the $(m_\psi, \lambda_{h\psi}/\Lambda_\psi)$ plane for $\cos\xi = 1$

a). Pure scalar interaction, $\cos\xi = 1$.

b). Equally mixed scalar-pseudoscalar interaction, $\cos\xi = 1/\sqrt{2}$.

c). Pure pseudoscalar interaction, $\cos\xi = 0$.
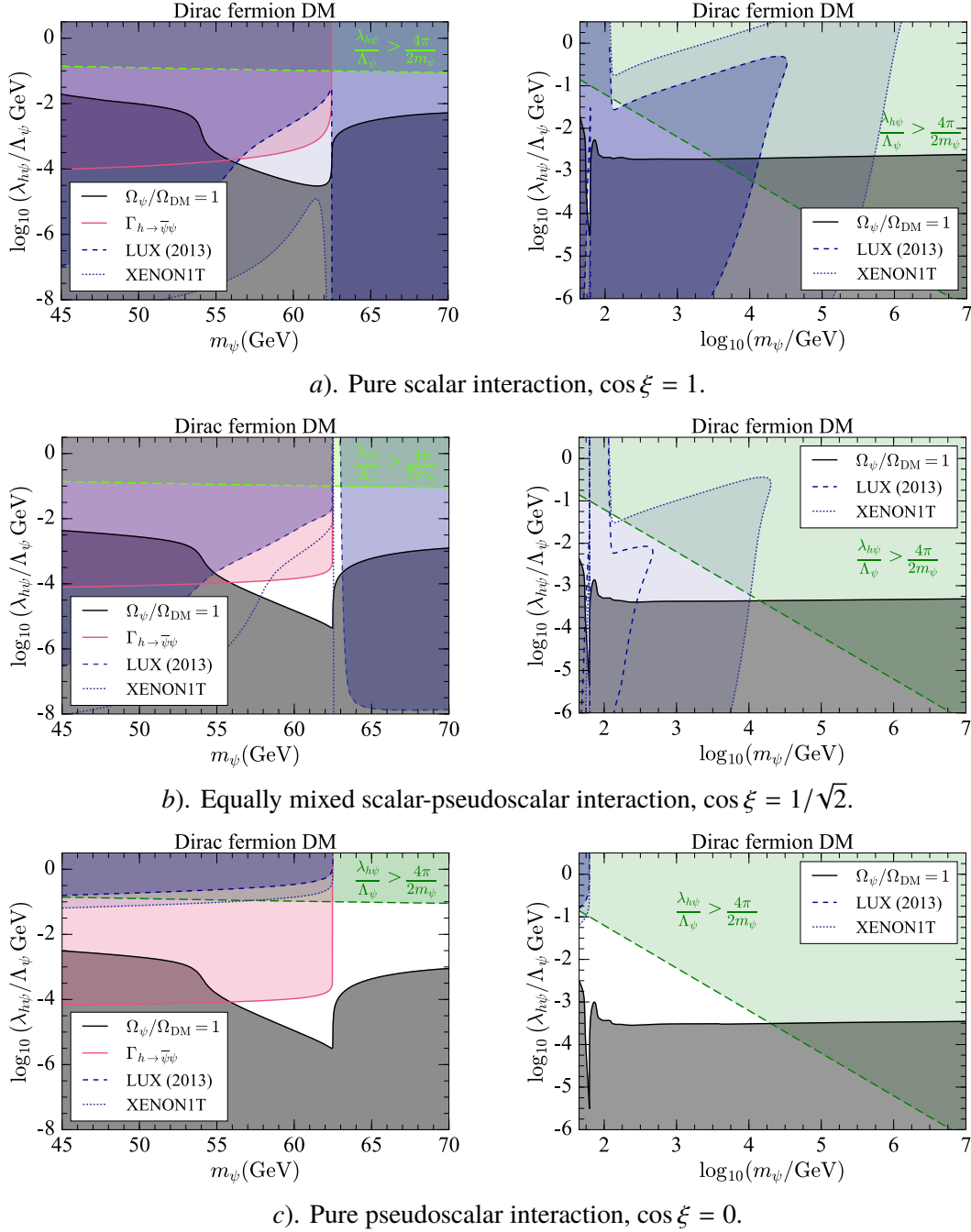
Figure 6.17: Same as Fig. 6.14 but for the Dirac fermion DM model.

(top row), $1/\sqrt{2}$ (middle row) and 0 (bottom row). Similar to the Majorana fermion model, the LUX/XENON1T limits within the green shaded regions are subject to UV corrections solely due to our scaling of the limits by the relic abundance parameter $f_{\text{rel}} = \Omega_\psi/\Omega_{\text{DM}}$. For the Dirac fermion masses above $\sim 3.3\,\text{TeV}$ ($\cos\xi = 1$), $\sim 14.2\,\text{TeV}$ ($\cos\xi = 1/\sqrt{2}$) and $\sim 19.7\,\text{TeV}$ ($\cos\xi = 0$), our limits cannot be guaranteed to keep the EFT approximation for DM annihilations valid, if ψ makes up all of the dark matter.

In the case of a pure pseudoscalar coupling ($\cos\xi = 0$), the SI cross-section is momentum suppressed by a factor of $q^2/4m_\psi^2$. Thus, the expected event rates are small. In

analogy with the Majorana fermion model when $\cos\xi = 0$, better prospects from indirect searches (see the bottom row in Fig. 6.16) make the latter class of observation the *only* type of experiment capable of probing the higher DM mass range if nature chooses to have DM interact with the SM Higgs boson only by a pure pseudoscalar coupling.

As interactions become pure scalar ($\cos\xi = 1$), the momentum suppression of the SI cross-section is lifted and results in significant direct detection rates. The LUX experiment excludes Dirac fermion masses up to $\sim 3.3\,\mathrm{TeV}$ ($\cos\xi = 1$) and $\sim 280\,\mathrm{GeV}$ ($\cos\xi = 1/\sqrt{2}$). In contrast with the Majorana fermion model when $\cos\xi = 1$, low Dirac fermion masses between $45\,\mathrm{GeV}$ and $m_h/2$ will be *entirely* excluded by the combined limits from the Dirac fermion relic density, Higgs invisible width and projected XENON1T experiment. Furthermore, the projected XENON1T experiment will reach higher sensitivity in excluding TeV-scale Dirac fermion masses, if ψ makes up all of the dark matter.

6.5   Summary

In this chapter, we performed an updated and combined analysis of effective scalar, vector, Majorana and Dirac fermion Higgs portal DM models. For the fermion models, we investigated the cases where interactions are either pure scalar, pure pseudoscalar or an equal mixture of the scalar and pseudoscalar terms. The presence of a pseudoscalar term and the requirement of a quadratic DM mass term lead us to redefine the post-EWSB fermion fields via a chiral rotation.

The combined constraints from the DM relic density and Higgs invisible width exclude most of the low mass parameter space in all portal models except for a small triangular region close to the resonance $m_X \sim m_h/2$ where $X \in (S, V_\mu, \chi, \psi)$. In the special case of a Dirac fermion DM interaction via a pure scalar coupling with the SM Higgs boson, the entire resonance region will be excluded by the projected XENON1T experiment.

For the first time, we have performed a consistent study of the indirect detection prospects in all four effective Higgs portal models. Using the current and projected future gamma-ray astronomy data, we looked for viable regions of the model parameter space that can be probed by the existing or future indirect searches. Below the resonance $m_X \sim m_h/2$, the indirect search limits are weaker than the combined constraints on the DM relic density and Higgs invisible width. Depending on the assumed DM density profile, indirect search experiments can provide strong limits at high DM masses, if the model makes up all of the dark matter. The forthcoming CTA experiment will be very useful in this regard.

In agreement with previous studies, direct search experiments will continue to provide the strongest limits on the parameter space of all models. The projected XENON1T experiment will have the sensitivity to probe TeV-scale DM masses. As past studies on fermionic DM models with a pure pseudoscalar interaction have naively applied the XENON100/LUX limits without properly taking account of the momentum-suppressed

SI cross-section, we have rederived these limits by including the factor $q^2/4m_X^2$ in our calculations. Although the resulting limits are weak, they are important in order to perform a consistent study. In such cases, indirect search experiments are our *only* hope of accessing the higher DM mass range in these models.

When both the indirect and direct search limits are available, as is the case for our portal models, a joint observation in both channels is a very realistic possibility at higher WIMP masses. Such detection in multiple experiments would provide a far more robust discovery than a single signal alone.

For the fermion DM models, the EFT approximation breaks down when DM annihilations are considered. A proper examination of the fermion portal models in these parameter regions require a detailed and systematic study of possible UV completions. Such a UV completion will be studied in chapter 8.

Chapter 7

Scalar singlet electroweak baryogenesis

7.1 Introduction

With the discovery of a SM-like Higgs boson at the LHC [10,56], it has probably confirmed the existence of an elementary scalar and its role in EWSB. In addition, it has opened up a new window to study the details of EWSB from the properties of the Higgs boson. On the other hand, recent observation of the first gravitational wave (GW) signal [396] has given us an entirely new way of probing the early history of the universe. As we saw in chapter 5, EWPT is a rather violent event in the early history of the universe. It is expected to leave GW imprints which can be detected in current or future GW experiments. In addition, the existence of DM as explained in chapter 4 also offers another way to probe the early history of our universe. In light of these experimental probes that are constantly developing, we study a scalar singlet extension of the SM.

In this chapter, we focus on the two main features of this model based on our work in Ref. [397]. As we saw in chapter 5, adding new scalar fields can help to facilitate EWBG [398] through a strong first-order EWPT. This phase transition is not first-order in the SM [399]. However, a scalar singlet extension of the SM can provide such a modification [400, 401], although an effective theory with the new scalar integrated out suggests otherwise [402–404]. Once an assumed $\mathbb{Z}_2$ symmetry is imposed on the new scalar field, it can also serve as a viable DM candidate [340, 405, 406].

All of the above features have equally attractive discovery prospects. Firstly, the new scalar inevitably modifies the Higgs potential, which can be probed at collider experiments [400, 407]. Secondly, a strong first-order phase transition generates a strong GW signal [317]. This fact has been used to constrain various EWBG models [408–420] and test the stability of the electroweak vacuum [347, 421]. Lastly, the presence of a DM candidate with a non-zero relic abundance provides strong direct detection limits on the model parameter space [30, 324, 422].

The early history of the universe is poorly constrained by astrophysical experiments. To identify regions where our model can be viable, we investigate how the allowed parameter

space changes when the cosmological history is modified. Specifically, we consider a modification where a new component dominates the energy budget of the early universe and redshifts faster than radiation. We also identify the experimental bounds on this scenario and show the extent to which the modification changes the allowed parameter space of the scalar singlet model. This cosmological amendment will have two main effects: first on baryogenesis, as it helps to avoid the sphaleron bound [423–427], and second on DM, as a faster expansion rate leads to an early freeze-out of the DM particles and larger DM abundance today.

We start by introducing a scalar singlet extension of the SM. After discussing the dynamics of the EWPT, we go over the discovery prospects of the model at colliders, gravitational wave and direct detection experiments. We also study the extent of the allowed model parameter space by considering a scenario with a modified cosmological history, and its impact on EWBG and DM abundance. The one-loop correction to the finite temperature effective potential is given in Appendix E.

7.2 Scalar singlet model

We extend the SM by adding a new real scalar singlet S which couples to the SM Higgs boson. Assuming $\mathbb{Z}_2$ symmetry: $S \to -S$, the tree-level scalar potential is given by[1]

$$V_{\text{tree}}(\Phi, S) = -\mu^2 \Phi^\dagger \Phi + \lambda(\Phi^\dagger \Phi)^2 + \lambda_{HS}\Phi^\dagger \Phi S^2 + \frac{1}{2}\mu_S^2 S^2 + \frac{1}{4}\lambda_S S^4, \qquad (7.1)$$

where Φ is the SM Higgs doublet as defined in Eq. (2.44). After EWSB, the physical mass of the new scalar S becomes

$$m_S^2 = \mu_S^2 + \lambda_{HS}v_0^2, \qquad (7.2)$$

where $v_0 \equiv \langle \phi \rangle = \mu/\sqrt{\lambda} \approx 246\,\text{GeV}$ is the SM Higgs VEV. At tree-level, the Higgs mass and its VEV fixes the constants μ and λ in Eq. (7.1) to $m_h = \sqrt{2}\mu = 125\,\text{GeV}$ and $\lambda = m_h^2/(2v_0^2) \simeq 0.129$. We work with the renormalisation conditions that do not modify these values.

We explore a wide range of scalar-Higgs couplings λ_{HS} for the scalar masses m_S above $m_h/2$.[2,3] We fix the scalar self-coupling to $\lambda_S = 1$. Our results depend on λ_S in a mild way; an increase in its value would only shift the allowed regions to slightly higher values of λ_{HS}. The one-loop corrections to the effective potential at zero and finite temperature are given in Appendix E. These corrections result in a barrier between the symmetric phase at $\langle \phi \rangle = 0$ and the EWSB one at $\langle \phi \rangle \neq 0$.

---

[1]To compare this expression against Eq. (6.1) in chapter 6, use the following substitution: $\lambda_{HS} \to \lambda_{hS}/2$ and $\lambda_S \to \lambda_S/6$.

[2] We only show results for $\lambda_{HS} \in [0.2, 4\pi]$. For values of λ_{HS} above 4π [400], the one-loop corrections to the effective potential becomes unreliable.

[3]When $m_S < m_h/2$, $h \to SS$ decay is kinematically allowed. For values of λ_{HS} that are of interest for EWBG, they are mostly excluded by the limits on the Higgs invisible branching ratio [30, 324].

7.3 Electroweak baryogenesis

The thermal corrections to the scalar potential restore the electroweak symmetry at very high temperatures. As the universe cools down, the EWSB minimum emerges. Due to the corrections arising from the new scalar, the electroweak minimum at $\langle\phi\rangle \neq 0$ can be separated from the symmetric one at $\langle\phi\rangle = 0$ by a potential barrier, thereby allowing a first-order phase transition which is absent in the SM [277].

As we saw in chapter 5, the necessary condition for EWBG is the decoupling of sphaleron processes after the EWPT. In the SM, the sphaleron processes are connected with the $SU(2)$ gauge interactions and provide baryon number (B) violation which is necessary for creating a baryon-antibaryon asymmetry. However, if these processes are not decoupled after the transition, they can quickly wash-out any previously created asymmetry. Being $SU(2)$ interactions, they are heavily suppressed once the electroweak symmetry is broken. This breaking is quantified by the Higgs VEV and leads to the following well-known condition

$$\frac{v}{T} \geq 1, \tag{7.3}$$

where v is the Higgs VEV at temperature T.

We start by approximating the transition temperature T_* as the critical temperature T_c at which the minima of the effective potential is degenerate. After discussing the dynamics of the phase transition, we outline our calculation of T_* at which the transition truly begins. The calculation of the sphaleron rate is technically complicated and leads to slightly different lower bounds on v/T [238, 407, 428, 429]. For simplicity, we work with the bound given in Eq. (7.3).

7.3.1 Vacuum structure

Before presenting the details of the transition dynamics, we study the model parameter space allowed by the vacuum structure. In Fig. 7.1, we show the regions of the model parameter space where the symmetric minimum at the origin and the EWSB one are separated by a barrier at the critical temperature T_c. In the yellow shaded region, the electroweak minimum is *not* the true minimum of the potential at $T = 0$ and is excluded. For low scalar masses, this happens because the minimum in the S direction is deeper while for very large couplings, the electroweak minimum is pushed up by quantum corrections to values above the minimum at the origin. In both cases, the universe would never transition to the broken EW symmetry phase, thus such situations are excluded. The region of small mass and coupling is also excluded as the negative mass terms start to overpower the $\phi^2 S^2$ coupling in the potential, and the new minimum appears in the general ϕ and S directions at $\langle S \rangle > 0, \langle\phi\rangle > 0$.
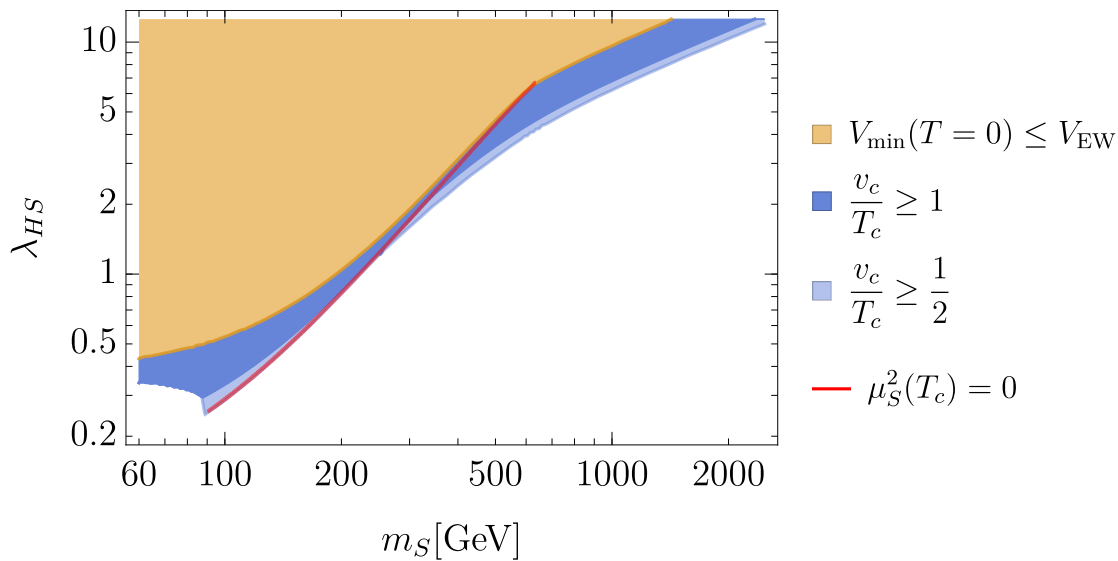
Figure 7.1: Parameter space of the scalar singlet model relevant for electroweak baryogenesis (EWBG). In the yellow shaded region, the electroweak minimum is not the global minimum at zero temperature and is excluded. The blue region is where the phase transition is strong first-order. The light blue region can still lead to a strong first-order phase transition in the modified cosmology scenario. The solid red line splits the regions where $\mu_S^2(T_c) < 0$ and $\mu_S^2(T_c) > 0$.

Depending on the sign of the bare scalar mass term μ_S^2, the EWPT in this model can proceed in two possible ways.

1. $\mu_S^2 > 0$: This occurs at large m_S and small λ_{HS}. In this case, the potential grows away from $S = 0$. Thus, the potential is one-dimensional along the h direction. This leads to a one-step phase transition where the field initially sits in a homogeneous configuration at the origin and tunnels through the barrier towards the electroweak minimum, i.e., $(\langle\phi\rangle, \langle S\rangle) = (0, 0) \rightarrow (v_0, 0)$.

2. $\mu_S^2 < 0$: This occurs at small m_S and large λ_{HS}. In this case, the universe can transition into a minimum along the S direction before the EWPT occurs, i.e., $(\langle\phi\rangle, \langle S\rangle) = (0, 0) \rightarrow (0, \neq 0) \rightarrow (v_0, 0)$. This scenario requires a precise numerical calculation to compute the details of the EWPT.

7.3.2 Dynamics of the phase transition

The EWPT occurs when the temperature of the universe drops below the critical temperature T_c and the EWSB minimum becomes the global minimum. Specifically, we require a first-order phase transition when the global EWSB minimum is separated from the EW symmetry preserving minimum by a potential barrier.

In the early universe, EWPT is driven by thermal fluctuations which eventually excite the field to cross the potential barrier. The calculation of the phase transition boils down

to finding the field profile that corresponds to such thermal excitations and appears most quickly to drive the transition. The crucial quantity for finding the transition temperature is the probability of finding a field configuration with action S_3 within a volume V [430, 431]

$$\frac{\Gamma}{V} \approx T^4 \exp\left(-\frac{S_3(T)}{T}\right). \tag{7.4}$$

Thus, the most probable configurations (as usual) are ones with the smallest action, which in turn are the most symmetric ones. Note that we can start with a static field configuration (as the time derivative can only increase the result), thus we can write down the action for an $O(3)$ symmetric field bubble. In addition, we are interested in cases where the S field cannot be neglected during the transition. This leads to a slightly more complicated action involving both scalar fields as

$$S_3 = 4\pi \int dr \, r^2 \left[\frac{1}{2} \left(\frac{dh}{dr} \right)^2 + \frac{1}{2} \left(\frac{dS}{dr} \right)^2 + V_{\text{eff}}(h, S, T) \right], \tag{7.5}$$

where V_{eff} is the finite temperature effective potential in Appendix E.

When the scalar mass m_S is large, the potential grows in the S direction. In this case, we can set $S = 0$ which leads to a much simpler analysis involving just the Higgs field direction [408, 426]. However, for small m_S, the universe transitions to the $\langle S \rangle > 0$, $\langle \phi \rangle = 0$ minimum before the EWPT. During this transition, no barrier is generated between the origin and the $\langle S \rangle > 0$ vacuum, i.e., the transition is a smooth crossover. The new problem when compared with the single field case is finding a trajectory in the field space which connects the initial vacuum ($\langle S \rangle > 0, \langle \phi \rangle = 0$) with the electroweak one ($\langle S \rangle = 0$, $\langle \phi \rangle = v_0$) and minimising the action in Eq. (7.5).

We follow a similar approach to the one outlined in Refs. [432–434]. We begin by choosing a path $\vec{\chi}(t) = (\phi(t), S(t))$ that connects the initial and final vacuum. We always set

$$\left| \frac{d\vec{\chi}}{dt} \right|^2 = \left(\frac{d\phi}{dt} \right)^2 + \left(\frac{dS}{dt} \right)^2 = 1 \tag{7.6}$$

such that $d\vec{\chi}/dt \, (d^2\vec{\chi}/dt^2)$ is a unit vector parallel (perpendicular) to the path. Thus, we can rewrite the equations of motion (EOMs) from the original action in Eq. (7.5), namely

$$\frac{d^2h}{dr^2} + \frac{2}{r}\frac{d\phi}{dr} = \frac{\partial V}{\partial \phi}, \quad \frac{d^2S}{dr^2} + \frac{2}{r}\frac{dS}{dr} = \frac{\partial V}{\partial S}, \tag{7.7}$$

in terms of the path $\vec{\chi}(t)$ as

$$\frac{d\vec{\chi}}{dt}\frac{d^2t}{dr^2} + \frac{d^2\vec{\chi}}{dt^2}\left(\frac{dt}{dr}\right)^2 + \frac{2}{r}\frac{d\vec{\chi}}{dt}\frac{dt}{dr} = \nabla V. \tag{7.8}$$

By taking the part proportional to $d\vec{\chi}/dt$, we get the following EOM along the path

$$\frac{d\vec{\chi}}{dt}\left(\frac{d^2t}{dr^2} + \frac{2}{r}\frac{dt}{dr}\right) = (\nabla V)_\parallel, \tag{7.9}$$

while by taking the part proportional to $d^2\vec{\chi}/dt^2$, we get the following EOM perpendicular to the path

$$\frac{d^2\vec{\chi}}{dt^2}\left(\frac{dt}{dr}\right)^2 = (\nabla V)_\perp . \tag{7.10}$$

For a given path (just as in the one-dimensional case), finding the bubble profile corresponds to solving Eq. (7.9) along the path as

$$\frac{d^2t}{dr^2} + \frac{2}{r}\frac{dt}{dr} = \frac{dV}{dt} \tag{7.11}$$

to find $t(r)$ subject to the following boundary conditions which are required for a finite action

$$\frac{dt}{dr}\bigg|_{r=0} = 0, \quad t(r \to \infty) = V_f. \tag{7.12}$$

Here V_f is the value of the potential in the decaying initial vacuum. The problem in choosing a certain path is that we are completely neglecting Eq. (7.10) which must also be satisfied to solve Eq. (7.7).

To solve both EOMs, we choose a certain initial path and require Eq. (7.11) to satisfy the boundary conditions in Eq. (7.12). This gives us dt/dr along the path which is used to calculate

$$\vec{N} = \frac{d^2\vec{\chi}}{dt^2}\left(\frac{dt}{dr}\right)^2 - (\nabla V)_\perp . \tag{7.13}$$

We modify our path until $\vec{N} = 0$ which corresponds to finding a solution of Eq. (7.10). In practice, this should be done iteratively. Each step consists of moving each point along our path in the direction of $\vec{N}$ and finding a modified path by fitting a polynomial to the modified points; fitting a function is necessary as otherwise, the algorithm becomes highly unstable. This is so because the result of one such modification is not a smooth function and the second derivative can grow uncontrollably, which would lead to an even bigger growth in subsequent modifications. We choose to fit a polynomial of order 5 after finding that the use of higher powers does not increase the accuracy of the results any further. After 20 such modifications, we again calculate the tunnelling action along the modified path by solving Eq. (7.11). This gives us the next approximation for S_3 and dt/dr along the path which are used for further path modification. After a few such steps, the action stabilises which means that a solution has been found.

We have checked that the above algorithm converges to the result expected from any reasonable initial guess for the path. However, in practice, it is most convenient to start with a path obtained by choosing S which minimises the potential for each h between the initial and final vacuum. In fact, in this model, this simple choice proves to be a good approximation, and the path obtained from the path modification algorithm decreases the resulting action only by a few percent. This leads to a negligible modification of the transition temperature T_*.

We can use the action in Eq. (7.5) and decay width in Eq. (7.4) to find T_*. We assume that the phase transition proceeds when at least one bubble is nucleated in every horizon

$$\int_{T_*}^{\infty} \frac{1}{TH} \Gamma V_H \, dT = \int_{T_*}^{\infty} \frac{1}{T} \left(\frac{1}{2\pi} \sqrt{\frac{45}{\pi g_{\text{eff}}}} \frac{M_p}{T} \right)^4 \exp\left(-\frac{S_3(T)}{T} \right) dT = 1, \qquad (7.14)$$

where V_H is the horizon volume, H is the Hubble rate and g_{eff} is the effective number of degrees of freedom at temperature T.[4] Under this assumption, our results depend on the thermal history of the universe. Indeed, this dependence is not negligibly small as previously shown in Ref. [426].

In Figs. 7.1 and 7.2, we show the model parameter space relevant for EWBG. The main difference between the simplified analysis using the critical temperature T_c in Fig. 7.1 and the actual transition temperature T_* in Fig. 7.2 is visible in the strong transition region, i.e., $v/T \geq 1$. Large values of v_c mean that the barrier between the electroweak minimum and the symmetric one is large; the probability of the transition is so low that the universe would remain until today in a vacuum that preserves EW symmetry, i.e., $T_* \sim 0$. This scenario is of course excluded.

7.4 Experimental probes

In the following subsections, we discuss three experimental probes for scalar singlet EWBG, namely collider, GW and DM signals.

7.4.1 Collider signals

The direct detection of the new scalar at the LHC is hopeless due to its small signal-to-background ratio. However, it could be detected at a 100 TeV collider as long as its mass (coupling) is small (large) enough [400]. This distinct possibility only covers a small portion of the model parameter space that is of interest to us. On the other hand, following indirect collider searches provide a far better probe of this scenario.

1. *Modification of the triple Higgs coupling*: The modification coming from the new scalar S is

$$\lambda_3 = \frac{1}{6} \frac{\partial^3 V(\phi, S = 0, T = 0)}{\partial h^3} \bigg|_{h=v_0} \approx \frac{m_h^2}{2v_0} + \frac{(\lambda_{HS} v_0)^3}{24\pi^2 m_S^2}. \qquad (7.15)$$

   The triple Higgs coupling λ_3 can only be measured at the HL-LHC in double Higgs production events where the very small cross sections again make the measurement difficult. The estimated precision on this coupling is roughly 30% at the HL-LHC [436] and can get up to 13% at 1 TeV ILC with 2.5 ab^{-1} of experimental data [437].

---

[4]We use the tabulated values of g_{eff} as a function of T from `microMEGAs_v3.6.9.2` [435].
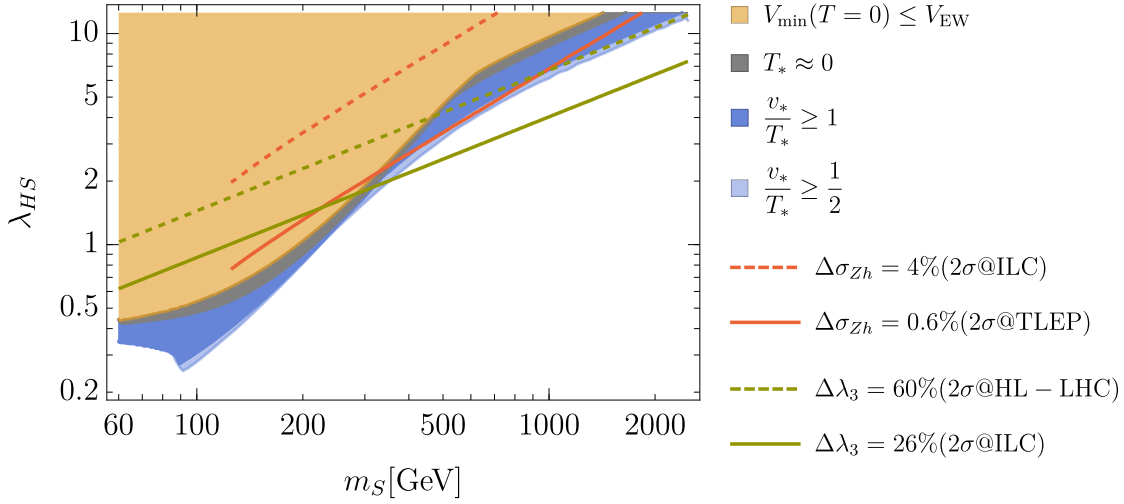
Figure 7.2: Parameter space of the scalar singlet model relevant for EWBG along with the reach of various collider experiments. In the yellow shaded region, the electroweak minimum is not the global minimum of the potential at zero temperature and is excluded. In the grey region, the universe is trapped in a metastable vacuum which preserves the electroweak symmetry. The blue region realises a strong first-order phase transition, whereas the light blue region can still be allowed due to the cosmological modification. Regions above the dotted and dashed lines can be tested at various collider experiments. Here $\Delta\lambda_3 \equiv (\lambda_3 - \lambda_3^{\mathrm{SM}})/\lambda_3^{\mathrm{SM}}$ is the modification of the triple Higgs coupling with respect to the SM expectation.

Much better precision is expected at the 100 TeV *pp* collider [438, 439]. Together with the direct detection of the new scalar via an off-shell Higgs decay [400], it could probe the entire model parameter space relevant for EWBG. However, the time frame of the 100 TeV collider is much bigger than other discussed experiments. Thus, we do not included it in our comparisons.

2. *Modification of the Zh production at lepton colliders*: The fractional change of the *Zh* production cross section relative to its SM value is [400, 440]

$$\Delta\sigma_{Zh} = \frac{1}{2}\frac{\lambda_{HS}^2 v_0^2}{4\pi^2 m_h^2}\left[1 + F\left(\frac{m_h^2}{4m_S^2}\right)\right], \qquad (7.16)$$

where

$$F(\tau) = \frac{1}{4\sqrt{\tau(\tau-1)}}\log\left(\frac{1-2\tau-2\sqrt{\tau(\tau-1)}}{1-2\tau+2\sqrt{\tau(\tau-1)}}\right). \qquad (7.17)$$

The ILC is expected to reach a precision of 2%, whereas FCC-ee/TLEP will reach about 0.6% accuracy at 95% C.L. [441].

In Fig. 7.2, we show parts of the model parameter space that are accessible at colliders. As evident, a measurement of λ_3 is the best probe of the neutral scalar scenario. The ILC and a 100 TeV *pp* collider would be able to probe most of model parameter space where a strong first-order phase transition occurs for scalar masses above ∼ 350 GeV. The *Zh*

production is a somewhat weaker probe. The ILC is not expected to see any modification if the model is realised as it can only probe the unphysical region of the model parameter space. On the other hand, FCC-ee/TLEP could probe a significant portion of the model parameter space where a one-step phase transition can occur. However, it will have a smaller reach in the low mass region than the ILC. In the high mass region, it cannot probe the full parameter space where a strong first-order phase transition occurs.

7.4.2 Gravitational wave signals

A strong first-order phase transition is a very violent event in the early history of the universe. The nucleation and subsequent collision of bubbles, which convert the symmetric vacuum to the electroweak one, is a process that is far away from equilibrium and brings about vast transfers of energy. As all the fields are flat and interact gravitationally, it offers the perfect setting for the creation of GW signals. This has been widely studied in the literature where three primary sources of GWs have been identified. These are the collisions of the bubble walls [311, 442, 443], sound waves generated after the transition [444, 445] and the magneto-hydrodynamical (MHD) turbulence in the plasma [446].

Using the details of the phase transition as outlined above, we can calculate the energy carried by the bubbles that drive the transition and the time scale on which they proceed. These quantities are required to obtain the GW signals from the transition [317]. The first crucial parameter is the ratio of latent heat released from the transition to the energy density of the plasma background [320]

$$\alpha = \frac{1}{\rho_R} \left[-(V_{\text{EW}} - V_f) + T \left(\frac{dV_{\text{EW}}}{dT} - \frac{dV_f}{dT} \right) \right] \Bigg|_{T=T_*}, \tag{7.18}$$

where V_f is the value of the potential in the unstable vacuum (in which the field initially resides) and V_{EW} is the value of the potential in the final vacuum. The second crucial parameter is the inverse time of the phase transition

$$\frac{\beta}{H} = \left[T \frac{d}{dT} \left(\frac{S_3(T)}{T} \right) \right] \Bigg|_{T=T_*}. \tag{7.19}$$

The parameters α and β/H in Eqs. (7.18) and (7.19) allow us to compute the GW signals arising from the phase transition.

The first important source of GWs is bubble collisions. The peak frequency of the resulting signal is [442]

$$f_{\text{col}} = 16.5 \times 10^{-6} \frac{0.62}{v_b^2 - 0.1 v_b + 1.8} \frac{\beta}{H} \frac{T_*}{100} \left(\frac{g_*}{100} \right)^{\frac{1}{6}} \text{Hz} \tag{7.20}$$

and the energy density is

$$\Omega h_{\text{col}}^2(f) = 1.67 \times 10^{-5} \left(\frac{\beta}{H} \right)^{-2} \frac{0.11 v_b^3}{0.42 + v_b^2} \left(\frac{\kappa \alpha}{1 + \alpha} \right)^2 \left(\frac{g_*}{100} \right)^{-\frac{1}{3}} \frac{3.8 \left(f/f_{\text{col}} \right)^{2.8}}{1 + 2.8 \left(f/f_{\text{col}} \right)^{3.8}}. \tag{7.21}$$

The efficiency factor κ and the bubble wall velocity v_b is given by

$$\kappa = \frac{\alpha_\infty}{\alpha}\left(\frac{\alpha_\infty}{0.73 + 0.083\sqrt{\alpha_\infty} + \alpha_\infty}\right), \quad v_b = \frac{1/\sqrt{3} + \sqrt{\alpha^2 + 2\alpha/3}}{1 + \alpha}. \tag{7.22}$$

This definition encompasses a fact that during a strong first-order phase transition, the energy deposited into the fluid saturates at [263, 264, 447]

$$\alpha_\infty = 4.9 \times 10^{-4}\left(\frac{v_*}{T_*}\right)^2. \tag{7.23}$$

We obtain values of $\alpha \in [10^{-3}, 10]$ and $\beta/H \in [1, 10^4]$. The condition $\alpha > \alpha_\infty$ is satisfied by a majority of points and gives hope for a detection in the near future. The bubble wall velocity in Eq. (7.22) provides only a lower bound on the true wall velocity [442]. However, we have checked that replacing it with $v_b = 1$ (more appropriate for a strong transition) does not modify our results noticeably. The same can be said about varying the bubble wall velocity within some uncertainty, say 20%. Although the GW spectrum changes slightly as their frequency and magnitude are multiplied by this $O(1)$ factor, the resulting reach of future GW experiments does not change significantly. For parameter points which give $\alpha < \alpha_\infty$, the contribution from bubble collisions to the GW signal can be removed.

The second source of GWs is sound waves generated in the plasma after the bubble collision. The corresponding peak frequency is [444, 445]

$$f_{\text{sw}} = 1.9 \times 10^{-5}\frac{\beta}{H}\frac{1}{v_b}\frac{T_*}{100}\left(\frac{g_*}{100}\right)^{\frac{1}{6}} \text{ Hz} \tag{7.24}$$

and the energy density is

$$\Omega h_{\text{sw}}^2(f) = 2.65 \times 10^{-6}\left(\frac{\beta}{H}\right)^{-1}\left(\frac{\kappa\alpha}{1+\alpha}\right)^2\left(\frac{g_*}{100}\right)^{-\frac{1}{3}}v_b\left(\frac{f}{f_{\text{sw}}}\right)^3\left(\frac{7}{4 + 3\left(f/f_{\text{sw}}\right)^2}\right)^{\frac{7}{2}}. \tag{7.25}$$

The last remaining source of GW signals is the MHD turbulence in the plasma. The peak frequency is [446]

$$f_{\text{turb}} = 2.7 \times 10^{-5}\frac{\beta}{H}\frac{1}{v_b}\frac{T_*}{100}\left(\frac{g_*}{100}\right)^{\frac{1}{6}} \text{ Hz} \tag{7.26}$$

and the energy density is

$$\Omega h_{\text{turb}}^2(f) = 3.35 \times 10^{-4}\left(\frac{\beta}{H}\right)^{-1}\left(\frac{\epsilon\kappa\alpha}{1+\alpha}\right)^{\frac{3}{2}}\left(\frac{g_*}{100}\right)^{-\frac{1}{3}}v_b\frac{(f/f_{\text{turb}})^3(1 + f/f_{\text{turb}})^{-\frac{11}{3}}}{[1 + 8\pi f a_0/(a_* H_*)]}, \tag{7.27}$$

where the efficiency factor $\epsilon \simeq 0.05$. The total energy density of GWs is a sum of all of the above mentioned sources [320]

$$\Omega_{\text{GW}}h^2(f) = \Omega h_{\text{col}}^2(f) + \Omega h_{\text{sw}}^2(f) + \Omega h_{\text{turb}}^2(f). \tag{7.28}$$
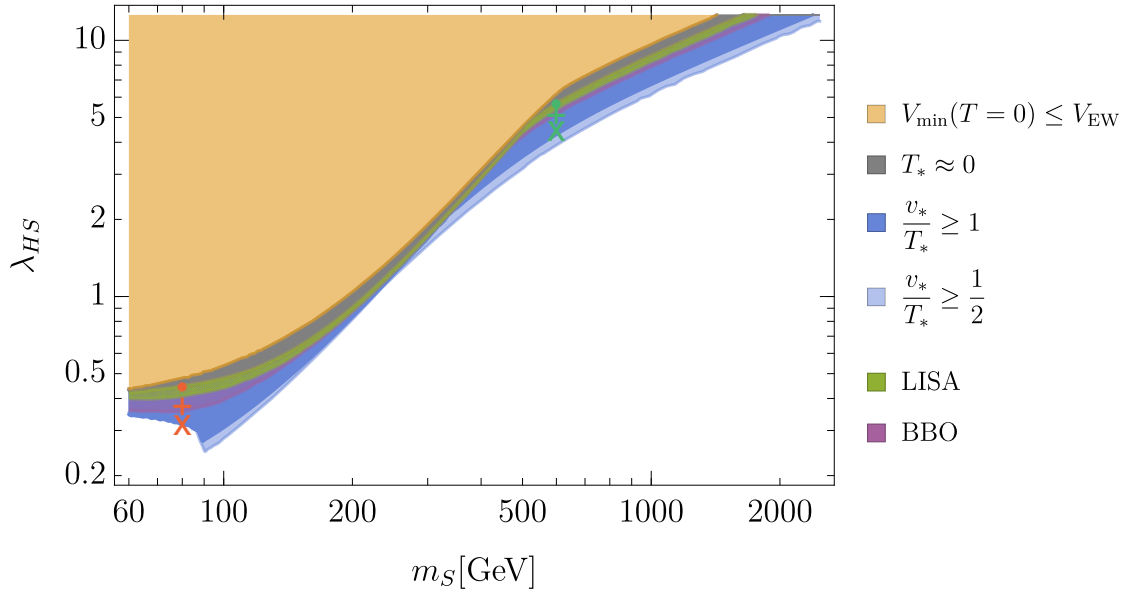
Figure 7.3: Parameter space of the scalar singlet model relevant for EWBG along with the gravitational wave (GW) signals. In the green and purple shaded regions, the GW signals from the phase transition will be accessible in LISA and BBO experiments respectively. A few example points are marked and their GW spectra are shown in Fig. 7.4.
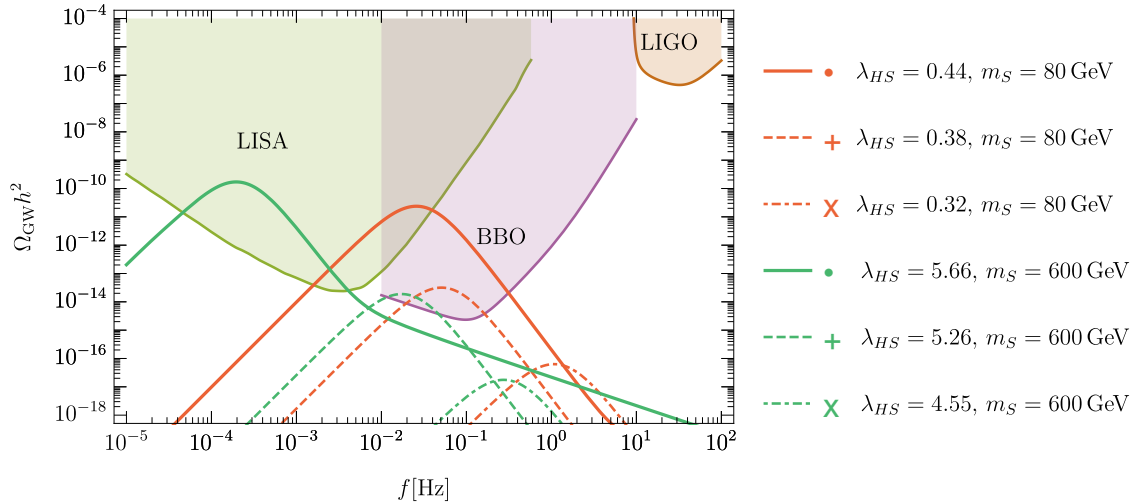
Figure 7.4: Spectra of GWs from EWPT for the example points marked in Fig. 7.3. Projected sensitivities of the future GW detectors such as LISA, BBO and the current LIGO experiment are also shown.

In general, the magnitude of the GW signal grows with the strength of the phase transition. In Figs. 7.3 and 7.4, we illustrate this effect and show the regions of the model parameter space that are accessible at future GW detectors, specifically LISA (using the most promising configuration A5M5) [448] and BBO [449]. For comparison sake, we also show the reach of LIGO [450] which cannot probe any part of the model parameter space relevant for EWBG.

For any value of the scalar mass m_S, the barrier separating the initial symmetric vacuum and the final EWSB one grows with λ_{HS}. This increases the Higgs VEV after the transition, reduces the transition temperature as tunnelling becomes suppressed, and results in an initial unstable configuration of the field which survives longer due to a larger barrier. This means that the action S_3 grows while the transition temperature T_* lowers. At some point, this leads to an over-suppression of the thermal tunnelling by a factor of S_3/T. This would cause the field to remain in the initial unstable configuration up until today, i.e., $T_* \sim 0$. This scenario is of course excluded.

For low transition temperatures, the vacuum decay is driven by quantum fluctuations and is only suppressed by the action S_4 [451] instead of S_3/T in the exponent. The quantum tunnelling action S_4 still depends on the temperature as the potential does. However, this dependence is rather weak as the potential is close to its zero temperature value when the quantum tunnelling becomes important. The calculation of the action is technically very similar to the procedure outlined above. In this case, one main difference is that the solution is four-dimensional as it also includes the Euclidean time. Numerically, the resulting action is similar to the 3D one and the decay probability is much smaller than in the thermally-induced decay case. In the end, this effect saves some part of the model parameter space as the integrated decay probability is increased by adding this small probability in the integral over the temperature when the quantum tunnelling dominates and the BBN temperature T_{BBN}. However, this is a subdominant effect and the part of the model parameter space where it enables the phase transition to occur is negligible. While the calculation of the GW signal is different in this case, the difference between the vacuum energies is still very large, and the resulting signal magnitude would be just as large as in the high-temperature case. This allows for an observation up to the border of the allowed model parameter space.

An important point to note is that for all possible values of the scalar mass m_S, there is a significant region of the model parameter space where a successful EWBG is followed by an observable GW signal. Specifically, for low scalar masses, the coupling λ_{HS} is too small for indirect detection at future based colliders, whereas the GW signal produced during the EWPT is within reach of planned GW detectors. Thus, we can conclude that the detection of GWs can be a more sensitive probe than the indirect collider searches.

7.4.3 Dark Matter signals

In this model, the new scalar S is stable and acts as a DM candidate. All the DM considerations can be avoided if the model is extended by adding new dark sector fields which couple to the SM only via the new scalar S [340,405,406,452]. In that case, the new scalar would decay into light dark sector particles, thereby avoiding all the DM detection limits. However, if the minimal model is realised, these bounds provide strong exclusion

limits on the model parameter space [30].

To calculate the relic abundance of S in the universe today, we follow the standard analysis by writing down the Boltzmann equation [453]

$$\frac{dY}{dx} = \frac{2\pi}{45} \frac{m_S^3}{x^4 H} \left(h_{\text{eff}} + \frac{T}{3} \frac{dh_{\text{eff}}}{dT} \right) \langle \sigma v_{\text{rel}} \rangle \left(Y_{\text{eq}}^2 - Y^2 \right), \tag{7.29}$$

where $Y = n/s$, $x = m_S/T$, $\langle \sigma v_{\text{rel}} \rangle$ is the thermally-averaged annihilation cross-section and h_{eff} is the effective number of entropy degrees of freedom. For the calculation of the σv into various SM final states, we use the results from Ref. [324]. We numerically solve Eq. (7.29) and obtain the number density n_0 of the scalar S today. Finally, the S relic density is

$$\Omega_S h^2 = \frac{m_S Y_0 s_0}{3 M_p^2 H_0^2} \sim m_S Y_0 \times 2.76 \times 10^8. \tag{7.30}$$

Assuming that S is the *only* DM candidate, its relic density must match with the *Planck* measured value [75]

$$\Omega_{\text{DM}} h^2 = 0.1188. \tag{7.31}$$

However, if we assume a multicomponent dark sector, the S abundance can be smaller but still cannot exceed the measured value.

To impose the direct search limits on the model parameter space, we calculate the spin-independent (SI) scalar-nucleon cross-section [30] as

$$\sigma_{\text{SI}} = \frac{\mu^2}{\pi} \frac{\lambda_{HS}^2 f_N^2 m_n^2}{4 m_S^2 m_h^4}, \tag{7.32}$$

where $\mu = m_n m_S/(m_n + m_S)$ is the DM-nucleon reduced mass, $m_n = 938.95\,\text{MeV}$ and $f_N = 0.3$ [324, 454, 455]. If the S abundance is smaller than the *Planck* measured value in Eq. (7.31), the SI cross-section in Eq. (7.32) must be scaled appropriately such that the parameter points with

$$\frac{\Omega_S}{\Omega_{\text{DM}}} \sigma_{\text{SI}} > \sigma_{\text{EXP}} \tag{7.33}$$

are excluded.

At the time when our study was performed, the best upper limit on the SI DM-nucleon cross-section came from the LUX (2016) experiment [193]. Using these limits, we show the regions of the model parameter space excluded by the LUX experiment in Fig. 7.5. In regions where EWBG is viable, the scalar S constitutes less than 1% of the total DM abundance. Even in this case, the LUX (2016) experiment can severely constrain the model parameter space. In fact, only a small region of the model parameter space is allowed where the S abundance is small, either requiring scalar masses $m_S > 700\,\text{GeV}$ or masses just above the Higgs resonance $m_S \sim m_h/2$.

Our results also take into account the vacuum structure of the theory. The region where no EWPT occurs is not constrained by these results as such cases lead to a freeze-out of
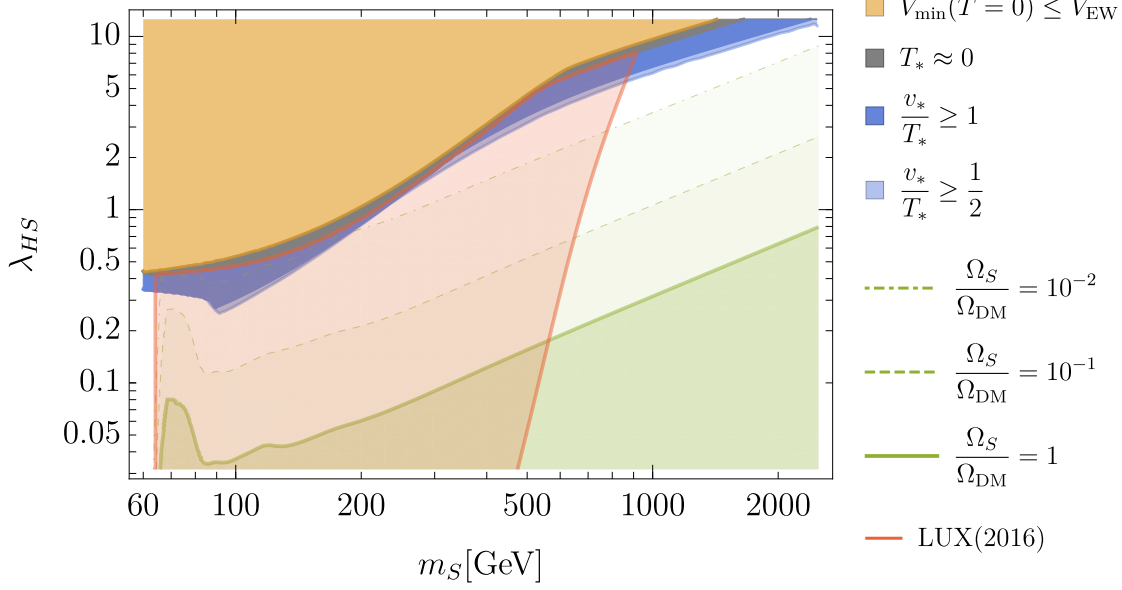
Figure 7.5: Parameter space of the scalar singlet model relevant for EWBG along with the DM abundance and LUX (2016) limits. Constraints from the vacuum structure of the theory are also taken into account. Thus, the correct abundance and the LUX (2016) limits do not enter in the grey and yellow shaded regions.

DM particles in the wrong vacuum; a much different computation of the DM relic density is required in that case. However, this is a pointless exercise to a large extent as the region is already excluded. There is a small loophole to this argument, namely in the region just below the no-EWPT excluded region where the transition proceeds at very low temperature. This means that the DM particles can freeze-out before EWPT occurs in a vacuum with $\langle S \rangle > 0$, $\langle \phi \rangle = 0$ for $m_S < 600$ GeV or $\langle S \rangle = \langle \phi \rangle = 0$ for $m_S > 600$ GeV. Even this exotic possibility is mostly ruled out. For $m_S > 600$ GeV, DM particles freeze-out in the symmetry preserving vacuum. This closes all the usual decay channels generated by the hSS vertex as the Higgs VEV is zero. The resulting abundance of DM particles is higher than it would be in the electroweak vacuum; this region is more constrained by direct detection experiments. The $m_S < 600$ GeV region has to be considered in two parts.

1. In the $m_S < 2m_h$ region, even though the S VEV generates a Shh vertex, the $S \to hh$ decay is kinematically forbidden. As discussed earlier, most of the decay channels via the Higgs decay into SM particles are closed due to a missing hSS vertex. Only the $SS \to hh$ channel is available, which results in a smaller cross-section and larger S abundance. This is again constrained by direct detection experiments.

2. The last possibility is $2m_h < m_S < 600$ GeV where the decay $S \to hh$ is possible. In principle, one could try to find points where the slightly larger DM abundance is depleted as S decays into Higgses in a short time between its freeze-out and EWPT. However, confirming this possibility would require a dedicated study in a negligibly

small region of the model parameter space. We leave this possibility unresolved as even if such points exist, they are very fine-tuned, and their existence is indeed open for questions.

In conclusion, S cannot play the role of a single-component DM in regions where EWBG is allowed. Secondly, in the regions where EWBG is realised, even a very small S abundance is enough to provide severe constraints from direct detection experiments. Moreover, the region of low mass and large coupling, which is considered as a hope for a successful EWBG in this scenario, is ruled out by the vacuum structure of the theory. However, we must keep in mind that by adding a lighter particle (e.g., a Dirac fermion [452, 456], another scalar [457]) which couples only to the scalar S, all the DM constraints can be removed without affecting our predictions for EWBG. This case would correspond to a freeze-out of the new scalar via its decay into the dark sector particles. This is an important realisation as the scalar S without any new dark sector particles *cannot* account for all of the observed DM abundance.

7.5 Cosmological modification

To ensure that the viability of the model parameter space is well-studied, we discuss a possible modification of the cosmological history which can expand this area significantly. We focus on a simple and generic cosmological modification that can describe the effects of current cosmological models.

We assume an additional contribution ρ_N to the energy budget of the early universe. In this case, the modified Friedmann equation is

$$H^2 \equiv \left(\frac{\dot{a}}{a}\right)^2 = \frac{8\pi}{3M_p^2}\left(\frac{\rho_R}{a^4} + \frac{\rho_N}{a^n}\right), \tag{7.34}$$

where $a \equiv a(t)$ is the scale factor and $n > 4$ such that the new component dilutes before it modifies any cosmological measurements. The first of such important measurements comes from BBN [458, 459]. The Hubble rate can be measured at the time of BBN as we precisely know when the neutrons need to freeze-out for a small fraction of them to recreate the observed abundance of light elements. While the observed expansion rate is consistent with a universe filled with the SM radiation, we are allowed to add a small fraction of the new component ρ_N within experimental uncertainties.

We translate the effective number of neutrino species into a modification of the Hubble rate [460] as

$$\frac{H}{H_R}\bigg|_{\text{BBN}} = \sqrt{1 + \frac{7}{43}\Delta N_{\nu_{\text{eff}}}}, \tag{7.35}$$

where H_R is the standard case (i.e., SM radiation) and

$$\Delta N_{\nu_{\text{eff}}} = (N_{\nu_{\text{eff}}} + 2\sigma) - N_{\nu_{\text{eff}}}^{\text{SM}} = (3.28 + 2 \times 0.28) - 3.046 = 0.794$$

is the difference between the effective number of neutrinos in the SM radiation case and the experimental upper bound at 2σ C.L. [458, 459]. We assume that the new component does not directly interact with the SM such that the usual relationship between the scale factor and temperature holds, namely

$$\frac{\rho_R}{a^4} = \frac{\pi^2}{30}gT^4, \tag{7.36}$$

where g is the number of degrees of freedom in the SM. This gives a known result for the Hubble rate in the radiation-dominated case

$$H_R = \sqrt{\frac{4\pi g}{45}}\frac{T^2}{M_p}. \tag{7.37}$$

We can calculate an upper bound on the expansion rate at an earlier time, i.e., high-temperature. The contribution arising from the new component grows quickly and dominates the total energy density. When this occurs, we can neglect ρ_R in Eq. (7.34) and arrive at the following result

$$\frac{H}{H_R} = \sqrt{\left(\left.\frac{H}{H_R}\right|_{\text{BBN}}\right)^2 - 1}\left[\left(\frac{g}{g_{\text{BBN}}}\right)^{\frac{1}{4}}\frac{T}{T_{\text{BBN}}}\right]^{(n-4)/2}, \tag{7.38}$$

where the quantities with the subscript "BBN" are calculated at the BBN temperature $T_{\text{BBN}} = 1\,\text{MeV}$. The resulting maximal modification of H is shown in the left panel of Fig. 7.6. In particular, $n = 6$ case can be realised in many cosmological models and results in an increase that can be as big as 10^5 in temperature around EWPT. This large modification has important consequences for DM and EWBG as discussed below.

7.5.1 The sphaleron bound

We revisit the sphaleron bound and its modification due to a non-standard cosmological history. The simplest criterion for the decoupling of sphalerons is

$$\Gamma_{\text{Sph}} = \mathcal{B}_0 T^4 \frac{g}{4\pi}\left(\frac{v}{T}\right)^7 \exp\left(-\frac{4\pi}{g}\frac{v}{T}\right) \leq H, \tag{7.39}$$

where the constant $\mathcal{B}_0$ encapsulate the details of the $SU(2)$ sphaleron calculation. Rigorous calculation of the value of $\mathcal{B}_0$ has generally proved to be difficult and a few different values have been used in the literature, leading to different bounds on v/T [238, 407, 428, 429]. We use the standard bound in Eq. (7.3) for the SM radiation dominated case, i.e., $H = H_R$. In the right panel of Fig. 7.6, we show the values of v_*/T_* needed to decouple the sphalerons after the EWPT as a function of the modified Hubble rate. In comparing the two panels in Fig. 7.6, we see that the required ratio can be as low as $v_*/T_* \sim 1/2$ for cosmological models with $n = 6$. We highlight this value in our results below and show its impact on the DM signals.
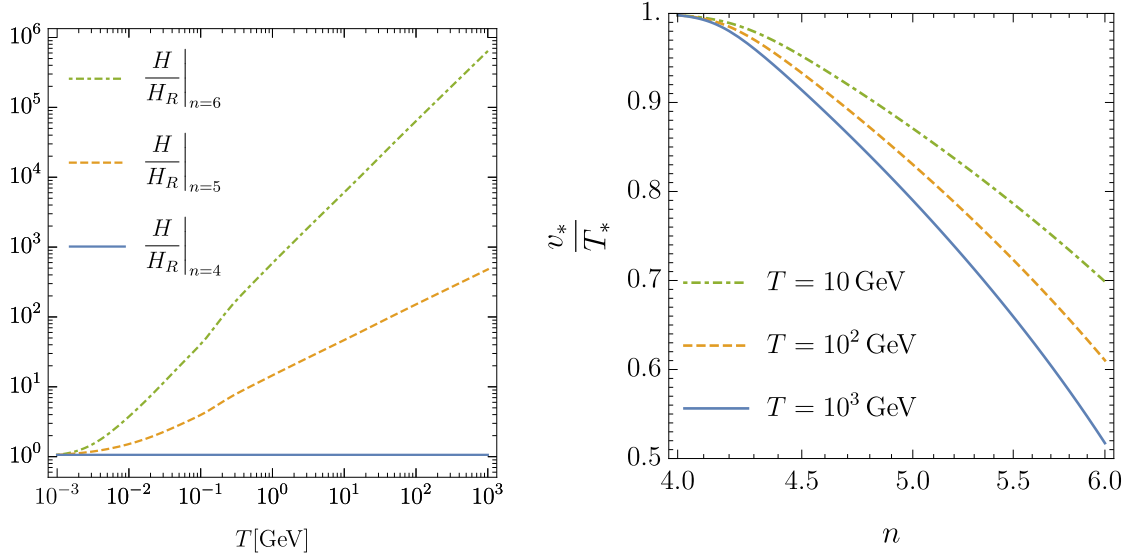
Figure 7.6: *Left panel*: Maximal modification of the Hubble rate H that is not in conflict with any experimental bounds. *Right panel*: Values of v_*/T_* needed to avoid the washout of the baryon asymmetry after the EWPT vs the modification of the Hubble rate.

7.5.2   Implications for dark matter

The abundance of S is very sensitive to any modifications in the cosmological history. An increased Hubble rate H would result in an earlier freeze-out of the new scalar S than in the case of standard cosmology. This would result in a larger abundance of S in the universe today. To see this effect in action, we simply replace H in Eq. (7.29) with a modified Hubble rate as given in Eq. (7.38). The result is shown in Fig. 7.7. The S abundance is evidently increased by orders of magnitude. The $n = 6$ case can achieve the correct abundance in all parts of the model parameter space up to the region excluded by the vacuum structure. However, no parameter space that allows for the observed DM abundance opens up due to this modification. This is so because the increased S abundance also results in severe direct detection limits from the LUX (2016) experiment.

It is interesting to note that a higher expansion rate increases the DM abundance for large couplings while allowing for smaller ones to be compatible with EWBG, thereby bringing the two regions closer.

7.6   Summary

In this chapter, we studied the viability and detection prospects of a scalar singlet extension of the SM. In particular, we have focused on two attractive features of this model, namely the possibility to facilitate EWBG and a DM candidate. We have discussed various experimental probes of this scenario and their reach in parts of the model parameter space. These include collider signals, detection of GW signals from the phase transition and
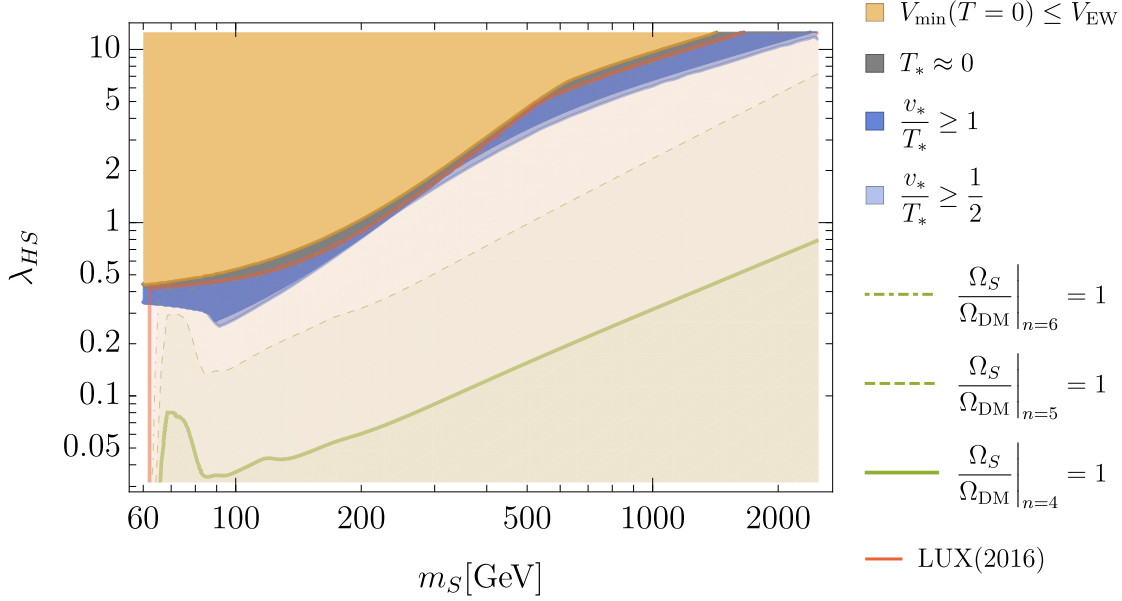
Figure 7.7: Parameter space of the scalar singlet model relevant for EWBG along with the DM abundance and LUX (2016) limits from a modified cosmological history. Values of λ_{HS} along the green lines give the correct DM abundance for cosmological modification at given n. For $n = 6$, the correct DM abundance can be obtained anywhere between the area excluded by the vacuum structure and the usual radiation domination case, $n = 4$. The LUX limit in the solid red line is based on the S abundance for $n = 6$.

direct DM detection limits.

We have studied the dynamics of the phase transition in regions where a two-step phase transition occurs. In this case, the universe first transitions into a minimum along the $\langle \phi \rangle = 0$, $\langle S \rangle > 0$ vacuum configuration and then subsequently decays to the electroweak vacuum $\langle \phi \rangle = v_0$, $\langle S \rangle = 0$. This allowed us to accurately compute the transition temperature T_* and its strength v_*/T_*. In turn, these enable us to predict the GW signals from the phase transition in all parts of the model parameter space.

Our most important conclusion is that a significant portion of the model parameter space will be accessible at the planned GW experiments but is beyond the reach at the future collider experiments. The region of small coupling is especially attractive as it guarantees that the use of a one-loop analysis is accurate and no Landau poles arise near the electroweak scale when the scalar coupling grows with the RGE. For more details, see Ref. [400].

We also extensively tested the possibility of the new scalar as a DM candidate. Using the standard freeze-out of S to compute its present relic density, we identified the model parameter space where S satisfies the observed DM abundance and is constrained by the limits from the LUX (2016) experiment. Here the conclusion is that the correct DM abundance *cannot* be obtained simultaneously with a strong first-order EWPT. The small abundance of S is enough to be constrained by direct DM searches. The situation becomes worse in the region of small scalar mass and large coupling as it is excluded by the vacuum

structure. In this case, our universe would never transition to the electroweak vacuum, at least for perturbative values of the couplings λ_S and λ_{HS}.

There are only two regions where EWBG is viable. The first is the region close to the Higgs resonance $m_S \sim m_h/2$ and the other at scalar masses $m_S > 700$ GeV. However, we must note that all the DM constraints can be avoided if the scalar only serves as a mediator between the SM and a new DM candidate. In that case, the details of EWPT would essentially remain the same.

Lastly, we have checked which parts of the model parameter space open up when the cosmological history is modified. We employed a simple cosmological model by assuming a new energy constituent ρ_N that redshifts faster than radiation, i.e., $\rho_N \propto a^{-n}$ for $n > 4$. We placed bounds on the expansion rate of the universe without spoiling any existing astrophysical observations. We concluded that the cosmological modification has significant implications for both EWBG and the DM abundance. This lead to a shift in the regions where the two requirements can be matched with observations. However, an increase in the DM abundance is always followed by severe constraints from direct search experiments. Thus, no new viable parameter space opens up.

Part III

Global fits

Chapter 8

Global fit of the extended scalar singlet model

8.1 Introduction

In chapter 7, we studied the phenomenology of the scalar singlet model in light of EWBG. With an assumed $\mathbb{Z}_2$ symmetry: $S \to -S$, we required the new scalar S to be a DM candidate. Using the standard freeze-out of S, we computed its relic density and constrained parts of the model parameter space using the observed DM abundance and direct detection limit from the LUX (2016) experiment. We found that the correct DM abundance *cannot* be obtained simultaneously with a strong first-order EWPT. These two requirements left us with two allowed regions, namely the Higgs resonance region $m_S \sim m_h/2$ and $m_S > 700\,\text{GeV}$. We also noted that all the DM constraints could be avoided if the new scalar S serves as a mediator between the SM and a new DM candidate. It is exactly this possibility that we wish to explore in this chapter. In particular, we study the phenomenology of an extended scalar singlet model with a fermionic DM candidate.

The singlet fermion DM model was first introduced in Ref. [461]. The model parameter space was constrained using the WMAP measured DM relic density, LEP2 limits on the Higgs boson mass and direct detection limits from the XENON100 and CDMS experiments. This study was further improved in Ref. [343] where constraints from electroweak precision tests, Higgs phenomenology at the LHC, relic density measurements from WMAP7 and direct detection limits from XENON100 experiment were imposed.

The model was revisited after the Higgs boson discovery in Ref. [462]. This study focused on the vacuum stability and triviality bounds (see also Ref. [463]). It was shown that the model is stable (without hitting a Landau pole) up to the Planck scale for a 125 GeV Higgs boson. It was also found that the regions where the electroweak vacuum is a global minimum of the potential are highly limited. This led to a strong bound on the second scalar mass m_2. A comparison with the fermion Higgs portal model was also made [464].

In light of EWBG, the model was first studied in Ref. [465]. Using a large Monte

Carlo scan of the model parameter space, the model was shown to account for the observed DM abundance. In addition, a strong first-order phase transition was realised without conflicting with any bounds from direct DM searches, electroweak precision tests and the latest Higgs data from the LHC. Similar results were obtained in Ref. [456] based on Markov Chain Monte Carlo (MCMC) scans of the model parameter space. Constraints from the latest Higgs searches at the LHC, direct detection limits from the LUX experiment, and limits from LEP and electroweak precision observables (EWPO) were taken into account. Both the tree- and loop-level barriers between the electroweak and symmetric minimum were studied.

In Ref. [452], the authors started out with a $\mathbb{Z}_2$ symmetric case, i.e., a scalar Higgs portal [340, 405, 406] and showed that the observed DM abundance could be explained by either a freeze-out or freeze-in mechanism. However, this simple model cannot simultaneously account for the observed DM abundance and baryon asymmetry (in agreement with our findings in chapter 7). Thus, the model was extended by relaxing the assumed $\mathbb{Z}_2$ symmetry and adding a new fermionic DM candidate. As the details of the EWPT mainly depend on the new scalar (however, the fermion DM does contribute at one-loop order), a strong first-order phase transition was realised in the extended model. The fermion DM was also shown to account for the observed DM abundance. Constraints from the vacuum stability and model perturbativity were also imposed at scales up to 10 TeV. For more recent studies of this model, see Refs. [421, 466–474].

In this chapter, we perform the most comprehensive study to date of the extended scalar singlet model with a fermionic DM candidate based on Ref. [475]. In our global fit, we include the latest results from the *Planck* measured DM relic density [75], direct detection limit from the PandaX-II experiment [19], EWBG, EWPO [476] and Higgs searches at colliders [477, 478]. We also find regions in the model parameter space where a successful EWBG is viable. This allows us to compute the gravitational wave (GW) signals arising from the phase transition and discuss their discovery prospects at current or future GW experiments.

We start by introducing the extended scalar singlet model with a fermionic DM candidate. After taking note of the free model parameters, we describe the set of constraints and likelihoods used in our global fit. We also present and discuss some of the preliminary results obtained from our global fit. Appendix F gathers supplementary information for understanding various expressions used in this chapter.

8.2   Model

We extend the SM by adding a new real scalar singlet S and a Dirac fermion DM field ψ. The fermion DM is assumed to be living in the hidden sector and communicates with the

SM only via the new scalar. The model Lagrangian is given by [343]

$$\mathscr{L} = \mathscr{L}_{SM} + \mathscr{L}_S + \mathscr{L}_\psi + \mathscr{L}_{portal}, \tag{8.1}$$

where $\mathscr{L}_{SM}$ is the SM Lagrangian,

$$\mathscr{L}_S = \frac{1}{2}(\partial_\mu S)(\partial^\mu S) + \frac{1}{2}\mu_S^2 S^2 + \frac{1}{3}\mu_3 S^3 - \frac{1}{4}\lambda_S S^4, \tag{8.2}$$

$$\mathscr{L}_\psi = \overline{\psi}(i\slashed{\partial} - \mu_\psi)\psi - g_S\overline{\psi}\psi S, \tag{8.3}$$

$$\mathscr{L}_{portal} = -\mu_{\Phi S}\Phi^\dagger\Phi S - \frac{1}{2}\lambda_{\Phi S}\Phi^\dagger\Phi S^2. \tag{8.4}$$

A linear term of the form $\mu_1^3 S$ is removed by a constant shift $S \to S+\sigma$. This transformation redefines μ_1^3, μ_S^2, μ_Φ^2, μ_3, g_S and $\mu_{\Phi S}$.[1] In writing the above Lagrangians, we have assumed that these parameters take their redefined values. When $\mu_3 = g_S = \mu_{\Phi S} = 0$, the model reduces to the scalar Higgs portal model studied in chapter 7.[2]

With an extra scalar field, the tree-level scalar potential is

$$V_{tree} = V_{SM} + V_S + V_{portal}, \tag{8.5}$$

where V_S and V_{portal} can be read directly from Eqs. (8.2) and (8.4) respectively. The SM part of the potential reads

$$V_{SM} = -\mu_\Phi^2\Phi^\dagger\Phi + \lambda_\Phi(\Phi^\dagger\Phi)^2, \tag{8.6}$$

where

$$\Phi = \begin{pmatrix} G^+ \\ \frac{1}{\sqrt{2}}\left(\phi + iG^0\right) \end{pmatrix} \tag{8.7}$$

is the SM Higgs doublet and $(G^\pm, G^0)$ are the "would-be" Goldstone bosons.

In general, both ϕ and S can develop non-trivial vacuum expectation values (VEVs). Denoting these VEVs at $T = 0$ by v_0 and s_0 respectively, i.e.,

$$\langle 0|\phi|0\rangle\Big|_{T=0} = v_0, \quad \langle 0|S|0\rangle\Big|_{T=0} = s_0, \tag{8.8}$$

we can expand Φ and S in the unitary gauge as

$$\Phi = \frac{1}{\sqrt{2}}\begin{pmatrix} 0 \\ v_0 + \varphi \end{pmatrix}, \quad S = s_0 + s, \tag{8.9}$$

where (φ, s) fields represent quantum fluctuations around the $T = 0$ VEVs.

After EWSB, the ϕ and S fields acquire their VEVs in Eq. (8.8). Using the results presented in Appendix F, we arrive at the following EWSB conditions

$$\mu_\Phi^2 = \lambda_\Phi v_0^2 + \mu_{\Phi S}s_0 + \frac{1}{2}\lambda_{\Phi S}s_0^2, \tag{8.10}$$

$$\mu_S^2 = -\mu_3 s_0 + \lambda_S s_0^2 + \frac{\mu_{\Phi S}v_0^2}{2s_0} + \frac{1}{2}\lambda_{\Phi S}v_0^2. \tag{8.11}$$

---

[1]The parameter μ_Φ^2 appears in the SM Higgs potential, see Eq. (8.6).
[2]The required substitution is $\mu_S^2 \to -\mu_S^2$ and $\lambda_{\Phi S} \to 2\lambda_{HS}$.

The portal interaction Lagrangian in Eq. (8.4) induces a mixing between the φ and s fields. Thus, the squared mass matrix

$$\mathcal{M}^2 = \begin{pmatrix} \mathcal{M}^2_{\varphi\varphi} & \mathcal{M}^2_{\varphi s} \\ \mathcal{M}^2_{s\varphi} & \mathcal{M}^2_{ss} \end{pmatrix} \tag{8.12}$$

is non-diagonal. As shown in Appendix F, its elements are given by

$$\mathcal{M}^2_{\varphi\varphi} = 2\lambda_\Phi v_0^2, \quad \mathcal{M}^2_{ss} = -\mu_3 s_0 + 2\lambda_S s_0^2 - \frac{\mu_{\Phi S} v_0^2}{2s_0}, \quad \mathcal{M}^2_{\varphi s} = \mathcal{M}^2_{s\varphi} = \mu_{\Phi S} v_0 + \lambda_{\Phi S} v_0 s_0.$$

The squared mass matrix in Eq. (8.12) can be diagonalised by rotating the interaction eigenstates (φ, s) into the physical mass eigenstates (h, H) as

$$\begin{pmatrix} h \\ H \end{pmatrix} = \begin{pmatrix} \cos\alpha & -\sin\alpha \\ \sin\alpha & \cos\alpha \end{pmatrix} \begin{pmatrix} \varphi \\ s \end{pmatrix}, \tag{8.13}$$

where α is the mixing angle. Thus, for small mixing, h is a SM-like Higgs boson, whereas H is dominated by the scalar singlet.

For the tree-level potential in Eq. (8.5) to be bounded from below, the following conditions must be satisfied (see Appendix F for more details)

$$\lambda_\Phi > 0, \quad \lambda_S > 0, \quad \lambda_{\Phi S} > -2\sqrt{\lambda_\Phi \lambda_S}. \tag{8.14}$$

After EWSB, the fermion DM Lagrangian in Eq. (8.3) reduces to

$$\mathcal{L}_\psi = \overline{\psi}(i\slashed{\partial} - m_\psi)\psi - g_S \overline{\psi}\psi s, \tag{8.15}$$

where

$$m_\psi = \mu_\psi + g_S s_0 \tag{8.16}$$

is the physical fermion DM mass.

8.3 Constraints

In light of the recent discovery of a SM-like Higgs boson at the LHC [10, 56], we take

$$m_h = 125\,\text{GeV}, \quad v_0 = 246.22\,\text{GeV}. \tag{8.17}$$

Thus, the model is fully described by the following 7 free parameters

$$m_H, \quad s_0, \quad \mu_3, \quad \lambda_S, \quad \alpha, \quad m_\psi, \quad g_S. \tag{8.18}$$

The remaining parameters in Eqs. (8.2) and (8.4) can be expressed as (see Appendix F for more details)

$$\lambda_\Phi = \frac{1}{2v_0^2}\left(m_h^2\cos^2\alpha + m_H^2\sin^2\alpha\right), \tag{8.19}$$

$$\mu_{\Phi S} = -\frac{2s_0}{v_0^2}\left(m_h^2\sin^2\alpha + m_H^2\cos^2\alpha + \mu_3 s_0 - 2\lambda_S s_0^2\right), \tag{8.20}$$

$$\lambda_{\Phi S} = \frac{1}{v_0 s_0}\left[(m_H^2 - m_h^2)\sin\alpha\cos\alpha - \mu_{\Phi S}v_0\right], \tag{8.21}$$

$$\mu_\Phi^2 = \lambda_\Phi v_0^2 + \mu_{\Phi S}s_0 + \frac{1}{2}\lambda_{\Phi S}s_0^2, \tag{8.22}$$

$$\mu_S^2 = -\mu_3 s_0 + \lambda_S s_0^2 + \frac{\mu_{\Phi S}v_0^2}{2s_0} + \frac{1}{2}\lambda_{\Phi S}v_0^2. \tag{8.23}$$

To study the model phenomenology, we implement the extended scalar singlet and fermion DM model in the `LanHEP_v3.2.0` [351] package. For the calculation of the fermion DM relic density and Higgs decay rates, we use `micrOMEGAs_v4.3.5` [435] which relies on the `CalcHEP` [479] package.

In the following subsections, we summarise a set of constraints used to explore the 7D model parameter space.

8.3.1 Thermal relic density

As described in chapter 4, the temperature and polarization anisotropies in the CMB places a strong bound on the present-day abundance of the DM particles. The most recent measurement comes from the *Planck* satellite [75]

$$\Omega_{\text{DM}}h^2 = 0.1188 \pm 0.0010. \tag{8.24}$$

In our model, the Dirac fermion ψ plays the role of a DM candidate. Its relic density is mainly determined by an s-channel annihilation into SM particles via an h/H exchange. Annihilation into hh, HH and hH final states via the t- and u-channels is also possible. Due to a mixing between the interaction eigenstates (φ, s), the decay rates go as

$$\Gamma(\overline{\psi}\psi \to h) \propto g_S^2\sin^2\alpha, \quad \Gamma(h \to \overline{X}X) \propto \cos^2\alpha, \tag{8.25}$$

$$\Gamma(\overline{\psi}\psi \to H) \propto g_S^2\cos^2\alpha, \quad \Gamma(H \to \overline{X}X) \propto \sin^2\alpha, \tag{8.26}$$

where X is a general SM final state, e.g., a quark, lepton or gauge boson. Thus, depending on the mixing angle α, three scenarios are possible.

1. $\alpha = 0$: In this case, H is the mediator particle. However, from Eq. (8.26), its decay rate into SM particles is suppressed. Thus, the only allowed final states from the fermion DM annihilation are hh, HH and hH.
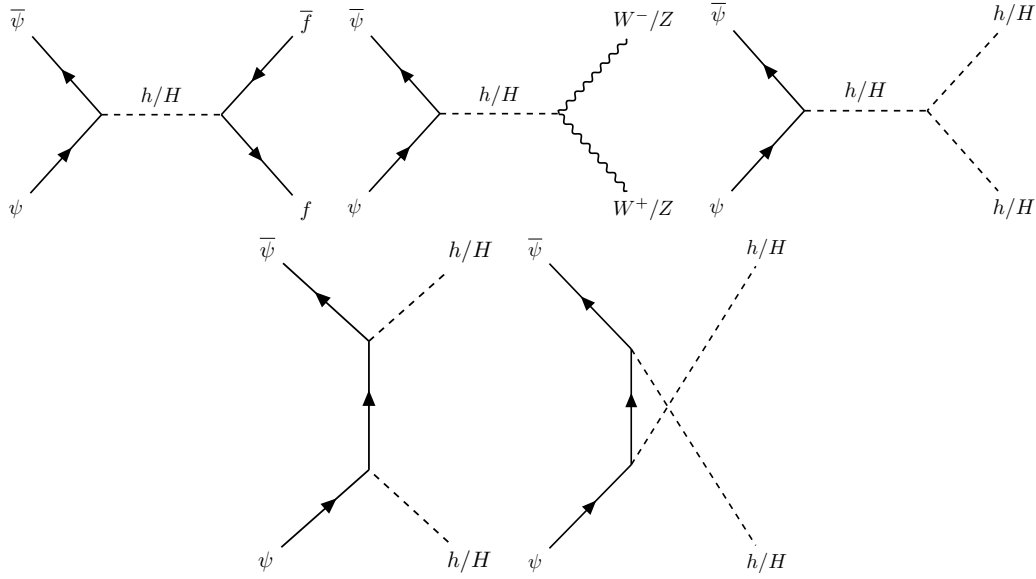
Figure 8.1: Feynman diagrams for the fermion DM annihilation into SM and h/H particles. Here f denotes a SM fermion.

2. $\alpha = \pi/4$: This corresponds to a maximal mixing between the interaction eigenstates. All the allowed final states from the fermion DM annihilation are shown in Fig. 8.1.

3. $\alpha = \pi/2$: In this case, h is the mediator particle. However, from Eq. (8.25), its decay rate into SM particles is suppressed. Thus, the only allowed final states from the fermion DM annihilation are hh, HH and hH, i.e., same as in the $\alpha = 0$ case.

With two scalar mediators h and H, the fermion DM annihilation rate into SM particles is enhanced when $m_\psi \sim m_{h,H}/2$. At these two resonances, the fermion DM relic density $\Omega_\psi h^2$ drops rapidly with increasing scalar-fermion DM coupling g_S. For the fermion DM to account for the observed DM abundance, i.e., $\Omega_\psi h^2 = \Omega_{DM} h^2$, small values of g_S are required to compensate for the enhanced annihilation rate into SM particles.

There is a strong possibility of a multicomponent dark sector where a given DM candidate makes up only a small fraction of the observed DM abundance. We address such scenarios by defining a relic abundance parameter as [30, 324, 480]

$$f_{\mathrm{rel}} = \frac{\Omega_\psi}{\Omega_{DM}}, \tag{8.27}$$

where $\Omega_{DM} h^2 = 0.1188$ is the *Planck* measured central value in Eq. (8.24). Consequently, indirect and direct detection signals must be scaled by f_{rel}^2 and f_{rel} respectively.[3] In regions of the model parameter space where $f_{\mathrm{rel}} > 1$, the model is robustly excluded by the relic density constraint.

---

[3]We do not discuss any indirect detection limits as the fermion DM annihilation rate into SM particles is suppressed by v^2 where $v \sim 10^{-3} c$ in the local halo [481]. However, if we add a pure pseudoscalar, parity-violating interaction term ($\propto \overline{\psi} i \gamma_5 \psi$), the resulting indirect detection limits can be sizeable [143, 482–486].

8.3.2 Direct detection

Direct detection experiments aim to measure the recoil of a nucleus from an elastic scattering off a DM particle. As we saw in chapter 4, such an event generates a typical recoil energy (E_R) on the order of a few keV. As most radioactive elements and high-energy cosmic rays induce nuclear recoils with energies well above this value, direct DM searches must be conducted in deep underground laboratories to shield them from potential background sources.

In our model, the DM-quark interaction proceeds via a t-channel exchange of h/H particles. With two neutral scalar mediators, the resulting DM-nucleus interaction is nuclear spin-independent (SI). The SI DM-nucleus cross-section is given by

$$\sigma_{\text{SI}}^{\psi N} = \frac{\mu_{\psi N}^2}{\pi} \left[Z G_p + (A - Z) G_n \right]^2, \tag{8.28}$$

where $\mu_{\psi N} = m_\psi m_N / (m_\psi + m_N)$ is the DM-nucleus reduced mass and $Z (A - Z)$ are the number of protons (neutrons) in the target nucleus N. The dimensionful parameters (G_p, G_n) are the effective DM-nucleon couplings. As shown in Appendix F, they are given by

$$G_N = \frac{g_S \sin \alpha \cos \alpha}{v_0} \left(\frac{1}{m_h^2} - \frac{1}{m_H^2} \right) m_N f_N, \tag{8.29}$$

where $N \in (p, n)$,

$$f_N = \frac{2}{9} + \frac{7}{9} \sum_{q=u, d, s} f_{Tq}^{(N)} \tag{8.30}$$

is the Higgs-nucleon coupling and $f_{Tq}^{(N)} \equiv m_q \langle N | \overline{q} q | N \rangle / m_N$ are the hadronic matrix elements.

When $G_p \simeq G_n$, the DM-nucleus cross-section in Eq. (8.28) is enhanced by a factor of A^2. This is expected as the matrix elements for a SI interaction involve a coherent sum over the individual protons and neutrons in the nucleus. For this reason, direct detection experiments rely on heavy target materials with large Z to better constrain the DM-nucleon cross-section $\sigma_{\text{SI}}^{\psi N}$.

8.3.3 Electroweak baryogenesis (EWBG)

In our model, the VEV of the new scalar S does not initially have to be zero. Thus, the transition pattern can be $(\langle \phi \rangle, \langle s \rangle) = (0, s_i) \rightarrow (v, s)$. At low temperatures, the latter minimum evolves slowly to become the electroweak minimum at $T = 0$, i.e., $(\langle \phi \rangle, \langle s \rangle) = (v_0, s_0)$. The initial transition can break the electroweak symmetry by tunnelling through a potential barrier to the broken phase minimum. It can proceed via nucleation of bubbles of the broken phase which provides a departure from thermal equilibrium [26, 230, 245, 398]. In addition, this transition can generate a significant GW signal [317]. Using the standard

notation, we define a strong first-order phase transition by

$$\frac{v}{T} \gtrsim 1, \tag{8.31}$$

where v is the Higgs VEV at temperature T. However, one should keep in mind that the calculation of the baryon asymmetry remaining after the transition is quite complicated. This has lead to slightly different exact lower bounds on v/T in the literature [238, 400, 407, 428, 429].

To find regions in the model parameter space where a successful EWBG is viable, we find the minima of the effective potential $V_{\text{eff}}(\phi, S, T)$ in Appendix F numerically, and compute the critical temperature T_c at which the initial and symmetry breaking minima are degenerate. This allows us to calculate the dimensionless parameter v_c/T_c and constrain the model parameter space, i.e., parameter points are excluded if they lead to a too weak phase transition. This approach is also used while performing a global fit of our model.

We also perform a complete analysis of the phase transition in this model by following our work on the $\mathbb{Z}_2$ symmetric case, i.e., scalar Higgs portal [397] as studied in chapter 7. This allows us to find the nucleation temperature T_* at which the phase transition truly proceeds and obtain a more accurate estimate of its strength v_*/T_*. More importantly, it allows us to compute the GW signals arising from the phase transition and discuss the discovery prospects of the model at current or future GW experiments.

8.3.4 Electroweak precision observables (EWPO)

With an extra scalar, the model can induce corrections to the gauge boson self-energy diagrams. Its effect on the EWPO can be parametrised by the oblique parameters S, T and U [487]. The $\gamma\gamma$ and γZ self-energies ($\Pi_{\gamma\gamma}$ and $\Pi_{\gamma Z}$ respectively) are not modified with respect to the SM values as the new scalar is electrically neutral. Thus, only the W and Z boson self-energies are subject to corrections.

In our model, the oblique parameters are shifted from their SM values, i.e., $\Delta O \equiv O - O_{\text{SM}}$ where $O \in (S, T, U)$ by [343]

$$\Delta T = \frac{3}{16\pi s_W^2} \left[\cos^2 \alpha \left\{ f_T \left(\frac{m_h^2}{m_W^2} \right) - \frac{1}{c_W^2} f_T \left(\frac{m_h^2}{m_Z^2} \right) \right\} + \sin^2 \alpha \left\{ f_T \left(\frac{m_H^2}{m_W^2} \right) \right. \right.$$
$$\left. \left. - \frac{1}{c_W^2} f_T \left(\frac{m_H^2}{m_Z^2} \right) \right\} - \left\{ f_T \left(\frac{m_h^2}{m_W^2} \right) - \frac{1}{c_W^2} f_T \left(\frac{m_h^2}{m_Z^2} \right) \right\} \right], \tag{8.32}$$

$$\Delta S = \frac{1}{2\pi} \left[\cos^2 \alpha f_S \left(\frac{m_h^2}{m_Z^2} \right) + \sin^2 \alpha f_S \left(\frac{m_H^2}{m_Z^2} \right) - f_S \left(\frac{m_h^2}{m_Z^2} \right) \right], \tag{8.33}$$

$$\Delta U = \frac{1}{2\pi} \left[\cos^2 \alpha f_S \left(\frac{m_h^2}{m_W^2} \right) + \sin^2 \alpha f_S \left(\frac{m_H^2}{m_W^2} \right) - f_S \left(\frac{m_h^2}{m_W^2} \right) \right] - \Delta S, \tag{8.34}$$

where m_W (m_Z) is the W (Z) boson mass, $c_W^2 = m_W^2/m_Z^2$ and $s_W^2 = 1 - c_W^2$. The loop functions $f_T(x)$ and $f_S(x)$ are given by [488]

$$f_T(x) = \frac{x \log x}{x - 1},$$

$$f_S(x) = \begin{cases} \frac{1}{12}\left[-2x^2 + 9x + \left((x-3)\left(x^2 - 4x + 12\right) + \frac{1-x}{x}\right) f_T(x) \right. \\ \left. +2\sqrt{(4-x)x}\left(x^2 - 4x + 12\right)\tan^{-1}\left(\sqrt{\frac{4-x}{x}}\right)\right], \quad 0 < x < 4, \\ \frac{1}{12}\left[-2x^2 + 9x + \left((x-3)\left(x^2 - 4x + 12\right) + \frac{1-x}{x}\right) f_T(x) \right. \\ \left. +\sqrt{(x-4)x}\left(x^2 - 4x + 12\right)\log\left(\frac{x - \sqrt{(x-4)x}}{x + \sqrt{(x-4)x}}\right)\right], \quad x \geq 4. \end{cases}$$

From Eqs. (8.32)–(8.34), it is evident that

$$\Delta O = (1 - \cos^2\alpha)\left[O_{\mathrm{SM}}(m_H) - O_{\mathrm{SM}}(m_h)\right], \tag{8.35}$$

where $\Delta O \in (\Delta S, \Delta T, \Delta U)$. Thus, at large values of m_H, $\alpha \sim 0$ is required, whereas for $m_H \sim m_h$, large mixing angles are compatible with the EWPO constraint.

8.3.5 Higgs searches at colliders

Due to a mixing between the interaction eigenstates (φ, s), the coupling strength between the mass eigenstates (h, H) and SM particles is suppressed. The effective squared couplings are defined as [456]

$$\left(\frac{g_{h\mathcal{X}\overline{\mathcal{X}}}}{g_{h\mathcal{X}\overline{\mathcal{X}}}^{\mathrm{SM}}}\right)^2 = \cos^2\alpha, \quad \left(\frac{g_{H\mathcal{X}\overline{\mathcal{X}}}}{g_{H\mathcal{X}\overline{\mathcal{X}}}^{\mathrm{SM}}}\right)^2 = \sin^2\alpha, \tag{8.36}$$

where $\mathcal{X}$ refers to a quark, lepton or gauge boson final state. For the loop-induced processes, the effective squared couplings are defined as [57]

$$\left(\frac{g_{h\mathcal{Y}\overline{\mathcal{Y}}}}{g_{h\mathcal{Y}\overline{\mathcal{Y}}}^{\mathrm{SM}}}\right)^2 = \frac{\Gamma_{h\to\mathcal{Y}\overline{\mathcal{Y}}}}{\Gamma_{h\to\mathcal{Y}\overline{\mathcal{Y}}}^{\mathrm{SM}}} = \cos^2\alpha, \quad \left(\frac{g_{H\mathcal{Y}\overline{\mathcal{Y}}}}{g_{H\mathcal{Y}\overline{\mathcal{Y}}}^{\mathrm{SM}}}\right)^2 = \frac{\Gamma_{H\to\mathcal{Y}\overline{\mathcal{Y}}}}{\Gamma_{H\to\mathcal{Y}\overline{\mathcal{Y}}}^{\mathrm{SM}}} = \sin^2\alpha, \tag{8.37}$$

where $\mathcal{Y}\overline{\mathcal{Y}} \in (\gamma\gamma, Z\gamma, gg, ggZ)$. Thus, a mixing between the interaction eigenstates modifies the branching ratios of h/H into SM final states.

For the two physical scalars (h, H), the signal strengths are given by [456]

$$\mu_h = \frac{\Gamma_h^{\mathrm{SM}}\cos^4\alpha}{\Gamma_h^{\mathrm{SM}}\cos^2\alpha + \Gamma_{h\to\overline{\psi}\psi} + \Gamma_{h\to HH}}, \tag{8.38}$$

$$\mu_H = \frac{\Gamma_H^{\mathrm{SM}}\sin^4\alpha}{\Gamma_H^{\mathrm{SM}}\sin^2\alpha + \Gamma_{H\to\overline{\psi}\psi} + \Gamma_{H\to hh}}. \tag{8.39}$$

In the absence of invisible and cross Higgs decay modes, μ_h and μ_H scale as $\cos^2 \alpha$ and $\sin^2 \alpha$ respectively. However, if these modes are kinematically allowed, they will suppress the h/H signal strengths with respect to the SM expectation.

8.4 Likelihoods

We adopt a frequentist approach and perform scans of the 7D model parameter space using the `Diver_v1.0.4` [489] package.[4] The combined log-likelihood function for our global fit is

$$\ln \mathcal{L}(\boldsymbol{\theta}) = \ln \mathcal{L}_{\Omega h^2}(\boldsymbol{\theta}) + \ln \mathcal{L}_{\mathrm{DD}}(\boldsymbol{\theta}) + \ln \mathcal{L}_{v_c/T_c}(\boldsymbol{\theta})$$
$$+ \ln \mathcal{L}_{\mathrm{EWPO}}(\boldsymbol{\theta}) + \ln \mathcal{L}_{\mathrm{HB}}(\boldsymbol{\theta}) + \ln \mathcal{L}_{\mathrm{HS}}(\boldsymbol{\theta}), \qquad (8.40)$$

where

- $\ln \mathcal{L}_{\Omega h^2}(\boldsymbol{\theta})$: log-likelihood for the *Planck* measured DM relic density, see subsection 8.4.1;

- $\ln \mathcal{L}_{\mathrm{DD}}(\boldsymbol{\theta})$: log-likelihood for the direct detection limit from the PandaX-II experiment, see subsection 8.4.2;

- $\ln \mathcal{L}_{v_c/T_c}(\boldsymbol{\theta})$: log-likelihood for the EWBG constraint, see subsection 8.4.3;

- $\ln \mathcal{L}_{\mathrm{EWPO}}(\boldsymbol{\theta})$: log-likelihood for the electroweak precision observables (EWPO) constraint, see subsection 8.4.4;

- $\ln \mathcal{L}_{\mathrm{HB}}(\boldsymbol{\theta})$: log-likelihood for the direct Higgs searches performed at the LEP, Tevatron and the LHC, see subsection 8.4.5;

- $\ln \mathcal{L}_{\mathrm{HS}}(\boldsymbol{\theta})$: log-likelihood for the Higgs signal strength and mass measurements at the Tevatron and the LHC, see subsection 8.4.5.

The parameter $\boldsymbol{\theta} = (m_H, s_0, \mu_3, \lambda_S, \alpha, m_\psi, g_S)$ denotes the free parameters of the model. Our choice for the free parameter ranges and priors is summarised in Table 8.1.

8.4.1 Relic density likelihood

We impose the relic density constraint as an *upper* limit by using a one-sided Gaussian likelihood function, i.e., we require the parameter points to satisfy

$$f_{\mathrm{rel}} = \frac{\Omega_\psi}{\Omega_{\mathrm{DM}}} \leq 1, \qquad (8.41)$$

where $\Omega_{\mathrm{DM}} h^2 = 0.1188$ [75]. A theoretical uncertainty of 5% is added in quadrature with the *Planck* measured uncertainty. This can potentially arise from the uncertainties in the relic density calculations in `microMEGAs`.

---

[4] http://diver.hepforge.org

Parameter	Minimum	Maximum	Prior
m_H	10 GeV	10 TeV	log
s_0	-1 TeV	1 TeV	flat
μ_3	-1 TeV	1 TeV	flat
λ_S	10^{-3}	10	log
α	$-\pi$	π	flat
m_ψ	10 GeV	10 TeV	log
g_S	10^{-3}	10	log

Table 8.1: Ranges and priors for the free parameters of our model.

8.4.2 Direct detection likelihood

In our model, the SI DM-nucleon cross-section is given by

$$\sigma_{\text{SI}}^{\psi N} = \frac{\mu_{\psi N}^2}{\pi} \left(\frac{g_S \sin\alpha \cos\alpha}{v_0} \right)^2 \left(\frac{1}{m_h^2} - \frac{1}{m_H^2} \right)^2 m_N^2 f_N^2, \tag{8.42}$$

where $N \in (p, n)$, $\mu_{\psi N} = m_\psi m_N / (m_\psi + m_N)$ is the DM-nucleon reduced mass, $m_N = 939$ MeV and $f_N = 0.3$ [324].

Currently, the best upper limit on the SI DM-nucleon cross-section comes from the PandaX-II experiment [19]. To impose PandaX-II limits on the model parameter space, we use a one-sided Gaussian likelihood function, i.e., we require the parameter points to satisfy

$$\sigma_{\text{SI}}^{\text{eff}} \leq \sigma_{\text{PandaX-II}}, \tag{8.43}$$

where $\sigma_{\text{PandaX-II}}$ is the 90% C.L. upper limit from the PandaX-II experiment and

$$\sigma_{\text{SI}}^{\text{eff}} = \begin{cases} \sigma_{\text{SI}}^{\psi N} f_{\text{rel}}, & f_{\text{rel}} < 1, \\ \sigma_{\text{SI}}^{\psi N}, & f_{\text{rel}} \geq 1, \end{cases} \tag{8.44}$$

is the effective SI DM-nucleon cross-section. The scaling by f_{rel} is done to suppress signals when $f_{\text{rel}} < 1$. In regions of the model parameter space where $f_{\text{rel}} > 1$, parameter points are ruled out by the relic density constraint.

A theoretical uncertainty of 5% is included in our calculations. This can arise from the uncertainties associated with the nuclear and astrophysical parameters. For more details, see Ref. [184].

8.4.3 EWBG likelihood

To find regions in the model parameter space where a successful EWBG is viable, we use a one-sided Gaussian likelihood function and require the parameter points to satisfy

$$\frac{v_c}{T_c} \geq 0.6 \tag{8.45}$$

as a conservative limit. A 5% uncertainty on the resulting v_c/T_c values is assumed to obtain a smooth likelihood function. The actual uncertainty can be much larger as the value of v_c/T_c required to facilitate EWBG is not yet settled [238, 407, 428].

In addition to finding parameter points that satisfy Eq. (8.45), we also perform several checks to guarantee a stable minimum of the effective potential. Specifically, we exclude parameter points if they exhibit any of the following three features.

1. *Incorrect minimum at $T = 0$* occurs when the electroweak vacuum (v_0, s_0) is not the true minimum of the potential at $T = 0$.

2. *Runaway directions in the potential* occur when the ϕ and S field values in the symmetric or broken phase are too large, or if the potential is unbounded from below in the general ϕ and S directions, i.e., when $\lambda_{\Phi S} \leq -2\sqrt{\lambda_\Phi \lambda_S}$ in Eq. (8.14).

3. *Non-perturbative couplings* when $|\lambda_\Phi| \geq 4\pi$ or $|\lambda_{\Phi S}| \geq 4\pi$. In this case, our 1-loop treatment of the effective potential is no longer reliable.

8.4.4   EWPO likelihood

The oblique parameters S, T and U are constrained from the global electroweak fit by computing the difference between the oblique corrections determined from the electroweak data and those arising from a SM reference point at fixed top quark and Higgs boson mass. In this definition, a non-zero value for the oblique parameters point towards a sign of new physics.

Using the SM reference as $m_h^{\text{ref}} = 125\,\text{GeV}$ and $m_t^{\text{ref}} = 173\,\text{GeV}$, the most recent global electroweak fit gives [476]

$$\Delta S = 0.05 \pm 0.11, \quad \Delta T = 0.09 \pm 0.13, \quad \Delta U = 0.01 \pm 0.11, \tag{8.46}$$

with the following correlation matrix

$$\rho_{ij} = \begin{pmatrix} 1 & 0.90 & -0.59 \\ 0.90 & 1 & -0.83 \\ -0.59 & -0.83 & 1 \end{pmatrix}. \tag{8.47}$$

We constrain the model parameter space from the electroweak precision observables (EWPO) by using the following likelihood function [490]

$$\ln \mathcal{L}_{\text{EWPO}}(\boldsymbol{\theta}) = -\frac{1}{2}\Delta\chi^2 = -\frac{1}{2}\sum_{i,j}(\Delta O_i - \overline{\Delta O_i})\left(\sigma^2\right)^{-1}_{ij}(\Delta O_j - \overline{\Delta O_j}), \tag{8.48}$$

where $\overline{\Delta O_i}$ denotes the central values for the shifts in Eq. (8.46), $\sigma^2_{ij} \equiv \sigma_i \rho_{ij} \sigma_j$ is the covariance matrix, ρ_{ij} is the correlation matrix in Eq. (8.47) and σ_i are the associated errors in Eq. (8.46).

8.4.5 Higgs search likelihood

We constrain the model parameter space from the direct Higgs searches performed at the LEP, Tevatron and the LHC using the `HiggsBounds_v4.3.1` [477] package. From the model predictions for the two scalar masses, total decay widths, branching ratios and effective squared couplings defined in Eqs. (8.36) and (8.37), it computes and compares the predicted signal rates for the search channels considered in multiple experimental analyses. By comparing the predicted signal rates against the expected and observed cross-section limits from the direct Higgs searches, we determine whether or not a given parameter point is excluded at 95% C.L.

We also constrain the model parameter space from the Higgs signal strength and mass measurements performed at the Tevatron and the LHC using the `HiggsSignals_v1.4.0` [478] package. Assuming a Gaussian p.d.f. for the two scalar masses, we calculate the signal strength chi-square χ_μ^2 using the *mass-centered* method. In this method, the signal strengths in Eqs. (8.38) and (8.39) are compared against the best-fit signal strength at the model predicted Higgs mass from multiple experimental analyses. The signal rates for the two scalars are combined if the signals cannot be resolved by a given experimental analysis. Finally, the computed χ_μ^2 is used to define the Higgs signal strength log-likelihood as

$$\ln \mathcal{L}_{\mathrm{HS}}(\boldsymbol{\theta}) = -\frac{1}{2}\chi_\mu^2. \tag{8.49}$$

Thus, a large χ_μ^2 indicates a large deviation between the model predicted signal strength and the best-fit value for a fixed Higgs boson mass.

8.5 Preliminary results

We present results in the form of 1D and 2D profile likelihood plots. For a model parameter θ_i where $i = (1, \ldots, 7)$, a 1D profile likelihood $\mathcal{L}_p(\theta_i)$ is defined as

$$\mathcal{L}_p(\theta_i) \equiv \max_{\{\theta_j \mid j \neq i\}} \mathcal{L}(\boldsymbol{\theta}). \tag{8.50}$$

Thus, $\mathcal{L}_p(\theta_i)$ is a function of θ_i only, i.e., all other parameters are *profiled out*. Similarly, a 2D profile likelihood $\mathcal{L}_p(\theta_i, \theta_j)$ is defined as

$$\mathcal{L}_p(\theta_i, \theta_j) \equiv \max_{\{\theta_k \mid k \neq i, \ k \neq j\}} \mathcal{L}(\boldsymbol{\theta}). \tag{8.51}$$

Thus, $\mathcal{L}_p(\theta_i, \theta_j)$ is a function of θ_i and θ_j only. Using Eqs. (8.50) and (8.51), we can define a profile likelihood ratio [491] as

$$\Lambda(\theta_i) = \frac{\mathcal{L}_p(\theta_i)}{\mathcal{L}(\hat{\boldsymbol{\theta}})}, \quad \Lambda(\theta_i, \theta_j) = \frac{\mathcal{L}_p(\theta_i, \theta_j)}{\mathcal{L}(\hat{\boldsymbol{\theta}})}, \tag{8.52}$$

where $\hat{\boldsymbol{\theta}} \equiv (\hat{\theta}_1, \ldots, \hat{\theta}_n)$ is the best-fit point, i.e., a parameter point which maximises the combined likelihood function $\mathcal{L}(\boldsymbol{\theta})$. Using Wilks' theorem [492], Eq. (8.52) can be used to construct 1σ (2σ) contours corresponding to $\sim 68.3\%$ (95.4%) C.L. regions.

In the following subsections, we present our model results in the form of 1D and 2D profile likelihood plots. These are generated using the `pippi_v2.0` [493] package.

8.5.1 EWBG only

We start by presenting results from a 7D scan of the model parameter space using *only* the EWBG constraint. Thus, the combined log-likelihood function is given by

$$\ln \mathcal{L}(\boldsymbol{\theta}) = \ln \mathcal{L}_{v_c/T_c}(\boldsymbol{\theta}), \tag{8.53}$$

where $\ln \mathcal{L}_{v_c/T_c}(\boldsymbol{\theta})$ is defined in subsection 8.4.3. The resulting 2D profile likelihood plots are shown in Fig. 8.2. In the dark blue regions where the profile likelihood ratio $\Lambda \equiv \mathcal{L}/\mathcal{L}_{\max} = 1$, a successful EWBG is viable. To understand these results, it is instructive to go through each panel one-by-one.

1. (m_H, s_0) plane: For $m_H \lesssim 1.6\,\text{TeV}$ and all values of s_0, some combination of the 5 profiled out parameters, namely $(\mu_3, \lambda_S, \alpha, m_\psi, g_S)$ give $v_c/T_c \geq 0.6$ and maximise the v_c/T_c log-likelihood, i.e., $\Lambda = 1$ everywhere. Due to the dependence of s_0 in Eq. (8.21), large values of $|s_0|$ should be invalidated by the runaway condition $\lambda_{\Phi S} \leq -2\sqrt{\lambda_\Phi \lambda_S}$ and non-perturbative coupling $|\lambda_{\Phi S}| \geq 4\pi$. However, this can be circumvented by choosing a small value for λ_S as its contribution in Eq. (8.21) appears as $-\lambda_S s_0^2$. In addition, small values of μ_3 can also aid in keeping $|\lambda_{\Phi S}| < 4\pi$. Thus, for $m_H \lesssim 1.6\,\text{TeV}$, large values of $|s_0|$ can facilitate EWBG.

   For $m_H \gtrsim 1.6\,\text{TeV}$ and $|s_0| \gtrsim 50\,\text{GeV}$, the white region is disfavoured ($\Lambda = 0$) as it leads to $|\lambda_{\Phi S}| \geq 4\pi$. This is expected as the contribution of m_H in Eq. (8.21) is dominant at large values of m_H. With large $|s_0|$, no choice of μ_3, λ_S and α can keep $|\lambda_{\Phi S}| < 4\pi$. In fact, the requirement $|\lambda_{\Phi S}| < 4\pi$ translates into an upper limit on m_H as a function of s_0. Using Eq. (8.21), we get

   $$f(m_H, s_0, \mu_3, \lambda_S, \alpha) < 8\pi v_0^2, \tag{8.54}$$

   where

   $$f(m_H, s_0, \mu_3, \lambda_S, \alpha) = \frac{v_0}{s_0}(m_H^2 - m_h^2)\sin 2\alpha + 4(m_h^2 \sin^2 \alpha + m_H^2 \cos^2 \alpha + \mu_3 s_0 - 2\lambda_S s_0^2).$$

   For a fixed m_H and s_0, Eq. (8.54) has 3 degrees of freedom. As μ_3, λ_S and α are profiled over in the plot, it is difficult to predict the exact functional dependence of the upper limit on m_H as a function of s_0. This upper limit becomes weaker as $|s_0|$ increases. For $m_H \gtrsim 5\,\text{TeV}$, a successful EWBG is viable as long as $|s_0| \lesssim 50\,\text{GeV}$.
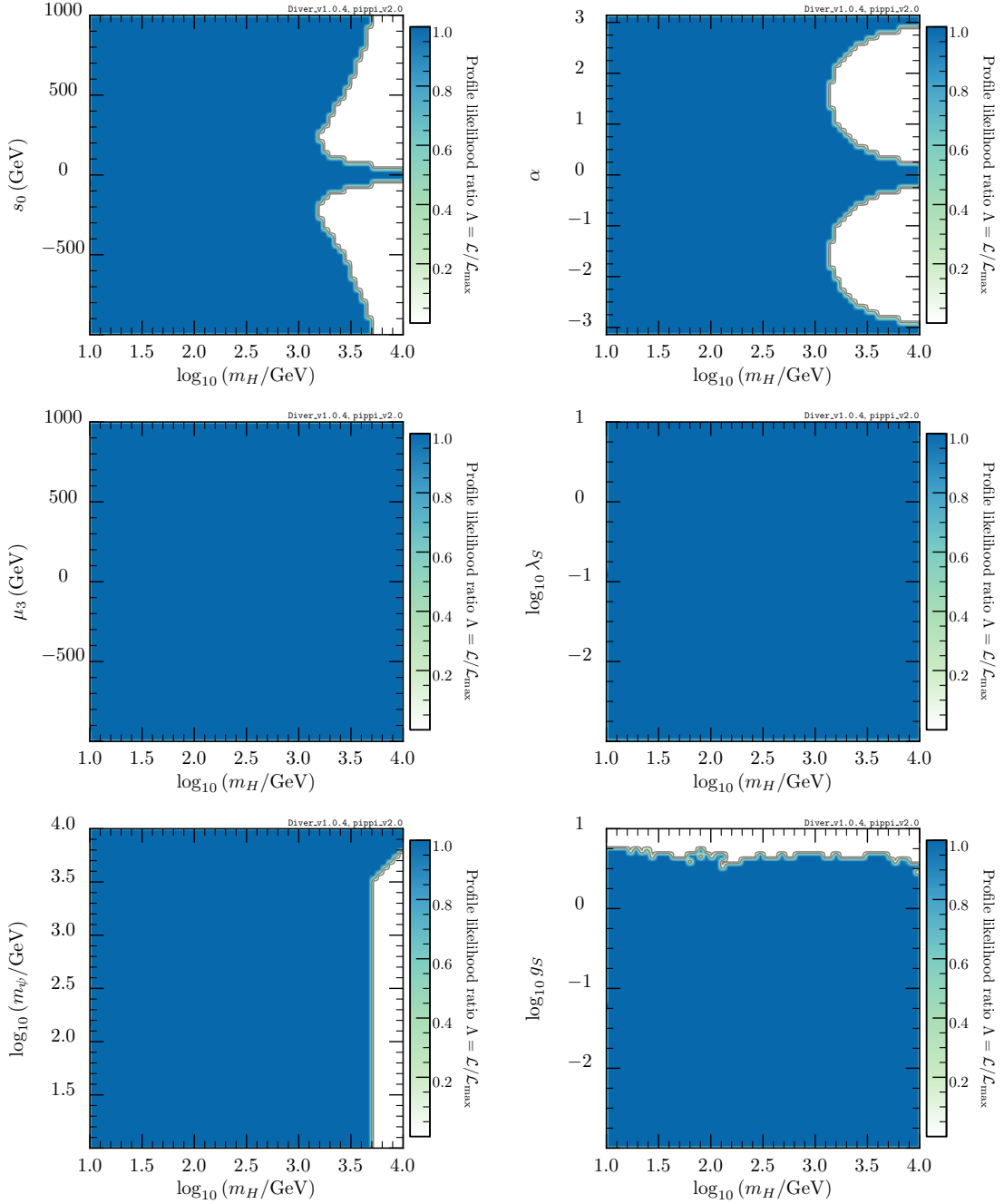
Figure 8.2: 2D profile likelihood plots from a 7D scan of the model parameter space using *only* the electroweak baryogenesis (EWBG) constraint. In regions where $\Lambda \equiv \mathcal{L}/\mathcal{L}_{\max} = 1$, a successful EWBG is viable, i.e., $v_c/T_c \geq 0.6$. The contour lines mark out the 1σ (68.3%) and 2σ (95.4%) C.L. regions.

2. (m_H, α) plane: Similar to the (m_H, s_0) plane for $m_H \lesssim 1.6\,\mathrm{TeV}$, some combination of the profiled out parameters in the (m_H, α) plane gives $v_c/T_c \geq 0.6$ at all values of α. However, when $m_H \gtrsim 1.6\,\mathrm{TeV}$ and $|\alpha| \neq 0, \pi$, the Higgs quartic coupling λ_Φ becomes non-perturbative as expected from Eq. (8.19). The requirement $|\lambda_\Phi| < 4\pi$ translates into an upper limit on m_H as a function of α. Using Eq. (8.19), we get

$$m_H^2 \sin^2 \alpha < 8\pi v_0^2 - m_h^2 \cos^2 \alpha. \tag{8.55}$$

When $|\alpha| = 0, \pi$, the above condition is satisfied at all values of m_H. On the other hand, when $|\alpha| = \pi/2$, Eq. (8.55) imposes an upper limit of $m_H \lesssim 1.23$ TeV. As $|\alpha| \to 0, \pi$, the upper limit on m_H becomes weaker as is evident in the plot.

3. (m_H, μ_3) and (m_H, λ_S) planes: In these planes, all values of m_H, μ_3, λ_S and suitable choices for the profiled out parameters give $v_c/T_c \geq 0.6$. Thus, the two planes are completely unconstrained by EWBG. In other words, the v_c/T_c likelihood depends weakly on the values of μ_3 and λ_S. This behaviour is expected from their dependency in Eq. (8.21). For instance, at large values of μ_3 or λ_S which would give $|\lambda_{\Phi S}| \geq 4\pi$ or $\lambda_{\Phi S} \leq -2\sqrt{\lambda_\Phi \lambda_S}$, small values of s_0 can be chosen to avoid these situations. Thus, there is no upper limit on m_H at fixed values of μ_3 or λ_S.

4. (m_H, m_ψ) plane: For $m_H \lesssim 5$ TeV, all values of m_ψ give $v_c/T_c \geq 0.6$. As m_ψ does not enter directly in Eqs. (8.19) and (8.21), the v_c/T_c likelihood is weakly dependent on the values of m_ψ. This is expected as the contribution from m_ψ in the effective potential appears only at one-loop order.

For $m_H \gtrsim 5$ TeV and $m_\psi \lesssim 3.2$ TeV, no combination of the profiled out parameters can keep $|\lambda_{\Phi S}| < 4\pi$. On the other hand, when $m_\psi \gtrsim 3.2$ TeV, the positive contribution from H to the effective potential is cancelled out by the negative contribution from ψ. Thus, the high mass region gives $v_c/T_c \geq 0.6$ and $\Lambda \simeq 1$.

5. (m_H, g_S) plane: For $g_S \lesssim 5.62$, all values of m_H and profiled out parameters can maximise the v_c/T_c likelihood. However, values of $g_S \gtrsim 5.62$ lead to runaway directions in the potential as the contribution from g_S in the 1-loop correction becomes large. This pushes the broken phase minimum too far away from the origin which results in a suppressed vacuum decay probability.

In summary, a successful EWBG is viable in all parts of the model parameter space provided $g_S \lesssim 5.62$. For the remaining parameters, namely $(m_H, s_0, \mu_3, \lambda_S, \alpha, m_\psi)$, the profile likelihood ratio Λ is roughly flat and equal to 1 at all parameter values. For $m_H \gtrsim 5$ TeV, values of $|s_0| \lesssim 50$ GeV, $|\alpha| \simeq 0, \pi$ and $m_\psi \gtrsim 3.2$ TeV can facilitate EWBG.

8.5.2 Global fit

With some intuition on the choice of free parameter values that can facilitate EWBG, we perform a global fit of the model using the combined log-likelihood function given in Eq. (8.40). The 2D and 1D profile likelihood plots are shown in Figs. 8.3 and 8.4 respectively.

The details of the best-fit point are summarised in Table 8.2, and is shown in the 1D (2D) profile likelihood plots as a black (red) star. It is compatible with the constraints from the *Planck* measured DM relic density, direct detection limit from the PandaX-II

m_H (GeV)	s_0 (GeV)	μ_3 (GeV)	λ_S	α	m_ψ (GeV)	g_S
95.88	−242.92	−11.20	5.88×10^{-2}	−0.72	45.52	3.29×10^{-2}

Table 8.2: Best-fit point from a global fit of our model.

experiment, EWBG, EWPO and Higgs searches at colliders. From the best-fit point in Table 8.2, we can make the following observations.

- The best-fit value for m_H lies outside the mass range of $[110, 135]$ GeV. Thus, only the h signal strength is taken into account in the Higgs signal strength analysis. As $|\alpha| \ll \pi/2$, h is predominately a SM-like Higgs boson with $m_h = 125$ GeV, whereas H is a singlet. The $h \to \overline{\psi}\psi$ decay mode is kinematically allowed as $m_\psi < m_h/2$. Although, this decay reduces the signal strength of h, the decay rate is relatively small as $g_S = 3.29 \times 10^{-2}$, see Eq. (8.25). Thus, the h signal strength is in good agreement with the observed one for a 125 GeV Higgs boson. In addition, the best-fit point is compatible with the direct Higgs searches and EWPO constraint.

- The best fit value for the fermion DM mass is $m_\psi = 45.52$ GeV $\sim m_H/2$. Being close to the second Higgs resonance, a small value for g_S is compatible with the *Planck* and direct detection limits. This is indeed the case as $g_S = 3.29 \times 10^{-2}$.

- The best-fit value for μ_3 and λ_S is small compared to s_0. Due to the dependence of these parameters in Eq. (8.21), a successful EWBG is viable as evident in Fig. 8.2. At the best-fit point, $T_c \simeq 120$ GeV and $v_c/T_c \simeq 1.23$.

It is instructive to go through the results in each panel of Fig. 8.3 one-by-one.

1. (m_H, s_0) and (m_H, α) planes: These planes can be studied in 4 separate mass regions.

    a) $m_H \lesssim m_h/2 = 62.5$ GeV: In this mass region, $h \to HH$ decay is kinematically allowed and is the dominant decay channel of h for all values of α. Thus, the signal strength of h, namely μ_h in Eq. (8.38), is reduced with respect to the SM expectation. This gives a large χ^2_μ in Eq. (8.49) when μ_h is compared against the best-fit value for $m_h \lesssim 62.5$ GeV. As we will see below, the contribution from the H signal strength is only taken into account when $m_H \in [110, 135]$ GeV. When m_H is outside this range, its signal strength is completely ignored in the Higgs signal strength analysis. Thus, Eq. (8.49) disfavours all values of $|s_0|$ and $|\alpha|$ in this mass region. For $|\alpha| \neq 0, \pi$, the region is also disfavoured by the direct Higgs searches performed at the LEP experiment.

    b) $m_H \in [m_h/2, 110$ GeV$]$: In this mass region, the $h \to HH$ decay is kinematically forbidden, and all values of $|s_0|$ and α fall inside the 1σ contour. Although the $h \to \overline{\psi}\psi$ decay can reduce the h signal strength with respect to the SM

expectation, profiling over the remaining parameters (including m_ψ) allow us to turn off the invisible decay mode, for instance, by choosing $m_\psi > m_h/2$ such that $h \to \overline{\psi}\psi$ decay is kinematically forbidden.

c) $m_H \in [110, 135]\,\text{GeV}$: This mass region appears in all panels as a vertical band with $\Lambda \simeq 1$. It is precisely where the H signal strength is taken into account. Specifically, the signal strength of the two scalars is combined and compared against the best-fit value at two *different* scalar masses. The chi-square of the two scalars is summed over. Although $h \to HH$ decay is kinematically forbidden in this mass region, $h \to \overline{\psi}\psi$ and $H \to \overline{\psi}\psi$ decays can reduce μ_h and μ_H if these modes are kinematically allowed. By profiling over m_ψ and other parameters, the invisible decay modes can be switched off. Thus, all values of $|s_0|$ and α in this band give $\Lambda \simeq 1$.

The effect of including a new scalar in the Higgs signal strength calculation is most noticeable when $m_H \simeq m_h = 125\,\text{GeV}$. In this case, the combined signal strength is compared against the best-fit value for a $125\,\text{GeV}$ Higgs boson. Thus, all values of α are consistent with the observed Higgs signal strengths as one of the two scalars can play the role of a SM-like Higgs boson, i.e., h is a SM-like Higgs when $|\alpha| = 0, \pi$, whereas H is a SM-like Higgs when $|\alpha| = \pi/2$. A scenario with two scalars and a non-zero mixing between them gives a better fit to the observed Higgs signal strengths than simply having a single SM-like Higgs boson.

d) $m_H \gtrsim 135\,\text{GeV}$: In analogy with the $m_H \lesssim m_h/2$ region, the contribution of the second scalar H in the Higgs signal strength analysis is completely ignored in this mass region. Values of $|\alpha| = 0, \pi$ are required for the parameter points to be compatible with the EWPO constraint, see Eq. (8.35). For $m_H \gtrsim 4\,\text{TeV}$, the allowed parameter space is determined by the EWBG constraint as in Fig. 8.2. Not only is this mass region disfavoured by the EWPO constraint, it also leads to $|\lambda_{\Phi S}| \geq 4\pi$ or $|\lambda_\Phi| \geq 4\pi$.

2. (m_H, μ_3) and (m_H, λ_S) planes: In these planes, all values of μ_3 and λ_S for $m_H \lesssim m_h/2$ are disfavoured by the direct Higgs searches performed at the LEP experiment, and the Higgs signal strength measurements. Above $m_h/2$, the contribution from the second scalar H provides a better fit to the observed Higgs signal strengths. At large values of m_H, all values of μ_3 and λ_S are disfavoured by the EWPO constraint.

3. (m_H, m_ψ) plane: The observed Higgs signal strengths and direct Higgs searches performed at the LEP experiment disfavour all values of m_ψ for $m_H \lesssim m_h/2$. Above $m_h/2$, the region is constrained by the *Planck* measured relic density and PandaX-II limits. For $m_\psi \lesssim 32\,\text{GeV}$, all values of m_H give $f_{\text{rel}} \equiv \Omega_\psi/\Omega_{\text{DM}} > 1$. At low DM masses, the fermion DM can only annihilate into light SM final states which gives
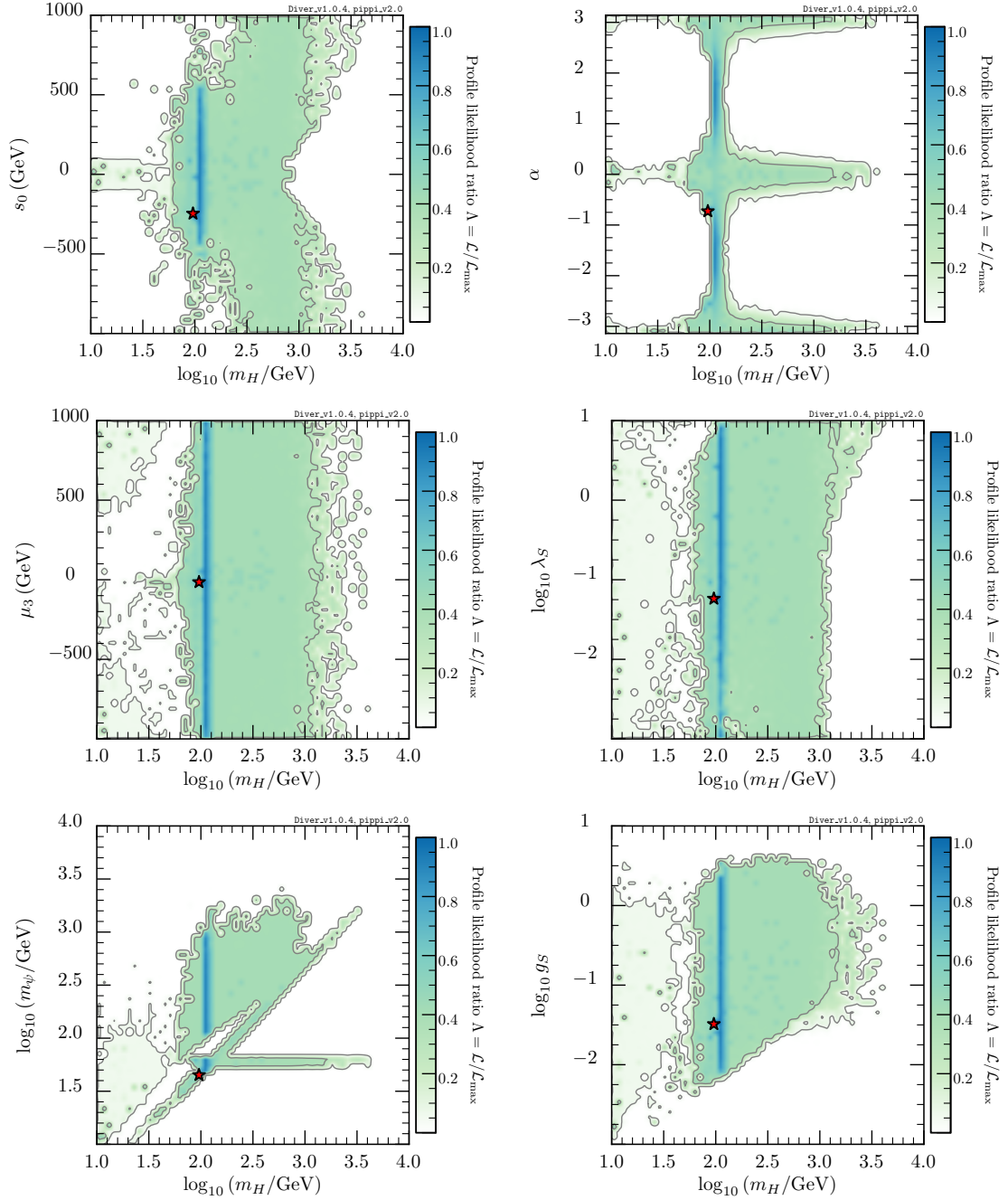
Figure 8.3: 2D profile likelihood plots from a global fit of our model. The best-fit point is shown by a red star in each panel. The contour lines mark out the 1σ (68.3%) and 2σ (95.4%) C.L. regions.

$f_{\rm rel} > 1$. When $m_\psi \simeq m_h/2$, all values of m_H up to $\sim 4\,{\rm TeV}$ are allowed by the relic density and PandaX-II limits; this region appears in the plot as a horizontal band. In this band, g_S can be sufficiently small to allow for $f_{\rm rel} \leq 1$ and remain compatible with the PandaX-II limits.

For $m_\psi \in [m_h/2, m_H/2]$, the region is disfavoured by either the *Planck* measured relic density or PandaX-II limits. This result is expected from an incompatibility between small values of g_S which are favoured by the PandaX-II limit (as this leads

to a smaller DM-nucleon cross-section $\sigma_{\text{SI}}^{\psi N}$) but disfavoured by the relic density constraint (as this leads to $f_{\text{rel}} > 1$) and vice versa.

The diagonal band in the (m_H, m_ψ) plane appears at the second resonance $m_\psi \simeq m_H/2$. All parameter points in this band are allowed by the relic density and PandaX-II limits. As g_S is profiled over, small values of g_S give $f_{\text{rel}} \leq 1$ and remain compatible with the PandaX-II limits. On the other hand, when $m_H \gtrsim 4\,\text{TeV}$, parameter points are disfavoured by the EWPO constraint. This region also leads to $|\lambda_{\Phi S}| \geq 4\pi$ as is evident in Fig. 8.2.

4. (m_H, g_S) plane: For $m_H \lesssim m_h/2$, all values of g_S are disfavoured by the direct Higgs searches performed at the LEP experiment. Above $m_h/2$, a lower limit on g_S comes from the relic density constraint as small values of g_S lead to an overabundance of the fermion DM. This limit becomes weaker as m_H increases. For $m_H \gtrsim 4\,\text{TeV}$, the coupling $\lambda_{\Phi S}$ becomes non-perturbative. On the other hand, values of $g_S \gtrsim 3.2$ are disfavoured for all values of m_H by the EWBG constraint as it leads to runaway directions in the potential. This result is also evident in Fig. 8.2.

In Fig. 8.4, we show the 1D profile likelihoods for all 7 free parameters. In each panel, the combined log-likelihood function in Eq. (8.40) is maximised by profiling over the remaining parameters. It is evident that the combined constraint places an upper limit on m_H, m_ψ and g_S, namely $m_H \lesssim 5\,\text{TeV}$, $m_\psi \lesssim 3.2\,\text{GeV}$ and $g_S \lesssim 3.2$.

8.5.3 Gravitational wave signals

The computation of the GW signals require a detailed study of the dynamics of the phase transition (PT). Luckily, the analysis of bubble nucleation is to some extent generic, and the steps required are always similar, albeit using a different potential. The main difficulty with our general scalar potential is that the transition always involve both scalar fields, and finding a correct tunnelling path in the 2D scalar field space is always necessary. We tackle this problem in the exact same way as we did in chapter 7. In particular, we use the method described there to find the appropriate tunnelling path and bubble solutions that drive the transition in each case.

The main drawback of this calculation is that it is computationally expensive when compared to all other constraints discussed in section 8.3. Thus, we first identify interesting points in the model parameter space using a global fit and check the detailed PT dynamics and GW signals afterwards.

For each viable point, we compute the tunnelling path and corresponding action as in chapter 7. In turn, this gives us the vacuum decay probability. This is used to find the nucleation temperature at which a bubble on average is nucleated in every horizon volume. We find that around 80% of the interesting points are excluded as the decay probability
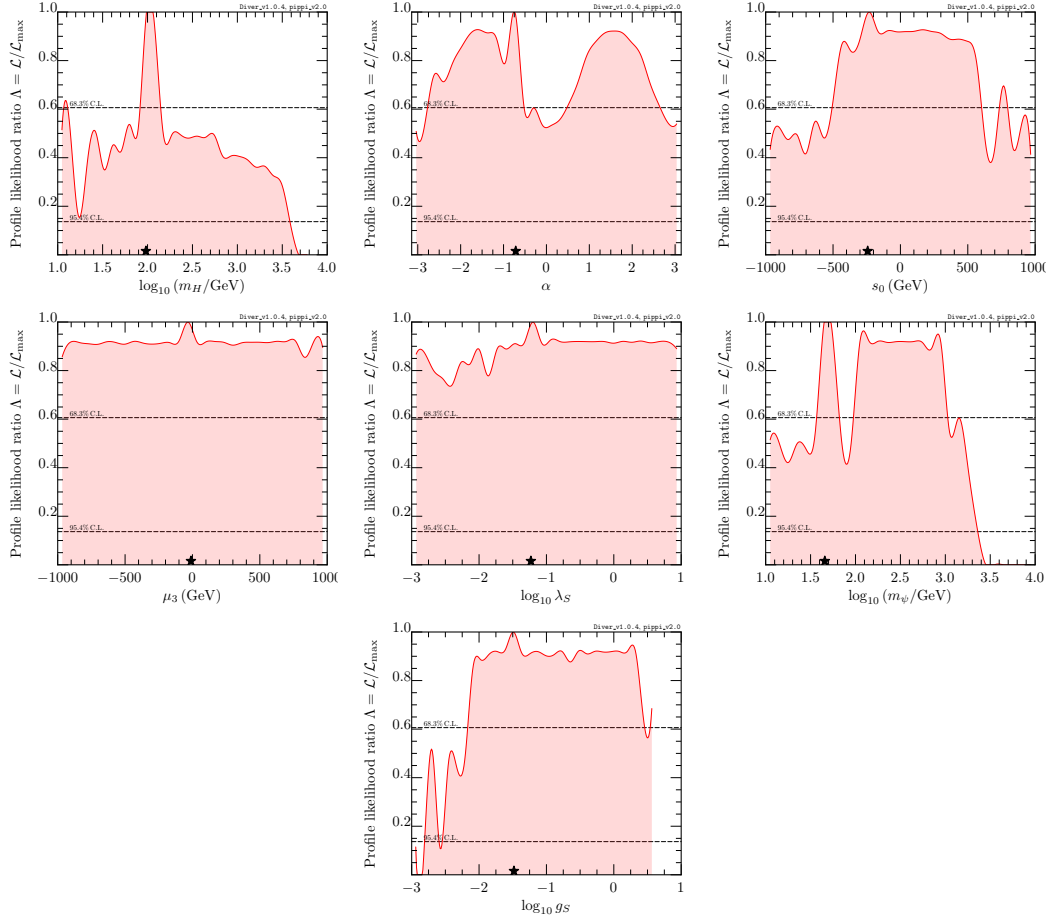
Figure 8.4: 1D profile likelihood plots for the free model parameters from our global fit. The best-fit point is shown by a black star in each panel.

is too suppressed and the tunnelling does not proceed. This result is not surprising as the potential depends on many parameters. The extended parameter space with respect to the scalar singlet model in chapter 7 allows for the formation of a large tree-level barrier, which can persist even at $T = 0$ and suppress the vacuum decay probability.

For the viable parameter points, we calculate the ratio of the released latent heat to the energy density of the plasma background (α) and the inverse time of the phase transition (β/H) [317, 320]. Using the expressions for the GW spectra from three main sources in chapter 7, we compute the total GW spectra as a function of the signal frequency. Finally, the GW spectra are compared with the current sensitivity bands of LIGO [450, 494, 495], the European Pulsar Timing Array (EPTA) [496], and detection prospects of LISA [448], DECIGO, BBO [449] and the Square Kilometre Array (SKA) [497].

In Fig. 8.5, we show the GW spectra of viable parameter points and their dependence on the transition temperature T_*. It is easier to find a strong GW signal from the viable points with a significant barrier as it postpones the tunnelling to lower temperatures. This relation is clear from Fig. 8.6 which shows the same result and its dependence on v_*/T_*. Again, larger values of v_*/T_* lead to a stronger phase transition and a stronger GW signal.
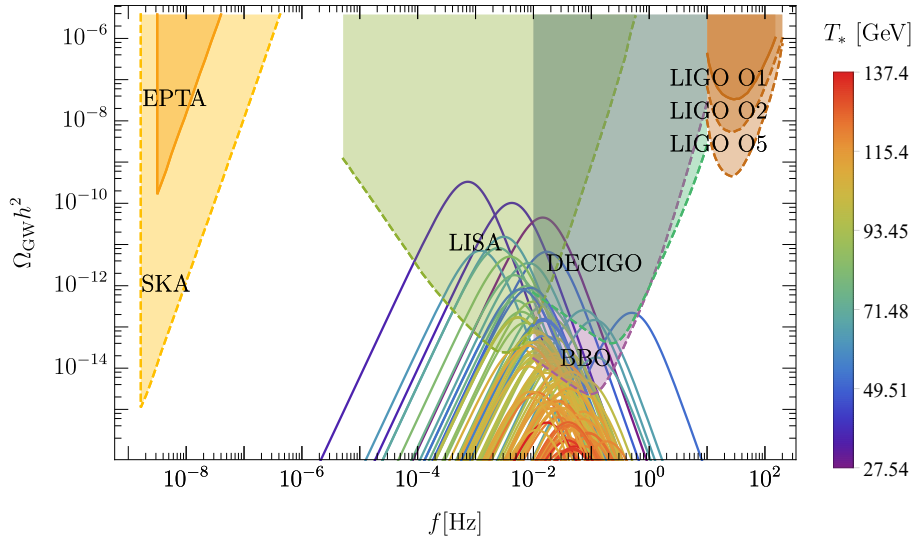
Figure 8.5: Gravitational wave (GW) spectra of viable points and their dependence on the transition temperature T_*. Current sensitivity bands of LIGO and the European Pulsar Timing Array (EPTA), as well as detection prospects of LISA, DECIGO, BBO and the Square Kilometre Array (SKA) are also shown for comparison.
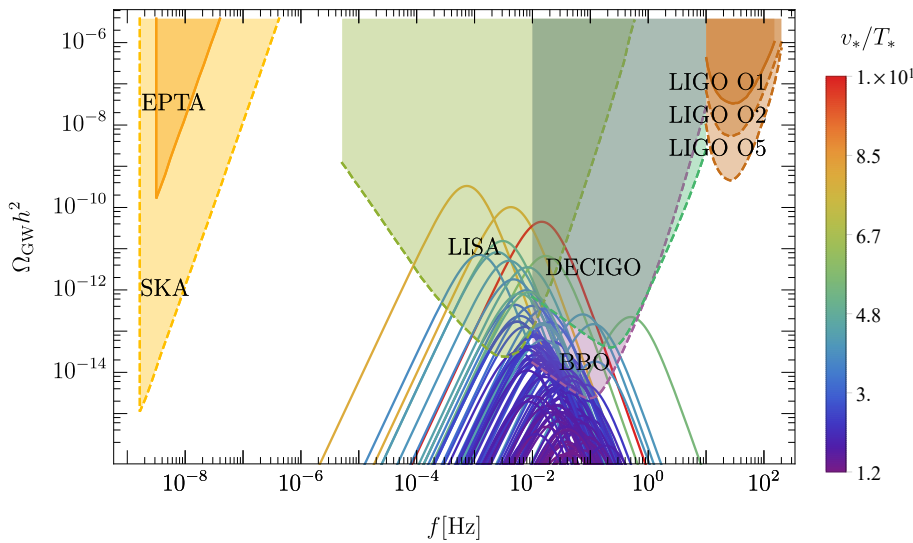
Figure 8.6: GW spectra of viable points and their dependence on v_*/T_*. The current sensitivity bands and detection prospects of GW experiments are same as in Fig. 8.5.

In particular, viable points with a small T_* lead to stronger GW signals and better prospects for discovery at future GW experiments.

From Figs. 8.5 and 8.6, we can see that the GW spectra of viable points are within reach of LISA, DECIGO and BBO experiment. On the other hand, the current LIGO experiment is insensitive to the GW spectra from the phase transition. This also agrees with our findings in chapter 7, since LIGO is particularly sensitive to high frequency signals from sources such as binary black holes and neutron stars, etc. Although EPTA and SKA can probe extremely low frequencies, the GW spectra of viable points peak at

frequencies that are higher than the expected reach of EPTA and SKA.

8.6   Summary

In this chapter, we have performed the most comprehensive and up-to-date study of the extended scalar singlet model with a fermionic DM candidate. After performing a 7D scan of the model parameter space using *only* the EWBG constraint, we found regions in the model parameter space that can facilitate EWBG. From the profile likelihood plots, we showed that a successful EWBG is viable in all parts of the model parameter space provided $g_S \lesssim 5.62$. In particular, for $m_H \gtrsim 5\,\text{TeV}$, $|s_0| \lesssim 50\,\text{GeV}$, $|\alpha| \simeq 0, \pi$ and $m_\psi \gtrsim 3.2\,\text{TeV}$ are required to facilitate EWBG.

After building intuition from the EWBG results, we performed a global fit of our model using all available constraints from the *Planck* measured relic density, direct detection limits from the PandaX-II experiment, EWBG, EWPO and Higgs searches at colliders. This allowed us to constrain parts of the 7D model parameter space. In particular, we imposed an upper limit on m_H, m_ψ and g_S, namely $m_H \lesssim 5\,\text{TeV}$, $m_\psi \lesssim 3.2\,\text{TeV}$ and $g_S \lesssim 3.2\,\text{GeV}$. We also confirmed that the model could simultaneously explain (at least a part of) the observed DM abundance and baryon asymmetry.

From the viable points that satisfied all of the available constraints, we computed their GW spectra and checked the discovery prospects of the model at current or future GW experiments. In doing so, we found that the GW spectra of viable points are often within reach of LISA, DECIGO and BBO experiments. On the other hand, the LIGO experiment will be insensitive to such low-frequency signals as it operates in a much higher frequency range. The EPTA and SKA experiments are designed to probe low-frequency signals. However, the GW spectra of viable points peak in a different frequency range than those probed by EPTA and SKA. Thus, it will be difficult to observe GW signals from the phase transition in these two experiments.

Chapter 9

Global fits with GAMBIT

9.1 Introduction

In chapter 6, we studied the phenomenology of effective Higgs portal DM models. They are continuing to generate much interest in the literature [336, 472, 486, 498–511]. For instance, a global fit of a spin $0\,(1/2)$ DM model using an EFT approach was performed in Ref. [512]. A total of 14 (6) operators for the fermion (complex scalar) DM candidates were included in the study. Constraints from the WMAP measured DM relic density, limits on the SI DM-nucleon cross-section from XENON100, SD DM-nucleon cross-section from XENON10, ZEPLIN-III and SIMPLE, cosmic antiproton flux from PAMELA, cosmic gamma-ray flux from *Fermi*-LAT, mono-jet and mono-photon production plus missing energy at the Tevatron and LHC were collectively used to place limits on the effective operators.

Global fits of the real and complex scalar DM candidates in the EFT framework were performed in Ref. [513]. All dimension-6 operators consisting of DM bilinears and gauge invariant combinations of quark and gluon fields were taken into account. Constraints on the free model parameters were imposed after combining the results from *Planck*, LUX and the *Fermi*-LAT experiment. The compatibility of the DM annihilation signal with the GC gamma-ray excess was also tested in this study.

The first global study of the scalar Higgs portal model was performed in Ref. [325]; for the most recent global fit, see Ref. [326]. The best-fit model parameters were obtained after combining the relic density constraint from WMAP-7, 225 live days of XENON100 data, upper limits on the gamma-ray flux from *Fermi*-LAT based on dwarf spheroidal galaxies, and a Higgs boson candidate with a mass of 125 GeV and an invisible branching ratio no larger than 40%. The fit parameters were used to predict various final states at the LHC such as the production of a mono-*b* jet, one and two charged leptons plus missing energy. The annihilation cross-section for the gamma-ray lines and muon anomalous magnetic dipole moment (a 2-loop process in this model) was also computed.

In this chapter, we present preliminary results for the vector and Dirac fermion Higgs

portal models as obtained using the GAMBIT software. [514]. We start by giving a brief review on GAMBIT, introduce our portal models, and discuss both the physics and the implementation of various constraints in GAMBIT. After performing scans of the model parameter space, we check the consistency of our preliminary results against those obtained in chapter 6; the latter is based on Ref. [30].

9.2   GAMBIT

In the past, it was a challenging task to properly and completely weigh the sum of data relevant to a theory from many experimental sources, and make rigorous statistical statements about which models are allowed and which are not. This problem can be addressed by *global fits*: simultaneous predictions of different observables from theory, coupled with a combined statistical analysis of various experimental searches that are sensitive to them.

Many global fitting tools in the past did not offer a public framework that could be easily extended to integrate new observables, datasets and likelihoods as they become available. They also did not provide a standardised way to deal with complex interfaces to external codes for calculating specific observables or experimental likelihoods. Another difficulty lies in carrying out detailed joint statistical analysis in many-dimensional BSM parameter spaces. This often requires a full understanding of a range of theoretical calculations as well as experiments, significant coding experience, large amounts of computing resources, and careful attention to statistical as well as numerical methods [515].

Making concrete statements across a range of parameters require adopting either the Bayesian or frequentist statistical framework. Both of these approaches impose specific mathematical conditions on how to discretely sample the parameter space and combine samples to make statements about a continuous parameter range. Most global fits performed so far have assumed either Bayesian or frequentist statistics, thus discarding the additional information available from the other approach. In addition, they have only employed a single parameter sampling algorithm, despite the availability and complementarity of a wide range of relevant numerical methods.

The Global And Modular BSM Inference Tool (GAMBIT) is a new global fitting software that addresses these issues.[1] It combines extensive calculations of many observables and likelihoods in particle/astroparticle physics with a hierarchical model database. In addition to offering advanced tools for automatically building analyses of essentially any BSM model, it provides a flexible and powerful system for interfacing to external codes, inclusion of various systematic uncertainties that are handled as nuisance parameters, a suite of different statistical methods and parameter scanning algorithms, and a host of

---

[1]https://gambit.hepforge.org

other utilities designed to perform faster, safer and more easily-extendible scans in both frequentist and Bayesian statistics [514].

GAMBIT is composed of multiple modules or *Bits*. Each module can be used separately or together within GAMBIT. Currently, there are six physics modules and a scanning module `ScannerBit` [489], which directly handles the scans of the model parameter space by choosing the parameters to be sampled during a scan using either internal algorithms or external codes. The physics modules can either calculate observables and likelihoods internally or make use of external codes (or *backends*) to determine these quantities. Each module in GAMBIT is designed to perform a specific calculation as summarised below [516].

1. `ColliderBit`: calculates particle collider observables, Higgs likelihoods, and searches for new particles at the LEP and the LHC [517].

2. `FlavBit`: calculates likelihoods from a range of flavour physics results, primarily decay rates and angular observables for *B* decays as observed in *B* factories and the LHCb experiment [518].

3. `DarkBit`: calculates DM observables and likelihood using results from the direct and indirect searches, and relic density constraints [184].

4. `SpecBit`: interfaces to external mass spectrum calculators to provide GAMBIT with pole masses and running parameters [519].

5. `DecayBit`: calculates decay rates of BSM particles and contains SM particle decay information [519].

6. `PrecisionBit`: calculates BSM corrections to a range of precision observables, including quantities such as the *W* boson mass and muon anomalous magnetic moment. It also provides likelihoods for these parameters/observables [519].

In addition to these modules, GAMBIT also contains a hierarchical model database. This allows for an easy translation between a constrained parameterisation of a given model to a more general form.

9.3 Models

Following chapter 6, we assume that the DM fields are SM gauge singlets and consider a vector V_μ and a Dirac fermion ψ DM candidate.[2] The model Lagrangians for the two

---

[2]We only present results for the Dirac fermion DM model. The results for a Majorana fermion DM χ are similar. For more details, see chapter 6.

scenarios are given by

$$\mathcal{L}_V = \mathcal{L}_{\text{SM}} - \frac{1}{4}W_{\mu\nu}W^{\mu\nu} + \frac{1}{2}\mu_V^2 V_\mu V^\mu - \frac{1}{4!}\lambda_V(V_\mu V^\mu)^2 + \frac{1}{2}\lambda_{hV}V_\mu V^\mu \Phi^\dagger \Phi, \tag{9.1}$$

$$\mathcal{L}_\psi = \mathcal{L}_{\text{SM}} + \overline{\psi}\left(i\slashed{\partial} - \mu_\psi\right)\psi - \frac{\lambda_{h\psi}}{\Lambda_\psi}\left(\cos\theta\,\overline{\psi}\psi + \sin\theta\,\overline{\psi}i\gamma_5\psi\right)\Phi^\dagger\Phi, \tag{9.2}$$

where λ_{hV} $(\lambda_{h\psi}/\Lambda_\psi)$ is the dimensionless vector (dimensionful fermion) Higgs portal coupling and Φ is the SM Higgs doublet. For a fermion DM candidate, we consider both the CP-even and CP-odd dimension-5 operators inducing a coupling to the SM Higgs boson with θ controlling their relative size. The choice $\cos\theta = 1$ (0) corresponds to a pure scalar, CP conserving (pure pseudoscalar, maximally CP violating) interaction between the fermion DM and the SM Higgs field. A possible UV completion of such a model is given in Ref. [334, 461].

After EWSB, the Higgs field acquires a VEV $v_0 = 246.22$ GeV. Thus, the $\Phi^\dagger\Phi$ term in the above Lagrangians generate mass and interaction terms for the DM fields. For the vector DM model, its tree-level physical mass is

$$m_V^2 = \mu_V^2 + \frac{1}{2}\lambda_{hV}v_0^2. \tag{9.3}$$

As we saw in chapter 6, the pseudoscalar term ($\propto \sin\theta$) in the Dirac fermion model generates a non-mass-type term. To eliminate this term, we perform a chiral rotation of the post-EWSB Dirac fermion field as

$$\psi \rightarrow e^{i\gamma_5\alpha/2}\psi, \tag{9.4}$$

where α is a real, space-time independent parameter. Using the results in Appendix D, we arrive at the following post-EWSB Dirac fermion DM Lagrangian

$$\mathcal{L}_\psi = \mathcal{L}_{\text{SM}} + \overline{\psi}(i\slashed{\partial} - m_\psi)\psi - \frac{\lambda_{h\psi}}{\Lambda_\psi}\left[\cos\xi\,\overline{\psi}\psi + \sin\xi\,\overline{\psi}i\gamma_5\psi\right]\left(v_0 h + \frac{1}{2}h^2\right),$$

where $\xi \equiv \theta + \alpha$,

$$\cos\xi = \frac{\mu_\psi}{m_\psi}\left(\cos\theta + \frac{1}{2}\frac{\lambda_{h\psi}}{\Lambda_\psi}\frac{v_0^2}{\mu_\psi}\right), \quad \sin\xi = \frac{\mu_\psi}{m_\psi}\sin\theta,$$

$$m_\psi = \sqrt{\left(\mu_\psi + \frac{1}{2}\frac{\lambda_{h\psi}}{\Lambda_\psi}v_0^2\cos\theta\right)^2 + \left(\frac{1}{2}\frac{\lambda_{h\psi}}{\Lambda_\psi}v_0^2\sin\theta\right)^2}.$$

Note that a CP-conserving theory before EWSB ($\cos\theta = 1$) is still CP-conserving after EWSB ($\cos\xi = 1$). Thus, this particular choice of ξ is well-motivated from the UV perspective.[3] A possible UV completion of this particular scenario was studied in chapter 8.

---

[3]This is not the case for the maximally CP-violating choice ($\cos\theta = 0$) as EWSB induces a scalar interaction with $\cos\xi \propto v_0^2$ [335].

Likelihoods	GAMBIT modules/backends	Ref.
Relic density (*Planck*)	`DarkBit`	[75]
Higgs invisible width	`DecayBit`	[356]
Fermi-LAT dSphs	`gamLike 1.0.0`	[367]
LUX (2013)	`DDCalc 2.0.0`	[392]
XENON1T (2017)	`DDCalc 2.0.0`	[192]

Table 9.1: Likelihoods and corresponding GAMBIT modules/backends that provide the relevant routines.

9.4 Constraints

The free parameters of the Lagrangians are subjected to a range of observational and theoretical constraints. For the vector DM model, the relevant parameters after EWSB are the vector DM mass m_V and its dimensionless coupling λ_{hV} with the SM Higgs boson.[4] The post-EWSB fermion DM Lagrangians contain 3 free parameters: the fermion DM mass m_ψ, its dimensionful coupling $\lambda_{h\psi}/\Lambda_\psi$ with the SM Higgs boson and the scalar-pseudoscalar mixing parameter ξ.

To compare our preliminary results from GAMBIT against the ones in chapter 6, we use the set of likelihoods summarised in Table 9.1. In the following subsections, we discuss both the physics and implementation of each of these constraints.

9.4.1 Thermal relic density

The time evolution of the DM number density n_X, where $X \in (V_\mu, \psi)$, is governed by the following Boltzmann equation [453]

$$\frac{dn_X}{dt} + 3Hn_X = -\langle \sigma v_{\rm rel} \rangle \left(n_X^2 - n_{X,\rm eq}^2 \right), \tag{9.5}$$

where $n_{X,\rm eq}$ is the number density at equilibrium, H is the Hubble rate and $\langle \sigma v_{\rm rel} \rangle$ is the thermally averaged annihilation cross-section given by

$$\langle \sigma v_{\rm rel} \rangle = \int_{4m_X^2}^{\infty} ds \, \frac{s\sqrt{s - 4m_X^2}K_1\left(\sqrt{s}/T\right)}{16Tm_X^4 K_2^2\left(m_X/T\right)} \sigma v_{\rm rel}^{\rm cms}. \tag{9.6}$$

Here $v_{\rm rel}^{\rm cms}$ is the relative velocity of the DM particles in the centre-of-mass frame.

In our models, the annihilation process of DM receives contributions from all kinematically accessible final states involving massive SM fields. Annihilations into SM gauge bosons and fermions are mediated by a SM Higgs boson in the *s*-channel. Near the resonance region $m_X \simeq m_h/2$, it is crucial to perform the actual thermal average as defined in

---

[4]The quartic self-coupling λ_V does not play any role in the DM phenomenology and can be ignored. However, it is vital if the constraints from the electroweak vacuum stability and model perturbativity are imposed [330].

Eq. (9.6) instead of expanding $\sigma v_{\text{rel}}^{\text{cms}}$ in the partial waves [520]. Moreover, we take into account the important contributions arising from the production of off-shell pairs of gauge bosons WW^* and ZZ^* [480].

For $45\,\text{GeV} \leq \sqrt{s} \leq 300\,\text{GeV}$, we compute the annihilation cross-section into SM gauge bosons and fermions in the narrow-width approximation via

$$\sigma v_{\text{rel}}^{\text{cms}} = \frac{2\lambda_{hX}^2 v_0^2 P(X)}{\sqrt{s}} \frac{\Gamma_h \left(\sqrt{s} = m_h^*\right)}{\left(s - m_h^2\right)^2 + m_h^2 \Gamma_h^2 (m_h)}, \tag{9.7}$$

where we have employ the tabulated Higgs boson width $\Gamma(m_h^*)$ as implemented in `DecayBit` [519]. The pre-factor $P(X)$ is given by

$$P(X) = \begin{cases} \dfrac{1}{9}\left(3 - \dfrac{s}{m_V^2} + \dfrac{s^2}{4m_V^4}\right), & X = V_\mu, \\[3ex] \dfrac{s}{2}\left(1 - \dfrac{4m_X^2 \cos^2 \xi}{s}\right), & X = \psi. \end{cases} \tag{9.8}$$

In particular, we note that for a CP-conserving interaction of a fermionic DM particle, the annihilation cross-section is *p*-wave suppressed. As shown in Ref. [480], for $\sqrt{s} \gtrsim 300\,\text{GeV}$, the Higgs one-loop self interaction begins to overestimate the tabulated Higgs boson width in Ref. [5]. Thus, in cases where $\sqrt{s} > 300\,\text{GeV}$ and off-shell production of gauge boson pairs is irrelevant, we revert to the tree-level expressions for the annihilation cross-section as given in Appendix G. For $m_X \geq m_h$, DM can annihilate into a pair of Higgs bosons, a process that is missing in Eq. (9.7); the corresponding analytical expression for the annihilation cross-section is also given in Appendix G.

Finally, we obtain the relic density of X by numerically solving Eq. (9.5) at each parameter point using the routines implemented in `DarkSUSY` [521] via `DarkBit`. We do *not* demand that the particle X constitutes all of the observed DM, i.e., we allow for the possibility of other DM species to contribute to the observed relic abundance, e.g., axions.

To compare our preliminary results against those presented in chapter 6, we implement the relic density constraint using a likelihood which is flat for predicted relic density values below the observed one, and is based on a Gaussian distribution with the *Planck* measured value $\Omega_{\text{DM}}h^2 = 0.1199 \pm 0.0027$ [354] for parameter points saturating or exceeding the observed value. For more details on this prescription, see Refs. [184, 514].

In regions of the model parameter space where the X relic abundance is less than the observed value, all indirect and direct detection signals are rescaled accordingly. In doing so, we conservatively assume that the remaining DM population does not contribute to signals in these experiments.

9.4.2 Higgs invisible decays

For $m_X < m_h/2$, the SM Higgs boson can decay into a pair of DM particles, with rates given by [30]

$$\Gamma_{\text{inv}}(h \to VV) = \frac{\lambda_{hV}^2 v_0^2 m_h^3}{128\pi m_V^4}\left(1 - \frac{4m_V^2}{m_h^2} + \frac{12m_V^4}{m_h^4}\right)\sqrt{1 - \frac{4m_V^2}{m_h^2}},\tag{9.9}$$

$$\Gamma_{\text{inv}}(h \to \overline{\psi}\psi) = \frac{m_h v_0^2}{8\pi}\left(\frac{\lambda_{h\psi}}{\Lambda_\psi}\right)^2\left(1 - \frac{4m_\psi^2\cos^2\xi}{m_h^2}\right)\sqrt{1 - \frac{4m_\psi^2}{m_h^2}}.\tag{9.10}$$

These processes give an extra contribution to the Higgs invisible width Γ_{inv}, which is constrained to be less than 19% of the total width at 2σ C.L. [356]. In GAMBIT, this constraint is accounted by using the `DecayBit` implementation of the Higgs invisible width likelihood, which in turn is based on an interpolation of Fig. 8 in Ref. [356].

9.4.3 Indirect detection via gamma rays

The most immediate prediction from the thermal freeze-out scenario is that DM particles can annihilate today, most notably in regions of enhanced DM density. In particular, gamma-ray observations from dwarf spheroidal galaxies (dSphs) of the Milky Way are strong and robust probes for any model of thermal DM with unsuppressed annihilations into SM particles.

As we saw in chapter 6, the flux of gamma rays in a given energy bin i from a target object labelled by k can be written in the factorised form as $\Phi_i \cdot J_k$, where Φ_i encodes all information about the particle physics of the DM annihilation process, and J_k depends on the spatial distribution of DM in the region of interest, namely

$$\Phi_i = \kappa \sum_j \frac{(\sigma v)_{0,j}}{8\pi m_X^2}\int_{\Delta E_i}\frac{dN_{\gamma,j}}{dE}\,dE,\tag{9.11}$$

$$J_k = \int_{\Delta\Omega_k}d\Omega\int_{\text{l.o.s.}}ds\,\rho_X^2.\tag{9.12}$$

Here κ is a phase space factor (equal to 1 for self-conjugate DM and 1/2 for non-self-conjugate DM), $(\sigma v)_{0,j}$ is the annihilation cross-section in the zero-velocity limit and $dN_{\gamma,j}/dE$ is the differential gamma-ray spectrum into final state j. In `DarkBit`, the latter is obtained from the correct routines in `DarkSUSY`. Moreover, the J-factor in Eq. (9.12) is defined as a line of sight (l.o.s.) integral over the square of the DM density ρ_X towards the target object k and extended over a solid angle $\Delta\Omega_k$. We assume an NFW profile [376] for the galactic halo within the Milky Way.

We use the `Pass-8` combined analysis of 15 dwarf galaxies using 6 years of the *Fermi*-LAT data [367], which currently provides the strongest limit on the DM annihilation cross-section into final states involving gamma rays. Concretely, we use the binned

likelihoods as implemented in `DarkBit` [184], which in turn is based on the `gamLike` `1.0.0` package.[5] The likelihood associated with the gamma-ray observations is

$$\ln \mathcal{L}_{\text{exp}} = \sum_{k=1}^{N_{\text{dSphs}}} \sum_{i=1}^{N_{\text{eBins}}} \ln \mathcal{L}_{ki} \left(\Phi_i \cdot J_k \right). \tag{9.13}$$

In addition, we include a term $\ln \mathcal{L}_J$ which parametrises the uncertainties on the J-factors [184, 367]. Finally, the overall *Fermi*-LAT likelihood used in our scans is obtained by profiling over all possible J-factors as nuisance parameters, namely

$$\ln \mathcal{L}_{\text{dwarfs}}^p = \max_{J_1, \dots, J_k} \left(\ln \mathcal{L}_{\text{exp}} + \ln \mathcal{L}_J \right). \tag{9.14}$$

For the Dirac fermion DM model with CP-conserving interactions ($\xi = 0$), the annihilation cross-section vanishes in the zero velocity limit. This opens up the parameter space of such scenarios. On the other hand, models with $\xi \neq 0$ come with the cost of an additional constraint from gamma-ray searches.

9.4.4 Direct detection

The predicted number of signal events in a given direct detection experiment is [184]

$$N_p = MT \int_0^\infty \phi(E) \frac{dR}{dE} \, dE, \tag{9.15}$$

where M is the detector mass, T is the exposure time and $\phi(E)$ is the detector efficiency function, i.e., the fraction of recoil events with energy E that are observed after applying all cuts in a given analysis. The differential recoil rate dR/dE for scattering off target isotope T is given by

$$\frac{dR}{dE} = \frac{2\rho_0}{m_X} \int v f(\boldsymbol{v}, t) \frac{d\sigma}{dq^2} \left(q^2, v \right) d^3 v, \tag{9.16}$$

where ρ_0 is the local DM density, $f(\boldsymbol{v}, t)$ is the three-dimensional, time-dependent DM velocity distribution, $d\sigma(q^2, v)/dq^2$ is the differential scattering cross-section with respect to the momentum transfer $q^2 = 2m_T E$.

For the evaluation of N_p in Eq. (9.15), we assume a Maxwell-Boltzmann velocity distribution in the galactic rest frame with a peak velocity v_{peak} and truncated at the local escape velocity v_{esc}. For more details about the conversion to the velocity distribution $f(\boldsymbol{v}, t)$ in the detector rest frame, see Ref. [184].

For the vector DM model, the SI DM-nucleon cross-section is given by

$$\sigma_{\text{SI}}^V = \frac{\mu^2}{\pi} \frac{\lambda_{hV}^2 f_N^2 m_N^2}{4 m_V^2 m_h^4}, \tag{9.17}$$

---

[5] http://gamlike.hepforge.org

where $\mu = m_V m_\mathcal{N}/(m_V + m_\mathcal{N})$ is the reduced mass of the DM-nucleon system and $f_\mathcal{N}$ is the effective Higgs-nucleon coupling. The latter is defined as

$$f_\mathcal{N} = \frac{2}{9} + \frac{7}{9} \sum_{q=u,d,s} f_{Tq}^{(\mathcal{N})}, \tag{9.18}$$

where $f_{Tq}^{(\mathcal{N})}$ are the hadronic matrix elements. These are calculated using the following matrix elements which describe the quark content of a nucleon, namely

$$\sigma_l \equiv m_l \langle \mathcal{N}|\bar{u}u + \bar{d}d|\mathcal{N}\rangle, \quad \sigma_s \equiv m_s \langle \mathcal{N}|\bar{s}s|\mathcal{N}\rangle, \tag{9.19}$$

where $m_l \equiv (m_u + m_d)/2$ and $\mathcal{N} \in \{p, n\}$. For more details, see Ref. [324].

For the Dirac fermion DM model, the SI DM-nucleon cross-section is given by

$$\sigma_{\text{SI}}^\psi = \frac{\mu^2}{\pi} \left(\frac{\lambda_{h\psi}}{\Lambda_\psi}\right)^2 \frac{f_\mathcal{N}^2 m_\mathcal{N}^2}{m_h^4} \left[\cos^2 \xi + \frac{q^2}{4m_\psi^2} \sin^2 \xi\right], \tag{9.20}$$

As typical momentum transfer in a scattering process is $|q| \simeq (1\text{–}100)$ MeV $\ll 4m_\psi^2$, direct detection constraints are weaker for (nearly) pseudoscalar interactions, i.e., $\xi \simeq \pi/2$.

To evaluate a Poisson-based likelihood for a given experiment, we use the `DarkBit` interface to `DDCalc 2.0.0`[6] as

$$\mathcal{L}(N_p|N_o) = \frac{(b + N_p)^{N_o} e^{-(b+N_p)}}{N_o!}, \tag{9.21}$$

where N_p is the number of predicted events, N_o is number of observed events and b is the predicted number of background events. We model the detector efficiencies and acceptance rates by interpolating between the pre-computed tables in `DDCalc`.

To make a fair comparison between our preliminary results and ones in chapter 6, we include the LUX (2013) [392] and XENON1T (2017) [192] constraints.

9.4.5 Nuisance likelihoods

In addition to the DM model parameters, the constraints mentioned above also depend on a set of *nuisance parameters*, i.e., parameters that are not of immediate interest but are required as inputs in various likelihoods. Examples include the hadronic matrix elements σ_s and σ_l in Eq. (9.19), the local DM density ρ_0, the parameters of the Maxwell-Boltzmann velocity distribution, namely v_{peak} and v_{esc}, and SM masses/couplings that are only known to a finite accuracy. One of the great virtues of a global fit is that such uncertainties can be taken into account in a fully consistent way, namely by including additional likelihoods in the combined likelihood function which parametrises these uncertainties.

In `DarkBit`, the nuisance likelihood for the local DM density ρ_0 is given by a log-normal distribution with a central value of $\rho_0 = 0.40$ GeV cm^{-3} and an error of

---

[6]http://ddcalc.hepforge.org/

$\sigma_{\rho_0} = 0.15\,\text{GeV cm}^{-3}$ [184]. To reflect the log-normal distribution, we can scan over an asymmetric range for ρ_0. For the parameters of the Maxwell-Boltzmann velocity distribution, namely v_{peak} and v_{esc}, we can use simple Gaussian likelihoods. In particular, a Gaussian likelihood for v_{peak} with a central value and 1σ error of $v_{\text{peak}} = 240 \pm 8\,\text{km s}^{-1}$; this is based on the determination of the rotational speed v_{rot} of the Sun in Ref. [187]. Assuming Gaussian errors, the 90% C.L. interval from the RAVE collaboration can be converted to give $v_{\text{esc}} = 533 \pm 31.9\,\text{km s}^{-1}$ [522]. A Gaussian likelihood for v_{esc} can also be used. In the absence of any other information about the DM distribution in our galaxy, we assume $v_{\text{peak}} \equiv v_{\text{rot}}$.

The uncertainties in the hadronic matrix elements can be parametrised using Gaussian likelihoods for $\sigma_l = 50 \pm 15\,\text{MeV}$ [523] and $\sigma_s = 43 \pm 8\,\text{MeV}$ [524]. The former deviates from the default choice in `DarkBit` as it reflects the recent lattice results which point towards smaller values of σ_s. The uncertainties on the light quark masses have a negligible impact on the Higgs-nucleon coupling f_N in Eq. (9.18). Thus, they can be ignored in a global study.

For the SM nuisance parameters, the uncertainty on the strong coupling α_s can be accounted by a Gaussian likelihood with $\alpha_s^{\overline{MS}}(m_Z) = 0.1185 \pm 0.0005$ [459]. Similarly, the uncertainity on the SM Higgs boson mass can be modelled by a Gaussian likelihood based on the PDG-2015 value of $m_h = 125.09 \pm 0.24\,\text{GeV}$ [525].

9.4.6 EFT validity

For the Dirac fermion model, the EFT approximation depends on the UV completion. As discussed in chapter 6, we consider a specific UV completion in which a heavy scalar mediator field φ couples to the fermions and the Higgs doublet as[7]

$$\mathscr{L} \supset -\varphi \left[\mu g_\Phi \Phi^\dagger \Phi + g_\psi \overline{\psi} \left(\cos\xi + i\gamma_5 \sin\xi \right) \psi \right], \qquad (9.22)$$

where μ has mass-dimension 1, e.g., from some Yukawa-type coupling. This heavy field can be integrated out to give a dimensionful coupling in the EFT approximation as

$$\mathscr{L} \supset -\frac{\mu g_\Phi g_\psi}{m_\varphi^2} \left(\cos\xi\, \overline{\psi}\psi + \sin\xi\, \overline{\psi} i\gamma_5\psi \right) \Phi^\dagger \Phi. \qquad (9.23)$$

By comparing this expression with Eq. (9.2), the coefficients can be related by $\lambda/\Lambda \simeq (\mu g_\Phi g_\psi)/m_\varphi^2$. The largest (realistic) value of the energy scale μ is m_φ. In this case, we get $\lambda/\Lambda \sim g_\Phi g_\psi/m_\varphi$. We also require the couplings to be perturbative, i.e., $g_\Phi g_\psi \leq 4\pi$. For DM annihilation, the relevant energy scale is $\sqrt{s} \approx 2m_X$. Thus, the EFT approximation becomes invalid when

$$\frac{\lambda_{h\psi}}{\Lambda_\psi} \geq \frac{4\pi}{2m_\psi}. \qquad (9.24)$$

---

[7]Note that the γ_5 term can be generated by having a complex mass term $\widetilde{m}_\psi$ in the original Dirac fermion Lagrangian and performing a chiral rotation. Full CP conservation, $\cos\xi = 1$, is equivalent to having a real mass term.

Parameter	Minimum	Maximum	Prior
λ_{hV}	10^{-4}	56.23	log
m_V (low mass)	$45\,\text{GeV}$	$70\,\text{GeV}$	flat
m_V (high mass)	$45\,\text{GeV}$	$10\,\text{TeV}$	log
m_h	$124.1\,\text{GeV}$	$127.3\,\text{GeV}$	flat

Table 9.2: Ranges and priors for the vector DM model, and the SM nuisance parameter m_h.

Parameter	Minimum	Maximum	Prior
$\lambda_{h\psi}/\Lambda_{\psi}$	$10^{-4}\,\text{GeV}^{-1}$	$10\,\text{GeV}^{-1}$	log
ξ	0	π	flat
m_{ψ} (low mass)	$45\,\text{GeV}$	$70\,\text{GeV}$	flat
m_{ψ} (high mass)	$45\,\text{GeV}$	$10\,\text{TeV}$	log
m_h	$124.1\,\text{GeV}$	$127.3\,\text{GeV}$	flat

Table 9.3: Ranges and priors for the Dirac fermion DM model, and the SM nuisance parameter m_h. Our choice for $\xi \in [0, \pi]$ reflects the fact that only odd powers of $\cos\xi$ appear in all included observables. Thus, our model results are symmetric under $\xi \to -\xi$.

Thus, we invalidate parameter points in the Dirac fermion model if they lead to a breakdown of the EFT approximation.

9.5 Preliminary results

In the following subsections, we present preliminary results for the vector and Dirac fermion models using the GAMBIT software. To make a fair comparison between these results and the ones presented in chapter 6, we scan over the same range of model parameters, and fix the nuclear and astrophysical parameters to [30]

$$\rho_0 = 0.4\,\text{GeV}\,\text{cm}^{-3}, \quad v_{\text{peak}} \equiv v_{\text{rot}} = 220\,\text{km}\,\text{s}^{-1}, \quad v_{\text{esc}} = 544\,\text{km}\,\text{s}^{-1},$$
$$\sigma_l = 58\,\text{MeV}, \quad \sigma_s = 40\,\text{MeV}. \tag{9.25}$$

More importantly, the chosen values for σ_s and σ_l reproduce $f_N = 0.3$ [30, 324].

For the Dirac fermion model, we extend the work presented in chapter 6 by scanning over the scalar-pseudoscalar mixing parameter ξ. The range and priors for the vector and Dirac fermion model is summarised in Tables 9.2 and 9.3 respectively.

In addition to the likelihoods listed in Table 9.1, we use a Gaussian likelihood for a SM Higgs boson with a mass of $m_h = 125.09 \pm 0.24\,\text{GeV}$ [525]. As the phenomenology of our models is strongly dependent on m_h (especially near the resonance region), we allow m_h to vary by more than 4σ. The range and prior-type for m_h is summarised in Tables 9.2 and 9.3.
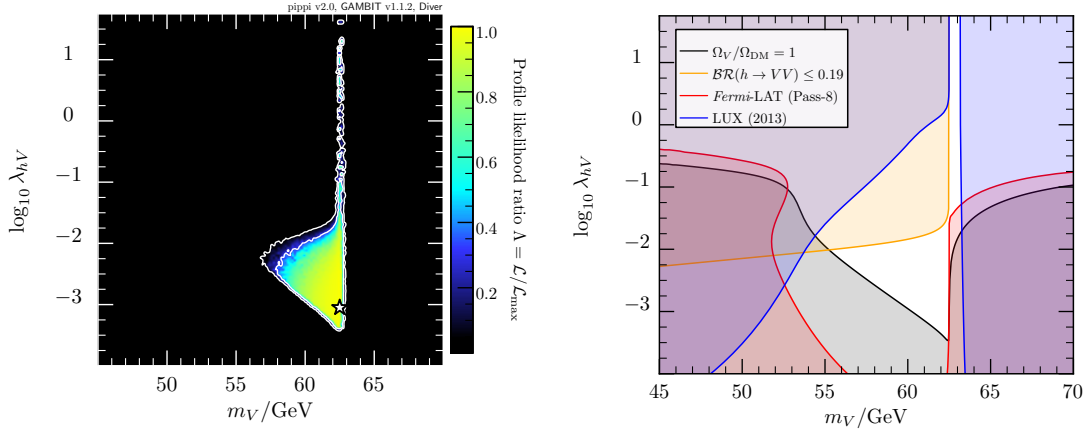
Figure 9.1: *Left panel*: Profile likelihood in the (m_V, λ_{hV}) plane for low vector DM masses. Contour lines mark out the 1σ and 2σ C.L. regions. *Right panel*: Vector DM model results from Ref. [30].
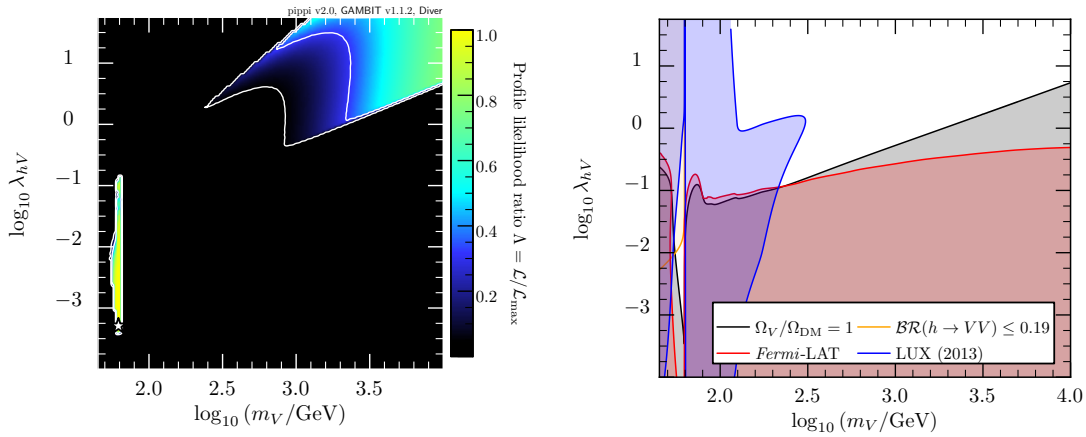
Figure 9.2: *Left panel*: Profile likelihood in the (m_V, λ_{hV}) plane for high vector DM masses. Contour lines mark out the 1σ and 2σ C.L. regions. *Right panel*: Vector DM model results from Ref. [30].

9.5.1 Vector model

We perform scans of the vector model parameter space using the `Diver 1.0.4` package. The ranges and priors for the free model parameters are summarised in Table 9.2. Specifically, we perform a scan in the low mass resonance region and another over the full range. The resulting profile likelihoods are shown in the left panels of Figs. 9.1 and 9.2 respectively. For comparison, we also show results for the vector DM model from chapter 6 in the right panels.

In the low mass region, we can see that the allowed region (shown as coloured in the left panel and as white in the right panel) is in good agreement. In both panels, the allowed region is tightly constrained from below by the relic density constraint, from upper left by the Higgs invisible decay, and from the right by direct search experiments. The inclusion of the XENON1T (2017) limit in the left panel results in a slightly stronger exclusion than the LUX (2013) limit in the right panel. In these plots, the SM Higgs boson mass m_h is
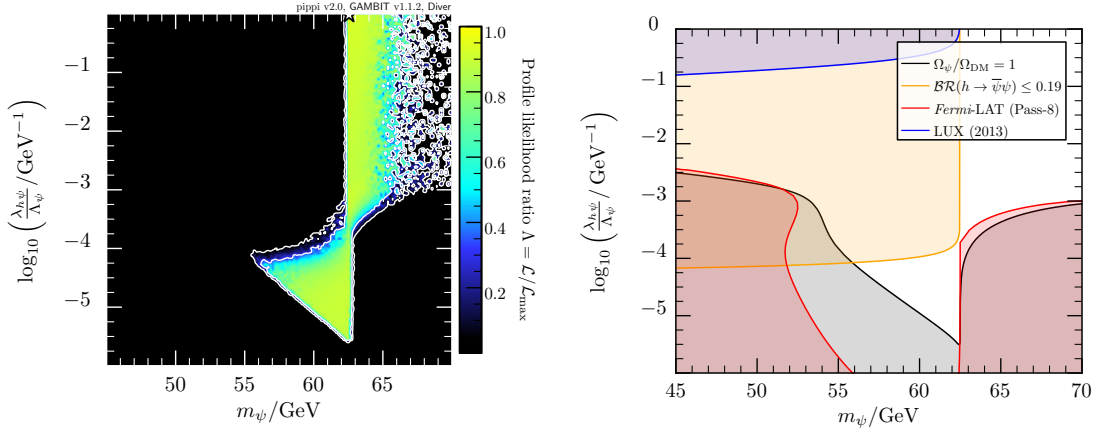
Figure 9.3: *Left panel*: Profile likelihood in the $(m_\psi, \lambda_{h\psi}/\Lambda_\psi)$ plane for low Dirac fermion masses. Contour lines mark out the 1σ and 2σ C.L. regions. *Right panel*: Dirac fermion model results from Ref. [30] for the case $\xi = \pi/2$.

profiled over. This broadens the allowed region near the Higgs resonance $m_V \simeq m_h/2$.

In the high mass region, constraints from the XENON1T (2017) experiment exclude vector DM masses between $m_h/2$ and $\sim 320\,$GeV. The profiled out SM nuisance parameter, namely m_h only has a small effect in this region when $VV \rightarrow hh$ annihilation mode is kinematically allowed. Again, the allowed region is constrained from below by the relic density limit as smaller values of λ_{hV} lead to an overabundance of DM. In fact, the lower boundary of the 2σ contour is where the vector DM relic density agrees exactly with the *Planck* measured value, i.e., $\Omega_V h^2 = 0.1199$. As evident in the right panel, the impact of *Fermi*-LAT limit on the model parameter space is small in comparison with the LUX (2013) limit. In the left panel, only two regions remain that are compatible with all constraints, one near the Higgs resonance $m_V \sim m_h/2$, and another at high vector DM masses $m_V \gtrsim 320\,$GeV.

9.5.2 Dirac fermion model

Similar to the vector DM model, we perform scans in the low and high mass region of the Dirac fermion DM model. In contrast to chapter 6 where results were presented for fixed values of $\cos\xi$ (or equivalently ξ), we scan over ξ in the range specified in Table 9.3. The resulting profile likelihoods in the low and high mass range are shown in the left panel of Figs. 9.3 and 9.4 respectively.

In the low mass region, a triangular region is allowed by the combined constraints. It is constrained from below by the relic density and from the upper left by the Higgs invisible decays. The parameter ξ is profiled over in these plots. As the CP-conserving case ($\xi = 0$) is severely constrained from direct DM searches, the net effect of profiling over ξ is to favour scenarios where $\xi \neq 0$, i.e., non-zero pseudoscalar coupling. This is especially favoured by direct detection experiments as the resulting limit is q^2-suppressed,
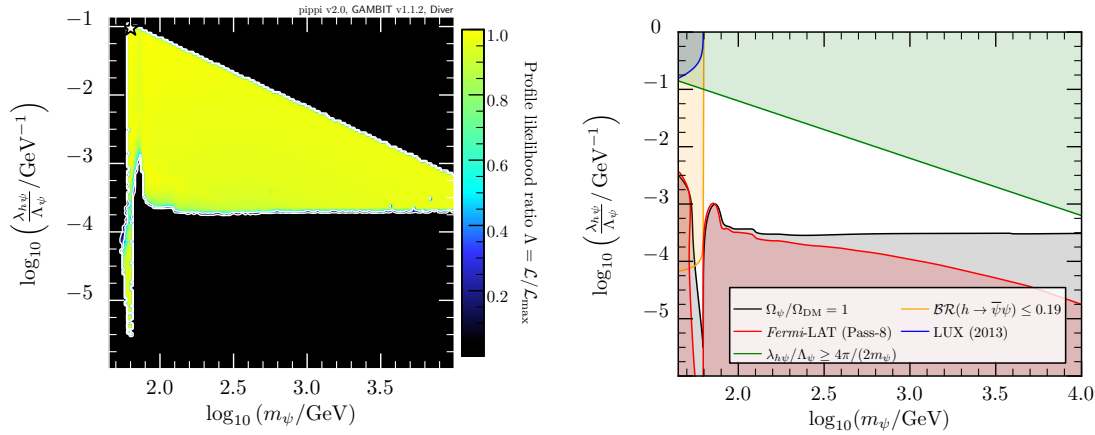
Figure 9.4: *Left panel*: Profile likelihood in the $(m_\psi, \lambda_{h\psi}/\Lambda_\psi)$ plane for high Dirac fermion masses. Contour lines mark out the 1σ and 2σ C.L. regions. *Right panel*: Dirac fermion model results from Ref. [30] for the case $\xi = \pi/2$.

see Eq. (9.20). In the $\xi \neq 0$ case, the allowed region is constrained from the right by the indirect gamma-ray searches. This is also evident in the right panel of Fig. 9.3, which is based on chapter 6 for the maximally CP-violating case, $\xi = \pi/2$.

In the high mass region, we also find a good agreement between our preliminary results using GAMBIT and those obtained in chapter 6. In this mass region, we invalidate parameter points if the EFT approximation is invalid, i.e., when $\lambda_{h\psi}/\Lambda_\psi \geq 4\pi/(2m_\psi)$. The EFT excluded region also agrees between the two panels. Similar to the low mass region, the parameter ξ is profiled over in these plots. Thus, $\xi \sim \pi/2$ is favoured as direct detection limits are weak in this case. For comparison sake, we also show the model results from chapter 6 for the case $\xi = \pi/2$. As expected, the results in the two panels agree. The allowed region is constrained from below by the relic density and from above by the EFT validity constraint.

9.6 Summary and future work

In this chapter, we have presented a few preliminary results for the vector and Dirac fermion Higgs portal DM models using the GAMBIT software. Using the same set of observables, parameter ranges, and fixed values for the nuclear and astrophysical nuisance parameters as in chapter 6, we constrained the model parameter space and checked the results for their consistency. In contrast to chapter 6, we also extended the study of the Dirac fermion DM model by scanning over the scalar-pseudoscalar mixing parameter ξ. We also included the SM Higgs boson mass as a nuisance parameter. In both of our models, the results were found to be in good agreement.

In the vector DM model, the low mass resonance region was found to be compatible with all constraints. This region is tightly constrained from below by the relic density, from the upper left by the Higgs invisible decay, and from the right by direct detection

experiments. A significant portion of the model parameter space is expected to be ruled out by the current generation of direct detection experiments. By profiling over the SM Higgs boson mass, the size of the allowed parameter space around $m_V \simeq m_h/2$ becomes larger. On the other hand, the high mass region is heavily constrained by the relic density and direct detection limits. In particular, the XENON1T experiment rules out all values of λ_{hV} for $m_h/2 \lesssim m_V \lesssim 320\,\text{GeV}$. Above this mass range, couplings of order unity are compatible with the direct detection limits. In addition, they can exactly reproduce the observed DM abundance.

For the Dirac fermion model, we performed scans of the model parameter space using 3 free model parameters: the DM mass m_ψ, the dimensionful coupling with the SM Higgs boson $\lambda_{h\psi}/\Lambda_\psi$, and the scalar-pseudoscalar mixing parameter ξ. In the low mass region with $m_\psi \lesssim m_h/2$, the parameter space is constrained in a similar way to the vector DM model, i.e., from below (upper left) by the relic density (Higgs invisible decays). As the CP-even case ($\xi = 0$) is severely constrained by direct detection experiments, the allowed region in the $(m_\psi, \lambda_{h\psi}/\Lambda_\psi)$ plane favours the CP-odd case, $\xi \simeq \pi/2$ when ξ is allowed to vary in our scans. In the $\xi \simeq \pi/2$ case, the resulting direct detection limits are weak due to a q^2-suppressed DM-nucleon cross-section. However, this scenario is constrained by indirect gamma-ray searches. The final model results are in good agreement with those obtained for the $\xi = \pi/2$ case in chapter 6. The EFT validity constraint on the Dirac fermion model excludes large values of $\lambda_{h\psi}/\Lambda_\psi$ and agrees with the result in chapter 6.

The work presented in this chapter can be easily extended by combining limits from multiple direct detection experiments, and the inclusion of the most important nuisance parameters from nuclear physics, astrophysics and the SM. An analysis of these models can be performed in both frequentist and Bayesian statistics. This includes a Bayesian model comparison, e.g., a comparison between scenarios where ξ is free vs cases when ξ is fixed, e.g., the CP-even case, $\xi = 0$. A prior sensitivity study can also be performed to understand any variation in the model results under a different choice of priors. This is important for the purpose of model comparison in Bayesian statistics (i.e., Bayes factor) as it is known to be prior-sensitive.

The GAMBIT software is flexible and modular, and allows users to add new observables and external interfaces. For our Higgs portal models, the extensions mentioned above can be easily realised. In a future work [526], we aim to perform the most comprehensive global fit of the vector and fermion Higgs portal DM models.

Chapter 10

Conclusions

In this thesis, we addressed two limitations of the Standard Model (SM), namely in providing a viable dark matter (DM) candidate and explaining the observed matter-antimatter asymmetry. We started with a pedagogical review of the SM and discussed the theories related to the electromagnetic, strong and weak forces. As the requirement of a local gauge invariant Lagrangian forbids mass terms for the gauge boson and fermions, we introduced the Higgs mechanism which generates the $W^{\pm}/Z$ and SM fermion masses after electroweak symmetry breaking. This mechanism also introduced a new scalar particle known as the Higgs boson h. In addition, the Higgs mechanism led to the origin of quark mixing.

As the Higgs boson mass m_h is not predicted by the SM, we reviewed various theoretical constraints ranging from unitarity, triviality, vacuum stability, electroweak precision measurements and fine-tuning to place upper and lower limits on m_h, assuming no new physics enters between the electroweak and a higher energy scale. The Higgs branching ratios were used to predict its production rate and decay modes at the LEP, Tevatron and the LHC. The LEP experiment placed a lower limit of $m_h > 114.4\,\text{GeV}$, whereas the Tevatron experiment ruled out various Higgs mass regions. It was only in 2012 when a signal for a SM-like Higgs boson with mass $m_h \sim 125\,\text{GeV}$ was discovered at the LHC. The properties of the new particle such as its spin, CP and coupling strengths to SM particles were all found to be in agreement with the SM expectation.

We presented various astrophysical evidence to support the existence of DM. These ranged from observations of galactic rotation curves, the CMB, and large-scale structures to results from N-body simulations and observations of collisions of galaxy clusters. The properties inferred from these observations pointed towards a cold and collision-less DM. Thus, we proposed viable DM candidates such as WIMPs and axions, and discussed their production in the early universe. We also studied various detection probes such as collider, direct and indirect searches for unravelling the nature of DM in our universe today.

We motivated the presence of matter-antimatter asymmetry in our universe. By outlining the three Sakharov conditions, we explained how such an asymmetry could be

generated dynamically from symmetric initial conditions. We subsequently studied the topic of electroweak baryogenesis (EWBG), a mechanism which aims to explain the observed baryon asymmetry via a strong first-order electroweak phase transition (EWPT). Both the perturbative and non-perturbative methods for studying the details of phase transition were discussed. In contrast to other mechanisms for baryogenesis, EWBG offered possible collider, indirect and gravitational wave (GW) signals.

In the second part of this thesis, we studied the phenomenology of Higgs portal DM models, i.e., models where the DM-SM interaction proceeds via a SM Higgs boson. In particular, we performed a combined analysis of effective scalar, vector, Majorana and Dirac fermion models. For the fermion models, both the CP-even and CP-odd interaction terms were included. The model parameter space was constrained using the limits from the DM relic density, Higgs invisible decay, indirect and direct detection experiments. Apart from the CP-odd case which led to suppressed direct detection rates, the parameter space of all models was found to be significantly constrained from direct DM searches. In general, this led to two allowed regions, one near the Higgs resonance $m_X \sim m_h/2$ and another at higher DM masses.

We also studied the viability and detection prospects of the scalar Higgs portal model by focusing on two main features, namely on the possibility to facilitate EWBG and serve as a DM candidate. After studying the collider, DM and GW signals of this scenario, we found that a significant portion of the model parameter space will be accessible at planned GW experiments such as LISA and BBO, but will be beyond the reach of future collider experiments. More importantly, it was found that the model could *not* simultaneously explain the observed DM abundance and facilitate a strong first-order EWPT. This left us with only two regions, one close to the Higgs resonance $m_S \sim m_h/2$ and the other at $m_S > 700\,\text{GeV}$. It was noted that the DM constraints could be avoided if the new scalar served as a mediator between the SM particles and a new DM candidate; the details of the EWPT would essentially remain the same. Lastly, we studied a scenario with modified cosmological history by employing a simple cosmological model with a new energy content ρ_N that redshifts faster than radiation, i.e., $\rho_N \propto a^{-n}$ where $n > 4$. This modification led to significant implications for both EWBG and the DM abundance. However, the increased DM abundance resulted in severe constraints from direct detection experiments. Thus, no new parameter space opened up.

In the third part of this thesis, we focused on global fits. Firstly, we performed a comprehensive and up-to-date study of the extended scalar singlet model with a fermionic DM candidate. This model was a generalisation of the scalar singlet model studied in previous chapters. By relaxing the $\mathbb{Z}_2$ symmetry which conventionally makes S a stable DM candidate, the new scalar S acquired a non-zero VEV. Due to additional interaction terms, the new scalar mixed with the SM Higgs boson. To diagonalise the squared mass matrix, the interaction eigenstates were rotated into the physical mass eigenstates (h, H).

The model parameter space was constrained using the *Planck* measured DM relic density, direct detection limit from the PandaX-II experiment, EWBG, electroweak precision observables and Higgs searches at colliders.

After performing 7-dimensional scans of the model using *only* the EWBG constraint, we found that all parts of the model parameter space can facilitate EWBG provided the scalar-fermion DM coupling $g_S \lesssim 5.62$. On the other hand, a strong upper limit on the second scalar mass m_H, the fermion DM mass m_ψ and g_S was obtained from our global fit. We also confirmed that the model could explain (at least a part of) the observed DM abundance and baryon asymmetry. From the viable points that satisfied all of the above constraints, the GW spectra from the phase transition were computed and checked against the discovery prospects of current or future GW experiments. In fact, the GW spectra of viable points were found to be within reach of LISA, DECIGO and BBO. On the other hand, experiments such as LIGO, EPTA and SKA would be immune to such GW signals.

Secondly, we presented preliminary results from a global fit of the vector and Dirac fermion Higgs portal models using the GAMBIT software. After discussing the main benefits of using GAMBIT, we scanned over the model parameter space using the same set of constraints, parameter ranges, and fixed values of nuclear and astrophysical parameters as in our previous study. The past analysis of the Dirac fermion model was extended by allowing the scalar-pseudoscalar mixing parameter ξ to vary in the scans. As the phenomenology of these models is strongly dependent on the SM Higgs boson mass (a SM nuisance parameter), especially near the Higgs resonance, we allowed m_h to vary by more than 4σ from its measured value. Despite these extensions, the model results were found to be in good agreement with our previous study.

We also discussed ways of improving upon our previous study of the vector and fermion Higgs portal models. In particular, we outlined the details for performing a more comprehensive study of these models using the GAMBIT software. This included a combination of results from many indirect and direct search experiments, inclusion of the most important nuclear, astrophysical and SM nuisance parameters, and analysis in both frequentist and Bayesian frameworks. In addition, we also proposed to compare models in the Bayesian approach, including a study of the prior dependence.

Appendix A

List of Papers

In preparation

- **A. Beniwal**, S. Bloor, J. M. Cornell *et al.*, *Global analyses of Higgs portal singlet dark matter models*, in preparation for *Eur. Phys. J. C*, (2018).

- **A. Beniwal**, M. Lewicki, M. White and A. G. Williams, *Gravitational waves and electroweak baryogenesis in a global study of the extended scalar singlet model*, in preparation for *JHEP*, (2018).

Journal publications

- **A. Beniwal**, M. Lewicki, J. D. Wells, M. White and A. G. Williams, *Gravitational wave, collider and dark matter signals from a scalar singlet electroweak baryogenesis*, *JHEP* **08** (2017) 108, [1702.06124].

- **A. Beniwal**, F. Rajec, C. Savage, P. Scott, C. Weniger, M. White and A. G. Williams, *Combined analysis of effective Higgs portal dark matter models*, *Phys. Rev. D* **93** (2016) 115016, [1512.06458].

Appendix B

Spontaneous Symmetry Breaking

One of the key ingredients of the electroweak sector is the concept of spontaneous symmetry breaking (SSB) [4]. It gives rise to massless Goldstone excitations which are related to the gauge boson masses. When a local gauge symmetry is spontaneously broken, the Higgs mechanism operates. In the Standard Model (SM), this mechanism is responsible for generating the gauge boson masses.

B.1   Global symmetry breaking

We start by considering a complex scalar field ϕ as

$$\phi = \frac{1}{\sqrt{2}}(\phi_1 + i\phi_2), \tag{B.1}$$

where ϕ_1 and ϕ_2 are two real scalar fields. Its Lagrangian density is given by

$$\mathscr{L}(\phi) = T - V = (\partial_\mu \phi)^*(\partial^\mu \phi) - \mu^2 \phi^* \phi - \lambda(\phi^* \phi)^2, \tag{B.2}$$

where $\lambda > 0$. It is invariant under a global $U(1)$ transformation

$$\phi \rightarrow \phi' = e^{i\alpha}\phi. \tag{B.3}$$

In terms of ϕ_1 and ϕ_2 fields, the Lagrangian expands to

$$\mathscr{L}(\phi_1, \phi_2) = \frac{1}{2}(\partial_\mu \phi_1)^2 + \frac{1}{2}(\partial_\mu \phi_2)^2 - \frac{1}{2}\mu^2(\phi_1^2 + \phi_2^2) - \frac{1}{4}\lambda(\phi_1^2 + \phi_2^2)^2. \tag{B.4}$$

Depending on the sign of μ^2 in Eq. (B.4), two distinct cases are possible. We investigate the particle spectrum in each case by studying the Lagrangian under small perturbations around the minimum of the potential.

1. $\mu^2 > 0$: In this case, the minimum of the potential occurs at $\phi_1 = \phi_2 = 0$. Thus, the Lagrangian in Eq. (B.4) describes two massive scalar particles, each with mass μ, and additional interactions.

2. $\mu^2 < 0$: In this case, there is no single minimum located at $\phi_1 = \phi_2 = 0$. Instead, there are an infinite number of vacuum configurations which satisfy

$$\sqrt{\phi_1^2 + \phi_2^2} = \sqrt{\frac{-\mu^2}{\lambda}} \equiv v. \tag{B.5}$$

From the infinite number of allowed vacuum configurations, we choose $\phi_1 = v$, $\phi_2 = 0$. We expand ϕ_1 and ϕ_2 fields around the minimum as

$$\phi_1 = \eta + v, \quad \phi_2 = \xi, \tag{B.6}$$

where η and ξ fields describe small oscillations around the minimum. Thus, the complex scalar field ϕ becomes

$$\phi = \frac{1}{\sqrt{2}}(\eta + v + i\xi).$$

Using $\phi^2 = \phi^*\phi = \left[(\eta + v)^2 + \xi^2\right]/2$ and $\mu^2 = -\lambda v^2$, the kinetic term and the potential expands to

$$(\partial_\mu \phi)^*(\partial^\mu \phi) = \frac{1}{2}\partial_\mu(\eta + v - i\xi)\,\partial^\mu(\eta + v + i\xi)$$
$$= \frac{1}{2}(\partial_\mu \eta)^2 + \frac{1}{2}(\partial_\mu \xi)^2,$$
$$\mu^2 \phi^*\phi + \lambda(\phi^*\phi)^2 = -\frac{1}{2}\lambda v^2\left[(\eta + v)^2 + \xi^2\right] + \frac{1}{4}\lambda\left[(\eta + v)^2 + \xi^2\right]^2$$
$$= -\frac{1}{4}\lambda v^4 + \lambda v^2 \eta^2 + \lambda v\eta^3 + \frac{1}{4}\lambda\eta^4 + \frac{1}{4}\lambda\xi^4 + \lambda v\eta\xi^2 + \frac{1}{2}\lambda\eta^2\xi^2.$$

Neglecting the constant and higher order terms, the full Lagrangian can be written as

$$\mathcal{L}(\eta, \xi) = \frac{1}{2}(\partial_\mu \eta)^2 - \lambda v^2 \eta^2 + \frac{1}{2}(\partial_\mu \xi)^2 + \text{higher order terms.} \tag{B.7}$$

From the above expression, we can identify a massive η particle and a *massless* ξ particle, namely

$$m_\eta = \sqrt{2\lambda v^2} = \sqrt{-2\mu^2} > 0, \quad m_\xi = 0.$$

Unlike the η field which describes radial excitations, there is no "force" acting on oscillations along the ξ field. This is a direct consequence of the $U(1)$ symmetry of the Lagrangian. The massless particle ξ is the so-called Goldstone boson and appears as a result of the Goldstone theorem [527]: For every spontaneously broken continuous symmetry, massless Goldstone bosons will appear. The number of Goldstone bosons is equal to the number of broken generators of the underlying symmetry group.
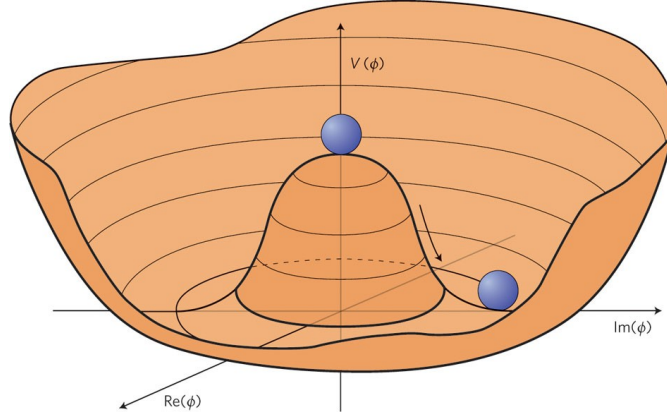
Figure B.1: The Mexican-hat potential for a complex scalar field ϕ with $\mu^2 < 0$. Figure from Ref. [31].

B.2 Local symmetry breaking

We study the implications of breaking a local gauge symmetry by using QED, a local $U(1)_Q$ gauge invariant theory as an example. We will see that this generates a mass term for the gauge (photon) field.[1]

We start with a local $U(1)_Q$ invariant Lagrangian for a complex scalar field ϕ as

$$\mathcal{L} = (\mathcal{D}^\mu \phi)^* (\mathcal{D}_\mu \phi) - \mu^2 \phi^* \phi - \lambda(\phi^* \phi)^2 - \frac{1}{4} F_{\mu\nu} F^{\mu\nu}, \tag{B.8}$$

where $\lambda > 0$ and $\mathcal{D}_\mu \equiv \partial_\mu + iQA_\mu$ is the covariant derivative. Again, depending on the sign of μ^2, we can study the particle spectrum in two cases.

1. $\mu^2 > 0$: In this case, the minimum of the potential is at $\phi_1 = \phi_2 = 0$. The exact symmetry of the Lagrangian is preserved in the vacuum as well. Thus, we have QED with a massless photon and two massive scalar particles ϕ_1 and ϕ_2, each with mass μ.

2. $\mu^2 < 0$: After expressing the ϕ field in terms of its components ϕ_1 and ϕ_2, we can see that the potential has a *Mexican hat* shape as shown in Fig. B.1. In this case, there are an infinite number of vacuum configurations that satisfy

$$|\phi|^2 = \phi_1^2 + \phi_2^2 = -\frac{\mu^2}{\lambda} = v^2.$$

We obtain the particle spectrum by studying the Lagrangian under small oscillations about the minimum. As a local gauge symmetry is broken, some important differences will appear. In particular, extra terms will appear in the kinetic term of the Lagrangian via the covariant derivative. Using the shifted fields η and ξ, we can

---

[1]This is done for illustration purposes only. A photon is known to be massless, i.e., $m_\gamma = 0$.

re-define the ϕ field as

$$\phi = \frac{1}{\sqrt{2}}(\eta + v + i\xi).$$

Consequently, the kinetic and potential terms in Eq. (B.8) expands to

$$(\mathcal{D}^\mu \phi)^*(\mathcal{D}_\mu \phi) = \frac{1}{2}(\partial^\mu - iQA^\mu)(\eta + v - i\xi)(\partial_\mu + iQA_\mu)(\eta + v + i\xi)$$

$$= \frac{1}{2}(\partial_\mu \eta)^2 + \frac{1}{2}(\partial_\mu \xi)^2 + \frac{1}{2}Q^2 v^2 A_\mu A^\mu + \frac{1}{2}Q^2(\eta^2 + \xi^2)A_\mu A^\mu$$

$$+ QvA_\mu(\partial^\mu \xi) + \ldots$$

$$\mu^2 \phi^* \phi + \lambda(\phi^* \phi)^2 = -\frac{1}{2}\lambda v^2 \left[(\eta + v)^2 + \xi^2\right] + \frac{1}{4}\lambda\left[(\eta + v)^2 + \xi^2\right]^2$$

$$= -\frac{1}{4}\lambda v^4 + \lambda v^2 \eta^2 + \lambda v \eta^3 + \frac{1}{4}\lambda \eta^4 + \frac{1}{4}\lambda \xi^4 + \lambda v \eta \xi^2 + \frac{1}{2}\lambda \eta^2 \xi^2.$$

Thus, the full Lagrangian is given by

$$\mathscr{L}(\eta, \xi) = \frac{1}{2}(\partial_\mu \eta)^2 - \lambda v^2 \eta^2 + \frac{1}{2}(\partial_\mu \xi)^2 - \frac{1}{4}F_{\mu\nu}F^{\mu\nu} + \frac{1}{2}Q^2 v^2 A_\mu A^\mu$$

$$+ QvA_\mu(\partial^\mu \xi) + \text{int. terms.}$$

This corresponds to a massive scalar η, a massless scalar ξ (same as before) and a massive photon field A_μ, namely

$$m_\eta = \sqrt{2\lambda v^2} = \sqrt{-2\mu^2} > 0, \quad m_\xi = 0, \quad m_\gamma = Qv. \tag{B.9}$$

However, we cannot easily interpret the term $QvA_\mu(\partial^\mu \xi)$. In QED, we can fix A_μ up to a term $\partial_\mu \alpha$ as in Eq. (2.6). In general, both A_μ and ϕ change simultaneously under the local $U(1)_Q$ transformations. We can exploit this freedom to re-define A_μ and remove all the terms involving the ξ field.

Looking only at the terms involving the ξ field, we can write them as

$$\frac{1}{2}(\partial_\mu \xi)^2 + QvA^\mu(\partial_\mu \xi) + \frac{1}{2}Q^2 v^2 A_\mu^2 = \frac{1}{2}Q^2 v^2 \left[A_\mu + \frac{1}{Qv}(\partial_\mu \xi)\right]^2 = \frac{1}{2}Q^2 v^2 (A_\mu')^2.$$

This specific choice, i.e., taking $\alpha(x) = \xi(x)/(Qv)$ in Eq. (2.4) corresponds to the *unitary gauge*. Of course, when choosing a gauge (the phase of the rotation angle α), the ϕ field changes simultaneously. Dropping terms of $O(\xi^2, \eta^2, \xi\eta)$, we get

$$\phi \to \phi' = e^{-iQ\alpha(x)}\phi = e^{-i\xi(x)/v}\frac{1}{\sqrt{2}}(\eta + v)e^{+i\xi(x)/v} = \frac{1}{\sqrt{2}}(v + h),$$

where h is the physical Higgs field. In writing the scalar Lagrangian in the unitary gauge, all the terms involving the ξ field will disappear and the associated degree of freedom will appear as a mass term for the gauge boson associated with the broken symmetry.
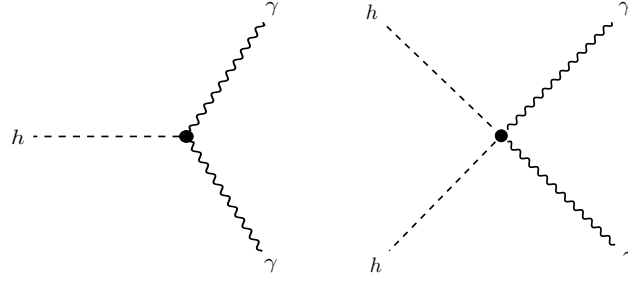
Figure B.2: Three- and four-point interaction between the Higgs boson and photon field.

In the unitary gauge, the Lagrangian can be written as

$$
\begin{aligned}
\mathscr{L}_{\text{scalar}} &= (\mathcal{D}^\mu \phi)^* (\mathcal{D}_\mu \phi) - V(\phi^*, \phi) \\
&= (\partial^\mu - iQA^\mu) \frac{1}{\sqrt{2}} (v + h)(\partial_\mu + iQA_\mu) \frac{1}{\sqrt{2}}(v + h) - V(\phi^*, \phi) \\
&= \frac{1}{2}(\partial_\mu h)^2 + \frac{1}{2}Q^2 A_\mu^2 (v + h)^2 - \lambda v^2 h^2 - \lambda v h^3 - \frac{1}{4}\lambda h^4 + \frac{1}{4}\lambda v^4.
\end{aligned}
$$

After expanding the $(v + h)^2$ term and ignoring the constant $\lambda v^4/4$, we get

$$
\begin{aligned}
\mathscr{L}_{\text{scalar}} &= \frac{1}{2}(\partial_\mu h)^2 - \lambda v^2 h^2 + \frac{1}{2}Q^2 v^2 A_\mu A^\mu + Q^2 v^2 h A_\mu A^\mu \\
&\quad + \frac{1}{2}Q^2 h^2 A_\mu A^\mu - \lambda v h^3 - \frac{1}{4}\lambda h^4.
\end{aligned}
$$

Thus, not only do we generate a mass term for the A_μ field, we also generate interaction terms between the Higgs h and the gauge boson field A_μ. After expanding the $Q^2 A_\mu^2 (v + h)^2/2$ term, we generate

- a term proportional to $Q^2 v^2 A_\mu A^\mu$ which corresponds to a mass term for the gauge (photon) field, namely $m_\gamma = Qv$.

- a term proportional to $Q^2 v^2 h A_\mu A^\mu$ which represents a three-point interaction between a Higgs boson and two-photon fields. A Feynman diagram for this interaction is shown in the left panel of Fig. B.2.

- a term proportional to $Q^2 h^2 A_\mu A^\mu$ which represents a four-point interaction between two photons and two Higgs bosons. A Feynman diagram for this interaction is shown in the right panel of Fig. B.2.

Appendix C

Big Bang Cosmology

C.1 Friedmann equations

The line-element for a homogeneous and isotropic universe is [32, 82]

$$ds^2 = dt^2 - a(t)^2 \left(\frac{dr^2}{1 - kr^2} + r^2 d\theta^2 + r^2 \sin^2 \theta d\phi^2 \right) = g_{\mu\nu} dx^\mu dx^\nu, \qquad \text{(C.1)}$$

where

$$g_{\mu\nu} = \begin{pmatrix} 1 & 0 & 0 & 0 \\ 0 & -\dfrac{a(t)^2}{1 - kr^2} & 0 & 0 \\ 0 & 0 & -a(t)^2 & 0 \\ 0 & 0 & 0 & -a(t)^2 \end{pmatrix} \qquad \text{(C.2)}$$

is a general space-time metric and $a(t)$ is the time-dependent scalar factor.[1] The time dependence of the scale factor indicates that the motion of objects in our universe is $r(t) \rightarrow a(t)r(t)$. The parameter k is the free curvature with values $k = -1, 0, 1$ for negatively, flat or positively curved universe respectively. When $k = 0$, $g_{\mu\nu}$ equals the Minkowski metric $\eta_{\mu\nu} = \text{diag}(1, -1, -1, -1)$.

Assuming the form of the metric given in Eq. (C.1), we can solve the following Einstein equations

$$R_{\mu\nu}(t) - \frac{1}{2} g_{\mu\nu}(t) R(t) + \Lambda(t) g_{\mu\nu}(t) = \frac{1}{M_p^2} T_{\mu\nu}(t), \qquad \text{(C.3)}$$

where $R_{\mu\nu}(t)$ is the Ricci tensor, $R = g^{\mu\nu} R_{\mu\nu}$ is the Ricci scalar, Λ is the cosmological constant and $M_p = 1/\sqrt{8\pi G}$ is the reduced Planck mass. The energy-momentum tensor $T_{\mu\nu}$ includes the energy density $\rho = T_{00}$ and the corresponding pressure p. The latter is defined as the direction-independent contribution to the diagonal entries T_{jj} of the energy-momentum tensor.

---

[1]From here onwards, we will work in natural units: $\hbar = c = k_B = 1$.

Using the time component of Eq. (C.3) to determine the scale factor $a(t)$, we arrive at the first Friedmann equation

$$\frac{\dot{a}(t)^2}{a(t)^2} + \frac{k}{a(t)^2} = \frac{\rho(t)}{3M_p^2} = \frac{\rho_m(t) + \rho_r(t) + \rho_\Lambda(t)}{3M_p^2}, \tag{C.4}$$

where $\rho_m(t)$, $\rho_r(t)$ and $\rho_\Lambda(t) = \Lambda(t)M_p^2$ is the energy density of matter, radiation and vacuum respectively. A similar, second condition from the symmetry of $T_{\mu\nu}$ and its derivatives gives

$$\frac{2\ddot{a}(t)}{a(t)} + \frac{\dot{a}(t)^2}{a(t)^2} + \frac{k}{a(t)^2} = -\frac{p(t)}{M_p^2}. \tag{C.5}$$

The two Friedmann equations in Eqs. (C.4) and (C.5) can be combined to give

$$\frac{\ddot{a}(t)}{a(t)} = -\frac{\rho(t) + 3p(t)}{6M_p^2}. \tag{C.6}$$

The cosmological model based on the above expression is known as *Friedmann-Lemaitre-Roberson-Walker* (FLRW) model.

In general, the relationship between pressure p and energy density ρ defines the thermodynamic equation of state as

$$p_j(t) = w_j \rho_j(t), \tag{C.7}$$

where

$$w_j = \begin{cases} 0, & \text{non-relativistic matter,} \\ 1/3, & \text{relativistic matter,} \\ -1, & \text{vacuum energy.} \end{cases} \tag{C.8}$$

Thus, it provides a crucial understanding of the matter content in our universe. By measuring w directly (or indirectly), we can estimate the matter/energy budget of our universe.

To track the evolution of the universe in terms of the scale factor $a(t)$ rather than time, we need to compute the time dependence of $a(t)$. The Friedmann equation gives a relation between $a(t)$ and $\rho(t)$, thus we need a relation between ρ and t (or a second relation between $a(t)$ and $\rho(t)$). It turns out that by using the second Friedmann equation in Eq. (C.5), we can extract the time dependence of the energy and matter densities as

$$\frac{d}{dt}\left(\rho_j a(t)^3\right) = -p_j \frac{d}{dt}\left(a(t)^3\right). \tag{C.9}$$

It relates the energy inside the volume a^3 to the work done by the pressure p. Using this conservation law, we find that [82]

$$\rho_j(a) = C a^{-3(1+w_j)}, \tag{C.10}$$

where C is the constant of integration. Using the values of w_j in Eq. (C.8), we get

$$\rho_j(a) \propto \begin{cases} a^{-3}, & \text{non-relativistic matter,} \\ a^{-4}, & \text{relativistic matter,} \\ C, & \text{vacuum energy.} \end{cases} \tag{C.11}$$

With the following definition for the Hubble parameter

$$H(t) \equiv \frac{\dot{a}(t)}{a(t)}, \tag{C.12}$$

we can rewrite Eq. (C.4) as

$$H(t)^2 = \frac{\rho_m(t)}{3M_p^2} + \frac{\rho_r(t)}{3M_p^2} + \frac{\Lambda(t)}{3} - \frac{k}{a(t)^2}. \tag{C.13}$$

A critical density ρ_c is the present-day density which gives $k = 0$, assuming $\Lambda = 0$ regardless of its actual value. After substituting these requirements in the above expression, we get [3]

$$\rho_c = 3H_0^2 M_p^2 = \frac{3H_0^2}{8\pi G} = 1.87847(23) \times 10^{-26} h^2 \, \text{kg m}^{-3}, \tag{C.14}$$

where $h = H_0/(100 \, \text{km}^{-1} \, \text{Mpc}^{-1})$ is the reduced Hubble constant.

It is standard to define the present-day density parameter Ω_x for various species as the dimensionless ratio

$$\Omega_x \equiv \frac{\rho_x(t = t_0)}{\rho_c} = \frac{\rho_x(t = t_0)}{3H_0^2 M_p^2}, \tag{C.15}$$

where $x \in (b, c, r, \Lambda)$ for baryons, cold dark matter (CDM), photons and relativistic neutrinos, and dark energy respectively. In this notation, Eq. (C.4) can be written as

$$1 + \frac{k}{H(t)^2 a(t)^2} = \frac{\rho(t)}{\rho_c(t)} = \Omega(t). \tag{C.16}$$

From this expression, we can see that the curvature k depends on the energy density of the universe, namely

$$k = a(t)^2 H(t)^2 \left[\Omega(t) - 1 \right]. \tag{C.17}$$

This expression holds for all time t including $t = t_0$, i.e., today. When $\Omega > 1$, the curvature is position as $k > 0$, i.e., the boundaries of the universe are well-defined. When $\Omega < 1$, the curvature is negative, whereas the universe is spatially flat ($k = 0$) when $\Omega = 1$.

From Eq. (C.11), we can see that the density of various species scale with different powers of the scale factor a. Thus, Eq. (C.13) can be conveniently expressed as

$$H(a) \equiv \frac{\dot{a}}{a} = H_0 \sqrt{(\Omega_c + \Omega_b)a^{-3} + \Omega_r a^{-4} + \Omega_k a^{-2} + \Omega_\Lambda a^{-3(1+w)}}, \tag{C.18}$$

where $\Omega_c + \Omega_b \equiv \Omega_m$ is the total matter density parameter, w is the dark energy equation of state, assuming negligible neutrino mass. By construction, the various Ω's add up to 1.

Using Eqs. (C.6) and (C.10), the time dependence of the scale factor is

$$a(t) = t^{2/[3(1+w_j)]}.$$ (C.19)

Thus, the time dependence of the Hubble parameter is

$$H(t) = \frac{\dot{a}(t)}{a(t)} = \frac{2}{3(1 + w_j)} \frac{1}{t}.$$ (C.20)

The above expressions for $a(t)$ and $H(t)$ fail for the vacuum energy with $w = -1$. For the vacuum energy density with $k = 0$ and in the absence of matter, Eq. (C.4) along with Eq. (C.12) gives

$$a(t) = e^{H(t)t} = e^{t\sqrt{\Lambda(t)/3}}.$$ (C.21)

Thus, the time dependence of $a(t)$ is

$$a(t) \sim \begin{cases} t^{2/3}, & \text{non-relativistic matter,} \\ t^{1/2}, & \text{relativistic matter,} \\ e^{t\sqrt{\Lambda(t)/3}}, & \text{vacuum energy.} \end{cases}$$ (C.22)

As a result, we can link three of the four measures for the evolution of our universe, namely (t, a, H). For the vacuum energy case $w = -1$, the scale factor and the expansion of the universe does not follow a simple power law, but rather an *exponential law*. This defines an inflationary expansion.

C.2 Matter and Radiation

To understand the implications of Eq. (C.8) on the evolution of the universe, we can study its composition in terms of the relativistic states (radiation), non-relativistic states (visible and dark matter), and a cosmological constant Λ. This is depicted in Fig. C.1. When the scale factor a increases, the relativistic energy density drops as a^{-4}. At the same time, the non-relativistic energy density drops as a^{-3}. This implies that as long as the relativistic energy density dominates, the relative fraction of matter increases linearly with a. When $a \sim 3 \times 10^{-4}$, the matter and radiation energy densities are approximately equal. On the other hand, the cosmological constant does not change and will eventually dominate the total energy density of the universe.

In Fig. C.1, we can see that neither the curvature k nor the vacuum energy density ρ_Λ plays a major role in the early universe. Thus, the first Friedmann equation in Eq. (C.4) can be written as

$$H(t)^2 \simeq \frac{\rho_m(t) + \rho_r(t)}{3M_p^2}.$$ (C.23)

The main change with respect to the previous discussion is on the use of temperature as an evolution variable rather than time.
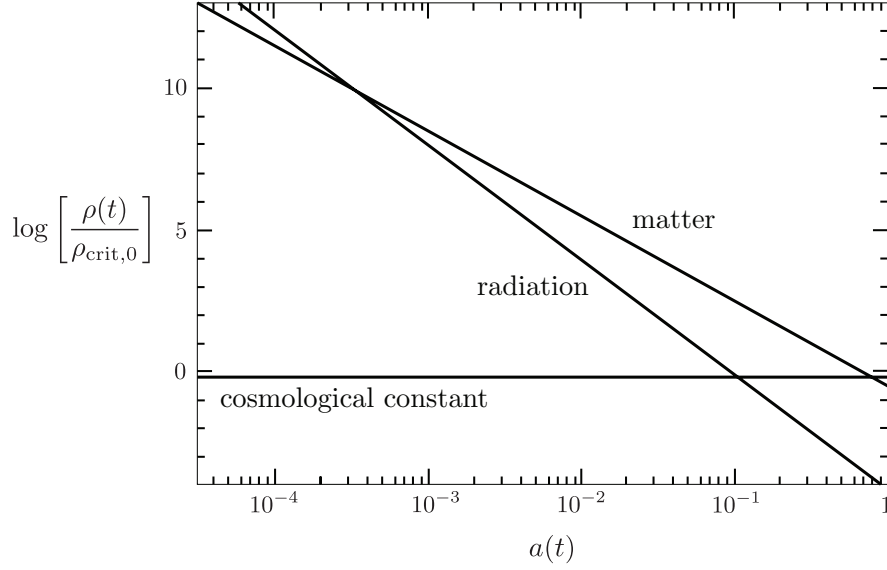
Figure C.1: Composition of the universe as a function of the scale factor $a(t)$. Figure from Ref. [32].

For relativistic and non-relativistic particles or radiation, we can obtain a unified picture in terms of their quantum fields. In doing so, we need to distinguish between the fermion and boson fields as well as the temperature T relative to the particle masses m. The number of degrees of freedom (e.g., anti-particle, spin, and colour states) is given by g. Assuming that the chemical potential can be neglected, we get [82]

$$n_{\mathrm{eq}}(T) = \begin{cases} g\left(\frac{mT}{2\pi}\right)^{3/2} e^{-m/T}, & \text{non-relativistic states, } T \ll m, \\ \frac{\zeta_3}{\pi^2} g T^3, & \text{relativistic bosons, } T \gg m, \\ \frac{3}{4}\frac{\zeta_3}{\pi^2} g T^3, & \text{relativistic fermions, } T \gg m, \end{cases} \tag{C.24}$$

where $\zeta_3 \simeq 1.202$. The quantum-statistical nature only matters when the state becomes relativistic and probe the relevant energy ranges. Similarly, we can compute the energy density in each case as

$$\rho_{\mathrm{eq}} = \begin{cases} mg\left(\frac{mT}{2\pi}\right)^{3/2} e^{-m/T}, & \text{non-relativistic states, } T \ll m, \\ \frac{\pi^2}{30} g T^4, & \text{relativistic bosons, } T \gg m, \\ \frac{7}{8}\frac{\pi^2}{30} g T^4, & \text{relativistic fermions, } T \gg m. \end{cases} \tag{C.25}$$

The number of *active* degrees of freedom depends on the temperature. For instance, above the electroweak scale $v_0 = 246.22\,\text{GeV}$, the effective number of degrees of freedom receives a contribution from all particles in the SM such that

$$g_f = g_{\mathrm{quark}} + g_{\mathrm{lepton}} + g_{\mathrm{neutrino}} = 6 \times 3 \times 2 \times 2 + 3 \times 2 \times 2 + 3 \times 2 = 90,$$

$$g_b = g_{\mathrm{gluon}} + g_{W/Z} + g_{\mathrm{photon}} + g_{\mathrm{Higgs}} = 8 \times 2 + 3 \times 3 + 2 + 1 = 28.$$
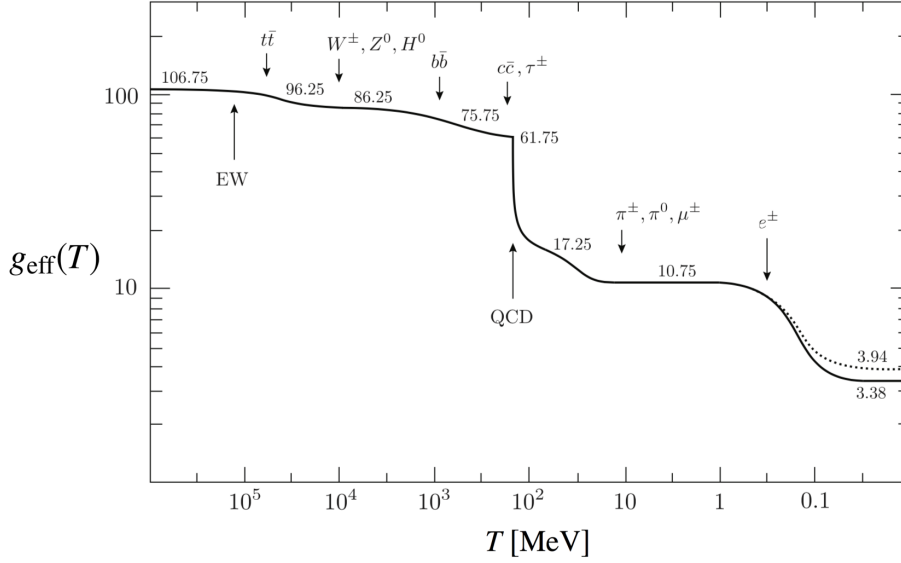
Figure C.2: Effective number of degrees of freedom $g_{\text{eff}}(T)$ vs temperature T. Figure from Ref. [32].

It is convenient to absorb the factor of $7/8$ in Eq. (C.25) into g. Thus, the relativistic matter energy density is given by

$$\rho_r = \frac{\pi^2}{30} g_{\text{eff}}(T) T^4. \tag{C.26}$$

This relation only holds if all states contributing to ρ_r have the same temperature, i.e., they are all in thermal equilibrium with each other. Of course, this does not have to be the case. In general, we can include states with different temperature and define $g_{\text{eff}}(T)$ as a weighted sum with the specific temperature of each component as

$$g_{\text{eff}}(T) = \sum_b g_b \left(\frac{T_b}{T}\right)^4 + \frac{7}{8} \sum_f g_f \left(\frac{T_f}{T}\right)^4, \tag{C.27}$$

where $b\,(f)$ refers to bosons (fermions). For the SM particle content at equal temperature, we get

$$g_{\text{eff}}(T > 175\,\text{GeV}) = 28 + \frac{7}{8} \times 90 = 106.75. \tag{C.28}$$

When the temperature lowers, the active number of degrees of freedom changes whenever a given particle species vanish at the respective threshold $T = m$. This is illustrated in Fig. C.2.

We can insert the expression for the relativistic matter density in Eq. (C.26) into Eq. (C.23) and obtain

$$H(t)^2 = \left(\frac{\pi \sqrt{g_{\text{eff}}}}{\sqrt{90}} \frac{T^2}{M_P^2}\right)^2. \tag{C.29}$$

This relation is important as it links the time, temperature and Hubble parameter together. i.e., the three possible scales in the evolution of our universe in the relativistic regime.

C.3 The ΛCDM model

The ΛCDM model is a parametrization of the Big Bang cosmological model in which the universe contains a cosmological constant Λ associated with dark energy, and cold dark matter (CDM). It is usually referred as the standard model of Big Bang cosmology as it is the simplest model that can account for following properties of the cosmos:

- the existence and structure of the cosmic microwave background (CMB);

- the large-scale structure in the distribution of galaxies;

- the abundances of hydrogen (including deuterium), helium, and lithium;

- the accelerating expansion of the universe as observed in the light coming from distant galaxies and supernovae.

The model is based on six parameters: physical baryon density parameter $\Omega_b h^2$; physical DM density parameter $\Omega_c h^2$; the age of the universe t_0; scalar spectral index n_s; curvature fluctuation amplitude Δ_R^2; and reionization optical depth τ. From these six parameters, the other model parameter values such as the Hubble constant H_0 and the dark energy density $\Omega_\Lambda h^2$ can be readily calculated. For the most up-to-date parameter estimates, see Ref. [75].

The most common set of observations that are fitted by the ΛCDM model includes the CMB anisotropy, the brightness/redshift relation for supernovae, and large-scale galaxy clustering including the baryon acoustic oscillation. Other observations such as the Hubble constant, the abundance of galaxy clusters, weak gravitational lensing and globular cluster ages are generally consistent and provide a check of the model, but are less precisely measured at present.

In accordance with Occam's razor, six is the smallest number of parameters needed to give an acceptable fit to current observations; other possible parameters are fixed at "natural" values, e.g., total density parameter $\Omega = 1$, $\Omega_k = 0$ and the dark energy equation of state $w = -1$. Thus, Eq. (C.18) simplifies to

$$H(a) = H_0 \sqrt{\Omega_m a^{-3} + \Omega_r a^{-4} + \Omega_\Lambda}. \tag{C.30}$$

Observations show that the radiation density is very small today, $\Omega_r \sim 10^{-4}$. If this term is neglected, the above expression has an analytical solution [528]

$$a(t) = (\Omega_m/\Omega_\Lambda)^{1/3} \sinh^{2/3}(t/t_\Lambda), \tag{C.31}$$

where $t_\Lambda \equiv 2/(3H_0\sqrt{\Omega_\Lambda})$. By solving for $a(t) = 1$, i.e., today, we can determine the present age of the universe t_0 in terms of the other ΛCDM model parameters.

Appendix D

Chiral rotation of fermion fields

D.1 Dirac fermion model

We start with the post-EWSB Lagrangian for the Dirac fermion DM field ψ as [30]

$$\mathcal{L}_\psi = \mathcal{L}_{\text{SM}} + \overline{\psi} i \partial\!\!\!/ \psi - \left[\mu_\psi \overline{\psi} \psi + \frac{1}{2} \frac{\lambda_{h\psi}}{\Lambda_\psi} v_0^2 \Big(\cos\theta \, \overline{\psi}\psi + \sin\theta \, \overline{\psi} i\gamma_5 \psi \Big) \right]$$
$$- \frac{\lambda_{h\psi}}{\Lambda_\psi} \Big(\cos\theta \, \overline{\psi}\psi + \sin\theta \, \overline{\psi} i\gamma_5 \psi \Big) \left(v_0 h + \frac{1}{2} h^2 \right). \tag{D.1}$$

The term in the square bracket contains a DM mass-type term, and a pseudoscalar coupling between the DM field and SM Higgs VEV v_0. It is convenient to remove the latter term ($\propto \sin\theta$) by redefining the field through a chiral rotation as

$$\psi \rightarrow e^{i\gamma_5 \alpha/2} \psi, \tag{D.2}$$

where α is a real, space-time-independent parameter. After expanding out the exponential and using the properties of the γ_5 matrix in the Dirac-representation, we get

$$e^{i\gamma_5 \alpha/2} = \cos(\gamma_5 \alpha/2) + i \sin(\gamma_5 \alpha/2) = \cos(\alpha/2) + i\gamma_5 \sin(\alpha/2),$$

where the property $\gamma_5^n = \gamma_5 \, (\mathbb{1}_{4\times4})$ for n odd (even) is used. Under the chiral rotation in Eq. (D.2), the term $\overline{\psi} i \partial\!\!\!/ \psi$ is invariant as

$$\overline{\psi} i \partial\!\!\!/ \psi \rightarrow \overline{\psi} e^{i\gamma_5 \alpha/2} i\gamma^\mu \partial_\mu \big(e^{i\gamma_5 \alpha/2} \psi \big) = \overline{\psi} e^{i\gamma_5 \alpha/2} \gamma^\mu e^{i\gamma_5 \alpha/2} i\partial_\mu \psi = \overline{\psi} i \partial\!\!\!/ \psi,$$

where we have used the property $\{\gamma_5, \gamma^\mu\} = 0$. On the other hand, $\overline{\psi}\psi$ and $\overline{\psi} i\gamma_5 \psi$ terms transform as

$$\overline{\psi}\psi \rightarrow \overline{\psi} e^{i\gamma_5 \alpha/2} e^{i\gamma_5 \alpha/2} \psi = \overline{\psi} e^{i\gamma_5 \alpha} \psi = \cos\alpha \, \overline{\psi}\psi + \sin\alpha \, \overline{\psi} i\gamma_5 \psi,$$
$$\overline{\psi} i\gamma_5 \psi \rightarrow \overline{\psi} e^{i\gamma_5 \alpha/2} i\gamma_5 e^{i\gamma_5 \alpha/2} \psi = \overline{\psi} e^{i\gamma_5 \alpha} i\gamma_5 \psi = \cos\alpha \, \overline{\psi} i\gamma_5 \psi - \sin\alpha \, \overline{\psi}\psi.$$

Thus, terms in the Dirac fermion Lagrangian transform as

$$\mu_\psi \overline{\psi}\psi \to \mu_\psi \cos\alpha\, \overline{\psi}\psi + \mu_\psi \sin\alpha\, \overline{\psi} i\gamma_5 \psi,$$

$$\frac{1}{2}\frac{\lambda_{h\psi}}{\Lambda_\psi} v_0^2 \Big(\cos\theta\, \overline{\psi}\psi + \sin\theta\, \overline{\psi} i\gamma_5 \psi\Big) \to \frac{1}{2}\frac{\lambda_{h\psi}}{\Lambda_\psi} v_0^2 \Big(\cos\theta\cos\alpha\, \overline{\psi}\psi + \cos\theta\sin\alpha\, \overline{\psi} i\gamma_5 \psi$$

$$+ \sin\theta\cos\alpha\, \overline{\psi} i\gamma_5\psi - \sin\theta\sin\alpha\, \overline{\psi}\psi\Big)$$

$$= \frac{1}{2}\frac{\lambda_{h\psi}}{\Lambda_\psi} v_0^2 \Big(\cos\xi\, \overline{\psi}\psi + \sin\xi\, \overline{\psi} i\gamma_5\psi\Big),$$

$$\frac{\lambda_{h\psi}}{\Lambda_\psi}\Big(\cos\theta\, \overline{\psi}\psi + \sin\theta\, \overline{\psi} i\gamma_5\psi\Big) \to \frac{\lambda_{h\psi}}{\Lambda_\psi}\Big(\cos\theta\cos\alpha\, \overline{\psi}\psi + \cos\theta\sin\alpha\, \overline{\psi} i\gamma_5\psi$$

$$+ \sin\theta\cos\alpha\, \overline{\psi} i\gamma_5\psi - \sin\theta\sin\alpha\, \overline{\psi}\psi\Big)$$

$$= \frac{\lambda_{h\psi}}{\Lambda_\psi}\Big(\cos\xi\, \overline{\psi}\psi + \sin\xi\, \overline{\psi} i\gamma_5\psi\Big),$$

where we have defined $\xi \equiv \theta + \alpha$ for future convenience and used the trigonometric identities $\cos\xi = \cos\theta\cos\alpha - \sin\theta\sin\alpha$ and $\sin\xi = \sin\theta\cos\alpha + \cos\theta\sin\alpha$. Thus, the mass and interaction terms expand to

$$-\Big[\mu_\psi \overline{\psi}\psi + \frac{1}{2}\frac{\lambda_{h\psi}}{\Lambda_\psi} v_0^2\Big(\cos\theta\, \overline{\psi}\psi + \sin\theta\, \overline{\psi} i\gamma_5\psi\Big)\Big] \to -\Big[\mu_\psi \cos\alpha\, \overline{\psi}\psi + \mu_\psi \sin\alpha\, \overline{\psi} i\gamma_5\psi$$

$$+ \frac{1}{2}\frac{\lambda_{h\psi}}{\Lambda_\psi} v_0^2\Big(\cos\xi\, \overline{\psi}\psi + \sin\xi\, \overline{\psi} i\gamma_5\psi\Big)\Big]$$

$$= -\Big[\mu_\psi \cos\alpha + \frac{1}{2}\frac{\lambda_{h\psi}}{\Lambda_\psi} v_0^2 \cos\xi\Big]\overline{\psi}\psi$$

$$- \Big[\mu_\psi \sin\alpha + \frac{1}{2}\frac{\lambda_{h\psi}}{\Lambda_\psi} v_0^2 \sin\xi\Big]\overline{\psi} i\gamma_5\psi,$$

$$\tag{D.3}$$

$$-\frac{\lambda_{h\psi}}{\Lambda_\psi}\Big(\cos\theta\, \overline{\psi}\psi + \sin\theta\, \overline{\psi} i\gamma_5\psi\Big)\Big(v_0 h + \frac{1}{2}h^2\Big) \to -\frac{\lambda_{h\psi}}{\Lambda_\psi}\Big(\cos\xi\, \overline{\psi}\psi + \sin\xi\, \overline{\psi} i\gamma_5\psi\Big)$$

$$\times \Big(v_0 h + \frac{1}{2}h^2\Big). \tag{D.4}$$

If $\alpha = \pi$, a sign change of the mass and interaction terms occur in the above expressions. Without any loss of generality, we can take $\mu_\psi > 0$ as long as the relative signs between these terms are preserved.

After the chiral rotation, we demand the coefficient of $\overline{\psi} i\gamma_5\psi$ term in Eq. (D.3) to vanish to go to the real mass basis. This defines a proper chiral rotation and gives mass to the Dirac fermion field after EWSB. Setting the coefficient of the $\overline{\psi} i\gamma_5\psi$ term to zero gives

$$\mu_\psi \sin\alpha = -\frac{1}{2}\frac{\lambda_{h\psi}}{\Lambda_\psi} v_0^2 \sin\xi = -\frac{1}{2}\frac{\lambda_{h\psi}}{\Lambda_\psi} v_0^2 \left(\cos\theta\sin\alpha + \sin\theta\cos\alpha\right).$$

Dividing the above expression on both sides by $\cos\alpha$ and re-arranging gives

$$\tan\alpha = \left(-\frac{1}{2}\frac{\lambda_{h\psi}}{\Lambda_\psi} v_0^2 \sin\theta\right)\left(\mu_\psi + \frac{1}{2}\frac{\lambda_{h\psi}}{\Lambda_\psi} v_0^2 \cos\theta\right)^{-1}. \tag{D.5}$$

Using the above expression, we can determine $\sin^2 \alpha$ and $\cos^2 \alpha$ as

$$\cos^2 \alpha = \frac{1}{1 + \tan^2 \alpha} = \frac{\left(\mu_\psi + \frac{1}{2}\frac{\lambda_{h\psi}}{\Lambda_\psi}v_0^2 \cos\theta\right)^2}{\left(\mu_\psi + \frac{1}{2}\frac{\lambda_{h\psi}}{\Lambda_\psi}v_0^2 \cos\theta\right)^2 + \left(\frac{1}{2}\frac{\lambda_{h\psi}}{\Lambda_\psi}v_0^2 \sin\theta\right)^2},$$

$$\sin^2 \alpha = \frac{\tan^2 \alpha}{1 + \tan^2 \alpha} = \frac{\left(\frac{1}{2}\frac{\lambda_{h\psi}}{\Lambda_\psi}v_0^2 \sin\theta\right)^2}{\left(\mu_\psi + \frac{1}{2}\frac{\lambda_{h\psi}}{\Lambda_\psi}v_0^2 \cos\theta\right)^2 + \left(\frac{1}{2}\frac{\lambda_{h\psi}}{\Lambda_\psi}v_0^2 \sin\theta\right)^2}.$$

After EWSB and chiral field rotation, we can define the DM mass m_ψ as the coefficient of the term proportional to $\overline{\psi}\psi$. Using Eq. (D.3), we get

$$m_\psi = \mu_\psi \cos\alpha + \frac{1}{2}\frac{\lambda_{h\psi}}{\Lambda_\psi}v_0^2 \cos\xi = \mu_\psi \cos\alpha + \frac{1}{2}\frac{\lambda_{h\psi}}{\Lambda_\psi}v_0^2\left(\cos\alpha\cos\theta - \sin\alpha\sin\theta\right)$$

$$= \left[\mu_\psi + \frac{1}{2}\frac{\lambda_{h\psi}}{\Lambda_\psi}v_0^2\left(\cos\theta - \tan\alpha\sin\theta\right)\right]\cos\alpha.$$

Using the expression for $\tan\alpha$ in Eq. (D.5), we get

$$m_\psi = \left[\frac{\left(\mu_\psi + \frac{1}{2}\frac{\lambda_{h\psi}}{\Lambda_\psi}v_0^2 \cos\theta\right)^2 + \left(\frac{1}{2}\frac{\lambda_{h\psi}}{\Lambda_\psi}v_0^2 \sin\theta\right)^2}{\mu_\psi + \frac{1}{2}\frac{\lambda_{h\psi}}{\Lambda_\psi}v_0^2 \cos\theta}\right]\cos\alpha.$$

Squaring both sides of the above expression and using the relation for $\cos^2 \alpha$ gives us a physical DM mass of

$$m_\psi^2 = \left[\frac{\left(\mu_\psi + \frac{1}{2}\frac{\lambda_{h\psi}}{\Lambda_\psi}v_0^2 \cos\theta\right)^2 + \left(\frac{1}{2}\frac{\lambda_{h\psi}}{\Lambda_\psi}v_0^2 \sin\theta\right)^2}{\mu_\psi + \frac{1}{2}\frac{\lambda_{h\psi}}{\Lambda_\psi}v_0^2 \cos\theta}\right]^2 \cos^2 \alpha$$

$$= \frac{\left[\left(\mu_\psi + \frac{1}{2}\frac{\lambda_{h\psi}}{\Lambda_\psi}v_0^2 \cos\theta\right)^2 + \left(\frac{1}{2}\frac{\lambda_{h\psi}}{\Lambda_\psi}v_0^2 \sin\theta\right)^2\right]^2}{\left(\mu_\psi + \frac{1}{2}\frac{\lambda_{h\psi}}{\Lambda_\psi}v_0^2 \cos\theta\right)^2 + \left(\frac{1}{2}\frac{\lambda_{h\psi}}{\Lambda_\psi}v_0^2 \sin\theta\right)^2}$$

$$= \left(\mu_\psi + \frac{1}{2}\frac{\lambda_{h\psi}}{\Lambda_\psi}v_0^2 \cos\theta\right)^2 + \left(\frac{1}{2}\frac{\lambda_{h\psi}}{\Lambda_\psi}v_0^2 \sin\theta\right)^2.$$

Notice that the signs of m_ψ, $\cos\alpha$ and $\sin\alpha$ are all common. Thus, we can choose the common sign to be "+" for m_ψ, $\cos\alpha = +\sqrt{\cos^2 \alpha}$ and $\sin\alpha = \sqrt{\sin^2 \alpha}$. The physical DM mass after EWSB is given by

$$m_\psi = \sqrt{\left(\mu_\psi + \frac{1}{2}\frac{\lambda_{h\psi}}{\Lambda_\psi}v_0^2 \cos\theta\right)^2 + \left(\frac{1}{2}\frac{\lambda_{h\psi}}{\Lambda_\psi}v_0^2 \sin\theta\right)^2}. \tag{D.6}$$

With the sign convention chosen above, the expression for $\cos\xi$ and $\sin\xi$ reduces to

$$
\cos\xi = \cos\alpha\,(\cos\theta - \sin\theta\tan\alpha) = \frac{\mu_\psi\cos\theta + \frac{1}{2}\frac{\lambda_{h\psi}}{\Lambda_\psi}v_0^2}{\sqrt{\left(\mu_\psi + \frac{1}{2}\frac{\lambda_{h\psi}}{\Lambda_\psi}v_0^2\cos\theta\right)^2 + \left(\frac{1}{2}\frac{\lambda_{h\psi}}{\Lambda_\psi}v_0^2\sin\theta\right)^2}}
$$

$$
= \frac{\mu_\psi}{m_\psi}\left(\cos\theta + \frac{1}{2}\frac{\lambda_{h\psi}}{\Lambda_\psi}\frac{v_0^2}{\mu_\psi}\right),
$$

$$
\sin\xi = \cos\alpha\,(\sin\theta + \cos\theta\tan\alpha) = \frac{\mu_\psi\sin\theta}{\sqrt{\left(\mu_\psi + \frac{1}{2}\frac{\lambda_{h\psi}}{\Lambda_\psi}v_0^2\cos\theta\right)^2 + \left(\frac{1}{2}\frac{\lambda_{h\psi}}{\Lambda_\psi}v_0^2\sin\theta\right)^2}}
$$

$$
= \frac{\mu_\psi}{m_\psi}\sin\theta,
$$

where we have used Eq. (D.6) to simplify the expressions. Thus, the final post-EWSB and chiral-rotated Dirac fermion Lagrangian is

$$
\mathcal{L}_\psi = \mathcal{L}_{\text{SM}} + \overline{\psi}(i\slashed{\partial} - m_\psi)\psi - \frac{\lambda_{h\psi}}{\Lambda_\psi}\left[\cos\xi\,\overline{\psi}\psi + \sin\xi\,\overline{\psi}i\gamma_5\psi\right]\left(v_0 h + \frac{1}{2}h^2\right), \qquad \text{(D.7)}
$$

where

$$
\cos\xi = \frac{\mu_\psi}{m_\psi}\left(\cos\theta + \frac{1}{2}\frac{\lambda_{h\psi}}{\Lambda_\psi}\frac{v_0^2}{\mu_\psi}\right), \quad \sin\xi = \frac{\mu_\psi}{m_\psi}\sin\theta,
$$

$$
m_\psi = \sqrt{\left(\mu_\psi + \frac{1}{2}\frac{\lambda_{h\psi}}{\Lambda_\psi}v_0^2\cos\theta\right)^2 + \left(\frac{1}{2}\frac{\lambda_{h\psi}}{\Lambda_\psi}v_0^2\sin\theta\right)^2}.
$$

D.2 Majorana fermion model

Consider the post-EWSB Lagrangian for the Majorana fermion field χ as

$$
\mathcal{L}_\chi = \mathcal{L}_{\text{SM}} + \frac{1}{2}\overline{\chi}i\slashed{\partial}\chi - \frac{1}{2}\left[\mu_\chi\overline{\chi}\chi + \frac{1}{2}\frac{\lambda_{h\chi}}{\Lambda_\chi}v_0^2\left(\cos\theta\,\overline{\chi}\chi + \sin\theta\,\overline{\chi}i\gamma_5\psi\right)\right]
$$

$$
- \frac{1}{2}\frac{\lambda_{h\chi}}{\Lambda_\chi}\left(\cos\theta\,\overline{\chi}\chi + \sin\theta\,\overline{\chi}i\gamma_5\chi\right)\left(v_0 h + \frac{1}{2}h^2\right).
$$

Apart from the conventional factor of $1/2$ in front of each Majorana field bilinear, the form of the post-EWSB Majorana fermion Lagrangian is analogous to Eq. (D.1). The proper chiral rotation again imposes the following condition

$$
\tan\alpha = \left(-\frac{1}{2}\frac{\lambda_{h\chi}}{\Lambda_\chi}v_0^2\sin\theta\right)\left(\mu_\chi + \frac{1}{2}\frac{\lambda_{h\chi}}{\Lambda_\chi}v_0^2\cos\theta\right)^{-1}.
$$

Finally, the post-EWSB and chiral-rotated Majorana fermion DM Lagrangian is

$$
\mathcal{L}_\chi = \mathcal{L}_{\text{SM}} + \frac{1}{2}\overline{\chi}(i\slashed{\partial} - m_\chi)\chi - \frac{1}{2}\frac{\lambda_{h\chi}}{\Lambda_\chi}\left[\cos\xi\,\overline{\chi}\chi + \sin\xi\,\overline{\chi}i\gamma_5\chi\right]\left(v_0 h + \frac{1}{2}h^2\right), \qquad \text{(D.8)}
$$

where

$$\cos\xi = \frac{\mu_\chi}{m_\chi}\left(\cos\theta + \frac{1}{2}\frac{\lambda_{h\chi}}{\Lambda_\chi}\frac{v_0^2}{\mu_\chi}\right), \quad \sin\xi = \frac{\mu_\chi}{m_\chi}\sin\theta,$$

$$m_\chi = \sqrt{\left(\mu_\chi + \frac{1}{2}\frac{\lambda_{h\chi}}{\Lambda_\chi}v_0^2\cos\theta\right)^2 + \left(\frac{1}{2}\frac{\lambda_{h\chi}}{\Lambda_\chi}v_0^2\sin\theta\right)^2}.$$

Appendix E

Scalar singlet effective potential

The one-loop correction to the zero temperature potential using the cutoff regularisation and on-shell scheme is [253, 400]

$$V_{1\text{-loop}}(\phi, S) = \sum_{i=\phi, \chi, W, Z}^{t, S} \frac{n_i}{64\pi^2} \left[m_i^4 \left(\log \frac{m_i^2}{m_{0i}^2} - \frac{3}{2} \right) + 2m_i^2 m_{0i}^2 \right], \tag{E.1}$$

where $n_{\{\phi, \chi, W, Z, t, S\}} = \{1, 3, 6, 3, -12, 1\}$ and m_0 are masses calculated at the electroweak VEV, i.e., $S = 0$, $\phi = v_0$. The field dependant masses are given by

$$m_W^2 = \frac{g^2}{4}\phi^2, \quad m_Z^2 = \frac{g^2 + g'^2}{4}\phi^2, \quad m_t^2 = \frac{y_t^2}{2}\phi^2, \quad m_\chi^2 = -\mu^2 + \lambda\phi^2 + \lambda_{HS}S^2. \tag{E.2}$$

The h and S masses are the eigenvalues of the following squared mass matrix

$$\mathcal{M}_{HS}^2 = \begin{pmatrix} -\mu^2 + 3\lambda\phi^2 + \lambda_{HS}S^2 & 2\lambda_{HS}\phi S \\ 2\lambda_{HS}\phi S & \mu_S^2 + 3\lambda_S S^2 + \lambda_{HS}\phi^2 \end{pmatrix}. \tag{E.3}$$

The finite temperature corrections are given by [238]

$$V_T(\phi, S, T) = \frac{T^4}{2\pi^2} \left[\sum_{i=\phi, \chi, W, Z, S} n_i J_b \left(\frac{m_i^2}{T^2} \right) + \sum_{i=t} n_i J_f \left(\frac{m_i^2}{T^2} \right) \right], \tag{E.4}$$

where

$$J_{b/f} \left(\frac{m_i^2}{T^2} \right) = \int_0^\infty dk \, k^2 \log \left[1 \mp \exp \left(-\sqrt{\frac{k^2 + m_i^2}{T^2}} \right) \right]. \tag{E.5}$$

The last important correction comes from resumming the multi-loop infrared divergent contributions to boson longitudinal polarizations [399, 529]. This is achieved by adding thermal corrections to scalars and longitudinal polarizations of the gauge bosons.

The thermal mass corrections are obtained by expanding Eq. (E.4) to the leading order in m^2/T^2 [399]. For the scalar singlet model, these are given by [400]

$$\Pi_\phi(T) = \Pi_\chi(T) = T^2 \left(\frac{g'^2}{16} + \frac{3g}{16} + \frac{\lambda}{2} + \frac{y_t^2}{4} + \frac{\lambda_S}{12} \right),$$

$$\Pi_S(T) = T^2 \left(\frac{\lambda_{HS}}{3} + \frac{\lambda_S}{4} \right), \quad \Pi_W(T) = \frac{11}{6}g^2 T^2. \tag{E.6}$$

For the two scalars ϕ and S, the thermal mass corrections are the eigenvalues of the following squared mass matrix

$$\mathcal{M}^2_{HS} + \begin{pmatrix} \Pi_\phi(T) & 0 \\ 0 & \Pi_S(T) \end{pmatrix}, \tag{E.7}$$

whereas the corrected Z and γ masses ($m^2_{Z/\gamma} + \Pi_{Z/\gamma}(T)$) are the eigenvalues of the following squared mass matrix

$$\begin{pmatrix} \frac{1}{4}g^2\phi^2 + \frac{11}{6}g^2T^2 & -\frac{1}{4}g'g\phi^2 \\ -\frac{1}{4}g'g\phi^2 & \frac{1}{4}g'^2\phi^2 + \frac{11}{6}g'^2T^2 \end{pmatrix}. \tag{E.8}$$

In all other cases, we simply use the substitution

$$m_i^2 \to m_i^2 + \Pi_i. \tag{E.9}$$

Finally, the finite temperature effective potential $V_{\text{eff}}(\phi, S, T)$ is given by

$$V_{\text{eff}}(\phi, S, T) = V_{\text{tree}}(\phi, S) + V_{\text{1-loop}}(\phi, S) + V_T(\phi, S, T), \tag{E.10}$$

where $V_{\text{tree}}(\phi, S)$ is the tree-level potential in Eq. (7.1).

Appendix F

Supplementary details

F.1 Tree-level scalar potential

The tree-level scalar potential in chapter 8 expands to

$$V_{\text{tree}} = -\mu_\Phi^2 \Phi^\dagger \Phi + \lambda_\Phi (\Phi^\dagger \Phi)^2 - \frac{1}{2}\mu_S^2 S^2 - \frac{1}{3}\mu_3 S^3 + \frac{1}{4}\lambda_S S^4 + \mu_{\Phi S}\Phi^\dagger \Phi S + \frac{1}{2}\lambda_{\Phi S}\Phi^\dagger \Phi S^2. \quad \text{(F.1)}$$

With the following definitions

$$\Phi = \begin{pmatrix} G^+ \\ \frac{1}{\sqrt{2}}(\phi + iG^0) \end{pmatrix}, \quad \Phi^\dagger = \begin{pmatrix} G^-, & \frac{1}{\sqrt{2}}(\phi - iG^0) \end{pmatrix},$$

where $G^- \equiv (G^+)^*$, the potential in Eq. (F.1) contains 2 complex (G^+, G^-) and 3 real (G^0, ϕ, S) scalar fields.

After EWSB, ϕ and S acquire their VEVs in Eq. (8.8). Thus, the following partial derivatives

$$\frac{\partial V_{\text{tree}}}{\partial G^0}, \frac{\partial V_{\text{tree}}}{\partial G^-}, \frac{\partial V_{\text{tree}}}{\partial G^+}, \frac{\partial V_{\text{tree}}}{\partial \phi}, \frac{\partial V_{\text{tree}}}{\partial S},$$

must vanish at the EWSB minimum

$$(\langle \phi \rangle|_{T=0}, \langle S \rangle|_{T=0}) = (v_0, s_0).$$

This gives

$$0 = \left.\frac{\partial V_{\text{tree}}}{\partial G^0}\right|_{(v_0,\, s_0)} = \left.\frac{\partial V_{\text{tree}}}{\partial G^-}\right|_{(v_0,\, s_0)} = \left.\frac{\partial V_{\text{tree}}}{\partial G^+}\right|_{(v_0,\, s_0)},$$

$$0 = \left.\frac{\partial V_{\text{tree}}}{\partial \phi}\right|_{(v_0,\, s_0)} = -\mu_\Phi^2 v_0 + \lambda_\Phi v_0^3 + \mu_{\Phi S}s_0 v_0 + \frac{1}{2}\lambda_{\Phi S}v_0 s_0^2,$$

$$0 = \left.\frac{\partial V_{\text{tree}}}{\partial S}\right|_{(v_0,\, s_0)} = -\mu_S^2 s_0 - \mu_3 s_0^2 + \lambda_S s_0^3 + \frac{1}{2}\mu_{\Phi S}v_0^2 + \frac{1}{2}\lambda_{\Phi S}s_0 v_0^2.$$

A simple rearrangement gives us the following EWSB conditions

$$\mu_\Phi^2 = \lambda_\Phi v_0^2 + \mu_{\Phi S} s_0 + \frac{1}{2}\lambda_{\Phi S} s_0^2, \tag{F.2}$$

$$\mu_S^2 = -\mu_3 s_0 + \lambda_S s_0^2 + \frac{\mu_{\Phi S} v_0^2}{2 s_0} + \frac{1}{2}\lambda_{\Phi S} v_0^2. \tag{F.3}$$

Now, we compute the second-order partial derivatives at the EWSB minimum. The only non-zero ones are given by

$$\left.\frac{\partial^2 V_{\text{tree}}}{\partial G^0\,\partial G^0}\right|_{(v_0,\,s_0)} = \left.\frac{\partial^2 V_{\text{tree}}}{\partial G^-\,\partial G^+}\right|_{(v_0,\,s_0)} = \left.\frac{\partial^2 V_{\text{tree}}}{\partial G^+\,\partial G^-}\right|_{(v_0,\,s_0)} = -\mu_\Phi^2 + \lambda_\Phi v_0^2 + \mu_{\Phi S} s_0 + \frac{1}{2}\lambda_{\Phi S} s_0^2,$$

$$\left.\frac{\partial^2 V_{\text{tree}}}{\partial \phi^2}\right|_{(v_0,\,s_0)} = -\mu_\Phi^2 + 3\lambda_\Phi v_0^2 + \mu_{\Phi S} s_0 + \frac{1}{2}\lambda_{\Phi S} s_0^2,$$

$$\left.\frac{\partial^2 V_{\text{tree}}}{\partial S^2}\right|_{(v_0,\,s_0)} = -\mu_S^2 - 2\mu_3 s_0 + 3\lambda_S s_0^2 + \frac{1}{2}\lambda_{\Phi S} v_0^2,$$

$$\left.\frac{\partial^2 V_{\text{tree}}}{\partial \phi\,\partial S}\right|_{(v_0,\,s_0)} = \left.\frac{\partial^2 V_{\text{tree}}}{\partial S\,\partial \phi}\right|_{(v_0,\,s_0)} = \mu_{\Phi S} v_0 + \lambda_{\Phi S} v_0 s_0.$$

Using Eqs. (F.2) and (F.3), these expressions can be simplified to

$$\left.\frac{\partial^2 V_{\text{tree}}}{\partial G^0\,\partial G^0}\right|_{(v_0,\,s_0)} = \left.\frac{\partial^2 V_{\text{tree}}}{\partial G^-\,\partial G^+}\right|_{(v_0,\,s_0)} = \left.\frac{\partial^2 V_{\text{tree}}}{\partial G^+\,\partial G^-}\right|_{(v_0,\,s_0)} = 0, \tag{F.4}$$

$$\left.\frac{\partial^2 V_{\text{tree}}}{\partial \phi^2}\right|_{(v_0,\,s_0)} = 2\lambda_\Phi v_0^2, \tag{F.5}$$

$$\left.\frac{\partial^2 V_{\text{tree}}}{\partial S^2}\right|_{(v_0,\,s_0)} = -\mu_3 s_0 + 2\lambda_S s_0^2 - \frac{\mu_{\Phi S} v_0^2}{2 s_0}, \tag{F.6}$$

$$\left.\frac{\partial^2 V_{\text{tree}}}{\partial \phi\,\partial S}\right|_{(v_0,\,s_0)} = \left.\frac{\partial^2 V_{\text{tree}}}{\partial S\,\partial \phi}\right|_{(v_0,\,s_0)} = \mu_{\Phi S} v_0 + \lambda_{\Phi S} v_0 s_0. \tag{F.7}$$

After EWSB, we can expand ϕ and S fields as

$$\phi = v_0 + \varphi, \quad S = s_0 + s. \tag{F.8}$$

As $\partial V_{\text{tree}}/\partial \phi = \partial V_{\text{tree}}/\partial \varphi$ and $\partial V_{\text{tree}}/\partial S = \partial V_{\text{tree}}/\partial s$, the mass term for the real scalar fields $\mathcal{A}^T = (\varphi, s)$ is

$$\mathscr{L}_{\text{mass–term}} = -\frac{1}{2}\mathcal{A}^T \mathcal{M}^2 \mathcal{A}, \tag{F.9}$$

where

$$\mathcal{M}^2 = \begin{pmatrix} \mathcal{M}_{\varphi\varphi}^2 & \mathcal{M}_{\varphi s}^2 \\ \mathcal{M}_{s\varphi}^2 & \mathcal{M}_{ss}^2 \end{pmatrix} \equiv \begin{pmatrix} \left.\frac{\partial^2 V_{\text{tree}}}{\partial \varphi^2}\right|_{(v_0,\,s_0)} & \left.\frac{\partial^2 V_{\text{tree}}}{\partial \varphi\,\partial s}\right|_{(v_0,\,s_0)} \\ \left.\frac{\partial^2 V_{\text{tree}}}{\partial s\,\partial \varphi}\right|_{(v_0,\,s_0)} & \left.\frac{\partial^2 V_{\text{tree}}}{\partial s^2}\right|_{(v_0,\,s_0)} \end{pmatrix} \tag{F.10}$$

is the squared mass matrix. Using Eqs. (F.5)–(F.7), the matrix elements are given by

$$\mathcal{M}_{\varphi\varphi}^2 = 2\lambda_\Phi v_0^2, \quad \mathcal{M}_{ss}^2 = -\mu_3 s_0 + 2\lambda_S s_0^2 - \frac{\mu_{\Phi S} v_0^2}{2 s_0}, \quad \mathcal{M}_{\varphi s}^2 = \mu_{\Phi S} v_0 + \lambda_{\Phi S} v_0 s_0. \tag{F.11}$$

For the EWSB minimum to be a stable (i.e., not a saddle point) solution of the potential, the symmetric 5×5 Hessian matrix $\mathcal{H}$ must be positive-definite. At the EWSB minimum, it is given by

$$
\mathcal{H}|_{(v_0, s_0)} = \begin{matrix} & \begin{matrix} G^0 & G^- & G^+ & \phi & \quad\quad S \end{matrix} \\ \begin{matrix} G^0 \\ G^- \\ G^+ \\ \phi \\ S \end{matrix} & \begin{pmatrix} 0 & 0 & 0 & 0 & 0 \\ 0 & 0 & 0 & 0 & 0 \\ 0 & 0 & 0 & 0 & 0 \\ 0 & 0 & 0 & 2\lambda_\Phi v_0^2 & \mu_{\Phi S} v_0 + \lambda_{\Phi S} v_0 s_0 \\ 0 & 0 & 0 & \mu_{\Phi S} v_0 + \lambda_{\Phi S} v_0 s_0 & -\mu_3 s_0 + 2\lambda_S s_0^2 - \frac{\mu_{\Phi S} v_0^2}{2 s_0} \end{pmatrix} \end{matrix}.
$$

The Hessian matrix is guaranteed to be positive-definite if the determinant (eigenvalue) of the 2×2 sub-matrix is non-zero (positive). This requires

$$
\lambda_\Phi > 0, \quad 2\lambda_S s_0^2 - \left(\mu_3 s_0 + \frac{\mu_{\Phi S} v_0^2}{2 s_0} \right) > 0. \tag{F.12}
$$

To study the bounds of the potential, Eq. (F.1) can be written in terms of the ϕ and S fields as

$$
V_{\text{tree}} \simeq -\frac{1}{2}\mu_\Phi^2 \phi^2 + \frac{1}{4}\lambda_\Phi \phi^4 - \frac{1}{2}\mu_S^2 S^2 - \frac{1}{3}\mu_3 S^3 + \frac{1}{4}\lambda_S S^4 + \frac{1}{2}\mu_{\Phi S}\phi^2 S + \frac{1}{4}\lambda_{\Phi S}\phi^2 S^2. \tag{F.13}
$$

Depending on the chosen direction in the ϕ–S plane, three scenarios are possible.

1. *Pure ϕ direction*: This corresponds to setting $S = 0$. Thus, the potential is bounded from below provided $\lambda_\Phi > 0$.

2. *Pure S direction*: The potential only depends on the S field. It is bounded from below provided $\lambda_S > 0$.

3. *General ϕ–S direction*: At large ϕ and S field values, the quartic terms in Eq. (F.13) dominate. In this case, the potential can be approximated by

$$
\begin{aligned}
V_{\text{tree}} &\approx \frac{1}{4}\lambda_\Phi \phi^4 + \frac{1}{4}\lambda_S S^4 + \frac{1}{4}\lambda_{\Phi S}\phi^2 S^2 \\
&= \frac{1}{4}\lambda_\Phi \phi^4 + \frac{1}{4}\lambda_S \left(S^4 + \frac{\lambda_{\Phi S}}{\lambda_S}\phi^2 S^2 \right) \\
&= \frac{1}{4}\lambda_\Phi \phi^4 + \frac{1}{4}\lambda_S \left(S^4 + \frac{\lambda_{\Phi S}}{\lambda_S}\phi^2 S^2 + \frac{1}{4}\frac{\lambda_{\Phi S}^2}{\lambda_S^2}\phi^4 \right) - \frac{1}{16}\frac{\lambda_{\Phi S}^2}{\lambda_S}\phi^4 \\
&= \frac{1}{4}\left(\lambda_\Phi - \frac{1}{4}\frac{\lambda_{\Phi S}^2}{\lambda_S} \right)\phi^4 + \frac{1}{4}\lambda_S \left(S^2 + \frac{1}{2}\frac{\lambda_{\Phi S}}{\lambda_S}\phi^2 \right)^2.
\end{aligned}
$$

Thus, the potential is bounded from below provided $\lambda_S > 0$ *and* $\lambda_{\Phi S} > -2\sqrt{\lambda_\Phi \lambda_S}$.

F.2 Mass eigenstate basis

The squared mass matrix $\mathcal{M}^2$ is real and symmetric. It can be diagonalised by an orthogonal matrix O. The mass eigenstates (h, H) are given by

$$
\begin{pmatrix} h \\ H \end{pmatrix} = \begin{pmatrix} \cos\alpha & -\sin\alpha \\ \sin\alpha & \cos\alpha \end{pmatrix} \begin{pmatrix} \varphi \\ s \end{pmatrix}, \tag{F.14}
$$

where (φ, s) fields are defined in the interaction eigenstate basis. Thus, we can write

$$
\begin{pmatrix} \varphi \\ s \end{pmatrix} = O \begin{pmatrix} h \\ H \end{pmatrix}, \quad O = \begin{pmatrix} \cos\alpha & \sin\alpha \\ -\sin\alpha & \cos\alpha \end{pmatrix}.
$$

We consider the following matrix product

$$
\begin{pmatrix} \varphi & s \end{pmatrix} \mathcal{M}^2 \begin{pmatrix} \varphi \\ s \end{pmatrix} = \begin{pmatrix} h & H \end{pmatrix} O^T \mathcal{M}^2 O \begin{pmatrix} h \\ H \end{pmatrix} \equiv \begin{pmatrix} h & H \end{pmatrix} \mathcal{D} \begin{pmatrix} h \\ H \end{pmatrix}, \tag{F.15}
$$

where $\mathcal{D} = \mathrm{diag}(m_h^2, m_H^2)$ is a diagonal squared mass matrix. The last equality in Eq. (F.15) requires

$$
O^T \mathcal{M}^2 O = \mathcal{D}. \tag{F.16}
$$

The left-hand side of the above equation expands to

$$
\begin{aligned}
O^T \mathcal{M}^2 O &= \begin{pmatrix} \cos\alpha & -\sin\alpha \\ \sin\alpha & \cos\alpha \end{pmatrix} \begin{pmatrix} \mathcal{M}_{\varphi\varphi}^2 & \mathcal{M}_{\varphi s}^2 \\ \mathcal{M}_{s\varphi}^2 & \mathcal{M}_{ss}^2 \end{pmatrix} \begin{pmatrix} \cos\alpha & \sin\alpha \\ -\sin\alpha & \cos\alpha \end{pmatrix} \\
&= \begin{pmatrix} \cos\alpha & -\sin\alpha \\ \sin\alpha & \cos\alpha \end{pmatrix} \begin{pmatrix} \mathcal{M}_{\varphi\varphi}^2 \cos\alpha - \mathcal{M}_{\varphi s}^2 \sin\alpha & \mathcal{M}_{\varphi\varphi}^2 \sin\alpha + \mathcal{M}_{\varphi s}^2 \cos\alpha \\ \mathcal{M}_{s\varphi}^2 \cos\alpha - \mathcal{M}_{ss}^2 \sin\alpha & \mathcal{M}_{s\varphi}^2 \sin\alpha + \mathcal{M}_{ss}^2 \cos\alpha \end{pmatrix}.
\end{aligned}
$$

Since $\mathcal{M}_{\varphi s}^2 = \mathcal{M}_{s\varphi}^2$, the elements of the $O^T \mathcal{M}^2 O$ matrix are

$$
\left[O^T \mathcal{M}^2 O \right]_{11} = \mathcal{M}_{\varphi\varphi}^2 \cos^2\alpha + \mathcal{M}_{ss}^2 \sin^2\alpha - 2\mathcal{M}_{\varphi s}^2 \sin\alpha \cos\alpha,
$$

$$
\left[O^T \mathcal{M}^2 O \right]_{22} = \mathcal{M}_{\varphi\varphi}^2 \sin^2\alpha + \mathcal{M}_{ss}^2 \cos^2\alpha + 2\mathcal{M}_{\varphi s}^2 \sin\alpha \cos\alpha,
$$

$$
\left[O^T \mathcal{M}^2 O \right]_{12} = \left[O^T \mathcal{M}^2 O \right]_{21} = -\frac{1}{2}(\mathcal{M}_{ss}^2 - \mathcal{M}_{\varphi\varphi}^2) \sin 2\alpha + \mathcal{M}_{\varphi s}^2 \cos 2\alpha.
$$

Using the above expressions and Eq. (F.16), we can write

$$
m_h^2 = \mathcal{M}_{\varphi\varphi}^2 \cos^2\alpha + \mathcal{M}_{ss}^2 \sin^2\alpha - 2\mathcal{M}_{\varphi s}^2 \sin\alpha \cos\alpha, \tag{F.17}
$$

$$
m_H^2 = \mathcal{M}_{\varphi\varphi}^2 \sin^2\alpha + \mathcal{M}_{ss}^2 \cos^2\alpha + 2\mathcal{M}_{\varphi s}^2 \sin\alpha \cos\alpha, \tag{F.18}
$$

$$
0 = -\frac{1}{2}(\mathcal{M}_{ss}^2 - \mathcal{M}_{\varphi\varphi}^2) \sin 2\alpha + \mathcal{M}_{\varphi s}^2 \cos 2\alpha. \tag{F.19}
$$

The last equality can be conveniently expressed as

$$
\tan 2\alpha = \frac{2\mathcal{M}_{\varphi s}^2}{\mathcal{M}_{ss}^2 - \mathcal{M}_{\varphi\varphi}^2}. \tag{F.20}
$$

We can write Eqs. (F.17)–(F.19) as the following matrix product

$$
\begin{pmatrix} m_h^2 \\ m_H^2 \\ 0 \end{pmatrix} = \begin{pmatrix} \cos^2 \alpha & \sin^2 \alpha & -2\sin\alpha\cos\alpha \\ \sin^2 \alpha & \cos^2 \alpha & 2\sin\alpha\cos\alpha \\ \sin\alpha\cos\alpha & -\sin\alpha\cos\alpha & \cos^2\alpha - \sin^2\alpha \end{pmatrix} \begin{pmatrix} \mathcal{M}_{\varphi\varphi}^2 \\ \mathcal{M}_{ss}^2 \\ \mathcal{M}_{\varphi s}^2 \end{pmatrix}.
$$

Taking the inverse of the 3×3 matrix above, i.e., $\alpha \to -\alpha$, we get

$$
\begin{pmatrix} \mathcal{M}_{\varphi\varphi}^2 \\ \mathcal{M}_{ss}^2 \\ \mathcal{M}_{\varphi s}^2 \end{pmatrix} = \begin{pmatrix} \cos^2 \alpha & \sin^2 \alpha & 2\sin\alpha\cos\alpha \\ \sin^2 \alpha & \cos^2 \alpha & -2\sin\alpha\cos\alpha \\ -\sin\alpha\cos\alpha & \sin\alpha\cos\alpha & \cos^2\alpha - \sin^2\alpha \end{pmatrix} \begin{pmatrix} m_h^2 \\ m_H^2 \\ 0 \end{pmatrix}.
$$

Using the above matrix product and Eq. (F.11), we can write

$$
\lambda_\Phi = \frac{\mathcal{M}_{\varphi\varphi}^2}{2v_0^2} = \frac{1}{2v_0^2} \left(m_h^2 \cos^2 \alpha + m_H^2 \sin^2 \alpha \right),
$$

$$
\mu_{\Phi S} = -\frac{2s_0}{v_0^2} \left(\mathcal{M}_{ss}^2 + \mu_3 s_0 - 2\lambda_S s_0^2 \right) = -\frac{2s_0}{v_0^2} \left(m_h^2 \sin^2 \alpha + m_H^2 \cos^2 \alpha + \mu_3 s_0 - 2\lambda_S s_0^2 \right),
$$

$$
\lambda_{\Phi S} = \frac{1}{v_0 s_0} \left(\mathcal{M}_{\varphi s}^2 - \mu_{\Phi S} v_0 \right) = \frac{1}{v_0 s_0} \left[(m_H^2 - m_h^2) \sin\alpha \cos\alpha - \mu_{\Phi S} v_0 \right].
$$

F.3 DM-nucleon coupling

The interaction eigenstates (φ, s) can be expressed in terms of the mass eigenstates (h, H) as

$$
\begin{pmatrix} \varphi \\ s \end{pmatrix} = \begin{pmatrix} \cos\alpha & \sin\alpha \\ -\sin\alpha & \cos\alpha \end{pmatrix} \begin{pmatrix} h \\ H \end{pmatrix}.
$$

Thus, the scalar-fermion DM and quark Yukawa term in the SM Lagrangian expands to

$$
\mathcal{L}_{\text{DM–quark}} = -g_S \bar{\psi}\psi s - \sum_{q=u,d,s}^{c,b,t} \frac{m_q}{v_0} \varphi \bar{q}q
$$

$$
= -g_S \bar{\psi}\psi (-\sin\alpha\, h + \cos\alpha\, H) - \sum_{q=u,d,s}^{c,b,t} \frac{m_q}{v_0} (\cos\alpha\, h + \sin\alpha\, H)\bar{q}q
$$

$$
= g_S \sin\alpha \bar{\psi}\psi h - \frac{\cos\alpha}{v_0} \sum_{q=u,d,s}^{c,b,t} m_q\, h\bar{q}q - g_S \cos\alpha \bar{\psi}\psi H - \frac{\sin\alpha}{v_0} \sum_{q=u,d,s}^{c,b,t} m_q\, H\bar{q}q.
$$

In a typical direct detection experiment, the momentum transfer q is roughly of the order of a few MeV. Assuming that the mediator mass $m_{h/H}$ is well above this value, i.e., $m_{h/H}^2 \gg q^2$, we can safely approach direct detection in the context of an effective field theory (EFT) and *integrate out* the scalar mediators [379]. This gives us an effective DM-quark interaction Lagrangian as

$$
\mathcal{L}_{\text{DM–quark}}^{\text{eff}} = - \sum_{q=u,d,s}^{c,b,t} G_q \bar{\psi}\psi\, \bar{q}q, \tag{F.21}
$$

where

$$G_q = \frac{g_S \sin\alpha \cos\alpha}{v_0} \left(\frac{1}{m_h^2} - \frac{1}{m_H^2} \right) m_q \tag{F.22}$$

is the effective DM-quark coupling.

To promote a DM-quark interaction to a DM-nucleon one, the quark contents of a nucleon must be taken into account. For a scalar mediator (as in our model), the quark Yukawa coupling scales with the mass of the interacting fermion. Thus, the dominant contribution comes from a nucleon strange quark content and gluons via heavy quark loops. These are parametrised by the hadronic matrix elements as

$$f_{Tq}^{(\mathcal{N})} \equiv \frac{m_q}{m_{\mathcal{N}}} \langle \mathcal{N} | \overline{q} q | \mathcal{N} \rangle, \tag{F.23}$$

where $\mathcal{N} \in (p, n)$. For a pure scalar interaction, the matrix elements parametrise the contribution of a quark mass m_q to the total mass of a nucleon $m_{\mathcal{N}}$. For more details, see Ref. [324] and references therein.

Using the heavy quark expansion [530], the contribution from gluons via heavy quark loops can be written as

$$f_{Tc}^{(\mathcal{N})} = f_{Tb}^{(\mathcal{N})} = f_{Tt}^{(\mathcal{N})} = \frac{2}{27} f_{TG}^{(\mathcal{N})} = \frac{2}{27} \left(1 - \sum_{q=u,d,s} f_{Tq}^{(\mathcal{N})} \right). \tag{F.24}$$

Thus, we can write

$$\frac{G_{\mathcal{N}}}{m_{\mathcal{N}}} \equiv \sum_{q=u,d,s}^{c,b,t} \frac{G_q}{m_q} f_{Tq}^{(\mathcal{N})} = \sum_{q=u,d,s} \frac{G_q}{m_q} f_{Tq}^{(\mathcal{N})} + \frac{2}{27} \left(1 - \sum_{q=u,d,s} f_{Tq}^{(\mathcal{N})} \right) \sum_{q=c,b,t} \frac{G_q}{m_q}.$$

Using Eq. (F.22), the above expression becomes

$$\frac{G_{\mathcal{N}}}{m_{\mathcal{N}}} = \frac{g_S \sin\alpha \cos\alpha}{v_0} \left(\frac{1}{m_h^2} - \frac{1}{m_H^2} \right) \left[\sum_{q=u,d,s} f_{Tq}^{(\mathcal{N})} + \frac{2}{9} \left(1 - \sum_{q=u,d,s} f_{Tq}^{(\mathcal{N})} \right) \right]$$

$$= \frac{g_S \sin\alpha \cos\alpha}{v_0} \left(\frac{1}{m_h^2} - \frac{1}{m_H^2} \right) f_{\mathcal{N}},$$

where

$$f_{\mathcal{N}} = \sum_{q=u,d,s} f_{Tq}^{(\mathcal{N})} + \frac{2}{9} \left(1 - \sum_{q=u,d,s} f_{Tq}^{(\mathcal{N})} \right) = \frac{2}{9} + \frac{7}{9} \sum_{q=u,d,s} f_{Tq}^{(\mathcal{N})}$$

is the Higgs-nucleon coupling. Thus, we can write down an effective DM-nucleon interaction Lagrangian as

$$\mathscr{L}_{\text{DM}-\mathcal{N}}^{\text{eff}} = - \sum_{\mathcal{N}=p,n} G_{\mathcal{N}} \overline{\psi} \psi \, \overline{\mathcal{N}} \mathcal{N}, \tag{F.25}$$

where

$$G_{\mathcal{N}} = \frac{g_S \sin\alpha \cos\alpha}{v_0} \left(\frac{1}{m_h^2} - \frac{1}{m_H^2} \right) m_{\mathcal{N}} f_{\mathcal{N}} \tag{F.26}$$

is the effective DM-nucleon coupling [481].

For a SI DM-nucleon interaction, the DM-nucleus interaction is a coherent sum over the number of protons Z and neutrons $(A - Z)$ in the nucleus. Thus, the SI cross-section for the DM-nucleus interaction is

$$\sigma_{\text{SI}}^{\psi N} = \frac{\mu_{\psi N}^2}{\pi} \left[ZG_p + (A - Z)G_n \right]^2, \tag{F.27}$$

where $\mu_{\psi N} = m_\psi m_N / (m_\psi + m_N)$ is the DM-nucleus reduced mass.

F.4   Effective potential

We include the following one-loop corrections to the zero temperature potential in the cutoff regularisation and on-shell scheme [253, 400]

$$V_{\text{1-loop}}(\phi, S) = \sum_{i=\phi, S, \chi}^{W, Z, t, \psi} \frac{n_i}{64\pi^2} \left[m_i^4 \left(\log \frac{m_i^2}{m_{0i}^2} - \frac{3}{2} \right) + 2m_i^2 m_{0i}^2 \right], \tag{F.28}$$

where $n_{\{\phi, S, \chi, W, Z, t, \psi\}} = \{1, 1, 3, 6, 3, -12, -4\}$. The subscript "0" denotes that the particle masses are calculated at the $T = 0$ minimum, i.e., $(\phi, S) = (v_0, s_0)$. The ϕ and S field dependant masses are given in section F.2, whereas the rest are given by

$$m_W^2 = \frac{g^2}{4}\phi^2, \qquad m_Z^2 = \frac{g^2 + g'^2}{4}\phi^2, \qquad m_t^2 = \frac{y_t^2}{2}\phi^2,$$
$$m_\chi^2 = -\mu_\Phi^2 + \lambda_\Phi \phi^2 + \mu_{\Phi S} S + \frac{1}{2}\lambda_{\Phi S} S^2, \quad m_\psi = \mu_\psi + g_S S. \tag{F.29}$$

The finite temperature corrections to the effective potential are given by

$$V_T(\phi, S, T) = \sum_{i=\phi, S, \chi}^{W, Z} \frac{n_i T^4}{2\pi^2} J_b\left(\frac{m_i^2}{T^2}\right) + \sum_{i=t, \psi} \frac{n_i T^4}{2\pi^2} J_f\left(\frac{m_i^2}{T^2}\right), \tag{F.30}$$

with

$$J_{b/f}\left(\frac{m_i^2}{T^2}\right) = \int_0^\infty dk \, k^2 \log\left[1 \mp \exp\left(-\sqrt{\frac{k^2 + m_i^2}{T^2}}\right)\right]. \tag{F.31}$$

The final important correction comes from resumming the multi-loop contributions to the boson longitudinal polarizations which are infrared divergent [399, 529]. We incorporate these corrections by supplementing the scalars and longitudinal polarizations of the gauge bosons with thermal mass corrections. These are obtained by expanding Eq. (F.30) to the leading order in m^2/T^2 [399]. In our model, these are given by

$$\Pi_\phi(T) = \Pi_\chi(T) = T^2 \left(\frac{g'^2}{16} + \frac{3g}{16} + \frac{\lambda_\Phi}{2} + \frac{y_t^2}{4} + \frac{\lambda_{\Phi S}}{24} \right),$$
$$\Pi_S(T) = T^2 \left(\frac{\lambda_{\Phi S}}{3} + \frac{\lambda_S}{4} + \frac{g_S^2}{6} \right), \quad \Pi_W(T) = \frac{11}{6} g^2 T^2. \tag{F.32}$$

For the ϕ and S fields, the corrected masses are the eigenvalues of the following squared mass matrix

$$\mathcal{M}^2 + \begin{pmatrix} \Pi_\phi(T) & 0 \\ 0 & \Pi_S(T) \end{pmatrix}, \tag{F.33}$$

where $\mathcal{M}^2$ is defined in Eq. (F.10). For Z and γ, i.e., $m_{Z/\gamma}^2 + \Pi_{Z/\gamma}(T)$, the mass corrections are the eigenvalues of the following squared mass matrix

$$\begin{pmatrix} \frac{1}{4}g^2\phi^2 + \frac{11}{6}g^2T^2 & -\frac{1}{4}g'g\phi^2 \\ -\frac{1}{4}g'g\phi^2 & \frac{1}{4}g'^2\phi^2 + \frac{11}{6}g'^2T^2 \end{pmatrix}. \tag{F.34}$$

In other cases, we simply use the substitution

$$m_i^2 \to m_i^2 + \Pi_i. \tag{F.35}$$

Finally, the effective potential $V_{\text{eff}}(\phi, S, T)$ is given by

$$V_{\text{eff}}(\phi, S, T) = V_{\text{tree}}(\phi, S) + V_{\text{1-loop}}(\phi, S) + V_T(\phi, S, T), \tag{F.36}$$

where $V_{\text{tree}}(\phi, S)$ is the tree-level scalar potential in section F.1.

Appendix G

Annihilation cross sections

For the Higgs portal models, the SM final states from the DM annihilation include W^+W^-, ZZ, $\tau^+\tau^-$, $t\bar{t}$, $b\bar{b}$, $c\bar{c}$ and hh. For all final states except hh, the DM annihilation proceeds via an s-channel Higgs exchange. For massive gauge bosons, the annihilation cross-section is given by

$$\sigma v_{\text{rel}}^{\text{cms}} = P(X)\delta_i v_i \lambda_{hX}^2 \frac{s}{8\pi}|D_h(s)|^2 \left(1 - 4x_i + 12x_i^2\right), \tag{G.1}$$

where $P(X)$ is defined in chapter 9, $i \in (W, Z)$, $\lambda_{hX} \in (\lambda_{hV}, \lambda_{h\psi}/\Lambda_\psi)$, $\delta_W = 1$, $\delta_Z = 1/2$, $v_i \equiv \sqrt{1 - 4x_i}$ and $x_i \equiv m_i^2/s$. The parameter $|D_h(s)|^2$ is the square of the full Higgs propagator and is given by

$$|D_h(s)|^2 = \frac{1}{\left(s - m_h^2\right)^2 + m_h\Gamma_h(\sqrt{s})}. \tag{G.2}$$

For final states involving SM fermion, the annihilation cross-section is given by

$$\sigma v_{\text{rel}}^{\text{cms}} = P(X)\frac{m_f^2}{4\pi}C_f v_f^3 \lambda_{hX}^2|D_h(s)|^2, \tag{G.3}$$

where C_f is a colour factor. For leptons, $C_f = 1$, whereas for quarks, it includes an important 1-loop vertex correction given by [531]

$$C_f = 3\left\{1 + \left[\frac{3}{2}\log\left(\frac{m_f^2}{s}\right) + \frac{9}{4}\right]\frac{4\alpha_s}{3\pi}\right\}, \tag{G.4}$$

where α_s is the strong coupling constant.

For the hh final state, additional contributions appear from the four-point contact interaction as well as the DM exchange in t- and u-channels. The annihilation cross-

section for $VV \to hh$ is

$$\sigma v_{\text{rel}}^{\text{cms}}(VV \to hh) = \frac{\lambda_{hV}^2 v_h}{2304\pi s x_V^4}|D_h(s)|^2\left[\frac{8\beta v_0^2 \lambda_{hV}}{1 - 2x_h^2}\coth^{-1}\beta\right.$$

$$\times\left\{2s\,(2x_h - 1)\,x_V\left((x_h - 1)\,(2x_h + 1) - x_\Gamma^2\right)\right.$$

$$\times\left(x_h^2 + 24x_V^3 + 2\,(x_h - 1)^2 - 4\,(2x_h + 1)\,x_V^2\right)$$

$$- v_0^2\lambda_{hV}\left[(3x_h^4 - 8x_h^3 x_V - x_h(x_h - 4x_V)(8x_V^2 + 1)\right.$$

$$\left.\left.-2x_V(24x_V^3 - 2x_V + 1))(x_h - 1)^2 + x_\Gamma^2))\right]\right\}$$

$$+ 4s^2 x_V^2\,(4x_V\,(3x_V - 1) + 1)\left((2x_h + 1)^2 + x_\Gamma^2\right)$$

$$- 4sx_V\lambda_{hV}v_0^2\,(2x_h\,(2x_V + 1) + 1 - 6x_V)\left(x_h\,(2x_h - 1) - 1 - x_\Gamma^2\right)$$

$$+ \frac{\lambda_{hV}^2 v_0^4\left[(x_h - 1)^2 + x_\Gamma^2\right]}{x_h^2 - 4x_V x_h + x_V}\left(6x_h^4 + 4x_h^3\,(1 - 8x_V)\right.$$

$$\left.\left.+ x_h^2\,(12x_V\,(4x_V - 1) + 1) - 64x_V^3 x_h + 96x_V^4 + x_V\right)\right], \tag{G.5}$$

where $\beta = (1 - 2x_h)/(v_h v_V)$ and $x_\Gamma = \Gamma_h m_h/s$. Similarly, the annihilation cross-section for $\overline{\psi}\psi \to hh$ is given by

$$\sigma v_{\text{rel}}^{\text{cms}}(\overline{\psi}\psi \to hh) = \left(\frac{\lambda_{h\psi}}{\Lambda_\psi}\right)^2\frac{v_h}{32\pi s}\left[3s^2|D_h(s)|^2 x_h\right.$$

$$\times\left(8v_0^2\cos\xi\,(x_h - 1)\frac{\lambda_{h\psi}}{\Lambda_\psi}m_\psi - ss\,(x_h + 2)\left(4x_\psi\cos^2\xi - 1\right)\right)$$

$$+ \frac{4\beta s^2|D_h(s)|^2 v_0^2\coth^{-1}\beta}{(1 - 2x_h)^2}\frac{\lambda_{h\psi}}{\Lambda_\psi}\left\{2m_\psi\cos\xi\,(2x_h - 1)\right.$$

$$\times\left(x_h\,(2x_h - 1) - x_\Gamma^2 - 1\right)\left(8x_\psi\cos^2\xi - 2x_h - 1\right)$$

$$+ \frac{\lambda_{h\psi}}{\Lambda_\psi}v_0^2\left(1 - 4x_h + 6x_h^2 - 16x_\psi\cos^2\xi\,(x_h - 1) - 32x_\psi^2\cos^4\xi\right)$$

$$\times\left.\left((x_h - 1)^2 + x_\Gamma^2\right)\right\}$$

$$- \left(\frac{\lambda_{h\psi}}{\Lambda_\psi}\right)^2\frac{2v_0^4\left(2x_\psi\,(8x_\psi\cos^4\xi + 1) - 8\,(1 + \cos^2\xi)\,x_h x_\psi + 3x_h^2\right)}{x_h^2 + x_\psi - 4x_h x_\psi}$$

$$+ \left.\left(s - 4sx_\psi\cos^2\xi - 8\frac{\lambda_{h\psi}}{\Lambda_\psi}m_\psi v_0^2\cos\xi\right)\right], \tag{G.6}$$

where $\beta = (1 - 2x_h)/(v_h v_\psi)$.

References

[1] *Standard Model of Elementary Particles*, https://upload.wikimedia.org/wikipedia/commons/0/00/Standard_Model_of_Elementary_Particles.svg.

[2] *Principal of Wu experiment (1956) to detect parity violation in nuclear beta decay*, https://upload.wikimedia.org/wikipedia/commons/f/f8/Wu_experiment.jpg.

[3] Particle Data Group Collaboration, C. Patrignani et al., *Review of Particle Physics*, *Chin. Phys. C* **40** (2016) 100001.

[4] I. V. Vulpen, *The Standard Model Higgs Boson*, pp. 1–49. Science Park, Amsterdam, 2013.

[5] LHC Higgs Cross Section Working Group Collaboration, S. Dittmaier et al., *Handbook of LHC Higgs Cross Sections: 1. Inclusive Observables*, [1101.0593].

[6] A. Denner, S. Heinemeyer, I. Puljak, D. Rebuzzi and M. Spira, *Standard Model Higgs-Boson Branching Ratios with Uncertainties*, *Eur. Phys. J. C* **71** (2011) 1753, [1107.5909].

[7] L. Reina, *TASI 2011: lectures on Higgs-Boson Physics*, in *The Dark Secrets of the Terascale: Proceedings, TASI 2011, Boulder, Colorado, USA, Jun 6 - Jul 11, 2011*, pp. 39–106, 2013, [1208.5504].

[8] Tev4LHC Higgs working group Collaboration, *Standard Model Higgs cross sections at hadron colliders*, http://maltoni.home.cern.ch/maltoni/TeV4LHC/SM.html.

[9] Tevatron New Physics Higgs Working Group, CDF, DØ Collaboration, *Updated Combination of CDF and DØ Searches for Standard Model Higgs Boson Production with up to 10.0 fb^{-1} of Data*, 2012, [1207.0449].

[10] ATLAS Collaboration, G. Aad et al., *Observation of a new particle in the search for the Standard Model Higgs boson with the ATLAS detector at the LHC*, *Phys. Lett. B* **716** (2012) 1–29, [`1207.7214`].

[11] ATLAS, CMS Collaboration, G. Aad et al., *Measurements of the Higgs boson production and decay rates and constraints on its couplings from a combined ATLAS and CMS analysis of the LHC pp collision data at $\sqrt{s}$ = 7 and 8 TeV*, *JHEP* **08** (2016) 045, [`1606.02266`].

[12] K. Garrett and G. Duda, *Dark Matter: A Primer*, *Adv. Astron.* **2011** (2011) 968283, [`1006.2483`].

[13] B. Koberlein, *Science in the raw*, `https://briankoberlein.com/2015/06/15/science-in-the-raw/`, 2015.

[14] J. Abdallah et al., *Simplified Models for Dark Matter Searches at the LHC*, *Phys. Dark Univ.* **9-10** (2015) 8–23, [`1506.03116`].

[15] M. A. Deliyergiyev, *Recent Progress in Search for Dark Sector Signatures*, *Open Phys.* **14** (2016) 281–303, [`1510.06927`].

[16] F. S. Queiroz, *Dark Matter Overview: Collider, Direct and Indirect Detection Searches*, in *Proceedings, 51st Rencontres de Moriond on Electroweak Interactions and Unified Theories: La Thuile, Italy, March 12-19, 2016*, pp. 427–436, ARISF, ARISF, 2016, [`1605.08788`].

[17] F. Kahlhoefer, *Review of LHC Dark Matter Searches*, *Int. J. Mod. Phys.* **A32** (2017) 1730006, [`1702.02430`].

[18] T. Saab, *An Introduction to Dark Matter Direct Detection Searches & Techniques*, in *The Dark Secrets of the Terascale: Proceedings, TASI 2011, Boulder, Colorado, USA, Jun 6 - Jul 11, 2011*, pp. 711–738, 2013, [`1203.2566`].

[19] PANDAX-II Collaboration, X. Cui et al., *Dark Matter Results From 54-Ton-Day Exposure of PandaX-II Experiment*, *Phys. Rev. Lett.* **119** (2017) 181302, [`1708.06917`].

[20] J. Liu, X. Chen and X. Ji, *Current status of direct dark matter detection experiments*, *Nature Phys.* **13** (2017) 212–216, [`1709.00688`].

[21] R. Bernabei et al., *DAMA/LIBRA results and perspectives, Bled 2013DAMA/LIBRA results and perspectives of phase 2*, *Bled Workshops Phys.* **14** (2013) 13–21, [`1403.1404`].

[22] SUPER-KAMIOKANDE Collaboration, K. Choi et al., *Search for neutrinos from annihilation of captured low-mass dark matter particles in the Sun by Super-Kamiokande*, *Phys. Rev. Lett.* **114** (2015) 141301, [`1503.04858`].

[23] PICO Collaboration, C. Amole et al., *Dark Matter Search Results from the PICO-2L C_3F_8 Bubble Chamber*, *Phys. Rev. Lett.* **114** (2015) 231302, [`1503.00008`].

[24] PICO Collaboration, C. Amole et al., *Dark matter search results from the PICO-60 CF_3I bubble chamber*, *Phys. Rev. D* **93** (2016) 052014, [`1510.07754`].

[25] J. M. Cline, *Baryogenesis*, in *Les Houches Summer School - Session 86: Particle Physics and Cosmology: The Fabric of Spacetime Les Houches, France, July 31-August 25, 2006*, 2006, [`hep-ph/0609145`].

[26] D. E. Morrissey and M. J. Ramsey-Musolf, *Electroweak baryogenesis*, *New J. Phys.* **14** (2012) 125003, [`1206.2942`].

[27] G. Belanger, F. Boudjema and A. Pukhov, *micrOMEGAs : a code for the calculation of Dark Matter properties in generic models of particle interaction*, in *The Dark Secrets of the Terascale: Proceedings, TASI 2011, Boulder, Colorado, USA, Jun 6 - Jul 11, 2011*, pp. 739–790, 2013, [`1402.0787`].

[28] M. Doro et al., *Dark matter and fundamental physics with the Cherenkov Telescope Array*, *Astropart. Phys.* **43** (2013) 189–214, [`1208.5356`].

[29] H. Silverwood, C. Weniger, P. Scott and G. Bertone, *A realistic assessment of the CTA sensitivity to dark matter annihilation*, *J. Cosmol. Astropart. Phys.* **1503** (2015) 055, [`1408.4131`].

[30] A. Beniwal, F. Rajec, C. Savage, P. Scott, C. Weniger, M. White et al., *Combined analysis of effective Higgs portal dark matter models*, *Phys. Rev. D* **93** (2016) 115016, [`1512.06458`].

[31] CMS Collaboration, W. de Boer, *The Discovery of the Higgs Boson with the CMS Detector and its Implications for Supersymmetry and Cosmology*, in *Time and Matter 2013 (TAM2013) Venice, Italy*, 2013, [`1309.0721`].

[32] D. Baumann, *Cosmology: Part III Mathematical Tripos*, http://www.damtp.cam.ac.uk/user/db275/Cosmology/Lectures.pdf.

[33] LHC HIGGS CROSS SECTION WORKING GROUP Collaboration, J. R. Andersen et al., *Handbook of LHC Higgs Cross Sections: 3. Higgs Properties*, [`1307.1347`].

[34] I. J. R. Aitchison and A. J. G. Hey, *Gauge theories in particle physics: A practical introduction. Vol. 1: From relativistic quantum mechanics to QED*. CRC Press, Bristol, UK, 2012.

[35] M. J. White, *Gauge Field Theory Course Notes*, pp. 1–187. Uni. of Adelaide, Australia, 2014.

[36] R. D. Young, *Quantum Field Theory*, pp. 1–113. Uni. of Adelaide, Australia, 2014.

[37] E. Noether, *Invariant variation problems*, *Transport Theory and Statistical Physics* **1** (Jan., 1971) 186–207, [`physics/0503066`].

[38] G. Rajasekaran, *Fermi and the Theory of Weak Interactions*, *Resonance J. Sci. Educ.* **19** (2014) 18–44, [`1403.3309`].

[39] E. Merzbacher, *Quantum Mechanics*. Jonh Wiley and Sons Ltd., New York, 2nd ed., 1970.

[40] C. S. Wu, E. Ambler, R. W. Hayward, D. D. Hoppes and R. P. Hudson, *Experimental test of parity conservation in beta decay*, *Phys. Rev.* **105** (Feb, 1957) 1413–1415.

[41] F. Englert and R. Brout, *Broken symmetry and the mass of gauge vector mesons*, *Phys. Rev. Lett.* **13** (Aug, 1964) 321–323.

[42] P. W. Higgs, *Broken symmetries and the masses of gauge bosons*, *Phys. Rev. Lett.* **13** (Oct, 1964) 508–509.

[43] P. W. Higgs, *Broken symmetries, massless particles and gauge fields*, *Phys. Lett.* **12** (1964) 132 – 133.

[44] P. W. Higgs, *Spontaneous symmetry breakdown without massless bosons*, *Phys. Rev.* **145** (May, 1966) 1156–1163.

[45] G. S. Guralnik, C. R. Hagen and T. W. B. Kibble, *Global conservation laws and massless particles*, *Phys. Rev. Lett.* **13** (Nov, 1964) 585–587.

[46] T. W. B. Kibble, *Symmetry breaking in non-abelian gauge theories*, *Phys. Rev.* **155** (Mar, 1967) 1554–1561.

[47] M. Kobayashi and T. Maskawa, *CP Violation in the Renormalizable Theory of Weak Interaction*, *Prog. Theor. Phys.* **49** (1973) 652–657.

[48] N. Cabibbo, *Unitary symmetry and leptonic decays*, *Phys. Rev. Lett.* **10** (Jun, 1963) 531–533.

[49] J. R. Fry, *CP violation and the standard model*, *Reports on Progress in Physics* **63** (2000) 117.

[50] Y. Nir, *CP violation in and beyond the standard model*, in *Proceedings, 27th SLAC Summer Institute on Particle Physics: CP Violation in and Beyond the Standard Model (SSI 99): Stanford, USA, July 7-16, 1999*, pp. 165–243, 1999, [hep-ph/9911321].

[51] L. Wolfenstein, *Parametrization of the kobayashi-maskawa matrix*, *Phys. Rev. Lett.* **51** (Nov, 1983) 1945–1947.

[52] CKMFITTER GROUP Collaboration, J. Charles, A. Hocker, H. Lacker, S. Laplace, F. R. Le Diberder, J. Malcles et al., *CP violation and the CKM matrix: Assessing the impact of the asymmetric B factories*, *Eur. Phys. J. C* **41** (2005) 1–131, [hep-ph/0406184].

[53] UTFIT Collaboration, M. Bona et al., *The 2004 UTfit collaboration report on the status of the unitarity triangle in the standard model*, *JHEP* **07** (2005) 028, [hep-ph/0501199].

[54] UTFIT Collaboration, M. Bona et al., *Model-independent constraints on $\Delta F = 2$ operators and the scale of new physics*, *JHEP* **03** (2008) 049, [0707.0636].

[55] Z. Maki, M. Nakagawa and S. Sakata, *Remarks on the unified model of elementary particles*, *Prog. Theor. Phys.* **28** (1962) 870–880.

[56] CMS Collaboration, S. Chatrchyan et al., *Observation of a new boson at a mass of 125 GeV with the CMS experiment at the LHC*, *Phys. Lett. B* **716** (2012) 30–61, [1207.7235].

[57] A. Djouadi, *The Anatomy of electro-weak symmetry breaking. I: The Higgs boson in the standard model*, *Phys. Rept.* **457** (2008) 1–216, [hep-ph/0503172].

[58] H.-J. He, Y.-P. Kuang and C. P. Yuan, *Equivalence theorem and probing the electroweak symmetry breaking sector*, *Phys. Rev. D* **51** (1995) 6463–6473, [hep-ph/9410400].

[59] *The LEP Electroweak Working Group*, http://lepewwg.web.cern.ch/LEPEWWG/.

[60] *The LEP Higgs Working Group*, http://lephiggs.web.cern.ch/LEPHIGGS/www/Welcome.html.

[61] C. F. Kolda and H. Murayama, *The Higgs mass and new physics scales in the minimal standard model*, *JHEP* **07** (2000) 035, [hep-ph/0003170].

[62] M. Veltman, *The Infrared - Ultraviolet Connection*, *Acta Phys. Polon. B* **12** (1981) 437.

[63] J. R. Espinosa, *Implications of the top (and Higgs) mass for vacuum stability*, *PoS* **TOP2015** (2016) 043, [`1512.01222`].

[64] A. Djouadi, J. Kalinowski and M. Spira, *HDECAY: A Program for Higgs boson decays in the standard model and its supersymmetric extension*, *Comput. Phys. Commun.* **108** (1998) 56–74, [`hep-ph/9704448`].

[65] A. L. Read, *Presentation of search results: The CL(s) technique*, *J. Phys.* **G28** (2002) 2693–2704.

[66] T. Junk, *Confidence level computation for combining searches with small statistics*, *Nucl. Instrum. Meth.* **A434** (1999) 435–443, [`hep-ex/9902006`].

[67] CMS Collaboration, S. Chatrchyan et al., *Combined results of searches for the standard model Higgs boson in pp collisions at $\sqrt{s}$ = 7 TeV*, *Phys. Lett. B* **710** (2012) 26–48, [`1202.1488`].

[68] ATLAS Collaboration, G. Aad et al., *Combined search for the Standard Model Higgs boson using up to 4.9 fb^{-1} of pp collision data at $\sqrt{s}$ = 7 TeV with the ATLAS detector at the LHC*, *Phys. Lett. B* **710** (2012) 49–66, [`1202.1408`].

[69] CMS Collaboration, S. Chatrchyan et al., *Study of the Mass and Spin-Parity of the Higgs Boson Candidate Via Its Decays to Z Boson Pairs*, *Phys. Rev. Lett.* **110** (2013) 081803, [`1212.6639`].

[70] ATLAS Collaboration, G. Aad et al., *Evidence for the spin-0 nature of the Higgs boson using ATLAS data*, *Phys. Lett. B* **726** (2013) 120–144, [`1307.1432`].

[71] CMS Collaboration, V. Khachatryan et al., *Constraints on the spin-parity and anomalous HVV couplings of the Higgs boson in proton collisions at 7 and 8 TeV*, *Phys. Rev. D* **92** (2015) 012004, [`1411.3441`].

[72] CMS Collaboration, V. Khachatryan et al., *Precise determination of the mass of the Higgs boson and tests of compatibility of its couplings with the standard model predictions using proton collisions at 7 and 8 TeV*, *Eur. Phys. J. C* **75** (2015) 212, [`1412.8662`].

[73] ATLAS Collaboration, G. Aad et al., *Measurements of the Higgs boson production and decay rates and coupling strengths using pp collision data at $\sqrt{s}$ = 7 and 8 TeV in the ATLAS experiment*, *Eur. Phys. J. C* **76** (2016) 6, [`1507.04548`].

[74] ATLAS, CMS Collaboration, G. Aad et al., *Combined Measurement of the Higgs Boson Mass in pp Collisions at $\sqrt{s}$ = 7 and 8 TeV with the ATLAS and CMS Experiments*, *Phys. Rev. Lett.* **114** (2015) 191803, [1503.07589].

[75] PLANCK Collaboration, P. A. R. Ade et al., *Planck 2015 results. XIII. Cosmological parameters*, *Astron. Astrophys.* **594** (2016) A13, [1502.01589].

[76] G. Bertone, D. Hooper and J. Silk, *Particle dark matter: Evidence, candidates and constraints*, *Phys. Rept.* **405** (2005) 279–390, [hep-ph/0404175].

[77] G. Bertone and D. Hooper, *A History of Dark Matter*, *Submitted to: Rev. Mod. Phys.* (2016) , [1605.04909].

[78] M. Lisanti, *Lectures on Dark Matter Physics*, in *Proceedings, Theoretical Advanced Study Institute in Elementary Particle Physics: New Frontiers in Fields and Strings (TASI 2015): Boulder, CO, USA, June 1-26, 2015*, pp. 399–446, 2017, [1603.03797].

[79] K. Freese, *Status of Dark Matter in the Universe*, *Int. J. Mod. Phys.* **1** (2017) 325–355, [1701.01840].

[80] P. J. E. Peebles, *How the Nonbaryonic Dark Matter Theory Grew*, [1701.05837].

[81] J. de Swart, G. Bertone and J. van Dongen, *How Dark Matter Came to Matter*, [1703.00013].

[82] T. Plehn, *Yet Another Introduction to Dark Matter*, [1705.01987].

[83] J. H. Oort, *The force exerted by the stellar system in the direction perpendicular to the galactic plane and some related problems*, *Bull. Astron. Inst. Netherlands,* **6** (Aug., 1932) 249.

[84] F. Zwicky, *On the Masses of Nebulae and of Clusters of Nebulae*, *Astrophys. J.* **86** (Oct., 1937) 217.

[85] V. C. Rubin and W. K. Ford, Jr., *Rotation of the Andromeda Nebula from a Spectroscopic Survey of Emission Regions*, *Astrophys. J.* **159** (Feb., 1970) 379.

[86] V. C. Rubin, *Dark matter in spiral galaxies*, *Scientific American,* **248** (June, 1983) 96–106.

[87] M. S. Roberts and R. N. Whitehurst, *The rotation curve and geometry of M31 at large galactocentric distances.*, *Astrophys. J.* **201** (Oct., 1975) 327–346.

[88] B. Ventrudo, *Gravity's Lens*, https://oneminuteastronomer.com/9237/gravitational-lens/, 2013.

[89] D. Walsh, R. F. Carswell and R. J. Weymann, *0957 + 561 A, B - Twin quasistellar objects or gravitational lens*, *Nature* **279** (1979) 381–384.

[90] R. Lynds and V. Petrosian, *Luminous arcs in clusters of galaxies*, *Astrophys. J.* **336** (Jan., 1989) 1–8.

[91] *Galaxy Cluster 0024+1654 as a Gravitational Lens*, https://www.spacetelescope.org/images/opo9610a/.

[92] A. E. Evrard, *Well of darkness*, *Nature* **394** (07, 1998) 122.

[93] R. N. Mohapatra and V. L. Teplitz, *Mirror matter MACHOs*, *Phys. Lett. B* **462** (1999) 302–309, [astro-ph/9902085].

[94] J. N. Bahcall, C. Flynn, A. Gould and S. Kirhakos, *M dwarfs, microlensing, and the mass budget of the galaxy*, *Astrophys. J.* **435** (1994) L51–L54, [astro-ph/9406019].

[95] D. Mera, G. Chabrier and R. Schaeffer, *Substellar mass function and maximum baryonic mass in the halo of the galaxy*, *Euro. Phys. Lett.* **33** (1996) 327.

[96] K. Freese, *Death of baryonic dark matter*, *Phys. Rep.* **333-334** (2000) 183 – 201.

[97] K. Freese, B. Fields and D. Graff, *Death of stellar baryonic dark matter candidates*, in *Proceedings, 3rd International Workshop on The identification of dark matter (IDM 2000): York, UK, September 18-22, 2000*, pp. 159–167, 2000, [astro-ph/0007444].

[98] MACHO Collaboration, K. Griest et al., *MACHO Collaboration search for baryonic dark matter via gravitational microlensing*, [astro-ph/9506016].

[99] MACHO Collaboration, C. Alcock et al., *The MACHO project: Microlensing results from 5.7 years of LMC observations*, *Astrophys. J.* **542** (2000) 281–307, [astro-ph/0001272].

[100] P. Tisserand et al., *Limits on the macho content of the galactic halo from the eros-2 survey of the magellanic clouds*, *Astron. & Astro.* **469** (July, 2007) 387–404.

[101] D. N. Schramm and M. S. Turner, *Big bang nucleosynthesis enters the precision era*, *Rev. Mod. Phys.* **70** (1998) 303–318, [astro-ph/9706069].

[102] R. H. Cyburt, *Primordial nucleosynthesis for the new cosmology: Determining uncertainties and examining concordance*, *Phys. Rev. D* **70** (2004) 023505, [astro-ph/0401091].

[103] COBE Collaboration, G. F. Smoot et al., *Structure in the COBE differential microwave radiometer first year maps*, *Astrophys. J.* **396** (1992) L1–L5.

[104] WMAP Collaboration, E. Komatsu et al., *Seven-Year Wilkinson Microwave Anisotropy Probe (WMAP) Observations: Cosmological Interpretation*, *Astrophys. J. Suppl.* **192** (2011) 18, [`1001.4538`].

[105] SDSS Collaboration, K. N. Abazajian et al., *The Seventh Data Release of the Sloan Digital Sky Survey*, *Astrophys. J. Suppl.* **182** (2009) 543–558, [`0812.0649`].

[106] SDSS Collaboration, D. J. Eisenstein et al., *Detection of the Baryon Acoustic Peak in the Large-Scale Correlation Function of SDSS Luminous Red Galaxies*, *Astrophys. J.* **633** (2005) 560–574, [`astro-ph/0501171`].

[107] 2DFGRS Collaboration, S. Cole et al., *The 2dF Galaxy Redshift Survey: Power-spectrum analysis of the final dataset and cosmological implications*, *Mon. Not. Roy. Astron. Soc.* **362** (2005) 505–534, [`astro-ph/0501174`].

[108] SDSS Collaboration, W. J. Percival et al., *Baryon Acoustic Oscillations in the Sloan Digital Sky Survey Data Release 7 Galaxy Sample*, *Mon. Not. Roy. Astron. Soc.* **401** (2010) 2148–2168, [`0907.1660`].

[109] M. Boylan-Kolchin, V. Springel, S. D. M. White, A. Jenkins and G. Lemson, *Resolving Cosmic Structure Formation with the Millennium-II Simulation*, *Mon. Not. Roy. Astron. Soc.* **398** (2009) 1150, [`0903.3041`].

[110] T. Di Matteo, J. Colberg, V. Springel, L. Hernquist and D. Sijacki, *Direct cosmological simulations of the growth of black holes and galaxies*, *Astrophys. J.* **676** (2008) 33, [`0705.2269`].

[111] J. R. Bond, G. Efstathiou and J. Silk, *Massive Neutrinos and the Large Scale Structure of the Universe*, *Phys. Rev. Lett.* **45** (1980) 1980–1984.

[112] M. Iye, K. Ota, N. Kashikawa, H. Furusawa, T. Hashimoto, T. Hattori et al., *A galaxy at a redshift z = 6.96*, *Nature* **443** (2006) 186–188, [`astro-ph/0609393`].

[113] P. J. E. Peebles, *Large scale background temperature and mass fluctuations due to scale invariant primeval perturbations*, *Astrophys. J.* **263** (1982) L1–L5.

[114] VIRGO CONSORTIUM Collaboration, A. Jenkins, C. S. Frenk, F. R. Pearce, P. A. Thomas, J. M. Colberg, S. D. M. White et al., *Evolution of structure in cold dark matter universes*, *Astrophys. J.* **499** (1998) 20, [`astro-ph/9709010`].

[115] D. Clowe, M. Bradac, A. H. Gonzalez, M. Markevitch, S. W. Randall, C. Jones et al., *A direct empirical proof of the existence of dark matter*, *Astrophys. J.* **648** (2006) L109–L113, [`astro-ph/0608407`].

[116] M. Bradac, S. W. Allen, T. Treu, H. Ebeling, R. Massey, R. G. Morris et al., *Revealing the properties of dark matter in the merging cluster MACSJ0025.4-1222*, *Astrophys. J.* **687** (2008) 959, [`0806.2320`].

[117] M. J. Jee et al., *Discovery of a Ringlike Dark Matter Structure in the Core of the Galaxy Cluster Cl 0024+17*, *Astrophys. J.* **661** (2007) 728–749, [`0705.2171`].

[118] S. Penny, C. Conselice, S. De Rijcke and E. Held, *Hubble Space Telescope survey of the Perseus Cluster I: The structure and dark matter content of cluster dwarf spheroidals*, [`0811.3197`].

[119] N. Jarosik et al., *Seven-Year Wilkinson Microwave Anisotropy Probe (WMAP) Observations: Sky Maps, Systematic Errors, and Basic Results*, *Astrophys. J. Suppl.* **192** (2011) 14, [`1001.4744`].

[120] L. Bergstrom, *Nonbaryonic dark matter: Observational evidence and detection methods*, *Rep. Prog. Phys.* **63** (2000) 793, [`hep-ph/0002126`].

[121] P. Langacker and M. Luo, *Implications of precision electroweak experiments for m_t, ρ_0, $sin^2\theta_W$, and grand unification*, *Phys. Rev. D* **44** (Aug, 1991) 817–822.

[122] F. Jegerlehner, *The hierarchy problem of the electroweak Standard Model revisited*, [`1305.6652`].

[123] T. Falk, K. A. Olive and M. Srednicki, *Heavy sneutrinos as dark matter*, *Phys. Lett. B* **339** (1994) 248–251, [`hep-ph/9409270`].

[124] E. J. Chun, H. B. Kim and J. E. Kim, *Dark matters in axino gravitino cosmology*, *Phys. Rev. Lett.* **72** (1994) 1956–1959, [`hep-ph/9305208`].

[125] T. Kaluza, *On the Problem of Unity in Physics*, *Sitzungsber. Preuss. Akad. Wiss. Berlin (Math. Phys.)* **1921** (1921) 966–972.

[126] O. Klein, *Quantum Theory and Five-Dimensional Theory of Relativity. (In German and English)*, *Z. Phys.* **37** (1926) 895–906.

[127] N. Arkani-Hamed, S. Dimopoulos and G. R. Dvali, *The Hierarchy problem and new dimensions at a millimeter*, *Phys. Lett. B* **429** (1998) 263–272, [`hep-ph/9803315`].

[128] T. Appelquist, H.-C. Cheng and B. A. Dobrescu, *Bounds on universal extra dimensions*, *Phys. Rev. D* **64** (2001) 035002, [`hep-ph/0012100`].

[129] G. Servant and T. M. P. Tait, *Is the lightest Kaluza-Klein particle a viable dark matter candidate?*, *Nucl. Phys. B* **650** (2003) 391–419, [`hep-ph/0206071`].

[130] D. Hooper and S. Profumo, *Dark matter and collider phenomenology of universal extra dimensions*, *Phys. Rept.* **453** (2007) 29–115, [hep-ph/0701197].

[131] O. Buchmueller, M. J. Dolan and C. McCabe, *Beyond Effective Field Theory for Dark Matter Searches at the LHC*, *JHEP* **01** (2014) 025, [1308.6799].

[132] G. Busoni, A. De Simone, E. Morgante and A. Riotto, *On the Validity of the Effective Field Theory for Dark Matter Searches at the LHC*, *Phys. Lett. B* **728** (2014) 412–421, [1307.2253].

[133] G. Busoni, A. De Simone, T. Jacques, E. Morgante and A. Riotto, *On the Validity of the Effective Field Theory for Dark Matter Searches at the LHC Part III: Analysis for the t-channel*, *JCAP* **1409** (2014) 022, [1405.3101].

[134] G. Busoni, A. De Simone, J. Gramling, E. Morgante and A. Riotto, *On the Validity of the Effective Field Theory for Dark Matter Searches at the LHC, Part II: Complete Analysis for the s-channel*, *JCAP* **1406** (2014) 060, [1402.1275].

[135] A. De Simone and T. Jacques, *Simplified models vs. effective field theory approaches in dark matter searches*, *Eur. Phys. J. C* **76** (2016) 367, [1603.08002].

[136] LHC New Physics Working Group Collaboration, D. Alves, *Simplified Models for LHC New Physics Searches*, *J. Phys. G* **39** (2012) 105005, [1105.2838].

[137] G. D'Ambrosio, G. F. Giudice, G. Isidori and A. Strumia, *Minimal flavor violation: An Effective field theory approach*, *Nucl. Phys. B* **645** (2002) 155–187, [hep-ph/0207036].

[138] A. De Simone, G. F. Giudice and A. Strumia, *Benchmarks for Dark Matter Searches at the LHC*, *JHEP* **06** (2014) 081, [1402.6287].

[139] N. Craig, H. K. Lou, M. McCullough and A. Thalapillil, *The Higgs Portal Above Threshold*, *J. High Energy Phys.* **02** (2016) 127, [1412.0258].

[140] J.-H. Yu, *Vector fermion-portal dark matter: Direct detection and Galactic Center gamma ray excess*, *Phys. Rev. D* **90** (2014) 095010, [1409.3227].

[141] F. S. Queiroz, K. Sinha and A. Strumia, *Leptoquarks, dark matter, and anomalous LHC events*, *Phys. Rev. D* **91** (2015) 035006, [1409.6301].

[142] S. Baek, P. Ko and W.-I. Park, *Invisible Higgs decay width vs. dark matter direct detection cross section in Higgs portal dark matter models*, *Phys. Rev. D* **90** (2014) 055014, [1405.3530].

[143] K. Ghorbani, *Fermionic dark matter with pseudo-scalar Yukawa interaction*, *J. Cosmol. Astropart. Phys.* **1501** (2015) 015, [1408.4929].

[144] P. Ko, W.-I. Park and Y. Tang, *Higgs portal vector dark matter for* GeV *scale γ-ray excess from galactic center*, *J. Cosmol. Astropart. Phys.* **1409** (2014) 013, [1404.5257].

[145] M. Duerr, P. Fileviez Perez and J. Smirnov, *Scalar singlet dark matter and gamma lines*, *Phys. Lett. B* **751** (2015) 119–122, [1508.04418].

[146] P. Ko, W.-I. Park and Y. Tang, *Higgs-portal dark matter for GeV gamma ray excess*, in *2nd Toyama International Workshop on Higgs as a Probe of ew Physics (HPNP2015) Toyama, Japan, February 11-15, 2015*, 2015, [1504.06944].

[147] H. Han and S. Zheng, *Higgs-portal Scalar Dark Matter: Scattering Cross Section and Observable Limits*, *Nucl. Phys. B* **914** (2017) 248–256, [1510.06165].

[148] M. Duerr, P. Fileviez Perez and J. Smirnov, *Scalar Dark Matter: Direct vs. Indirect Detection*, *JHEP* **06** (2016) 152, [1509.04282].

[149] R. D. Peccei and H. R. Quinn, *CP Conservation in the Presence of Instantons*, *Phys. Rev. Lett.* **38** (1977) 1440–1443.

[150] G. Raffelt and A. Weiss, *Red giant bound on the axion - electron coupling revisited*, *Phys. Rev. D* **51** (1995) 1495–1498, [hep-ph/9410205].

[151] ADMX Collaboration, S. J. Asztalos et al., *An Improved RF cavity search for halo axions*, *Phys. Rev. D* **69** (2004) 011101, [astro-ph/0310042].

[152] D. Budker, P. W. Graham, M. Ledbetter, S. Rajendran and A. Sushkov, *Proposal for a Cosmic Axion Spin Precession Experiment (CASPEr)*, *Phys. Rev.* **X4** (2014) 021030, [1306.6089].

[153] Y. Kahn, B. R. Safdi and J. Thaler, *Broadband and Resonant Approaches to Axion Dark Matter Detection*, *Phys. Rev. Lett.* **117** (2016) 141801, [1602.01086].

[154] S. Coleman, *Q-balls*, *Nucl. Phys. B* **269** (June, 1986) 744–744.

[155] M. Holthausen and R. Takahashi, *GIMPs from Extra Dimensions*, *Phys. Lett. B* **691** (2010) 56–59, [0912.2262].

[156] J. A. R. Cembranos, A. Dobado and A. L. Maroto, *Brane world dark matter*, *Phys. Rev. Lett.* **90** (2003) 241301, [hep-ph/0302041].

[157] G. Steigman, B. Dasgupta and J. F. Beacom, *Precise Relic WIMP Abundance and its Impact on Searches for Dark Matter Annihilation*, *Phys. Rev. D* **86** (2012) 023506, [1204.3622].

[158] M. Laine and Y. Schroder, *Quark mass thresholds in QCD thermodynamics*, *Phys. Rev. D* **73** (2006) 085009, [`hep-ph/0603048`].

[159] T. M. Undagoitia and L. Rauch, *Dark matter direct-detection experiments*, *J. Phys. G* **43** (2016) 013001, [`1509.08767`].

[160] T. R. Slatyer, *TASI Lectures on Indirect Detection of Dark Matter*, in *Theoretical Advanced Study Institute in Elementary Particle Physics: Anticipating the Next Discoveries in Particle Physics (TASI 2016) Boulder, CO, USA, June 6-July 1, 2016*, pp. 297–353, 2018, [`1710.05137`].

[161] J. Diemand, M. Kuhlen, P. Madau, M. Zemp, B. Moore, D. Potter et al., *Clumps and streams in the local dark matter distribution*, *Nature* **454** (2008) 735–738, [`0805.1244`].

[162] T. Lin, E. W. Kolb and L.-T. Wang, *Probing dark matter couplings to top and bottom quarks at the LHC*, *Phys. Rev. D* **88** (2013) 063510, [`1303.6638`].

[163] P. Agrawal, B. Batell, D. Hooper and T. Lin, *Flavored Dark Matter and the Galactic Center Gamma-Ray Excess*, *Phys. Rev. D* **90** (2014) 063512, [`1404.1373`].

[164] ATLAS Collaboration, G. Aad et al., *Search for dark matter in events with heavy quarks and missing transverse momentum in pp collisions with the ATLAS detector*, *Eur. Phys. J. C* **75** (2015) 92, [`1410.4031`].

[165] ATLAS Collaboration, T. A. collaboration, *Search for Dark Matter production associated with bottom quarks with 13.3 fb?1 of pp collisions at ?s = 13 TeV with the ATLAS detector at the LHC*, .

[166] CMS Collaboration, C. Collaboration, *Search for Dark Matter produced in association with bottom quarks*, .

[167] L. M. Carpenter, A. Nelson, C. Shimmin, T. M. P. Tait and D. Whiteson, *Collider searches for dark matter in events with a Z boson and missing energy*, *Phys. Rev. D* **87** (2013) 074005, [`1212.3352`].

[168] ATLAS Collaboration, M. Aaboud et al., *Search for new phenomena in events with a photon and missing transverse momentum in pp collisions at $\sqrt{s}$ = 13 TeV with the ATLAS detector*, *JHEP* **06** (2016) 059, [`1604.01306`].

[169] CMS Collaboration, V. Khachatryan et al., *Searches for invisible decays of the Higgs boson in pp collisions at $\sqrt{s}$ = 7, 8, and 13 TeV*, *JHEP* **02** (2017) 135, [`1610.09218`].

[170] ATLAS Collaboration, G. Aad et al., *Search for invisible decays of the Higgs boson produced in association with a hadronically decaying vector boson in pp collisions at $\sqrt{s}$ = 8 TeV with the ATLAS detector*, *Eur. Phys. J.* **C75** (2015) 337, [`1504.04324`].

[171] ATLAS Collaboration, T. A. collaboration, *Search for new phenomena in the $Z(\to \ell\ell) + E_\mathrm{T}^\mathrm{miss}$ final state at $\sqrt{s}$ = 13 TeV with the ATLAS detector*, .

[172] D. L. Rainwater and D. Zeppenfeld, *Searching for $H \to \gamma\gamma$ in weak boson fusion at the LHC*, *JHEP* **12** (1997) 005, [`hep-ph/9712271`].

[173] ATLAS Collaboration, G. Aad et al., *Search for invisible decays of a Higgs boson using vector-boson fusion in pp collisions at $\sqrt{s}$ = 8 TeV with the ATLAS detector*, *JHEP* **01** (2016) 172, [`1508.07869`].

[174] ATLAS Collaboration, G. Aad et al., *Constraints on new phenomena via Higgs boson couplings and invisible decays with the ATLAS detector*, *JHEP* **11** (2015) 206, [`1509.00672`].

[175] R. C. Cotta, J. L. Hewett, M. P. Le and T. G. Rizzo, *Bounds on Dark Matter Interactions with Electroweak Gauge Bosons*, *Phys. Rev. D* **88** (2013) 116009, [`1210.0525`].

[176] A. Crivellin, U. Haisch and A. Hibbs, *LHC constraints on gauge boson couplings to dark matter*, *Phys. Rev. D* **91** (2015) 074028, [`1501.00907`].

[177] L. Carpenter, A. DiFranzo, M. Mulhearn, C. Shimmin, S. Tulin and D. Whiteson, *Mono-Higgs-boson: A new collider probe of dark matter*, *Phys. Rev. D* **89** (2014) 075017, [`1312.2592`].

[178] Y. Bai, P. J. Fox and R. Harnik, *The Tevatron at the Frontier of Dark Matter Direct Detection*, *JHEP* **12** (2010) 048, [`1005.3797`].

[179] P. J. Fox, R. Harnik, J. Kopp and Y. Tsai, *Missing energy signatures of dark matter at the LHC*, *Phys. Rev. D* **85** (2012) 056011, [`1109.4398`].

[180] P. J. Fox, R. Harnik, R. Primulando and C.-T. Yu, *Taking a Razor to Dark Matter Parameter Space at the LHC*, *Phys. Rev. D* **86** (2012) 015010, [`1203.1662`].

[181] I. M. Shoemaker and L. Vecchi, *Unitarity and Monojet Bounds on Models for DAMA, CoGeNT, and CRESST-II*, *Phys. Rev. D* **86** (2012) 015023, [`1112.5457`].

[182] M. Endo and Y. Yamamoto, *Unitarity Bounds on Dark Matter Effective Interactions at LHC*, *JHEP* **06** (2014) 126, [`1403.6610`].

[183] J. Engel and P. Vogel, *Neutralino inelastic scattering with subsequent detection of nuclear gamma-rays*, *Phys. Rev. D* **61** (2000) 063503, [`hep-ph/9910409`].

[184] T. Bringmann et al., *DarkBit: A GAMBIT module for computing dark matter observables and likelihoods*, *Eur. Phys. J. C* **77** (2017) 831, [`1705.07920`].

[185] K. Freese, M. Lisanti and C. Savage, *Colloquium: Annual modulation of dark matter*, *Rev. Mod. Phys.* **85** (2013) 1561–1581, [`1209.3339`].

[186] J. Bovy, D. W. Hogg and H.-W. Rix, *Galactic masers and the Milky Way circular velocity*, *Astrophys. J.* **704** (2009) 1704–1709, [`0907.5423`].

[187] M. J. Reid et al., *Trigonometric Parallaxes of Massive Star Forming Regions: VI. Galactic Structure, Fundamental Parameters and Non-Circular Motions*, *Astrophys. J.* **700** (2009) 137–148, [`0902.3913`].

[188] P. J. McMillan and J. J. Binney, *The uncertainty in Galactic parameters*, *Mon. Not. Roy. Astron. Soc.* **402** (2010) 934, [`0907.4685`].

[189] J. D. Sloane, M. R. Buckley, A. M. Brooks and F. Governato, *Assessing Astrophysical Uncertainties in Direct Detection with Galaxy Simulations*, *Astrophys. J.* **831** (2016) 93, [`1601.05402`].

[190] N. Bozorgnia, F. Calore, M. Schaller, M. Lovell, G. Bertone, C. S. Frenk et al., *Simulated Milky Way analogues: implications for dark matter direct searches*, *JCAP* **1605** (2016) 024, [`1601.04707`].

[191] C. Kelso, C. Savage, M. Valluri, K. Freese, G. S. Stinson and J. Bailin, *The impact of baryons on the direct detection of dark matter*, *JCAP* **1608** (2016) 071, [`1601.04725`].

[192] XENON Collaboration, E. Aprile et al., *First Dark Matter Search Results from the XENON1T Experiment*, *Phys. Rev. Lett.* **119** (2017) 181301, [`1705.06655`].

[193] LUX Collaboration, D. S. Akerib et al., *Results from a search for dark matter in the complete LUX exposure*, *Phys. Rev. Lett.* **118** (2017) 021303, [`1608.07648`].

[194] LUX Collaboration, D. S. Akerib et al., *Results on the Spin-Dependent Scattering of Weakly Interacting Massive Particles on Nucleons from the Run 3 Data of the LUX Experiment*, *Phys. Rev. Lett.* **116** (2016) 161302, [`1602.03489`].

[195] PANDAX-II Collaboration, C. Fu et al., *Spin-Dependent Weakly-Interacting-Massive-Particle-Nucleon Cross Section Limits from First Data of PandaX-II Experiment*, *Phys. Rev. Lett.* **118** (2017) 071301, [`1611.06553`].

[196] PICO Collaboration, C. Amole et al., *Improved dark matter search results from PICO-2L Run 2*, *Phys. Rev. D* **93** (2016) 061101, [`1601.03729`].

[197] R. Bernabei et al., *DAMA results*, in *Neutrino telescopes. Proceedings, 10th International Workshop, Venice, Italy, March 11-14, 2003. Vol. 1+2*, pp. 403–423, 2003, [`astro-ph/0305542`].

[198] XENON100 Collaboration, E. Aprile et al., *XENON100 Dark Matter Results from a Combination of 477 Live Days*, *Phys. Rev. D* **94** (2016) 122001, [`1609.06154`].

[199] SᴜᴘᴇʀCDMS Collaboration, R. Agnese et al., *New Results from the Search for Low-Mass Weakly Interacting Massive Particles with the CDMS Low Ionization Threshold Experiment*, *Phys. Rev. Lett.* **116** (2016) 071301, [`1509.02448`].

[200] P. Gondolo and G. Gelmini, *Compatibility of DAMA dark matter detection with other searches*, *Phys. Rev. D* **71** (2005) 123520, [`hep-ph/0504010`].

[201] SABRE Collaboration, F. Froborg, *SABRE: WIMP modulation detection in the northern and southern hemisphere*, *J. Phys. Conf. Ser.* **718** (2016) 042021, [`1601.05307`].

[202] COSINE Collaboration, J. Park, *Status of the COSINE Experiment*, in *Proceedings, 12th Patras Workshop on Axions, WIMPs and WISPs (PATRAS 2016): Jeju Island, South Korea, June 20-24, 2016*, pp. 125–128, 2017.

[203] DM-Iᴄᴇ Collaboration, E. Barbosa de Souza et al., *First search for a dark matter annual modulation signal with NaI(Tl) in the Southern Hemisphere by DM-Ice17*, *Phys. Rev. D* **95** (2017) 032006, [`1602.05939`].

[204] J. Amare et al., *Status of the ANAIS Dark Matter Project at the Canfranc Underground Laboratory*, in *Proceedings, 11th Patras Workshop on Axions, WIMPs and WISPs (Axion-WIMP 2015): Zaragoza, Spain, June 22-26, 2015*, 2015, [`1508.07213`].

[205] J. Billard, L. Strigari and E. Figueroa-Feliciano, *Implication of neutrino backgrounds on the reach of next generation dark matter direct detection experiments*, *Phys. Rev. D* **89** (2014) 023524, [`1307.5458`].

[206] J. Cooley, *Overview of non-liquid noble direct detection dark matter experiments*, *Physics of the Dark Universe* **4** (2014) 92 – 97.

[207] J. M. Gaskins, *A review of indirect searches for particle dark matter*, *Contemp. Phys.* **57** (2016) 496–525, [`1604.00014`].

[208] T. Toma, *Gamma rays constraint on Higgs production from dark matter annihilation*, in *1st Toyama International Workshop on Higgs as a Probe of New Physics 2013 (HPNP2013) Toyama, Japan, February 13-16, 2013*, 2013, [1305.1601].

[209] P. Ko and Y. Tang, *Galactic center γ-ray excess in hidden sector DM models with dark gauge symmetries: Local Z_3 symmetry as an example*, *J. Cosmol. Astropart. Phys.* **1501** (2015) 023, [1407.5492].

[210] L. Goodenough and D. Hooper, *Possible Evidence For Dark Matter Annihilation In The Inner Milky Way From The Fermi Gamma Ray Space Telescope*, [0910.2998].

[211] D. Hooper and L. Goodenough, *Dark Matter Annihilation in The Galactic Center As Seen by the Fermi Gamma Ray Space Telescope*, *Phys. Lett. B* **697** (2011) 412–428, [1010.2752].

[212] P. Agrawal, B. Batell, P. J. Fox and R. Harnik, *WIMPs at the Galactic Center*, *JCAP* **1505** (2015) 011, [1411.2592].

[213] S. K. Lee, M. Lisanti, B. R. Safdi, T. R. Slatyer and W. Xue, *Evidence for Unresolved γ-Ray Point Sources in the Inner Galaxy*, *Phys. Rev. Lett.* **116** (2016) 051103, [1506.05124].

[214] D. Gaggero, M. Taoso, A. Urbano, M. Valli and P. Ullio, *Towards a realistic astrophysical interpretation of the gamma-ray Galactic center excess*, *JCAP* **1512** (2015) 056, [1507.06129].

[215] R. Bartels, S. Krishnamurthy and C. Weniger, *Strong support for the millisecond pulsar origin of the Galactic center GeV excess*, *Phys. Rev. Lett.* **116** (2016) 051102, [1506.05104].

[216] T. Bringmann, J. Edsjo, P. Gondolo, P. Ullio and L. Bergstrom, *DarkSUSY 6 : An Advanced Tool to Compute Dark Matter Properties Numerically*, [1802.03399].

[217] ICECUBE Collaboration, M. G. Aartsen et al., *Improved limits on dark matter annihilation in the Sun with the 79-string IceCube detector and implications for supersymmetry*, *JCAP* **1604** (2016) 022, [1601.00653].

[218] PAMELA Collaboration, O. Adriani et al., *An anomalous positron abundance in cosmic rays with energies 1.5-100 GeV*, *Nature* **458** (2009) 607–609, [0810.4995].

[219] Fermi-LAT Collaboration, A. A. Abdo et al., *Measurement of the Cosmic Ray e+ plus e- spectrum from 20 GeV to 1 TeV with the Fermi Large Area Telescope*, *Phys. Rev. Lett.* **102** (2009) 181101, [`0905.0025`].

[220] HESS Collaboration, F. Aharonian et al., *Observations of the Crab Nebula with H.E.S.S*, *Astron. Astrophys.* **457** (2006) 899–915, [`astro-ph/0607333`].

[221] AMS Collaboration, L. Accardo et al., *High Statistics Measurement of the Positron Fraction in Primary Cosmic Rays of 0.5–500 GeV with the Alpha Magnetic Spectrometer on the International Space Station*, *Phys. Rev. Lett.* **113** (2014) 121101.

[222] A. Lopez, C. Savage, D. Spolyar and D. Q. Adams, *Fermi/LAT observations of Dwarf Galaxies highly constrain a Dark Matter Interpretation of Excess Positrons seen in AMS-02, HEAT, and PAMELA*, *JCAP* **1603** (2016) 033, [`1501.01618`].

[223] A. Scaffidi, K. Freese, J. Li, C. Savage, M. White and A. G. Williams, *Gamma rays from muons from WIMPs: Implementation of radiative muon decays for dark matter analyses*, *Phys. Rev. D* **93** (2016) 115024, [`1604.00744`].

[224] B. D. Fields, *The primordial lithium problem*, *Ann. Rev. Nucl. Part. Sci.* **61** (2011) 47–68, [`1203.3551`].

[225] W. Hu and S. Dodelson, *Cosmic microwave background anisotropies*, *Ann. Rev. Astron. Astrophys.* **40** (2002) 171–216, [`astro-ph/0110414`].

[226] E. W. Kolb and M. S. Turner, *The Early Universe*, *Front. Phys.* **69** (1990) 1–547.

[227] A. D. Sakharov, *Violation of CP Invariance, C Asymmetry, and Baryon Asymmetry of the Universe*, *Pisma Zh. Eksp. Teor. Fiz.* **5** (1967) 32–35.

[228] R. Lehnert, *CPT Symmetry and Its Violation*, *Symmetry* **8** (2016) 114.

[229] G. 't Hooft, *Symmetry Breaking Through Bell-Jackiw Anomalies*, *Phys. Rev. Lett.* **37** (1976) 8–11.

[230] V. A. Kuzmin, V. A. Rubakov and M. E. Shaposhnikov, *On the Anomalous Electroweak Baryon Number Nonconservation in the Early Universe*, *Phys. Lett.* **155B** (1985) 36.

[231] F. R. Klinkhamer and N. S. Manton, *A Saddle Point Solution in the Weinberg-Salam Theory*, *Phys. Rev. D* **30** (1984) 2212.

[232] P. B. Arnold and L. D. McLerran, *Sphalerons, Small Fluctuations and Baryon Number Violation in Electroweak Theory*, *Phys. Rev. D* **36** (1987) 581.

[233] P. B. Arnold, D. Son and L. G. Yaffe, *The Hot baryon violation rate is* $O(\alpha - w^5 T^4)$, *Phys. Rev. D* **55** (1997) 6264–6273, [`hep-ph/9609481`].

[234] D. Bodeker, G. D. Moore and K. Rummukainen, *Chern-Simons number diffusion and hard thermal loops on the lattice*, *Phys. Rev. D* **61** (2000) 056003, [`hep-ph/9907545`].

[235] C. Jarlskog, *Commutator of the Quark Mass Matrices in the Standard Electroweak Model and a Measure of Maximal CP Violation*, *Phys. Rev. Lett.* **55** (1985) 1039.

[236] G. R. Farrar and M. E. Shaposhnikov, *Baryon asymmetry of the universe in the standard electroweak theory*, *Phys. Rev. D* **50** (1994) 774, [`hep-ph/9305275`].

[237] A. Riotto, *Theories of baryogenesis*, in *Proceedings, Summer School in High-energy physics and cosmology: Trieste, Italy, June 29-July 17, 1998*, pp. 326–436, 1998, [`hep-ph/9807454`].

[238] M. Quiros, *Finite temperature field theory and phase transitions*, in *Proceedings, Summer School in High-energy physics and cosmology: Trieste, Italy, June 29-July 17, 1998*, pp. 187–259, 1999, [`hep-ph/9901312`].

[239] M. Trodden, *Electroweak baryogenesis*, *Rev. Mod. Phys.* **71** (1999) 1463–1500, [`hep-ph/9803479`].

[240] W. Bernreuther, *CP violation and baryogenesis*, *Lect. Notes Phys.* **591** (2002) 237–293, [`hep-ph/0205279`].

[241] W. Buchmuller, *Baryogenesis: 40 Years Later*, in *Proceedings on 13th International Symposium on Particles, strings, and cosmology (PASCOS 2007): London, UK, July 2-7, 2007*, 2007, [`0710.5857`].

[242] E. Senaha, *Overview of Electroweak Baryogenesis*, in *Proceedings, 1st Toyama International Workshop on Higgs as a Probe of New Physics 2013 (HPNP2013): Toyama, Japan, February 13-16, 2013*, 2013, [`1305.1563`].

[243] L. Dolan and R. Jackiw, *Symmetry Behavior at Finite Temperature*, *Phys. Rev. D* **9** (1974) 3320–3341.

[244] D. A. Kirzhnits and A. D. Linde, *Macroscopic Consequences of the Weinberg Model*, *Phys. Lett. B* **42** (1972) 471–474.

[245] A. G. Cohen, D. B. Kaplan and A. E. Nelson, *Progress in electroweak baryogenesis*, *Ann. Rev. Nucl. Part. Sci.* **43** (1993) 27–70, [`hep-ph/9302210`].

[246] F. R. Klinkhamer and N. S. Manton, *A saddle-point solution in the weinberg-salam theory*, *Phys. Rev. D* **30** (Nov, 1984) 2212–2220.

[247] A. I. Bochkarev and M. E. Shaposhnikov, *Electroweak Production of Baryon Asymmetry and Upper Bounds on the Higgs and Top Masses*, *Mod. Phys. Lett.* **A2** (1987) 417.

[248] K. Kajantie, M. Laine, K. Rummukainen and M. E. Shaposhnikov, *The Electroweak phase transition: A Nonperturbative analysis*, *Nucl. Phys. B* **466** (1996) 189–258, [`hep-lat/9510020`].

[249] M. B. Gavela, P. Hernandez, J. Orloff and O. Pene, *Standard model CP violation and baryon asymmetry*, *Mod. Phys. Lett.* **A9** (1994) 795–810, [`hep-ph/9312215`].

[250] P. Huet and E. Sather, *Electroweak baryogenesis and standard model CP violation*, *Phys. Rev. D* **51** (1995) 379–394, [`hep-ph/9404302`].

[251] D. A. Kirzhnits, *Weinberg model in the hot universe*, *JETP Lett.* **15** (1972) 529–531.

[252] S. Weinberg, *Gauge and Global Symmetries at High Temperature*, *Phys. Rev. D* **9** (1974) 3357–3378.

[253] C. Delaunay, C. Grojean and J. D. Wells, *Dynamics of Non-renormalizable Electroweak Symmetry Breaking*, *JHEP* **04** (2008) 029, [`0711.2511`].

[254] M. B. Gavela, P. Hernandez, J. Orloff, O. Pene and C. Quimbay, *Standard model CP violation and baryon asymmetry. Part 2: Finite temperature*, *Nucl. Phys. B* **430** (1994) 382–426, [`hep-ph/9406289`].

[255] J. I. Kapusta and C. Gale, *Finite-temperature field theory: Principles and applications*. Cambridge University Press, 2011.

[256] A. K. Das, *Finite Temperature Field Theory*. World Scientific, New York, 1997.

[257] S. R. Coleman and E. J. Weinberg, *Radiative Corrections as the Origin of Spontaneous Symmetry Breaking*, *Phys. Rev. D* **7** (1973) 1888–1910.

[258] G. W. Anderson and L. J. Hall, *The Electroweak phase transition and baryogenesis*, *Phys. Rev. D* **45** (1992) 2685–2698.

[259] D. J. Gross, R. D. Pisarski and L. G. Yaffe, *QCD and Instantons at Finite Temperature*, *Rev. Mod. Phys.* **53** (1981) 43.

[260] R. R. Parwani, *Resummation in a hot scalar field theory*, *Phys. Rev. D* **45** (1992) 4695, [`hep-ph/9204216`].

[261] G. D. Moore and K. Rummukainen, *Electroweak bubble nucleation, nonperturbatively*, *Phys. Rev. D* **63** (2001) 045002, [`hep-ph/0009132`].

[262] G. D. Moore, *Electroweak bubble wall friction: Analytic results*, *JHEP* **03** (2000) 006, [`hep-ph/0001274`].

[263] A. Megevand and A. D. Sanchez, *Velocity of electroweak bubble walls*, *Nucl. Phys. B* **825** (2010) 151–176, [`0908.3663`].

[264] J. R. Espinosa, T. Konstandin, J. M. No and G. Servant, *Energy Budget of Cosmological First-order Phase Transitions*, *JCAP* **1006** (2010) 028, [`1004.4187`].

[265] L. Dolan and R. Jackiw, *Gauge Invariant Signal for Gauge Symmetry Breaking*, *Phys. Rev. D* **9** (1974) 2904.

[266] N. K. Nielsen, *On the Gauge Dependence of Spontaneous Symmetry Breaking in Gauge Theories*, *Nucl. Phys. B* **101** (1975) 173–188.

[267] R. Fukuda and T. Kugo, *Gauge Invariance in the Effective Action and Potential*, *Phys. Rev. D* **13** (1976) 3469.

[268] M. Laine, *Gauge dependence of the high temperature two loop effective potential for the Higgs field*, *Phys. Rev. D* **51** (1995) 4525–4532, [`hep-ph/9411252`].

[269] D. Metaxas and E. J. Weinberg, *Gauge independence of the bubble nucleation rate in theories with radiative symmetry breaking*, *Phys. Rev. D* **53** (1996) 836–843, [`hep-ph/9507381`].

[270] D. Boyanovsky, D. Brahm, R. Holman and D. S. Lee, *The Gauge invariant effective potential: Equilibrium and nonequilibrium aspects*, *Phys. Rev. D* **54** (1996) 1763–1777, [`hep-ph/9603337`].

[271] H. H. Patel and M. J. Ramsey-Musolf, *Baryon Washout, Electroweak Phase Transition, and Perturbation Theory*, *JHEP* **07** (2011) 029, [`1101.4665`].

[272] J. Baacke and S. Junker, *Quantum fluctuations of the electroweak sphaleron: Erratum and addendum*, *Phys. Rev. D* **50** (1994) 4227–4228, [`hep-th/9402078`].

[273] C. Wainwright, S. Profumo and M. J. Ramsey-Musolf, *Gravity Waves from a Cosmological Phase Transition: Gauge Artifacts and Daisy Resummations*, *Phys. Rev. D* **84** (2011) 023521, [`1104.5487`].

[274] M. Garny and T. Konstandin, *On the gauge dependence of vacuum transitions at finite temperature*, *JHEP* **07** (2012) 189, [`1205.3392`].

[275] N. S. Manton, *Topology in the Weinberg-Salam Theory*, *Phys. Rev. D* **28** (1983) 2019.

[276] C. L. Wainwright, S. Profumo and M. J. Ramsey-Musolf, *Phase Transitions and Gauge Artifacts in an Abelian Higgs Plus Singlet Model*, *Phys. Rev. D* **86** (2012) 083537, [1204.5464].

[277] K. Kajantie, M. Laine, K. Rummukainen and M. E. Shaposhnikov, *A Nonperturbative analysis of the finite T phase transition in SU(2) × U(1) electroweak theory*, *Nucl. Phys. B* **493** (1997) 413–438, [hep-lat/9612006].

[278] K. Jansen, *Status of the finite temperature electroweak phase transition on the lattice*, *Nucl. Phys. Proc. Suppl.* **47** (1996) 196–211, [hep-lat/9509018].

[279] K. Farakos, K. Kajantie, K. Rummukainen and M. E. Shaposhnikov, *3-d physics and the electroweak phase transition: A Framework for lattice Monte Carlo analysis*, *Nucl. Phys. B* **442** (1995) 317–363, [hep-lat/9412091].

[280] K. Kajantie, K. Rummukainen and M. E. Shaposhnikov, *A Lattice Monte Carlo study of the hot electroweak phase transition*, *Nucl. Phys. B* **407** (1993) 356–372, [hep-ph/9305345].

[281] J. Ambjorn, T. Askgaard, H. Porter and M. E. Shaposhnikov, *Sphaleron transitions and baryon asymmetry: A Numerical real time analysis*, *Nucl. Phys. B* **353** (1991) 346–378.

[282] J. Ambjorn, T. Askgaard, H. Porter and M. E. Shaposhnikov, *Lattice Simulations of Electroweak Sphaleron Transitions in Real Time*, *Phys. Lett. B* **244** (1990) 479–487.

[283] J. Ambjorn, M. L. Laursen and M. E. Shaposhnikov, *Baryon Asymmetry Generation in the Electroweak Theory: A Lattice Study*, *Nucl. Phys. B* **316** (1989) 483–508.

[284] J. Ambjorn, M. Laursen and M. E. Shaposhnikov, *Baryon Asymmetry of the Universe: A Monte Carlo Study on the Lattice*, *Phys. Lett. B* **197** (1987) 49.

[285] Y. Brihaye and J. Kunz, *Electroweak bubbles and sphalerons*, *Phys. Rev. D* **48** (1993) 3884–3890, [hep-ph/9304256].

[286] M. Laine and K. Rummukainen, *What's new with the electroweak phase transition?*, *Nucl. Phys. Proc. Suppl.* **73** (1999) 180–185, [hep-lat/9809045].

[287] M. Laine and K. Rummukainen, *The MSSM electroweak phase transition on the lattice*, *Nucl. Phys. B* **535** (1998) 423–457, [hep-lat/9804019].

[288] F. Csikor, Z. Fodor, J. Hein, A. Jaster and I. Montvay, *Numerical tests of the electroweak phase transition and thermodynamics of the electroweak plasma*, *Nucl. Phys. B* **474** (1996) 421–445, [hep-lat/9601016].

[289] K. Kajantie, M. Laine, K. Rummukainen and M. E. Shaposhnikov, *Is there a hot electroweak phase transition at m(H) larger or equal to m(W)?*, *Phys. Rev. Lett.* **77** (1996) 2887–2890, [`hep-ph/9605288`].

[290] F. Csikor, Z. Fodor and J. Heitger, *Endpoint of the hot electroweak phase transition*, *Phys. Rev. Lett.* **82** (1999) 21–24, [`hep-ph/9809291`].

[291] G. D. Moore, *Measuring the broken phase sphaleron rate nonperturbatively*, *Phys. Rev. D* **59** (1999) 014503, [`hep-ph/9805264`].

[292] Y. Aoki, F. Csikor, Z. Fodor and A. Ukawa, *The Endpoint of the first order phase transition of the SU(2) gauge Higgs model on a four-dimensional isotropic lattice*, *Phys. Rev. D* **60** (1999) 013001, [`hep-lat/9901021`].

[293] M. Carena, M. Quiros and C. E. M. Wagner, *Opening the window for electroweak baryogenesis*, *Phys. Lett. B* **380** (1996) 81–91, [`hep-ph/9603420`].

[294] M. Carena, M. Quiros, A. Riotto, I. Vilja and C. E. M. Wagner, *Electroweak baryogenesis and low-energy supersymmetry*, *Nucl. Phys. B* **503** (1997) 387–404, [`hep-ph/9702409`].

[295] J. M. Cline and G. D. Moore, *Supersymmetric electroweak phase transition: Baryogenesis versus experimental constraints*, *Phys. Rev. Lett.* **81** (1998) 3315–3318, [`hep-ph/9806354`].

[296] S. J. Huber and M. G. Schmidt, *Electroweak baryogenesis: Concrete in a SUSY model with a gauge singlet*, *Nucl. Phys. B* **606** (2001) 183–230, [`hep-ph/0003122`].

[297] A. T. Davies, C. D. Froggatt and R. G. Moorhouse, *Electroweak baryogenesis in the next-to-minimal supersymmetric model*, *Phys. Lett. B* **372** (1996) 88–94, [`hep-ph/9603388`].

[298] T. Cohen, D. E. Morrissey and A. Pierce, *Electroweak Baryogenesis and Higgs Signatures*, *Phys. Rev. D* **86** (2012) 013009, [`1203.2924`].

[299] A. Noble and M. Perelstein, *Higgs self-coupling as a probe of electroweak phase transition*, *Phys. Rev. D* **78** (2008) 063518, [`0711.3018`].

[300] B. Jain, S. J. Lee and M. Son, *On the Validity of the Effective Potential and the Precision of Higgs Self Couplings*, [`1709.03232`].

[301] M. Reichert, A. Eichhorn, H. Gies, J. M. Pawlowski, T. Plehn and M. M. Scherer, *Probing Baryogenesis through the Higgs Self-Coupling*, [`1711.00019`].

[302] S. J. Huber, T. Konstandin, T. Prokopec and M. G. Schmidt, *Baryogenesis in the MSSM, nMSSM and NMSSM*, *Nucl. Phys. A* **785** (2007) 206–209, [hep-ph/0608017].

[303] K. Blum, C. Delaunay, M. Losada, Y. Nir and S. Tulin, *CP violation Beyond the MSSM: Baryogenesis and Electric Dipole Moments*, *JHEP* **05** (2010) 101, [1003.2447].

[304] S. Tulin and P. Winslow, *Anomalous B meson mixing and baryogenesis*, *Phys. Rev. D* **84** (2011) 034013, [1105.2848].

[305] T. Liu, M. J. Ramsey-Musolf and J. Shu, *Electroweak Beautygenesis: From* $b \to s$ *CP-violation to the Cosmic Baryon Asymmetry*, *Phys. Rev. Lett.* **108** (2012) 221301, [1109.4145].

[306] ATLAS Collaboration, G. Aad et al., *Search for Massive Colored Scalars in Four-Jet Final States in* $\sqrt{s}$ = 7 *TeV proton-proton collisions with the ATLAS Detector*, *Eur. Phys. J. C* **71** (2011) 1828, [1110.2693].

[307] L. V. Keldysh, *Diagram technique for non-equilibrium processes*, *Zh. Eksp. Teor. Fiz.* **47** (1964) 1515–1527.

[308] K. T. Mahanthappa, *Multiple production of photons in quantum electrodynamics*, *Phys. Rev.* **126** (1962) 329–340.

[309] P. M. Bakshi and K. T. Mahanthappa, *Expectation value formalism in quantum field theory. 1.*, *J. Math. Phys.* **4** (1963) 1–11.

[310] A. Kosowsky, M. S. Turner and R. Watkins, *Gravitational waves from first order cosmological phase transitions*, *Phys. Rev. Lett.* **69** (1992) 2026–2029.

[311] M. Kamionkowski, A. Kosowsky and M. S. Turner, *Gravitational radiation from first order phase transitions*, *Phys. Rev. D* **49** (1994) 2837–2851, [astro-ph/9310044].

[312] J. M. No, *Large Gravitational Wave Background Signals in Electroweak Baryogenesis Scenarios*, *Phys. Rev. D* **84** (2011) 124025, [1103.2159].

[313] R.-G. Cai, Z. Cao, Z.-K. Guo, S.-J. Wang and T. Yang, *The Gravitational-Wave Physics*, *Natl. Sci. Rev.* **4** (2017) 687–706, [1703.00187].

[314] D. J. Weir, *Gravitational waves from a first order electroweak phase transition: a brief review*, in *Phil. Trans. R. Soc. A 2018 376 20170126*, vol. A2018, p. 376, 2017, [1705.01783].

[315] A. Kosowsky, A. Mack and T. Kahniashvili, *Gravitational radiation from cosmological turbulence*, *Phys. Rev. D* **66** (2002) 024030, [`astro-ph/0111483`].

[316] A. Nicolis, *Relic gravitational waves from colliding bubbles and cosmic turbulence*, *Class. Quant. Grav.* **21** (2004) L27, [`gr-qc/0303084`].

[317] C. Grojean and G. Servant, *Gravitational Waves from Phase Transitions at the Electroweak Scale and Beyond*, *Phys. Rev. D* **75** (2007) 043507, [`hep-ph/0607107`].

[318] C. Balazs, M. Carena and C. E. M. Wagner, *Dark matter, light stops and electroweak baryogenesis*, *Phys. Rev. D* **70** (2004) 015007, [`hep-ph/0403224`].

[319] eLISA Collaboration, P. A. Seoane et al., *The Gravitational Universe*, [`1305.5720`].

[320] C. Caprini et al., *Science with the space-based interferometer eLISA. II: Gravitational waves from cosmological phase transitions*, *JCAP* **1604** (2016) 001, [`1512.06239`].

[321] N. Seto, S. Kawamura and T. Nakamura, *Possibility of direct measurement of the acceleration of the universe using 0.1-Hz band laser interferometer gravitational wave antenna in space*, *Phys. Rev. Lett.* **87** (2001) 221103, [`astro-ph/0108011`].

[322] G. M. Harry, P. Fritschel, D. A. Shaddock, W. Folkner and E. S. Phinney, *Laser interferometry for the big bang observer*, *Classical and Quantum Gravity* **23** (2006) 4887.

[323] S. J. Huber and T. Konstandin, *Production of gravitational waves in the nMSSM*, *JCAP* **0805** (2008) 017, [`0709.2091`].

[324] J. M. Cline, K. Kainulainen, P. Scott and C. Weniger, *Update on scalar singlet dark matter*, *Phys. Rev. D* **88** (2013) 055025, [`1306.4710`].

[325] K. Cheung, Y.-L. S. Tsai, P.-Y. Tseng, T.-C. Yuan and A. Zee, *Global study of the simplest scalar phantom dark matter model*, *J. Cosmol. Astropart. Phys.* **1210** (2012) 042, [`1207.4930`].

[326] GAMBIT Collaboration, P. Athron et al., *Status of the scalar singlet dark matter model*, *Eur. Phys. J. C* **77** (2017) 568, [`1705.07931`].

[327] A. Djouadi, O. Lebedev, Y. Mambrini and J. Quevillon, *Implications of LHC searches for Higgs-portal dark matter*, *Phys.Lett. B* **709** (2012) 65–69, [`1112.3299`].

[328] M. Endo and Y. Takaesu, *Heavy WIMP through Higgs portal at the LHC*, *Phys. Lett. B* **743** (2015) 228–234, [`1407.6882`].

[329] A. Djouadi, A. Falkowski, Y. Mambrini and J. Quevillon, *Direct detection of Higgs-portal dark matter at the LHC*, *Eur. Phys. J. C* **73** (2013) 2455, [`1205.3169`].

[330] F. Kahlhoefer and J. McDonald, *WIMP dark matter and unitarity-conserving inflation via a gauge singlet scalar*, *J. Cosmol. Astropart. Phys.* **1511** (2015) 015, [`1507.03600`].

[331] H. Han and S. Zheng, *New constraints on Higgs-portal scalar dark matter*, *J. High Energy Phys.* **12** (2015) 044, [`1509.01765`].

[332] L. Feng, S. Profumo and L. Ubaldi, *Closing in on singlet scalar dark matter: LUX, invisible Higgs decays and gamma ray lines*, *J. High Energy Phys.* **03** (2015) 045, [`1412.1105`].

[333] A. Urbano and W. Xue, *Constraining the Higgs portal with antiprotons*, *J. High Energy Phys.* **03** (2015) 133, [`1412.3798`].

[334] L. Lopez-Honorez, T. Schwetz and J. Zupan, *Higgs portal, fermionic dark matter, and a Standard Model like Higgs at 125 GeV*, *Phys. Lett. B* **716** (2012) 179–185, [`1203.2064`].

[335] M. A. Fedderke, J.-Y. Chen, E. W. Kolb and L.-T. Wang, *The fermionic dark matter Higgs portal: an effective field theory approach*, *J. High Energy Phys.* **08** (2014) 122, [`1404.2283`].

[336] S. Matsumoto, S. Mukhopadhyay and Y.-L. S. Tsai, *Singlet Majorana fermion dark matter: a comprehensive analysis in effective field theory*, *J. High Energy Phys.* **10** (2014) 155, [`1407.1859`].

[337] S. Kanemura, S. Matsumoto, T. Nabeshima and N. Okada, *Can WIMP dark matter overcome the nightmare scenario?*, *Phys. Rev. D* **82** (2010) 055026, [`1005.5651`].

[338] V. Silveira and A. Zee, *Scalar phantoms*, *Phys. Lett.* **161B** (1985) 136.

[339] J. McDonald, *Gauge singlet scalars as cold dark matter*, *Phys. Rev. D* **50** (1994) 3637.

[340] C. P. Burgess, M. Pospelov and T. ter Veldhuis, *The Minimal model of nonbaryonic dark matter: A singlet scalar*, *Nucl. Phys. B* **619** (2001) 709–728, [`hep-ph/0011335`].

[341] S. Baek, P. Ko, W.-I. Park and E. Senaha, *Higgs portal vector dark matter : Revisited*, *J. High Energy Phys.* **1305** (2013) 036, [`1212.2131`].

[342] M. Duch, B. Grzadkowski and M. McGarrie, *A stable Higgs portal with vector dark matter*, *J. High Energy Phys.* **09** (2015) 162, [`1506.08805`].

[343] S. Baek, P. Ko and W.-I. Park, *Search for the Higgs portal to a singlet fermionic dark matter at the LHC*, *J. High Energy Phys.* **1202** (2012) 047, [`1112.1847`].

[344] M. Gonderinger, H. Lim and M. J. Ramsey-Musolf, *Complex scalar singlet dark matter: Vacuum stability and phenomenology*, *Phys. Rev. D* **86** (2012) 043511, [`1202.1316`].

[345] M. Gonderinger, Y. Li, H. Patel and M. J. Ramsey-Musolf, *Vacuum stability, perturbativity, and scalar singlet dark matter*, *J. High Energy Phys.* **01** (2010) 053, [`0910.3167`].

[346] M. Kadastik, K. Kannike, A. Racioppi and M. Raidal, *Implications of the 125 GeV Higgs boson for scalar dark matter and for the CMSSM phenomenology*, *J. High Energy Phys.* **05** (2012) 061, [`1112.3647`].

[347] N. Khan and S. Rakshit, *Study of electroweak vacuum metastability with a singlet scalar dark matter*, *Phys. Rev. D* **90** (2014) 113008, [`1407.6015`].

[348] R. N. Lerner and J. McDonald, *Gauge singlet scalar as inflaton and thermal relic dark matter*, *Phys. Rev. D* **80** (2009) 123507, [`0909.0520`].

[349] Z.-z. Xing, H. Zhang and S. Zhou, *Impacts of the Higgs mass on vacuum stability, running fermion masses and two-body Higgs decays*, *Phys. Rev. D* **86** (2012) 013013, [`1112.3112`].

[350] J. Elias-Miro, J. R. Espinosa, G. F. Giudice, G. Isidori, A. Riotto and A. Strumia, *Higgs mass implications on the stability of the electroweak vacuum*, *Phys. Lett. B* **709** (2012) 222–228, [`1112.3022`].

[351] A. Semenov, *LanHEP: A package for automatic generation of Feynman rules from the Lagrangian. Updated version 3.2*, *Comput. Phys. Commun.* (2014) , [`1412.5016`].

[352] A. Semenov, *LanHEP: A package for the automatic generation of Feynman rules in field theory. Version 3.0*, *Comput. Phys. Commun.* **180** (2009) 431–454, [`0805.0555`].

[353] G. Belanger, F. Boudjema, A. Pukhov and A. Semenov, *microOMEGAs_3: A program for calculating dark matter observables*, *Comput.Phys.Commun.* **185** (2014) 960–985, [`1305.0237`].

[354] Planck Collaboration, P. Ade et al., *Planck 2013 results. XVI. Cosmological parameters*, *Astron.Astrophys.* **571** (2014) A16, [`1303.5076`].

[355] R. P. Brent, *Algorithms for Minimisation Without Derivatives*. Prentice Hall, Englewood Cliffs, NJ, 1973.

[356] G. Belanger, B. Dumont, U. Ellwanger, J. Gunion and S. Kraml, *Global fit to Higgs signal strengths and couplings and implications for extended Higgs sectors*, *Phys. Rev. D* **88** (2013) 075008, [`1306.2941`].

[357] M. E. Peskin, *Comparison of LHC and ILC capabilities for Higgs boson coupling measurements*, [`1207.2516`].

[358] W. B. Atwood, A. A. Abdo, M. Ackermann, W. Althouse, B. Anderson, M. Axelsson et al., *The Large Area Telescope on the Fermi Gamma Ray Space Telescope mission*, *Astrophys. J.* **697** (2009) 1071–1102, [`0902.1089`].

[359] A. Abramowski et al., *Search for a Dark Matter Annihilation Signal from the Galactic Center Halo with H.E.S.S.*, *Phys. Rev. Lett.* **106** (2011) 161301, [`1103.3266`].

[360] AMS Collaboration, C. Claudio, *The cosmic ray electron and positron spectra measured by AMS-02*, in *10th International Symposium on Cosmology and Particle Astrophysics (CosPA 2013) Honolulu, Hawaii, USA, November 12-15, 2013*.

[361] CTA Consortium Collaboration, R. M. Wagner, E. J. Lindfors, A. Sillanpää and Wagner, S., *The CTA Observatory*, [`0912.3742`].

[362] J. M. Cline and P. Scott, *Dark Matter CMB Constraints and Likelihoods for Poor Particle Physicists*, *JCAP* **1303** (2013) 044, [`1301.5908`].

[363] D. P. Finkbeiner, S. Galli, T. Lin and T. R. Slatyer, *Searching for dark matter in the CMB: A compact parameterization of energy injection from new physics*, *Phys. Rev. D* **85** (2012) 043522, [`1109.6322`].

[364] T. R. Slatyer, *Energy injection and absorption in the cosmic dark ages*, *Phys. Rev. D* **87** (2013) 123513, [`1211.0283`].

[365] E. Komatsu et al., *Seven-year Wilkinson Microwave Anisotropy Probe (WMAP) Observations: Cosmological interpretation*, *Astro. Phys. J.* **192** (2011) 18, [`1001.4538`].

[366] T. R. Slatyer, *Indirect dark matter signatures in the cosmic dark ages. I. Generalizing the bound on s-wave dark matter annihilation from Planck results*, *Phys. Rev. D* **93** (2016) 023527, [`1506.03811`].

[367] FERMI-LAT Collaboration, M. Ackermann et al., *Searching for Dark Matter Annihilation from Milky Way Dwarf Spheroidal Galaxies with Six Years of Fermi Large Area Telescope Data*, *Phys. Rev. Lett.* **115** (2015) 231301, [`1503.02641`].

[368] J. Aleksić et al., *Performance of the MAGIC stereo system obtained with Crab Nebula data*, *AstroPhys.* **35** (2012) 435–448, [`1108.1477`].

[369] J. Holder et al., *Status of the VERITAS Observatory*, *AIP Conf. Proc.* **1085** (2009) 657–660, [`0810.0474`].

[370] K. Bernlöhr et al., *Monte Carlo design studies for the Cherenkov Telescope Array*, *Astropart. Phys.* **43** (2013) 171–188, [`1210.3503`].

[371] M. Doro et al., *Dark matter and fundamental physics with the Cherenkov Telescope Array*, *Astropart. Phys.* **43** (2013) 189–214, [`1208.5356`].

[372] M. Pierre, J. M. Siegal-Gaskins and P. Scott, *Sensitivity of CTA to dark matter signals from the Galactic Center*, *JCAP* **1406** (2014) 024, [`1401.7330`].

[373] M. Actis et al., *Design concepts for the Cherenkov Telescope Array CTA: An advanced facility for ground-based high-energy gamma ray astronomy*, *Experimental Astronomy* **32** (2011) 193–316, [`1008.3703`].

[374] J. F. Navarro, E. Hayashi, C. Power, A. Jenkins, C. S. Frenk, S. D. M. White et al., *The inner structure of Lambda-CDM halos 3: Universality and asymptotic slopes*, *Mon. Not. R. Astron. Soc.* **349** (2004) 1039, [`astro-ph/0311231`].

[375] L. Pieri, J. Lavalle, G. Bertone and E. Branchini, *Implications of high-resolution simulations on indirect dark matter searches*, *Phys. Rev. D* **83** (2011) 023518, [`0908.0195`].

[376] J. F. Navarro, C. S. Frenk and S. D. M. White, *A universal density profile from hierarchical clustering*, *Astrophys. J.* **490** (1997) 493–508, [`astro-ph/9611107`].

[377] D. G. Cerdeno and A. M. Green, *Direct detection of WIMPs*, in *Particle Dark Matter : Observations, Models and Searches* (G. Bertone, ed.), p. 347. Cambridge University Press, England, 2010.

[378] P. Gondolo, *Phenomenological introduction to direct dark matter detection*, in *Dark matter in cosmology, quantum measurements, experimental gravitation. Proceedings, 31st Rencontres de Moriond, 16th Moriond Workshop, Les Arcs, France, January 20-27, 1996*, 1996, [`hep-ph/9605290`].

[379] A. Berlin, D. Hooper and S. D. McDermott, *Simplified dark matter models for the Galactic Center gamma ray excess*, *Phys. Rev. D* **89** (2014) 115022, [`1404.0022`].

[380] J. D. Lewin and P. F. Smith, *Review of mathematics, numerical factors, and corrections for dark matter experiments based on elastic nuclear recoil*, *Astropart. Phys.* **6** (1996) 87–112.

[381] G. Duda, A. Kemper and P. Gondolo, *Model independent form factors for spin independent neutralino-nucleon scattering from elastic Electron scattering data*, *J. Cosmol. Astropart. Phys.* **0704** (2007) 012, [`hep-ph/0608035`].

[382] Y. Akrami, C. Savage, P. Scott, J. Conrad and J. Edsjö, *How well will ton-scale dark matter direct detection experiments constrain minimal supersymmetry?*, *J. Cosmol. Astropart. Phys.* **4** (2011) 12, [`1011.4318`].

[383] M. Shifman, A. Vainshtein and V. Zakharov, *Remarks on higgs-boson interactions with nucleons*, *Phys. Lett. B* **78** (1978) 443 – 446.

[384] XENON1T Collaboration, E. Aprile, *The XENON1T dark matter search experiment*, *Springer Proc. Phys.* (2012) 148, [`1206.6288`].

[385] XENON Collaboration, P. Beltrame et al., *Direct dark matter search with the XENON program*, in *Proceedings, 48th Rencontres de Moriond on Electroweak Interactions and Unified Theories*, pp. 143–148, 2013, [`1305.2719`].

[386] XENON Collaboration, E. Aprile et al., *Physics reach of the XENON1T dark matter experiment*, *J. Cosmol. Astropart. Phys.* **1604** (2016) 027, [`1512.07501`].

[387] XENON100 Collaboration, E. Aprile et al., *Dark Matter Results from 225 Live Days of XENON100 Data*, *Phys. Rev. Lett.* **109** (2012) 181301, [`1207.5988`].

[388] LUX Collaboration, M. Woods, *Underground commissioning of LUX*, in *Proceedings, 48th Rencontres de Moriond on Very High Energy Phenomena in the Universe*, pp. 211–214, 2013, [`1306.0065`].

[389] LUX Collaboration, S. Fiorucci, *The LUX Dark Matter Search - Status Update*, *J. Phys. Conf. Ser.* **460** (2013) 012005, [`1301.6942`].

[390] G. J. Feldman and R. D. Cousins, *A unified approach to the classical statistical analysis of small signals*, *Phys. Rev. D* **57** (1998) 3873–3889, [`physics/9711021`].

[391] C. Savage, A. Scaffidi, M. White and A. G. Williams, *LUX likelihood and limits on spin-independent and spin-dependent WIMP couplings with LUXCalc*, *Phys. Rev. D* **92** (2015) 103519, [`1502.02667`].

[392] LUX Collaboration, D. Akerib et al., *First Results from the LUX Dark Matter Experiment at the Sanford Underground Research Facility*, *Phys. Rev. Lett.* **112** (2014) 091303, [`1310.8214`].

[393] C. Savage et al., *TPCMC: A time projection chamber Monte Carlo for dark matter searches*,.

[394] M. Szydagis, N. Barry, K. Kazkaz, J. Mock, D. Stolp et al., *NEST: A comprehensive model for scintillation yield in liquid xenon*, *JINST* **6** (2011) P10002, [`1106.1613`].

[395] M. Szydagis, A. Fyhrie, D. Thorngren and M. Tripathi, *Enhancement of NEST capabilities for simulating low-energy recoils in liquid xenon*, *JINST* **8** (2013) C10003, [`1307.6601`].

[396] Virgo, LIGO Scientific Collaboration, B. P. Abbott et al., *Observation of Gravitational Waves from a Binary Black Hole Merger*, *Phys. Rev. Lett.* **116** (2016) 061102, [`1602.03837`].

[397] A. Beniwal, M. Lewicki, J. D. Wells, M. White and A. G. Williams, *Gravitational wave, collider and dark matter signals from a scalar singlet electroweak baryogenesis*, *JHEP* **08** (2017) 108, [`1702.06124`].

[398] A. Riotto and M. Trodden, *Recent progress in baryogenesis*, *Ann. Rev. Nucl. Part. Sci.* **49** (1999) 35–75, [`hep-ph/9901362`].

[399] P. B. Arnold and O. Espinosa, *The Effective potential and first order phase transitions: Beyond leading-order*, *Phys. Rev. D* **47** (1993) 3546, [`hep-ph/9212235`].

[400] D. Curtin, P. Meade and C.-T. Yu, *Testing Electroweak Baryogenesis with Future Colliders*, *JHEP* **11** (2014) 127, [`1409.0005`].

[401] A. V. Kotwal, M. J. Ramsey-Musolf, J. M. No and P. Winslow, *Singlet-catalyzed electroweak phase transitions in the 100 TeV frontier*, *Phys. Rev. D* **94** (2016) 035022, [`1605.06123`].

[402] P. H. Damgaard, D. O'Connell, T. C. Petersen and A. Tranberg, *Constraints on New Physics from Baryogenesis and Large Hadron Collider Data*, *Phys. Rev. Lett.* **111** (2013) 221804, [`1305.4362`].

[403] P. H. Damgaard, A. Haarr, D. O'Connell and A. Tranberg, *Effective Field Theory and Electroweak Baryogenesis in the Singlet-Extended Standard Model*, *JHEP* **02** (2016) 107, [`1512.01963`].

[404] T. Brauner, T. V. I. Tenkanen, A. Tranberg, A. Vuorinen and D. J. Weir, *Dimensional reduction of the Standard Model coupled to a new singlet scalar field*, *JHEP* **03** (2017) 007, [`1609.06230`].

[405] V. Silveira and A. Zee, *Scalar Phantoms*, *Phys. Lett. B* **161** (1985) 136–140.

[406] J. McDonald, *Gauge singlet scalars as cold dark matter*, *Phys. Rev. D* **50** (1994) 3637.

[407] A. Katz and M. Perelstein, *Higgs Couplings and Electroweak Phase Transition*, *JHEP* **07** (2014) 108, [1401.1827].

[408] M. Artymowski, M. Lewicki and J. D. Wells, *Gravitational wave and collider implications of electroweak baryogenesis aided by non-standard cosmology*, *JHEP* **03** (2017) 066, [1609.07143].

[409] V. Vaskonen, *Electroweak baryogenesis and gravitational waves from a real scalar singlet*, *Phys. Rev. D* **95** (2017) 123515, [1611.02073].

[410] A. Ashoorioon and T. Konstandin, *Strong electroweak phase transitions without collider traces*, *JHEP* **07** (2009) 086, [0904.0353].

[411] K. Enqvist, S. Nurmi, T. Tenkanen and K. Tuominen, *Standard Model with a real singlet scalar and inflation*, *JCAP* **1408** (2014) 035, [1407.0659].

[412] T. Tenkanen, K. Tuominen and V. Vaskonen, *A Strong Electroweak Phase Transition from the Inflaton Field*, *JCAP* **1609** (2016) 037, [1606.06063].

[413] P. Huang, A. J. Long and L.-T. Wang, *Probing the Electroweak Phase Transition with Higgs Factories and Gravitational Waves*, *Phys. Rev. D* **94** (2016) 075008, [1608.06619].

[414] M. Kakizaki, S. Kanemura and T. Matsui, *Gravitational waves as a probe of extended scalar sectors with the first order electroweak phase transition*, *Phys. Rev. D* **92** (2015) 115007, [1509.08394].

[415] K. Hashino, M. Kakizaki, S. Kanemura and T. Matsui, *Synergy between measurements of gravitational waves and the triple-Higgs coupling in probing the first-order electroweak phase transition*, *Phys. Rev. D* **94** (2016) 015005, [1604.02069].

[416] K. Hashino, M. Kakizaki, S. Kanemura, P. Ko and T. Matsui, *Gravitational waves and Higgs boson couplings for exploring first order phase transition in the model with a singlet scalar field*, *Phys. Lett. B* **766** (2017) 49–54, [1609.00297].

[417] A. Kobakhidze, A. Manning and J. Yue, *Gravitational waves from the phase transition of a nonlinearly realized electroweak gauge symmetry*, *Int. J. Mod. Phys. D* **26** (2017) 1750114, [1607.00883].

[418] M. Chala, G. Nardini and I. Sobolev, *Unified explanation for dark matter and electroweak baryogenesis with direct detection and gravitational wave signatures*, *Phys. Rev. D* **94** (2016) 055006, [1605.08663].

[419] J. Choi and R. R. Volkas, *Real Higgs singlet and the electroweak phase transition in the Standard Model*, *Phys. Lett. B* **317** (1993) 385–391, [hep-ph/9308234].

[420] P. S. B. Dev and A. Mazumdar, *Probing the Scale of New Physics by Advanced LIGO/VIRGO*, *Phys. Rev. D* **93** (2016) 104001, [1602.04203].

[421] C. Balazs, A. Fowlie, A. Mazumdar and G. White, *Gravitational waves at aLIGO and vacuum stability with a scalar singlet extension of the Standard Model*, *Phys. Rev. D* **95** (2017) 043505, [1611.01617].

[422] X.-G. He and J. Tandean, *New LUX and PandaX-II Results Illuminating the Simplest Higgs-Portal Dark Matter Models*, *JHEP* **12** (2016) 074, [1609.03551].

[423] M. Joyce, *Electroweak Baryogenesis and the Expansion Rate of the Universe*, *Phys. Rev. D* **55** (1997) 1875–1878, [hep-ph/9606223].

[424] M. Joyce and T. Prokopec, *Turning around the sphaleron bound: Electroweak baryogenesis in an alternative postinflationary cosmology*, *Phys. Rev. D* **57** (1998) 6022–6049, [hep-ph/9709320].

[425] G. Servant, *A Way to reopen the window for electroweak baryogenesis*, *JHEP* **01** (2002) 044, [hep-ph/0112209].

[426] M. Lewicki, T. Rindler-Daller and J. D. Wells, *Enabling Electroweak Baryogenesis through Dark Matter*, *JHEP* **06** (2016) 055, [1601.01681].

[427] M. Lewicki, *EW baryogenesis via DM*, in *28th Rencontres de Blois on Particle Physics and Cosmology Blois, France, May 29-June 3, 2016*, 2016, [1611.02387].

[428] K. Funakubo and E. Senaha, *Electroweak phase transition, critical bubbles and sphaleron decoupling condition in the MSSM*, *Phys. Rev. D* **79** (2009) 115024, [0905.2022].

[429] K. Fuyuto and E. Senaha, *Improved sphaleron decoupling condition and the Higgs coupling constants in the real singlet-extended standard model*, *Phys. Rev. D* **90** (2014) 015015, [1406.0433].

[430] A. D. Linde, *Decay of the False Vacuum at Finite Temperature*, *Nucl. Phys. B* **216** (1983) 421.

[431] A. D. Linde, *Fate of the False Vacuum at Finite Temperature: Theory and Applications*, *Phys. Lett. B* **100** (1981) 37.

[432] J. M. Cline, G. D. Moore and G. Servant, *Was the electroweak phase transition preceded by a color broken phase?*, *Phys. Rev. D* **60** (1999) 105035, [`hep-ph/9902220`].

[433] S. Profumo, L. Ubaldi and C. Wainwright, *Singlet Scalar Dark Matter: monochromatic gamma rays and metastable vacua*, *Phys. Rev. D* **82** (2010) 123514, [`1009.5377`].

[434] C. L. Wainwright, *CosmoTransitions: Computing Cosmological Phase Transition Temperatures and Bubble Profiles with Multiple Fields*, *Comput. Phys. Commun.* **183** (2012) 2006–2013, [`1109.4189`].

[435] G. BÃľlanger, F. Boudjema, A. Pukhov and A. Semenov, *micrOMEGAs4.1: two dark matter candidates*, *Comput. Phys. Commun.* **192** (2015) 322–329, [`1407.6129`].

[436] F. Goertz, A. Papaefstathiou, L. L. Yang and J. Zurita, *Higgs Boson self-coupling measurements using ratios of cross sections*, *JHEP* **06** (2013) 016, [`1301.3492`].

[437] D. M. Asner et al., *ILC Higgs White Paper*, in *Proceedings, Community Summer Study 2013: Snowmass on the Mississippi (CSS2013): Minneapolis, MN, USA, July 29-August 6, 2013*, 2013, [`1310.0763`].

[438] R. Contino et al., *Physics at a 100 TeV pp collider: Higgs and EW symmetry breaking studies*, *CERN Yellow Report* (2017) 255–440, [`1606.09408`].

[439] A. J. Barr, M. J. Dolan, C. Englert, D. E. Ferreira de Lima and M. Spannowsky, *Higgs Self-Coupling Measurements at a 100 TeV Hadron Collider*, *JHEP* **02** (2015) 016, [`1412.7154`].

[440] C. Englert and M. McCullough, *Modified Higgs Sectors and NLO Associated Production*, *JHEP* **07** (2013) 168, [`1303.1526`].

[441] S. Dawson et al., *Working Group Report: Higgs Boson*, in *Proceedings, 2013 Community Summer Study on the Future of U.S. Particle Physics: Snowmass on the Mississippi (CSS2013): Minneapolis, MN, USA, July 29-August 6, 2013*, 2013, [`1310.8361`].

[442] S. J. Huber and T. Konstandin, *Gravitational Wave Production by Collisions: More Bubbles*, *JCAP* **0809** (2008) 022, [`0806.1828`].

[443] R. Jinno and M. Takimoto, *Gravitational waves from bubble collisions: analytic derivation*, *Phys. Rev. D* **95** (2017) 024009, [`1605.01403`].

[444] M. Hindmarsh, S. J. Huber, K. Rummukainen and D. J. Weir, *Gravitational waves from the sound of a first order phase transition*, *Phys. Rev. Lett.* **112** (2014) 041301, [`1304.2433`].

[445] M. Hindmarsh, S. J. Huber, K. Rummukainen and D. J. Weir, *Numerical simulations of acoustically generated gravitational waves at a first order phase transition*, *Phys. Rev. D* **92** (2015) 123009, [`1504.03291`].

[446] C. Caprini, R. Durrer and G. Servant, *The stochastic gravitational wave background from turbulence and magnetic fields generated by a first-order phase transition*, *JCAP* **0912** (2009) 024, [`0909.0622`].

[447] D. Bodeker and G. D. Moore, *Can electroweak bubble walls run away?*, *JCAP* **0905** (2009) 009, [`0903.4099`].

[448] N. Bartolo et al., *Science with the space-based interferometer LISA. IV: Probing inflation with gravitational waves*, *JCAP* **1612** (2016) 026, [`1610.06481`].

[449] K. Yagi and N. Seto, *Detector configuration of DECIGO/BBO and identification of cosmological neutron-star binaries*, *Phys. Rev. D* **83** (2011) 044011, [`1101.3940`].

[450] LIGO Scientific Collaboration, J. Aasi et al., *Advanced LIGO*, *Class. Quant. Grav.* **32** (2015) 074001, [`1411.4547`].

[451] S. R. Coleman, *The Fate of the False Vacuum. 1. Semiclassical Theory*, *Phys. Rev. D* **15** (1977) 2929–2936.

[452] T. Alanne, K. Tuominen and V. Vaskonen, *Strong phase transition, dark matter and vacuum stability from simple hidden sectors*, *Nucl. Phys. B* **889** (2014) 692–711, [`1407.0688`].

[453] P. Gondolo and G. Gelmini, *Cosmic abundances of stable particles: Improved analysis*, *Nucl. Phys. B* **360** (1991) 145–179.

[454] J. M. Alarcon, J. Martin Camalich and J. A. Oller, *The chiral representation of the πN scattering amplitude and the pion-nucleon sigma term*, *Phys. Rev D* **85** (2012) 051503, [`1110.3797`].

[455] J. M. Alarcon, L. S. Geng, J. Martin Camalich and J. A. Oller, *The strangeness content of the nucleon from effective field theory and phenomenology*, *Phys. Lett. B* **730** (2014) 342–346, [`1209.2870`].

[456] T. Li and Y.-F. Zhou, *Strongly first order phase transition in the singlet fermionic dark matter model after LUX*, *JHEP* **07** (2014) 006, [1402.3087].

[457] W. Chao, H.-K. Guo and J. Shu, *Gravitational Wave Signals of Electroweak Phase Transition Triggered by Dark Matter*, *JCAP* **1709** (2017) 009, [1702.02698].

[458] R. Cooke, M. Pettini, R. A. Jorgenson, M. T. Murphy and C. C. Steidel, *Precision measures of the primordial abundance of deuterium*, *Astrophys. J.* **781** (2014) 31, [1308.3240].

[459] PARTICLE DATA GROUP Collaboration, K. A. Olive et al., *Review of Particle Physics*, *Chin. Phys. C* **38** (2014) 090001.

[460] V. Simha and G. Steigman, *Constraining The Early-Universe Baryon Density And Expansion Rate*, *JCAP* **0806** (2008) 016, [0803.3465].

[461] Y. G. Kim, K. Y. Lee and S. Shin, *Singlet fermionic dark matter*, *J. High Energy Phys.* **05** (2008) 100, [0803.2932].

[462] S. Baek, P. Ko, W.-I. Park and E. Senaha, *Vacuum structure and stability of a singlet fermion dark matter model with a singlet scalar messenger*, *JHEP* **11** (2012) 116, [1209.4163].

[463] J. R. Espinosa, T. Konstandin and F. Riva, *Strong Electroweak Phase Transitions in the Standard Model with a Singlet*, *Nucl. Phys. B* **854** (2012) 592–630, [1107.5441].

[464] Y. G. Kim and K. Y. Lee, *The minimal model of fermionic dark matter*, *Phys. Rev. D* **75** (2007) 115012, [hep-ph/0611069].

[465] M. Fairbairn and R. Hogan, *Singlet Fermionic Dark Matter and the Electroweak Phase Transition*, *JHEP* **09** (2013) 022, [1305.3452].

[466] A. Falkowski, C. Gross and O. Lebedev, *A second Higgs from the Higgs portal*, *JHEP* **05** (2015) 057, [1502.01361].

[467] D. Buttazzo, F. Sala and A. Tesi, *Singlet-like Higgs bosons at present and future colliders*, *JHEP* **11** (2015) 158, [1505.05488].

[468] M. Heikinheimo, T. Tenkanen, K. Tuominen and V. Vaskonen, *Observational Constraints on Decoupled Hidden Sectors*, *Phys. Rev. D* **94** (2016) 063506, [1604.02401].

[469] I. M. Lewis and M. Sullivan, *Benchmarks for Double Higgs Production in the Singlet Extended Standard Model at the LHC*, *Phys. Rev. D* **96** (2017) 035037, [1701.08774].

[470] P. H. Ghorbani, *Electroweak Baryogenesis and Dark Matter via a Pseudoscalar vs. Scalar*, *JHEP* **08** (2017) 058, [1703.06506].

[471] C.-Y. Chen, J. Kozaczuk and I. M. Lewis, *Non-resonant Collider Signatures of a Singlet-Driven Electroweak Phase Transition*, *JHEP* **08** (2017) 096, [1704.05844].

[472] T. Kamon, P. Ko and J. Li, *Characterizing Higgs portal dark matter models at the ILC*, *Eur. Phys. J. C* **77** (2017) 652, [1705.02149].

[473] M. Ettefaghi and R. Moazzemi, *Analyzing of singlet fermionic dark matter via the updated direct detection data*, *Eur. Phys. J. C* **77** (2017) 343, [1705.07571].

[474] M. J. Baker, M. Breitbach, J. Kopp and L. Mittnacht, *Dynamic Freeze-In: Impact of Thermal Masses and Cosmological Phase Transitions on Dark Matter Production*, [1712.03962].

[475] A. Beniwal, M. Lewicki, M. White and A. G. Williams, *Gravitational waves and electroweak baryogenesis in a global study of the extended scalar singlet model*, in preparation for *JHEP* (2018) .

[476] GFITTER GROUP Collaboration, M. Baak, J. C?th, J. Haller, A. Hoecker, R. Kogler, K. M?nig et al., *The global electroweak fit at NNLO and prospects for the LHC and ILC*, *Eur. Phys. J. C* **74** (2014) 3046, [1407.3792].

[477] P. Bechtle, O. Brein, S. Heinemeyer, O. St?, T. Stefaniak, G. Weiglein et al., *HiggsBounds-4: Improved Tests of Extended Higgs Sectors against Exclusion Bounds from LEP, the Tevatron and the LHC*, *Eur. Phys. J. C* **74** (2014) 2693, [1311.0055].

[478] P. Bechtle, S. Heinemeyer, O. St?, T. Stefaniak and G. Weiglein, *HiggsSignals: Confronting arbitrary Higgs sectors with measurements at the Tevatron and the LHC*, *Eur. Phys. J. C* **74** (2014) 2711, [1305.1933].

[479] A. Belyaev, N. D. Christensen and A. Pukhov, *CalcHEP 3.4 for collider physics within and beyond the Standard Model*, *Comput.Phys.Commun.* **184** (2013) 1729–1769, [1207.6082].

[480] J. M. Cline and K. Kainulainen, *Electroweak baryogenesis and dark matter from a singlet Higgs*, *J. Cosmol. Astropart. Phys.* **1301** (2013) 012, [1210.4196].

[481] P. Agrawal, Z. Chacko, C. Kilic and R. K. Mishra, *A Classification of Dark Matter Candidates with Primarily Spin-Dependent Interactions with Matter*, [1003.1912].

[482] S. Esch, M. Klasen and C. E. Yaguna, *Detection prospects of singlet fermionic dark matter*, *Phys. Rev. D* **88** (2013) 075017, [`1308.0951`].

[483] Z. Bagherian, M. M. Ettefaghi, Z. Haghgouyan and R. Moazzemi, *A new parameter space study of the fermionic cold dark matter model*, *JCAP* **1410** (2014) 033, [`1406.2927`].

[484] T. H. Franarin, C. A. Z. Vasconcellos and D. Hadjimichef, *On the possibility of a 130 GeV gamma-ray line from annihilating singlet fermionic dark matter*, *Astron. Nachr.* **335** (2014) 647–652, [`1404.0406`].

[485] Y. G. Kim, K. Y. Lee, C. B. Park and S. Shin, *Secluded singlet fermionic dark matter driven by the Fermi gamma-ray excess*, *Phys. Rev. D* **93** (2016) 075023, [`1601.05089`].

[486] C. Balazs, T. Li, C. Savage and M. White, *Interpreting the Fermi-LAT gamma ray excess in the simplified framework*, *Phys. Rev. D* **92** (2015) 123520, [`1505.06758`].

[487] M. E. Peskin and T. Takeuchi, *Estimation of oblique electroweak corrections*, *Phys. Rev. D* **46** (1992) 381–409.

[488] W. Grimus, L. Lavoura, O. M. Ogreid and P. Osland, *The Oblique parameters in multi-Higgs-doublet models*, *Nucl. Phys. B* **801** (2008) 81–96, [`0802.4353`].

[489] GAMBIT Collaboration, G. D. Martinez, J. McKay, B. Farmer, P. Scott, E. Roebber, A. Putze et al., *Comparison of statistical sampling methods with ScannerBit, the GAMBIT scanning module*, *Eur. Phys. J. C* **77** (2017) 761, [`1705.07959`].

[490] S. Profumo, M. J. Ramsey-Musolf, C. L. Wainwright and P. Winslow, *Singlet-catalyzed electroweak phase transitions and precision Higgs boson studies*, *Phys. Rev. D* **91** (2015) 035018, [`1407.5342`].

[491] G. Cowan, K. Cranmer, E. Gross and O. Vitells, *Asymptotic formulae for likelihood-based tests of new physics*, *Eur. Phys. J. C* **71** (2011) 1554, [`1007.1727`].

[492] S. S. Wilks, *The Large-Sample Distribution of the Likelihood Ratio for Testing Composite Hypotheses*, *Annals Math. Statist.* **9** (1938) 60–62.

[493] P. Scott, *Pippi - painless parsing, post-processing and plotting of posterior and likelihood samples*, *Eur. Phys. J. Plus* **127** (2012) 138, [`1206.2245`].

[494] VIRGO, LIGO SCIENTIFIC Collaboration, B. P. Abbott et al., *GW150914: Implications for the stochastic gravitational wave background from binary black holes*, *Phys. Rev. Lett.* **116** (2016) 131102, [1602.03847].

[495] E. Thrane and J. D. Romano, *Sensitivity curves for searches for gravitational-wave backgrounds*, *Phys. Rev. D* **88** (2013) 124032, [1310.5300].

[496] R. van Haasteren et al., *Placing limits on the stochastic gravitational-wave background using European Pulsar Timing Array data*, *Mon. Not. Roy. Astron. Soc.* **414** (2011) 3117–3128, [1103.0576].

[497] G. Janssen et al., *Gravitational wave astronomy with the SKA*, *PoS* **AASKA14** (2015) 037, [1501.00127].

[498] C. Balazs and T. Li, *Simplified Dark Matter Models Confront the Gamma Ray Excess*, *Phys. Rev. D* **90** (2014) 055026, [1407.0174].

[499] F. Bishara, J. Brod, P. Uttayarat and J. Zupan, *Nonstandard Yukawa Couplings and Higgs Portal Dark Matter*, *JHEP* **01** (2016) 010, [1504.04022].

[500] M. A. Fedderke, T. Lin and L.-T. Wang, *Probing the fermionic Higgs portal at lepton colliders*, *JHEP* **04** (2016) 160, [1506.05465].

[501] C.-H. Chen and T. Nomura, *Searching for vector dark matter via Higgs portal at the LHC*, *Phys. Rev. D* **93** (2016) 074019, [1507.00886].

[502] A. DiFranzo, P. J. Fox and T. M. P. Tait, *Vector Dark Matter through a Radiative Higgs Portal*, *JHEP* **04** (2016) 135, [1512.06853].

[503] A. Aravind, M. Xiao and J.-H. Yu, *Higgs Portal to Inflation and Fermionic Dark Matter*, *Phys. Rev. D* **93** (2016) 123513, [1512.09126].

[504] P. Ko and H. Yokoya, *Search for Higgs portal DM at the ILC*, *JHEP* **08** (2016) 109, [1603.04737].

[505] A. Cuoco, B. Eiteneuer, J. Heisig and M. Kramer, *A global fit of the γ-ray galactic center excess within the scalar singlet Higgs portal model*, *JCAP* **1606** (2016) 050, [1603.08228].

[506] G. Dupuis, *Collider Constraints and Prospects of a Scalar Singlet Extension to Higgs Portal Dark Matter*, *JHEP* **07** (2016) 008, [1604.04552].

[507] A. Das, N. Okada and O. Seto, *Galactic center excess by Higgs portal dark matter*, *J. Phys. Conf. Ser.* **718** (2016) 042054.

[508]   P. Di Bari, P. O. Ludl and S. Palomares-Ruiz, *Unifying leptogenesis, dark matter and high-energy neutrinos with right-handed neutrino mixing via Higgs portal*, *JCAP* **1611** (2016) 044, [`1606.06238`].

[509]   G. Arcadi, C. Gross, O. Lebedev, S. Pokorski and T. Toma, *Evading Direct Dark Matter Detection in Higgs Portal Models*, *Phys. Lett. B* **769** (2017) 129–133, [`1611.09675`].

[510]   J. A. Casas, D. G. Cerdeno, J. M. Moreno and J. Quilis, *Reopening the Higgs portal for single scalar dark matter*, *JHEP* **05** (2017) 036, [`1701.08134`].

[511]   B. Dutta, T. Kamon, P. Ko and J. Li, *Prospects of Higgs portal DM models and their cousins at 100 TeV p-p collider*, [`1712.05123`].

[512]   K. Cheung, P.-Y. Tseng, Y.-L. S. Tsai and T.-C. Yuan, *Global Constraints on Effective Dark Matter Interactions: Relic Density, Direct Detection, Indirect Detection, and Collider*, *JCAP* **1205** (2012) 001, [`1201.3402`].

[513]   S. Liem, G. Bertone, F. Calore, R. Ruiz de Austri, T. M. P. Tait, R. Trotta et al., *Effective Field Theory of Dark Matter: a Global Analysis*, *JHEP* **09** (2016) 077, [`1603.05994`].

[514]   GAMBIT Collaboration, P. Athron et al., *GAMBIT: The Global and Modular Beyond-the-Standard-Model Inference Tool*, *Eur. Phys. J. C* **77** (2017) 784, [`1705.07908`].

[515]   C. Strege, R. Trotta, G. Bertone, A. H. G. Peter and P. Scott, *Fundamental statistical limitations of future dark matter direct detection experiments*, *Phys. Rev. D* **86** (2012) 023507, [`1201.3631`].

[516]   GAMBIT Collaboration, J. M. Cornell, *Global fits of scalar singlet dark matter with GAMBIT*, [`1611.05065`].

[517]   GAMBIT Collaboration, C. Balazs et al., *ColliderBit: a GAMBIT module for the calculation of high-energy collider observables and likelihoods*, *Eur. Phys. J. C* **77** (2017) 795, [`1705.07919`].

[518]   THE GAMBIT FLAVOUR WORKGROUP Collaboration, F. U. Bernlochner et al., *FlavBit: A GAMBIT module for computing flavour observables and likelihoods*, *Eur. Phys. J. C* **77** (2017) 786, [`1705.07933`].

[519]   P. Athron et al., *SpecBit, DecayBit and PrecisionBit: GAMBIT modules for computing mass spectra, particle decay rates and precision observables*, *Eur. Phys. J. C* **78** (2018) 22, [`1705.07936`].

[520] T. Binder, T. Bringmann, M. Gustafsson and A. Hryczuk, *Early kinetic decoupling of dark matter: when the standard way of calculating the thermal relic density fails*, *Phys. Rev. D* **96** (2017) 115010, [1706.07433].

[521] P. Gondolo, J. Edsjo, P. Ullio, L. Bergstrom, M. Schelke and E. A. Baltz, *DarkSUSY: Computing supersymmetric dark matter properties numerically*, *JCAP* **0407** (2004) 008, [astro-ph/0406204].

[522] T. Piffl et al., *The RAVE survey: the Galactic escape speed and the mass of the Milky Way*, *Astron. Astrophys.* **562** (2014) A91, [1309.4293].

[523] F. Bishara, J. Brod, B. Grinstein and J. Zupan, *From quarks to nucleons in dark matter direct detection*, *JHEP* **11** (2017) 059, [1707.06998].

[524] H.-W. Lin, *Lattice QCD for Precision Nucleon Matrix Elements*, [1112.2435].

[525] PARTICLE DATA GROUP Collaboration, K. A. Olive et al., *Review of Particle Physics*, update to Ref. [459] (2015) .

[526] A. Beniwal, S. Bloor, J. M. Cornell et al., *Global analyses of Higgs portal singlet dark matter models*, in preparation for *Eur. Phys. J. C* (2018) .

[527] J. Goldstone, A. Salam and S. Weinberg, *Broken Symmetries*, *Phys. Rev.* **127** (Aug., 1962) 965–970.

[528] J. Frieman, M. Turner and D. Huterer, *Dark Energy and the Accelerating Universe*, *Ann. Rev. Astron. Astrophys.* **46** (2008) 385–432, [0803.0982].

[529] M. E. Carrington, *The Effective potential at finite temperature in the Standard Model*, *Phys. Rev. D* **45** (1992) 2933–2944.

[530] M. Shifman, A. Vainshtein and V. Zakharov, *Remarks on higgs-boson interactions with nucleons*, *Phys. Lett. B* **78** (1978) 443 – 446.

[531] M. Drees and K.-i. Hikasa, *Note on QCD Corrections to Hadronic Higgs Decay*, *Phys. Lett. B* **240** (1990) 455.